FACULDADE DE ENGENHARIA DA UNIVERSIDADE DO PORTO

Risk-based Analysis of Bridge Scour Prediction

Ana Margarida Lopes Saraiva Alves Bento

Programa Doutoral em Engenharia Civil

Supervisor: Doctor Maria Teresa Fontelas dos Santos Viseu

Co-Supervisor: Doctor João Pedro Gomes Moreira Pêgo

Co-Supervisor: Doctor Lúcia Teixeira Couto Garcia Ribeiro

August 31, 2020

© Ana Margarida Bento, 2020

Risk-based Analysis of Bridge Scour Prediction

Ana Margarida Lopes Saraiva Alves Bento

Programa Doutoral em Engenharia Civil

August 31, 2020

Aos meus Pais,

Irmãos e Sobrinhas

Resumo

As pontes são susceptíveis de colapsar devido ao fenómeno de erosão localizada, uma das maiores ameaças para a estabilidade e segurança destas infraestruturas em todo o mundo. Apesar de décadas de investigação sobre o processo erosivo, persistem ainda muitas incertezas que afectam a concepção das suas fundações. As variáveis hidrológicas e hidráulicas são dos aspectos mais críticos e menos explorados deste processo. Assim, o objectivo do presente trabalho de investigação consistiu em desenvolver uma nova e pragmática metodologia para a avaliação e classificação do risco associado à erosão em fundações de pontes, utilizando um factor prioritário semi-quantitativo. Os eventos hidrológicos, as condições hidráulicas e as características da fundação da ponte são exemplos das muitas incertezas subjacentes que são tomadas em consideração nesta metodologia, em reconhecimento da sua influência no fenómeno de erosão e no risco resultante. Foi utilizada uma ponte Portuguesa como caso de estudo para validar a metodologia proposta. Este caso de estudo foi selecionado pela variabilidade da batimetria no local da ponte e disponibilidade de dados relevantes de monitorização de caudais afluentes.

Na presente tese, a avaliação do risco de erosão baseou-se numa abordagem interdisciplinar que combinou análise experimental e numérica para alcançar uma compreensão mais avançada e abrangente deste fenómeno na proximidade das fundações de pontes, com e sem transporte generalizado de sedimentos. O trabalho de investigação está, assim, organizado em três módulos que visam objetivos específicos: "Análise de Risco", "Estudo Experimental" e "Modelação Numérica".

O módulo "Análise de Risco" propõe uma nova metodologia para a avaliação do risco de erosão. Esta é uma metodologia dividida em três etapas que compreendem: (i) a modelação hidrológica de eventos extremos; (ii) o cálculo de variáveis de escoamento e de erosão para modelar o comportamento do rio; e (iii) a atribuição de uma classificação qualitativa de risco de erosão da ponte, com base na relação entre a profundidade relativa de erosão e a vulnerabilidade da infraestrutura em questão. Dois artigos científicos são apresentados neste módulo: "Improvement assessment of maximum streamflow approaching a bridge over Douro river. A case study" que fornece uma visão detalhada da primeira etapa da metodologia, e "Risk-based methodology for scour analysis at bridge foundations" onde a metodologia é descrita e aplicada utilizando dados de campo de um caso de estudo. Das potenciais pontes para caso de estudo, a "nova ponte Hintze Ribeiro", localizada no rio Douro, foi identificada como a mais adequada para a investigação. Esta ponte, inaugurada em Maio de 2002, foi construída na sequência do colapso da ponte Hintze Ribeiro, do século XIX, localizada 7,5 m a montante da posição da antiga ponte.

O módulo "Estudo Experimental" aborda dois aspectos-chave do processo de erosão localizada em pontes: (i) a geometria da cavidade de erosão em torno dos modelos de pilar de ponte e (ii) o campo de escoamento turbulento no início do processo de erosão e no interior da cavidade de erosão entretanto desenvolvida. O escoamento na proximidade de pilares de pontes oblongas foi reproduzido num canal rectangular de paredes laterais de vidro, com 40,7 m de comprimento, 2,0 m de largura e 1,9 m de profundidade, sito no laboratório de hidráulica do Laboratório Nacional de Engenharia Civil (LNEC) em Lisboa (Portugal). Foi adoptado um sistema de medição abrangente para a caracterização tridimensional dos efeitos de erosão e do

seu respectivo conjunto. Consistiu na captura de fotografias durante os ensaios experimentais, através do desenvolvimento de um processamento de imagens subaquáticas e rotinas de visão por computador, e na aquisição de dados no início e no final dos ensaios utilizando o sensor Kinect V2 e técnicas de fotogrametria de curta distância. Foram alcançados níveis significativos de precisão. Os resultados permitiram a caracterização do fenómeno ao longo do tempo, tirando partido do recente e crescente desenvolvimento da tecnologia de câmaras submersíveis e ferramentas de processamento. A estrutura tridimensional turbulenta foi também objeto de estudo através de um medidor acústico de velocidades no início do processo de erosão e dentro das respetivas cavidades de erosão desenvolvidas. Dois artigos científicos são apresentados neste módulo: "Characterizing bridge scour using image-based techniques in laboratory environment" que fornece uma caracterização detalhada da geometria das cavidades de erosão e "Experimental characterization of the flow field around oblong bridge piers" onde o campo de escoamento turbulento é estudado nas proximidades de modelos de pilar oblongo. Os resultados obtidos constituem uma contribuição importante para a compreensão das variáveis hidrodinâmicas associadas aos processos de erosão, bem como para a calibração e validação de modelos numéricos.

Finalmente, o módulo "Modelação Numérica" descreve as simulações numéricas do transporte de sedimentos na proximidade de modelos de pilar de pontes criados para as condições experimentais. As simulações numéricas foram realizadas utilizando a ferramenta de Dinâmica de Fluidos Computational (CFD) SSIIM (um acrónimo para *Sediment Simulation Intakes with Multiblock option*). O artigo científico apresentado neste módulo, "Numerical simulations of scour development around an oblong bridge pier laboratory model", é dedicado à modelação tanto do movimento do leito sedimentar como da tensão de arrastamento do leito na proximidade do modelo de pilar de ponte oblongo. Em termos de computação das variáveis hidrodinâmicas, estas simulações revelaram um desempenho satisfatório do modelo numérico ao replicar as alterações morfológicas observadas. Os objectivos da ferramenta de CFD adoptada foram a obtenção de uma visão integrada das interações entre as estruturas de turbulência e o fenómeno de erosão, o alargamento das observações experimentais e a exploração de opções que permitam a sua aplicação na avaliação do risco de erosão de pontes existentes, bem como auxiliar no processo de concepção de novas infraestruturas.

Palavras-chave: erosão localizada, metodologia de risco de erosão, técnicas de caracterização baseadas em imagem, ferramentas CFD, análise de incerteza

Abstract

Bridges are susceptible to failure due to the local scour phenomenon, one of the greatest threats to the stability and safety of these infrastructures worldwide. Despite decades of research, there are still many uncertainties affecting the design process of bridge foundations. The hydrological and hydraulic variables are among the most critical and least explored aspects of this process. Therefore, the main aim of the present research work was to develop a new and pragmatic methodology for the assessment and rating of risk associated with scour at bridge foundations, using a semi-quantitative priority factor. Hydrological events, hydraulic conditions and bridge pier characteristics are examples of the many underlying uncertainties that are taken into consideration in this methodology, in recognition to their influence on the scouring phenomenon and the resulting bridge scour risk. A Portuguese bridge case study was used to validate the proposed methodology. This case study was selected due to the variability of the bathymetry at the bridge site and the availability of relevant flow monitoring data.

In this thesis, the scour risk evaluation was based on an interdisciplinary approach combining experimental and numerical analysis to attain a more advanced and comprehensive understanding of the scour phenomenon at the vicinity of bridge foundations, both under clear water and live bed scour regimes. The research work is, thus, organized in three modules that aim specific achievements: "Risk-based Analysis", "Experimental Study" and "Numerical Modelling".

The "Risk-based Analysis" module addresses the new scour risk assessment methodology proposed. This is a three-step methodology that comprises: (i) the hydrological modelling of extreme events; (ii) the computation of flow and scour variables to model river behavior; and (iii) the assignment of a bridge scour qualitative risk rating based on the relation between relative scour depth and the vulnerability of the infrastructure in question. Two scientific papers are presented in this module: "Improvement assessment of maximum streamflow approaching a bridge over Douro river. A case study" that provides a detailed insight to the first step of the methodology, and "Risk-based methodology for scour analysis at bridge foundations" where the methodology is described and applied using a case study field data. Of the potential bridge case studies, the "new Hintze Ribeiro" bridge, located in the Douro river, was identified as the most suitable for the investigation. This bridge, inaugurated in May 2002, was built in the sequence of the collapse of the 19th century Hintze Ribeiro bridge in 2001, 7.5 m upstream of the old bridge's position.

The "Experimental Study" module addresses two key aspects of the bridge scouring process: (i) the geometry of the scour hole around bridge pier models and (ii) the turbulent flow field at the beginning of the scouring process and within the developed scour hole. The flow in the vicinity of oblong bridge piers was thus reproduced in a glass-sided rectangular tilting flume, 40.7 m long, 2.0 m wide, and 1.9 m deep, located in the experimental facilities of the National Laboratory of Civil Engineering (LNEC) in Lisbon (Portugal). A comprehensive measurement system was adopted for the three-dimensional characterization of the scouring effects and its respective ensemble. It consisted of capturing underwater images during experiments, through a novel development of underwater image processing and computer vision routines, or acquiring data at the beginning and at the end of experiments using the Kinect V2 sensor and close-range photogrammetry techniques.

Significant levels of accuracy were achieved. The results enabled the characterization of the phenomenon with time, taking advantage of the continuous development of low cost technology of submersible cameras and processing tools. The three-dimensional turbulent structure was also studied using a high-resolution acoustic velocimeter at the beginning of the scouring process and within the respective developed scour holes. Two scientific papers are presented in this module: "Characterizing bridge scour using image-based techniques in laboratory environment" that provides a detailed characterization of the scour hole geometry, and "Experimental characterization of the flow field around oblong bridge piers" where the turbulent flow field is studied at the vicinity of oblong bridge pier models. The obtained results were an important contribution to the understanding of the hydrodynamic variables associated with the scouring processes and constitute a basis for the calibration and validation of numerical models.

Finally, the "Numerical Modelling" module describes the numerical simulations of the sediment bed transport in the vicinity of bridge pier models that were conducted for the experimental boundary conditions. The numerical simulations were performed by using the Computational Fluid Dynamics (CFD) tool SSIIM (an acronym for *Sediment Simulation In Intakes with Multiblock option*). One scientific paper is presented in this module, entitled "Numerical simulations of scour development around an oblong bridge pier laboratory model" that is devoted to modelling both the sediment bed movement and the bed shear stress in the vicinity of an oblong bridge pier model. In terms of computing the hydrodynamic variables, the results revealed a satisfying performance of the numerical model in replicating the observed morphological changes. The purpose of the herein adopted CFD tool was to gain insight into the coupling between turbulence structures and the scour interaction process, to augment the experimental observations, and to explore options for enabling its application for evaluating the scour risk of existing bridges, as well as aiding the design of new bridges.

Keywords: local scour, scour risk methodology, image-based characterization techniques, CFD tools, uncertainty analysis

Acknowledgements

This thesis was developed in the Doctoral Program in Civil Engineering (PRODEC), under the guidance and supervision of Doctor Teresa Viseu and Doctor Lúcia Couto from the National Laboratory of Civil Engineering (LNEC), and Doctor João Pedro Pêgo from the Faculty of Engineering of the University of Porto (FEUP).

I would like to express my deepest gratitude to my supervisors, Doctor Teresa Viseu, Doctor Lúcia Couto and Doctor João Pedro Pêgo, for their exemplary guidance, patience and constant encouragement throughout the course of this thesis. Their supervision, knowledge and experience, and above all, the support provided at times when things were not at its best and the motivation weakened, were fundamental to the accomplishment of this research. I acknowledge the dedication, availability, and feedback on the articles, for both conferences and scientific journals. I also want to thank Doctor Teresa Viseu and Doctor Lúcia Couto for providing the necessary conditions at LNEC for the development of this thesis. To Doctor Lúcia Couto, I wish to express special thanks for the support and by relentlessly drawing the best out of myself over the course of this study. To Doctor João Pedro Pêgo, I acknowledge for having facilitated contacts (both formal and informal), which were so essential for the good course of the work, as well as for the resources made available at FEUP.

To Engineer João Gonçalo Morais, from Infraestruturas de Portugal, and to Engineer Fernando Barbosa Teixeira, from Energias de Portugal, I thank the collaboration and information exchange, quite relevant for this work's progress.

I would also like to thank the committee members from the Research Thesis Project's defence, Doctor Francisco Taveira Pinto, Doctor Rodrigo Maia and Doctor Cristina Fael for the important insights, comments and suggestions for this two-year period, thank you.

During my stay at LNEC, I had the opportunity and pleasure to meet other researchers that made my experience even more enriching, Doctor João Rocha, Doctor José Melo, Doctor Rui Rodrigues and Doctor Laura Caldeira.

I would also like to express my sincere gratitude to the inspiring discussions concerning underwater monitoring techniques to Doctor José Alberto Gonçalves, Doctor Francisco Piqueiro, Doctor Maria João Henriques, Doctor João Santos, Doctor Juana Fortes, Doctor Rute Lemos, Doctor Andry Markol, Doctor Renato Henriques, Doctor Jorge Isidoro and Doctor Paulo Avilez-Valente.

I also thank the technical assistance provided by the team of the Laboratory of Construction and Modelling, the Urban Water Unit, and the Center of Scientific Instrumentation of LNEC for their help and meticulous work to make possible the experimental work. To Fahetem Vojoudi, Maria José Henriques, Luís Dias, Pedro Guerreiro, I want to thank the spirit of camaraderie at my two years-long experimental work.

Many thanks to Raquel Néri, João Tiago Pereira, Abril Uriarte, Rute Coelho, Henrique Martins, Mahdi Alemi, Mário Moreno, Luís Mendes, Danilo Jodas, Beatriz Monteiro, Vanessa Araújo, Joana Ribeiro and Mike Duarte for all the valuable time, friendship, and patience throughout the course of this thesis. To Andreia Gomes, I acknowledge her willingness, impressive dedication and friendship.

I would also like to thank all my friends, who have been by my side during this time, keeping my spirit and motivation up. In particular, my friends at FEUP, Vanessa Ramos, Andreia Moreira, Tiago Ferradosa, Daniel Conde, Fábio Paiva, Saeid Okhravi, Arlon André, Eliamin Rosendo, Guilherme Paredes and Bruno Oliveira, and my friends at LNEC, Teresa Alvarez, Sílvia Amaral, Solange Mendes, Soraia Canelas, Joana Simão, Ana Rilo, Liliana Pinheiro, Natália Lopes, Francisco Borralho, Pedro Lopes, João Fernandes, João Oliveira, António Muralha and Lourenço Mendes for the good moments we shared, which contributed to excellent work environments.

Special thanks go to my parents, Margarida and António, my sisters Filipa and Carla, my brother João Miguel and my little nieces, Mariana and Mafalda, for their endless help and moral support offered throughout the work period. I deeply thank my parents for inculcating in me the dedication and discipline to do whatever I undertake well, their continuous encouragement and inexhaustible patience. My brother and sisters have never left my side and are very special. To Filipa, I thank the outstanding support throughout the study. To my little nieces, Mariana and Mafalda, I thank their contagious joy and incessant curiosity that have always been a ray of hope and a fountain of inspiration for the research part of the thesis, and for me.

Finally, I acknowledge the financial support of the Portuguese Foundation for Science and Technology (FCT), through the PhD scholarship PD/BD/127798/2016, in the framework of the Doctoral Program InfraRisk - “Analysis and Mitigation of Risks in Infrastructures”.

"There will be obstacles.
There will be doubters.
But with hard work,
there are no limits."

– Michael Phelps –

x

Contents

1. Introduction **1**
1.1. Background and Motivation . . . 1
1.2. Objectives and Methodological Approaches . . . 4
1.2.1. General considerations . . . 4
1.2.2. *Risk-based Analysis* . . . 4
1.2.3. *Experimental Study* . . . 5
1.2.4. *Numerical Modelling* . . . 6
1.3. Thesis Layout . . . 7

2. A Review of Bridge Scour Research **9**
2.1. Introduction . . . 9
2.2. Types of Erosion . . . 10
2.2.1. General considerations . . . 10
2.2.2. General scour . . . 11
2.2.3. Contraction scour . . . 11
2.2.4. Local scour . . . 12
2.2.5. Sediment types and behaviour . . . 13
2.3. Bridge Scour Process . . . 15
2.4. Scour Parameter Framework . . . 18
2.4.1. Scour variables and parameters . . . 18
2.4.2. Effects of parameters on local scour . . . 20
2.5. Erosion and Scour Prediction . . . 29
2.5.1. Introduction . . . 29
2.5.2. General scour . . . 29
2.5.3. Contraction scour . . . 30
2.5.4. Local scour . . . 30
2.6. Numerical Modelling . . . 33
2.6.1. CFD analysis . . . 33
2.6.2. Numerical studies . . . 38
2.7. Bridge Scour Monitoring . . . 40
2.8. Scour Risk Assessment . . . 41

3. Risk-based Analysis **47**
3.1. General Considerations . . . 47
3.2. Improvement assessment of maximum streamflow approaching a bridge over Douro river. A case study. *Paper submitted* . . . 49
3.2.1. Abstract . . . 50
3.2.2. Introduction . . . 50
3.2.3. Hydrological modelling methodology . . . 52

3.2.4. Case study and database . . . 55
3.2.5. Results and discussion . . . 60
3.2.6. Conclusions . . . 70
3.2.7. Data availability statement . . . 71
3.2.8. Acknowledgments . . . 71
3.3. Risk-based methodology for scour analysis at bridge foundations. *Paper published* 72
3.3.1. Abstract . . . 73
3.3.2. Introduction . . . 73
3.3.3. Scour risk analysis . . . 75
3.3.4. New Hintze Ribeiro bridge case study . . . 83
3.3.5. Conclusions . . . 94
3.3.6. Declaration of competing interest . . . 95
3.3.7. Acknowledgments . . . 95

4. Experimental Study **97**
4.1. General Considerations . . . 97
4.2. Experimental facility and apparatus . . . 100
4.2.1. Introductory considerations . . . 100
4.2.2. Pumping and impulsion systems . . . 100
4.2.3. Supply tank . . . 101
4.2.4. Tilting flume . . . 102
4.2.5. Discharge system . . . 105
4.2.6. Sand bed material . . . 106
4.2.7. Critical flow velocity equations . . . 107
4.3. Characterizing bridge scour using image-based techniques in laboratory environment. *Paper under preparation* . . . 108
4.3.1. Abstract . . . 109
4.3.2. Introduction . . . 109
4.3.3. Local scouring experiments . . . 111
4.3.4. Scour depth predictors . . . 115
4.3.5. Scour hole and deposition characterization . . . 118
4.3.6. Results and discussions . . . 122
4.3.7. Conclusions . . . 135
4.3.8. Data availability statement . . . 136
4.3.9. Acknowledgments . . . 136
4.4. Experimental characterization of the flow field around oblong bridge piers. *Paper under preparation* . . . 137
4.4.1. Abstract . . . 138
4.4.2. Introduction . . . 138
4.4.3. Flow field experiments . . . 139
4.4.4. Results and discussions . . . 143
4.4.5. Conclusions . . . 159
4.4.6. Data availability statement . . . 159
4.4.7. Acknowledgements . . . 159

5. Numerical Modelling **161**
5.1. General Considerations . . . 161
5.2. Numerical simulations of scour development around an oblong bridge pier laboratory model. *Paper under preparation* . . . 162

5.2.1. Abstract . . . 163
5.2.2. Introduction . . . 163
5.2.3. The hydrodynamic model . . . 166
5.2.4. Local scouring experimental data . . . 168
5.2.5. Numerical model setup . . . 169
5.2.6. Results and discussion . . . 171
5.2.7. Conclusions . . . 177
5.2.8. Data availability statement . . . 177
5.2.9. Acknowledgements . . . 177

6. Conclusions and Future Research **179**
6.1. Main Conclusions . . . 179
6.1.1. General considerations . . . 179
6.1.2. *Risk-based Analysis* . . . 180
6.1.3. *Experimental Study* . . . 181
6.1.4. *Numerical Modelling* . . . 182
6.2. Future Research . . . 183

References **187**

A. Bridge Failures Causes **219**

B. Portuguese bridges suggested as potential case studies **221**

C. Experimental Study. Framework and Results **227**
C.1. Experimental campaign . . . 227
C.2. Experimental procedure . . . 228
C.3. Cameras calibration parameters . . . 230
C.4. Movable bed experiments carried out for bridge scour characterization . . . 232
C.5. Fixed bed experiments carried out for flow field characterization . . . 242

D. Conference Submissions and Communications **259**
D.1. Caracterização da cavidade de erosão em torno de fundações de pontes. Relação entre volume erodido e profundidade de erosão . . . 260
D.2. Evolution of local pier scour under unsteady flow conditions . . . 279
D.3. Advanced characterization techniques of the scour hole around a bridge pier model 282
D.4. Hydrological risk and associated scour risk: Case study sensitivity analysis . . . 291

List of Figures

1.1. Examples of collapses due to scour at bridge foundations. 2

2.1. Components of scour at a bridge, adapted from DTMN (2013). 12
2.2. Main flow features around a circular pier, adapted from Sumer (2007). 15
2.3. Narrow pier, adapted from Ettema *et al.* (2011). 16
2.4. Transitional pier, adapted from Ettema *et al.* (2011). 17
2.5. Wide pier, adapted from Ettema *et al.* (2011). 17
2.6. Scour hole around a bridge pier, in Portugal (Universidade do Algarve, 2006). . . 18
2.7. Variables influencing scour at an oblong pier, adapted from Ettema *et al.* (2011). . 19
2.8. Evolution scour depth with time under (a) clear water and (b) live bed regimes, adapted from Moreno (2016). 21
2.9. Influence of h/W on local scour depth expressed as d_s/W under clear water scour conditions, adapted from Melville & Coleman (2000). 23
2.10. Local scour depth variation with sediment non-uniformity, adapted from Melville & Coleman (2000). 25
2.11. Relative scour depth (d_s/W) as function of W/D_{50} for clear-water and live bed field, adapted from Lança *et al.* (2013). *RMSE* denotes Root Mean Square Error. 26
2.12. Basic single pier shapes: (a) single cylindrical, (b) oblong, and (c) rectangular (Sheppard *et al.*, 2011). 27
2.13. Cylinders differing in cross-sectional shape, but having the same projected width to the flow, adapted from Mostafa (1994). 27
2.14. Local scour depth variation with pier alignment, adapted from Melville & Coleman (2000). 28
2.15. Steps in numerical simulation applied for a bridge pier scour problem. 34
2.16. Schematic view of the differences between DNS, LES, and RANS methodologies (from André Bakker's lectures: `https://www.bakker.org/Lectures-Applied-CFD.pdf`). 36
2.17. Qualitative risk matrix, adapted from Pakrashi *et al.* (2016). 44
2.18. Risk method, adapted from Lamb *et al.* (2017). 46

3.1. Photograph of the new Hintze Ribeiro bridge (downstream view). 55
3.2. Map of the vicinity of the new Hintze Ribeiro bridge, over the Douro river Google Earth (n.d.). 56
3.3. Maximum annual flow discharges from the mean daily values for the three gauging stations. 58
3.4. *Method A* - Maximum annual flow discharges from Q_F hydrological time series. . 61
3.5. *Method B* - Flow-duration curves of Q_T hydrological time series. 62
3.6. Correlation between observed and estimated instantaneous discharge values from the Q_{FT} hydrological time series. 63

3.7. Box-plot graphs of Q_{HR} for the hydrological scenarios under consideration. . . . 63
3.8. Graphical adjustments (Q-Q plots) of the four probabilistic distributions to the Scenario 3 data time series. . . . 65
3.9. Histogram of the Scenario 3 data time series. . . . 67
3.10. Kernel density estimate applied to the Scenario 3 data time series. . . . 68
3.11. Cumulative distribution functions ($F(x)$) obtained by the parametric and the non-parametric distributions. . . . 68
3.12. Relative differences of the design floods normalized by the respective non-parametric estimates. . . . 69
3.13. Comparison between the KDE and the arithmetic model averaging methods. . . . 69
3.14. Proposed methodology for bridge scouring risk analysis. . . . 76
3.15. Conceptual hypothesis of obtaining D_e, through the sum of equivalent diameters of each element from a pile-supported foundation: c for column, pc for pile cap, and pg for pile group. Variable h stands for approach flow depth while d_{sm} is the maximum local scour depth. Adapted from Moreno (2016). . . . 80
3.16. Definition of the pier foundation depth (D_F) according to the alluvial riverbed level (from (a) to (c)). $W.S.$ refers to water surface. . . . 80
3.17. Scour risk rating (Highways Agency, 2012). . . . 82
3.18. Location of the case study, the new Hintze Ribeiro bridge, over the Douro river (Google Earth, n.d.). . . . 85
3.19. Upstream view of the new Hintze Ribeiro bridge, with indication of $P2$, adapted from Milhazes (2016). . . . 86
3.20. Hydraulic model built within HEC-RAS software. . . . 89
3.21. Maximum local scour depth estimates using four empirical predictors. . . . 90
3.22. Scour risk rating of the new Hintze Ribeiro bridge. . . . 93

4.1. Tilting flume at LNEC's experimental facilities. . . . 97
4.2. Longitudinal scheme of CIV (Moreno, 2016). . . . 100
4.3. Components of pumping and impulsion systems. . . . 101
4.4. Control panels of the flow discharge in CIV. . . . 101
4.5. Flow entrance in the flume (top view). . . . 102
4.6. Downstream working section of CIV. . . . 102
4.7. Sluice gates of CIV. . . . 103
4.8. Slope controllers of CIV. . . . 103
4.9. Moving carriages of CIV to aid flow and scour monitoring. . . . 104
4.10. Flow depth controllers along CIV. . . . 104
4.11. Surge tank operation (Moreno, 2016). . . . 105
4.12. Suction pump controlling panels and downstream tanks. . . . 105
4.13. Sand grain size distribution curve. . . . 106
4.14. Longitudinal scheme of the experimental facility. . . . 112
4.15. Oblong bridge pier model. . . . 113
4.16. Spatial reference for the 3D bed morphology models. . . . 119
4.17. Scheme of the underwater cameras' acquisition during scour experiment (dimensions in meters). . . . 121
4.18. Hydraulic conditions of $Exp.\ 4U$. . . . 124
4.19. Hydraulic conditions of $Exp.\ 4D$. . . . 125
4.20. Temporal evolution of the scour depths for *Run* 1 (upper panel) and *Run* 4 (lower panel). . . . 125

4.21. Three-dimensional eroded bed models from close-range photogrammetry (left panel) and Kinect V2 sensor (right panel). 127
4.22. Contour bed surfaces around the oblong pier model from close-range photogrammetry (left panel) and Kinect V2 sensor (right panel). 129
4.23. Scheme of the scour bed profiles under analysis. 130
4.24. Scour bed profiles normalized by the approach flow depth from close-range photogrammetry (continuous line) and Kinect V2 sensor (dashed line) for end of $Exp.\ 1U$. 131
4.25. Scour bed profiles normalized by the approach flow depth from close-range photogrammetry (continuous line) and Kinect V2 sensor (dashed line) for end of $Exp.\ 1D$. 131
4.26. Scour bed profiles normalized by the approach flow depth from close-range photogrammetry (continuous line) and Kinect V2 sensor (dashed line) for end of $Exp.\ 4U$. 132
4.27. Scour bed profiles normalized by the approach flow depth from close-range photogrammetry (continuous line) and Kinect V2 sensor (dashed line) for end of $Exp.\ 4D$. 132
4.28. Underwater photograph (left panel) and 2D bed profiles at different instants of $Exp.\ 1D$ (right panel). 133
4.29. Experimental facility and bridge pier models. 140
4.30. Geometry of the oblong bridge pier models. 141
4.31. Setup for the flow velocity measurements. 142
4.32. Downlooking vectrino: photo (left panel) and scheme (right panel, adapted from Quaresma (2017)). 143
4.33. Hydraulic conditions of $Exp.\ 1U\ Fbed$. 144
4.34. Hydraulic conditions of $Exp.\ 1U\ Ebed$. 144
4.35. Hydraulic conditions of $Exp.\ 1D\ Fbed$. 145
4.36. Hydraulic conditions of $Exp.\ 1D\ Ebed$. 145
4.37. Hydraulic conditions of $Exp.\ 4U\ Fbed$. 146
4.38. Hydraulic conditions of $Exp.\ 4U\ Ebed$. 146
4.39. Schematic diagram of the velocity point measurements. 147
4.40. Longitudinal velocity profile measured in the flume mid-plane and at the distance 0.50 m upstream the oblong pier's front. Experimental data ($\circ$) and theoretical approximation line (dashed line). 148
4.41. Vertical profiles of the velocity components along the mid-plane of the pier for $Exp.\ 1U\ Fbed$. 149
4.42. Vertical profiles of the velocity components along the mid-plane of the pier for $Exp.\ 1U\ Ebed$. 150
4.43. Vertical profiles of the velocity components along the mid-plane of the pier for $Exp.\ 1D\ Fbed$. 151
4.44. Vertical profiles of the velocity components along the mid-plane of the pier for $Exp.\ 1D\ Ebed$. 151
4.45. Vertical profiles of the velocity components along the mid-plane of the pier for $Exp.\ 4U\ Fbed$. 152
4.46. Vertical profiles of the velocity components along the mid-plane of the pier for $Exp.\ 4U\ Ebed$. 152
4.47. Vertical profiles of the Reynolds shear stresses along the mid-plane of the pier for $Exp.\ 1U\ Fbed$. 153

4.48. Vertical profiles of the Reynolds shear stresses along the mid-plane of the pier for *Exp.* 1*U Ebed*. 154
4.49. Vertical profiles of the Reynolds shear stresses along the mid-plane of the pier for *Exp.* 1*D Fbed*. 155
4.50. Vertical profiles of the Reynolds shear stresses along the mid-plane of the pier for *Exp.* 1*D Ebed*. 156
4.51. Vertical profiles of the Reynolds shear stresses along the mid-plane of the pier for *Exp.* 4*U Fbed*. 157
4.52. Vertical profiles of the Reynolds shear stresses along the mid-plane of the pier for *Exp.* 4*U Ebed*. 158

5.1. Plan view of the grid mesh around the oblong bridge pier: whole and local mesh. 170
5.2. Calibration of the bed roughness height. 172
5.3. Experimental and computed scour depths. 172
5.4. Scour hole and deposition region around the oblong bridge pier (dimensions in meters). 174
5.5. Scoured bed hole profiles on the longitudinal mid-plane (5.5a) and on the plane normal to the flow direction (5.5b). Flow direction: x-axis. 175
5.6. Normalized bed shear stress (τ/τ_m) contours around the oblong bridge pier. . . . 176

A.1. Debris effects at the vicinity of Portuguese bridge foundations (Universidade do Algarve, 2006). 220

B.1. Portuguese bridges suggested by Infraestruturas de Portugal as potential case studies (Google Maps, n.d.). 221

C.1. Schematic layout of the camera setup adopted in the experimental study. Courtesy of Doctor Renato Henriques. 230

List of Tables

2.1. Classification of local scour processes at bridge piers in terms of h/W (Melville & Coleman, 2000). 22

3.1. Time series and database available. Periods that require extrapolation of streamflow data. 58
3.2. Hydrological scenarios considered for Q_{HR} estimation. 59
3.3. Statistics of Q_{HR} for the hydrological scenarios under consideration (m^3s^{-1}). . . 64
3.4. Design floods of Scenario 3 estimated by the four probabilistic models (m^3s^{-1}). . 65
3.5. Design floods at the new Hintze Ribeiro bridge (Q_{HR}). Here MM stands for the $modified\ MM$ method. 66
3.6. Values for the parameters contributing for Priority factor (Highways Agency, 2012). 81
3.7. Main advantages and limitations of the proposed risk-based methodology. 83
3.8. Main dimensions of the new Hintze Ribeiro bridge components. 86
3.9. Design floods at the new Hintze Ribeiro bridge (Q_{HR}). Here MM stands for the $modified\ MM$ method. 87
3.10. Hydraulic variables and scour depths at pier $P2$ through HEC-RAS model. 90
3.11. Scour risk rating for the new Hintze Ribeiro bridge. 92
3.12. Contributing parameters for the priority factor of the new Hintze Ribeiro bridge. . 92

4.1. Experimental campaign of the present study. 99
4.2. Geometry dimensions of the oblong bridge pier models. 113
4.3. Estimates of the spatial coordinates of the control points on the top surface of the bridge pier models (coordinates in $\times 10^{-3}$ meters). 120
4.4. Estimates of the spatial coordinates of the control points on the graduated scale (coordinates in $\times 10^{-3}$ meters). 120
4.5. Hydraulic variables of *Run* 1 and *Run* 4. 123
4.6. Reference basis for the time duration of the experiments. 124
4.7. Equilibrium scour depth estimates and measured maximum scour depths. 126
4.8. Statistical results in the computation of the reference lines. 134
4.9. Hydraulic variables of the fixed bed experiments, including uncertainties. 144

5.1. Hydraulic variables of $Exp.\ 1U$. 169
5.2. Scour depth relative error (e_i), determined by Equation 5.11. 173

A.1. Percentages of cause of bridge failure rate, adapted from Cook *et al.* (2015). . . . 219

C.1. Experimental campaign initial plan. 227
C.2. Intrinsic parameters of the action cameras, obtained from "Camera Calibration Toolbox for Matlab". 231

Symbols and Acronyms

The symbols with their fundamental dimensions used in this document are listed below:

a	Distance from the concentration point to the bed	[L]
AD	Anderson-Darling test	[−]
Ai	Acoustic probe data (being i = 1, 2 or 3)	[L]
bw	Kernel bandwidth	[L]
B	Flume width	[L]
B_s	Constant of log-law profile	[L]
c	Sediment concentration	$[\mathrm{MT}^{-1}]$
C	Consequences	[−]
C_{bed}	Equilibrium sediment concentration at the bed	$[\mathrm{MT}^{-1}]$
C_μ	Adjustable constant	[−]
d_{cs}	Depth of contraction scour	[L]
d_{ms}	Short-term general eroded flow depth	[L]
d_s	Scour depth time evolution	[L]
$d_{s,computed}$	Scour depth measured experimentally	[L]
$d_{s,measured}$	Scour depth obtained numerically	[L]
d_{se}	Equilibrium scour depth	[L]
d_{sm}	Maximum local scour depth	[L]
$d_{se-HEC18}$	Equilibrium scour depth estimate given by HEC-18 equation	[L]
d_{se-MM}	Equilibrium scour depth estimate given by Moreno equation	[L]
d_{s-MS}	Scour depth time evolution estimate given by M/S equation	[L]
d_{se-SM}	Equilibrium scour depth estimate given by S/M equation	[L]
D	Downstream sand recess box	[−]
D_{ec}	Equivalent diameter of the column from a pile-supported foundation	[L]
D_{epc}	Equivalent diameter of the pile cap from a pile-supported foundation	[L]
D_{epg}	Equivalent diameter of the pile group from a pile-supported foundation	[L]
D_e	pier equivalent diameter	[L]
D_i	Sediment diameter for which i% of sediments are finer (being i = 16, 84 or 90)	[L]
D_m	Effective mean diameter of the bed material	[L]
D_{50}	Median grain size diameter	[L]
D_F	Pier foundation depth	[L]
D_{FT}	Pier available foundation depth	[L]
D_R	Pier relative scour depth	[L]
D_T	Pier total depth of scour	[L]
D^*	Dimensionless sediment diameter	[−]
e_i	Relative error	[−]
f_1	flow-structure interactions factor	[−]
f_2	Flow-sediment interactions factor	[−]

f_3	Sediment-structure interactions factor	$[-]$
F	Foundation type factor	$[-]$
Fi	Filliben test	$[-]$
Fr	Froude number	$[-]$
$F(x)$	Cumulative distribution function	$[-]$
g	Gravity acceleration	$[\mathrm{LT}^{-2}]$
h	Mean approach flow depth	$[\mathrm{L}]$
h_1	Average depth in the main channel	$[\mathrm{L}]$
h_2	Average depth in the contracted section	$[\mathrm{L}]$
H	History of scour problems factor	$[-]$
H_A	Hazard	$[-]$
H_c	Pile cap top position	$[-]$
If	Mean approach flow intensity	$[-]$
$If1$	Mean approach flow intensity by considering $R1$ data	$[-]$
$If1$	Mean approach flow intensity by considering $R2$ data	$[-]$
If_{mean}	Mean approach flow intensity by considering R_{mean} data	$[-]$
k	Turbulence kinetic energy	$[\mathrm{L}^2\mathrm{T}^{-2}]$
k_1	Exponent for mode of bed material transport	$[-]$
k_s	Roughness height	$[\mathrm{L}]$
K	Von Kárman constant	$[-]$
K_C	Coefficient of proportionality of the hydrological time series of Q_C	$[-]$
K_F	Coefficient of proportionality of the hydrological time series of "Fridão (R.E.) (06I/03H)" gauging station	$[-]$
K_T	Coefficient of proportionality of the hydrological time series of Q_T	$[-]$
K_d	Sediment coarseness factor	$[-]$
K_{hD_e}	Flow shallowness factor	$[-]$
Ki	Control points at the pier top surface (being i = 1, 2, 3, 4, 5 or 6)	$[-]$
K_I	Flow intensity factor	$[-]$
KS	Kolmogorov-Smirnov test	$[-]$
K_{sc}	Column shape factor	$[-]$
K_t	Melville/Sheppard (M/S)'s time factor	$[-]$
K_u	Coefficient of Laursen (1963)'s critical velocity predictor	$[-]$
K_w	Wide pier factor	$[-]$
K_1	Pier shape factor	$[-]$
K_2	Pier alignment factor	$[-]$
K_3	Bed forms factor	$[-]$
l	Integral scale	$[\mathrm{L}]$
L	Pier total length	$[\mathrm{L}]$
L_s	Losses	$[-]$
$L1$	Pier flat side surface length	$[\mathrm{L}]$
LT	Provisional life of a bridge (100 years)	$[\mathrm{T}]$
n	Design life	$[\mathrm{T}]$
n_s	Data series record length	$[-]$
n_v	Shedding frequency	$[\mathrm{T}^{-1}]$
p	Number of parameters of a probability distribution	$[-]$
P_A	Annual probability of scour failure	$[-]$
P_f	Infrastructure priority factor	$[-]$
Pi	Control points at the graduated scale marks (being i from 10 to 110)	$[-]$
P_{LT}	Lifetime risk of scour failure	$[-]$

q	Flow discharge per unit width of the main channel	$[L^2T^{-1}]$
q_{ti}	Total load (bed and suspended load) discharge in stream- or cross-wise direction (being $i = x$ or y, respectively)	$[L^3T^{-1}]$
Q	Flow discharge	$[L^3T^{-1}]$
Q_C	"Carrapatelo Dam (EDP) (07/01A)" records	$[L^3T^{-1}]$
Q_T	"Torrão Dam (EDP) (07H/01A)" records	$[L^3T^{-1}]$
Q_{FT}	"Fragas da Torre (EDP) (08H/02H)" records	$[L^3T^{-1}]$
Q_{HR}	Discharge flow approaching the new Hintze Ribeiro bridge	$[L^3T^{-1}]$
$Q_{instantaneous}$	Instantaneous discharge flow records	$[L^3T^{-1}]$
Q_{mean}	Mean discharge flow records	$[L^3T^{-1}]$
Q_1	Flow discharge in the main channel	$[L^3T^{-1}]$
Q_2	Flow discharge in the contraction section	$[L^3T^{-1}]$
$Q-Q$	Quantile-Quantile	$[-]$
r	reduction factor	$[-]$
R	Pier semi-cylindrical surface ratio	[L]
$R1$	Upstream resistive probe data	[L]
$R2$	Downstream resistive probe data	[L]
R_H	Hydrological risk	$[-]$
R_{mean}	Arithmetic average of $R1$ and $R2$ data	[L]
Re	Flow Reynolds number	$[-]$
Re_D	Pier Reynolds number	$[-]$
Re^*	Particle Reynolds number	$[-]$
s	Specific gravity of bed material	$[-]$
S	Flume slope	$[-]$
S_R	Scour risk of a bridge to failure	$[-]$
t	Time	[T]
t_e	Equilibrium time	[T]
t_r	Reference time	[T]
t_{90}	Time required to reach 90% of d_{se-SM}	[T]
T	Return period	[T]
T_R	Type of river factor	$[-]$
u	Stream-wise velocity	$[LT^{-1}]$
u'	Stream-wise velocity fluctuation	$[LT^{-1}]$
u^*	Shear velocity	$[LT^{-1}]$
u_c^*	Critical friction velocity	$[LT^{-1}]$
U	Upstream sand recess box	$[-]$
v	Cross-wise velocity	$[LT^{-1}]$
v'	Cross-wise velocity fluctuation	$[LT^{-1}]$
V	Mean approach flow velocity	$[LT^{-1}]$
V_c	Critical mean velocity for the beginning of sediment motion	$[LT^{-1}]$
V_f	Importance factor	$[-]$
V_{lp}	Live-bed peak velocity	$[LT^{-1}]$
V_{ref}	Reference velocity	$[LT^{-1}]$
V_u	Vulnerability	$[-]$
w	Vertical velocity	$[LT^{-1}]$
w'	Vertical velocity fluctuation	$[LT^{-1}]$
w_s	Sediment particles fall velocity	$[LT^{-1}]$
W	Pier width	[L]

W_1	Approach channel width	$[\mathrm{L}]$
W_2	Channel width in the contracted section	$[\mathrm{L}]$
W^*	Pier effective width	$[\mathrm{L}]$
x	Longitudinal coordinate/direction	$[\mathrm{L}]$
x_T	Random variable for a return period T	$[-]$
X	Random variable	$[-]$
y	Transverse coordinate/direction	$[\mathrm{L}]$
y_w	Distance from the wall to the center of the cell	$[\mathrm{L}]$
z	Vertical coordinate/direction	$[\mathrm{L}]$
z_0	Coefficient of Sheppard & Renna (2010)'s critical velocity predictor	$[\mathrm{L}]$
α	Significance level	$[-]$
α_b	Angle between the flow direction and a line perpendicular to bed plane	$[-]$
Γ_T	Diffusion coefficient	$[\mathrm{L}^2\mathrm{T}^{-1}]$
δ_{ij}	Kronecker delta	$[-]$
ε	Turbulent dissipation	$[\mathrm{L}^2\mathrm{T}^{-3}]$
η	Kolmogorov length scale	$[\mathrm{L}]$
θ	Skew angle	$[-]$
θ_s	Slope parameter	$[-]$
λ	Bed material porosity	$[-]$
μ	Dynamic viscosity coefficient	$[\mathrm{L}^2\mathrm{T}^{-1}]$
ν	Kinematic viscosity coefficient	$[\mathrm{L}^2\mathrm{T}^{-1}]$
ν_T	Eddy viscosity	$[\mathrm{L}^2\mathrm{T}^{-1}]$
ρ	Flow density	$[\mathrm{ML}^{-3}]$
ρ_s	Sediment density	$[\mathrm{ML}^{-3}]$
σ	Standard deviation	$[-]$
σ_D	Sediment diameter standard deviation	$[-]$
τ	Bed shear stress	$[\mathrm{ML}^{-1}\mathrm{T}^{-2}]$
τ_m	Bed shear stress of the approach flow	$[\mathrm{ML}^{-1}\mathrm{T}^{-2}]$
τ_c	Critical bed shear stress	$[\mathrm{ML}^{-1}\mathrm{T}^{-2}]$
ϕ	Diameter of the Kinect control points	$[\mathrm{L}]$
φ_s	Slope angle	$[-]$
χ^2	Chi-square test	$[-]$
Ω	Pier shape parameter	$[-]$

The acronyms presented in the current document are listed below:

APA	Agência Portuguesa do Ambiente (in Portuguese)
APRH	Associação Portuguesa de Recursos Hídricos (in Portuguese)
ADV	Acoustic Doppler Velocimetry
AASHTO	American Association of State Highway and Transportation Officials
BLESS	Bed LEvel Seeking System
BRISENT	BRIdge–Pier Scour ENTropic model
CFD	Computational Fluid Dynamics
CIC	Centro de Instrumentação Científica (in Portuguese)
CPU	Central Process Unit
DEM	Digital Elevation Model
DES	Detached Eddy Simulation
DNS	Direct Numerical Simulation
Ebed	Eroded bed
ECTS	European Credit Transfer and Accumulation System
EDP	Energias de Portugal (in Portuguese)
Fbed	Flat bed
FBG	Fiber-Bragg Grating
FCT	Portuguese Foundation for Science and Technology (in English)
	Fundação para a Ciência e a Tecnologia
FDOT	Florida Department Of Transportation
FEUP	Faculty of Engineering of the University of Porto (in English)
	Faculdade de Engenharia da Universidade do Porto (in Portuguese)
FORM	First-Order Reliability Method
FOSM	First-Order Second-Moment Method
FHWA	Federal Highway Administration
FSI-CURVIB	Fluid-structure Interaction Curvilinear Immersed Boundary
GCI	Grid Convergence Index
GEV	General Extreme Values
HEC	Hydraulic Engineering Circular
HEC-RAS	Hydrologic Engineering Center - River Analysis System
INFRARISK	Analysis and Mitigation of Risks in Infrastructures
IP	Infraestruturas de Portugal
KDE	Kernel Density Estimate
LES	Large Eddy Simulation
LNEC	National Laboratory of Civil Engineering (in English)
	Laboratório Nacional de Engenharia Civil (in Portuguese)
LRFD	Load Resistance Factor Design
LSE	Least Square Estimate method
MCS	Monte Carlo Simulation
M	Foundation material factor
MA	Weighted model averaging method
MM	Arithmetic model averaging method
modified MM	Modified arithmetic model averaging method
MS	Model selection method
NBI	National Bridge Inventory
NCHRP	National Cooperative Highway Research Program
NES	Urban Water Unit

OpenFOAM	Open Field Operation and Manipulation
POW	Power-Law scheme
PRODEC	Doctoral Program in Civil Engineering (in English) Programa Doutoral em Engenharia Civil (in Portuguese)
RANS	Reynolds-Averaged Navier-Stokes
RANSAC	RANdom SAmple Consensus
RMSE	Root Mean Square Error
RSSes	Reynolds Shear Stresses
SGS	Subgrid-Scale
SIMPLE	Semi-Implicit Method for Pressure-Linked Equation
SNR	Signal-to-Noise Ratio
SNIRH	National Water Resources Information System (in English) Sistema Nacional de Informação de Recursos Hídricos (in Portuguese)
SOU	Second-Order Upstream scheme
SSIIM	Sediment Simulation In Intakes with Multiblock option
TDR	Time-Domain Reflectometry
TI	Turbulence Intensity
TDDS	Theoretically Derived Distribution of Scour
UNISDR	United Nations Office for Disaster Risk Reduction
URANS	Unsteady Reynolds Averaged Navier Stokes
USACE	U.S. Army Corps of Engineers
USGS	United States Geological Survey
VOF	Volume of Fluid
WS	Water Surface

Chapter 1

Introduction

1.1 Background and Motivation

Bridges are a key infrastructure, for they overcome land barriers and waterways that would otherwise prevent the transport of people and goods from one place to another. Bridges, particularly those in waterways, are exposed to many natural hazards that need to be appropriately addressed at the early stages of their design. Bridge scour is one of the most important natural hazards and widely recognized as a major cause of bridge collapses (Melville & Coleman, 2000; Cook *et al.*, 2015; Proske, 2018).

In the United States of America (USA), 60% of the bridge collapses registered over a period of 30 years (in excess of one thousand), resulted from scour at the bridge foundation (Shirole & Holt, 1991). Additionally, bridge damage repair works accounts for an annual cost of US$50 million (Lagasse *et al.*, 2012). The collapse of the Schoharie Creek bridge on April 5, 1987, caused by scouring beneath a concrete pier footing after an estimated 50-year flood (NTSB, 1988; Lagasse & Richardson, 2001), led to the death of ten people (Figure 1.1a). Serious bridge scour problems can also be found in many East Asian countries, mainly in regions subject to yearly typhoon induced floods. For instance, numerous bridges with busy traffic collapsed and led to remarkable losses during the 1996 Typhoon Herb flood event (Milliman & Kao, 2005). Recently, the intensification of flood events, possibly due to climate changes, have caused numerous collapses and increased the global awareness of the academia and bridge engineering industry to this issue (Hsieh *et al.*, 2010; Millilo *et al.*, 2014; Flint *et al.*, 2017).

Within the Portuguese context, scouring problems have also been a common cause of bridge collapses. In 1979, the basal displacement of the central pier led to the partial collapse of the Penacova bridge. Later in 1994, the local scour around the central piers of Gafanha bridge in Aveiro also caused its structural failure. The most recent and hazardous case of scour registered in Portugal occurred in 2001 with the collapse of the Hintze Ribeiro bridge (Rocha *et al.*, 2008), causing 59 casualties (Figure 1.1b). According to national authorities, it occurred in the sequence of three months of floods exceeding 8,000 m^3s^{-1} that corresponded to a return period of 5 years (much lower than the typical design criterion of bridges), alongside two decades of uncontrolled sand extraction which compromised the bridge's stability (Rocha *et al.*, 2008; Sousa & Bastos, 2013).

(a) Schoharie Creek bridge, USA (USGS, 2012). (b) Hintze Ribeiro bridge, Portugal (CEP, 2002).

Figure 1.1: Examples of collapses due to scour at bridge foundations.

In light of the considerable threats against human lives and economic losses, bridge scour research has gained great attention in the last decades as a way to prevent further disasters. Local scour is one of the three main process of erosion at any given bridge site, which also include the general and the contraction scour (Melville & Coleman, 2000). The consideration of these three erosion forms is essential for the depth evaluation of the scour hole formed around foundations and the magnitude of their contribution is known to be site specific (Sturm *et al.*, 2018). In addition, these erosion forms and respective interactions add complexity to the prediction of maximum scour depth for bridge design purposes. As a conservative estimate, it is recommended that the engineer considers each erosion form in isolation and then to add them as though they were independent of one another (Arneson *et al.*, 2012). However, the development of scour holes at foundation level also pose a threat to the safety and serviceability of bridges (Sturm *et al.*, 2018). Scour holes are caused by flow pattern changes and the resulting increase in sediment transport capacity.

The design standards and recommendations practices provided in European codes are often conservative; they consider scour corresponding to an extreme peak discharge acting on the riverbed over a theoretically infinite duration, as noted by Simarro *et al.* (2011) and Link *et al.* (2017). This assumption implies that the flood duration is at least as long as the time needed to achieve equilibrium scour. Several researchers have pointed out that after a single hydrological event, scour may be smaller than the one at the equilibrium stage (Lai *et al.*, 2009; Borghei *et al.*, 2012; López *et al.*, 2014). Since the time to reach equilibrium is somewhat misleading, many researchers assessed the accuracy of the available bridge scour predictors, namely equilibrium scour depth and time evolution of scour depth. The general consensus amongst authors is that most existing equations are conservative (Gaudio *et al.*, 2010; Sheppard *et al.*, 2011; Park *et al.*, 2017).

Despite the decades of research on local scouring phenomenon, there are still many uncertainties that potentially affect the design process of bridge piers. The hydrological and hydraulic variables

are the most critical and less explored uncertainties (Kowalik, 2009; Briaud *et al.*, 2014; Ettema *et al.*, 2017). As a result of their stochastic nature, a risk-based methodology accounting for the uncertainty of those variables inherently enhance the scouring analysis and reduce the vulnerability of bridges to scour effects, thus reducing the scour risk (Tubaldi *et al.*, 2017; Rausand & Haugen, 2020). Following the pioneer studies of Johnson (1992) and Johnson & Ayyub (1992), other researchers have applied probabilistic design approaches as a measure of the bridge pier reliability index or probability of failure (Tubaldi *et al.*, 2017; Barbetta *et al.*, 2017; Manfreda *et al.*, 2018; Akay *et al.*, 2019).

Lagasse *et al.* (2013) mention that the uncertainties in hydrological and hydraulic variables are inherently more complicated than the ones that define the applied loads and the material properties, as considered in the Load Resistance Factor Design (LRFD) approach, extensively used by contemporary bridge designers in the United States of America (Barker & Puckett, 2013). More recently, a study conducted by Johnson *et al.* (2015) quantified the model uncertainty in commonly used scour equations; their results have led to a set of scour design factors that are based on the reliability of the design estimate. Notwithstanding the above, there is still scope for further improvements in this field, particularly in placing most hydrologic and hydraulic aspects of bridge design at similar levels of reliability as structural and geotechnical facets, as suggested by Kallias & Imam (2016), Ettema *et al.* (2017) and Pizarro *et al.* (2020).

A detailed understanding of bridge pier scouring arises, thus, as a fundamental step to prevent catastrophic consequences with their collapse, either partial or total. Moreover, it is crucial to define a structured approach to estimate scour depth that encompasses the complex flow field and bed bathymetry at the vicinity of a bridge pier (Oliveto & Hager, 2005; Link *et al.*, 2017). To attain this goal, it is strongly advisable to adopt approaches involving semi-empirical methodologies and advanced flume experiments, aided by contemporary instrumentation, and Computational Fluid Dynamics (CFD) tools (Ettema *et al.*, 2017; Pizarro *et al.*, 2020).

The sediment transport processes, such as erosion, transport and deposition of particles in fluvial environment, are not yet fully understood. It is known that the sediment motion is highly related to flow features that develop in the viscous sublayer (Ninto & Garcia, 1996; Mattioli *et al.*, 2012) as well as on the forces exerted on the surface of the particles. Moreover, many works demonstrated the ability of CFD tools to provide a detailed flow description over the whole domain even in the viscous sublayer of the flow (Rodi, 2017). In general, the Navier-Stokes and continuity equations are the foundation of the numerical simulations in hydraulic engineering (Moukalled *et al.*, 2016; Hackl *et al.*, 2018).

Beyond the usefulness of CFD tools for understanding complex pier flow fields (Ettema *et al.*, 2006a; Kirkil *et al.*, 2008; Kirkil & Constantinescu, 2009; Khosronejad *et al.*, 2012a; Kirkil & Constantinescu, 2015; Chang *et al.*, 2013; Chang & Constantinescu, 2015), their ability to simulate erosion and scour at a pier vicinity is still limited, preventing its current practicability for estimating scour depths. Hence, a reliable use of CFD tools for an improved design of bridge scour depth estimation remains an issue of continuing research interest.

1.2 Objectives and Methodological Approaches

1.2.1 General considerations

The main aim of the present research work was to develop a new and pragmatic methodology to evaluate the risks associated with scour at bridge foundations, founded on alluvial beds. This methodology can serve two key purposes: (i) to consolidate the connection between the recent advances on scour depth prediction and its applicability on industry practices; and (ii) to provide oriented measures and practical recommendations for reducing the vulnerability and enhancing the capacity of infrastructures in coping with scouring effects. The ultimate accomplishment of the present work is to define a methodology to be used into the important decision-making process of bridge engineers and designers, and its incorporation into regular bridge inspection schedules. The core focus of the investigation, in the context of the risk methodology, was the modelling of flood events and dealing with the uncertainty associated with adverse hydraulic conditions, which are the main drivers of the scouring phenomenon.

For a more advanced and comprehensive understanding of the scour phenomenon, the two sediment transport modes, clear water *vs* live bed scour regimes, were considered in the study by combining the scour risk evaluation with two other research approaches, namely experimental and numerical modelling. For this reason, the research work of this thesis was organized in three interconnected modules: "Risk-based Analysis", "Experimental Study" and "Numerical Modelling". Each module incorporated adequate sensitivity and uncertainty analyses. The following subsections describe the particular objectives and methodological approaches of each module.

1.2.2 *Risk-based Analysis*

The "Risk-based Analysis" module concerns the proposed new risk-based methodology with particular emphasis on the statistical analysis of hydraulic events using case study data.

- *Research design / Conceptualization:* An initial phase was devoted to devise the theoretical framework of the risk-based methodology. This framework was used to structure the research process and helped to systematize the underlying steps of such methodology. A validation phase with a real case study bridge constitutes a key aspect of the methodology's reliability and thus an adequate selection of the case study bridge was undertaken.

- *Preparatory work / Data collection:* The following sets of data were required for the case study selection process: (i) detailed bathymetry at the bridge location (its variability over time was taken as a favourable factor for selection); (ii) bridge structural characteristics (including substructure and superstructure components); (iii) continuous measurements of discharge at a near gauging (if possible, during flood events); and (iv) grain size distribution and other geotechnical properties of the riverbed material in the vicinity of the bridge foundations. The bathymetry data and bridge structural characteristics were provided by "Infraestruturas de Portugal (IP)", one of the Portuguese authorities responsible for the conservation of bridges, with whom both institutions (LNEC and FEUP) signed a collaboration and information

exchange agreement. The hydraulic and hydrological data were available at the National Water Resources Information System (SNIRH, Portugal) - `http://snirh.apambiente.pt/`. Part of this data was made accessible thanks to "Energias de Portugal (EDP)".

- *Statistical modelling / Data treatment:* A statistical analysis of hydrological variables approaching the case study bridge was undertaken. It used the flood frequency analysis technique allied to parametric and non-parametric methods for providing reliable estimates of the extreme flow discharges (design floods). The statistical results were then associated with the bridge susceptibility to scour phenomenon, taking into consideration the bridge geometry and location, for assessing its scour risk rating.

- *Main outputs:* A novel modelling method to provide reliable estimates of extreme discharge flows was proposed in a scientific paper (Section 3.2). This paper was submitted to the "Journal of Hydrological Engineering", in July 2020 and is currently waiting for response. The risk-based methodology developed for bridge scour risk assessments was described and implemented to a bridge case study in a scientific paper (Section 3.3), published in "Engineering Structures" in July 2020.

1.2.3 *Experimental Study*

The "Experimental Study" module describes the experiments performed in the experimental facilities of the National Laboratory of Civil Engineering (LNEC) in Lisbon (Portugal). Some of this facility's features were kept the same as previously prepared and used for Moreno (2016)'s study.

- *Research design / Conceptualization:* The experimental facility was prepared and adapted for the movable and fixed bed experiments envisaged for the experimental campaign. This preliminary step comprised trial runs, in which sophisticated measurement techniques and instrumentation were explored for comprehensive characterization of the scouring effects and their respective ensemble. It culminated with the definition of the experimental campaign, procedure and the selection of the measuring variables and techniques/tools to be adopted.

- *Experimental campaign / Data collection:* The experimental campaign was conceived to address two key aspects of the bridge scouring process: (i) the geometry of the scour hole around bridge piers and (ii) the turbulent flow field at the beginning of the scouring process and within the developed scour hole. Ten experiments were performed in a glass-sided rectangular tilting flume, where the two types of scour regimes, clear water and live bed, were carried out. Two different widths of oblong bridge piers and a sand of known granulometric composition were considered. The bridge piers were part of the models used by Moreno (2016) and Moreno *et al.* (2016b).

- *Results / Recommendations:* Digital elevation models (DEMs) of the scour hole geometries and their respective ensembles were retrieved by using two image-based techniques, namely

by use of the Kinect V2 sensor and by applying close-range photogrammetry. A continuous monitoring method was developed to obtain two-dimensional bed profiles during experiment, through the application of underwater image processing techniques and computer vision routines. Detailed flow field patterns associated with the scouring process were measured by using a high-resolution acoustic velocimeter.

- *Main outputs:* The mechanism of the scour hole formation at the vicinity of oblong bridge pier models were characterized in a scientific paper (Section 4.3). The hydrodynamic erosion process was explored in an independent paper (Section 4.4). These two papers are under preparation for submission to international scientific journals.

1.2.4 *Numerical Modelling*

The "Numerical Modelling" module discusses the role and adequacy of the CFD tools for simulating bridge scour phenomenon under the experimental conditions.

- *Research design / Conceptualization:* Different advanced numerical modelling techniques were evaluated and their abilities addressed in order to select the appropriate one to study the dynamics of turbulent flows and to deepen the understanding of their interactions with the erodible bed around bridge foundations. As with all loose-bed hydraulic modelling, the duality between the accuracy of the results and the time of computation were considered and discussed without underestimating the main goals of the current investigation.

- *Numerical analysis / Data collection:* A selection of the appropriate CFD tool for simulating the mechanism of the scour hole formation in the laboratory environment was performed. The database resulting from the experimental campaign was used to calibrate and validate the numerical model. A careful preparation of the numerical setup regarding the experimental boundary conditions and the grid mesh was undertaken. Due to the amount of data and the required computational time, the platform GridFEUP (`https://grid.fe.up.pt/web/index.php?page=welcome`), provided by the Faculty of Engineering of the University of Porto (FEUP), was used to perform the numerical simulations.

- *Results / Recommendations:* Numerical simulations of the sediment bed movement and the bed shear stress in the vicinity of an oblong bridge pier model were carried out. A large set of data relative to bed morphology and flow field patterns was produced.

- *Main outputs:* The adequacy and accuracy of the selected CFD tool to characterize the scouring process at the vicinity of bridge foundations was explored in a scientific paper (Section 5.2). This paper is under preparation for submission to an international scientific journal.

1.3 Thesis Layout

The current work comprises six chapters and five appendices. The present chapter presents the general framework and motivation of this thesis. The main objectives, the methodological approaches and the structure of the present document are also detailed.

Chapter 2, "A Review of Bridge Scour Research", provides a broad review of recent research undertaken concerning bridge scour prediction, as well as existing risk-based approaches applied to evaluate scour at bridges.

Chapter 3 to Chapter 5 present the studies developed by the author to achieve the objectives of this investigation. Each of these chapters begins with an introductory section to provide the reader with the necessary context to understand the respective main sections.

The main sections of Chapter 3, "Risk-based Analysis", present the two scientific papers produced within the risk module of the thesis, the first submitted and the second published, namely "Improvement assessment of maximum streamflow approaching a bridge over Douro river. A case study" and "Risk-based methodology for scour analysis at bridge foundations", respectively in sections 3.2 and 3.3.

Chapter 4, "Experimental Study", is focused on the performed experimental campaign. The description of the experimental setup and its components precede the obtained achievements in the form of two independent manuscripts. The scientific papers in preparation "Characterizing bridge scour using image-based techniques in laboratory environment" and "Experimental characterization of the flow field around oblong bridge piers" are presented in sections 4.3 and 4.4, respectively.

Chapter 5, "Numerical Modelling", discusses the role and adequacy of the CFD tools for simulating bridge scour phenomenon under the experimental conditions. A systematic methodology to pursue the aims of the "Numerical Modelling" module is therein provided by the elaboration of the "Numerical simulations of scour development around an oblong bridge pier laboratory model" scientific paper under preparation and included in Section 5.2.

Chapter 6, "Conclusions and Future Research", summarizes the more significant findings of this dissertation and presents a discussion on future works.

The four appendices provide further information that supports the research presented in the main chapters.

Appendix A presents a brief compilation of the most common bridge failures causes.

Appendix B contains a summary of the thirteen Portuguese bridges suggested by Infraestruturas de Portugal (IP) as potential candidates for the research purpose of the "Risk-based Analysis" module.

Appendix C details the experimental campaign, the general experimental procedure, and the hydraulic and scour conditions in which the tests were conducted.

Finally, Appendix D includes the three scientific conference papers in one national and in two international events, as well as an abstract accepted for oral communication.

The numbering of the figures, tables and equations follows the order of this document.

Chapter 2

A Review of Bridge Scour Research

2.1 Introduction

Erosion phenomenon is characterized by the lowering of the riverbed level under the effect of flowing water, either along a channel riverbed or around an obstacle (e.g. a bridge foundation), leading to its exposure (AASHTO, 2017). The stability of a riverbed is, thus, closely related with variables that are difficult to measure and control. River scouring complexities arise from the consideration of a variety of factors. They comprise bridge foundations' geometry and construction, flow temporal variability under local channel conditions, generated flow field at the structure's vicinity, diverse riverbed sediments, and erosion/deposition dynamics along the river channel, as well as their relations with riverbanks or other structures. The impact of the flowing water on the dynamic behaviour of the riverbed and its repercussion on the structural stability of bridge foundations has been receiving a greater recognition and attention from scientists and engineers nowadays.

It is worth mentioning that scour at the vicinity of bridges plays a vital role in a variety of fields, especially due to the morphological evolution of alluvial riverbed channels as a consequence of altering the sediment-flow equilibrium and thus seriously affecting the ecosystems at the cross-section scale. Flood vulnerability and the modification of local geomorphological characteristics have also to be accounted for when analysing the integrity of bridges. Despite a vast number of studies focusing on bridge failure causes (Appendix A), and on the main mechanism of soil removal around bridge single piers as well described in Melville & Coleman (2000) and Richardson & Davis (1995), bridge resistance to scour effects, and the mechanisms of soil degradation, have not yet been fully clarified. Consequently, an accurate relationship between flow magnitude and its temporal duration in a scouring event at a specific site is important for a better understanding of bridge failure modes. It is, thus, crucial to understand the flow field and its erosion capacity for a variety of pier characteristics and foundation materials. The dynamic nature of these phenomena should be properly investigated and understood in order to obtain adequate relations between the fluid flow and the erodible boundary. Such investigation requires a methodology sufficiently comprehensive to account for the most important individual parameters and the influence of non-independent relations, as well.

The three-dimensional and unsteady flow field coupled to the diversity of riverbed materials complicate the design method for scour depth estimation at bridge foundations (Ettema *et al.*, 2011). Rather, the design of bridges has been relying on empirical and semi-empirical relations, and on hydraulic models, to relate scour depths to the erosive action of the pier flow fields and erosion resistance of riverbed foundation materials. Notwithstanding, laboratory experiments are typically simulated in simplified conditions that do not replicate the complexities of scour at actual bridge sites. As these factors are inevitably difficult and even impracticable to investigate fully with laboratory experiments or numerical simulations, much reliance has to be placed on the monitoring system at individual bridge sites to protect those structures against scour. Monitoring systems may also be useful in detecting the need for immediate scour mitigation measures during a flood event or simply to establish a schedule for structural countermeasures. This monitoring demand increases since the scouring process at bridge components (piers and abutments) and at channel riverbanks are complex due to increasing interactions with each other and thereby causing scour depths to be estimated inaccurately (Ettema *et al.*, 2006c; Sturm *et al.*, 2018). Hence, a fully coupled methodology generally comprises experimental work and numerical simulations under the considered experimental conditions. These two modes have been used for evaluating scour and failure risk of existing bridges as well as its design.

2.2 Types of Erosion

2.2.1 General considerations

Riverbed erosion may result from either natural or man-made phenomena, both capable of causing adverse consequences over long reaches of the river or solely at a particular location. It is strongly dependent on the sediment regime of rivers or streams and can occur under normal or flood flow (Melville & Coleman, 2000). The process of erosion might, thus, develop gradually over time or rapidly during flood events. This phenomenon occurs in alluvial riverbeds.

The scouring process may occur at bridge foundations, such as piers and abutments, or at river banks, since the erosive action of the flowing water has the strength to excavate and carry away material from, respectively, the bottom or the banks of the channel (Richardson & Davis, 1995). Scouring at bridge foundations is the most common cause of bridge collapses (Appendix A), whilst the scour at river banks may lead to the changing of the natural stream course and to outflank the bridge (Raudkivi, 1986).

Therefore, the overall scour for any stream is typically categorized into three components: general erosion, contraction scour, and local scour at piers or abutments (Melville & Coleman, 2000). These may occur either isolated or simultaneously. The different origins require an accurate understanding of its nature and consequent different estimation of each individual scour contribution (Melville & Coleman, 2000). The present section briefly describes these three forms of erosion.

2.2.2 General scour

A riverbed is exposed to general scour when it takes place regardless of the presence of a riverine structure. It is mainly a result of riverbed degradation under geomorphological processes induced by either hydro-meteorological background or anthropogenic impacts on watershed (Gilja *et al.*, 2012). Ettema *et al.* (2006c) have identified climate change and land activities (landslides, mud flows) as factors of natural phenomena, while some land-use changes (deforestation, urbanization), dam and reservoir construction, channel straightening, and riverbed material mining have been recognized as due to human activities. In Italy, for instance, stream bed gravel mining was identified as number one of general scour cause, which increased after second World War, causing exacerbated bed channel degradation (Brandimarte *et al.*, 2012).

Regarding the time scale, general scour is commonly divided into long-term and short-term. The former is defined as the scour that occurs in a relatively long time scale or even several years, and, encompasses progressive degradation and aggradation[1] of the riverbed (Melville & Coleman, 2000; Ettema *et al.*, 2006c), and lateral bank migration. On the other hand, short-term scour develops during flood events or between two shortly spaced flood waves (Gilja *et al.*, 2012; Harrigan, 2012).

2.2.3 Contraction scour

Unlike general scour, contraction scour is directly influenced by riverine structure positioning, such as bridges, in the movable channel. It consists on the removal of bed materials in the constriction section, resultant from either the presence of a bridge or when overbank flow is confined by roadway embankments (Arneson *et al.*, 2012).

The reduction of the flow area of a certain stream produces an increase of the mean flow velocity and bed shear stress (Richardson & Davis, 1995; Graf, 1998). This pattern leads to increased erosive strength in the contraction area and more riverbed material leaving than entering. The resulting overall lowering of the riverbed level causes the increase of the flowing area, the velocity and the bed shear stress change until equilibrium is reached, i.e. when the bed shear stress decreases such that no sediment is transported out of the reach (Arneson *et al.*, 2012). The equilibrium concept is addressed later in subsection 2.4.2.1. In addition, contraction scour differs from long-term degradation (see subsection 2.2.2) on the presence of a constriction/obstacle (bridge or other riverine structure), it can be intermittent and/or associated to the occurrence of a particular flood event.

The contraction scouring phenomenon is also affected by the type of vegetation in the catchment area and by floating woody debris, which also narrow the flow area by clogging partially or totally the structure (Brandimarte *et al.*, 2012; Gilja *et al.*, 2012).

[1] This term is generally used to characterize the deposition of material being carried by the flowing water from upstream.

2.2.4 Local scour

The presence of riverine structures such as bridge piers and abutments, cross-dykes, dams or ground sills, among others, induce a significant local increase of the shear stress, resulting in scour of the surrounded riverbed (Richardson & Davis, 1995; Graf, 1998). This kind of scour is known as local scour and is the major cause of structural instability in bridges with foundations in riverbeds (Tanasić *et al.*, 2013; Deng *et al.*, 2016; Flint *et al.*, 2017), which justifies in part the more emphasis given to this particular type of scour over decades (Figure 2.1).

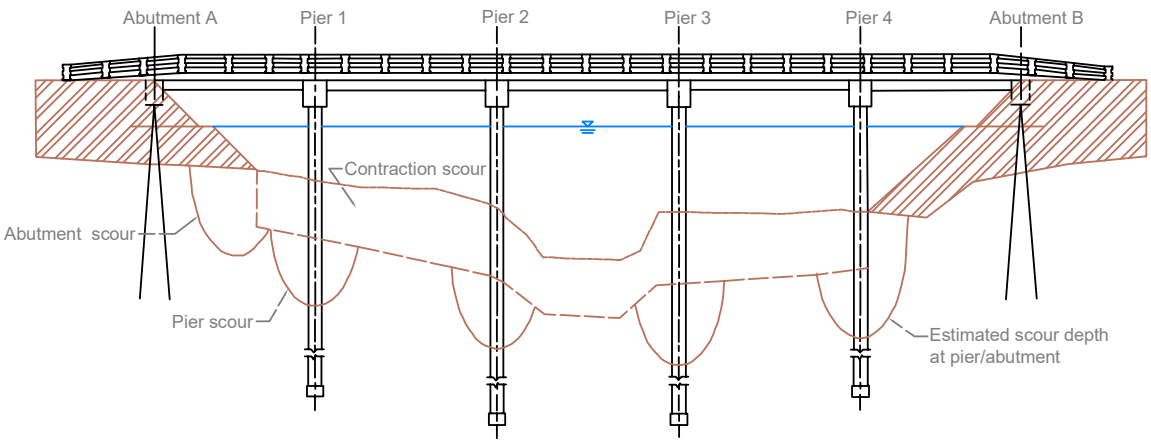

Figure 2.1: Components of scour at a bridge, adapted from DTMN (2013).

The formation of highly turbulent vortex systems as result of the locally deflection of the approach flow by the presence of a bridge foundation (pier and abutment) leads to increased local velocities. The latter induce also increased bottom shear stress and the scour rate of the riverbed material. The scour of the riverbed at the vicinity of bridge components is usually evaluated in terms of scour depth. An increase in scour depth may lead to a significant reduction of the lateral resistance of the soil supporting the foundation, which increases the lateral deflection of the foundation head (Daniels *et al.*, 2007; Lin *et al.*, 2010; Deng *et al.*, 2016). Moreover, when the scour depth reaches a certain magnitude, bending and buckling of the foundation may occur under the combined effect of the dead load of bridge superstructures and the traffic load (Walton *et al.*, 1982; Hughes *et al.*, 2007; Deng *et al.*, 2016).

Local scouring at bridge abutments is fairly complex specially due to their location in compound channels (most common case) whose morphology such as alignment and bathymetry are not entirely known. The process involves the consideration of flow field, riverbed material as well as the mix of geotechnical failure modes that can develop at and near abutments (Brandimarte *et al.*, 2012). In many cases, the channel where the abutment is founded is composed by a mixture of materials (Ettema *et al.*, 2004a). The role of these different sediment types on the scouring phenomenon is further explained in Subsection 2.2.5. More details regarding the mode of failures of bridge abutments can be found in Melville & Coleman (2000) and Ettema *et al.* (2006c), among others.

2.2.5 Sediment types and behaviour

2.2.5.1 Sediments role

Sediments have influence on the storage capacity of dam reservoirs, the stability of bridges, and the navigation conditions of rivers, among others. High sediment transport rates may lead to poor water quality, habitat degradation and, depending on the local geology and terrain, damage aquatic ecosystems in downstream sites as well as in upstream headwaters as the deposits grow (Walling & Fang, 2003). Both high and low values of sediment transport are responsible for environmental issues. Sediment starvation, in turn, is increasingly affected by anthropogenic impacts, which seriously alter riverbed properties and may represent considerable economic losses, often leading to maintenance interventions in fluvial hydraulic systems (Álvares & Pimenta, 1998; Kondolf *et al.*, 2014). Further, river sediment is a valuable economic resource used in construction, thus requiring the prediction of the values of sustainable extraction that are compatible with the ecosystem equilibrium and the safety of riverine structures, mainly bridges. In fact, the excessive extraction may cause serious degradation of the riverbed at the the vicinity of bridge foundations that may lead to structural instability and consequent collapse. An accurate assessment of eroded and transported sediment, within a certain stretch of a hydrological watershed, is, therefore, vital to inform adequate river engineering solutions and to identify unstable river stretches, where resources may be targeted and management/restoration efforts prioritised (Thorne *et al.*, 2010a,b).

2.2.5.2 Sediments displacement mode

In a stretch of a riverbed, sediment transport may occur in two main modes: bed and suspended load (Cardoso & Cunha, 1998). Several researchers have attempted the quantification of sediment transport rates. DuBoys (1879) proposed the first successful relationship for bed load. Subsequently, other works have followed resulting in the derivation of either empirical or semi-empirical equations for the bed, suspended or even total sediment load (Shields, 1936; Lane & Kalinske, 1939; Meyer-Peter & Müller, 1948; Einstein *et al.*, 1950; Bagnold, 1966; Shen *et al.*, 1970; Ackers & White, 1973; Parker *et al.*, 1983; Brownlie, 1982; Rijn, 1984; Hassanzadeh, 2007, among others). Since Bagnold (1966)'s contribution on this topic, various predictive equations of sediment transport rate based on stream power concepts were proposed (Soar *et al.*, 2017), such as works of Engelund & Hansen (1967), Yang (1973, 1984), and Eaton & Church (2010). Further studies on sediment transport in suspension and sediment transport in steep channels were compiled and reported recently by Mueller & Sumer (2020).

2.2.5.3 Cohesive and non-cohesive sediments

The capacity of the flowing water to transport sediments from the bed and/or suspended load is highly affected by the type and properties of the riverbed material as it determines the mechanism of scour. The characterization of the riverbed material is extremely complex and usually divided into cohesive and non-cohesive sediments. These two sediment types respond quite differently to scour phenomenon due to their own features.

For a riverbed markedly composed by cohesive sediments, the resistance to erosion depends mostly on the strength of the cohesive bond between particles, which may far overweight the influence of the individual particles features (Briaud, 2015). The erosion resistance of cohesive sediments is a very complex problem and at present the understanding of the inherent physics is somewhat limited (Kothyari *et al.*, 2014). In a mainly non-cohesive sediment riverbed, the individual particle properties, namely size, shape, and density, determines the erosion threshold conditions. Generally, the scour depth in gravel beds is more than that in sand beds (Raikar & Dey, 2005).

Even within non-cohesive sediments it is important to distinguish sand from gravel riverbed materials. The magnitude of scour depth at the immediacy of structures changes, for instance, depends on the bed roughness, which affects the vortex flow system around the obstacle and, consequently, the mobility of the bed material.

2.2.5.4 Sediment layering and armouring

In major studies, the riverbed is usually represented as a homogeneous geological structure and the spatial disposition of riverbed layers of material is thus neglected. However, neglecting this spatial variation can lead to systematic underestimation of the scour depth and may have important implications for the integrity of structures founded in the riverbed. In the past, Raudkivi & Ettema (1985) and Dey & Raikar (2007b) have investigated experimentally the influence of layer thicknesses and median diameters of two types of sand. They have concluded that there is a dependency of these two parameters on the scour depth, which can be reduced or increased compared to that obtained for a uniform bed of the underlying sand type under the same flow conditions, depending on whether the upper coarse sand layer is breached and whether a secondary armour layer is formed in the scour hole.

Comparatively few researchers have studied the bed armouring phenomenon in the context of a layered bed, composed by a coarse sediment layer overlying finer sand. It is known that armouring phenomenon, in which the median grain size of the surface is significantly larger than that of the subsurface (Ferdowsi *et al.*, 2017), may show a significant influence on local scour due to the different mobility of non-homogeneous bed soils. As scour develops in time, the finer bed particles are carried away and, when the flow has no strength to erode all sizes of widely-graded bed sediments, an armour layer is formed by the coarser materials, protecting the riverbed from the flow erosive action. However, if the armour layer is not stable and the flow exceeds the mobility threshold for the coarser materials, the underlying riverbed material is highly exposed to erosion and deeper scour holes are expected to occur (Brandimarte *et al.*, 2012). Molinas (2003) studied the effect of sediment distribution shape on the scour process, under constant median diameter and non-uniformity coefficient, by skewing the distribution towards the coarse fraction. The researcher has found that as coarse fraction enhanced, the scour depth reduced, which was explained by the impact of bed armouring on scour development. These experimental tests have demonstrated the significance and influence of the sediment distribution shape on the scouring process, which needs further investigation.

2.3 Bridge Scour Process

The development of scour holes are a result of the locally accelerated flow and the consequent vortices formed at the immediacy of bridge foundations. This very complex flow and resulting mechanism of scouring has been addressed by several studies, experimentally by laboratory work, using analytical/theoretical approaches, as well as, more recently, through numerical methods by means of Computational Fluid Dynamic (CFD) tools either coupled or not with a 3D morphodynamic code (Sumer, 2007).

Laursen & Toch (1956) were some of the pioneers to describe the mechanism of flow and scour development in the vicinity of a circular bridge pier; others have followed for other types of flow conditions, bridge foundations, and sediment characteristics (e.g. Melville & Raudkivi (1977); Dargahi (1989); Graf & Istiarto (2002); Muzzammil & Gangadhariah (2003); Ettema *et al.* (2006b); Dey & Raikar (2007a); Unger & Hager (2006); Kirkil *et al.* (2009); Diab *et al.* (2010); Radice & Tran (2012)). Figure 2.2 illustrates the main flow processes that take place around a classic circular bridge pier, exposed to a steady approach flow on a plane sediment bed. They comprise the "horseshoe vortices" formed in front of the pier, the "lee-wake vortices" (usually called "vortex shedding"), the contracted streamlines at the side edges of the pier, and the "downflow" process due to the deceleration of the flow in front of the pier.

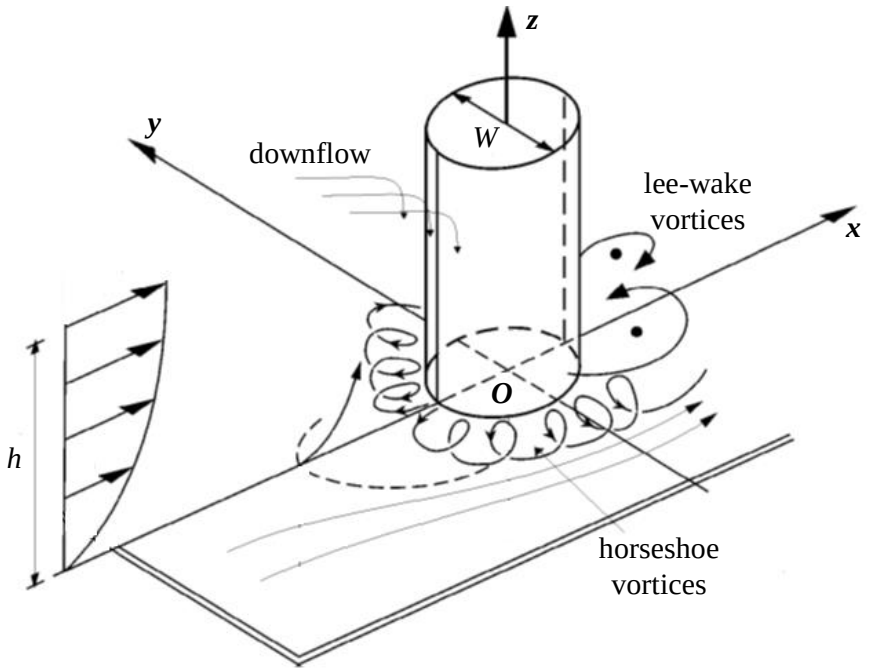

Figure 2.2: Main flow features around a circular pier, adapted from Sumer (2007).

The mechanism of scouring and formation of the scour hole are as follows. At the upstream side of the pier, the approach flow is brought to a stall by the obstacle, causing an increase in pressure and consequently swelling of the water surface level in front of the pier (commonly referred to "surface roller" or"upflow"). As the flow velocity decreases from the water surface to the bed

level, the dynamic pressure on the pier face also decreases downwards. This adverse pressure gradient enforces a three-dimensional boundary layer separation just in front of the pier footing and results in a vortical structure, horseshoe vortices, surrounding the upstream perimeter of the pier and fading away downstream, this vortex system causes local scour at the pier base. The formation of the vortex system occurs on both sides of the pier simultaneously. The pair of vortices is unstable, causing one of the vortices to be pulled across the wake, cutting off the other. For the next shedding cycle, lee-wake vortices, a vortex is cut off at the other side of the cylinder, rotating in the opposite direction; this process continues throughout the vortex shedding process, converging at the downstream of the pier. The overall action of the vortices system removes material from the stream or riverbed adjacent to the foundation. If the transport rate of sediment away from the vicinity of the bridge pier is greater than the transport rate into the area, a scour hole will develop. Scour holes usually are deepest at the upstream nose of a foundation element and extend some distance along the sides. At the downstream end of the element, where the water velocities are generally lower, transported material can be deposited. The variation of pier width (W) and shape, and approach flow depth (h) modify the flow field, enhancing or weakening these flow features. The ratio h/W, known as flow shallowness, is used to differentiate the three categories of pier flow field, namely narrow piers (Figure 2.3), transitional piers (Figure 2.4) and wide piers (Figure 2.5), which produce significantly different pier scour morphologies as follows:

- Narrow piers ($h/W > 1.4$) - the scour is typically deepest at the pier front, previously described (Figure 2.3);

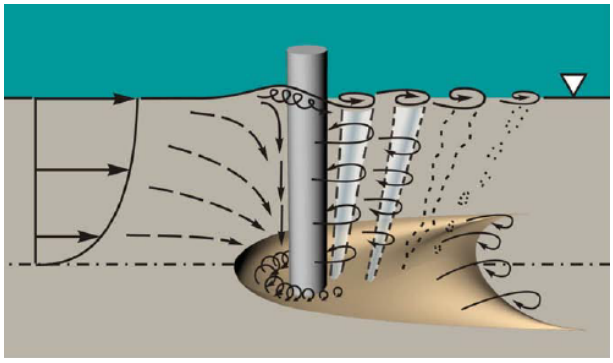

Figure 2.3: Narrow pier, adapted from Ettema *et al.* (2011).

- Transitional piers ($0.2 < h/W < 1.4$) - the reduction in h/W results in shallower scour depths;
- Wide piers ($h/W < 0.2$) - the scour is typically deepest at the pier sides.

Figures 2.3 to 2.5 illustrate a sequence of flow field patterns consistent with three values of h/W, representing how the scour capacity of flow field reduces. The “Downflow” (as indicated in Figure 2.2) becomes less developed since it has a shortened length over which to develop whilst the upflow remains unaltered. Additionally, the vorticity of the “Horseshoe vortex”, aligned nearly horizontally in the pier flow field weakens as the “Downflow” weakens, and the “Lee-Wake vortices” also weaken owing to the increased importance of bed friction in a shallower flow.

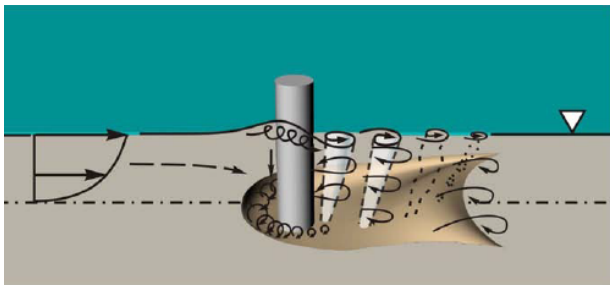

Figure 2.4: Transitional pier, adapted from Ettema *et al.* (2011).

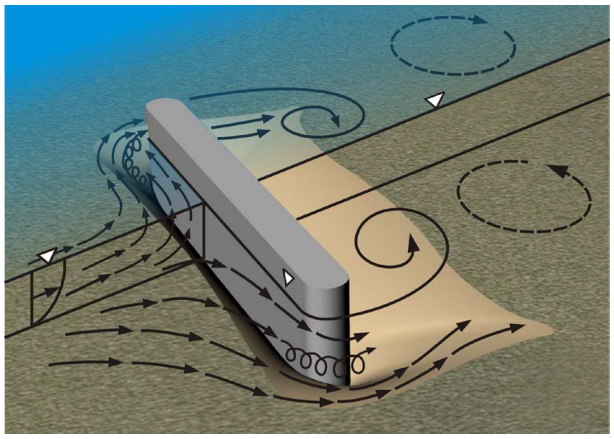

Figure 2.5: Wide pier, adapted from Ettema *et al.* (2011).

The main flow field features previously described for narrow piers exist in the flow field of piers within the transitional range of flow shallowness (Figure 2.4), although the features starts to modify in response to reductions of h and/or increases in W. The closer proximity of the water surface to the foundation boundary (for constant pier width), or the increased width of a pier (for constant flow depth), partially disrupt the formation of the features, and thereby reduce their capacity to erode the foundation material (Ettema *et al.*, 2011). Though the ample data showing that the reduction of the flow shallowness (h/W) leads to smaller scour depths for the transitional category of flow field, further research is needed to systematically describe and document the flow field changes (Ettema *et al.*, 2006a; Kirkil *et al.*, 2008; Sheppard *et al.*, 2011; Ettema *et al.*, 2017).

The aforementioned flow features are responsible for the development of scour holes around bridge foundations (Figure 2.6). Therefore, to understand how scour develops, to model scour and to estimate scour depth, it is necessary to understand the main variables that govern the scouring phenomenon and how they influence the entrainment and transport of foundation material from the scour hole (issue addressed on Section 2.4).

The measurement of sediment transport can be performed using a Eulerian approach that targets measurement of sediment fluxes, or a Lagrangian one that aims at measuring trajectories of individual grains as they move. Since pioneering works appeared some decades ago, the use of image-based techniques for the study of river sediment transport has been constantly increasing.

Image processing techniques offer unique possibilities for particle tracking in comparison to

Figure 2.6: Scour hole around a bridge pier, in Portugal (Universidade do Algarve, 2006).

other Eulerian methods. This technique indeed proved its capability to provide relatively high-resolution and low-cost data for detailed analyses of physical phenomena. However, despite these potentialities, the application of image analysis to scouring process monitoring suffers from some critical experiment limitations, in terms of spatial/temporal support scales for the measurement and size of data samples. For example, it is difficult to achieve simultaneously an appropriate combination of a large spatial area, long duration of an experiment and high measuring frequency, without compromising the quality and quantity of data. Significant improvements can also be obtained for both hardware and software tools.

2.4 Scour Parameter Framework

2.4.1 Scour variables and parameters

The scouring process at single piers may be described by the set of independent variables shown in Figure 2.7. The functional relation between the scour depth (d_s) and the pertinent variables can be written as in Equation 2.1.

$$d_s = function[flow(\rho,\mu,V,h,g), bed\,material(D_{50},\sigma_D,\rho_s,V_c), pier(W,L,\Omega,\theta), time(t)] \quad (2.1)$$

Variables ρ and μ are the density and dynamic viscosity of the flow, respectively; V is the mean approach flow velocity; h stands for the flow depth; g is the gravity acceleration; and t refers to time. Regarding the bed material variables, D_{50} and σ_D are the median diameter and the geometrical standard deviation of the bed material. Parameter ρ_s denotes the sediment density while V_c is the critical mean approach flow velocity for entrainment of bed sediment. Considering the single pier parameters, W is the pier width while L is the pier length. The non-dimensional parameter Ω describes the shape of the pier front whereas θ is the angle of the approaching flow relative to

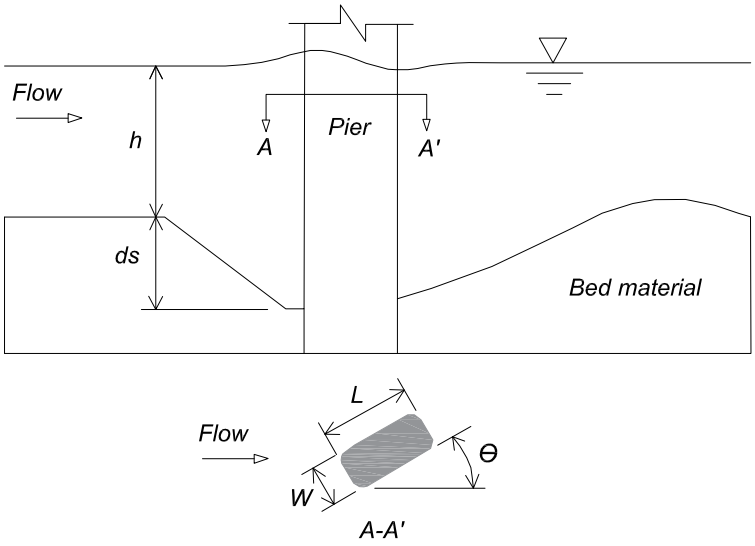

Figure 2.7: Variables influencing scour at an oblong pier, adapted from Ettema *et al.* (2011).

pier alignment. It is, then, common to rewrite Equation 2.1 by normalizing its parameters by the independent variables W, V and ρ (Equation 2.2).

$$\frac{d_s}{W} = function\left(\Omega, \theta, \frac{W}{L}, \frac{h}{W}, \frac{D_{50}}{W}, \frac{V}{V_c}, \frac{V^2}{gW}, \frac{\rho VW}{\mu}, \sigma_D, \frac{\rho_s}{\rho}, \frac{tV}{W}\right) \tag{2.2}$$

According to Ettema *et al.* (2011), Equation 2.2 mainly comprises sets of primary and secondary parameters. The primary parameters define the structure and the geometric scale of the pier flow field, determining, thus, the potential maximum scour depth as follows:

- $\frac{h}{W}$: Indicates the geometric scale of the pier flow field, above termed as flow shallowness;

- $\frac{W}{D_{50}}$: Relates the length scales of pier width and median diameter of bed material, also known as sediment coarseness;

- Ω, $\frac{W}{L}$, θ: Define pier face shape, aspect ratio of pier cross-section and approach flow alignment to pier, respectively. These variables are usually combined to form the compound variable W^* denoting the effective pier width. The above length scale parameters are, therefore, expressed as h/W^* and W^*/D_{50}.

The secondary parameters characterize scour depth sensitivities within the geometric scale limit, leading to reduced scour depths than the potential maximum; those values are more susceptible to more uncertainties at pier sites. They include the following:

- $\frac{V}{V_c}$: Expresses the extent (or stage) of sediment transport on the approach flow bed, often termed the flow intensity. Such parameter distinguishes whether clear water or live bed scour (issue addressed later) conditions prevail in the approach flow;

- $\frac{V^2}{gW}$: Ratio relating vorticity induced inertial forces in the pier flow field relative to gravity acceleration;

- $\frac{\rho VW}{\mu}$: Pier Reynolds number (Re_D). While viscous effects are unlikely to have an effect on the scour depth at the pier due to the fully turbulent flow at its vicinity, the inclusion of a Reynolds number accounts for the dependency of lee-wake vortices (indicated in Figure 2.2) on pier Reynolds number;

- σ_D: Geometrical standard deviation of bed material, which characterizes sediment uniformity;

- $\frac{tV}{W}$: Characterizes the temporal development of scour associated with pier flow field and nature of foundation material.

On the following subsection, the influences of these individual parameters on the scouring phenomena (Equation 2.2) are presented as well as the interaction between some of them. Melville & Coleman (2000) published a comprehensive in-depth review of the state of the art of such parameters. Other researchers as Sheppard *et al.* (2004), Lee & Sturm (2009) and Lança *et al.* (2013) disputed the assumption that the sediment coarseness did not influence the scour depth for relations ($\frac{W}{D_{50}}$) higher than 50, proving experimentally that such dependency decreases for increasing sediment coarseness ratio (i.e. $\frac{W}{D_{50}} > 50$).

2.4.2 Effects of parameters on local scour

2.4.2.1 Flow intensity and time rate

The first major issue when considering flow intensity and time rate in scour development is the distinction between clear water and live bed regimes. This categorization was firstly performed by Chabert & Engeldinger (1956) according to the approach flow velocity. Clear water scour occurs when sediments move from scour holes and are not replaced by the sediments carried out by the approaching flow, whereas under live bed conditions, the approach flow induces a general movement of sediments leading to a continuous transport of sediments into the scour hole (Richardson & Davis, 1995; Graf, 1998; Melville & Coleman, 2000). The deciding criterion between these two scour regimes is the ratio of the approach flow velocity (V) to the critical velocity (V_c), referring to the velocity for sediment incipient motion - $V/V_c \leq 1$ - clear water scour conditions; $V/V_c > 1$ - live bed scour conditions. Several empirical formulations were derived for estimating the critical velocity (V_c); some of the most used are presented in Subsection 4.2.7.

Different evolution of the scouring hole development is expected. For clear water conditions, the approach flow has no movement of bed particles. The maximum scour depth in the vicinity of the foundation structure increases relatively rapidly in the initial period of the scouring process and then tends to reach a stable solution, an equilibrium scour depth (d_{se}), when the flow can no

longer remove sediment particles from the scour hole. Under live bed conditions, the beginning of the scouring process is characterized by an imbalance between the quantity of material that leaves the scour hole and the quantity of material coming in and produced by the general motion of bed particles in the approach flow, leading to a sudden increase of the scour depth. Therein, a typically cyclic phenomenon is registered due to the interaction between erosion and deposition. A continuous process of adding and removing bed materials into the scour hole occurs until an equilibrium between the amount of sediment being removed from the scour hole and the amount entering is reached. At the end, the scour depth tends to fluctuate around an equilibrium value, also known as a dynamic equilibrium scour depth. In Figure 2.8, examples of two experimental tests performed in laboratory conditions clearly show the different evolution of the scour hole maximum depth with time, where (a) represents the result for clear water and the expected static equilibrium (Sheppard *et al.*, 2004, from Test 10) and (b) the dynamic equilibrium obtained in live bed flow (Sheppard & Miller, 2006, from Test 8). Under live bed sour conditions, the maximum scour depth (d_{sm}) depends on the semi-amplitude of bed forms as explained in the published works of Chee (1982) and Chiew (1984). Bed forms can occur when non-cohesive sediments are subject to currents and/or surface waves. These bed forms are divided mainly into ripples, mega ripples, dunes, sand waves, and antidunes, according to their size, shape, method of generation, among others (Sheppard & Renna, 2010).

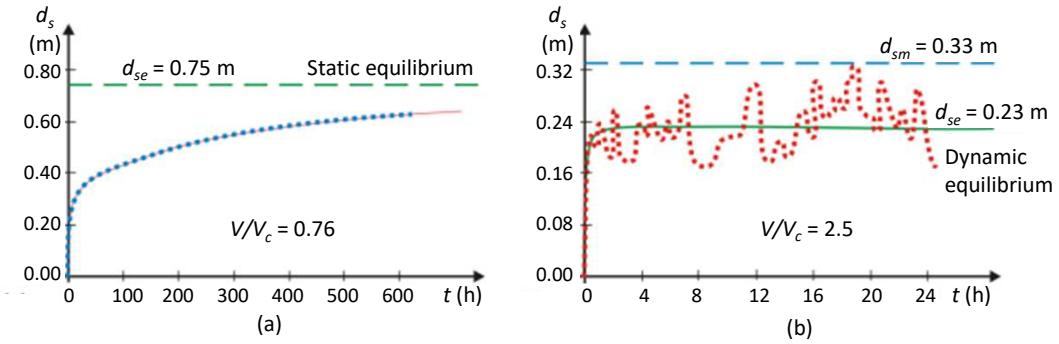

Figure 2.8: Evolution scour depth with time under (a) clear water and (b) live bed regimes, adapted from Moreno (2016).

Time plays an important role in the scouring process, regardless the approach flow regime (clear water *vs* live bed). It is possible to consider the existence of three phases of evolution of the scour depth (Cardoso & Cunha, 1998): (i) initial phase, in which the maximum scour depth increases very rapidly; (ii) development phase, in which the cavity accentuates in depth and in shape extension systematic although at a progressively decreasing pace; and (iii) equilibrium phase, in which the scour hole practically ceases to evolve. This concept of equilibrium condition is, however, somewhat controversial. Some researchers have attempted to establish reliable criteria for equilibrium time in experimental environments for single piers and abutments. Kumar *et al.* (1999) stopped their experiments when the scour depth did not change by more than 1 mm over a period of 3 hours. Melville & Chiew (1999) defined the equilibrium time when the scour depth did not change by more than 5% of the pier diameter (which may also correspond to the pier width

for the current study) over a period of 24 hours. Moreno (2016) discussed the latter criterion for pile-supported piers based on long-duration experiments (about 25 days each). Mia & Nago (2003) stopped their experiments when there was less than 1 mm of scour by 1 hour. As reported by Breusers (1966) and Hoffmans & Verheij (1997), among others, the initial and development phases are, among the three scouring phases, the ones with more considerable scour capacity; with the maximum scour depth ranging from 85 to 95% of the equilibrium scour depth. Regarding the scour regime, the equilibrium scour depths for live bed conditions are slightly smaller than those in clear water cases, as early stated by Breusers *et al.* (1977).

In addition, Hancu (1971) has stated that no scour would exist at bridge piers if the flow intensity is smaller than 0.5 (for $V < 0.5\ V_c$). Others, such as Chiew (1995), have suggested that the critical value of the flow intensity is 0.3, while Hager & Oliveto (2002) indicated that such value depends on the flow contraction (this ratio is, commonly, referred as the condition of scour inception).

2.4.2.2 Flow shallowness

Flow shallowness, h/W, defines the geometric scale of the pier flow field. Melville & Coleman (2000) classified pier scour flow field and correspondent processes in respect to the three classes of h/W (Table 2.1). The ranges in Table 2.1 were derived from laboratory plots as can be seen in Figure 2.9. The same data were also used on the establishment of functional relations for $d_s = function\,(h/W)$ in Table 2.1.

Table 2.1: Classification of local scour processes at bridge piers in terms of h/W (Melville & Coleman, 2000).

Pier class	h/W	Pier scour dependence
Narrow	$h/W > 1.4$	$d_s \propto W$
Transitional	$0.2 \leq h/W \leq 1.4$	$d_s \propto \sqrt{Wh}$
Wide	$h/W < 0.2$	$d_s \propto h$

For narrow piers, the scour depth increases proportionally with pier width (W) and is independent of flow depth (h). The characteristic flow field of this pier category is exemplified in Figure 2.3. For non-single piers, the width (W) should be replaced by the effective width of the pier (W^*) in the evaluation of the pier category (Table 2.1). For instance, the maximum depth of scour at a relatively narrow circular bridge pier is about 2.4 times the pier diameter, irrespective of the flow depth (Richardson & Davis, 2001).

In the transitional pier category, the flow depth influences the local scour depth once the horseshoe vortex is also affected by the formation of the surface roller (previously termed “upflow”). These two vortex systems have opposite directions of rotation. Therefore, the scour depth rely on both h and W (Figure 2.4). According to Melville & Coleman (2000), the local scour depth is independent of flow depth; in other words, the scour occurs at a narrow pier. By decreasing flow depth, the surface roller becomes more prevalent and renders the base vortices less capable of entraining sediment. This trend shows a reduction on scour depth for shallower flows, as mentioned on previous studies of Chabert & Engeldinger (1956), Laursen & Toch (1956), Laursen (1963),

Breusers *et al.* (1977), Ettema (1980), Chiew (1984), and Raudkivi & Ettema (1985). Contrarily, for wide piers, the scour depth increases in proportion to flow depth, regardless of pier width. Figure 2.5 illustrates the correspondent flow field. The scouring process features a zone of slow moving fluid existing at the pier front on the line of symmetry. In this zone, the scour activity is reduced and the central portion of the pier width is ineffective in generating scour. It should be noted that the wider the pier, the deeper the scour hole will be developed even though it requires greater time. Further details on flow field patterns around a pier are given in Subsection 2.3.

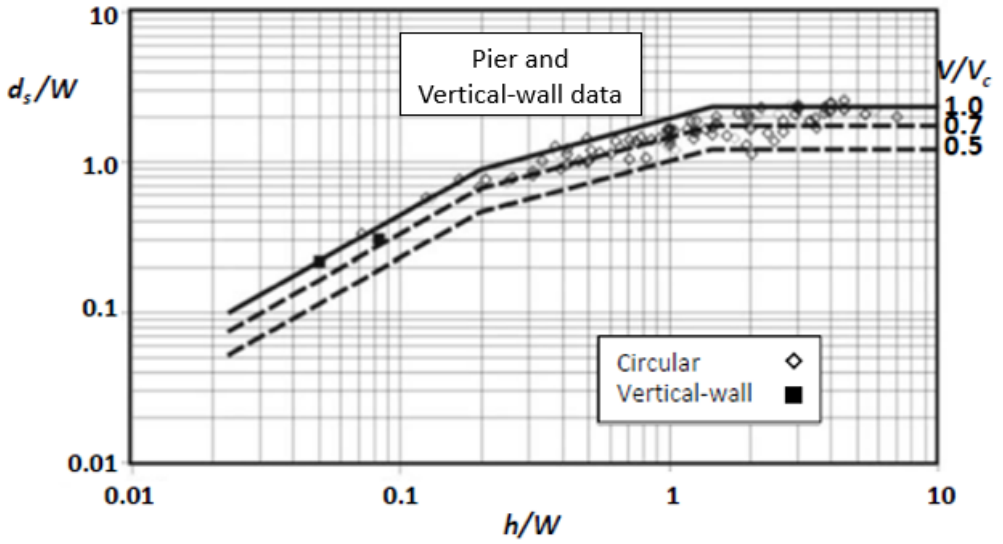

Figure 2.9: Influence of h/W on local scour depth expressed as d_s/W under clear water scour conditions, adapted from Melville & Coleman (2000).

In Figure 2.9, the solid line envelops the experimental data and applies to wide, transitional and narrow pier categories, respectively, under clear water scour conditions. The dashed lines present the scour depths for different flow intensities, showing lesser scour depths for lower values of V/V_c. These lines assume a linear relation between scour depth and flow velocity (Ettema *et al.*, 2011). Under the influence of other parameters, namely sediment gradation, abutment shape and channel geometry, the actual scour depths would be further reduced from the solid one in Figure 2.9. An identical figure applicable to live bed scour conditions has yet to be developed. Such information would aid the scour depth formulation for a typical condition of pier scour.

2.4.2.3 Power of turbulence structures

The turbulence structures in the flow field around a pier may be characterized by two parameters, namely pier Reynolds number (Re_D) and the Froude number (Fr). The former characterizes the relationship between inertial and viscous forces, whereas the latter expresses the frequency of vortex formation and break-up/shedding (Ettema *et al.*, 1998, 2006b).

In several local scouring studies, the dependency of the scour depth on the Reynolds number (Re_D) is assumed to be negligible due to the highly turbulent nature of flow structures around a bridge pier (Manes & Brocchini, 2015; Rogers, 2019). Notwithstanding, the strength, evolution

and instability of the vortices that are developed upstream the pier are well-known to be dependent on the Reynolds number, dictating the momentum transfer mechanisms at the sediment-flow boundary (Ettema *et al.*, 2011). Early works performed by Shen *et al.* (1970) have demonstrated some dependency of the scour depth on Re_D due to its effect on both the size and strength of the horseshoe vortex. Ettema *et al.* (2006b), in turn, have observed that vortex dependency on Re_D is extandable to the piers' wake. They also noticed the ability of the wake vortex system to move the sediment for narrower piers is also increased which can induce distorted scour depths when scaled to field equivalents.

Few studies have considered the implications of viscosity forces on the scouring development processes. However, Lança *et al.* (2016) performed a dimensional analysis in which the viscosity effects were separated. It was shown that the flow viscosity plays a minor, yet important, influence on the scour depth. The authors also state that an assumption of negligible viscosity influence assumes a fully-rough turbulent approach flow, where the critical shear stress (as first introduced by Shields (1936)), is independent of the particle Reynolds number ($Re^* = \frac{u^* D_{50}}{\nu}$, being u^* the shear velocity and ν the kinematic viscosity of the water). Fully-rough conditions are applicable to sediments defined as very coarse sand or gravel, while most experimental research into scour has typically used fine to medium sands (defined within the transitionally-rough regime). As such, it is very plausible that there is some dependency of the scour depth on viscosity.

The Froude number, in turn, can be interpreted as expressing the vorticity of wake vortices. Ettema *et al.* (2006b) have identified that narrower piers yield stronger eddies relative to their large scale counterparts, for the same approach flow. They also pointed out the difficulty in simultaneously satisfying the three length scales, such as h, W and D_{50} in flume experiments and in field. Thus, small model piers are seen to have a greater potential for the flow to remove sediment away from the scour hole. Although adjustment factors to account for this eddy scaling concern have been developed, their inclusion has yet to be validated using field data and thus the physics underlying the proposed adjustment are not well understood.

2.4.2.4 Sediment non-uniformity

The effect of sediment non-uniformity on local scour depth has been tackled from early laboratory studies undertaken, among others, by Ettema (1976) and Ettema (1980) under clear water conditions as well as by Chiew (1984) and Baker (1986) under live bed conditions. Moreno (2016) has plotted the relative equilibrium scour depth (d_{se}/W) as a function of σ_D for laboratory studies with cylindrical piers, $D_{50} \geq 0.6$ mm, $h/W \geq 2$, $0.8 \leq V/V_c \leq 1.0$ and $30 \leq W/D_{50} \leq 100$. For uniform bed mixtures, i.e. $\sigma_D \leq 1.50$, d_{se}/W is assumed constant. Conversely, for non-uniform bed mixtures, selective sediment transport of the finer sediment grains typically occurs for flow velocities smaller than the critical velocity, associated with D_{50}. The distinct threshold conditions for sediment transport leads to the development of a superficial armour layer (Subsection 2.2.5.4), composed by the coarser grains that in the end inhibits sediment transport as well as the development of scour holes (even partially). For such cases, a general decrease trend of the relative equilibrium scour depth (d_{se}/W) was observed for increasing values of σ_D for clear water conditions (Cheng

et al., 2020, and references therein). Under live bed conditions, a decrease trend of d_{se}/W with increasing values of σ_D was also found, albeit not so pronounced as in the clear water condition cases.

Figure 2.10 schematically summarizes the trends associated with varying flow intensities (V/V_c). Near the threshold condition ($V/V_c \approx 1$), armouring occurs on the approach flow bed and at the base of the scour hole. The armoured bed in the erosion zone, at the base of the scour hole, significantly reduces the local scour depth. Contrarily, at higher values of V/V_c, the flow is capable of entraining most grain sizes within the non-uniform sediment, at which stage sediment non-uniformity has only a minor effect on the local scour depth. At the intermediate values of flow intensity, the effect of σ_D reduces progressively with increasing flow velocity between these two limits, as more grains are transported by the flow (Ettema *et al.*, 2011).

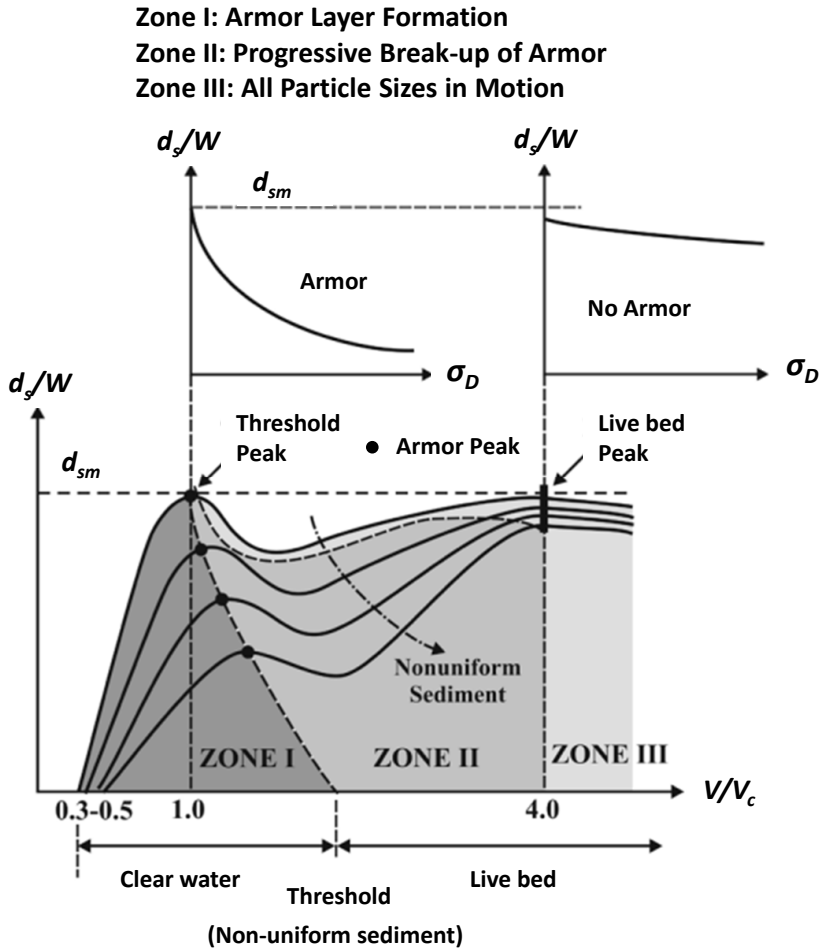

Figure 2.10: Local scour depth variation with sediment non-uniformity, adapted from Melville & Coleman (2000).

2.4.2.5 Sediment coarseness

Possibly one of the most influential parameter relating to sediment size is the ratio of the pier width (W) to median diameter of the bed material (D_{50}). This relationship is commonly called sediment coarseness. Numerous researchers have devoted their studies to explaining the relationship between W/D_{50} and relative scour depth d_{se}/W.

Results from small-scale experiments have shown that the scour depth is only affected by the sediment coarseness if the sediment is relatively large, for uniform sediments ($\sigma_D \leq 1.50$). For smaller values of W/D_{50}, individual particles are large relative to the groove excavated by the downflow and erosion is impeded because the rough and porous bed dissipates some energy of the downflow (Ettema *et al.*, 2011). For $W/D_{50} < 8$, individual particles are so large relative to the pier that scour is mainly due to erosion at the sides of the pier and scour is further reduced (Melville & Coleman, 2000). For the range $8 < W/D_{50} < 50$, the sediment diameter is large relative to the scour hole dimension and erosion is impeded due to the porous bed which dissipates the horseshoe vortex strength (Ettema *et al.*, 2011; Moreno, 2016). In an intermediate zone, characterized by $50 < W/D_{50} < 100$, the sediment is entrained mainly from the groove with only a limited entrainment under the horseshoe vortices. The sediment supply to the groove is achieved by sliding down the lateral slope in the hole. Such range of sediment coarseness is characterized by a decrease in relative scour depth (Figure 2.11).

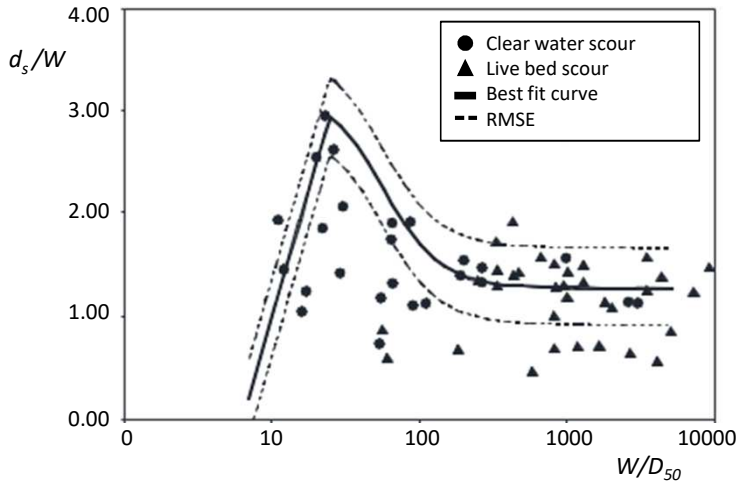

Figure 2.11: Relative scour depth (d_s/W) as function of W/D_{50} for clear-water and live bed field, adapted from Lança *et al.* (2013). *RMSE* denotes Root Mean Square Error.

Recent large-scale studies (Sheppard & Glasser, 2004; Lee & Sturm, 2009; Sheppard & Renna, 2010; Lança *et al.*, 2011, 2013), have shown that for $W/D_{50} > 50$, the relative scour depth decreases significantly and eventually plateaus around 1.4 for $W/D_{50} > 400$. Such a reason is not yet well understood. As field sites presents particularly high values of W/D_{50} relative to small-scale laboratory studies, this lack of understanding raises concerns that the true behaviour of field scour may be poorly accounted for in empirical predictive models.

2.4.2.6 Pier face shape

Pier's face shape has influence on the depth and geometry of the scour hole. The basic face shapes are illustrated in Figure 2.12. It is known that the degree to which a pier face shape is aerodynamic greatly influences the frequency of vortex shedding and the amount of vorticity in the wake of a pier (Ettema *et al.*, 2006b). Diab (2011) has experimentally investigated the scour hole development around piers of different shapes in gravel and sand beds. The same researcher has observed that steeper scour slopes and higher gradients of the scour hole bottom were encountered for square piers shape. The longitudinal extent of the scour hole at square and rectangular pier was roughly 50% longer than at circular pier. The effect of more complex shapes, composed by column, pile cap and piles, are addressed in Ettema *et al.* (2011).

The shape effects for the pier face are commonly given as a multiplying factor (K_1), which accounts for the difference in local scour between a particular pier shape and a circular pier, subject to the narrow pier category (Table 2.1). The factor K_1 is less accurate for transitional piers and might not be applied for the wide pier category (Ettema *et al.*, 2011). Researchers such as Chabert & Engeldinger (1956), Laursen & Toch (1956) and more recently Fael *et al.* (2014) and Fael *et al.* (2016), among others, have published such multiplying factors. Moreno (2016) performed a compilation of the variation of the shape factor as a function of L/W for rectangular piers, oblong piers, lenticular piers and elliptical piers.

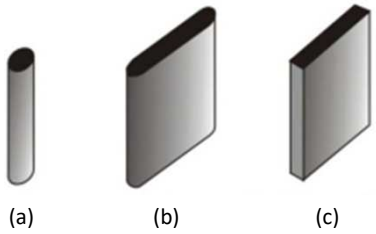

Figure 2.12: Basic single pier shapes: (a) single cylindrical, (b) oblong, and (c) rectangular (Sheppard *et al.*, 2011).

2.4.2.7 Pier aspect ratio

Pier aspect ratio, W/L, defines the ratio between the width and the length of the pier and Mostafa (1994) has proposed the influence of such ratio depending on the cross-sectional shape of the pier for equally effective pier width (piers of the same projected width to the flow - Figure 2.13).

Figure 2.13: Cylinders differing in cross-sectional shape, but having the same projected width to the flow, adapted from Mostafa (1994).

For identical projected pier width (W^*) Mostafa (1994) showed significant variations of the scour depth. Such differences are due to variations in the flow field developed by each cylindrical form (Ettema *et al.*, 2011). More research should be devoted to document flow field changes and associate them to scour depth. However, this issue is beyond the scope of the present work.

2.4.2.8 Pier alignment

The pier alignment strongly influences the local scour depth at piers of all shapes except the circular one. The skew angle (θ), also know as the alignment angle, is the one defined between the pier axis and the approach flow direction. As θ increases, scour depth increases since the effective width of the pier is also increased.

A multiplying factor to account for the influence of the pier alignment on the scour depth for non-circular piers (K_2) is greatly recommended (Figure 2.14). The alignment factor values have resulted from Laursen & Toch (1956) study for rectangular piers by normalization of the measured scour depth by the corresponding depth for $\theta = 0^\circ$. The factor K_2 increases with θ until the alignment reaching a maximum value, which occurs when the projected width of the pier (or equivalently, effective pier width) is the largest (Ettema *et al.*, 1998). Moreno (2016) presents illustrative diagrams of scour hole around rectangular piers oriented in different angles to flow direction.

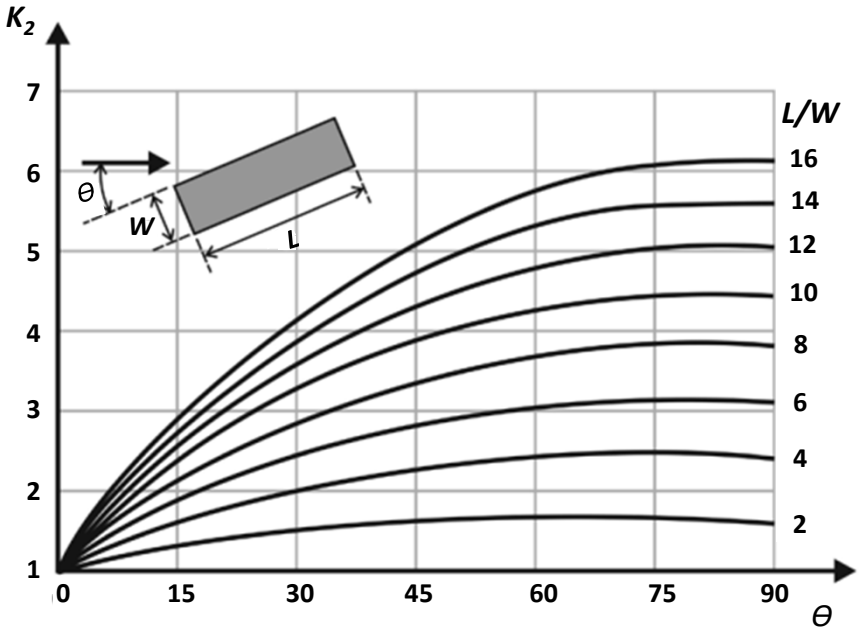

Figure 2.14: Local scour depth variation with pier alignment, adapted from Melville & Coleman (2000).

2.5 Erosion and Scour Prediction

2.5.1 Introduction

The complexity of flow dynamics at hydraulic structures hinders the theoretical estimation of the scouring process. Moreover, the criteria for assessing and estimating the process of scour also depend on the type of scour. Different scour types have different affecting factors involved (presented in Section 2.4), resulting in different formulas for scour depth prediction (Arneson *et al.*, 2012, among others). In order to fully evaluate the nature of scour problems it is, thus, important to take into account the hydraulic and structural issues as well as the complexities of the channel morphology and sediment/soil disposition. This section concentrates on existing formulas for general erosion, contraction scour, and local scour (pier and abutment) treated as they occur independently (without interaction). Detailed investigation on the relationships among individual scour components for the same aproach flow at a bridge site may be found in Sturm *et al.* (2018).

2.5.2 General scour

There are a variety of factors that influence the magnitude of general scour in a riverbed and consequently its stability. Bettess (2002), for instance, pointed out the change in the flow section area and in discharge, the sediment grading, the upstream sediment supply and the flow duration.

Lauchlan & May (2002) summarized several general scour prediction equations and gave special emphasis to a particular empirical formula, the Blench (1969)'s formula (Equation 2.3). Equation 2.3 depends on the flow discharge per unit width of the main channel (q) and on the median sediment diameter (D_{50}). These empirical formulas, however, have usually certain limitations on their application due to the scale effect; the time scale is, for instance, of the order of several years or longer, and include progressive degradation or aggradation of the channel bed, and lateral riverbank scour due to channel widening or meander migration (Ettema *et al.*, 2006c).

$$d_{ms} = \begin{cases} 1.20 \left[\dfrac{q^{2/3}}{D_{50}^{1/6}} \right], & \text{for sand bed of } 0.06 < D_{50} \leq 2 \text{ mm} \\ 1.23 \left[\dfrac{q^{2/3}}{D_{50}^{1/6}} \right], & \text{for gravel bed of } D_{50} \geq 2 \text{ mm} \end{cases} \tag{2.3}$$

According to Lu *et al.* (2012), a lack of accurate field data measurements in intermittent rivers with relatively steep slopes does exist. The same authors have measured the eroded flow depth and the maximum scour depth during the peak flow of a single flood on both sand and gravel riverbeds material. The investigation ended with the derivation of an empirical formula (Equation 2.4) for predicting the short-term general scour for the high gradient intermittent rivers. In line with their investigation, besides the discharge per unit width for the main channel (q) and the median sediment diameter (D_{50}), the short-term general eroded flow depth (d_{ms}) also should be related to the bed slope (S_0) and the geometric standard deviation of the bed material (σ_D). This new formula brings

more tools to engineers for bridge design and safety evaluation, although further field data should be tested to improve such prediction.

$$d_{ms} = 1.26 \left[\frac{q^{0.80} S_0^{0.27} \sigma_D^{0.74}}{D_{50}^{0.23}} \right] \tag{2.4}$$

2.5.3 Contraction scour

The prediction of the contraction scour is normally separated into the two flow conditions: clear water scour and live bed scour. The clear water contraction scour occurs when the bed material sediment transport in the uncontracted approach section is less than the carrying capacity of the flow (Arneson *et al.*, 2012). On the other hand, live bed contraction scour occurs when bed material is already being transported into the contracted bridge section from upstream of the approach section. The equation derived by Laursen (1963) is commonly used for the determination of the critical velocity, V_c:

$$V_c = K_u h_1^{1/6} D_{50}^{1/3} \tag{2.5}$$

where h_1 stands for the average depth in the main channel, and K_u is dependent on the mode of sediment transport.

The predictor of the average depth after scour in the contracted section (h_2) for steady uniform flows and simple geometries is given by Equation 2.6, depending on the flow regime; the expressions follow the recommendations of Richardson & Davis (2001). The depth of contraction scour (d_{cs}) is given by the simple equation: $d_{cs} = h_2 - h_1$.

$$h_2 = \begin{cases} 0.13 h_1 \left[\dfrac{Q_2}{D_m^{1/3} h_1^{7/6} W_2} \right]^{6/7} - h_1, & \text{clear water contraction scour} \\ h_1 \left[\dfrac{Q_2}{Q_1} \right]^{6/7} \left[\dfrac{W_1}{W_2} \right]^{K_1}, & \text{live bed contraction scour} \end{cases} \tag{2.6}$$

For the clear water contraction scour, Q_2 is the flow discharge in the main channel at the contracted section, D_m is the effective mean diameter of the bed material (D_m = 1.25D_{50}), W_1 is the approach channel width, W_2 is the bottom width of the main channel at the contracted section (subtracted from the pier widths). Regarding the live bed contraction scour, Q_1 stands for the flow discharge in the main channel at the approach section and k_1 is an exponent for mode of bed material transport (Sheppard & Renna, 2010).

2.5.4 Local scour

Once significant uncertainty is inherent to flow and bed material at bridges waterways, design prudence requires the estimation of a potential maximum scour depth. This means the highest scour depth attainable for a given flow field, and may be computed using the parameters identified in Subsection 2.4.1. Several equations have been proposed for estimating the equilibrium scour depth

through the decades, which prediction ability is nearly good especially for structures of relatively simple geometry.

In Ettema *et al.* (2011) work, two well established equations are recommended in bridge design, namely HEC-18 scour depth predictor (Arneson *et al.*, 2012) and the S/M equation, given below by Equations 2.7 and 2.8, respectively.

$$\frac{d_{se-HEC18}}{W} = 2K_1K_2K_3K_w\left(\frac{h}{W}\right)^{0.35}Fr^{0.43}, \tag{2.7}$$

$$\frac{d_{se-SM}}{W^*} = \begin{cases} 2.5f_1f_2f_3, & 0.47 < \dfrac{V}{V_c} < 1.0 \\ f_1\left[2.2\left(\dfrac{\dfrac{V}{V_c}-1}{\dfrac{V_{lp}}{V_c}-1}\right)+2.5f_3\left(\dfrac{\dfrac{V_{lp}}{V_c}-\dfrac{V}{V_c}}{\dfrac{V_{lp}}{V_c}-1}\right)\right], & 1 < \dfrac{V}{V_c} < \dfrac{V_{lp}}{V_c} \\ 2.2f_1, & \dfrac{V}{V_c} > \dfrac{V_{lp}}{V_c} \end{cases} \tag{2.8}$$

In Equation 2.7, $d_{se-HEC18}$ is the equilibrium scour depth at the pier front given by HEC-18 (Arneson *et al.*, 2012) and Fr is the Froude number ($Fr = V/\sqrt{gh}$). The factors K_1, K_2 and K_3 account for pier shape, pier alignment and bed forms, respectively (given in Arneson *et al.* (2012)). This equation was derived from a set of laboratory data for circular piers, selected from Chabert & Engeldinger (1956) and Colorado State University (Shen *et al.*, 1966). The HEC-18 method has been progressively modified over the years and is currently recommended by the United States of America Federal Highway Administration (FHWA) for estimating equilibrium scour depths at simple piers (Richardson & Davis, 1995, 2001; Arneson *et al.*, 2012). It also includes a multiplying factor (K_w) to account for the wide pier category, developed by Johnson & Torrico (1994). This equation can also be adapted for more complex (3-element) substructure configurations, multiple columns skewed to the flow, estimating scour from debris on piers and scour in tidal waterways.

Sheppard *et al.* (2011) developed a new equation by melding the Sheppard's (Sheppard & Miller, 2006) and Melville's (Melville & Raudkivi, 1977) predictors, referred as Sheppard/Melville (S/M) equation (Equation 2.8). The variables f_1, f_2, and f_3 represent the interactions of flow-structure, flow-sediment, and sediment-structure, respectively (given in Sheppard *et al.* (2011)) and V_{lp} is the live-bed peak velocity, estimated using Van Rijn *et al.* (1993) equations for determining plane bed velocity (i.e., coincident with an upstream flat bed stage of sediment transport); the larger of $V_{lp} = 0.6\sqrt{gh}$ or $V_{lp} = 5V_c$ is assigned as the V_{lp} value. The S/M equation (Equation 2.8) has been recommended since it better reflects the physical mechanisms and parameters that influence the pier scour depth, as well as due to its large database, specially covering piers of various width classes. Such method reduces over-predictions and the unwarranted need for countermeasures. The developed equation uses the effective pier diameter (W^*) as the diameter of a circular pier which will experience the same equilibrium scour depth as the subjected structure under the same flow

and sediment conditions. Also, a set of equations relying on bed material mobility is included, which make it suitable for both laboratory and field data (Sheppard *et al.*, 2011). Equations 2.7 and 2.8 might be applied for both clear water and live bed scour conditions.

Researchers as Coleman (2005), Ataie-Ashtiani *et al.* (2010) and Moreno *et al.* (2016b); Moreno (2016); Moreno *et al.* (2017) have focused their studies on the prediction of the equilibrium scour depth around pile groups and complex piers. In Moreno (2016) and Moreno *et al.* (2016b), an extensive research to systematically map equilibrium scour at pile-supported piers was developed. Among the conceptual approaches, the new formulation for predicting the equilibrium scour depth at complex piers have shown better performance (in terms of accuracy). This predictor was derived by integration and adjustment of the equations developed by Sheppard *et al.* (2014) and Lança *et al.* (2013) for cylindrical piers to pile-supported piers, wherein the pier diameter was replaced by the equivalent diameter (D_e). Regarding the position of the pile cap top (H_c, for the pile-supported piers therein studied), d_{se} changes markedly. Moreno (2016)'s predictor was based on an extensive experimental campaign performed in the tilting flume located in the experimental facilities of the National Laboratory of Civil Engineering (LNEC) in Lisbon (Portugal).

In the research project conducted by Sheppard *et al.* (2011), methods and procedures for predicting time-dependent local scour at wide piers and at long skewed piers were also developed for non-cohesive sediments and steady flow conditions. They state that the current methods for predicting local scour at bridge piers, including those described in HEC-18 (Arneson *et al.*, 2012), generally over-predict local scour at such piers, leading to the use of unwarranted and costly foundations or countermeasures. The literature review undertaken within that project revealed a scarcity of information regarding predictive equations and data for related piers. Most of the temporal scour predictions at the vicinity of bridge foundations were derived from laboratory experiments, simulated in simplified conditions that not always replicate the complexities of bridge sites. However, the predictive equations in the literature are intended to apply equally well to large as well as small piers (Harrigan, 2012). Those researchers have evaluated both the equilibrium scour (addressed above) and scour evolution equations, in an initial phase, and then made improvements to the best performing equations/methods for a significant quantity of both laboratory and field equilibrium scour data. The research has contributed for the derivation of an equation that predicts the time-dependent local scour (Equation 2.9), with d_{se-SM} and K_t as given in Sheppard *et al.* (2011).

$$d_{s-MS} = K_t d_{se-SM} \tag{2.9}$$

It is worth to mention that Melville & Raudkivi (1977)'s equation was developed for clear water scour, whilst the S/M equation (Equation 2.8) seems to predict equally well for live bed scour data. Since time to equilibrium is somewhat misleading, Sheppard *et al.* (2011) have derived an expression for the time required to reach 90% of the equilibrium scour depth, t_{90}, in terms of the reference time t_r and the flow intensity (Equation 2.10).

$$t_{90} = exp\left(-1.83\frac{V}{V_c}\right) t_r \tag{2.10}$$

Many researchers have given more emphasis on local scour around bridge piers while others at the vicinity of abutments. A review of scour estimation difficulties at bridge abutments was carried out by Ettema *et al.* (2004b).

2.6 Numerical Modelling

2.6.1 CFD analysis

Computational Fluid Dynamics (CFD) analysis aims at a deeper understanding of the scouring problem by means of numerical simulation to study and forecast future outcomes, by capturing the essentials of the real response of such an issue. In a fluvial environment, the flow is assumed incompressible; therefore, many successful numerical methods developed in CFD may be applied. However, the river flow has a free surface and movable bed, which make the numerical simulation relatively complicated and difficult. Some assumptions and empirical formulas are normally used to close the mathematical systems and the approximate solution sought may not be unique. Thus, a simulation requires a good knowledge about numerical techniques as well as enough experience/sensibility to scouring processes.

According to Moges (2010), the reliability of numerical simulations deeply relies on the following items: (i) how well the physical processes are mathematically described through governing equations, boundary conditions, and empirical formulas; (ii) how accurately the differential governing equations are discretized using numerical schemes; (iii) how effectively the discretized algebraic equations are solved using direct or iterative solution methods; and (iv) whether the numerical solution procedures are correctly coded.

Regardless of the numerical tool selected, the CFD model analysis may be subdivided into five major components, namely (i) Problem definition, (ii) Mathematical modelling, (iii) Pre-processing and mesh generation, (iv) Algebraic equations system solving, and (v) Post-processing. Some of these components must be performed several times in order to finally obtain results of the desired quality (see Figure 2.15).

A proper definition of the scouring problem is necessary, which should attain the simplest form without compromising the accuracy of the real phenomenon in question. Some of the system features and its behaviour might include: dimensionality; steady, quasi-steady, or unsteady; laminar or turbulent; subcritical, supercritical or mixed; gradually or rapidly varied flow; fixed or movable bed; bed load, suspended load, or total load; low or high sediment concentration; uniform and multiple sediment sizes; equilibrium or non-equilibrium transport; cohesive or non-cohesive; and, initial and boundary conditions.

Once a clear **problem definition** is done, it has to be formulated mathematically by using a set of algebraic and differential equations that are subject to the conservation laws of mass and momentum. The solver choice requires a good understanding of the models used to describe different physical phenomena. Choosing the right one is fundamental for obtaining a valid solution to the simulated problem. The mathematical model describes the details of the flow, which means that the numerical simulation, that only approximates the solution of the model at best, cannot

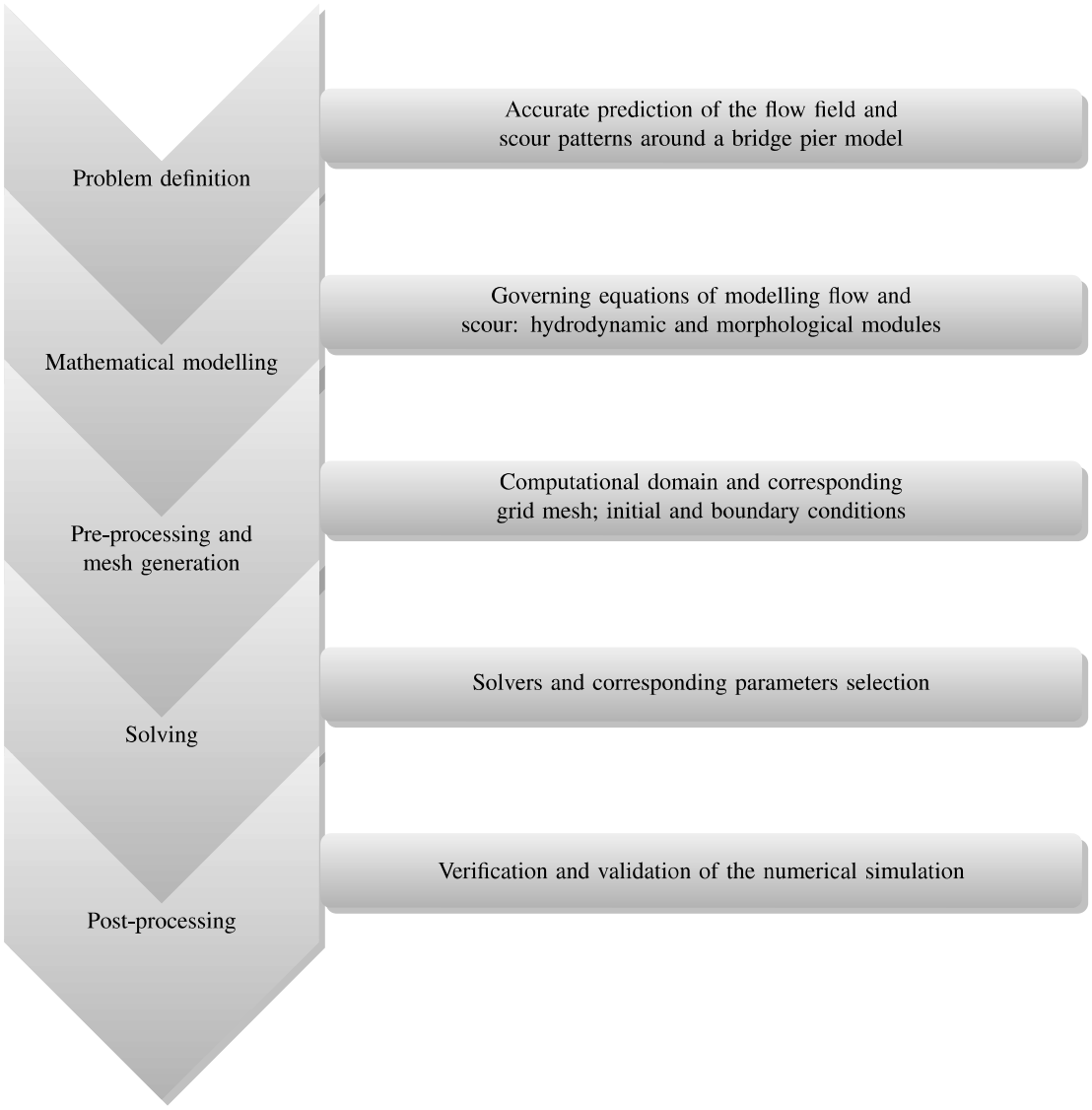

Figure 2.15: Steps in numerical simulation applied for a bridge pier scour problem.

produce more information about the flow than described by the model itself. The numerical consideration of the flow, sediment transport and morphological change processes in the study of local scour are generally done by considering a hydrodynamic module and a morphological module, respectively.

The **hydrodynamic module** solves the Navier-Stokes equations for the flow field whilst the sediment-laden flow may be treated as either a two-phase flow, which includes the water and the sediment phase, or a one-phase flow, in which the two phases are modeled as a mixture. The two-phase flow model can be classified as the Euler-Euler type and the Euler-Lagrange type. The former describes the dispersed phase in a similar way to the one used for the continuous phase and efforts have been directed to this type of model by Li *et al.* (2008), Jha & Bombardelli (2010), and Chen *et al.* (2011). As indicated by Chen *et al.* (2011), the Euler-Euler type of the two-phase model is particularly complex. It needs to solve the continuity and momentum equation for both

of the phases. The Euler-Lagrange type, in its turn, treats the sediment phase as motions of a certain number of individual particles. This approach requires a rather large number of particles to correctly simulate practical problems and this also needs large computational resources and time. Though the successful studies proposing such approach (Li *et al.*, 2014; Finn *et al.*, 2016; Sun & Xiao, 2016) in hydraulic applications - including the estimation of scour holes - the one-phase flow is generally used.

The major advantage of the one-phase model consists on neglecting the dispersed phase effects on the continuous phases, and solving the volumetric concentration of the dispersed phase by using an advection-diffusion model. Roulund *et al.* (2005) have applied the advection-diffusion model with considerable success. Notwithstanding, the advection-diffusion model is only valid for cases where the suspended load concentration is not large enough to influence the main properties of the flow field.

Other concern regarding the hydrodynamic module consists on the way the **free surface** effects are included in the model. When the flow encounters the obstacle (in this case, a bridge pier) the interface between water and air varies, causing fluctuations in the flow depth (h). For higher variations, compared with flow depth, the free surface effects have an important influence on the flow field and consequently on scour evolution. Such situation is what typically occurs in scour problems, and many numerical models for flow and scour issues include the free surface effect in the model (Liu & García, 2008).

The effective representation of **turbulence** is another issue concerning the hydrodynamic module. While increased energy dissipation caused by turbulence at the boundary shear flows such as in pipes or open channels is well known (Chen & Wu, 2019), its contribution to enhanced mixing and transport of sediment is a subject of continuing research (Kyrousi, 2017). One of the confounding aspects of turbulence with respect to CFD models is that its properties include a wide range in the physical size of eddies, from large-scale eddies (given by the integral scale l) that depend on the geometry of the flow domain to the smallest sizes (given by the *Kolmogorov* length η), where viscosity becomes relevant due to high gradients and kinetic energy is irreversible converted (dissipated) in internal energy (Pope, 2000, and references therein). Because the ratio of large-scale to small-scale eddy sizes increases with increasing Reynolds number, modelling high Reynolds number turbulent flows in hydraulic engineering becomes particularly challenging. There are mainly three approaches: Direct Numerical Simulation (DNS), Large Eddy Simulations (LES) and Reynolds-Averaged Navier-Stokes (RANS), as exemplified in Figure 2.16.

A direct numerical simulation (DNS) of the full Navier-Stokes equations resolves the whole range of spatial and temporal scales of the turbulence. For practical engineering applications, where the Reynolds number is large, this approach requires large computational time and resources, rendering it only suitable for simple geometry cases of basic fluid mechanics research. The wide application of Large Eddy Simulation (LES) for the computation of unsteady turbulent flows, which are three-dimensional and have strong separation and vortex shedding features, has been well documented in the literature and lies between the DNS and the RANS approaches (Rodi, 2017). In LES, the unsteady dynamics of the energetically important scales in the flow is directly

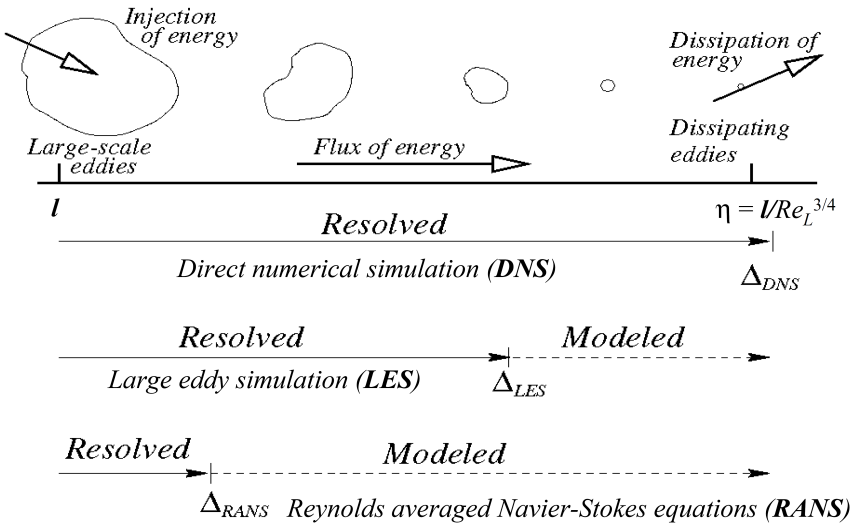

Figure 2.16: Schematic view of the differences between DNS, LES, and RANS methodologies (from André Bakker's lectures: `https://www.bakker.org/Lectures-Applied-CFD.pdf`).

computed and only the effect of the filtered (small) scales on the resolved sub-grid are modelled (Sturm *et al.*, 2018). Generally, the flow through a square cylinder is used as a benchmark case for testing various sub-grid scale models of LES (Rodi *et al.*, 1997; Sohankar *et al.*, 1999, among others). The numerical results are comprehensive and are frequently compared with experimental works such as the ones of Durão *et al.* (1988) and Lyn *et al.* (1995). Other works have employed the time-averaged form of the Navier-Stokes equations (RANS or URANS), which requires less computational time than the previous DNS method, LES model or even Detached Eddy Simulation (DES) model.

Detached Eddy Simulation (DES) is an hybrid method that combines the solutions of the RANS equations in the entirely boundary-layers with the solutions of the LES equations in the separated regions. Regions where the turbulent length scale is less than the maximum grid dimension (such as regions near solid boundaries) are assigned with RANS model. As the turbulent length scale exceeds the grid dimension, the regions are solved using the LES model. Within such model, the grid resolution is rather less demanding as pure LES, reducing significantly the computational cost. Since DES was originally formulated by Spalart *et al.* (1997) to resolve separated flows of high Reynolds number, Nikitin *et al.* (2000) have employed DES as a wall-modeled LES in calculations of the channel flow at a wide range of Reynolds numbers without introducing any complexity. Generally speaking, DES model is applied as a plausible Subgrid-Scale (SGS) model in the LES of channel flow and it acts as both RANS and LES models for the near-wall layer and outer flow, respectively.

By using the time-averaged equations, each instantaneous quantity is, therefore, decomposed into its time-averaged and fluctuating components. The turbulent fluctuations are also averaged over time and presented by the Reynolds stress terms, which has to be modelled independently by

a turbulence model (Alemi & Maia, 2016). On the other hand, an unsteady state solution of the time-averaged equations (URANS) of the flow field might integrate the vortex shedding effects while the steady state solution (RANS) has no ability to incorporate those effects on the local scour prediction. It should be noted that a larger computational time is required for the unsteady state. Several studies have analysed the influence of the choice of turbulence model on the results of scour simulations. For instance, Aghaee & Hakimzadeh (2010) simulated the scour caused by the presence of bridge piers with RANS and LES turbulence models and concluded that although LES simulates the flow more accurately, RANS gives satisfactory estimates of scour development. The main disadvantages of the RANS approach is that it cannot accurately predict massively separated flows and flows in which large adverse pressure gradient are present (Sturm *et al.*, 2018), both of which are present in the flow past a bridge pier.

The turbulence characteristics have, thus, significant role towards the mobility of sediment particles inside the scour hole. The scour simulations are dependent on the **morphological module**. Usually, it includes a sediment transport model and a mass conservation equation (known as Exner equation) to compute the bed level change (Fukuoka, 2013). The sediment transport model usually includes bed and suspended load. As previously mentioned, the suspended load in scour problems is often resolved by the advection-diffusion model, with a reference concentration given at a certain reference height (Zhou, 2017). Such reference concentration can be estimated by empirical models of sediment entrainment, such as the ones of Rijn (1984) and Garcia & Parker (1991). For estimation the bed load, Hassanzadeh (2007) has proposed many empirical formulas, relying most of them on the bed shear stress.

The study domain must be discretized in order to approximate the model solution numerically. The spatial discretization of the simulation domain consists on separating the study domain into a grid mesh composed by volumes (cells). All of these volumes taken together are referred to as the **computational domain**, as shown in Figure 2.15. Usually, the grid mesh must be refined in the area of most interest, i.e, where large gradients of field values are expected to occur. Increasing the mesh resolution for transient simulations might slow down the simulation due to a very small value, set for the discrete time step in order to obtain a stable solution, when explicit discretization schemes are used. The cells size is quite important with respect to accuracy and convergence of the numerical algorithms used in the approximation and solution of the governing equation - **Mathematical modelling** in Figure 2.15.

Besides the mesh generation, the **solving** step is the most time consuming task of a CFD analysis. The time required highly depends on the mathematical model, the numerical scheme used to approximate its solution, as well as the geometrical and topological nature of the computational mesh. Herein, the differential (analytical) model gets replaced by a system of (linear) algebraic equations. These algebraic equation systems are solved using algorithms developed especially for this purpose.

After the simulation finished successfully, the data must be visualized and analysed in order to inspect the details of the simulated problem. At this point, it is necessary to determine if the results are trustful. Considering that many empirical formulas are used to close the mathematical

problems, the applicability of such computational simulation needs to be verified and validated.

The **verification** is normally done by analytical solutions. The agreement between analytical and numerical solutions should certify the correctness of the mathematical formulation, numerical methods, and computer programming. It may also determine errors of numerical solution quantitatively, by analysis of the residual values. The residual is one of the most fundamental measures of an iterative solution's convergence since it quantifies directly the error in the solution of the system of equations. It measures the local imbalance of a conserved variable in each control volume. Thus, every cell in the model has its own residual value for each of the equations being solved, which never reaches the exact value of zero. As the iteration proceeds, the variables converge to their final solution and the residuals decrease. Furthermore, the lower the residual value is, the more numerically accurate is the solution. The maximum acceptable residual levels depends on the CFD tool and on the variable under analysis (Date, 2009). Maximum acceptable residual levels should be established according to the the CFD tool in use and the variable under consideration (Olsen, 2018a).

Regarding the **validation** of the numerical model, two types of validation might be performed. Since the laboratory experiments are usually conducted in controlled environments, the numerical model should be able to reproduce the same physical phenomena measured in laboratories. On the other hand, the validation can also be done by field measurements. For this case, a portion of the field data should be used to calibrate the physical parameters in the model and the remaining data can be used to determine whether the computational domain can simulate the real problem. It should be noted that the numerical results may only approximately agree with the measured data, since the computational model only represents a simplified version of the physical processes in natural rivers. However, the realistic trend of spatial and temporal variations should be correctly predicted. If the simulation results are unsatisfactory, the previous steps of CFD analysis must be revisited and improved.

2.6.2 Numerical studies

Briley & McDonald (1981) made numerical solutions of the compressible Navier-Stokes equations for a laminar steady horseshoe vortex at the junction between an elliptic strut and a flat plate whilst Kwak *et al.* (1986) computed the laminar steady junction flow using a three-dimensional incompressible Navier-Stokes code. However, when the flow is turbulent, the computational prediction of the separation flow is a process of crucial relevance. The physical phenomenon that arises is a matter of concern in many engineering components and systems; for streamlined car bodies, low-pressure turbine blades and highly loaded aircraft wings, among others, the flow separation may influence significantly its respective ability for an effective performance. The fluctuation of turbulent flows on a wide range of time and length scales makes its numerical computation difficult and requires a specific way to model that turbulence. RANS (Reynolds-averaged Navier-Stokes) are such model equations and were employed in the first application of CFD tools, by Deng & Piquet (1992), to study the three-dimensional turbulent flow around an airfoil. The adoption of an iterative fully decoupled technique to compute the RANS equations

revealed an interesting approach to capture the main features of horseshoe vortices although lacking some accuracy on modelling the scour process. The rapid development of computer science has widened the application of numerical methods in many fields, for instance, for studying the local scour phenomena, as it boasts such advantages as high precision, low expenses, and modelling scale independence (Zhang *et al.*, 2017). In recent years, several numerical models have been constructed for simulating the 3D flow field and bed morphological changes around circular piers. Olsen & Melaaen (1993) were among the first to predict local scour developing processes by combining the three-dimensional flow field with a sediment transport model around a circular pier.

Another computational study about flow around circular cylinders was carried out by Beaudan & Moin (1994). Nakamura *et al.* (1996) studied numerical and experimentally the vortex shedding from a rectangular pier. Yulistiyanto *et al.* (1998) simulated the flow over a cylinder on shallow-water. The work of Olsen & Melaaen (1993) was limited to the initial stage of scouring while the entire scour process was contemplated by Olsen & Kjellesvig (1998), where good qualitative and quantitative agreement with the experimentally measured scour patterns were achieved. Richardson & Panchang (1998) conducted three-dimensional simulations of the flow around a circular cylinder with fixed scour holes at an intermediate and equilibrium phases, employing FLOW3D software. Comparing the numerical results with experimental observations of Melville & Raudkivi (1977), the researchers founded that the FLOW3D hydrodynamic model simulates well the complex flow patterns around the bridge pier. Chang *et al.* (1999) performed three-dimensional calculations of the flow around a bridge pier with a fixed bed and no scour, using a Large-Eddy Simulation (LES) model. In Tseng *et al.* (2000), simulation runs were performed to study various properties of the three-dimensional flow around both circular and square piers by LES model, exposed to a steady current. Their model results were validated against the results of Dargahi (1989)'s experiments. Despite the discussion about the influence of flow patterns in the scouring process, no scour simulation was undertaken.

Chen (2002) employed the RANS equations to predict scour in an array of piers in a side-by-side arrangement. The bed material was cohesive, and the scour rate was assumed to vary linearly with the bed shear stress. Roulund *et al.* (2005) developed an experimental and numerical study of the flow and the scour around a circular pier subject to a steady current. The flow field was simulated using the hydrodynamic model EllipSys3D with a k-ω turbulence model; the free surface effects were neglected. They considered the Engelund & Fredsøe (1976)'s model to account for bed load sediment transport as well as for bed-slope modifications. The authors devoted special attention to horseshoe and lee-wake vortices, to the influence of the boundary-layer thickness, Reynolds number, and bed roughness on those mechanisms. They also elaborated a non-cohesive sediment model, obtaining equilibrium scour depths 30% larger than the experimental data.

Liu & García (2008) developed a mathematical model for simulating the local scour phenomenon around bridge piers, by using the volume of fluid (VOF) method to track the free surface between water and air, and the moving mesh method to modify the simulation domain. Similar to the previous researchers, Liu & García (2008) also chose the bed load sediment transport model, given by Engelund & Fredsøe (1976). The simulation results showed good agreement

with the experimental data, albeit not included a sand-sliding mechanism to limit the bed slope at scour holes. In Khosronejad *et al.* (2012b), the scour caused by different pier shapes was studied experimental and numerically. The latter was performed by using the fluid-structure interaction curvilinear immersed boundary (FSI-CURVIB) method with a k-ω turbulence model. The sediment transport model was analogous to the one presented in Khosronejad *et al.* (2011). The authors observed that the pier bluntness plays an important role on the estimation ability of the numerical model.

A review of the recent advances in the numerical simulation of local scour is presented by Sumer (2015). More recent studies were conducted by Baykal *et al.* (2015) and Baykal *et al.* (2017), where flow and scour around a vertical pier subject to currents and waves were numerically simulated, respectively. The backfilling process of the scour hole was also considered in both works by using the same model used in Fuhrman *et al.* (2014). The experimental data of Roulund *et al.* (2005), Sumer & Fredsøe (1997) and Sumer *et al.* (2013) were used for model validation as well as for evaluation of the suspended load influence on the scouring process. The unsteady flow features, namely the horseshoe and the lee-wake vortices were also discussed. It is worth to notice that some previous numerical studies, particularly the works of Liu & García (2008), Baykal *et al.* (2015) and Baykal *et al.* (2017) were conducted by using the CFD tool OpenFOAM. Other commercial CFD tools have also been adapted to simulate scour and some have given reasonable results, as the example of Zhang *et al.* (2017)'s work. The authors investigated the mechanisms of local scour around three adjacent piles with different arrangements under steady currents by using Flow3D. They opted by the RANS equations closed with a *RNG* k-ε turbulence model to simulate the flow field. A sediment scour model was adopted to predict the motion of the sediment by estimating the erosion, advection, and deposition of the sediment.

Recently, Alemi *et al.* (2019) developed a proper numerical model to predict the flow behaviour around pile-supported piers on fixed eroded beds in a simple, fast and accurate way. In his study, the numerical results revealed good agreement with two different benchmark cases: (i) periodic hill-channel flow and (ii) single bridge pier on a scoured bed. The numerical model solves the space-filtered Navier-Stokes and continuity equations (LES Smagorisky model) in the Cartesian coordinate system using a fractional-step method. In Grivalszki *et al.* (2020)'s study, steady flow conditions around a hydraulic structure of complex geometry were investigated with the open-source CFD tool OpenFOAM. The numerical simulations were calibrated and validated with the results acquired by using an Acoustic Doppler Velocimeter (ADV) device.

2.7 Bridge Scour Monitoring

The difficulty of performing accurate predictions of scour formation with the available models (Johnson *et al.*, 2015) has contributed to the development of several measuring devices to monitor the scour hole development *in situ*. Prendergast & Gavin (2014) categorize six broad different device groups: (i) single-use devices, pulse or radar devices; (ii) buried or driven rod systems; (iii) sound-wave devices; (iv) fiber-Bragg grating (FBG) devices; and (iv) electrical conductivity

devices. Despite the successful application of radar (Millard *et al.*, 1998) and sonar (Falco & Mele, 2002) in the detection of the bridge scour profile, they are generally only used to determine the final status of the sedimentation surrounding a pier (Deng & Cai, 2007). Hence, it is difficult to employ these techniques for a continuous monitoring of the scour process during flood events, since debris may hit and destroy sensors. In addition, they can have a serious influence on the measurements, reducing the reliability of the results (Crotti *et al.*, 2016).

Techniques for continuous monitoring scour process are, therefore, desirable since real-time scour information can provide a warning prior to bridge failures and help bridge engineers to make important decisions during flood events. Devices using time-domain reflectometry (TDR) techniques (Yu & Zabilansky, 2006) and fiber-Bragg grating (FBG) sensors (Lin *et al.*, 2005) have been developed and used for real-time monitoring of bridge scour. In addition, an innovative device, called BLESS (Bed LEvel Seeking System), was developed by Crotti *et al.* (2016) to allow the continuous monitoring of riverbed in real time during flood events on the Scisciano Bridge on the River Ensino. Despite the short duration of the tests performed by Crotti *et al.* (2016), it appears to be a promising device. Hence, the development of sophisticated engineering devices is fundamental to know whether the bridge structure can be used, mainly during flood events (Crotti *et al.*, 2016). In Pizarro *et al.* (2020), a compilation of the main advantages and disadvantages of sensors for field scour monitoring is provided.

Notwithstanding, the real-time monitoring of both flow field and scour hole development in field is still not a generalized practice in bridges worldwide. The prevailing method for scour monitoring has been undertaking visual inspections using divers to obtain the depth of scour around a bridge foundation. For instance, one of the Portuguese authorities responsible for the conservation of bridges, Infraestruturas de Portugal, has the practice of conducting underwater inspections aiming the observation and the diagnosis of the structural condition of submerged bridge components. To date, the emergency decisions are often based on the subjective experience of technicians. This approach requires increased robustness and to be substantiated by data and objective measurements. Particularly, it is important to study the effect of the dynamic system and take into account the inherent uncertainties for a specific site to mitigate the potential damage owing to hazardous events like floods. A viable way to consider such uncertainty is to perform risk and reliability analysis, which topic is addressed on Section 2.8.

2.8 Scour Risk Assessment

Besides the efficiency of assessment, monitoring and maintenance activities in reducing risk, addressed in Section 2.7, scour-related bridge collapses still occur, indicating that some residual risk remains (Lamb *et al.*, 2017). A scour risk assessment involves the outcomes that could result from a combination of drivers, hazard events, and the performance of the bridge foundations when subject to those events (Johnson *et al.*, 2015). The management of scour usually leads to the prioritization of resources allocations for more detailed evaluations where either scour is more susceptible to occur or its consequences may be worst. In addition, the availability of sufficient

investments to undertake all the necessary improvements usually occurs. Normally, limited budgets are in tandem with the need of taking difficult decisions in order to decide how and where resources should be invested, i.e. where intervention is financially justified (Roca & Whitehouse, 2012). Understanding risk is, thus, a fundamental step for the bridge safe operation and provides a base for future management operations.

The underlying hazard events are mainly flood flows to which bridges and their foundations may be vulnerable (Flint *et al.*, 2017). A multidisciplinary understanding of the aggressivenesses of the hydraulic conditions, the riverbed material features and the bridge foundation geometry/performance are, thus, of crucial importance in a scour analysis. The interrelations of them in and around the scour hole make the phenomenon extremely complex, which explains the somewhat limited applicability of experimental studies, considering only certain aspects whereas others are underestimated. Additionally, calibrating scour prediction models by field data is also limited mainly owing to observational difficulties (Yanmaz, 2002b). Such lack of relevant information may lead to increased model and parameter uncertainties used in bridge scour prediction (Lagasse *et al.*, 2013). Therefore, the inherent uncertainties associated with the flowing water, riverbed material, and bridge structural performance pose a particular risk on the safe design of bridge foundations by the application of deterministic bridge scour predictors (issue addressed in Section 2.5). In order to tackle this problem, the scientific community has been recommending probabilistic assessments (Lamb *et al.*, 2017).

Probabilistic approaches to the scour depth prediction have been applied for reliability and risk analysis. As pointed out in Chapter 1, Johnson (1992) and Johnson & Ayyub (1992) were probably the first who raised the issue of the reliability-based pier assessment presenting a risk-based method by incorporating uncertainty into the bridge pier design. Johnson (1992) employed Monte Carlo simulations to compute the probability of failure. The correlation among the various random variables was, however, neglected. Johnson & Ayyub (1992) developed a method to assess the risk of bridge failure caused by scour during the bridge life. Chang *et al.* (1994) have proposed a procedure to generate multivariate, non-normal, correlated random variate relying on the specified marginal distribution and correlation coefficients using the empirical equations provided in the literature for the Monte Carlo simulation of interacted variables. Such simulation procedure was used in the reliability analysis of bridge pier scour by using the scour model derived in Johnson (1992). The researchers have concluded that higher probabilities of failures are obtained whether the correlation among the stochastic parameters is not considered. Johnson & Dock (1998) have considered the HEC-18 scour depth predictor with the hydraulic variables associated to a large event storm for the reliability analysis. Ghosn & Johnson (2000) have derived a reliability model for the analysis of bridges subject to the combined effect of scour and earthquake. Johnson & Niezgoda (2004) have developed a risk-based method for rating, contrasting, and finally select the most appropriate scour countermeasures using failure modes. Muzammil *et al.* (2006) have developed a reliability analysis for bridge piers by using the scour model of Coleman & Melville (2001); the correlations among the scour variables was ignored.

The loading-resistance interference approach for the assessment of the reliability of bridge

scour was also employed by Yanmaz & Cicekdag (2001), Yanmaz & Üstün (2001), and Yanmaz (2002a), among others. Though seemingly straightforward, the evaluation of the involved integrals is mostly difficult. Such integration involves certain numerical techniques, which accuracy might be not appropriate. Further, the probability distribution of the scour independent variables will not be known or it may be difficult to obtain. In addition, the joint distribution of all the basic variables is commonly impossible to get in the field environment. When the failure function is highly non-linear, it can be difficult to numerically evaluate the integral even if the marginal distributions of the variables are known (Ranganathan, 1990; Nowak & Collins, 2012). Such complexity have led to the development of approximate and simulation methods, namely the First-Order Second-Moment Method (FOSM), the First-Order Reliability Method (FORM), or the Monte Carlo Simulation (MCS) method, among others (Muzzammil *et al.*, 2008; Muzzammil & Siddiqui, 2009). More recently, Lagasse *et al.* (2013) quantified uncertainty in common hydraulic parameters based on data from experiments and field observations, which probabilistic procedures are consistent with Load and Resistance Factor Design (LRFD) approaches. They pointed out that field data - only pier scour due to the lack of abutment and contraction scour data - show significantly higher bias compared to laboratory data sets because of the difficulty in estimating the hydraulic conditions associated with the event causing the scour, as well as the uncertainty in determining the maturity of the scour hole depths. Reliability analysis are, thus, commonly used to express the performance of a bridge foundation exposed to a certain condition in terms of its likelihood of failure under a specific hydraulic loading (Melchers & Beck, 2018).

The development and application of risk analysis held great promise to quantify and explicitly incorporate uncertainties in hydrologic, hydraulic, and geotechnical parameters in bridge pier's design analysis. Various risk methodologies have been developed. The methodology developed within the scope of the FUTURENET project (Roca & Whitehouse, 2012) aimed to estimate the annual probability of failure at each particular bridge site due to scour. Moreover, other risk approaches have been proposed entirely based on expert judgement, which may be inconsistent given the distinct backgrounds on hydraulics, engineering or geomorphology and indirectly hinders such assessments for risk quantification at a certain bridge site. Other research works (Briaud *et al.*, 2014; Johnson *et al.*, 2015, among others) involve some probabilistic analysis, typically introduced through the estimation of potential scour depth for an assumed "design flood", specified in terms of an annual exceedance probability or, equivalently, a return period (T). Conversely, it is expected that a flood of similar magnitude will occur every T years. Such "design flood" estimate may be compared with a predicted or known foundation depth to calculate a risk score (Lamb *et al.*, 2017). In line with Kirby (2015), the design condition of bridges in USA is typically $T = 100$ years, but with a margin of safety that the bridge should not fail for a return period of 500 years. Moreover, the probabilistic analysis is a major part of the scour risk assessment protocols used in industries. Within damages, there is a distinction between direct damages, such as the bridge failure, and indirect damages or consequences, which are often more important like human fatalities.

Therefore, the still reduced number of studies regarding scour risks and vulnerability highlights the need for a systematization of a coherent and straightforward methodology for assessing the scour

risk of hydraulic infrastructures, as bridges. Bride scour risk may be defined as the probability of losses of different types due to the removal of riverbed material at the vicinity of bridge foundations over a future time period. Mathematically, risk may be expressed by the product of the probability of failure (P_A) with the consequences C. Consequent functions are usually expert opinion-based or empirical, and are used to convert damage to loss, either in terms of repair or replacement cost, or fatalities. A qualitative assessment of the risk failure may be performed by using, for instance, the risk matrix presented in Figure 2.17. This qualitative risk assessment derives from the product of the likelihood of occurrence of hazardous event (*Likelihood*) by the severity of hazard consequence (*Severity*), both obtained from the HYRISK methodology, which was developed by the Federal Highway Administration (FHWA) in USA. *Likelihood* depends on the lifetime risk of scour failure (P_{LT}), givenby Equation 2.11 and the values scale, established by the National Bridge Inventory (NBI).

Qualitative Risk Matrix

Likelihood of occurrence of hazardous event (L_s)						
	Frequent: The hazard will occur on a regular basis during the life of the asset / process / system / procedure. The hazard will be continually experienced	10	10 *Undesirable*	20 *Intolerable*	30 *Intolerable*	40 *Intolerable*
	Probable: The hazard will occur several times during the life of the asset / process / system / procedure. The hazard will occur often	7	7 Tolerable	14 *Undesirable*	21 *Intolerable*	28 *Intolerable*
	Occasional: The hazard will occur a number of times during the life of the asset / process / system / procedure. The hazard will occur infrequently	5	5 Tolerable	10 *Undesirable*	15 *Undesirable*	20 *Intolerable*
	Remote: The hazard is likely to occur at some times during the life of the asset / process / system / procedure.	4	4 Negligible	8 Tolerable	12 *Undesirable*	16 *Intolerable*
	Improbable: The hazard is unlikely to occur but possible at some times during the life of the asset / process / system / procedure. The hazard may occur in exceptional circumstances	2	2 Negligible	4 Negligible	6 Tolerable	8 Tolerable
	Incredible: The hazard is extremely unlikely during the life of the asset / process / system / procedure.	1	1 Negligible	2 Negligible	3 Negligible	4 Negligible
			1	2	3	4
Severity of hazard consequence (C)	**Description**		**Insignificant**	**Marginal**	**Critical**	**Catastrophic**
	Consequence to persons		Possible minor Injury	Minor injury	Single fatality or severe injury	Fatalities or multiple severe injuries
	Property loss & environmental Consequence		€20k	€200k	€2m	€20m

Figure 2.17: Qualitative risk matrix, adapted from Pakrashi *et al.* (2016).

The variable P_A is the annual probability of scour failure, while LT is the provisional life of a

bridge (100 years). The annual probability (P_A) is a function of overtopping frequency and scour vulnerability. *Likelihood* and *Severity* are then merged into one descriptive variable through the risk matrix (Figure 2.17), which is based on more than 100 case studies and for which there are quantitative data. Such matrix divides the scour risk in four classes: *Intolerable*, *Undesirable*, *Tolerable*, and *Negligible*. The higher the likelihood of a risk occurring, and the harsher the consequences, the more the risk is considered critical.

$$P_{LT} = 1 - (1 - P_A)^{LT} \tag{2.11}$$

According to Lamb *et al.* (2017), the establishment of the probabilistic risk failure for bridge foundations (and consequently, bridge structures) is based on hydraulic and hydrological characteristics of a river stretch for a particular bridge site under consideration and can follow the scheme in Figure 2.18. In its methodology, fragility curves were developed to predict the probability of failure under the action of variable loadings (as indicated in Figure 2.18). The final outcome corresponds to a relation between the probability of an event and the probability of failure, if such event occurs. The integration of such curve provides, thus, the annual probability of failure.

Mathematically, the scour risk of a bridge to failure (S_R) may be, simply, defined as the probability of failure (P_A) multiplied by the consequences (C) if that failure occurs (Equation 2.12). The computation of risk might also be expressed as the product of hazard (H_A), vulnerability (V_u) and losses (L_s), as schematically presented in Figure 2.18. Therefore, vulnerability (V_u) expresses the damage and losses (L_s) conditional on a given scour depth value for certain flood events (H_A).

$$S_R = P_A \cdot C = H_A \cdot V_u \cdot L_s \tag{2.12}$$

Hazard analysis consists mainly in the identification of the likelihood of occurrence of a hazardous phenomenon (flood flows) with a given intensity within a specified period of time. Vulnerability assessment, in turn, focuses on the factors, regardless their origin, which together or separately drive and shape the susceptibility of the receptor (infrastructure) to a certain hazardous event (scour effects). These drivers are, however, uncertain owing to the stochastic nature of hydrological events but also it is not certain how the system (river morphodynamics and infrastructure) will respond to them, especially when conditions exceed design specifications (Kallias & Imam, 2016; Ettema *et al.*, 2017; Pizarro & Tubaldi, 2019).

Tubaldi *et al.* (2017) proposed a probabilistic distribution of the scour depth, by combining information from hydrological, hydraulic and scour analyses in a Markov-model approach. The same authors have concluded that not only the random occurrence of subsequent extreme flood events contribute to the scour development, but also the hydrograph duration and shape. Results confirmed that assuming both independence of scour events and always attained equilibrium scour depths, they may lead to unrealistic estimates of scour. On these findings, Pizarro & Tubaldi (2019) included more realistic flood shapes into the Markovian framework, identifying the most influencing hydraulic parameters in the computation of scour depths. Results corroborated the high sensitivity of the exceedance probability to the choice of the time-dependent scour model, while

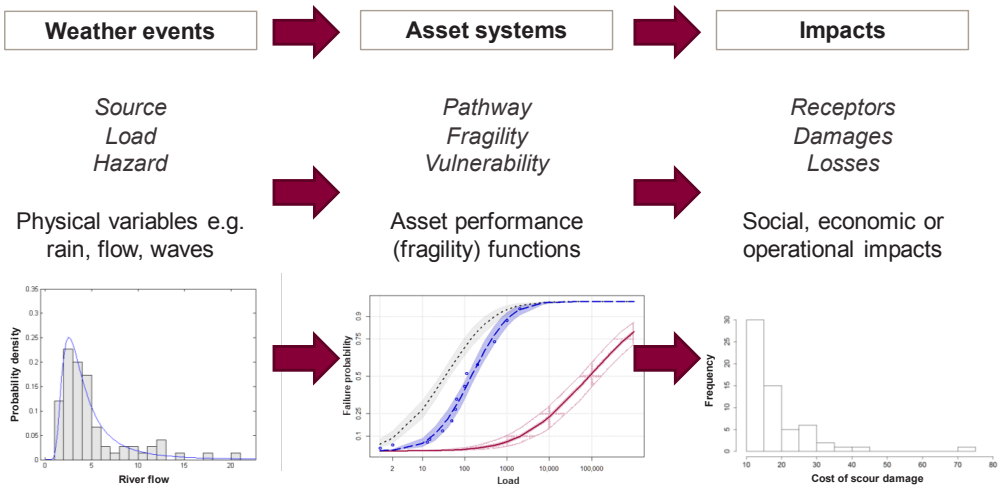

Figure 2.18: Risk method, adapted from Lamb *et al.* (2017).

the effects of the epistemic uncertainty associated with the equilibrium scour models were lower than those associated with the time-dependent scour ones.

In Manfreda *et al.* (2018), a probability distribution of scour, based on the probability distribution of floods, the velocity-area rating curve (Manfreda, 2018) and BRISENT model (Pizarro *et al.*, 2017), is theoretically derived (TDDS) to reduce uncertainty in the hydraulic design of bridges and their scour assessment. It focuses on the impact that the contributing variables, such as river basin hydrology, hydraulic river characteristics, sediment and pier geometry have on the scour depth probability distribution, which can be used for design or scour risk assessment purposes.

Several approaches have been proposed to deal with the issue of predicting the scour depth at bridge foundations. Among them, physical modelling, empirical formulations, and numerical, data-driven and non-deterministic methods give undoubtedly extra effort to the research in question, but on the other hand, there is still a tremendous lack of consensus within the scientific community. The science behind the scour phenomenon at bridge foundations is currently characterized by high empiricism and uncertainty, especially at real-scale bridges (Pizarro *et al.*, 2020). Physical modelling and empirical approaches are usually developed at small-geometric-scales (laboratory flumes) under controlled hydraulic and boundary conditions. Therefore, their applicability to real-geometric-scale bridges is not fully validated. Field scour data is critical to deal with the aforementioned issue as highlighted in Section 2.7, motivating also the possibility to develop better scour risk frameworks.

Chapter 3

Risk-based Analysis

3.1 General Considerations

Understanding risk is a fundamental step for the safe operation of bridges and the foundation for any future management operations. However, as pointed out in Section 2.8, the number of studies that address scour risks and vulnerability is currently reduced. This confirms the need for a systematic, coherent and straightforward methodology for assessing the scour risk of hydraulic infrastructures, such as bridges (Pizarro *et al.*, 2020, and references therein). As stated by Johnson *et al.* (2015), a scour risk assessment involves the outcomes that could result from a combination of drivers, hazard events, and the performance of the bridge foundations when subject to those events. The focus of the present chapter is thus to propose and discuss a new and pragmatic three-step methodology for assessing risks associated with scour at bridge foundations on alluvial riverbeds.

The risk-based methodology steps comprise: (i) the hydrological modelling of extreme events (hazards), (ii) the computation of flow and scour variables to model river behaviour, and (iii) the assignment of a bridge scour qualitative risk rating based on the relation between scour depth to foundation depth ratio and the vulnerability of the infrastructure in question (level of risk). The proposed methodology was applied and validated using a case study bridge in Portugal. The selection of the most appropriate case study bridge considered the following requirements: the availability of hydrological and bed level monitoring data, and the variability of the bathymetry over time at the bridge location. Of the potential bridge case studies summarized in Appendix B, the "new Hintze Ribeiro" bridge, located in the Douro river, was identified as the most suitable for the investigation. This bridge, inaugurated in May 2002, was built in the sequence of the collapse, in 2001, of the 19th century Hintze Ribeiro bridge, which was located 7.5 m downstream of the new bridge's position.

Two scientific papers are presented in the following sections. The "Improvement assessment of maximum streamflow approaching a bridge over Douro river. A case study" (Section 3.2) concerns the first step of the risk-based methodology: the assessment of the hydrological events. The paper proposes a novel modelling method to provide reliable estimates of extreme discharge flows approaching hydraulic infrastructures, validated by the selected case study. This paper was submitted to "Journal of Hydrologic Engineering" in July 2020 and is currently waiting for response.

The “Risk-based methodology for scour analysis at bridge foundations” (Section 3.3) concerns the implementation of the three-step risk-based methodology for bridge scour risk assessments to the case study. The aim of this methodology is to propose a practical and useful approach for bridge inspection and risk management measures. This paper was published in “Engineering Structures” in July 2020. A conference contribution, “Hydrological risk and associated scour risk: Case study sensitivity analysis” (Appendix D.4) was submitted in May 2020 and accepted for oral communication in the “V International Congress on Risks”, to be held in Coimbra (Portugal) from 12 to 16 October 2020. The latter explores the relationship between hydrological risks and associated scour risks for the case study bridge.

3.2 Improvement assessment of maximum streamflow approaching a bridge over Douro river. A case study. *Paper submitted*

TITLE: Improvement assessment of maximum streamflow approaching a bridge over Douro river. A case study[1]

Paper submitted to "Journal of Hydrologic Engineering"
Submitted: July 9th, 2020

Author contributions:
Bento, A.M. and Gomes, A. collected and processed the data. Bento, A.M. wrote the manuscript and designed the figures. Pêgo, J.P., Viseu, T. and Couto, L. aided in interpreting the results and worked on the manuscript. All authors discussed the results and commented on the manuscript.

[1]Bento, A.M., Gomes, A., Pêgo, J.P., Viseu T. & Couto, L. (Submitted). Improvement assessment of maximum streamflow approaching a bridge over Douro river. A case study. In: Journal of Hydrologic Engineering

3.2.1 Abstract

A novel hydrological modelling methodology was developed to provide reliable estimates of extreme discharge flows approaching hydraulic infrastructures and their probability of occurrence. It was applied to estimate the design floods approaching the case study "new Hintze Ribeiro" bridge, located in the Douro river, one of the three main rivers in Portugal, and one of Europe's largest river flood flows. An extrapolation technique for the missing instantaneous discharge data was derived and validated. The estimates are accurate with a mean deviation of 7.2% relative to the observed data. Probabilistic models were considered and their performance verified. Model uncertainties were addressed by comparing the estimated design floods through the best fit model (MS) with the arithmetic model averaging (MM), and the herein proposed model ($modified\ MM$). This comparative analysis was performed using the non-parametric Kernel Density Estimate (KDE) as benchmark model. The $modified\ MM$ method showed a lower discrepancy (24.4%) to KDE estimates, when compared with the MM results. Given the obtained results, the $modified\ MM$ is considered a better calibrate method for the design floods estimation.

Keywords: design flood, extrapolation technique, hydrological risk, $modified\ MM$ method, new Hintze Ribeiro bridge, uncertainty analysis

3.2.2 Introduction

Bridges, like other hydraulic infrastructures as dams, play an important role in the economic development of a society. In recognition of their relevance, the assessment of the associated hydrological risk plays a vital role in the design process, as well as during their operation, namely when such bridges are founded on alluvial riverbeds (Simonovic, 2012). The risks associated with the likelihood of extreme events and their respective consequences call for the prediction, as accurate as possible, of the maximum annual flow discharges that approach the section of a bridge for different return periods (called design floods), as those may compromise its stability. According to Pizarro *et al.* (2020), a deterministic approach is often employed, neglecting the natural and the epistemic sources of uncertainty that may affect the scour problem, and leading to a one-to-one relationship between the design flood discharge and the design scour depth (Melville & Coleman, 2000; Highways Agency, 2012; Arneson *et al.*, 2012).

The estimation of design floods approaching hydraulic structures requires the determination of instantaneous peak flows from the historical flood data since there may be significant streamflow fluctuations within hours or even minutes, especially for small watersheds (Dastorani *et al.*, 2013). An interesting aspect concerns the process by which hydro-metereological agencies evaluate and make accessible the hydrological data. Most of the times, these agencies publish only the mean daily flow data, for which the consideration of the mean data in flood studies may cause underestimation of the design flood thus resulting the sizing of the hydraulic infrastructure for a higher risk of collapse.

The extreme events and their occurrence rate depend, among other factors, on the physical characteristics of the river basin, the dominant run-off generation mechanisms (Robinson *et al.*,

1995), the magnitude and variability of the temporal distribution of rainfall (Kusumastuti *et al.*, 2007), and the stream network geometry and river routing (Rogger *et al.*, 2012a,b). These factors may change along time as a result of the influence of climate change or socio-economic development aspects, so their estimation remains an area of continuous research interest. In the literature, several methods can be used, from which the statistical methods (flood frequency analysis) and hydro-meteorological methods stand out. Whilst both these methods have strengths and weaknesses (Calver *et al.*, 2009; Sordo-Ward *et al.*, 2014), the hydro-meteorological methods require a higher computational capacity.

Flood frequency analysis relates the magnitude of annual maximum flood events to the likely frequency of occurrence of natural events (Moran, 1957; Beven, 2019), by employing probability distribution models that describe the observed data. From the application of a set of different distributions, statistical tests are commonly used to select the model that best fits the given time series data from a number of candidate probabilistic distribution models. The selection of a single best distribution model (i.e. model selection, *MS*) represents an implicit assumption that the selected model can adequately describe the frequency of observed and future flood flow events (Okoli *et al.*, 2018). Many hydrologists have pointed out ways to deal with the inherent uncertainties, always present in any mathematical evaluation, such as from the parameter or model selection (McMillan *et al.*, 2018; Beven, 2019).

The quantification of model uncertainty, in flood frequency analysis, can be tackled through the consideration of all candidate probability distribution models in the estimation of the design floods, where the final floods estimate is an average of all individual estimates, known as model averaging (Okoli *et al.*, 2018). The model averaging can be performed either by taking the arithmetic mean of the design flood estimates (i.e. arithmetic model averaging, *MM*) or by attributing weights to the design floods of each individual candidate probability model (i.e. weighted model averaging, *MA*) depending on how best each model fits the time series data (Hoeting *et al.*, 1999; Yan & Moradkhani, 2014). According to Okoli *et al.* (2019), the selection of the best fitting probability distribution is associated with several outliers in comparison with multiple probability distributions, especially when facing short sample sizes (30 - 50 hydrological years).

Therefore, the present study proposes a hydrological modelling methodology for providing reliable estimates of extreme discharge flows and their occurrence probabilities, constituting thus a relevant input data for the assessment of the safety of new or existing hydraulic infrastructures. In order to demonstrate the hydrological modelling herein presented, the methodology was applied to estimate the flood events approaching the new Hintze Ribeiro bridge, built in 2002, over the Douro river, in Portugal. Various ways of accounting with the inherent uncertainties were also proposed.

Following this introduction, Subsection 3.2.3 of this paper presents and discusses the time series analysis techniques and properties, and describes the assessment of how to deal with the uncertainties inherent to a flood frequency application. In Subsection 3.2.4, the river basin defined by the case study bridge cross-section is described, and a set of hydrological plausible scenarios are defined. The application of the hydrological modelling methodology to the new Hintze Ribeiro bridge is presented and discussed in Subsection 3.2.5. A comparative analysis of the design flood

estimate methods and the inherent hydrological risks was also undertaken. Finally, the main conclusions are provided in Subsection 3.2.6.

3.2.3 Hydrological modelling methodology

3.2.3.1 Data reliability analysis

The applicability of any statistical method is preceded by a reliability analysis of the hydrological series under consideration. Such analysis consists on the verification of the consistency and the hypothesis of randomness of that series (Naghettini & Pinto, 2007; Kite, 2019, among others).

The conformity of data consistency refers to the detection and elimination of gross and/or systematic errors, for instance, using the usual double-mass technique, firstly developed by Searcy & Hardison (1960). A consistency check can reveal inconsistencies entailed by a variety of causes, including changes in land use (e.g. agricultural to forest), the construction of new control infrastructures (e.g. dams) or modifications in the operation of these structures, changes in the amount of water diverted into or out of the watershed, the effect of large forest fires, alterations in agricultural practices, and changes to measurement methods or practices. Moreover, this consistency verification can reveal information regarding magnitude and timing of these aforementioned causes and determine whether the streamflow data need to be adjusted.

The randomness of an historical series is verified if it guarantees the assumptions of independence, homogeneity and stationarity (Naghettini & Pinto, 2007; Kite, 2019). Those assumptions are usually performed by using non-parametric tests (Lencastre *et al.*, 1984; Hipólito & Vaz, 2011). The independence of the data series is usually assessed by the auto-correlation coefficient test whereas the homogeneity is verified by the application of the non-parametric test of Mann & Whitney (1947) or the local extremes number test. The Mann-Kendall trend test (Mann, 1945; Kendall, 1975) or the Spearman tests are typically used to identify trends on hydrological series. The Wald & Wolfowitz (1943)'s test is also used as a general verification of the randomness of a series. According to Hipólito & Vaz (2011) when the hypothesis of randomness is not rejected in more than two of the four tests, the hydrological series is assumed random and reliable for statistical analyses at a 95% confidence level.

3.2.3.2 Statistical methods

Flood frequency analysis Given reliable historical streamflow records, the statistical method known as "flood frequency analysis" can be used to extend them and hence predict the likely frequency of occurrence of natural events, typically designated as "design floods" (Chow *et al.*, 1988). It often consists of fitting probability distribution functions to records of annual maximum flows that likely occur at a certain river location, namely at a bridge site for the current study. The accuracy of the estimated design floods, such as the 100-year flood (a flood with 1% annual frequency of exceedance), is essentially dependent on the record length, which should be longer than 30 hydrological years.

In flood frequency analysis it is common practice to employ probability distribution models that describe the observed data (Chow *et al.*, 1988; Cunnane, 1989; Castellarin *et al.*, 2012; Hassan *et al.*, 2019). In the present study, six models were considered and their confidence intervals determined, namely for the following distributions: two- and three-parameter LogNormal ($2p$ and $3p$, respectively, being p the number of parameters), Gumbel, Gamma, LogPearson III, and Weibull. For estimating the parameters of each probability distribution, the method of moments, the L-moments method and the method of maximum likelihood are the most advisable by hydrologists (Kite, 2019).

Goodness-of-fit tests and graphical methods Once the probability distributions are adjusted, the performance of each model is usually assessed based on goodness-of-fit tests and accuracy measures (D'Agostino, 1986; Naghettini & Pinto, 2007). Generally speaking, goodness-of-fit tests describe how well a statistical model fits a set of observations, through the analysis of the discrepancy between observed and expected values under the probabilistic model in consideration.

Goodness-of-fit tests may be divided into qualitative and quantitative non-parametric tests. The former refers to the Kolmogorov-Smirnov (KS) test (Massey, 1951), while the latter assigns the Chi-square (χ^2) test (Kenney & Keeping, 1957). Other tests include the Filliben (Fi) test (Filliben, 1975) and the Anderson-Darling (AD) test (Anderson & Darling, 1954). The Anderson-Darling (AD) test constitutes a modification of the Kolmogorov-Smirnov (KS) test, giving more weight to the tails than the latter (KS test). Each of the goodness-of-fit tests has its own set of particularities, which inherently interferes with the rejection (or not) of a certain probabilistic model for the representation of the time series data under analysis (Maity, 2018b; Naghettini & Pinto, 2007).

A measure of accuracy given by the graphical method assessment obtained by the Quantile - Quantile plot (Q-Q plot) is also advised in the evaluation of those models' performance (D'Agostino, 1986). The Q-Q plot checks the validity of a distributional assumption for a data set by computing the theoretically expected value for each data point based on the distribution in question. Whenever the data indeed follow the assumed distribution, the points on the Q-Q plot will fall approximately on a straight line. For determining the theoretical probability of non-exceedance of each data point, "plotting position" formulas are assigned and used depending on the type of distribution being fitted. The commonly used unbiased plotting positions comprise the formulas of Weibull, Blom, Cucane, Gringorten, Hazen, Chegodayev and Turkey (Stedinger, 1993; Naghettini & Pinto, 2007).

Uncertainty and proposed methods Despite the wide practice of selecting a single best probability distribution (i.e. the model selection, MS) in the field of flood frequency analysis, the technique itself does not take into account the inherent uncertainties (Okoli *et al.*, 2018). Moreover, any model faces uncertainty and its quantification is crucial for ensuring data quality and usability (Beven, 2006; McMillan *et al.*, 2018; Kiang *et al.*, 2018). Besides the advances in the development of tools for quantitative uncertainty analyses, its quantification is not yet a standard practice in water resources planning, design, and operation (Yen, 2002; Beven, 2019).

The uncertainty in flood frequency analysis, as in any other area, can be divided into two distinct categories: natural uncertainty - irreducible uncertainty, and epistemic uncertainty - reducible

uncertainty (Yen, 2002; Huang *et al.*, 2018; Leandro *et al.*, 2019; Beven, 2019). While the first stems from variability of the underlying stochastic process, the second results from incomplete knowledge about the process under study. In the present investigation, the natural uncertainty refers to the variability that exists in the amount of annual flow discharge in consecutive hydrological years. The epistemic uncertainty is related to the ability of understanding and describing the system under analysis (Merz & Thieken, 2005; Maity, 2018a), namely model and parameter uncertainties.

In accordance with Okoli *et al.* (2018), model uncertainty can be reduced by using all candidate probability distributions for the design floods estimation, where the final estimate is a weighted average of all individual estimates. This procedure is known as model averaging (Bumham & Anderson, 2002; Höge *et al.*, 2019). The model averaging technique can be performed through two distinct ways: (i) by taking the arithmetic mean of the design flood estimates from the candidate probabilistic distributions (i.e. the arithmetic model averaging, *MM*) or (ii) by attributing different weights to the design floods of each candidate probability model (i.e. weighted model averaging, *MA*), depending on how best the probability function fits the data under analysis (Hoeting *et al.*, 1999; Yan & Moradkhani, 2014). Bayesian inference is one of the possibilities to estimate the weights assigned to a range of models considered for flood estimation purposes and Wood & Rodríguez-Iturbe (1975) showed, for the first time, an example of application in flood frequency analysis. A review on theoretical backgrounds of Bayesian model averaging (and selection) is provided in Höge *et al.* (2019).

In the present investigation, a modification of the original *MM* method (Okoli *et al.*, 2018), is introduced, which consists of considering the distributions that ensure good performance on both goodness-of-fit tests and graphical methods. The comparative analysis between the widely applied *MS* and the $modified\ MM$ methods (hereinafter designated as $modified\ MM$) will provide insights and explain the importance of considering more than a single probability distribution for the representation of the time series data under analysis. A brief sensitivity analysis was undertaken for the two *MM* methods to obtain the final design floods.

Parameter uncertainty, in turn, results from the inability to accurately quantify the model input parameters. The estimation of a random variable (x_T) for a particular return period (T), for each probabilistic distribution, is inherently dependent on the available sample size, which carries uncertainty to the system. In order to tackle such uncertainty, in the model selection method (*MS*), the computed flow rates should be estimated with 95% of confidence interval for the full range of design floods (i.e. with lower and upper boundaries) as per best practice. This has been considered in the *MS* method presented herein.

3.2.3.3 Hydrological risk

Frequency analysis is of great relevance in the interpretation and assessment of flood flows, as well as in the evaluation of the flood occurrence risks for specific return periods. The hydrological risk is typically considered during the design process of any hydraulic infrastructure (Ojha *et al.*, 2008), such as a bridge or a dam, due to the aforementioned uncertainties.

The designer is generally concerned with the return period for which the infrastructure should be designed. Based on the acceptable risk and on the design life (n) of an hydraulic infrastructure, the return period for which the structure should be designed can be ascertained. Hydrological risk (R_H) is thus defined as the probability of occurrence of an event at least once $[P(X \geq x_T)]$ over a period of n successive years (see Equation 3.1).

$$R_H = P(X \geq x_T) = 1 - \left(1 - \frac{1}{T}\right)^n \tag{3.1}$$

3.2.4 Case study and database

3.2.4.1 Case study framework

In Portugal, the persistence of discharge peaks exceeding 8,000 m^3s^{-1} in a three-months period have contributed to the collapse of the 19^{th} century Hintze Ribeiro bridge on the night of 4 March 2001, during the fifth flood event over the Douro river. This tragic accident caused the death of 59 people who were crossing the bridge, in a bus and three cars, when one of its piers collapsed and the central sections plunged into the river.

The 19^{th} century Hintze Ribeiro bridge was built in 1885 and linked Castelo de Paiva and Entre-os-Rios. Following the disaster, preliminary studies were planned for the rehabilitation of the 19^{th} century Hintze Ribeiro bridge, considering the importance of maintaining the crossing at the lower Douro level, particularly for those local populations. However, the underwater inspections undertaken promptly excluded that hypothesis and in April 2001 the Portuguese government announced the tendering procedure for the construction of the new bridge over the Douro river. The old bridge was, thus, replaced by the new Hintze Ribeiro bridge, inaugurated in May 2002, 7.5 m upstream of the old bridge's position (Figure 3.1).

Figure 3.1: Photograph of the new Hintze Ribeiro bridge (downstream view).

The severe socio-economical impact of the collapse of the 19^{th} century Hintze Ribeiro bridge dictated its importance for the purposes of the current study, providing data and highlighting the importance for reliable estimates of extreme discharge flows and their occurrence probabilities at the new bridge's approach section.

3.2.4.2 Hydrographic region characterization

The Portuguese region of the Douro watershed, representing 19.07% of its total area (97,477.66 km^2), is characterized by embedded valleys, strong riverbed slopes and overly narrow floodplains APA (2019). As a result, the extraordinary floods of the Douro river are characterized by a strong water level rise, especially in the narrowest sections, with fast hydrological response and for a short duration of about 2 to 3 days APA (2016). The highest flood peaks took place in the years of 1727, 1739, 1779, 1788, 1823, 1843, 1850, 1855, 1860, 1877, 1888, 1909, 1962 and 1989 Silva & Oliveira (2002), all of which caused great damage to farms, long-distance ships, coastal, fishing vessels and river traffic, and loss of human lives. The 1739 flood, with a recorded maximum value of 18,000 m^3s^{-1}, was not exceeded until now. The historical flood data collection and compilation, although mostly empirical, is an indispensable basis for establishing danger trends or flood-related disasters Tato (1966); Vieira & Costa (2017), as occurred with the collapse of the 19^{th} century Hintze Ribeiro bridge in 2001.

The new Hintze Ribeiro bridge lies 500 m from the mouth of the Tâmega river (at the confluence with the Douro river), a right tributary of Douro river (Fig. 3.18). The bridge section is located in the downstream reach of the Douro river, at the Crestuma-Lever dam reservoir (at a distance of 25.5 km). Upstream of the bridge section are the Torrão dam, on the Tâmega river, at a distance of 3.8 km, and the Carrapatelo dam, on the Douro river, at 16.7 km from the bridge. The Paiva river, a left tributary of Douro river, also contributes to the flow rates that approach the new Hintze Ribeiro bridge, through the records of "Fragas da Torre (EDP) (08H/02H)" gauging station (Fig. 3.2).

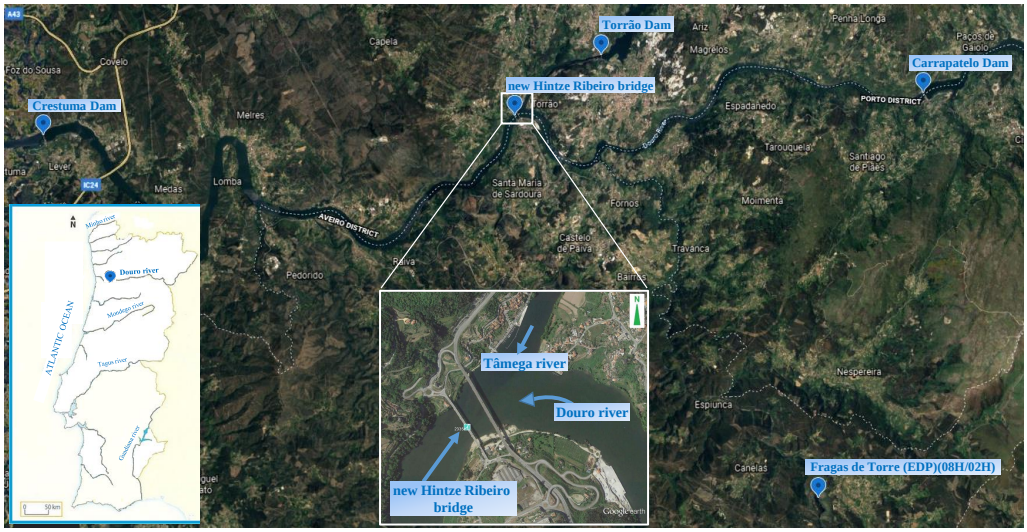

Figure 3.2: Map of the vicinity of the new Hintze Ribeiro bridge, over the Douro river Google Earth (n.d.).

3.2.4.3 Hydrometric data collection

In the Douro river watershed, a real-time hydro-metereological network is operating since the beginning of the 20th century (Tato, 1966; Vieira & Costa, 2017). Since 2012, its management is under the responsibility of the "Portuguese Environment Agency" (APA). The availability of streamflow data at gauging stations, located in the vicinity of the new Hintze Ribeiro bridge, represent indeed an important tool towards the assessment of the design floods that approach such bridge section. Those gauging stations are identified as follows:

(i) "Crestuma Dam (EDP) (07G/01A)";

(ii) "Carrapatelo Dam (EDP) (07I/01A)";

(iii) "Torrão Dam (EDP) (07H/01A)";

(iv) "Fragas da Torre (EDP) (08H/02H)".

Although the easiest and direct method to compute maximum flow discharges approaching the new Hintze Ribeiro Bridge would be the consideration of the streamflow approaching the Crestuma-Lever dam, the estimates of natural affluences to a reservoir are subject to several uncertainties. These are mainly related to the estimate of water volumes flowing into the reservoir, from fluvial flows or direct precipitation, as well as to the estimate of the effluent flows for losses due to supply and evaporation Portela & da Silva (2014). In addition to these issues, the stream of the Douro river that separates the case study bridge and the Crestuma-Lever dam is characterized by a meandering path along 25.5 km. Therefore, streamflow data from the "Crestuma Dam (EDP) (07G/01A)" (item (i)) gauging station was no longer considered, although the dam's design flood was taken as reference.

The new Hintze Ribeiro bridge is subject to the effects of flow which are highly dependent on the discharges from the dams situated upstream of the bridge, Torrão and Carrapatelo dams (from records of items (ii) and (iii), respectively), and the flow from the Paiva river (from records of item (iv)). The resulting flow discharge approaching the case study bridge was thus considered by combining the contributions of the three aforementioned gauging stations (items (ii) to (iv)).

Table 3.1 summarizes the streamflow data availability and the periods of required extrapolation. Mean daily and instantaneous flow data were taken from the "Water Resources Information System" (SNIRH, Portugal) platform and were made accessible by "Energias de Portugal" (EDP, Portugal), the Portuguese entity responsible for the management of the dams considered, respectively.

3.2.4.4 Hydrological modelling hypothesis

The resulting flow discharge approaching the new Hintze Ribeiro bridge was herein considered by combining the contributions of the three aforementioned gauging stations (items (ii) to (iv) mentioned in Subsection 3.2.4.3). In light of the hydrographic location of the bridge, the resulting flow discharge approaching the new Hintze Ribeiro bridge was the direct sum of the flow discharges from the three gauging stations.

Table 3.1: Time series and database available. Periods that require extrapolation of streamflow data.

Gauging stations	**Mean daily data**		**Instantaneous data**	
	N.º of annual records	Records period	N.º of annual records	Records period
"Carrapatelo Dam (EDP) (07I/01A)"	47	1972/73 to 2018/19	10	2009/10 to 2018/19
"Torrão Dam (EDP) (07H/01A)"	31	1988/89 to 2018/19	10	2009/10 to 2018/19
"Fragas da Torre (EDP) (08H/02H)"	68	1946/47 to 2018/19	66	1948/49 to 2018/19
Periods of required extrapolation				
"Carrapatelo Dam (EDP) (07I/01A)"	-	-	21	1988/89 to 2008/09
"Torrão Dam (EDP) (07H/01A)"	-	-	21	1988/89 to 2008/09

Following individual analyses to the preponderance that each gauging station plays on the approach flow discharges at the bridge section, the proposed direct sum hypothesis resulted in more conservative values. As such, this was selected as the modelling hypothesis. This combination assumes the temporal coincidence of flood peaks between the three gauging stations' records and simultaneously disregards the streamflow losses and gains between those stations and the bridge section. Figure 3.3 plots the maximum annual discharges from the mean daily values for the coincident recording years, i.e. from 1988/89 to 2018/19, comprising a total number of 31 hydrological years.

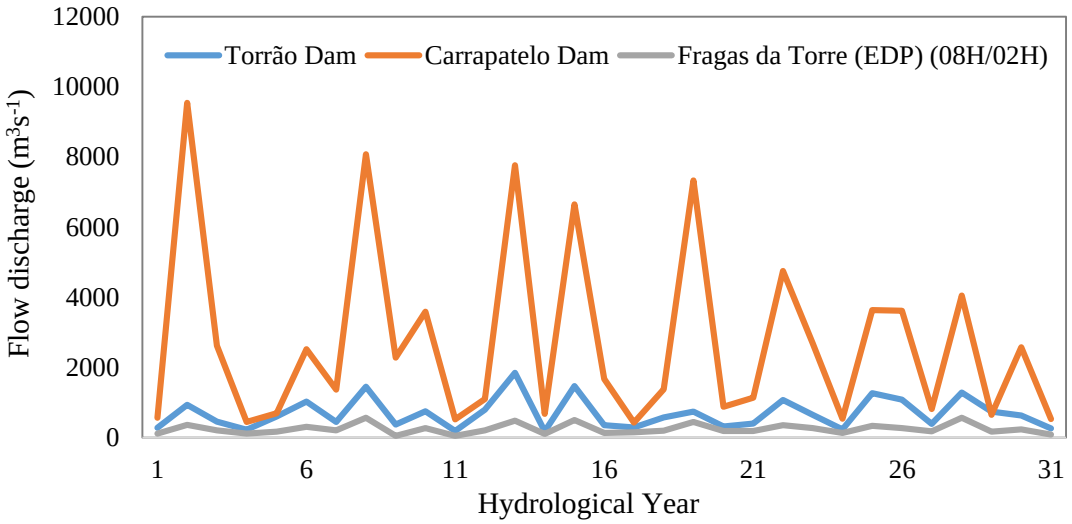

Figure 3.3: Maximum annual flow discharges from the mean daily values for the three gauging stations.

3.2.4.5 Hydrological scenarios definition

By using the assumption of direct sum, four possible hydrological scenarios were considered to evaluate the maximum annual flow discharge approaching the new Hintze Ribeiro bridge (Q_{HR}) - Table 3.2.

Table 3.2: Hydrological scenarios considered for Q_{HR} estimation.

Database	Description	Scenarios
Mean daily	Sum of the design floods obtained independently for each gauging station	0
	Sum of the maximum annual discharges of the three gauging stations	1
	Sum of the discharges from the three gauging stations and calculation of the maximum annual values	2
Instantaneous	Sum of the maximum annual discharges of the three gauging stations	3

The total flow rate was determined through the sum of the aforesaid records: $Q_{HR} = Q_C + Q_T + Q_{FT}$, where Q_C, Q_T and Q_{FT} stand for the streamflows extracted from the gauging stations "Carrapatelo Dam (EDP) (07I/01A)", "Torrão Dam (EDP) (07H/01A)" and "Fragas da Torre (EDP) (08H/02H)", respectively, either mean daily or instantaneous data. Table 3.2 summarizes how Q_{HR} was assessed, as well as the database under consideration.

Scenario 0 was promptly unconsidered. The hydrological time series of streamflow data, from the three gauging stations, does not follow the same statistical distribution, rejecting the hypothesis of data homogeneity and the synchrony of return period exceedances.

Following individual analyses to the preponderance that each gauging station plays on the approach flow discharges at the bridge section (by their characteristic years), it can be concluded that the maximum annual discharges tend to occur on different days for the considered stations. Higher discrepancies are found between the dams' records, "Carrapatelo Dam (EDP) (07I/01A)" and "Torrão Dam (EDP) (07H/01A)", and the flow rates collected from the "Fragas da Torre (EDP) (08H/02H)" gauging station. This behaviour was expected due to the significantly reduced area of the latter river watershed compared with the basins of Douro and Tâmega rivers, respectively. The resultant effect of considering the daily coincidence of the three gauging stations' annual maxima is assessed by comparing the results of Q_{HR} from Scenario 1 and Scenario 2 (an issue addressed later).

Scenarios 1 and 2 can be considered more feasible due to the higher availability of the database. The mean daily flow data, the database of those scenarios (Table 3.2), are often made accessible by hydro-meteorological agencies. However, the consideration of those mean daily data in flood studies (as the current work) may cause underestimation of the design flood resulting in the sizing of the hydraulic structure for higher risk of collapse case study bridge.

Scenario 3, in turn, represents undoubtedly the more conservative scenario since it considers all exceptional flow rates that occurred at the approach section of the new Hintze Ribeiro bridge. This combination assumes the temporal coincidence of flood peaks between the three gauging stations'

records and simultaneously disregards the streamflow losses and gains between those stations and the bridge section. An ideal scenario would consider the sum of the discharges from the three gauging stations, equivalent to Scenario 2, using instantaneous daily flow as the database instead. Notwithstanding the rich vein of information available in the online platform SNIRH, often neither instantaneous data nor reliable records are available for an extended period of time. As such, this assumption was disregarded in this study.

The proposed Scenario 3 resulted, as expected, in more conservative values (an issue resumed later) and it was selected as the preferable one for the aim of the current study.

3.2.5 Results and discussion

3.2.5.1 Data analysis and extrapolation

Some data gaps in the mean daily records from the three gauging stations were filled in order to guarantee data continuity (on the mean daily series) for scenarios 1 and 2. Such task was performed through application of a linear regression function for either one or two consecutive gap days. For three or more consecutive data gaps, a linear correlation was applied to the records of the station under study with its neighbouring station records.

After analysing the historical time series with regard to record length and quality of data, only records from the period between 1988/89 to 2018/19 were considered for further analysis, namely flood frequency analysis (ensuring the minimum required sample size of 30 years). As indicated in Table 3.1, from 1988/89 to 2008/09, the instantaneous streamflow data for "Carrapatelo Dam (EDP) (07I/01A)" and "Torrão Dam (EDP) (07H/01A)" were not available. For that period, an extrapolation of the missing instantaneous discharge data was needed.

Hence, the extrapolation of the missing instantaneous discharge data was derived by factoring the corresponding mean discharge in that year by a coefficient of proportionality. This coefficient was the result of averaging the yearly instantaneous discharge to mean discharge ratio ($Q_{instantaneous}/Q_{mean}$), for the available 10 hydrological years. Coefficients of proportionality of $K_C = 1.322 \pm 0.138$ ($\sigma = 0.222$) and $K_T = 1.568 \pm 0.190$ ($\sigma = 0.306$) were obtained for the hydrological time series of Q_C and Q_T, respectively. These coefficients were applied to the respective maximum annual mean daily discharges (Q_{mean}) to estimate the associated instantaneous data. For these cases, the adoption of different discharge classes for the estimation of each coefficient of proportionality (K_C or K_T) did not seem to influence the estimates. The limited size of the sample precludes its application, since what could be gained in differentiation would be lost in increased sample error, and consequent uncertainty. In order to validate the developed approach of estimating the instantaneous missing data, this technique was verified by two distinct methods (herein designated *Method A* and *Method B*). For that purpose, the resultant value for K_T was considered; a similar procedure can be performed for the Q_C case.

Method A - The magnitude of K_T was compared with the one obtained from the records of a neighboring station of "Torrão Dam", namely the gauging station of "Fridão (R.E.) (06I/03H)", for which both mean and instantaneous streamflow data were accessible.

Method B - The construction of the flow-duration curves, representative of the 10 years of available mean and instantaneous data, allowed for another estimate of K_T.

Regarding the application of *Method A*, the approach herein developed resulted in an coefficient of $K_F = 1.511 \pm 0.095$ ($\sigma = 0.270$) for the "Fridão (R.E.) (06I/03H)" gauging station. For this station, a total of 25 hydrological years of records was considered for the ratio $Q_{instantaneous}/\ Q_{mean}$ (Figure 3.4 - discharges were sorted in descending order based on the mean daily data). Also for this case, no classes were considered for the estimation of that coefficient due to the limited data sample size for an adequate statistical procedure. Besides the similar order of magnitude of the obtained proportional coefficients (K_T and K_F), the different sample sizes explain the lower sample error obtained for the "Fridão (R.E.) (06I/03H)" time series data.

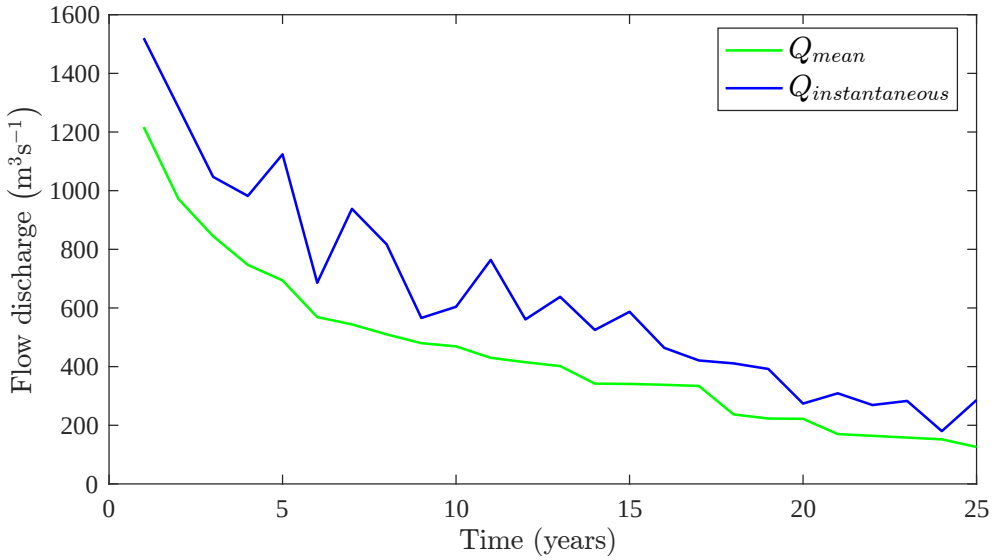

Figure 3.4: *Method A* - Maximum annual flow discharges from Q_F hydrological time series.

In regard to *Method B*, the 10 years of available mean daily and instantaneous data for Q_T (indicated in Table 3.1) were used in obtaining the correspondent flow-duration curves (Figure 3.5a). The flow-duration curve of the mean daily data presents an expected behaviour. The same is not true for the instantaneous records, at least to some extent. If we revisit the function of these curves, their construction for instantaneous flow regimes is not usual. Such curves indicate the number of days in which a given flow discharge (Q_{mean} or $Q_{instantaneous}$) has been exceeded or equalized in that 10-year period of records.

A minimum mean daily discharge of 242.21 m^3s^{-1} was registered in the 2011/12 hydrological year, whereas a minimum instantaneous discharge of 322.66 m^3s^{-1} was attained in 1998/99. In order to cope with the strange behaviour of the instantaneous flow-duration curve, the coefficient of proportionality (K_T) was considered for two separated instances: (i) the minimum mean daily discharge, and (ii) minimum instantaneous discharge. The former was reached and exceeded for 25 days, while the second was exceeded in 35 days of the year. Following these thresholds, the resultant coefficients of proportionality from the "Torrão Dam" gauging station data were: (i) $K_T = 1.474 \pm 0.018$ ($\sigma = 0.045$), and (ii) $K_T = 1.481 \pm 0.013$ ($\sigma = 0.040$). The flow-duration

curves for the second limit (ii) are plotted in Figure 3.5b. These curves do not represent annual duration. Rather, they correspond to 35 annual days from the 10 representative years, and present a sufficiently acceptable behavior to trust the estimated proportionality coefficients (very similar estimates for (i) and (ii)).

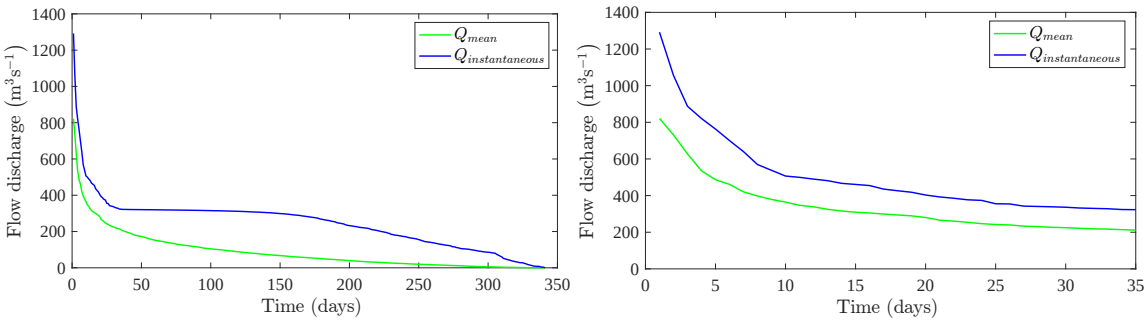

(a) For the available 10 years of records. (b) Until the minimum instantaneous discharge (ii).

Figure 3.5: *Method B* - Flow-duration curves of Q_T hydrological time series.

Another way to establish these limits is to impose the base flow for this watercourse, the Tâmega river. However, such information was not available on SNIRH's online platform. It is known that the base flow of Douro river is about 500 m^3s^{-1}, and that the affluence of Tâmega river represents 14.5% of the Douro river discharge in the bridge area. Therefore, it is reasonable to conclude that the base flow of Tâmega river is much lower, possibly in the order of the minimum mean daily discharge, as previously referred.

An additional verification was undertaken. The availability of mean daily and instantaneous Q_{FT} records for the same 10-year time period (from 2009/10 to 2018/19) allowed the quantification of the associated discrepancy, through the comparison of estimated and recorded instantaneous streamflow data. For that purpose, the coefficient of proportionality was estimated for the "Fragas da Torre (EDP) (08H/02H)" gauging station data, using the available sample of 66 hydrological years (Table 3.1). A value of $K_{FT} = 1.621 \pm 0.075$ ($\sigma = 0.316$) was obtained for Q_{FT} data. By imposing that coefficient to the mean daily data for the aforementioned 10-year period, new instantaneous discharge values were estimated, showing an average over-prediction of 7.2% when compared with the recorded data (Figure 3.6). Therefore, for the purposes of the current investigation, the estimated coefficients of proportionality for the Q_T and Q_C data were deemed to be conservative estimates of reasonable order of magnitude.

3.2.5.2 Reliability analysis and scenario selection

Regarding the data reliability analysis, the verification of consistency and the hypothesis of randomness of the three hydrological time series were performed. The verification of consistency was not an issue, since there were neither changes in the location of the gauging stations nor the creation of obstacles nearby. The hypothesis of randomness was analyzed through the tests referred in Subsection 3.2.3.1, following the procedures outlined in Hipólito & Vaz (2011). The hypothesis

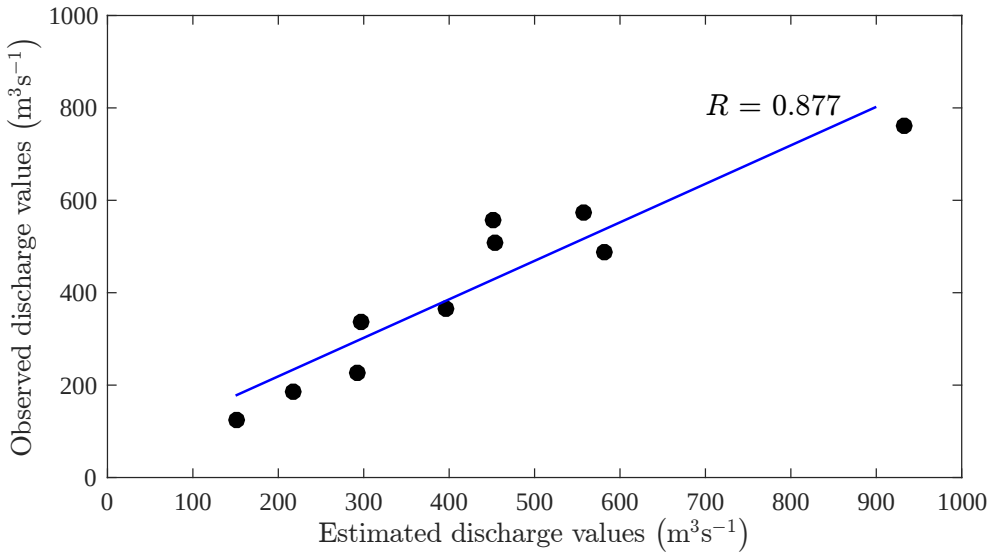

Figure 3.6: Correlation between observed and estimated instantaneous discharge values from the Q_{FT} hydrological time series.

of randomness was thus satisfied for all the three scenarios, since the assumptions of independence and homogeneity were confirmed.

The hydrological scenarios, considered to evaluate the maximum annual flow discharge approaching the new Hintze Ribeiro bridge (Q_{HR}), are depicted in Figure 3.7 in the form of box-plots graphs, which include the median, and the lower and upper quantiles (defined as the 25^{th} and 75^{th} percentiles) for each of the scenarios. The long upper tails show the lack of symmetry in the data values for all of the scenarios. The red plus signs are outliers that should be investigated carefully. In the current study, they are all mild outliers and contain trustful information; for Scenario 3, for instance, the higher outlier corresponds to the 1989 flood, referenced in Subsection 3.2.4.2, with a magnitude of 14,597.05 m^3s^{-1}.

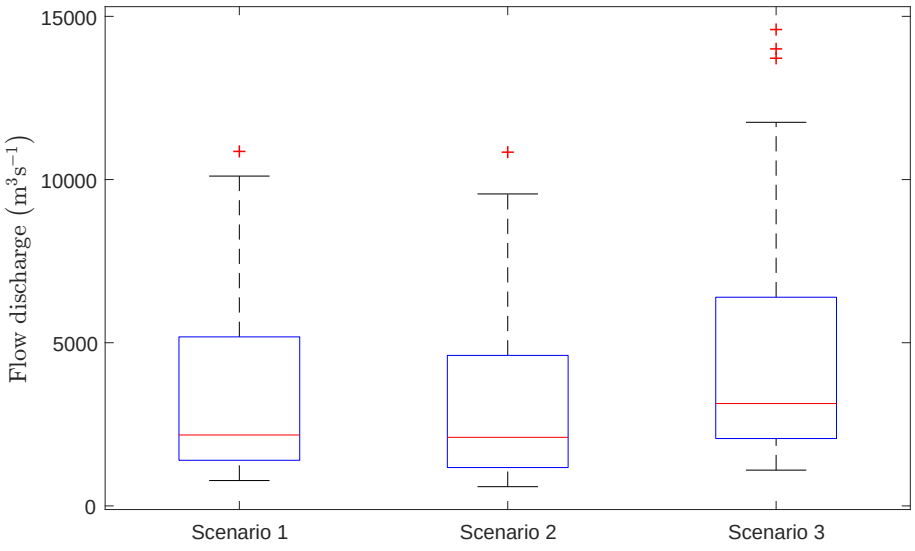

Figure 3.7: Box-plot graphs of Q_{HR} for the hydrological scenarios under consideration.

It is relevant to note that, when compared with the Scenario 1, Scenario 2 leads to lower resultant discharge values (Q_{HR}). In practice this behavior have led us to the conclusion that flood peaks do not coincide in all rivers, namely Douro, Tâmega and Paiva rivers. Scenario 1 is more conservative, but less realistic. However, this difference is not significant, representing solely an over-prediction of 6.3% of the mean value (as indicated in Table 3.3). As expected and previously mentioned, Scenario 3 is clearly the one which contains the higher discharge values. It over-predicts the Scenario 1 mean discharge value in a percentage of 26.8%. Further statistics for each scenario are given in Table 3.3.

Table 3.3: Statistics of Q_{HR} for the hydrological scenarios under consideration (m^3s^{-1}).

Variables	Scenario 1	Scenario 2	Scenario 3
Mean	3,691.80	3,460.40	5,045.60
Minimum	776.80	589.10	1,096.00
Median	2,173.40	2,101.10	3,137.00
Maximum	10,862.00	10,839.00	14,597.10
Standard Deviation	3,095.30	2,976.90	4,105.30
Coef. of Skewness	0.13	1.16	1.21
Coef. of Kurtosis	0.14	0.32	0.41
Coef. of Variation	0.84	0.86	0.81

Bearing in mind the main objective of the current study, providing a reliable estimate of extreme flow discharges at the bridge's approach section, the scenario that led to higher floods was desired and Scenario 3 was thus the one selected for the following analyses.

3.2.5.3 Probabilistic models' performance

The frequency of flood events, considering the peak discharge and return period, was statistically analyzed by individually employing the six parametric distributions referred in Subsection 3.2.3.2. Eight different return periods were considered: T = 2, 5, 10, 20, 50, 100, 500 and 1000 years. The methods of moments was used to estimate the parameters of the aforementioned distributions. The performance of these probabilistic models was assessed by the goodness-of-fit tests (KS, χ^2, Fi and AD), as well as by the corresponding Q-Q plots.

The models with potential for the design floods estimation were the two- and three-parameter LogNormal distributions, the Gumbel distribution, and the Gamma distribution. The estimated design floods, computed with the free Matlab code developed by Benkaci (2019), are presented in Table 3.4. From the goodness-of-fit tests, only the quantitative χ^2 test did not give satisfying results for the Log-Normal ($3p$) distribution and the Gumbel distribution; however, these two were also accepted as potential representatives of the data time series under analysis (Scenario 3), since the remaining tests did not reject them. The graphical adjustments of those four probabilistic distributions of the maximum annual flow discharge approaching the new Hintze Ribeiro bridge (given by Q-Q plots) are shown in Figure 3.8. It should be noted that the design floods (Table 3.4) were estimated at a 95% confidence level, in which the upper and the lower boundaries are represented by dashed borderlines in Figure 3.8.

Table 3.4: Design floods of Scenario 3 estimated by the four probabilistic models (m^3s^{-1}).

T (years)	LogNormal ($2p$)	LogNormal ($3p$)	Gumbel	Gamma
2	3,706	3,635	4,371	3,986
5	7,302	7,286	7,999	7,801
10	10,410	10,545	10,401	10,496
20	13,950	14,338	12,705	13,113
50	19,395	20,296	15,688	16,497
100	24,160	25,604	17,923	19,018
500	37,689	41,029	23,087	24,788
1,000	44,713	49,196	25,307	27,247

The Q-Q plots were built by using the empirical Weibull plotting position for all the distribution models, except for the Gumbel distribution, in which the Gringorten formula was selected. Figure 3.8 shows that the aforementioned four parametric distributions may produce satisfying results for Scenario 3 and that the Gamma distribution is the best fit for the available data (model selection, *MS*). The Gamma distribution not only passed the four goodness-of-fit tests, but also returned the highest correlation coefficient (R = 0.979). Despite the good performance of the Gamma distribution, the current study also considered an arithmetic average of the considered candidate models in order to reduce the model uncertainty, especially due to the available record length of only 31 hydrological years.

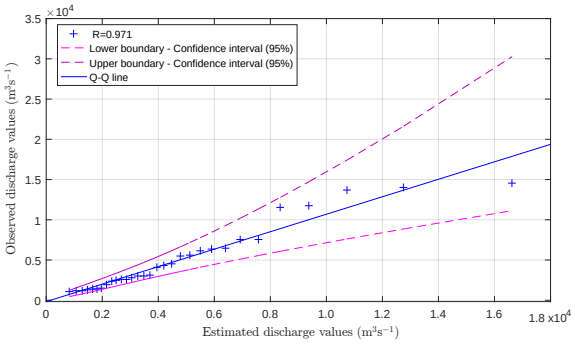

(a) LogNormal ($2p$) distribution.

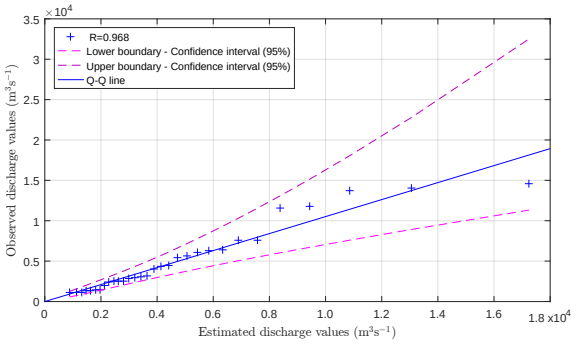

(b) LogNormal ($3p$) distribution.

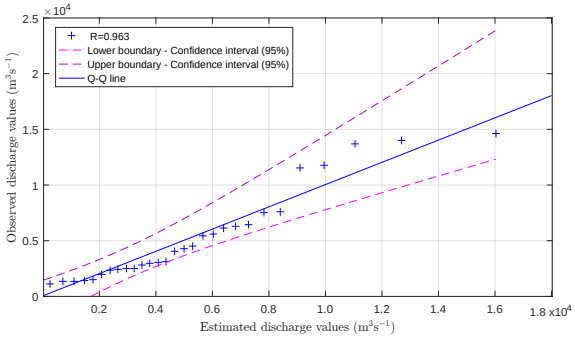

(c) Gumbel distribution.

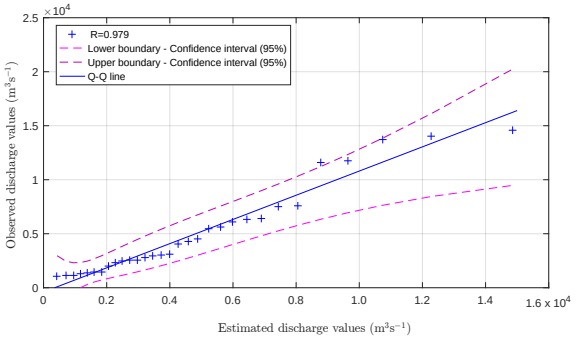

(d) Gamma distribution.

Figure 3.8: Graphical adjustments (Q-Q plots) of the four probabilistic distributions to the Scenario 3 data time series.

Comparative analysis of the hydrological modeling methods In order to take model uncertainties into account and thus reduce some of the epistemic uncertainties (reducible uncertainty), the weighted averaging technique was also considered in the present study. For the purposes of this investigation, only a modified arithmetic model averaging method was considered, namely the *modified MM*.

The design floods estimated by both methods are given in Table 3.5 (therein *MM* stands for the *modified MM* method). The *MS* design floods ranged from 3,986 m^3s^{-1} for T = 2 years of return period to 27,247 m^3s^{-1} for T = 1,000 years, whilst for the *modified MM* method, the flood events varied between 3,925 m^3s^{-1} and 36,616 m^3s^{-1} for the same return periods, respectively. In spite of the record length of only 31 historical records, the obtained flood designs included the major floods registered in the Douro valley. The 1739 flood corresponded roughly to the design flood reached for T = 50 years in the *modified MM* method. The first hydraulic infrastructure situated downstream of the case study bridge (Crestuma-Lever dam) was designed to withstand a discharge flow of 26,000 m^3s^{-1} for a correspondent return period of T = 1,000 years, in close proximity to *MS* estimate. A "relative difference" between the *modified MM* and *MS* methods was computed and it is also indicated in Table 3.5. For return periods ranging from 20 to 1,000 years, the "relative difference" varied between 3.1% and 25.6%. For T = 2 to 10 years, the *modified MM* method slightly underestimated the flood designs in comparison to *MS*. Higher differences between the methods, *MS* and *modified MM*, are expected for increasing return periods.

Table 3.5: Design floods at the new Hintze Ribeiro bridge (Q_{HR}). Here *MM* stands for the *modified MM* method.

T (years)	Q_{HR} (m^3s^{-1})		relative difference (%)
	MS	*MM*	$(MM-MS)/MM$
2	3,986	3,925	-1.6
5	7,801	7,597	-2.7
10	10,496	10,463	-0.3
20	13,113	13,527	3.1
50	16,497	17,969	8.2
100	19,018	21,676	12.3
500	24,788	31,648	21.7
1,000	27,247	36,616	25.6

In order to get further insight into the accuracy of the modelling methods herein considered, both parametric representations (*MS* and *modified MM*), a non-parametric method was also applied for the present case study. A Kernel density estimate (*KDE*) is a non-parametric way of estimating the probability density function of a random variable (Lall *et al.*, 1993; Apipattanavis *et al.*, 2010), in this case, the maximum annual discharges that approach the new Hintze Ribeiro bridge. It constitutes a fundamental data smoothing problem where inferences about the hydrological series are made, based on a finite data sample size. Such estimates are closely related to histograms; the histogram of the Scenario 3 data time series is presented in Figure 3.9.

Figure 3.9 gives thus an idea of the frequency of the flood events, as well as their magnitudes, occurred at the bridge approach section along the 31 hydrological years (from 1988/89 to 2018/19).

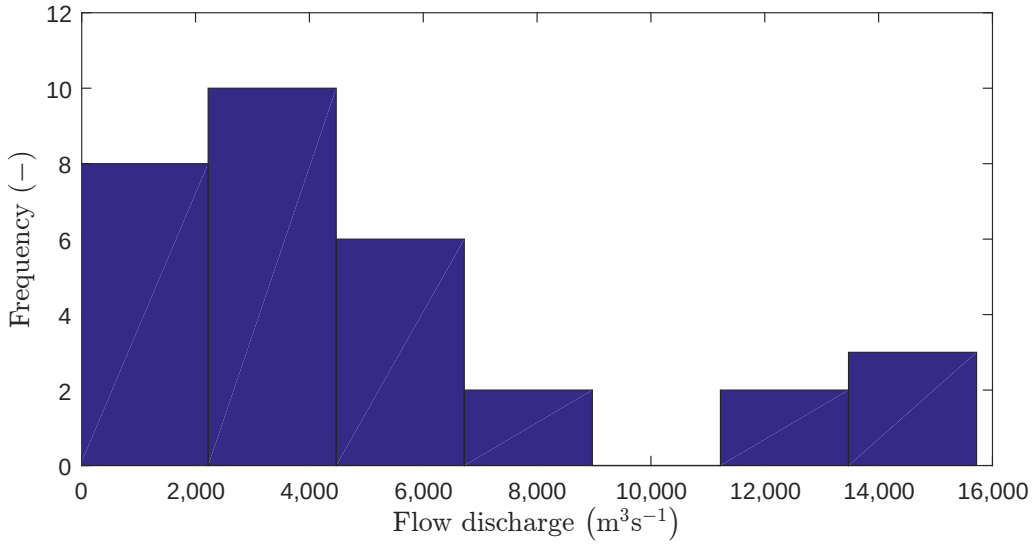

Figure 3.9: Histogram of the Scenario 3 data time series.

Regarding the standard deviation (σ) and the record length of the data series (n_s), estimates for the suitable Kernel bandwidth (bw) can be computed through the rule-of-thumb formula (Silverman, 1986, Equation 3.2), as well as by a variant in order to better fit tailed and skewed distributions of data (Equation 3.3).

$$bw = \left[\frac{4\sigma^5}{3n_s}\right]^{-\frac{1}{5}} \tag{3.2}$$

$$bw = 0.9 \min\left[\sigma; \frac{IQ}{1.34}\right] n_s^{-\frac{1}{5}} \tag{3.3}$$

Kernel bandwidths of 0.14 and 0.15 were obtained by equations 3.2 and 3.3, respectively, so a value of 0.15 was assumed for the Kernel optimal bandwidth, represented in Figure 3.10. The empirical cumulative distribution function ($F(x)$) of the data series is also shown in Figure 3.10. The long stair-step, in Figure 3.10, ranging from the flow rate of 7,592 $\mathrm{m^3 s^{-1}}$ to 11,559 $\mathrm{m^3 s^{-1}}$ was due to the nonexistence of records within that interval. This situation is corroborated with the histogram of the Scenario 3 data time series, shown in Figure 3.9.

Figures 3.11 and 3.12 comprise a shorter range of return periods due to the available Kernel estimates (maximum return period of 23 years). Nevertheless, it can be concluded that all four probabilistic distributions as well as the two *MM* methods (*modified MM* and *MM* (Okoli *et al.*, 2018)) exhibited a very similar design flood for T = 10 years. These results show an under-prediction of the non-parametric method (15.5%). For T = 2 years, the Gumbel distribution showed the highest percentage of relative difference (circa 26.5%). For 5 years of return period, a general discrepancy of 1.5% was obtained. While the individual and averaging methods under-predicted the *KDE* estimate in different percentages (not exceeding 12%) for T = 20 years, the LogNormal ($3p$) distribution estimate was practically coincident (showing a non-significant 0.1%

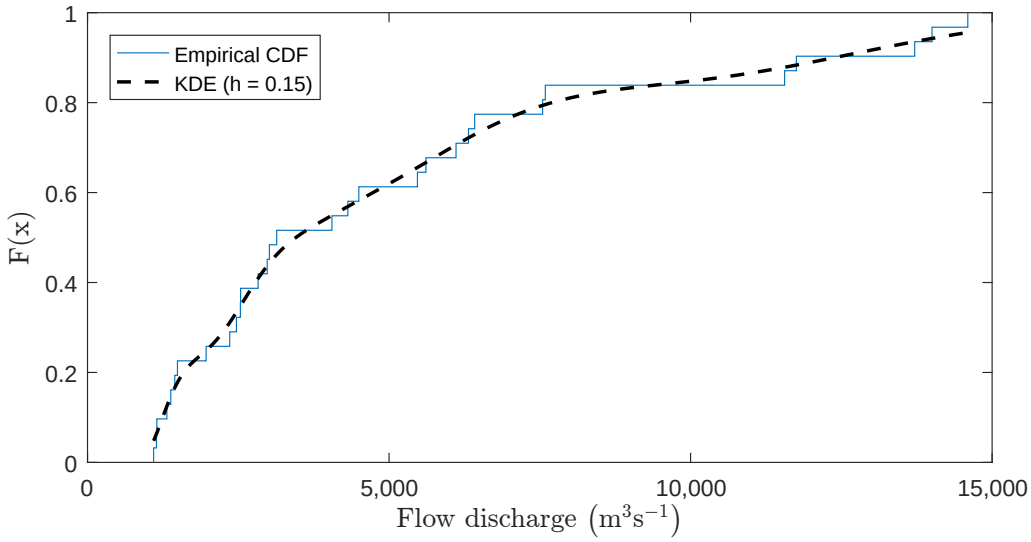

Figure 3.10: Kernel density estimate applied to the Scenario 3 data time series.

of relative difference). The arithmetic model averaging method proposed by Okoli *et al.* (2018), also represented in Figure 3.12, was taken from design flood estimates from the four probabilistic distributions referred in Subsection 3.2.3.2. The arithmetic model averaging methods - *modified MM* and *MM* (Okoli *et al.*, 2018) - display similar behavior (Figure 3.13).

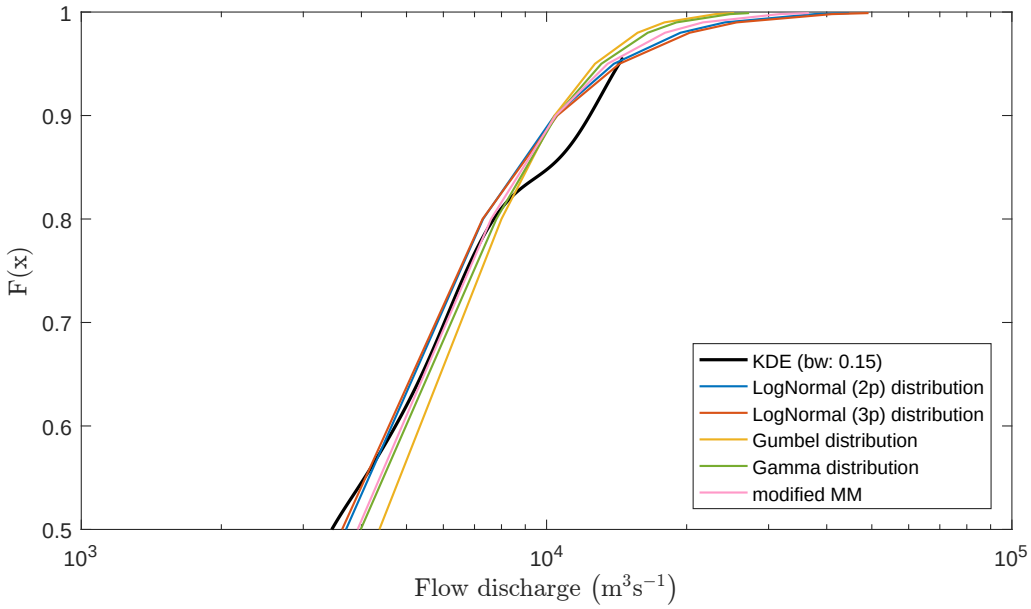

Figure 3.11: Cumulative distribution functions ($F(x)$) obtained by the parametric and the non-parametric distributions.

By considering the four return periods, from 2 to 20 years, the resulting prediction of the *modified MM* method presents a 2.19% lower average than the *KDE* results. The *MM* (Okoli *et al.*, 2018) under-predicts about 2.90% in relation with the non-parametric method; a relative difference of 24.4% is obtained when such method is compared with the *modified MM* method

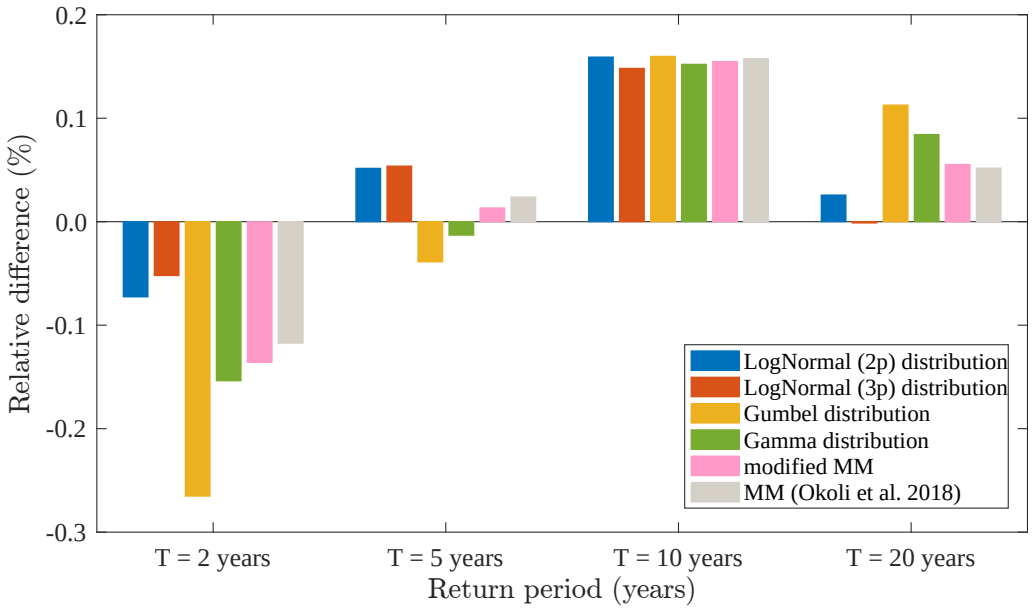

Figure 3.12: Relative differences of the design floods normalized by the respective non-parametric estimates.

herein proposed. If individual analyses are considered, different conclusions may be derived for the distribution model assigned as the *MS* when compared against *KDE* estimates. As stated in Subsection 3.2.5.3, Gamma distribution was assigned as the best fit for the available record length of 31 hydrological years. For a shorter range of return period (until $T = 20$ years), the Gumbel distribution gave a general over-prediction of 0.79% whereas the Gamma distribution showed an overall under-prediction of 1.74% (Figure 3.12). The LogNormal ($2p$) and ($3p$) distributions returned, in turn, average under-predictions of 4.10% and 3.71% in relation to *KDE* results.

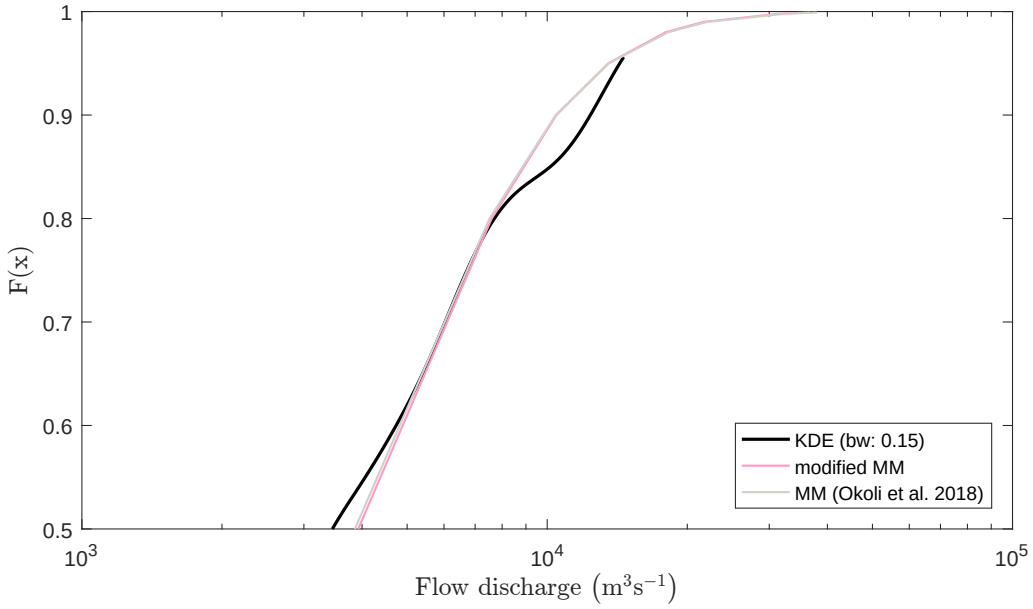

Figure 3.13: Comparison between the KDE and the arithmetic model averaging methods.

The conclusion that can be drawn from the information related to Figures 3.11 and 3.12 is that for the range analyzed (until roughly $T = 20$ years of return period), the behaviors of the parametric methods (individual and averaging models) were very similar and followed the non-parametric trend. This justifies the validity of all four models for the given data, i.e., through the *modified MM* method herein developed. The exception arose for the aforementioned range, in which there were no records of flood events within the 31-hydrological years considered in this study. Given the observed results (Figures 3.12 and 3.13), *modified MM* is considered a better calibrate method (in relation to *MS* and *MM* (Okoli *et al.*, 2018) methods) since it gives closer estimations to the non-parametric method (*KDE*), assumed as most reliable in the current investigation.

By assuming the typical 50 years for the expected design life of the new Hintze Ribeiro bridge, different return periods could be plausibly used, depending on the acceptance risks, through the application of Equation 3.1. Whereas a 100-year return period of the design flood event corresponds to a risk of 40%, the flood associated to 1,000 years of return period presents a hydrological risk of 5%. It should be noted that the adopted return period as a design criterion, and associated design flood, also plays a significant role on the assessment of admissible scour risk (i.e., maximum scour depths at the bridge foundations level) for the bridge structural stability.

3.2.6 Conclusions

A hydrological modeling methodology is herein presented that uses the flood frequency analysis technique allied to parametric and non-parametric methods for providing reliable estimates of design floods that approach hydraulic infrastructures. The new Hintze Ribeiro bridge, over the Douro river, in Portugal, was selected as case study. The frequency analysis is also relevant for the assessment of the hydrological risk considered, or to be adopted, as a design criterion of those infrastructures.

The extrapolation of the missing instantaneous discharge data was herein derived by factoring the corresponding mean discharge in that year by a coefficient of proportionality. This procedure was key to satisfy the minimum required sample size for the application of the flood frequency analysis technique on hydrological time series data. Such extrapolation was performed to obtain the "Carrapatelo Dam" and "Torrão Dam" instantaneous data. Two validation methods verified the output, including the associated sample errors, and consequent uncertainties of their estimations. The associated discrepancy between estimated and recorded instantaneous data is an over-prediction of 7.2%. Thus, the estimated coefficients of proportionality for the Q_T and Q_C data were deemed to be conservative estimates of reasonable order of magnitude.

A variety of probabilistic models were considered in the assessment of the maximum annual flow discharges at the bridge approach section, and the models' performance verified by the goodness-of-fit tests and graphical methods (by the *Q-Q* plots). Besides the widely applied model selection method (*MS*, Gamma distribution), in the present work, a modified method of the arithmetic model averaging (*modified MM*) was also performed. In order to take into account the parameter uncertainties, all design floods were estimated at a 95% confidence interval. Contrarily to what performed by Okoli *et al.* (2019), herein the proposed *modified MM* method considered solely the

contribution of the probability distributions that fitted well the Scenario 3 data, attributing equal contribution of the candidate probabilistic models on the estimation of the design flood events (four of the distribution models analyzed).

While slight differences were observed between the two methods (*MS* and *modified MM*) for lower return periods, for return periods higher than 20 years, the methods become increasingly different. The proposed arithmetic model averaging (*modified MM*) method was therefore entirely justified to cope with the model uncertainties. An additional analysis was performed by comparing both of the parametric representations (*MS* and *modified MM*) with a non-parametric method, the Kernel density estimate (*KDE*). Unlike its parametric counterparts, no prior assumption of the underlying distribution was required, which makes it suitable for the assessment of the parametric methods' accuracy. Despite the shorter range of validity of the Kernel estimates (maximum return period of 23 years), the behaviors of the parametric methods (individual and averaging models) were similar and followed the non-parametric trend, justifying the contribution of the all four models in fitting the data under study, through the *modified MM* method herein proposed. The discrepancy between *KDE* and *MM* (Okoli *et al.*, 2018) was 24.4% higher than the ones obtained by the *modified MM* method. Given the obtained results, the *modified MM* is considered a better calibrate method for the design floods estimation.

Based on the acceptable risk of flood occurrence in specific return periods (hydrological risk), and on the design life of a hydraulic infrastructure, the return period for which a structure should be designed can be ascertained. The selected return period and correspondent design flood also play a significant role on the assessment of admissible scour risk for any bridge structural stability, as for the new Hintze Ribeiro bridge.

3.2.7 Data availability statement

Some or all data, models, or code that support the findings of this study are available from the corresponding author upon reasonable request.

3.2.8 Acknowledgments

The first author thanks the Portuguese Foundation for Science and Technology (FCT) for financial support through the PhD scholarship (PD/BD/127798/2016). This manuscript is an outcome of the Doctoral Program INFRARISK - "Analysis and Mitigation of Risks in Infrastructures". This research was also supported by Centro Interdisciplinar de Investigação Marinha e Ambiental (CIIMAR) through the project with reference UID/Multi/04423/2019. Streamflow data was partly made accessible thanks to "Energias de Portugal (EDP)".

3.3 Risk-based methodology for scour analysis at bridge foundations. *Paper published*

TITLE: Risk-based methodology for scour analysis at bridge foundations[1]

Paper published in "Engineering Structures"
Received: March 19th, 2020 / Accepted: July 10th, 2020

Author contributions:
Bento, A.M. and Viseu, T. devised the main conceptual ideas and proof outline. Bento, A.M. and Gomes, A. conceived the present idea and performed the analytic calculations. Gomes, A. carried out the numerical simulations. Bento, A.M. wrote the manuscript. Viseu T., Couto, L. and Pêgo, J.P. discussed the results and contributed to the final manuscript.

[1] Bento, A.M., Gomes, A., Viseu T., Couto, L. & Pêgo, J.P. (2020) Risk-based methodology for scour analysis at bridge foundations. *Engineering Structures.* 223:111115. doi: 10.1016/j.engstruct.2020.111115

3.3.1 Abstract

The collapse of bridges inevitably leads to economical losses and may also be responsible for human fatalities. A bridge may fail due to several reasons, with local scouring around its foundation being the most common. Despite decades of scouring research, there are still many uncertainties affecting the design process of bridge piers. The most critical and least explored are the hydrological and hydraulic variables. The recent intensification of floods may also increase the vulnerability of bridges to scour effects. Therefore, the present work aims to propose a risk-based methodology for considering scour at bridge foundations. It is composed of three main steps: (i) assessing extreme hydrological events (hazards); (ii) modeling river behavior through the computation of flow characteristics and bridge scour depths; and (iii) assessing bridge scour risk by associating its scour depth to foundation depth ratio with the priority factor (vulnerability) and assigning a qualitative evaluation of the scour risk rating (level of risk). The hydrological modeling incorporates uncertainty with an averaging approach in the design floods definition. The flow characteristics are simulated with the HEC-RAS model, which also contains a scour module for bridge scour assessment. However, other empirical estimates are considered for simple and pile-supported foundations. This study ends with a qualitative assessment of how the scouring phenomenon affects bridge vulnerability and its safety. The proposed risk-based methodology - validated through a case study, the new Hintze Ribeiro bridge in Portugal - can be potentially incorporated into regular bridge inspection schedules as a useful tool for risk management measures, assisting in catastrophic events' prevention.

Keywords: bridge scour, design flood, HEC-RAS, new Hintze Ribeiro bridge, risk rating, scour risk

3.3.2 Introduction

One of the most significant issues with bridges over watercourses is the scouring around their foundations, often associated with high velocity flows. Scour can cause costly damage, leading to compromised safety, service restrictions for the bridge users and in certain circumstances to structural collapse (Lamb *et al.*, 2017). The removal of bed material at the vicinity of bridge foundations has been appointed to be the cause of numerous bridge collapses worldwide (Melville & Coleman, 2000; Wardhana & Hadipriono, 2003; Brandimarte *et al.*, 2012; Cook *et al.*, 2015). Over a period of 30 years, more than 1,000 bridges have collapsed in the United States, 60% of which as a result of scour at the bridge foundation (Shirole & Holt, 1991). Proske (2018) performed a compilation of the main causes of bridges collapses according to studies undertaken all around the world. He ranged scour as being one of the main causes of bridge failures, responsible for more than 50% of recorded collapses over the world. In 2001 the fall of the 19th century Hintze Ribeiro bridge, Portugal, caused the loss of 59 lives. According to national authorities, it occurred in the sequence of three months of floods exceeding 8,000 m^3s^{-1}, together with two decades of uncontrolled sand extraction which compromised the bridge's stability (Rocha *et al.*, 2008; Sousa & Bastos, 2013).

The recent intensification of floods, characterized by an increase in frequency and magnitude of such events, has generated a global awareness on the likely susceptibility of bridges to scouring effects (Flint *et al.*, 2017). Current design standards and recommendations often assume that bridges must be designed to cope with a prefixed return period, typically of the order of 100 to 200 years (Arneson *et al.*, 2012; Highways Agency, 2012; Pizarro *et al.*, 2020, among others). However, recent studies have concluded that such rule does not comprehend the variability related with collapse return periods, compromising their impact on the assessment of bridge risk due to scour effects (Ellingwood, 2001; Flint *et al.*, 2017; Ashraf & Flint, 2019).

Acknowledging the impossibility to eliminate the risk of scour, a comprehensive assessment of such risk is therefore essential to define design criteria and also establish procedures for their inspection. Despite decades of research, there are still many uncertainties (Kowalik, 2009; Briaud *et al.*, 2014) affecting the design process of bridge foundations, being the most critical ones and less explored (Lagasse *et al.*, 2013; Ettema *et al.*, 2017) the hydrological and hydraulic variables. As a result of their stochastic nature, a risk-based methodology accounting the uncertainty of those variables will enhance scouring analysis and reduce the vulnerability of bridges to scour effects, thus reducing the scour risk (Rausand & Haugen, 2020). Tubaldi *et al.* (2017) have proposed a probabilistic distribution of the scour depth, by combining information from hydrological, hydraulic and scour analyses in a Markov-model approach. The same authors have concluded that not only the random occurrence of subsequent extreme flood events contribute to the scour development, but also the hydrograph duration and shape. In Manfreda *et al.* (2018), a probability distribution of scour, by assuming a simplified hydrograph shape, is theoretically derived to reduce uncertainty in the hydraulic design of bridges and their scour assessment. It focuses on the impact that the contributing variables, as river basin hydrology, hydraulic river characteristics, sediment and pier geometry have on the scour depth probability distribution.

A risk analysis framework comprehends a combination between hazard analysis and vulnerability assessment (Todinov, 2006; Goerlandt *et al.*, 2015; Rausand & Haugen, 2020). Hazard analysis consists mainly in the identification of the likelihood of occurrence of a hazardous phenomenon (flood flows) with a given intensity within a specified period of time. Vulnerability assessment, in turn, focuses on the factors, regardless their origin, which together or separately drive and shape the susceptibility of the receptor (infrastructure) to a certain hazardous event (scour effects). These drivers are uncertain owing to the stochastic nature of hydrological events but also it is not certain how the system (river morphodynamics and infrastructure) will respond to them, especially when conditions exceed design specifications (Kallias & Imam, 2016; Ettema *et al.*, 2017; Pizarro & Tubaldi, 2019). Barbetta *et al.* (2017) performed a comparison of two procedures for a qualitative assessment of bridge piers vulnerability to scour, applied to 46 bridges in the Tiber River basin, Italy. While the first quantifies the Scour Vulnerability Index (SVI) considering the combined effects of local and contraction scour, the second method identifies a vulnerability index to vertical instability depending on several indicators (presence of debris, foundation protections, among others). Similar results were obtained, yielding the former a quicker assessment of the bridge pier vulnerability to undermining. In Akay *et al.* (2019), a structural assessment is also

added to the qualitative safety-inspection method therein developed for bridges in Turkey.

Hence, the present study addresses bridge scouring, through the development of a methodology to assess how it affects the bridge safety and level of risk. A three-step approach is herein presented: (i) assessing extreme hydrological events causing river floods (hazards), through field data acquisition and hydrological modeling; (ii) modeling the river behavior through the computation of flow and bridge scour variables; and (iii) assessing the bridge scour risk by associating its scour depth to foundation depth ratio with the priority factor (vulnerability, based on important characteristics that may increase or reduce the likelihood of failure, such as the type of foundation, the material on which the bridge is founded or the history of scour problems, for example) and assigning a qualitative evaluation of the scour risk rating (level of risk).

Different probability distributions are analyzed in order to properly estimate the extreme discharges approaching a bridge cross-section. The definition of such design floods are then used in the computation of flow variables (approach flow depths and velocities) and maximum scour depths. Modeling scour in a close proximity to infrastructures, founded on alluvial beds, is subject to major sources of incertitude. These uncertainties are tied to the input parameters whilst the modeling errors are associated with the chosen scour calculation procedure (Briaud *et al.*, 2007). Within the proposed methodology, the maximum scour depths are estimated by HEC-RAS software (Brunner, 2016), and compared with other well-established empirical predictors (Sturm *et al.*, 2018), regarding the respective flow regimes and bridge foundations' shape. The maximum scour depth at a bridge foundation is then compared with the correspondent foundation depth and the scour risk rating is evaluated. In order to validate such methodology, a field implementation was performed for the new Hintze Ribeiro bridge, located in the Douro river, Portugal.

Following this Introduction, Subsection 3.3.3 presents the proposed methodology for scouring risk analysis and its key components. Subsection 3.3.4 illustrates the case study and the application of the proposed methodology. Detailed features and results from each step of the methodology are given. Finally, Subsection 3.3.5 clarifies the most important conclusions of this research.

3.3.3 Scour risk analysis

3.3.3.1 Proposed methodology

Risk analysis involves combining the possible consequences of an event, such as a bridge failure, with that event's occurrence likelihood, and results in a level of risk. Two types of risk analysis can be used: qualitative and quantitative, depending on the objective of the analysis (Rausand & Haugen, 2020). They differ significantly in the level and availability of information required as well as in the degree of accuracy achieved (Haimes *et al.*, 2008).

A qualitative risk analysis prioritizes risks according to their potential impact on project objectives, by using a pre-defined rating level. Quantitative risk analysis, in turn, is the process of analyzing mathematically the likelihood of each risk event and its impact. It estimates practical values for consequences and their probabilities, and produces values of the level of risk in specific units. Full quantitative analysis may not always be possible or desirable due to insufficient information about the system or activity being analyzed, lack of reliable and adequate data, influence

of human factors, among others, or simply because the effort of a quantitative analysis is not warranted or required (Andrić & Lu, 2016, among others). In such circumstances, a qualitative ranking of risks by specialists/experts may still be effective (Lamb *et al.*, 2017, and references therein). In the present work, a general methodology to evaluate the risks associated with scour at bridges, as a result of extreme hydrological events and based on a qualitative risk approach, is presented. Such methodology is based on modeling hydrological and hydraulic characteristics of rivers basins, taking into consideration the bridge geometry and the site under study. The evaluation of consequences, i.e., the quantification of the socio-economic damages was not carried out. Its assessment would require an independent study of the possible costs, expressed in monetary units, concerning different levels of damages in the infrastructure due to scouring but also intangible costs related to its possible operation interruption, not forgetting the ultimate costs related to possible loss of lives if failure is considered. Those issues were considered to be out of the scope of the current investigation. Therefore, the proposed risk analysis methodology is based on three main steps as presented in Figure 3.14. It indicates the prerequisites, the techniques and the final results for each stage.

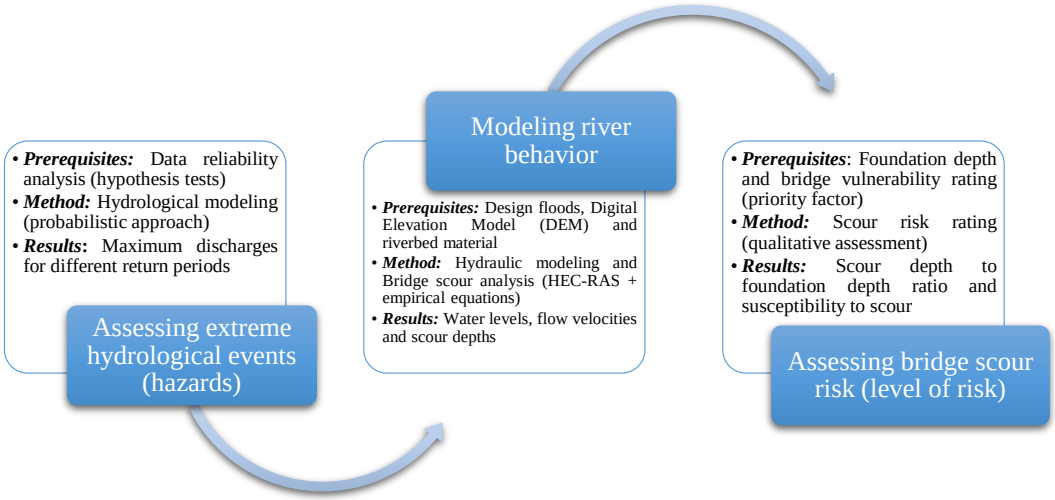

Figure 3.14: Proposed methodology for bridge scouring risk analysis.

In the first step, the hydrological series (maximum annual flow discharge data) of the river at the bridge site are statistically analyzed and the frequency of flood events, considering the peak discharge and return period, is assessed. As a second step, the hydrological events allow the derivation of the correspondent hydraulic variables, namely the approach flow depths and velocities at a bridge site, by using the open-source HEC-RAS software (5.0.7 version) developed by the U.S. Army Corps of Engineers (Brunner, 2016). Then, taking into account the hydraulic parameters of the flow, the characteristics of the riverbed material and the geometric dimensions of the bridge under analysis, the maximum scour depth around bridge foundations is herein estimated. Such estimation is performed taking advantage of the HEC-RAS scour computation capability and compared with adequate empirical prediction methods (Sturm *et al.*, 2018; Yang *et al.*, 2019).

Finally, in step 3, the maximum scour depth, calculated using the sum of contraction and local scour, is compared with the correspondent foundation depth (relative scour depth), and is related to a level of risk of failure due to scouring through the qualitative risk rating, presented in Highways Agency (2012). Each step is further detailed on the following subsections (Subsection 3.3.3.2 to 3.3.3.4).

3.3.3.2 Hydrological modelling

Hydrological modeling aims at obtaining a reliable estimate of extreme discharge flows and their occurrence probabilities (Okoli *et al.*, 2018) that might occur at a given location, namely at a bridge site. To estimate such extreme discharge flows (hereinafter referred as "design floods"), statistical methods, generally referred as "flood frequency analysis", are commonly considered (Klemeš, 2000; Moran, 1957; Beven, 2019, and references therein).

In flood frequency analysis it is common to consider a range of models as potential representations of the observed data. Six probability models are suggested in the proposed methodology, namely the following distributions: two and three-parameter LogNormal ($2p$ and $3p$, respectively, being p the number of parameters), Gumbel, Weibull, Gamma and LogPearson III. These models are usually recommended to both site and regional contexts (Chow *et al.*, 1988; Cunnane, 1989; Castellarin *et al.*, 2012; Hassan *et al.*, 2019). For estimating the parameters of each probability distribution, the method of moments, the L-moments method and the method of maximum likelihood are the most advisable by hydrologists (Kite, 2019). The performance of each probability distribution is assessed based on goodness-of-fit tests and graphical methods (Naghettini & Pinto, 2007).

The selection of a single best distribution function (i.e. the model selection, *MS*) in the field of flood frequency analysis, represents an implicit assumption that the selected model can adequately describe the frequency of observed and future floods, including the extreme events (Okoli *et al.*, 2018). Nevertheless, any model faces uncertainty and its quantification is crucial for ensuring data quality and usability (McMillan *et al.*, 2018). According to Okoli *et al.* (2018), one of the possibilities to deal with model uncertainty is to use all candidate probability distributions for the estimation of the design floods, where the final estimate is an average of all individual estimates, known as model averaging (Bumham & Anderson, 2002; Höge *et al.*, 2019). The model averaging can be performed either by taking the arithmetic mean of the design flood estimates from the candidate probabilistic models (i.e. the arithmetic model averaging, *MM*) or by attributing weights to the design floods of each individual candidate probability distribution (i.e. the weighted model averaging, *MA*) depending on how best the probability model fits the data (Hoeting *et al.*, 1999; Yan & Moradkhani, 2014). Okoli *et al.* (2019) concluded that selecting the best fitting probability distribution is associated with several outliers in comparison with multiple probability functions, specially when facing short sample sizes (30-50 hydrological years). Hence in the present methodology, a modification of the arithmetic averaging method, derived by Okoli *et al.* (2018) (*MM*), is employed as proposed in Bento *et al.* (Submitted). Such method consists of considering only the distributions that ensure good performance on both goodness-of-fit tests and graphical

methods in the definition of the design floods (hereinafter referred as $modified\ MM$). The latter are the outcome of this first step.

3.3.3.3 Hydraulic modelling and bridge scour analysis

Hydraulic simulations aid the understanding of the spatial and temporal changes in the nature of a river and its effects on the surrounding environment. Factors such as anthropogenic activities and topographic changes lead to increased rates of erosion and deposition, which modify the riverbed configuration and results in increasing the susceptibility of bridge foundations to scouring effects (Anees *et al.*, 2016).

In the proposed methodology, the propagation of the design floods approaching a certain bridge section is performed using the HEC-RAS model. The latter has been widely applied for one- and two-dimensional hydraulic modeling and has been proven trustworthy by many researchers (Horritt & Bates, 2002; Brandimarte & Baldassarre, 2012; Lagasse *et al.*, 2013; Link *et al.*, 2020). Further details regarding the modeling capabilities of HEC-RAS may be found in Brunner (2016).

The adoption of steady flow conditions, within the HEC-RAS river analysis module, is herein consistent with the proposed methodology by maintaining it simple and pragmatic as also performed in the studies of Brandimarte & Baldassarre (2012) and Link *et al.* (2020), and usually used by regulatory agencies (Baldassarre *et al.*, 2010). In addition, the steady flow component is capable of modeling the subcritical, the supercritical and the mixed flow regimes (Chow, 1959), being the first one the mostly encountered in the large bridges all around the world.

The application of this hydrodynamic model requires the definition of the channel geometry, the upstream and downstream boundary conditions, and the channel features (Ramesh, 2012; Brunner, 2016). An adequate resolution of the digital representation of the river bathymetry and the bridge geometry is crucial regarding spatial input data dealing with the river behavior, flow and sediment, in both stream and floodplain areas. The RAS Mapper routine (Ackerman *et al.*, 2010) of HEC-RAS is herein considered to import the Digital Elevation Model (DEM), adequately generated by the ArcMap software. The bridge configuration is also introduced in HEC-RAS according to its geometrical features, including its deck and foundations. Upstream the bridge section, cross-sections of the riverbed are defined in order to evaluate long-term effects of the bridge on the water surface profile upstream (Brunner, 2016). Downstream, in turn, other cross-sections are required to guarantee that the hydraulic simulation results, at the bridge section and immediately upstream the bridge section, will not be affected by defining the downstream boundary condition (for subcritical flow regimes). Such condition may be set to a rating curve, a normal depth, a known water surface elevation, or a critical depth. For steady and subcritical flow conditions, upstream boundary conditions are the approaching discharges (i.e. design floods).

Among the hydraulic parameters, the channel roughness plays an important role on the accuracy of both the computed water surface elevations and the flow velocities. The channel roughness is highly variable, which is dependent on several factors such as surface roughness, vegetation cover, channel irregularities and alignment, scour and deposition, obstructions, size and shape of the channel, stage and discharge, seasonal changes, temperature, suspended material and bedload

(Ramesh *et al.*, 2000; Dey, 2014). The roughness coefficient is advisably calibrated by using typical values for streams and floodplains and, once possible, it should be validated by appropriate field data. A summary of roughness prediction techniques, and their theoretical bases, can be found in McKay *et al.* (2011). The channel bed is commonly characterized by its median grain size diameter, D_{50}, as well as by its D_{90}. Once the hydraulic model has been calibrated, the water surface profiles and respective flow velocities can be computed for the different design floods.

Bearing in mind that significant uncertainty is associated with flow and riverbed material at a bridge site, design prudence requires the estimation of a potential maximum scour depth, that is, the deepest scour attainable for a given design flood, considering both the contraction and the local scouring. For decades, several equations have been proposed for estimating the maximum local scour depth, whose prediction ability is especially suitable for structures of relatively simple geometry. For simple bridge pier's geometry, the empirical estimates given in the latest version of HEC-18 equation (Arneson *et al.*, 2012, Chapter 7), and the Sheppard/Melville (S/M) equation (Sheppard *et al.*, 2014, Equations 1 to 6), are herein considered as recommended by Sturm *et al.* (2018). For pile-supported piers, the computation of the local scour may require adaptations such as the consideration of an equivalent diameter, D_e (Figure 3.15) in order to apply the methods of FDOT (Sheppard & Renna, 2010, *Florida Department of Transportation*, Chapters 3 and 4), HEC-18 (Arneson *et al.*, 2012, Chapter 7), and Yang *et al.* (2019) (Equations 1 to 7). The aforementioned empirical predictors can be applied for both clear water and live bed scour conditions.

HEC-RAS model also supports a bridge scour computation routine, within the "Hydraulic Design Functions" window. The aforesaid empirical estimators of the maximum local scour depth are calculated and compared with the scour evaluation method available in the HEC-RAS model, namely the previous version of HEC-18 equation (Richardson & Davis, 2001). For the contraction scour, HEC-RAS uses the Laursen's clear water (Laursen, 1963) and the Laursen's live bed (Laursen, 1960) equations, respectively. Thus, total scour at bridge piers is then estimated by simply adding the contraction and the local scouring, inherently assuming that the scour processes for each are independent, although other authors dispute this assumption (Sturm *et al.*, 2018). Finally, the output consists on a final estimate of the maximum scour depth encountered in the most vulnerable foundation in order to rank the bridge, under analysis, in terms of scour risk (aim of step 3 - Subsection 3.3.3.4).

3.3.3.4 Scour risk rating

The ratio between the maximum scour depth that potentially could occur under the hydraulic conditions (obtained in Subsection 3.3.3.3) with the depth of the bridge foundation is the major parameter affecting the safety of a bridge. This can be expressed by a relative scour depth parameter given by $D_R = D_T/D_F$, where D_T is the total depth of scour and D_F is the foundation depth. Such factor (D_F) is a key parameter for determining its resistance to scour and the risk of scour-related failure. The determination of D_F differs regarding the type of foundation, either simple or pile-supported piles, and whether the piles reach (or not) the underlying bedrock. Thus, D_F is the depth from the average bed level to the underside of a spread footing (Figure 3.16 (a)) or to the

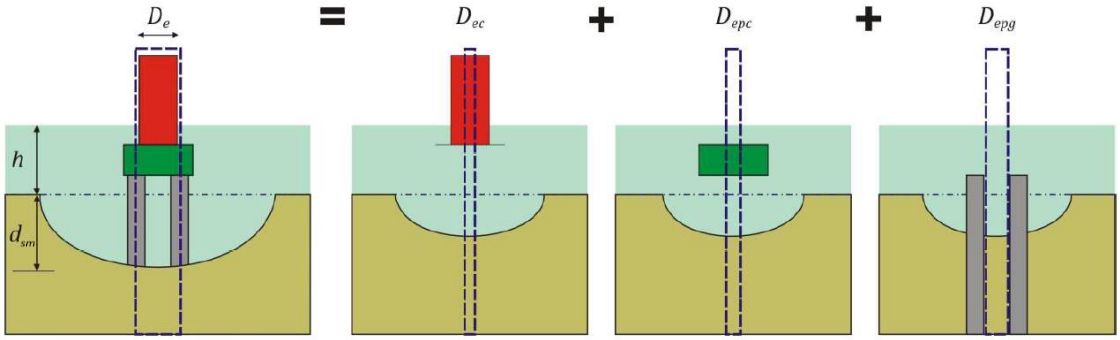

Figure 3.15: Conceptual hypothesis of obtaining D_e, through the sum of equivalent diameters of each element from a pile-supported foundation: c for column, pc for pile cap, and pg for pile group. Variable h stands for approach flow depth while d_{sm} is the maximum local scour depth. Adapted from Moreno (2016).

underside of the pile-cap in the case of a piled foundation (Figure 3.16 (b)). Though there is less risk of scour causing damage to a pile-supported foundation, it is undesirable for the piles themselves to be exposed, as this may affect their bearing capacity or the lateral stability of the bridge (Highways Agency, 2012). On that case, D_F should consider all thick layer of alluvial deposits at the foundation vicinity (Figure 3.16 (c)).

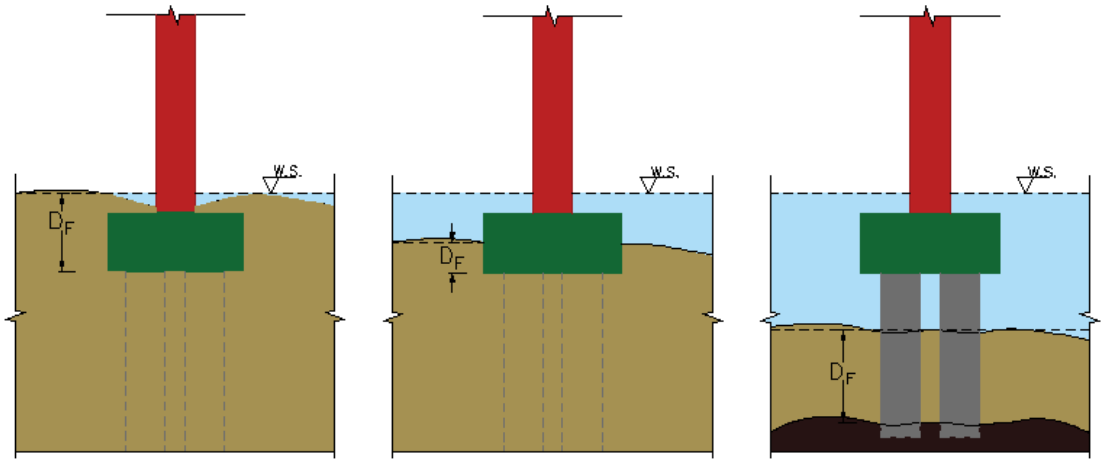

Figure 3.16: Definition of the pier foundation depth (D_F) according to the alluvial riverbed level (from (a) to (c)). $W.S.$ refers to water surface.

Besides the hydraulic characteristics of the flow (mentioned in the previous subsection), other parameters may increase or reduce the likelihood of failure. They can be more difficult to assess, nonetheless, should be considered. According to Highways Agency (2012), these include: (i) the type of foundation (F) and material on which the bridge is founded (M); (ii) the history of scour problems (H); (iii) the type of river (T_R); and (iv) the importance of the bridge as indicated by vehicle traffic volume and other factors (V_f). These parameters can be combined to provide a Priority factor, P_f, defined as $P_f = FHMT_RV$, which is used to define the vulnerability of an

infrastructure. Such factors are assessed and described in Table 3.6.

The scour risk rating is assessed from Figure 3.17, based on the magnitude of the relative scour depth (D_R) and the Priority factor (P_f) for a certain bridge, considered as an indicative statement of relative risk. Figure 3.17 shows five bands which define the risk rating, with 1 being the highest risk and 5 the lowest. Bridges falling in band 5 have a very low risk of scour damage or have been assessed as having a depth of foundation greater than the estimated maximum depth of scour. If the scour depth does not exceed the depth to the underside of the foundation for each pier and abutment, then the structure should be designated as "Scour risk rating" 5. Otherwise, it should be allocated a "Scour risk rating" in the range of 1 to 4 and must be designated as "Scour susceptible".

Table 3.6: Values for the parameters contributing for Priority factor (Highways Agency, 2012).

Foundation type factor (F)	
Spread footing	1.00
Piled foundation	0.75
History of scour problems factor (H)	
History of scour problems	1.50
No history of scour problems	1.00
Foundation material factor (M)	
No information on the foundation material or the material is granular (silts, sands, gravels, etc.)	1.00
Some evidence that the bridge is founded in clay	0.75
Strong evidence that the bridge is founded in clay or there is a reasonable possibility of rock under the foundations	0.50
Type of river factor (T_R)	
Mountainous terrain	1.50
Upland terrain	1.30
Hilly terrain	1.20
Lowland terrain or estuary	1.00
Importance factor (V_f)	
Motorway/A road (12-hour traffic flow: $\geq$ 30,000)	1.00
Motorway/A road (12-hour traffic flow: 10,000 - 29,999)	0.90
A/B class road (12-hour traffic flow: 1,000 - 9,999)	0.80
A/B class road (12-hour traffic flow: $\leq$ 1,000)	0.70

With regards to the obtained risk rating for a certain bridge, different actions, typically comprising a selection of risk management measures, can be suggested. Bridges with risk ratings 1 and 2 are of greater concern and must be subject to a strict monitoring and assessment in order to define scour protection measures. For bridges falling in bands 3 and 4, underwater inspections, both as part of regular bridge surveys and after major floods, should check for signs of scour and bank erosion. If conditions at the bridge change then re-assessment should be carried out. These are of less concern with regard to potential scour damage, nonetheless, its potential should not be neglected. For bridges with a risk rating of 5, no special action is required other than routine inspections, according with the local regulatory laws and standards.

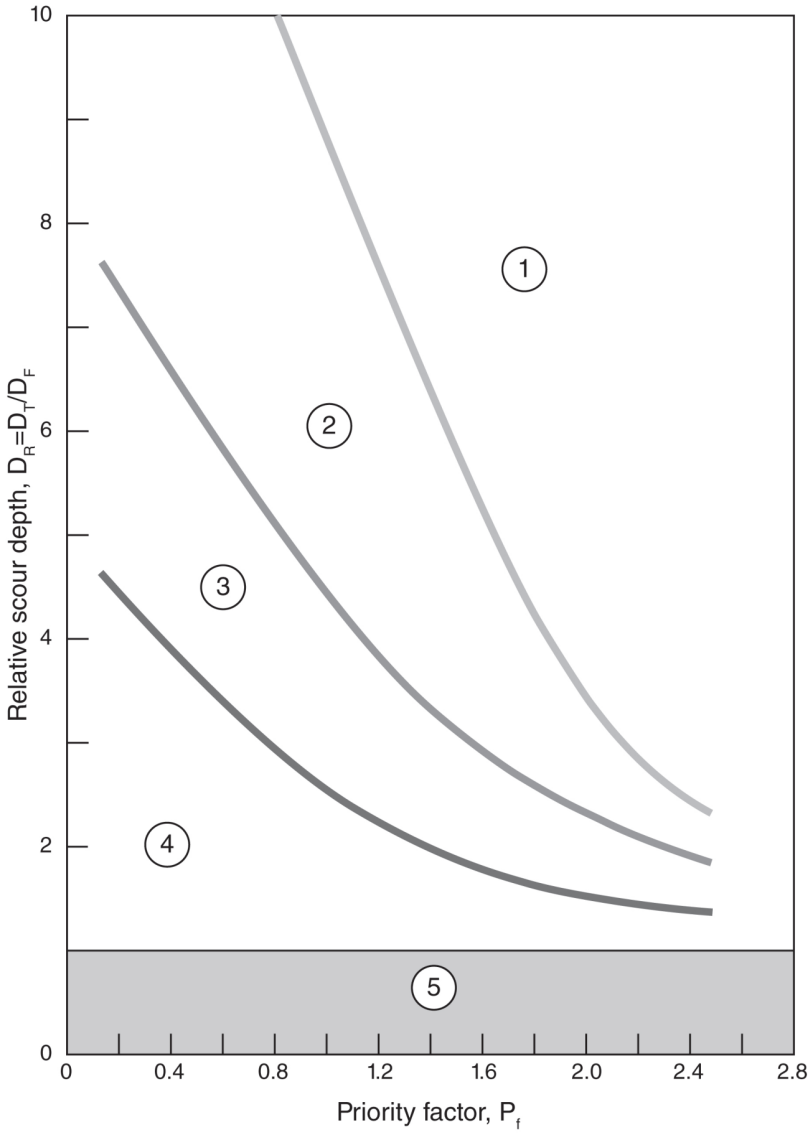

Figure 3.17: Scour risk rating (Highways Agency, 2012).

3.3.3.5 Applicability considerations

A risk management approach, able to consolidate a connection between the recent advances on scour depth predictors and its usefulness on industry practices (calibration of the HEC-RAS results for scour depth estimates), was herein sought. The proposed methodology's three main steps provide, thus, a simple and pragmatic methodology for rating and assessing scour risk to bridges using a semi-quantitative priority factor. Many underlying uncertainties, concerning how different pier characteristics, hydrological events and hydraulic conditions, are accounted for in recognition to their influence on the scouring phenomenon and the resulting bridge scour risk. As with any model, the presented methodology (Subsection 3.3.3.1) has strengths and weaknesses; the major advantages and limitations of each step are highlighted in Table 3.7.

In line with Table 3.7, the proposed methodology also assumes that the empirical formulas of local and contraction scour depths, herein employed, are reliable and in the safety side to estimate

Table 3.7: Main advantages and limitations of the proposed risk-based methodology.

	Step 1
Advantage	Accounting for hydological uncertainties in the design floods estimation by opting for the *modified MM* method
Limitation	Assuming the extreme hydrological events (design floods) as independent occurrences
	Step 2
Advantage	Freely available HEC-RAS scour computation capability, which estimates are validated by recent and adequate empirical predictors
Limitation	Assuming the direct sum of the contraction and the local scouring as independent processes
	Step 3
Advantage	Reliable assessment of the relative scour depth and how it affects the available foundation depth
Limitation	Factors as the presence of debris or countermeasures are not accounted for in the quantification of the bridge's priority factor

the maximum scour depth attained in field bridge foundations. On the other hand, the foundation depth of a certain bridge pier, important parameter in the scour risk assessment, should be used with caution since its value may be affected by uncertainties inherent to the difficulties of carrying out the survey (observation uncertainty). The multidisciplinary analysis, covering concepts from the large branches of civil engineering (structural, hydraulics, geotechnical, transport and urban planning areas) within the aforementioned three main steps, make it a useful tool for being incorporated into regular bridge inspection schedules, as well as being used in the hydraulic design of new infrastructures.

3.3.4 New Hintze Ribeiro bridge case study

3.3.4.1 Case study selection considerations

Due to the inherent complexity of site- and bridge-specific cases, the selection of a Portuguese bridge for the proposed risk analysis was preceded by an extensive investigation on the availability of monitoring data as well as their potential susceptibility to the scouring phenomenon. The required data consisted on: (i) detailed bathymetry taken upstream from the bridge (approach section), at the bridge, and downstream from the bridge (exit section); (ii) bridge structural characteristics, including substructure (geometry and shape of the foundations elements) and superstructure (e.g. deck thickness) components; (iii) continuous measurements of discharge at a near gauging station (if possible during flood events); and (iv) grain size distribution and other geotechnical properties of the riverbed material in the vicinity of the bridge foundations. The variability of the bathymetry over time at the bridge site was also taken as a favorable factor for selection. Therefore, special preference was given to bridges crossing the watersheds of Tagus and Douro rivers due to the higher abundance of streamflow data, within the Portuguese context.

The selection of the case study was made with the assistance of Infraestruturas de Portugal (Portuguese authority for the conservation of bridges) personnel who were able to confirm the availability of data specific to the aforementioned requirements and conditions. Of the potential

bridge case studies, the new Hintze Ribeiro bridge, located in the Douro river, was identified as the most suitable for the present investigation. This bridge, inaugurated in May 2002, was built in the sequence of the collapse of the 19^{th} century Hintze Ribeiro bridge in 2001, which was located 7.5 m downstream of the new bridge's position.

3.3.4.2 Hydrographic region characterization

The new Hintze Ribeiro bridge is located in the Douro river, about 500 m downstream of the Tâmega river confluence, a tributary of the right bank of Douro river (Figure 3.18). The bridge section is located in the downstream reach of the Douro river, at the Crestuma-Lever dam (at a distance of 25.5 km) reservoir. The bridge is subject to the effects of flow which are essentially dependent on the discharges from the Torrão dam, on the Tâmega river, and from the Carrapatelo dam, on the Douro river (Lopes, 2019). The former is situated 3.8 km upstream the bridge section while the latter is located at a distance of 16.7 km. The discharges from Torrão dam consist of clean waters, without sediments which are held by that dam, while the flood flows of the Douro river carry high concentrations of sediment, as evident by the light color of the flow from Tâmega river in Figure 3.18 (Rocha *et al.*, 2008). The Paiva river, a left tributary of Douro river, also contributes to the flow rates that approach the new Hintze Ribeiro bridge, through the records of "Fragas da Torre (R.E.) (08H/02H)" gauging station (identified in Figure 3.18).

A real time hydro-meteorological network is operating in the Douro river basin, since the beginning of the 20^{th} century (Tato, 1966; Vieira & Costa, 2017), nowadays under the responsibility of the Portuguese Environment Agency (APA). However, given the importance that the floods have for the riverside populations, dispersed records of flood marks exist along the Douro river, which enabled the assessment of maximum flow discharges since at least the 18^{th} century (Tato, 1966; Vieira & Costa, 2017). The extraordinary floods of the Douro river are characterized by a large volume, rapid propagation, strong water level rise (especially in the narrowest sections) and for a short duration of 2 to 3 days, since the water level falls relatively quickly (APA, 2016). Those flood peaks, reaching the Portuguese region of the Douro watershed, are mainly due to the combination of several factors such as the intensity of precipitation (1200-3000 mm/year), although with a rather irregular regime, and to its shape not so elongated in relation to that of its tributaries (APA, 2019). The intensity of precipitation is out of the scope of the present study. The tributaries are roughly parallel to each other, with strong slopes, and without floodplains. In addition to the characteristics of the embedded valley and the inclination of the Douro riverbed and its tributaries, the geological constitution of the basin and the construction of the Portuguese and Spanish dams are also determining factors for the flow regime. According to APA (2019), the Douro river basin has a total area of 97,477.66 km^2, of which 18,587.85 km^2 are in Portugal (19.07%) and 78,889.00 km^2 are in Spain (80.93%). The geology of the Portuguese part of the Douro watershed consists predominantly of granitoid and highly deformed metasedimentary units. At the bridge site, the Douro riverbed is mainly made up of sandy alluvial with scattered pebbles (Nazareth & Sousa Cruz, 2002).

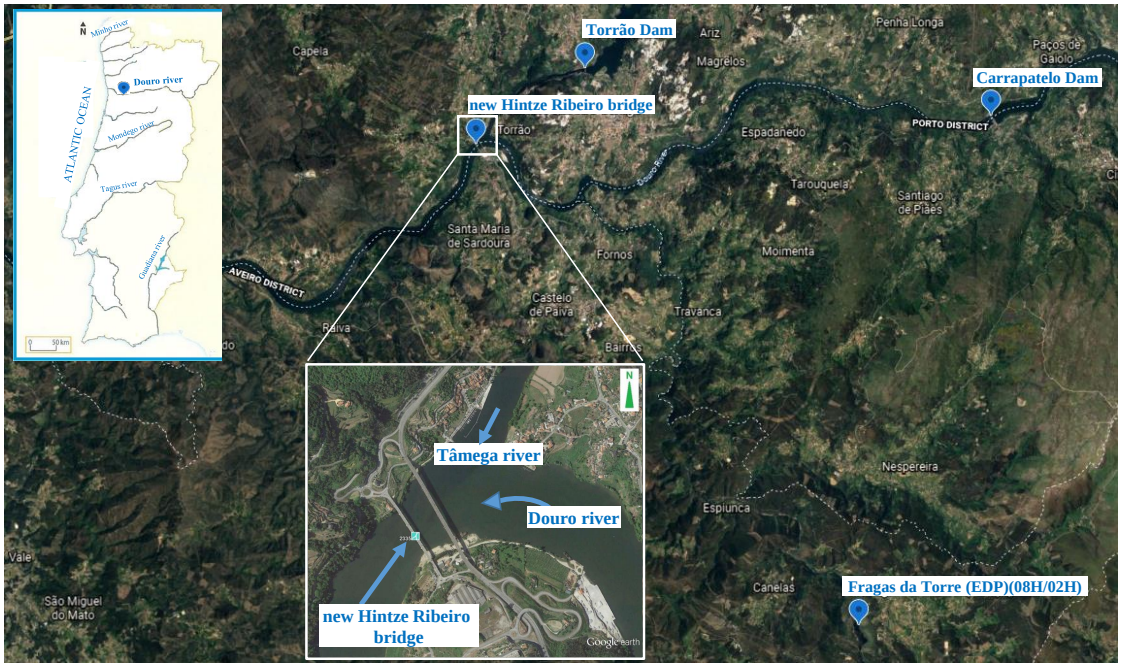

Figure 3.18: Location of the case study, the new Hintze Ribeiro bridge, over the Douro river (Google Earth, n.d.).

3.3.4.3 Bridge characteristics

The foundations of the new Hintze Ribeiro bridge were laid longitudinally outside the rip-rap cones of the older bridge piers to facilitate the execution of the works. Similar bridge spans were considered, although they were more evenly set between the intermediates and the extremes (Barata, 2001). Special caution was taken with the total length of the bridge deck in order to make the connection of the old abutments compatible with the new ones. Thus, a continuous deck was built with 40.7 m extreme spans and five intermediate spans of 55 m, by an incremental launching method of the steel structure which evolves in the final situation into a composite steel-reinforced concrete structure. The bridge, presented in Figure 3.19, is supported on two lateral abutments, and on five piers, three of which stand in the main channel. The bridge foundations have a pile-supported piers geometry, which consist of elliptical columns (with 2.0 m as minor axis and 7.5 m as major axis) founded on oblong pile caps (10.7 m long and 7.0 m wide), supported by 2 x 2 pile groups of 2.0 m of diameter (Barata, 2001). Further dimensions can be found in Table 3.8, where the bridge piers are numerated from 1 to 5, from right riverbank to left riverbank.

For the risk analysis of this case study, only the bridge foundation $P2$ (Figure 3.19) was considered since it is the pier appearing to be more vulnerable to scour due to its position in relation to the flow direction as well as for being the one founded in the highest alluvial layer thickness. Pier $P2$ is founded on end-bearing piles within a 17 m thick layer of alluvial deposits. Such information was derived by the geological and geotechnical part of the execution project (Nazareth & Sousa Cruz, 2002) as well as in the underwater inspections, performed by the conservation of bridges authority in Portugal (Lopes, 2019, Infraestruturas de Portugal).

Figure 3.19: Upstream view of the new Hintze Ribeiro bridge, with indication of $P2$, adapted from Milhazes (2016).

Table 3.8: Main dimensions of the new Hintze Ribeiro bridge components.

Bridge dimensions (m)							
Deck			Piers' height				
length	width	thickness	$P1$	$P2$	$P3$	$P4$	$P5$
301.4	11.0	2.6	37.4	61.9	53.9	48.9	37.9

3.3.4.4 Results and discussion

Hydrological modelling application Records from three gauging stations located at the new Hintze Ribeiro bridge vicinity (Figure 3.18) were considered, namely: (i) "Carrapatelo Dam (EDP) (07I/01A)" - Q_C; (ii) "Torrão Dam (EDP) (07H/01A)" - Q_T; and (iii) "Fragas da Torre (EDP) (08H/02H)" - Q_{FT}. The variables Q_C, Q_T and Q_{FT} denote the streamflows extracted from those stations, either mean daily or instantaneous data. The mean daily data were taken from the National Water Resources Information System (SNIRH, Portugal) platform, whereas the instantaneous data were made accessible by Energias de Portugal (EDP), the entity responsible for the management of the dams used in the current work. After analyzing the historical series with regard to record length and quality of data, only records from the period between 1988/89 and 2018/19 (31 hydrological years of records) were considered for further analysis. All data were scanned for outliers and data gaps. The continuity, consistency, and the hypothesis of randomness were first verified. Therefore, distinct hydrological scenarios were considered to evaluate the maximum annual discharge flow

approaching the new Hintze Ribeiro bridge (Q_{HR}), through the sum of the aforesaid records, i.e., $Q_{HR} = Q_C + Q_T + Q_{FT}$. Such determination ($Q_{HR}$) and the corresponding results, for each scenario, are given in detail in Bento *et al.* (Submitted).

With regard to the aforementioned study and correspondent results (Bento *et al.*, Submitted), only the scenario estimated based on the instantaneous streamflow data are herein presented and further analyzed. The instantaneous streamflow data for Q_C and Q_T were only available between the period of 2009/10 and 2018/19. For the remaining period, from 1988/89 to 2008/09, the instantaneous streamflow data was estimated through proportional relations between mean and instantaneous records of the gauging stations of Q_C and Q_T, respectively. Such approach was validated with the records of a neighbor station of Q_T, namely the gauging station of "Fridão (R.E) (06I/03H)", for which mean and instantaneuos streamflow data were accessible. Further details can be found in Bento *et al.* (Submitted).

In the current investigation, seven return periods were considered, namely T = 5, 10, 20, 50, 100, 500, and 1000 (see Table 3.9). From the six parametric distributions, referred in Subsection 3.3.3.2, four of them produced satisfying results. Those distributions were: LogNormal ($2p$ and $3p$), Gumbel and Gamma. Table 3.9 shows the obtained design floods, by considering either the best fitting distribution (MS) or the $modified\ MM$ method, as discussed in Subsection 3.3.3.2. The MS design floods were estimated by the Gamma distribution, since it fits best the data under analysis. The goodness-of-fit tests, performed on the series of maximum annual instantaneous flows approaching the new Hintze Ribeiro bridge, were not rejected when using this probabilistic model. Furthermore, the Gamma distribution produced a better graphical adjustment, compared with the other three probability models. The flood frequency analysis was performed by using a free *matlab* code, developed by Benkaci (2019).

Table 3.9: Design floods at the new Hintze Ribeiro bridge (Q_{HR}). Here MM stands for the $modified\ MM$ method.

T (years)	Q_{HR} (m^3s^{-1})		relative difference (%)
	MS	MM	$(MM-MS)/MM$
2	3,986	3,925	-1.6
5	7,801	7,597	-2.7
10	10,496	10,463	-0.3
20	13,113	13,527	3.1
50	16,497	17,969	8.2
100	19,018	21,676	12.3
500	24,788	31,648	21.7
1,000	27,247	36,616	25.6

The MS discharge values ranged from 7,801 m^3s^{-1} for 5 years of return period to 27,247 m^3s^{-1} for T = 1,000 years, while for the $modified\ MM$ method the design floods varied between 7,597 m^3s^{-1} and 36,616 m^3s^{-1}, respectively (Table 3.9). It is worth mentioning that the analyzed historical records included the major floods registered in the Douro valley. According to records of Tato (1966) and Vieira & Costa (2017), the highest flood occurred in 1739 with a magnitude of 18,000 m^3s^{-1}. Such discharge corresponded roughly to the design flood attained for 50 years of

return period in the *modified MM* method. In addition, the design flood of the Crestuma-Lever dam, the first hydraulic infrastructure downstream the bridge (see Subsection 3.3.4.2 for more details), of 26,000 m^3s^{-1}, was already included in the estimated peak discharge values. Within the execution project of the new Hintze Ribeiro bridge, a logarithmic regression was adopted (*MS* approach).

Table 3.9 also includes the "relative difference" between both approaches. For return periods ranging from 20 to 1,000 years, the "relative difference" varied between 3.1% and 25.6%. For T = 5 years and T = 10 years, the *modified MM* method slightly underestimated the flood designs in comparison to the *MS* approach. Higher differences between the two methods, *MS* and *modified MM*, are expected for increasing return periods. In agreement with the final purpose of the present study, the approach that gives the worst-case scenario is undoubtedly the modified arithmetic model averaging (*modified MM*), which returned higher discharge values (Table 3.9), specially for higher return periods. This method (*modified MM*) accounts with model uncertainty, which derives from the inadequacy of models to represent such real-world phenomena. As stated in subsection 3.3.3.2, mathematical models are always simplifications of reality and therefore introduce uncertainty. Therefore, only the results obtained by *modified MM* were considered for the following steps.

Hydraulic modeling and bridge scour assessment Topographic and bathymetric surveys of the Douro river were conducted by Infraestruturas de Portugal in July 2019 (Lopes, 2019), along a 200 meter extension, including the location of the new Hintze Ribeiro bridge. Details of the bridge structure information were provided in the execution project (Barata, 2001). The RAS Mapper routine of HEC-RAS was used to import the Digital Elevation Model (DEM), generated in ArcMap, with a spatial resolution of 0.5 m, forming the basis of the hydraulic model and providing a detailed level in the reach upstream and downstream of the bridge section. Following river delineation, a total of 80 cross-sections, spaced 2 m apart, were extracted for the hydraulic computations (Figure 3.20).

The roughness coefficient was estimated based on the guidelines of Chow (1959) and Lencastre & Franco (1992). Hence, a roughness coefficient of 0.050 $m^{-1/3}s$ was used in the riverbanks whereas a value of 0.033 $m^{-1/3}s$ was adopted for the main channel. A calibration of the roughness coefficient, at the main channel, was enabled by using the water level data registered for the flood of 1962 and the longitudinal riverbed profile at the bridge site, which corroborated the first estimate. As a downstream boundary condition, a known rating curve, provided in Martins (1992), was considered.

As carried out within the hydraulic part of the execution project (Pinheiro & André, 2002), the one-dimensional hydrodynamic model was used to simulate the steady flow regimes obtained in Subsection 3.3.4.4 (from $Q5$ to $Q1000$). For the present study, the local hydraulic quantities, namely flow depth, flow velocity, and Froude number, close to pier $P2$, were derived for each flood design and considered in the scour depth evaluation (see Table 3.10).

Based on the information gathered from historical records (Rocha & Cardoso, 1984), the median grain size diameter, D_{50}, was set as 8.5 mm while the D_{90} was assumed as 50 mm, which are in

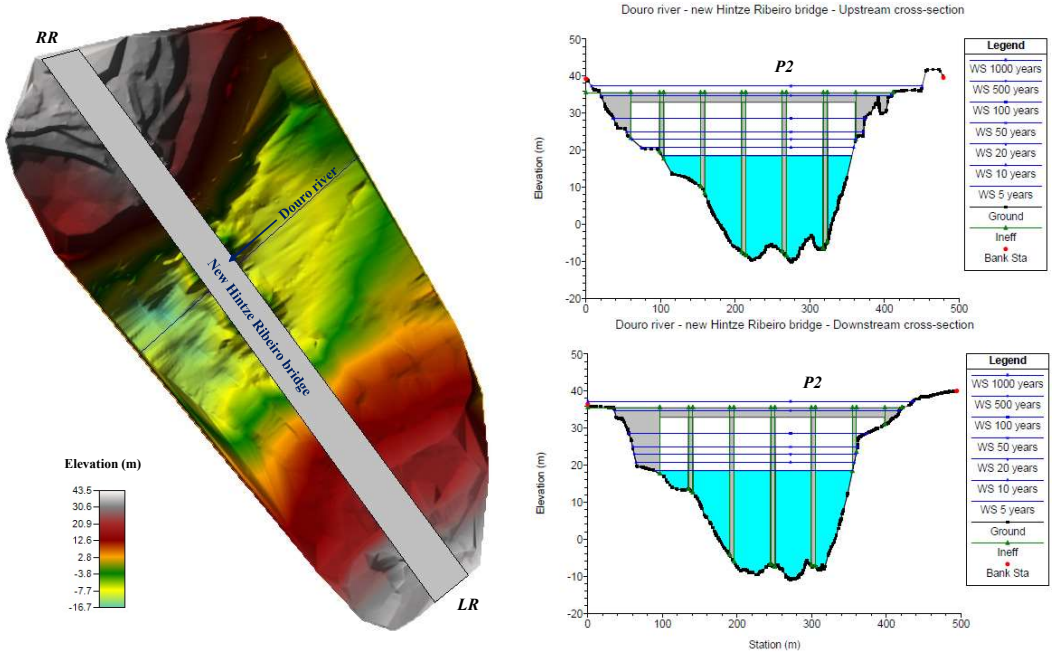

Figure 3.20: Hydraulic model built within HEC-RAS software.

conformity with the riverbed surveys performed for the execution project (Nazareth & Sousa Cruz, 2002). Such data was required for the total scour depth (D_T) estimation at $P2$ front.

Table 3.10 summarizes the resultant hydraulic variables, as well as the scour estimates obtained through the HEC-RAS scour module at the vicinity of $P2$. Previously to scour depth computations, the respective equivalent diameters (D_e) were accordingly determined.

The simulated flow velocities varied between 1.78 ms^{-1} and 3.87 ms^{-1}, albeit always under subcritical regime conditions (Froude number < 1). The design floods occurred under live bed conditions, except the corresponding to a 5 years of return period (clear water conditions). The flow depth, in turn, varied by as much as 19 m between the lower and the upper inflow discharges. In this study, the water level regarding the design flood $Q500$ reached the bridge deck, whilst in the case of $Q1000$ flood event the bridge was submerged (as can be seen in Figure 3.20).

In order to assure the simple and pragmatic methodology, invoked in Subsection 3.3.3.3, the total scour depth was evaluated within HEC-RAS. The scour module available in HEC-RAS allowed the estimation of both the contraction and the local scour depths as can be seen in Table 3.10.

The contraction scour depths indicate that the considered design floods gave acceptable values up to the 100-year return period; the depths of contraction scour were of an order of magnitude lower than the corresponding local scouring depths. The contraction scour depths are, thus, much less significant than the local scouring estimates. For the present study, an assumption was made by equaling the contraction scour depth for $Q100$ (of 0.85 m) to the contraction depths for the flood flows of $Q500$ and $Q1000$, due to the limitation of HEC-RAS for pressure-flow scour and overtopping flow, respectively. It should be noted that for $Q500$ there is already another concern

Table 3.10: Hydraulic variables and scour depths at pier $P2$ through HEC-RAS model.

Design flood (-)	Flow depth (m)	Flow velocity (ms^{-1})	Froude number (-)	Equivalent diameter D_e (m)	Contraction scour depth (m)	Local scour depth (m)	Total scour depth D_T (m)
$Q5$	26.46	1.78	0.11	4.16	0.00	6.78	6.78
$Q10$	28.72	2.20	0.13	4.64	1.32	8.06	9.38
$Q20$	30.94	2.53	0.15	4.82	1.41	8.87	10.28
$Q50$	32.90	3.10	0.17	5.51	1.32	10.64	11.96
$Q100$	36.58	3.16	0.17	5.10	0.85	10.35	11.20
$Q500$	42.62	3.72	0.18	5.25	0.85*	11.55	12.40
$Q1000$	45.17	3.87	0.18	5.16	0.85*	11.70	12.55

* Assumed equal to the contraction scour obtained for $Q100$.

related with the impact of the flow towards the bridge's deck. In addition, under some circumstances, the flow may induce lift on the bridge's deck. However, these sources of instability were out of the scope of the current work.

Regarding the estimation of the local scouring component, HEC-RAS uses an older version of HEC-18 method (Richardson & Davis, 2001) to estimate the maximum local scour depth. Such scour depths were compared with estimated depths through other three well-developed empirical formulations in order to evaluate the former's model performance (Figure 3.21). Those methods comprise the predictors of HEC-18 (Arneson *et al.*, 2012), FDOT (Sheppard & Renna, 2010) and Yang *et al.* (2019), and the correspondent results are plotted in Figure 3.21.

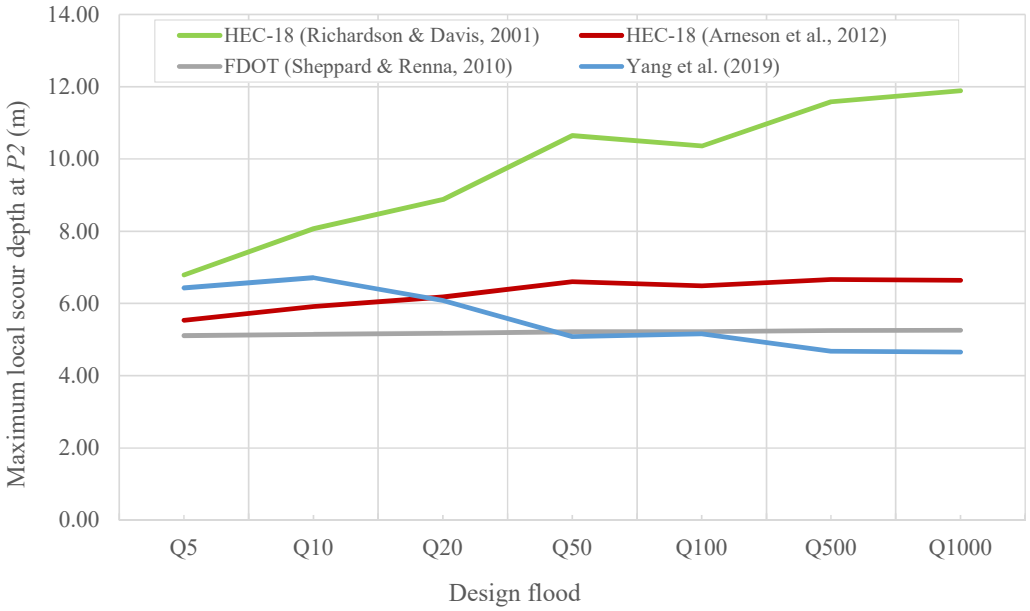

Figure 3.21: Maximum local scour depth estimates using four empirical predictors.

It can be observed that HEC-18 predictions (Richardson & Davis, 2001) show a significant increase with increasing the design flood condition. This estimate also demonstrates that the maximum local scour depth does not reach a peak for $Q1000$ (the higher design flood under consideration) and would continue to increase by increasing the magnitude of hydrological extreme

events (by decreasing their occurrence probabilities), even though at a reduced rate. This version of HEC-18 method over-predicts largely the other estimators.

The HEC-18 equation (Arneson *et al.*, 2012) provided local scour depths closer to the other empirical estimates herein considered. The correspondent results also show higher scour depths, although at a rate much less strongly than with the previous version (Richardson & Davis, 2001, HEC-18 method). Differences of 18% to 43% are encountered with the increase of the design floods, showing a difference of 5 m in scour depth calculations for $Q1000$.

The maximum local scour depths estimated by the FDOT method (Sheppard & Renna, 2010) are almost constant regardless of the occurring design floods. On the other hand, the method of Yang *et al.* (2019) shows a slight increase between the design floods of 5 and 10 years of return period, at which a maximum scour depth is reached, of 6.71 m of magnitude. From $Q10$ to $Q50$, it is possible to observe a decay on the scouring process at the bridge foundation ($P2$). From there on, the predictor oscillates around a central value of 5 meters of maximum local scour depth. The estimate of Yang *et al.* (2019) under-predicts the scour depths from a range of 5% to 60% in comparison with HEC-18 method (Richardson & Davis, 2001). Higher differences are encountered when comparing the method of Richardson & Davis (2001) with the FDOT method estimates, varying from 25% to 55%.

In addition to the graphical comparison performed in Figure 3.21, the relative quality of the computations, in comparison to HEC-18 (Richardson & Davis, 2001) results, was determined through the root mean square error (RMSE). Those values were 0.5831, 0.9251, and 0.8743, corresponding to the estimates of HEC-18 (Arneson *et al.*, 2012), FDOT (Sheppard & Renna, 2010), and Yang *et al.* (2019), respectively. The obtained values corroborated with the discrepancies visible in Figure 3.21.

The validation of HEC-RAS model results may constitute a very complex process. However, in this work, that validation was addressed indirectly, through analyses of historical records of floods and observed scour depths at pier $P2$ of the new Hintze Ribeiro bridge. Underwater inspections performed at two different moments (by Infraestruturas de Portugal) in 2010 and 2013, were used as a reference base (DEM of 2010) and as a comparative base (DEM of 2013), respectively. The comparison of the cross-sectional profiles between 2013 and 2010 at pier $P2$ shows a total scour depth of 2.35 m for that 3-year period, though this value may not truly represent the maximum scour depth occurred.

Following the assumptions considered previously, an independent hydraulic model was built with HEC-RAS using the topographic and bathymetric data from 2010. The main flow characteristics and the total scour depths at $P2$ were computed by imposing the flood events observed within that period of time (from 2010/11 to 2012/13). The hydraulic simulation results showed maximum annual discharges ranging from 1,491.09 m^3s^{-1} and 7,546.38 m^3s^{-1}, flow depths varying between 23.53 m and 28.39 m and Froude numbers between 0.03 and 0.12. In terms of total scour depths, the scour module within HEC-RAS estimated a value of 3.31 m.

It can be concluded that the scour prediction computed by the HEC-RAS scour module is in a reasonable agreement with the observed scour depth, as the variation of less than 1 m is not

relevant to the analysis of change of the alluvial bed material for Douro river (Rocha & Alves, 2002). Thus, the total scour depths obtained by HEC-RAS were used for the subsequent risk assessments addressed next.

Risk rating assessment The total depth of scour (D_T), calculated for each design flood (Table 3.10), was compared with the foundation depth at $P2$, determined from the underwater inspection survey performed in 2019 (D_F = 17 m). Such comparison, D_T/D_F, itself provides the dominant parameter in any prioritization (D_R) and is given in Table 3.11. The resultant depth of foundation due to the occurrence of each design flood and correspondent return period, D_{FT}, is also indicated in Table 3.11.

Table 3.11: Scour risk rating for the new Hintze Ribeiro bridge.

Design flood	D_T (m)	D_{FT} (m)	D_R (-)	Scour risk rating
$Q5$	6.78	10.22	0.40	
$Q10$	9.38	7.62	0.55	
$Q20$	10.28	6.72	0.60	
$Q50$	11.96	5.04	0.70	5
$Q100$	11.20	5.80	0.66	
$Q500$	12.40	4.60	0.73	
$Q1000$	12.55	4.45	0.74	

The relative scour depth (D_R) was then related to the priority factor (P_f), which is solely dependent on the variables indicated in Table 3.6. Those parameters, indicated in Table 3.12, were combined to provide the priority factor (P_f) of 0.90 for the new Hintze Ribeiro bridge. The pile-supported pier type ($P2$) has a reduced priority on the foundation type (F). The history of scour-related problems due to collapse of the 19th century Hintze Ribeiro bridge in 2001 aggravated the associated factor for the new bridge. As stated in subsection 3.3.4.2, the riverbed is made of granular material which have no influence on the priority factor. Likewise, the type of river factor at the bridge area (T_R) has no significant impact on the priority factor. According to Highways Agency (2012) guidelines, the importance of a bridge (V_f) is directly related to its traffic flow. For a 6,242 12-hour traffic flow of the new Hintze Ribeiro bridge, a value of 0.80 was assigned for V_f factor.

Table 3.12: Contributing parameters for the priority factor of the new Hintze Ribeiro bridge.

Factors	Value	Observations
F	0.75	Piled foundation
H	1.50	History of scour problems
M	1.00	Material is granular (silts, sands and gravels)
T_R	1.00	Lowland terrain
V_f	0.80	A/B class road (12-hour traffic flow: 1,000 - 9,999)

A resulting scour risk rating, based on the magnitudes of the relative scour depth (D_R) and the priority factor (P_f), were assigned through Figure 3.22. The design floods considered in the present

study contributed to a scour risk rating of 5 for the new Hintze Ribeiro bridge. At this risk rating there is no special action than the routine inspections that are, in Portugal, being conducted by the National Authority (Infraestruturas de Portugal) every three years. It should be noted that the obtained rating should be considered as indicative and not a definitive statement of relative risk, as indicated in Highways Agency (2012).

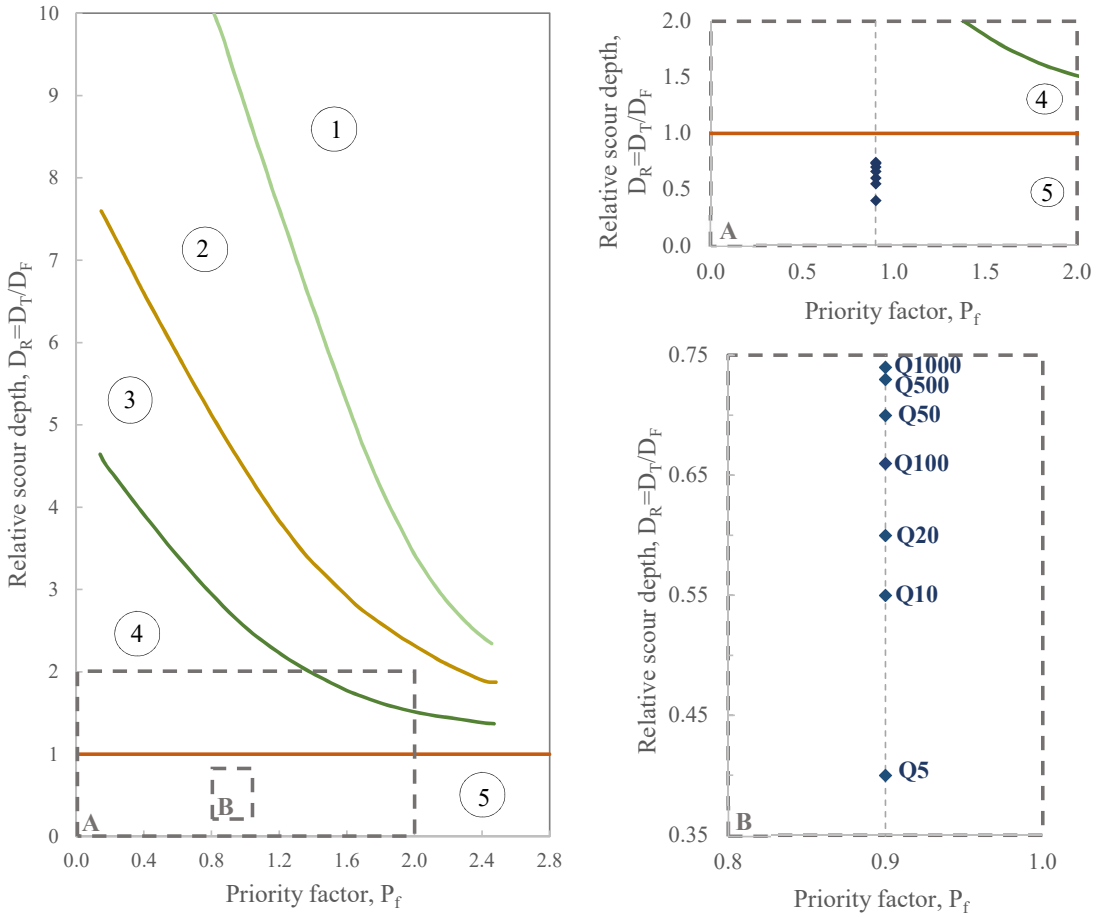

Figure 3.22: Scour risk rating of the new Hintze Ribeiro bridge.

The adopted risk analysis assume that the design floods occurred as independent events, i.e., the relative scour depth was estimated by considering the foundation depth (D_F = 17 m) determined from the survey of 2019 (the basis of the present study). However, if the cumulative effect would be considered, the increase of the total scour depth at $P2$ would affect the available foundation depth. Such influence is traduced on the results of D_{FT} in Table 3.11.

This may constitute a concern when, in the geotechnical design, the mobilization of the pile's surface resistance by friction with the surrounding alluvial bed (known as skin fraction) is considered in the bearing capacity of such pile. It is usual to disregard the contribution of the first meters of the alluvial layer to the lateral pile's resistance. According with the geological and geotechnical part of the execution project of the case study bridge (Nazareth & Sousa Cruz, 2002), the first 5 meters of alluvial layer were neglected. In line with the values obtained for D_{FT}, the

mobilization of the surface resistance, through the pile friction with the surrounding alluvial bed material, should not be considered for return periods greater that 50 years.

3.3.5 Conclusions

This paper proposes a three-step risk-based methodology to evaluate the risks associated with scour at bridge foundations, founded on alluvial beds. The methodology steps consist of, firstly, the assessment of hydrological events (hazards), secondly, the modeling of the river behavior through the computation of flow and bridge scour variables, and thirdly, the assessment of the bridge scour risk by associating its relative scour depth with the priority factor of such infrastructure (vulnerability) and assigning a qualitative evaluation of the scour risk rating (level of risk). Each step is detailed, specifying the required input data, the methodological process and its outcomes. Specific management strategies are suggested and recommended for the risk rating level obtained according with Highways Agency (2012) guidelines. The proposed methodology was applied and validated to the new Hintze Ribeiro bridge, over the Douro river, in Portugal.

The results of the first step confirm the importance of considering the variability of hydrological events, by taking into account the model uncertainty. Such uncertainty aspects should be taken into account in the early stages of the design, instead of the standard model selection (MS) method. In the present work, the modified arithmetic model averaging method ($modified\ MM$ (Bento *et al.*, Submitted)) is recommended in the definition of the design floods to deal with the inherent model uncertainties. The $modified\ MM$ method resulted in a worst-case scenario for the case study bridge, since it returned higher discharge values, specially for greater return periods.

For step 2, the hydraulic variables, flow depths and velocities approaching a bridge foundation, were simulated in the $1D$ open-source HEC-RAS model. The determination of the maximum scour depth, performed by using the scour module available within HEC-RAS, which is based on HEC-18 (Richardson & Davis, 2001), proved to reasonably reproduce the scour phenomenon, with safety margins, namely at the new Hintze Ribeiro bridge foundation $P2$. Three other well-established formulations were also considered when evaluating the HEC-RAS model performance. Those formulations comprise the predictors of HEC-18 (Arneson *et al.*, 2012), FDOT (Sheppard & Renna, 2010), and Yang *et al.* (2019). It was concluded that the 2001 version of HEC-18 method used in HEC-RAS largely over-predicted the other three estimates, whilst being in accordance with the literature. The model capabilities and limitations were indicated, as well as the calibration and validation of the set of the involved variables. This pragmatic assessment of the total scour depth was recommended for proceeding to the bridge risk assessment (step 3).

Based on a relative scour depth and a measure of the priority factor of the case study bridge, the scour is assessed using a qualitative risk rating. The risk rating of the new Hintze Ribeiro bridge fell within risk rating band 5, regardless the flood return period. Within this level, risk can be accepted, and no important damages are expected. The frequency of underwater inspections currently being undertaken by the Portuguese authority for the conservation of bridges, once in every three years, is deemed appropriate for the level of risk obtained using the proposed methodology.

Although the present methodology was solely applied to a single case study, the findings indicate that it is expected to translate well to other bridges, regardless of the shape of the bridge foundations, and on the most vulnerable pier. It is, however, advisable that more case studies are undertaken to further support and validate the potential of the proposed methodology to assess the risk of scour at bridges foundations. Advanced calibrations for this methodology (namely in step 2) may be attained by using more sophisticated models such as the Computational Fluid Dynamics (CFD) software tools; nonetheless, out of the scope of the current study.

In the opinion of the authors, the proposed risk-based methodology can be potentially incorporated into regular bridge inspection schedules as well as being used for providing support to decision making, under uncertainty, of bridges subject to more adverse hydraulic conditions, which are the main drivers of the scouring phenomenon.

3.3.6 Declaration of competing interest

The authors declare that they have no known competing financial interests or personal relationships that could have appeared to influence the work reported in this paper.

3.3.7 Acknowledgments

The first author gratefully acknowledges support from the Portuguese Foundation for Science and Tecnology (FCT), through the PhD scholarship PD/BD/127798/2016, in the framework of the Doctoral Program INFRARISK – “Analysis and Mitigation of Risks in Infrastructures”. The authors thank FCT for the funding to this research with project reference UID/Multi/04423/2019. The authors also express gratitude for the insightful comments and contributions offered by Dr. João Rocha, former principal researcher at LNEC. The provision of bathymetry data and bridge structural characteristics from “Infraestruturas de Portugal (IP)”, the Portuguese Authority responsible for the conservation of bridges, with whom the authors’ institutional affiliations signed a collaboration and information exchange agreement. Streamflow data was partly made accessible thanks to a collaboration agreement with “Energias de Portugal (EDP)”.

Chapter 4

Experimental Study

4.1 General Considerations

The experimental campaign of the present study was conceived to address two key aspects of the bridge scouring process: firstly, the geometry of the scour hole around bridge pier models, and secondly, the turbulent flow field at the beginning of the scouring process and within the developed scour hole. The flow in the vicinity of oblong bridge piers was thus reproduced in a glass-sided rectangular tilting flume, 40.7 m long, 2.0 m wide and 1.0 m deep, located in the experimental facilities of the National Laboratory of Civil Engineering (LNEC) in Lisbon, Portugal (Figure 4.1). This facility was used in several previous studies, namely in local scour experiments (Moreno *et al.*, 2016a; Moreno, 2016). Oblong bridge pier models were chosen as those geometries are the most common shape of Portuguese bridge foundations of the 19th and 20th centuries.

(a) View from upstream. (b) View from inside. (c) View from downstream.

Figure 4.1: Tilting flume at LNEC's experimental facilities.

A total of ten experiments were undertaken, consisting of four movable bed experiments (*Exp.* 1*U*, *Exp.* 1*D*, *Exp.* 4*U* and *Exp.* 4*D*), to depict the geometry of the scour hole, and six fixed bed experiments (*Exp.* 1*U Fbed*, *Exp.* 1*U Ebed*, *Exp.* 1*D Fbed*, *Exp.* 1*D Ebed*, *Exp.* 4*U Fbed*, and *Exp.* 4*U Ebed*) to evaluate the turbulent flow field developed. These experiments are identified in Table 4.1. Tests were carried out under two types of approach flow conditions, namely clear water and live bed. Two different widths of oblong bridge piers were considered (Appendix C.1). The scouring experiments were conducted until the time required to reach 90% of the equilibrium depth (t_{90}) as per Equation 2.10. Table 4.1 summarizes the conditions in which the experiments were developed, indicating the approach flow condition, the pier model dimensions, the type of characterization, the monitoring variables and techniques that were used. Specific details regarding the tilting flume, the hydraulic circuit, the sand bed material properties and the general experimental procedure are given in Section 4.2. Flow and scour particularities of the experimental campaign are also reported in Appendix C.4 and C.5.

Two scientific papers, under preparation, are presented in the following sections, based on the results of the experimental campaign undertaken in this facility. "Characterizing bridge scour using image-based techniques in laboratory environment" (Section 4.3) concerns the characterization of the scour hole geometry and its respective ensemble, either based on underwater images during experiments (through the application of underwater image processing and computer vision routines) or on captures acquired at the beginning and at the end of experiments (by application of close-range photogrammetry and Kinect V2 sensor). The validation of the image-based techniques using the point-wise evolution of the scour depth is also presented. "Experimental characterization of the flow field around oblong bridge piers" (Section 4.4) concerns the study of the flow field around the oblong bridge pier models by using a downlooking vectrino. The measurements were performed at the beginning of the scouring process and within the respective developed scour holes. The two scientific papers that compose this chapter are under preparation for submission to international scientific journals.

The preliminary tests undertaken before the experimental campaign led to the submission and publication of three conference papers in 2018. The first, "Caracterização da cavidade de erosão em torno de fundações de pontes. Relação entre volume erodido e profundidade de erosão" (Appendix D.1), was presented in March 2018 in the "14° Congresso da Água", in Évora (Portugal). A compilation of the relations between the maximum scour depth and the eroded volume at the vicinity of bridge foundations is presented in this paper. The second paper, "Evolution of local pier scour under unsteady flow conditions" (Appendix D.2), was presented in June 2018 in the "5th IAHR Europe Congress" in Trento (Italy). The paper explores the scour depth evolution at a circular pier for a stepwise discharge hydrograph, conducted experimentally under clear water scour conditions. The third, "Advanced characterization techniques of the scour hole around a bridge pier model" (Appendix D.3), was presented in September 2018 in the "9th International Conference on Fluvial Hydraulics" in Lyon (France). This paper analyses two different methodologies for the three-dimensional characterization of the scour hole: the close-range photogrammetry technique and the use of the Kinect V2 sensor, thus verifying the feasibility of both for this type of research issue.

Table 4.1: Experimental campaign of the present study.

Approach flow condition	Clear water - *Run* 1						Live bed - *Run* 4			
Oblong pier ID (width)	*Pier* 11			*Pier* 14			*Pier* 11			*Pier* 14
Label	*Exp.* 1*U*	*Exp.* 1*U Fbed*	*Exp.* 1*U Ebed*	*Exp.* 1*D*	*Exp.* 1*D Fbed*	*Exp.* 1*D Ebed*	*Exp.* 4*U*	*Exp.* 4*U Fbed*	*Exp.* 4*U Ebed*	*Exp.* 4*D*
Type of bed	Movable	Fixed		Movable	Fixed		Movable	Fixed		Movable
Type of characterization	Scour hole geometry	Flow field		Scour hole geometry	Flow field		Scour hole geometry	Flow field		Scour hole geometry
Flow depth and discharge	x	x	x	x	x	x	x	x	x	x
Point-wise time evolution of scour depth	x	-	-	x	-	-	x	-	-	x
Close-range photogrammetry (3D)	x	-	-	x	-	-	x	-	-	x
Kinect V2 sensor (3D)	x	-	-	x	-	-	x	-	-	x
Underwater monitoring (2D)	$*$	-	-	x	-	-	$**$	-	-	$***$
Downlooking vectrino	-	x	x	-	x	x	-	x	x	-

Fbed = Flat bed; *Ebed* = eroded bed

$*$ The action cameras acquired images of *Exp.* 1*D*.

$**$ The water quality prevented an underwater monitoring (Appendix C.4).

$***$ The experiment stopped at half of the planned duration time (Appendix C.4).

4.2 Experimental facility and apparatus

4.2.1 Introductory considerations

The titling flume (CIV in the Portuguese acronym), designed for free surface flows involving sediment transport, is illustrated in figures 4.1 and 4.2, highlighting its main components. It is composed by a supply tank [9], the flume itself [17], a downstream tank [2] ("Discharge tank"), the return circuit, as well as the corresponding pumping system [5] and impulsion pipes [7].

CIV works in a closed hydraulic circuit. The pumping system supplies the upstream tank through the impulsion pipes; the flow, either with or without sediments, drains, by gravity, from the supply tank to the channel itself until it outflows in the discharge tank ([2] in Figure 4.2), which constitutes the supply source of the closed circuit. This hydraulic circuit is further explained in the following subsections.

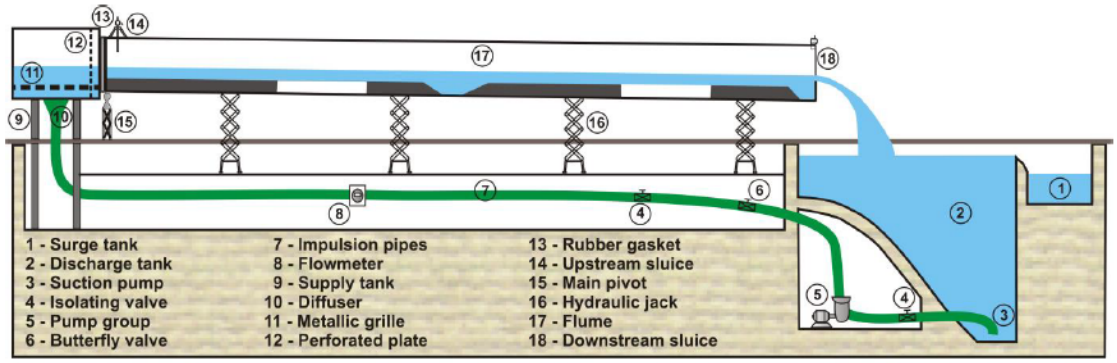

Figure 4.2: Longitudinal scheme of CIV (Moreno, 2016).

4.2.2 Pumping and impulsion systems

The pumping system is composed by three independent pump groups ([5] in Figure 4.2). Each group comprises an alternating current motor, a variable speed drive, a rotational speed and a centrifugal pump. In accordance with Cardoso (1982), the three centrifugal pumps allow flow discharges to be pumped with a total capacity of 1.0 m^3s^{-1} (two of 0.25 and one of 0.5 m^3s^{-1}). The impulsion system consists of three pipes in parallel ([7] in Figure 4.2; Figure 4.3a) with internal diameters of 0.25, 0.30 and 0.45 meter, associated to each pump group ([5] in Figure 4.2; Figure 4.3b).

Each impulsion pipe comprises a set of accessories, namely: (i) an isolating valve ([4] in Figure 4.2), which allows the confinement of a part of the system for maintenance and repair operations at either the pump or impulsion system; (ii) an electromagnetic flowmeter ([8] in Figure 4.2; Figure 4.4a) for flow discharge measurement; and (iii) a butterfly valve ([6] in Figure 4.2) for the regulation of the flow inside the pipe. This system establishes the link between the discharge tank ([2] in Figure 4.2) and the supply tank ([9] in Figure 4.2), designed with distinct names - Circuit I, Circuit II, and Circuit III - according to Figure 4.3. In the current study only two circuits were considered

(Circuit I and Circuit II). The pumped flow discharge is controlled by regulating the rotational speed of the pumps on the correspondent control panels (Figure 4.4b).

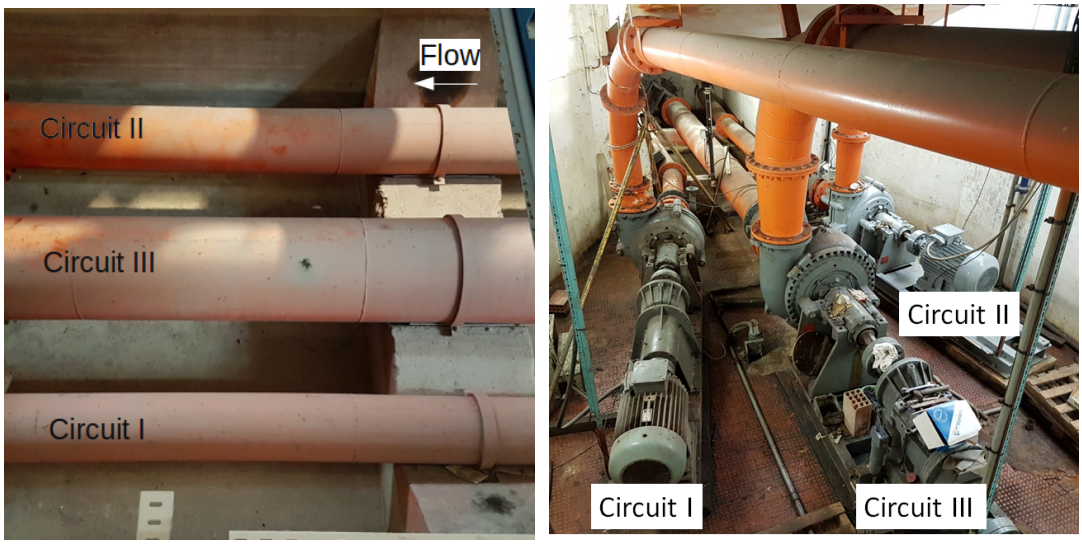

(a) Feeder pipes.

(b) Pump room.

Figure 4.3: Components of pumping and impulsion systems.

(a) Control panel of Circuit I.

(b) Control panel of Circuit II.

Figure 4.4: Control panels of the flow discharge in CIV.

4.2.3 Supply tank

The flow is supplied close to the bottom of the supply tank - 3.0 m long, 2.5 m wide and 1.4 m deep (Figure 4.5a) - through three diffusers ([10] in Figure 4.2), reducing the entry inflow rate in the tank. At the exit of the diffuser section, an horizontal grille ([11] in Figure 4.2) and a detachable vertical perforated plate ([12] in Figure 4.2) to curb large turbulent scales and evenly distribute the flow towards the flume (Figure 4.5b).

(a) Horizontal grille. (b) Vertical perforated plate.

Figure 4.5: Flow entrance in the flume (top view).

4.2.4 Tilting flume

A concrete false bottom was installed in order to obtain two sand filled recess boxes, 5.0 m long and 0.4 m deep, where the pier models were installed at $\approx$ 2 m from their upstream borders, allowing to perform two experiments simultaneously (Figure 4.6a). Each of the sand recess boxes is preceded by a 2.0 m long accelerating ramp and a 7.0 m long fixed bed reach and is followed by a 3.0 m long fixed-bed reach. The stilling recess area, at the end of the first 3.0 m long fixed bed reach, was designed to store the sand transported by the flowing water from the upstream recess box, as well as to restore the uniform flow regime. The accelerating ramp at both the inlet of the flume (Figure 4.5b) and the stilling recess boxes (visible in Figure 4.2) conduce to the development of an uniform flow distribution in the two working sections (i.e. at the sand recess boxes).

(a) Sand recess box. (b) Gravel mattress.

Figure 4.6: Downstream working section of CIV.

A 0.2 m thick and 0.5 m long fine gravel mattress, embedded at the upstream end of the sand recess boxes and properly levelled with the adjacent concrete, allows a smooth and progressive transition, avoiding scouring at the transition between the fixed and the movable bed. The gravel mattress was placed inside a metallic mesh as can be seen in Figure 4.6b.

Figure 4.7 displays the two sluice gates of the tilting flume - one placed at the upstream section ([14] in Figure 4.2; Figure 4.7a) and the other at the downstream section ([18] in Figure 4.2; Figure 4.7b) - that enable the flow depth adjustment inside the flume. The flow passes either under or over the sluice gate at the upstream or at the downstream, respectively.

(a) Upstream (b) Downstream

Figure 4.7: Sluice gates of CIV.

CIV is supported by a metallic structure with a fixed support at upstream (denominated "15 - Main Pivot" in Figure 4.2). There are four pairs of hydraulic jacks ([16] in Figure 4.2), 9.5 m apart, which may vary the bottom slope of the flume continuously from 0% to 2.5% through an independent control console placed in the room adjacent to CIV (Figure 4.8a). At the exit of the supply tank, a rubber gasket ([13] in Figure 4.2) allows the movement (slope variation) of CIV. The slope is controlled by mechanical screws (Figure 4.8b) located along the flume length, and is equipped with a calibrated scale (Figure 4.8c - 3.8 cm for null slope) that indicates the vertical movement of CIV. This calibrated scale allows the tilted vertical distance to be determined up to an accuracy of $\pm$ 1 mm.

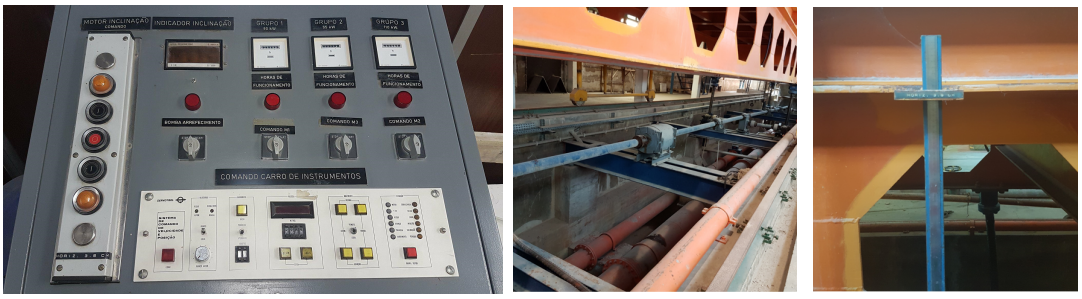

(a) Console (b) Mechanical screws (c) Calibrated scale

Figure 4.8: Slope controllers of CIV.

The tilting flume is equipped with three moving carriages that move along the longitudinal axis of the flume on two precisely levelled rails (Figure 4.9). They permit the access of the experiment area for controlling and measuring purposes, namely for flow and scour characterization.

(a) For the upstream working section. (b) For the downstream working section.

Figure 4.9: Moving carriages of CIV to aid flow and scour monitoring.

Two aluminium bars, supporting a point gauge each (hereinafter termed as “hydrometer”), are positioned at downstream of each sand recess box to check the flow depth before and during experiments (Figure 4.10a and 4.10b, respectively). Two graduated vertical rulers, designed for the current study and positioned strategically on the flume side walls, also aid the control of the flow depth before and during experiments (Figure 4.10c). Two hydrometers, coupled to the upstream face of the bridge pier models, allow the registration of the scour depth evolution at that vertical with a $\pm$ 0.05 mm of accuracy. One of these is visible in Figure 4.9b.

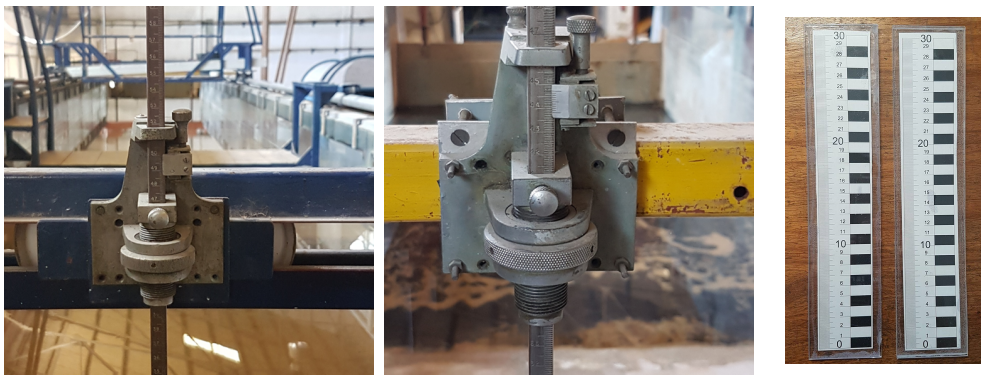

(a) Upstream working section (b) Downstream working section (c) Flume side walls

Figure 4.10: Flow depth controllers along CIV.

4.2.5 Discharge system

The discharge tank ([2] in Figure 4.2; Figure 4.11) is 18.1 m long, 2.5 m wide, and 6.9 m deep, with approximately 150 m^3 of maximum stored volume. The deepest zone of the tank works as a suction chamber of the pumps that carry the flow through impulsion pipes to the supply tank ([9] in Figure 4.2). Further downstream, a surge tank ([1] in Figure 4.2) is also part of the discharge system.

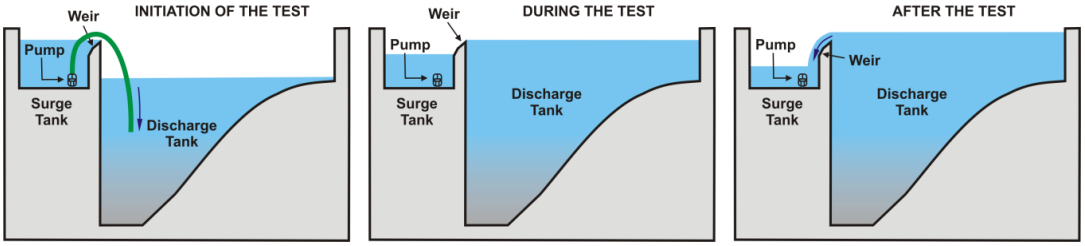

Figure 4.11: Surge tank operation (Moreno, 2016).

At the beginning of the experiments, flow is pumped from the surge tank, using a suction pump ([3] in Figure 4.2; Figure 4.12a), to the discharge tank to supply the volume of flow that will be on the flume while at the end of the experiments the flow returns to the surge tank, thereby closing the hydraulic circuit (Figure 4.11; Figure 4.12b). A surface spillway, between the discharge tank and the surge tank, assures a constant hydraulic head for proper pump operation. Photos of the suction pump controlling panels as well as of the downstream tanks (discharge and surge tanks) are shown in Figure 4.12.

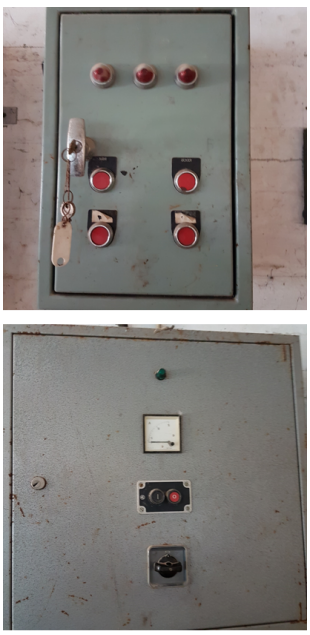

(a) Controlling pannels

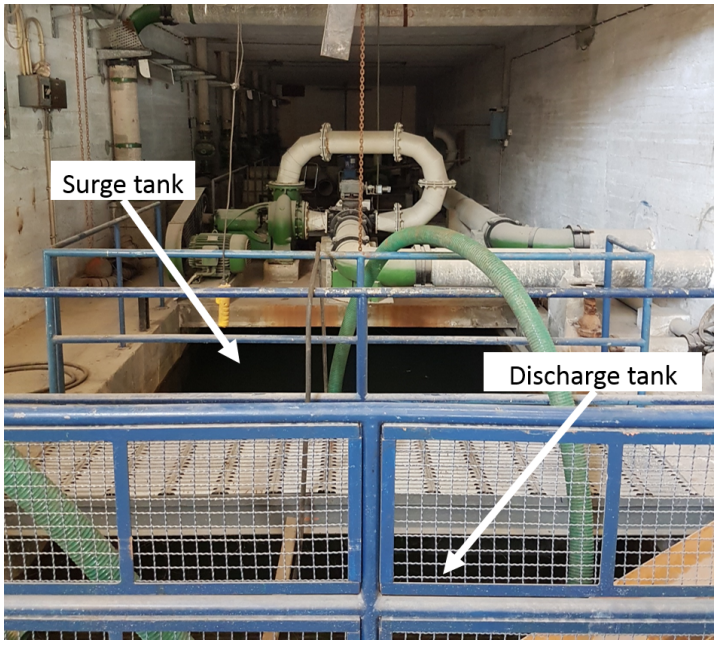

(b) Downstream tanks

Figure 4.12: Suction pump controlling panels and downstream tanks.

4.2.6 Sand bed material

A total volume of 8 m^3 of uniform quartz sand was used to fill both sand recess boxes for the scouring experiments. The grain-size distribution curve of the bed material was obtained by mechanical sieving and is shown in Figure 4.13. This sand was characterized by a median sediment diameter (D_{50}) of 0.86 mm, a specific gravity (s) of 2.65, and a geometrical standard deviation ($\sigma_D = \sqrt{D_{84}/D_{16}}$) of 1.28, thus considered a uniform sand. The corresponding dimensionless sediment diameter ($D^* = \left[(s-1)\,g/\nu^2\right]^{1/3} \cdot D_{50}$) is 21.7.

Following the review in Chapter 2, the non-ripple-forming sediment ($D_{50} \geq 0.7$ mm) criterion was respected (Raudkivi & Ettema, 1983). In line with Chiew & Melville (1987) and Lee & Sturm (2009), if geometrical standard deviation (σ_D) is lower than 1.5, the effect of non-uniformity of sediment on the depth of the scour hole became negligible. The sediment coarseness ratio (W/D_{50}, being W the pier width) took the values of 127.9 and 162.8, regarding to each pier model (0.11 m and 0.14 m of pier width, respectively). The pier models used were kept the same of the structures used in studies performed by Moreno *et al.* (2016a) and Moreno (2016). According to the envelope curve presented by Moreno (2016), such ratios implied an influence on the scour depths of about 2.1 to 2.4 times the respective pier widths.

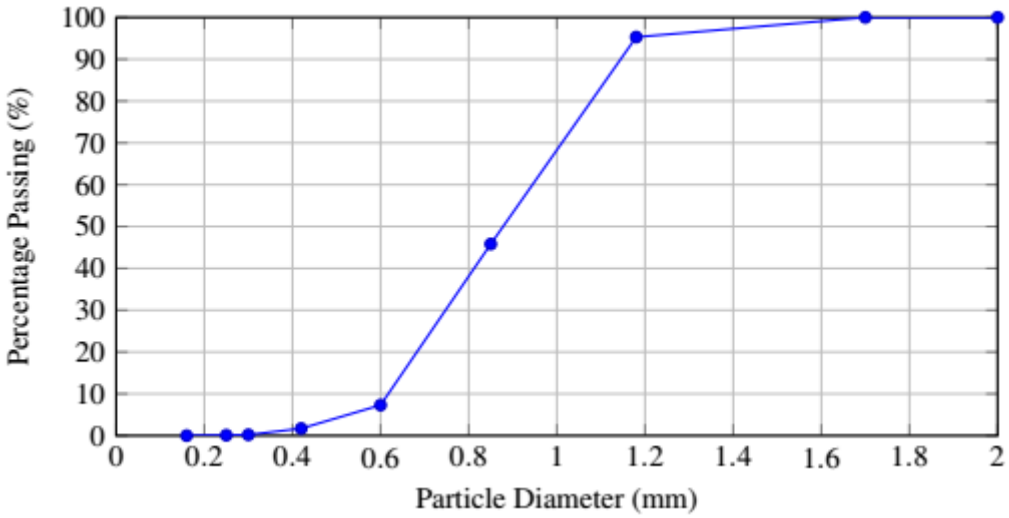

Figure 4.13: Sand grain size distribution curve.

4.2.7 Critical flow velocity equations

There are several empirical formulations for estimating the velocity at which the sediment grains start moving (V_c) have been derived. Some of the most used are presented below and were considered in the present study.

- Shields (1936) equation (for $Re > 70$):

$$V_c = 2.5u_* \ln\left(\frac{2.21h}{D_{50}}\right) \tag{4.1}$$

- Neill (1967) equation:

$$V_c = \sqrt{2.5\left(\frac{h}{D_{50}}\right)^{0.2} gsD_{50}} \tag{4.2}$$

- Garde (1970) equation:

$$V_c = \left[0.5\log\left(\frac{h}{D_{50}}\right) + 1.63\right]\sqrt{gsD_{50}} \tag{4.3}$$

- Melville & Coleman (2000) equation:

$$V_c = 5.75u_{*_c} \log\left(5.53\frac{h}{D_{50}}\right) \tag{4.4}$$

- Sheppard & Renna (2010) equation:

$$V_c = 2.5u_{*_c} \ln\left(\frac{h}{2.72z_0}\right) \tag{4.5}$$

4.3 Characterizing bridge scour using image-based techniques in laboratory environment. *Paper under preparation*

TITLE: Characterizing bridge scour using image-based techniques in laboratory environment[1]

Paper under preparation and to be submitted for publication in an international scientific journal

Author contributions:
All authors conceived the experimental campaign. Bento, A.M. planned and performed the experiments. Bento, A.M. analysed the results, derived the post-processing models and wrote the manuscript. Couto, L., Viseu, T., and Pêgo, J.P. provided critical feedback and helped shape the research, analysis and manuscript.

[1] Bento, A.M., Couto, L., Viseu T. & Pêgo, J.P. (Under preparation). Characterizing bridge scour using image-based techniques in laboratory environment.

4.3.1 Abstract

Bridge foundations, often inserted on non-cohesive riverbeds, are weakened by age and exposure to flood events. Consequently, scouring near foundations can occur, leading to the development of scour holes at their vicinity that may compromise the infrastructure's stability. For further understanding of how local scour may readily undermine such foundations, local scouring experiments around two transitional oblong bridge piers were performed in a tilting flume of the Portuguese National Laboratory of Civil Engineering (LNEC). Clear water and live bed scour conditions for steady flow conditions were considered. The current ability to characterize the scour hole at the piers' proximity is mostly limited to point-wise measurements during or at the end of experiments. To tackle these measuring limitations, 2D and 3D image-based techniques - close-range photogrammetry and Kinect V2 sensor - have proved powerful and non-intrusive capabilities for characterizing the scouring effects and its respective ensemble, either based on underwater images during experiments or on captures acquired before and after them.

4.3.2 Introduction

Bridges are susceptible to failure due to the local scour phenomenon, one of the greatest threats to the stability and safety of bridges around the world (Melville & Coleman, 2000; Cook *et al.*, 2015; Proske, 2018). Bridge collapses lead to severe disruption to infrastructures networks, socio-economic problems and, in some circumstances, human casualties. Pizarro *et al.* (2020) collected and reported repair costs and associated financial losses of noteworthy worldwide scour-induced bridge collapses. In Germany, these repair costs amounted to €577 million in consequence of the 2002 flooding events. In Portugal, the most hazardous case of scour occurred in 2001 with the collapse of the 19th century Hintze Ribeiro bridge, which caused 59 fatalities. The vital role of bridges in society and the catastrophic consequences of a potential bridge failure justify the need to actively research ways to improve the prediction of local scour and its implications in the hydraulic bridge design (Chiew *et al.*, 2020).

The design typically considers the prediction of the expected scour at foundation level through the estimate of the maximum equilibrium scour depth. There are two scour conditions which are dictated by the sediment transport characteristics in the approaching flow: clear water occurs when there is no general sediment transport and live bed occurs when sediments are transported in the approach flow (Graf, 1998; Melville & Chiew, 1999; Richardson & Davis, 2001). Normal flow conditions (typically clear water conditions) can cause continuous scour at the bridge foundations, in which the scouring process is often slow enough to allow countermeasures via regular maintenance works, but if unacknowledged may be responsible for silently reaching dangerous scour depth values. Although there is a wide number of studies on clear water scour condition, the majority of the scour-induced bridge failures occurs during floods, where a significant sediment flux is transported by the river flow and the flow intensity is high (Ballio *et al.*, 2010). In this live bed condition, the equilibrium scour hole (when the scour depth fluctuates around a mean equilibrium value) is reached faster than when in clear water condition (Hoffmans & Verheij, 1997; Melville &

Coleman, 2000). Several formulations can be found in the literature concerning the quantification of equilibrium and time evolution of scour depth for both conditions.

Many researchers assessed the accuracy of the available bridge scour depth predictors (Gaudio *et al.*, 2010; Sheppard *et al.*, 2011, 2014; Park *et al.*, 2017), and despite some differences in opinion, the general consensus is that most of the existing equations are conservative. According to those models, the scour depth is strongly related to three key factors: sediment properties, flow dynamics, and foundation structure geometry. However, due to laboratory limitations or numerical simplifications, investigations, focused on the isolated effects of each factor, are not considered comprehensive enough. For instance, the most recent version of the HEC-18 equation (Arneson *et al.*, 2012) does not allow for the effects of bed particle size, an important aspect driving scour, and the Froude number dependency is not valid when comparing results for distinct bed materials. Sheppard *et al.* (2014) have demonstrated that the Sheppard/Melville (S/M) equation, when compared to other widely known equations, results in a better performance, for both clear water and live bed conditions. This was corroborated by Sturm *et al.* (2018)'s study. The S/M equation is specifically recommended when dealing with simple foundation shapes, founded in non-cohesive beds.

The dynamic process of the local scour phenomenon occurs when flowing water erodes the sediment around the bridge foundations, leading to the formation of scour holes. The sediment entrainment and transport are controlled by the turbulent flow field therein developed (Dargahi, 1989; Ettema *et al.*, 2017). Once formed, the scour hole interferes significantly with the scouring process in several ways, for instance, by modifying the incoming flow features. Therefore, a three-dimensional survey of the scour hole and the characterization of the deposition features are essential in order to assess scour vulnerability and risk. This survey is used to find mechanisms and improve tools that minimize potential consequences to bridge stability (Bento *et al.*, 2020). Several efforts have evolved from point-wise measurements (Oliveto & Hager, 2002; Diab, 2011, among others) into techniques capable of reconstructing the 3D model of the scour effects and its ensemble in the vicinity of the foundations. To the authors' knowledge, few experimental works have used non-intrusive methods to characterize the evolution of the scour hole in clear water and live bed conditions (Müller *et al.*, 2001; Visconti *et al.*, 2012; Bouratsis *et al.*, 2013; Poggi & Kudryavtseva, 2019, among others).

Müller *et al.* (2001) have used the Moiré effect to map surface contours of the scour development around physical models of a railway bridge across the Rhine river and assess their evolution by comparing the initial and final fringe images. Visconti *et al.* (2012) have proposed a new method to measure the scour hole evolution in shallow water and under live bed conditions, based on laser and ultrasonic level transmitters. Bouratsis *et al.* (2013) have presented a photogrammetry-based method for the three-dimensional survey of the river bed topography, without interrupting the scouring experiments; the method consisted of two cameras recording the sediment bed during its evolution, and a number of algorithms for camera calibration, image rectification, and stereo-triangulation. In Hackl *et al.* (2018)'s work, an unmanned aerial vehicle and photogrammetric technology were used to obtain the three-dimensional mesh of the terrain in which a concrete bridge

in the Canton of Grisons (Switzerland) was founded. The close-range photogrammetry technique was successfully adopted in the reconstruction of the scour hole around bridge foundations of simple or complex shapes in experimental environments by Pfleger *et al.* (2010) and Ramos *et al.* (2015), respectively. Chourasiya *et al.* (2017), in turn, have explored the potential of the Kinect V2 sensor for three-dimensional surveys. Recently, Poggi & Kudryavtseva (2019) have presented a new technique for measuring the two-dimensional shape of an evolving scour hole, based on the use of line laser source and a commercial camera that acquired the bed evolution during the experiment.

The accuracy and reduced financial outlay of the image-based techniques, namely the close-range photogrammetry and the use of the Kinect sensor, are of key importance when planning surveys of three-dimensional surface maps (Linder, 2016; Bento *et al.*, 2018). Both methods have revealed satisfactory accuracy and non-intrusive particularities. Therefore, a more advanced and comprehensive level of bridge scour prediction is herein described for clear water and live bed flow scouring experiments based on these techniques.

To attain this aim, laboratory experiments were undertaken in order to provide: (i) detailed measurements of geometry and evolution of the scour hole (and deposition zone) in the vicinity of oblong bridge pier models; (ii) increased understanding of the mechanism of the scouring phenomenon; and (iii) valuable database for calibration and validation of numerical models, such as Computational Fluid Dynamics (CFD) tools. For a continuous monitoring of the scouring process, an additional method was developed to obtain two-dimensional bed profiles during experiment, through the application of underwater image processing and computer vision routines.

This paper is organized as follows. Subsection 4.3.3 describes the experimental facility, the bridge pier models, the devices, the measured variables and the instrumentation. Subsection 4.3.4 indicates the scour depth estimates considered in the current study and highlights their applicability conditions. Subsection 4.3.5 briefly describes the image-based techniques herein employed and their respective experimental apparatus. Subsection 4.3.6 presents the results of the study and provides a discussion. Finally, Subsection 4.3.7 summarizes the main conclusions of this research.

4.3.3 Local scouring experiments

In the present subsection, the experimental facility and the bridge pier models are presented in detail as well as a characterization of the bed material in which the pier models were embedded. Then, the flow conditions considered for the experiments are reported. The instrumentation and measuring techniques are, thereafter, specified and explained. Finally, the experimental procedure is presented, highlighting the role of each task for the experiments' success.

4.3.3.1 Experimental facility and bridge pier models

Four local scouring experiments, reproducing the flow at the vicinity of bridge pier models, embedded in a sediment bed, were performed in the 40.7 m long, 2.0 m wide and 1.0 m deep glass-sided rectangular tilting flume (hereinafter termed CIV) of the National Laboratory of Civil Engineering (LNEC), in Lisbon, Portugal (Figure 4.14).

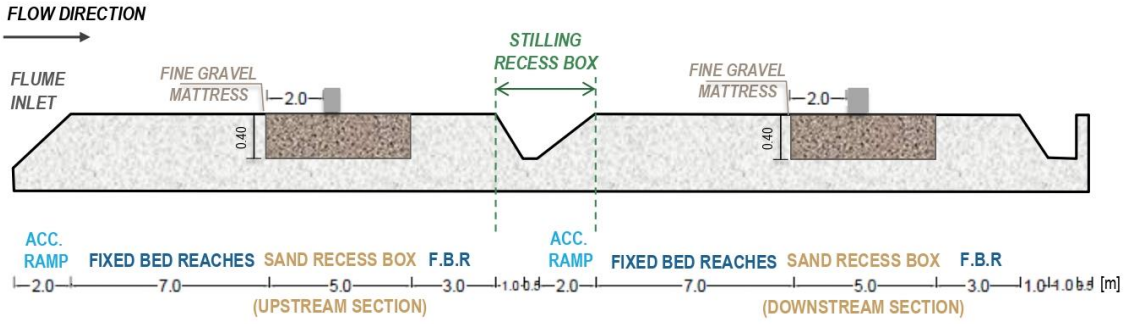

Figure 4.14: Longitudinal scheme of the experimental facility.

At the inlet of the flume, a metallic grid was installed to guarantee the uniform distribution of the transversal flow. A false concrete bottom was installed to perform simultaneously two experiments per run. Two recess boxes, 5.0 m long and 0.4 m deep, filled with sand, were left in the false bottom, where the bridge piers were installed (Figure 4.14). A 0.2 m thick and 0.5 m long fine gravel mattress, embedded at the upstream end of the recess boxes, and properly levelled by the adjacent concrete, allows for a smooth and progressive transition, avoiding scouring at the transition between the fixed and the movable bed. Each of the sand recess boxes is preceded by a 2.0 m long accelerating ramp and a 7.0 m long fixed bed reach and is followed by a 3.0 m long fixed bed reach (Figure 4.14). The accelerating ramp at both the flume inlet and the stilling recess box also contribute to the development of a uniform flow distribution in the two working sections (i.e. at the sand recess boxes). The stilling recess area between the two working sections prevents any sand bed materials carried by the flowing water from the upstream section to be transported to the downstream section, and restores the flow regime for the downstream working section (Figure 4.14). Four pairs of hydraulic jacks, 9.5 m apart, allow the variation of the flume bottom slope from 0% to 2.5%. A 0.019% slope of the CIV bottom was herein imposed. Mechanical screws along its length control the slope and a calibrated scale indicates the vertical movement of CIV up to an accuracy of $\pm$ 0.5 mm.

The bridge pier models were not representative of specific piers, but replicate the most common oblong shape of Portuguese bridge foundations of the 19th and 20th centuries. Thus, two bridge pier models (henceforth called oblong bridge pier models), made of rectangular round-nose concrete columns, were used with widths, W, of 0.11 m and 0.14 m. For the sake of simplicity, the pier models are herein designated as *Pier* 11 and *Pier* 14. The use of these pier models allowed also the analysis and discussion in terms of the results of a previous study carried out in the same facility (Moreno *et al.*, 2012; Moreno, 2016). The geometry of the oblong bridge pier models is schematically presented in Figure 4.15 as well as a photograph of *Pier* 14. The correspondent dimensions are given in Table 4.2. The oblong pier models were placed vertically in the recess boxes at a distance of $\approx$ 2.0 m from their upstream borders. The longitudinal axis of the oblong piers coincided with the working section mid-plane and was aligned with the approaching flow; thus, a skew angle (θ) of 0° was used. The contraction and wall effects of the flume on the scour hole development were avoided according to the criterion of Chiew & Melville (1987) since the

pier width was lower than 10% of the flume width (W/B assumed the values of 5.5% and 7%, being B the flume width).

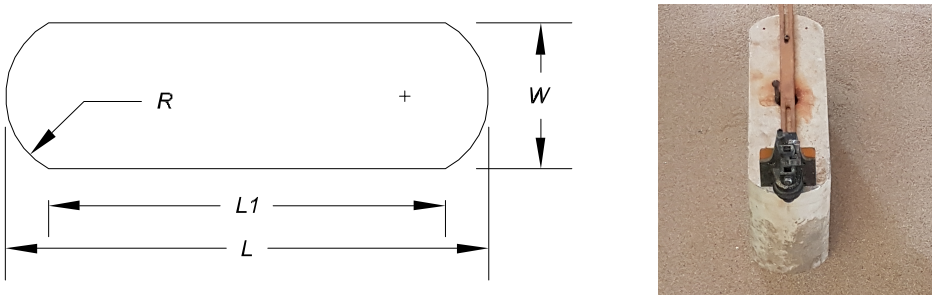

(a) Geometry.

(b) Photograph of *Pier* 14.

Figure 4.15: Oblong bridge pier model.

Table 4.2: Geometry dimensions of the oblong bridge pier models.

Pier geometry dimensions (m)		
Oblong bridge pier models	*Pier* 11	*Pier* 14
Width, W	0.110	0.140
Total length, L	0.433	0.463
Flat side surface length, $L1$	0.372	0.380
Semi-cylindrical surface ratio, R	0.065	0.080
Symbols are represented in Figure 4.15.		

4.3.3.2 Bed material properties and scour conditions

The recess boxes were filled with a uniform quartz sand as bed material for the scouring experiments, characterized by a median grain size diameter, D_{50}, of 0.86 mm, a specific gravity, s, of 2.65 and a sediment diameter standard deviation, σ_D (where $\sigma_D = \sqrt{D_{84}/D_{16}}$), of 1.28. The corresponding dimensionless sediment diameter ($D^* = \left[(s-1)\,g/\nu^2\right]^{1/3} \cdot D_{50}$, being g the gravity acceleration and ν the kinematic viscosity coefficient) was equal to 21.7. The non-ripple-forming sediment criterion was respected (Raudkivi & Ettema, 1983) and the effect of non-uniformity of sediment on the depth of the scour hole was avoided (Chiew & Melville, 1987; Lee & Sturm, 2009). Sediment coarseness ratios (W/D_{50}) of 127.9 and 162.8 were obtained for *Pier* 11 and *Pier* 14, respectively, which effects were not negligible according to recent studies (Lee & Sturm, 2009; Lança *et al.*, 2011).

Two experimental runs were performed, namely *Run* 1 and *Run* 4, for different flow conditions. Whilst *Run* 1 was carried out under clear water condition, *Run* 4 was developed under live bed flow. The selection of a flow intensity slightly below the threshold condition of sediment motion allowed to obtain the maximum scour depth, without the generalized sediment transport, guaranteeing the clear water flow regime for *Run* 1. In contrast, a flow intensity higher than the unity assured the live bed condition for *Run* 4. Each run comprised two local scouring experiments; in *Run*

1, the experiments were performed simultaneously. Hence, *Run* 1 included $Exp.\ 1U$ and $Exp.\ 1D$, whereas *Run* 4 consisted of $Exp.\ 4U$ and $Exp.\ 4D$ experiments. *Pier* 11 was installed in the upstream working section, whereas *Pier* 14 was embedded in the downstream recess box for *Run* 1. A 0.019% slope of the CIV bottom was imposed for *Run* 1. For experiments of *Run* 4, the pier models were installed on the upstream sand box.

Five critical mean velocity predictors for the beginning of sediment motion were considered (Shields (1936), Neill (1967), Garde (1970), Melville & Coleman (2000), and Sheppard & Renna (2010), as given in Subsection 4.2.7). Preliminary tests have showed that the sand grains start moving for conditions close to the prediction given by Neill (1967). Thus, the critical velocities obtained by Neill (1967) were herein assumed for the different hydraulic conditions of the local scouring experiments.

4.3.3.3 Devices, measured variables and instrumentation

Several variables were measured before, during and after the local scouring experiments. They comprise (i) the flow depth within CIV and at the immediacy of each working section, which will be the approaching flow depth upstream the obstacles; (ii) the flow discharge at the flume entrance; (iii) the scour depth at piers' front; and (iv) the bed morphology at the pier's vicinity, including scour holes and the deposition regions.

Two sluice gates of the tilting flume, one placed at the upstream section and the other at the downstream end, enabled the flow depth adjustment inside the flume. During the scouring experiments, the approach flow depth was measured by resistive probes, suitably deployed within the flume so as not to interfere with the experiments' development. Two aluminum bars, supporting a limnimeter each, were positioned close to the working sections to check the flow depth before and during experiments. Two vertical rulers, designed for the current study and positioned on the flume side walls, also aided the flow depth control. The flow discharge was regulated by the rotational speed of the associated pump, set at a constant value, and monitored by an electromagnetic flowmeter (Badger's Magnetoflow®, Badger (2007)) with a rate accuracy of $\pm$ 0.25%. The signal from the resistive probes as well as from the electromagnetic flowmeter was acquired at a sampling frequency of 25 Hz.

Limnimeters, coupled to the upstream faces of the oblong bridge pier models, allowed the registration of the scour depth evolution with an accuracy of $\pm$ 0.05 mm. The limnimeters were installed at 0.03 m from *Pier* 1l ($Exp.\ 1U$) and at 0.05 m from *Pier* 14 ($Exp.\ 1D$) fronts. The difference in the positions was due to the presence of the cameras support structure, previously installed at the top surface of *Pier* 14 ($Exp.\ 1D$). In Run 4, $Exp.\ 4U$ and $Exp.\ 4D$, the scour depth measurements were performed at 0.05 m from the piers' front, as well. The tilting flume was equipped with three moving carriages that moved along the longitudinal axis of the flume on two precisely levelled rails. They enabled the access of the experiment area for controlling and measuring purposes, namely for flow and scour particularities.

A comprehensive measurement system for the two- and three-dimensional characterization of scour and deposition areas at the vicinity of the pier models was implemented. Four

submersible action cameras (Action Cam NK 3056 Full HD) enabled the acquisition of synchronized images of the scouring phenomenon during the experiments. Frames with a spatial resolution of 3,000 $\times$ 4,000 px^2 were acquired, which allowed the extraction of bed profiles for specific instants by employing underwater image-processing and computer vision routines. For the three-dimensional characterization of the initial and final stages of the scouring experiments, two advanced image-based techniques were employed, specifically the close-range photogrammetry and the use of the Kinect V2 sensor.

4.3.3.4 Experimental Procedure

Prior to the scouring experiments, a set of steps was undertaken: (i) the bridge pier models were installed in each working section; (ii) the recess boxes were filled with the graduated sand, arranged and levelled with the adjacent concrete bed level; (iii) the flume was filled slowly and allowed to stand until the air trapped in the sediment had escaped; (iv) the flume was then drained and the sand arranged once again; (v) the pier models were protected with metallic plaques to preclude undesirable scour at the beginning of experiments; (vi) the flume was filled again by increasing the rotational speed of the associated pump and by gradually adjust the level of the downstream sluice gate until reaching the desired hydraulic conditions (mean approach flow depth and discharge); and (vii) the protective plaques were removed with the aid of wires, establishing the initiation of each scouring experiment.

An inspection of all instrumentation and measuring supports were properly conducted before the beginning of experiments. Between steps (iv) and (v), scan images and photos of the flat (initial) bed morphology were captured for their characterization by using the Kinect V2 sensor and by the application of the close-range photogrametry technique. These procedures were repeated at the end of the scouring experiments, after the flow was stopped and the flume was slowly made empty, with the aim of characterizing the eroded (final) bed morphology.

During experiments, the temporal evolution of the scour depth at the piers' front was measured. The temporal distribution of the scour depths' measurements was adapted in line with the development of the scouring phenomena; higher periodicity was used for the first instants of experiments as scour develops more rapidly. Thus, measurements were performed every five minutes for the first hour to capture the initial high rate of scouring, after which the frequency reduced to every 30 min. They were recorded every two hours after 48 h had passed.

Synchronized underwater captures of the scour hole were acquired at certain instants along the experiments' duration. Each experiment corresponded to a previously designated time duration, specified and justified in the following subsection.

4.3.4 Scour depth predictors

4.3.4.1 Equilibrium scour depth

Several equations have been proposed for estimating the equilibrium scour depth in the past decades. In the present study, two well established equations, namely the latest version of HEC-18

scour depth predictor (Arneson *et al.*, 2012) and the Sheppard/Melville (S/M) method (Sheppard *et al.*, 2014), were selected. As recently indicated in Sturm *et al.* (2018), these predictors are recommended for use in estimating local scour depths at foundations of simple shapes founded in non-cohesive beds, as is the case of the current investigation. The prediction method given by the latest version of HEC-18 (Arneson *et al.*, 2012) is stated as Equation 4.6:

$$\frac{d_{se-HEC18}}{W} = 2K_1K_2K_3K_w\left(\frac{h}{W}\right)^{0.35}Fr^{0.43}, \tag{4.6}$$

where $d_{se-HEC18}$ is the equilibrium scour depth at the pier front, and Fr is the Froude number ($Fr = V/\sqrt{gh}$). The factors K_1, K_2 and K_3 account for pier shape, pier alignment and bed forms, respectively (given in Arneson *et al.* (2012)). This equation was derived from a set of laboratory data for circular piers, selected from Chabert & Engeldinger (1956) and Shen *et al.* (1966) studies, which has been progressively modified over the years and is currently recommended by the Federal Highway Administration (FHWA) for estimating maximum scour depths at single piers (Arneson *et al.*, 2012). The last version of HEC-18 also includes a multiplying factor, K_w, to be applied to wide piers in shallow flows, i.e., when the ratio of flow depth to pier width is less than 0.8 ($h/W < 0.8$), the ratio of pier width to the median sediment diameter is greater than 50 ($W/D_{50} > 50$), and the Froude number of the flow is sub-critical ($Fr < 1$). Such factor was derived by Johnson & Torrico (1994) using laboratory and field data for large piers and is estimated by Equation 4.7.

$$K_W = \begin{cases} 2.58\left(\dfrac{h}{W}\right)^{0.34}Fr^{0.65}, & \dfrac{V}{V_c} < 1.0 \\ 1.0\left(\dfrac{h}{W}\right)^{0.13}Fr^{0.25}, & \dfrac{V}{V_c} \geq 1 \end{cases} \tag{4.7}$$

The Sheppard/Melville (S/M) method (Sheppard *et al.*, 2014) is expressed by Equation 4.8, in which W^* is the pier effective width and V_{lp} is the live-bed peak velocity. The variables f_1, f_2, and f_3 represent the interactions of flow-structure, flow-sediment, and sediment-structure, respectively (given in Sheppard *et al.* (2014)). In Equation 4.8, V_c is computed by using the Neill (1967)'s predictor (in the current investigation), while V_{lp} is estimated using Van Rijn *et al.* (1993) equations for determining plane bed velocity (i.e., coincident with a upstream flat bed stage of sediment transport); the larger of $V_{lp} = 0.6\sqrt{gh}$ or $V_{lp} = 5V_c$ is assigned as the V_{lp} value. The S/M equation (Sheppard *et al.*, 2014) resulted from a melding, and slight modifications, of Sheppard's (Sheppard & Miller, 2006) and Melville's (Melville, 1997) equilibrium equations. The modifications consisted of: (i) changing the 1.75 coefficient to 1.2 in the f_2 computation, (ii) modifying the value of V/V_c where local scour is initiated from 0.47 (considered in Sheppard & Miller (2006)) to 0.4, and (iii)

simplifying the manner in which the V_{lp} is computed.

$$\frac{d_{se-SM}}{W^*} = \begin{cases} 2.5 f_1 f_2 f_3, & 0.47 < \dfrac{V}{V_c} < 1.0 \\ f_1 \left[2.2 \left(\dfrac{\dfrac{V}{V_c} - 1}{\dfrac{V_{lp}}{V_c} - 1} \right) + 2.5 f_3 \left(\dfrac{\dfrac{V_{lp}}{V_c} - \dfrac{V}{V_c}}{\dfrac{V_{lp}}{V_c} - 1} \right) \right], & 1 < \dfrac{V}{V_c} < \dfrac{V_{lp}}{V_c} \\ 2.2 f_1, & \dfrac{V}{V_c} > \dfrac{V_{lp}}{V_c} \end{cases} \tag{4.8}$$

Both predictors, equations 4.6 and 4.8, might be applied for both clear water and live bed conditions. Additionally, the proposed formulation of Moreno *et al.* (2016b) to predict the equilibrium scour depth (d_{se-MM}) is also considered in this investigation (Equation 4.9). This predictor was derived by integration and adjustment of the equations developed by Sheppard *et al.* (2011) and Lança *et al.* (2013) for cylindrical piers to pile-supported piers, wherein the pier diameter was replaced by the equivalent diameter (D_e). Regarding the position of the pile cap top (H_c, for the pile-supported piers therein studied), d_{se-MM} changes markedly. For single piers, which is equivalent to a scenario where the pile cap top is below the base of the scour hole (Situation 3 in Moreno (2016)), $D_e = K_{sc} D_c$, where K_{sc} is the column shape factor (given in Moreno *et al.* (2016b)) and D_c corresponds, in the current investigation, to W. The variables K_I, K_{hD_e} and K_d (given by equations 4.10 to 4.12) stand for the factors of flow intensity, flow shallowness, and sediment coarseness, respectively. Moreno *et al.* (2016b)'s predictor was based on an extensive experimental campaign performed in the same tilting flume and bed material of the ones used in the current investigation, though for clear water conditions.

$$\frac{d_{se-MM}}{D_e} = 2.6 K_I K_{hD_e} K_d \tag{4.9}$$

$$K_I = 1.0 - 1.2 \left[ln \left(\frac{V}{V_c} \right) \right]^2 \tag{4.10}$$

$$K_{hD_e} = \tanh \left[\left(1.3 \frac{h}{D_e} \right)^{0.7} \right] \tag{4.11}$$

$$K_d = \begin{cases} 1, & 50 \leq \dfrac{D_e}{D_{50}} \leq 100 \\ 0.2 + \dfrac{3.5}{\left(\dfrac{D_e}{D_{50}} \right)^{0.32}}, & \dfrac{D_e}{D_{50}} > 100 \end{cases} \tag{4.12}$$

4.3.4.2 Local scour depth evolution

Sheppard *et al.* (2014) have stated that the current methods for predicting the equilibrium scour depth at bridge piers, including those described in HEC-18 (Arneson *et al.*, 2012), generally over-predict the field scour depths, leading to the use of unwarranted and costly foundations or

countermeasures. Moreover, the equilibrium scour depth does not fully replicate the scouring phenomenon in nature, requiring thus a prediction of the temporal progression of scour depth. Few studies on the scour depth temporal evolution can be found (Kothyari *et al.*, 2007; Sheppard *et al.*, 2011; Lança *et al.*, 2013, among others), although not extensively used and tested for the live bed scour conditions. Hence, the possibility of improving the accuracy of the better performing predictors was investigated in Sheppard *et al.* (2011). For that purpose, methods such as the Miller & Sheppard (2002) model are complex and modifications would require significant effort. In contrast, the Melville & Chiew (1999) model is less complex and easy to apply and modify. Thus, in Sheppard *et al.* (2011) an adjustment of the coefficients of Melville & Chiew (1999)'s model and the replacement of the equilibrium scour depth equation with the S/M equation (Equation 4.8) improved its accuracy. The resulting equation, named as the Melville/Sheppard (M/S) equation, is given by Equation 4.13, with K_t given in Sheppard *et al.* (2011).

$$d_{s-MS} = K_t d_{se-SM} \tag{4.13}$$

Since time to equilibrium is somewhat misleading, Sheppard *et al.* (2011) have also derived an expression for the time required to reach 90% of the equilibrium scour depth, t_{90}, in terms of the reference time, t_r, and the flow intensity, V/V_c, as expressed by Equation 4.14. Such parameter, t_{90}, was considered for the definition of the experiments' time duration of the current study (addressed later).

$$t_{90} = exp\left(-1.83\frac{V}{V_c}\right) t_r \tag{4.14}$$

4.3.5 Scour hole and deposition characterization

4.3.5.1 Flat and eroded 3D bed morphology models

In the experimental runs, besides the monitoring of the temporal evolution of the maximum scour depth at piers' front, two image-based techniques were herein considered: close-range photogrammetry and Kinect V2 sensor for characterizing both the flat (initial) and the eroded (final) stages of the bed morphology, resulting from the local scouring experiments. These methods required the previous emptying of the tilting flume and a set of control points, suitably deployed so as to enable the spatial reference of the three-dimensional (3D) bed morphology models.

Photo captures of the scour hole and of the surrounding affected area were acquired using a 12 MP action camera at a mean height of 0.50 m from the flat bed case, as used in Bento *et al.* (2018). The areal extent of the scouring phenomenon have dictated the number of captures for each case. The acquired photos were then processed in a Structured from Motion (SfM) software, namely *Agisoft Metashape Professional Edition*, version 64 bit 1.6.3 (Agisoft, 2020) to reconstruct the beds morphology. The digital elevation models (DEMs) were then extracted and post-processed to enable the creation of bed contour surfaces, bed profiles, among others.

For a successful completion of the digital elevation model (DEM), an image overlap of about 60% should be guaranteed. Since Agisoft Metashape Professional Edition applies Brown model

(Duane, 1971) to simulate lens assembly, automatic calibration works perfectly well for "standard" optics (i.e. with 50 mm focal length, 35 mm film equivalent). However, to process the data captured with the ultra-wide angle lenses of the cameras used in the current investigation, the automatic calibration is likely to fail. Thus, a calibration of the cameras lens was required in order to achieve good reconstruction results. The cameras parameters, including intrinsic, extrinsic and distortion coefficients, were estimated by "Camera Calibration Toolbox for Matlab" through the analysis of the multiple images of a calibration pattern, namely a chess plaque with squares 28 mm wide; the correspondent results are given in Appendix C.3. The images were then corrected and introduced into the photogrammetry software.

A Kinect V2 sensor was also employed as an alternative for the full characterization of the bed morphology (Lachat *et al.*, 2015; Jiao *et al.*, 2017; Zhou *et al.*, 2020). This sensor, composed by a projector and two internal cameras, captured the area of interest from a vertical distance of $\simeq$ 0.50 m. This technique works as follows: (i) the infrared projector transmits a predefined pattern of light; (ii) the distance of various points of the object to the sensor deforms that pattern of light; (iii) the infrared camera captures the deformed pattern and correlates it against a reference speckle pattern projected at a known distance from the sensor. The resulting point clouds were then introduced in the 3D net processing *CloudCompare* software, version 64 bit 2.11, to build topographic 3D maps. This technique allows corroborating the accuracy of the close-range photogrammetry technique by performing a direct comparison between the two approaches, with some preliminary work in Bento *et al.* (2018).

The bridge pier models as well as specific marks on them, serving as spatial reference of the aforementioned 3D models, were properly characterized through a three-dimensional coordinate measuring machine, *MMC* 3D (Lages Martins *et al.*, 2019, DEA, Gamma 2203 model); an accuracy of $\pm$ 7.3x10^{-6} m was ensured. The origin (x, y, z) = (0; 0; 0) was taken at the center of the pier at the CIV mid-plane surface (as can be observed in Figure 4.16a).

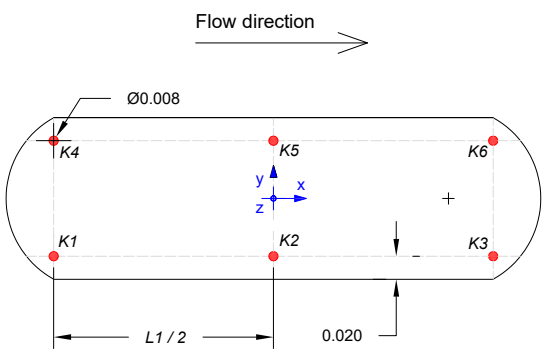

(a) Red circles on the piers' top surface (dimensions in meters).

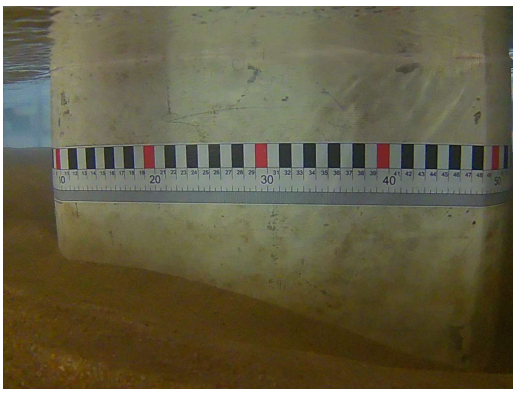

(b) Graduated scale marks.

Figure 4.16: Spatial reference for the 3D bed morphology models.

The symbols x, y and z are, respectively, the longitudinal, transverse, and vertical coordinates. Red circles of 5/16 inch of diameter ($\simeq$ 8 mm - ϕ in Figure 4.16a), glued directly on the top surface of the pier models, represent control points, herein denoted marks $K1$ to $K6$. Graduated

scale marks were also considered for spatial reference, denoted by the letter P, from $P10$ to $P110$, corresponding the number to the lower right corner-centimeter of the graduated scale, as can be seen in Figure 4.16b. Table 4.3 and 4.4 give the spatial coordinates of the control points considered by these image-based techniques.

Table 4.3: Estimates of the spatial coordinates of the control points on the top surface of the bridge pier models (coordinates in $\times 10^{-3}$ meters).

Control Point	*Pier* 11			*Pier* 14		
	x	y	z	x	y	z
$K1$	-188.9442	-36.3563	-0.0394	-189.8233	-48.3533	0.1372
$K2$	-1.3662	-36.9695	-0.0775	-3.6916	-47.2551	-0.2022
$K3$	185.1313	-34.9231	0.3109	191.7488	-45.9323	-0.0959
$K4$	-187.7066	30.7833	0.0879	-192.1237	51.9048	-0.0295
$K5$	0.7866	33.7361	0.0114	-1.9779	51.8607	-0.3258
$K6$	187.8264	32.0585	0.1001	194.1220	51.7658	0.1947

Table 4.4: Estimates of the spatial coordinates of the control points on the graduated scale (coordinates in $\times 10^{-3}$ meters).

Control Point	*Pier* 11			*Pier* 14		
	x	y	z	x	y	z
$P10$	217.5354	4.3695	102.6217	177.0651	71.5489	-172.6304
$P20$	217.0231	4.9234	-202.8070	76.9439	71.1280	-172.5741
$P30$	216.5695	6.0479	-303.0150	-23.1808	71.0893	-172.6096
$P50$	85.1119	54.8684	-136.0736	-215.8753	51.8635	-173.2206
$P60$	-14.7762	55.0847	-137.7383	-219.4160	-42.5139	-173.5513
$P70$	-114.7376	54.8325	-139.0786	-128.7941	-67.7587	-173.4699
$P80$	-207.3938	38.0033	-142.6432	-28.2131	-68.0255	-172.8390
$P90$	-194.1236	-51.7155	-146.1127	71.6660	-68.2625	-172.3487
$P100$	-95.2123	-56.3560	-149.9365	171.8344	-68.2441	-172.4323
$P110$	4.4581	-56.1443	-153.0610	231.6173	-1.831	-173.0584

4.3.5.2 Continuous 2D bed profiles

In the present work, real-time measurements of the scour hole profile were envisaged. To attain that purpose, submersible cameras were considered for the acquisition of underwater images of the scouring phenomenon. Several dispositions were considered and the one selected is schematically illustrated in Figure 4.17. A metallic structure was designed to withstand the possible vibrations that the cameras could be subjected to, which could compromise the quality of the acquired images. It is worth mentioning that preliminary tests were conducted in order to ensure that this structure did not unduly disturb the whole scouring process. For that purpose, an aqueous tracer was used for flow visualization in order to identify the surface streamlines generated by the presence of the cameras'

support structure on the flow approaching the oblong bridge pier model. A solution of potassium permanganate (dark violet in color) was injected uniformly across the flume to understand its influence, as reported in other studies (Aberle *et al.*, 2017); it proved to not interfere with the flow structure at the pier model's immediacy.

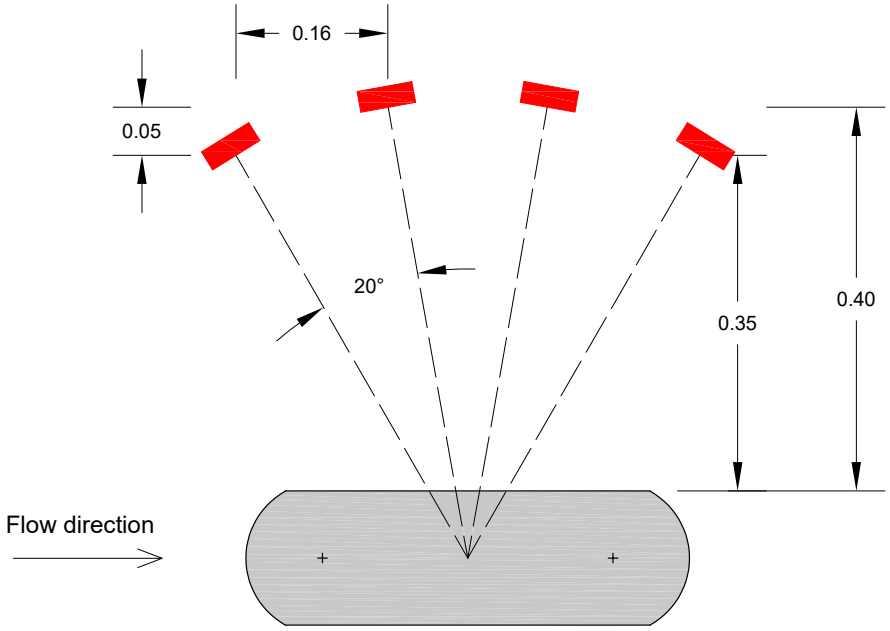

Figure 4.17: Scheme of the underwater cameras' acquisition during scour experiment (dimensions in meters).

Four submersible action cameras (Action Cam NK 3056 Full HD, waterproof with remote control) enabled the acquisition of synchronized images of the scour hole and the surrounding affected areas. Therefore, real-time information of the scour hole patterns was gathered at predetermined instants of the scouring experiments. Acquisitions were made every minute for two blocks of two hours each day of experiment. At the end of each block of acquisition, the cameras' support was removed to make sure that the cameras' batteries would be fully charged for the next sequence of acquisitions. The 12 MP resolution of the cameras proved fit for the intended purpose. Thanks to the submersible feature of the cameras, their optical path were neither impacted by refraction nor by the "ripples" of the water surface, formed due to the presence of the pier and to the large-scale turbulence. The four cameras were positioned so that they were able to frame both the upstream and the downstream eroded bed. By processing each sequence of images was possible to obtain the scour hole evolution in the form of 2D bed profiles during the scouring experiments.

Besides the expected potential of the underwater technique, some critical issues had to be faced during the images' processing (Poggi & Kudryavtseva, 2019; Pinto & Matos, 2020), namely: (i) identification, in each image, of the border between the sand and the pier model; (ii) conversion of pixels into metric distances; and (iii) the adjustment of perspective, distortion, scale and rotation of the cameras' lens. The border between the sand and the pier model was a rather manual detection task, since the pier lateral surface was not completely homogeneous for a successful employment

of image segmentation operations in the whole border's width. To minimize that detection error, the sand-pier border at a certain instant corresponded to the border average from two consecutive images. For the remaining issues, a Python code was developed. A total of 18 vertical lines were defined, obtained by the extraction of the planar coordinates of 38 points of the graduated scale at pier's lateral surface (the same ruler considered for spatial reference of the aforementioned image-based techniques) to fulfil the (ii) issue. In order to minimize the error due to the existence of outliers, the iterative method Random sample consensus (*RANSAC*), firstly published by Fischler & Bolles (1981), was used for aiding the selection of the points that better corroborated a single line (vertical or horizontal). An horizontal line, referred to as reference line, was also determined by using the *RANSAC* method, at the ruler lower border (Figure 4.16b). The correspondent equations were determined by the Least Squares Estimate (LSE) method. The correction of perspective, scale and rotation was performed by employing 2D projective transformations between points in the world plane and in the image plane, known as "Homographies". Distortion effects are inherent in all the acquired images and bring non-linear errors that can be overcome through the cameras' calibration. In the present investigation, the "Camera Calibration Toolbox for Matlab" was used for the extraction of the intrinsic cameras' parameters, required for their lens' distortion corrections. The respective results are given in Appendix C.3. Once the calibration of the model and the detection of the sand-pier border line were performed, the code computed its distance to the reference line, enabling, this way, the construction of the 2D bed profiles.

4.3.6 Results and discussions

4.3.6.1 Hydraulic conditions

Table 4.5 depicts the main hydraulic variables concerning the approach flow, namely, discharge (Q), depth (h), velocity (V), flow intensity ($I_f = \frac{V}{V_c}$, being V_c the critical mean approach flow velocity for sediment incipient motion), Froude number ($Fr = \frac{V}{\sqrt{gh}}$), flow Reynolds number ($Re = \frac{Vh}{\nu}$, being ν the kinematic viscosity), and, the parameters concerning the obstacle: pier width (W) and pier Reynolds number ($Re_D = \frac{VW}{\nu}$). Despite the flow intensity of 1.0 for $Exp.\ 1U$, this experiment was considered as being conducted under clear water scour conditions.

Whilst the flow discharge and water levels within the flume in *Run* 1 experiments were controlled on a point-wise basis, the experiments of *Run* 4 were undertaken with a continuous acquisition of the flow discharge and water levels data. For this reason, the main hydraulic parameters for experiments $Exp.\ 4U$ and $Exp.\ 4D$, undertaken under live bed conditions, were estimated with an associated uncertainty. In Table 4.5, the main hydraulic parameters of *Run* 4 are presented with a 95% of confidence interval; the estimated error corresponded to the sample error, given by $\frac{1.96\sigma}{\sqrt{n_s}}$.

The results of $Exp.\ 4U$ and $Exp.\ 4D$ are illustrated in Figure 4.18 and Figure 4.19, respectively, each comprising a set of four plots. Plots (a) show the time evolution of the flow discharge, in which different methods for data filtering were tested and applied, namely, the Butterworth filter, the Smoothing spline and the Moving average. Plots (b), (c) and (d) depict, in the form of box-plot graphs, the variability of the approach flow discharge, flow depth and flow intensity, respectively. Such graphs include the median, the lower and upper quantiles (defined as the 25^{th}

Table 4.5: Hydraulic variables of *Run* 1 and *Run* 4.

Run 1							
Experiment	Q (m^3s^{-1})	h (m)	V (ms^{-1})	If $(-)$	Fr $(-)$	Re $(-)$	Re_D $(-)$
Exp. 1*U*	0.0923	0.1440	0.3205	1.0295	0.2696	46150	35253.47
Exp. 1*D*		0.1500	0.3077	0.9843	0.2536		43073.33
Exp. 4*U*	0.1226±6x10^{-7}	0.1453±1x10^{-6}	0.4222±3x10^{-6}	1.3550±1x10^{-5}	0.2964±5x10^{-6}	61069±0.3	46254±0.4
Exp. 4*D*	0.1244±1x10^{-6}	0.1570±2x10^{-6}	0.3964±6x10^{-6}	1.2626±2x10^{-5}	0.2575±6x10^{-6}	61977±0.6	55281±0.8

and 75^{th} percentiles) and the outliers for each variable. The long upper (Figure 4.18c) or lower (Figure 4.18d) tails show the lack of symmetry (skewness) in the data values. The red plus signs, in turn, are outliers that should be investigated carefully. The mild outliers were kept since they contained trustful information, whilst the extreme outliers were filtered out and removed from the analysis.

The slight variability in the trend observable in Figure 4.18a and Figure 4.19a coincided with heavy construction working hours in the vicinity of the experiments. Notwithstanding, the registered differences were almost negligible as Figure 4.18b and Figure 4.19b demonstrate: in $Exp.\ 4U$, the differences of the minimum and maximum flow discharges to the mean value were 3.1% and 1.4%, respectively, whereas in $Exp.\ 4D$, the same differences were 2.6% and 1.1%, respectively. Figure 4.18c and 4.19c show the estimates of water level within the flume at each resistive probe position of the working section: upstream ($R1$) and downstream ($R2$). The variable R_{mean} is the arithmetic average of $R1$ and $R2$ data, which was herein the selected approach. Similar analysis was also performed for the evaluation of the flow intensity of each experiment as shown in Figure 4.18d and Figure 4.19d. These analyses constitute a relevant and efficient source of information to account for the uncertainty in the hydraulic and scour conditions of each experiment.

In both runs, the oblong bridge pier models behaved as transitional piers (Melville & Coleman, 2000), yielding a flow shallowness (h/W) varying between 1.07 ($Exp.\ 1U$) and 1.32 ($Exp.\ 4U$). The effect of secondary currents due to flume side walls on the flow was negligible given the values of the ratio of the flume width to flow depth (B/h) obtained: 13.9, 13.3, 13.8 and 12.7, respectively. According to Yang *et al.* (2004), the aforementioned effect intrudes near the free surface and develops a dip phenomenon in the velocity profiles for ratios less than 6. Therefore, the flow was free from the secondary currents at the flume mid-plane (Cardoso *et al.*, 1989), where the pier models were installed. The experiments were carried out under subcritical flow conditions ($Fr < 1.0$). The flow and pier Reynolds numbers (Re and Re_D in Table 4.5) ensured fully turbulent incoming flows for all experiments.

4.3.6.2 Evolution of scour depth with time

Regardless of the clear water or live bed approach flow condition (*Run* 1 or *Run* 4), the time required to reach 90% of the respective equilibrium scour depth (t_{90}, given by Equation 4.14), dependent of the reference time (t_r, given in Sheppard *et al.* (2011)), was used as a basis criterion for the time duration of the experiments. These estimates as well as the real duration of experiments (t) are given in Table 4.6.

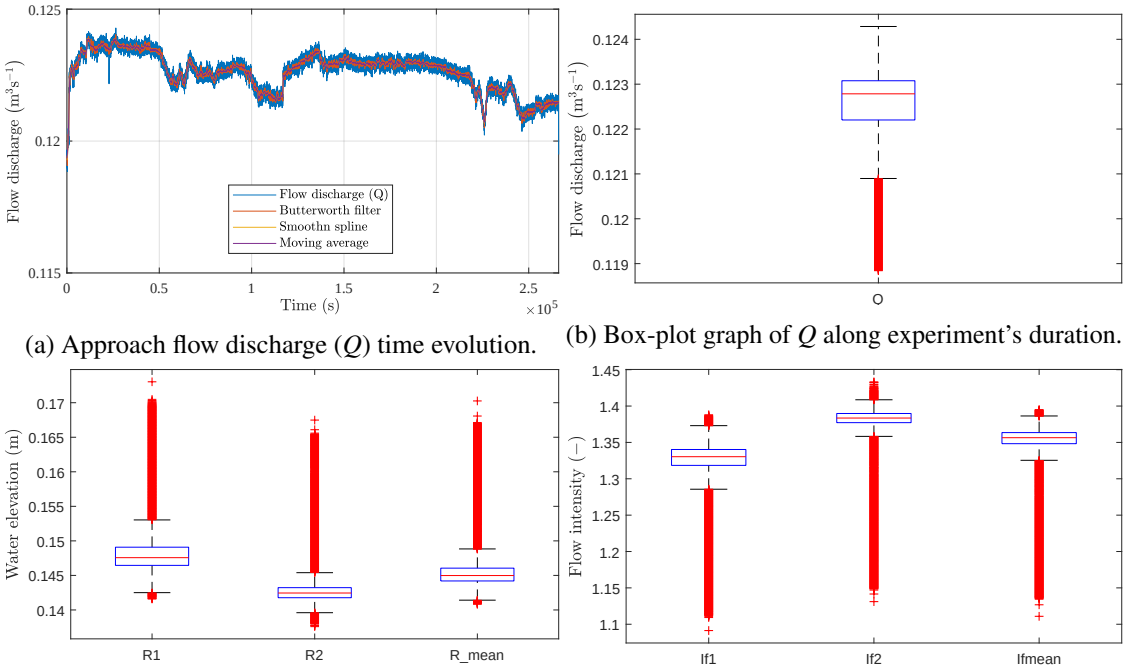

(a) Approach flow discharge (Q) time evolution.

(b) Box-plot graph of Q along experiment's duration.

(c) Box-plot graphs of the water level within flume.

(d) Box-plot graphs of the approach flow intensity.

Figure 4.18: Hydraulic conditions of *Exp*. 4*U*.

Table 4.6: Reference basis for the time duration of the experiments.

Experiment	t_r (days)	t_{90} (days)	t (days)
Exp. 1*U*	30.4100	4.6200	5.8979
Exp. 1*D*	34.0300	5.6200	5.9000
Exp. 4*U*	$34.5801 \pm 8\text{x}10^{-5}$	$2.8984 \pm 8\text{x}10^{-5}$	3.1000
Exp. 4*D*	$40.8442 \pm 1\text{x}10^{-4}$	$4.0537 \pm 2\text{x}10^{-4}$	1.8208

Figure 4.20 displays the evolution of the scour depth at the piers' front with time (Figure 4.20a and Figure 4.20c) and with the correspondent logarithmic scales (Figure 4.20b and Figure 4.20d), for *Run* 1 and *Run* 4, respectively. Despite the estimated values for t_{90}, *Run* 1 lasted 5.90 days instead of 5.62 days obtained for the longest experiment, *Exp*. 1*D*. *Exp*. 4*U* lasted 3.1 days instead of 2.9 days estimated in Table 4.6. Due to mechanical faults, *Exp*. 4*D* was interrupted before reaching 4.1 days, namely after 1.8 days of the scouring process; the experiment ran roughly to 44.4% of the planned duration (Table 4.6).

For *Run* 1 experiments, under clear water conditions, the scour depth values differed roughly in 5.4%, with higher depths for *Exp*. 1*U* in more than 60% of the registered instants (Figure 4.20a and Figure 4.20b). Similar trends between experiments are explained by their proximity in flow intensity as well as to the critical condition ($V = V_c$) and the mean approach flow depth (h). As transitional piers, the scour depths have a non-linear dependence on pier width and flow depth ($\propto \sqrt{Wh}$). Despite different dimensions of the piers (higher width of *Pier* 14), it should be noted that the hydraulic conditions, under which both experiments were developed, were also lightly

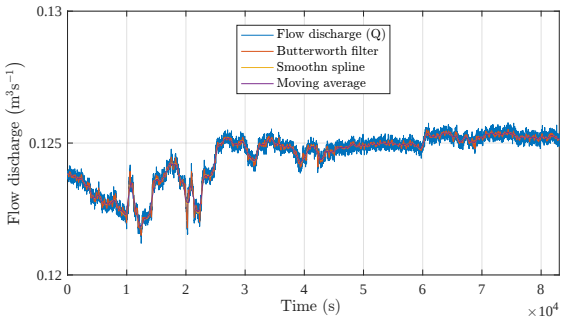

(a) Approach flow discharge (Q) time evolution.

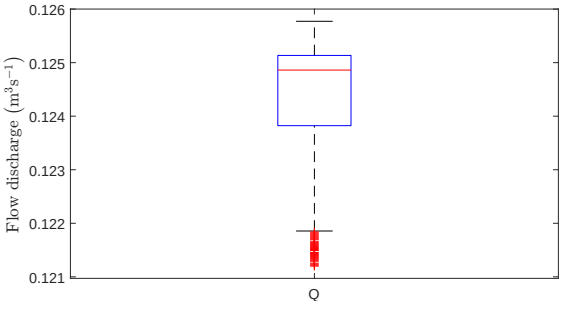

(b) Box-plot graph of Q along experiment's duration.

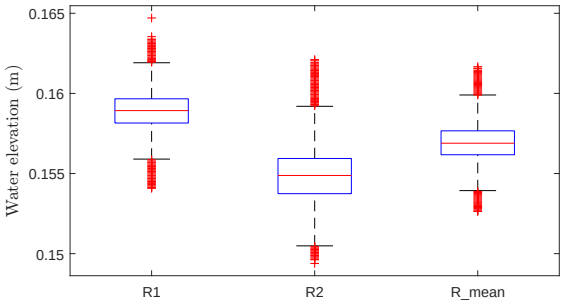

(c) Box-plot graphs of the water level within flume.

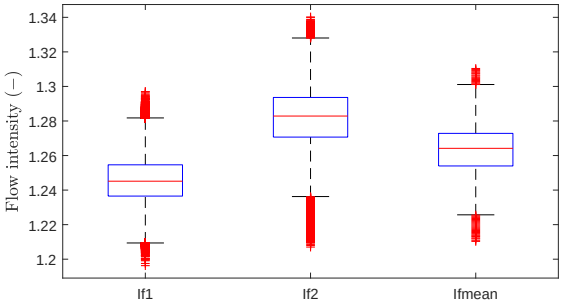

(d) Box-plot graphs of the approach flow intensity.

Figure 4.19: Hydraulic conditions of $Exp.\ 4D$.

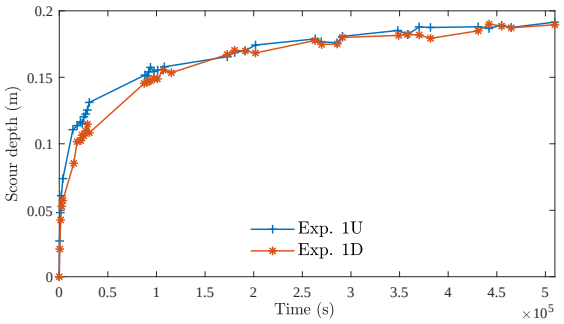

(a) Scour depth time evolution for *Run* 1.

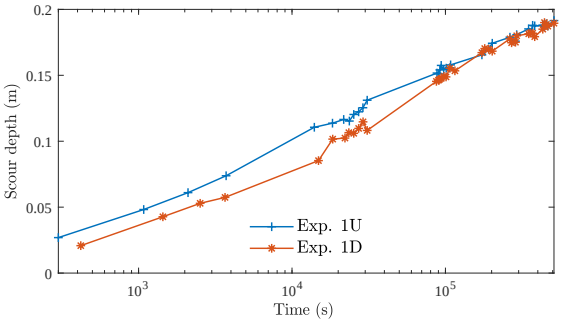

(b) Scour depth time evolution in logarithmic scale.

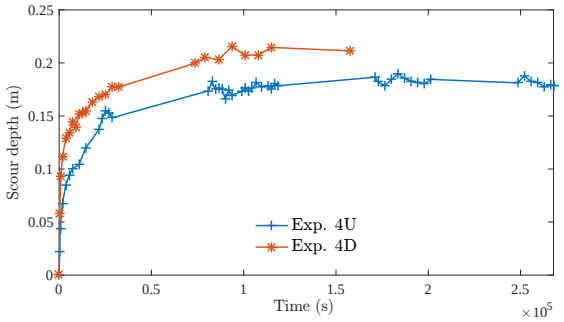

(c) Scour depth time evolution for *Run* 4.

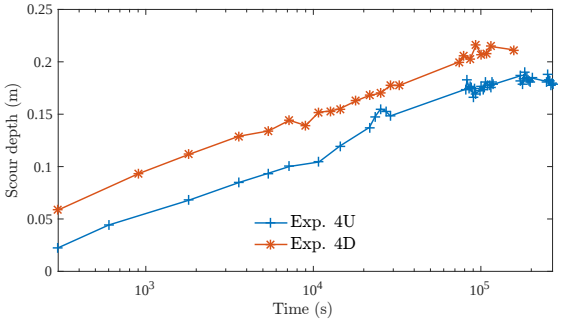

(d) Scour depth time evolution in logarithmic scale.

Figure 4.20: Temporal evolution of the scour depths for *Run* 1 (upper panel) and *Run* 4 (lower panel).

different. The slightly higher flow intensity and lower mean approach flow depth of $Exp.\ 1U$ have led to higher scour depths. At the end of *Run* 1, the final scour depths, d_{sm}, were 0.1915 m ($Exp.$

$1U$) and 0.1895 m ($Exp.\ 1D$), equating to a relative difference of the order of 1.04%.

However, scour depth time evolution for the *Run* 4 experiments under live bed conditions revealed evident differences between $Exp.\ 4U$ and $Exp.\ 4D$ (Figure 4.20c and Figure 4.20d). For this run, the higher width of Pier 14 ($Exp.\ 4D$), explained the temporal evolution of the scour depths towards higher scour depths than for $Exp.\ 4U$. At the end of the first hour of $Exp.\ 4U$, the measured scour depth attained was of 0.085 m, whereas for $Exp.\ 4D$ such value almost reached the value of 0.13 m. The night period (of almost 11 hours, from the last measurement performed on the first day and the first one on the second day), registered an increase of the scour depth of 0.0225 m. During the second day of experiments a reduction of slope was visible. At the end of *Run* 4, the final scour depths, d_{sm}, were 0.1790 m ($Exp.\ 4U$) and 0.2114 m ($Exp.\ 4D$). This latter scour depth registered at roughly 1.8 days of $Exp.\ 4D$, was higher than the correspondent scour depth of $Exp.\ 4U$, as can be observed in Figure 4.20c and Figure 4.20d.

As aforementioned, the equilibrium scour depth estimated by Sheppard/Melville equation (Equation 4.8) was used as reference for the experiments' time duration; however, other predictions were computed, particularly the ones derived by Arneson *et al.* (2012) and Moreno *et al.* (2016b). Table 4.7 presents their values for the scouring experiments herein performed.

Table 4.7: Equilibrium scour depth estimates and measured maximum scour depths.

Experiment	$d_{se-HEC18}$ (m)	d_{se-SM} (m)	d_{se-MM} (m)	d_{sm} (m)
$Exp.\ 1U$	0.1514	0.2014	0.2176	0.1915
$Exp.\ 1D$	0.1749	0.2370	0.2509	0.1895
$Exp.\ 4U$	$0.1581 \pm 7\text{x}10^{-7}$	$0.2012 \pm 4\text{x}10^{-7}$	-	0.1790
$Exp.\ 4D$	$0.1789 \pm 1\text{x}10^{-6}$	$0.2395 \pm 5\text{x}10^{-7}$	-	0.2114

Their differences can be assigned to their own features, addressed previously. These predictions have evidenced that estimates by Moreno (2016)'s approach over-predict by 6.4% (being a very good approximation) and that estimates by Arneson *et al.* (2012)'s approach under-predict by 25.5%.

4.3.6.3 Scour holes and deposition zones at piers' vicinity

A total of 16 three-dimensional (3D) maps of bed morphology at the vicinity of the oblong bridge pier models were derived, either from the application of close-range photogrammetry or by using the Kinect V2 sensor, at the beginning and at the end of experiments. The three-dimensional eroded bed models are displayed in Figure 4.21 for the four local scouring experiments: $Exp.\ 1U$, $Exp.\ 1D$, $Exp.\ 4U$ and $Exp.\ 4D$, respectively. In the same figure, the pier models were introduced, highlighting the $K's$ and $P's$ control points as represented in Figure 4.16.

Different length extensions of the characterization were obtained (Figure 4.21). Longitudinal and transversal overlaps of the photographs for the close-range photogrammetry, or of the scans acquired by the Kinect V2 sensor, dictated the extension for upstream and downstream, as well as for the left and right sides of the pier model. Each of the beds' morphology were built for

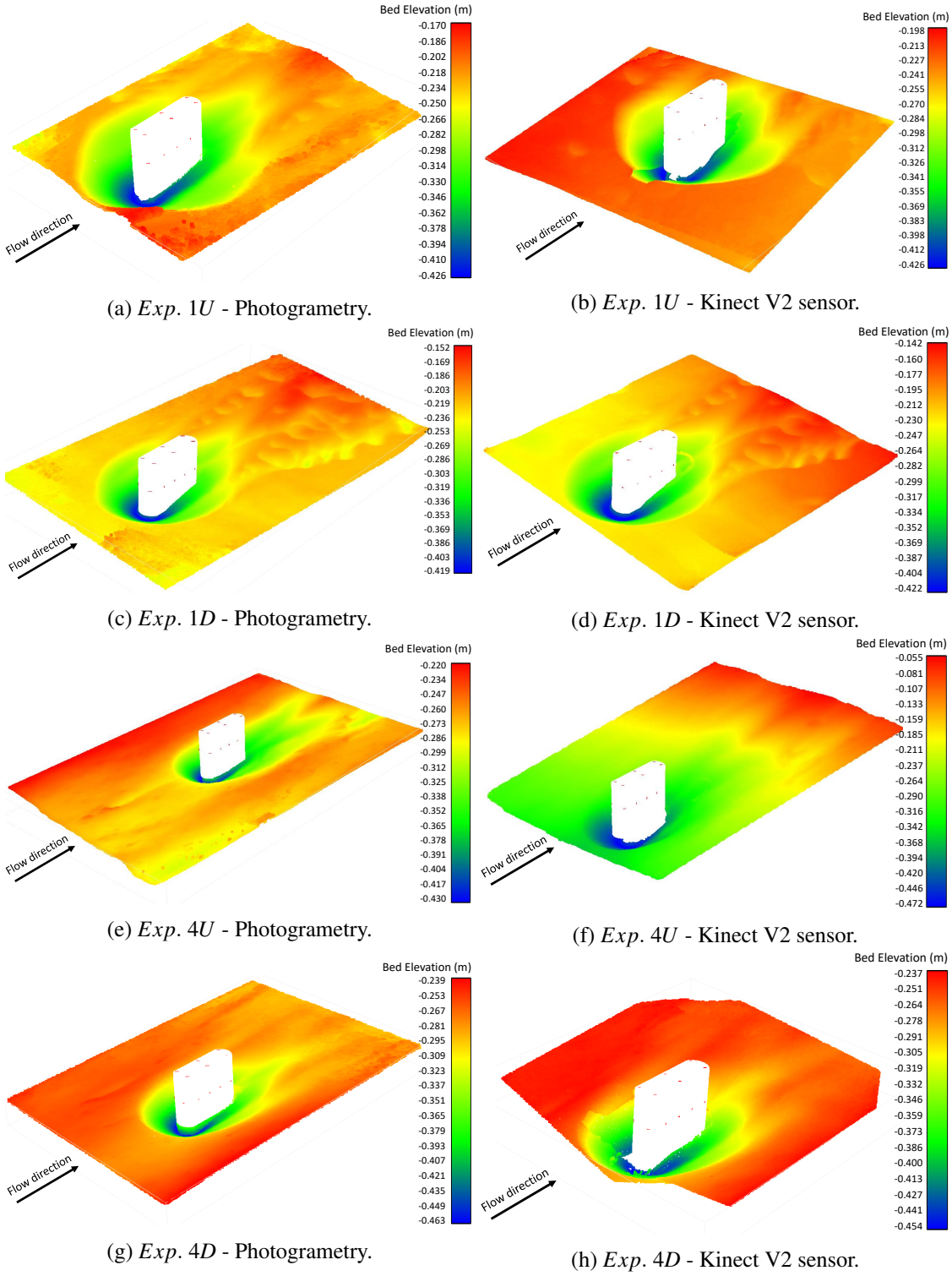

(a) *Exp*. 1*U* - Photogrametry.

(b) *Exp*. 1*U* - Kinect V2 sensor.

(c) *Exp*. 1*D* - Photogrametry.

(d) *Exp*. 1*D* - Kinect V2 sensor.

(e) *Exp*. 4*U* - Photogrametry.

(f) *Exp*. 4*U* - Kinect V2 sensor.

(g) *Exp*. 4*D* - Photogrametry.

(h) *Exp*. 4*D* - Kinect V2 sensor.

Figure 4.21: Three-dimensional eroded bed models from close-range photogrammetry (left panel) and Kinect V2 sensor (right panel).

the flat condition, for each experiment, allowing for the assessment of the initial stage of the bed elevation model. On average, those elevations were 0.215 m for *Exp*. 1*U*, 0.219 m for *Exp*. 1*D*, 0.230 m for *Exp*. 4*U* and 0.225 m for *Exp*. 4*D* below zero. Generally, they are quite similar despite

slight differences due to the quality of captures and techniques' accuracy, that had to be carefully analysed.

The accuracy of the 3D models was assessed based on the reference points of the respective models and their absolute coordinates. Position average errors of 1.52 mm, 2.21 mm, 0.79 mm and 0.63 mm were obtained from the application of close-range photogrammetry for $Exp.\ 1U$, $Exp.\ 1D$, $Exp.\ 4U$ and $Exp.\ 4D$, respectively. Besides the high accuracy obtained for this image-based technique, experiments of *Run* 1 showed a position error higher than the median sand grain diameter in 43.4% and 61.1% for $Exp.\ 1U$ and $Exp.\ 1D$, respectively. $Exp.\ 4U$ and $Exp.\ 4D$, in turn, returned errors lower than D_{50} in 26.7% and 8.1%. The scans acquired from the Kinect V2 sensor were spatially referenced with a resulting Root Mean Square Error (RMSE) kept lower than 0.03 for obtaining a reliable model. In all cases, more than one point cloud (representing the scene under analysis) was used to build the final 3D bed models. The number and displacement of the control points across the area to be reconstructed revealed of great importance to achieve result of highest quality, both in terms of the geometrical precision and spatial-referencing accuracy.

For the application of the close-range photogrammmetry technique only photographs with a minimum quality of 0.70 were considered since such feature also plays a relevant role in the success of the different processing phases in the generation of the 3D bed models. In order to process the point clouds acquired by the Kinect V2 sensor, a careful quality inspection was also previously carried out.

By subtracting the eroded beds' morphologies from the respective flat beds, it allowed to obtain the bed contour surfaces by using each image-based technique as a function of scour depth-to-approach flow depth (d_s/h), represented in Figure 4.22. The contour surfaces obtained for *Run* 1, from Figure 4.22a to Figure 4.22d, present quite similar results, showing the maximum scour depth at the piers' front (therein defined by a darker color).

Despite the perception of distinct scour holes, obtained through the image-based techniques under analysis, for $Exp.\ 4U$, the approaches are, in general, in accordance with each other. However, by inspection of the 3D models (Figure 4.21e and Figure 4.21f) it is possible to infer that the characterization given by the close-range photogrametry technique was more reliable since a maximum scour depth of 0.20 m is closer to the measurement performed with the aid of a limnimeter at the end of the experiment (registering the value of 0.179 m at 5 cm from the pier front). According to Figure 4.22f, the maximum scour depth, given by the Kinect V2 sensor, resulted in 0.242 m, which corresponds to a difference of 26%. Such differences were responsible for the distinctive color shadows of Figure 4.21e and Figure 4.21f.

The processing phases of the Kinect V2 sensor scans, for $Exp.\ 4D$, did not allow a more length characterization of the bed morphology, mainly at the upstream side of *Pier* 14, as it was performed by the application of the close-range photogrammetry technique. In this experiment, the close-range photogrammetry gave a little deeper scour depth immediately upstream of the pier model; a difference of 0.009 m between approaches was attained. Although the difference, the close-range photogrammetry technique remains the more suitable approach as can be confirmed by the eroded bed models in Figure 4.21g and Figure 4.22g. There are some discontinuities, even

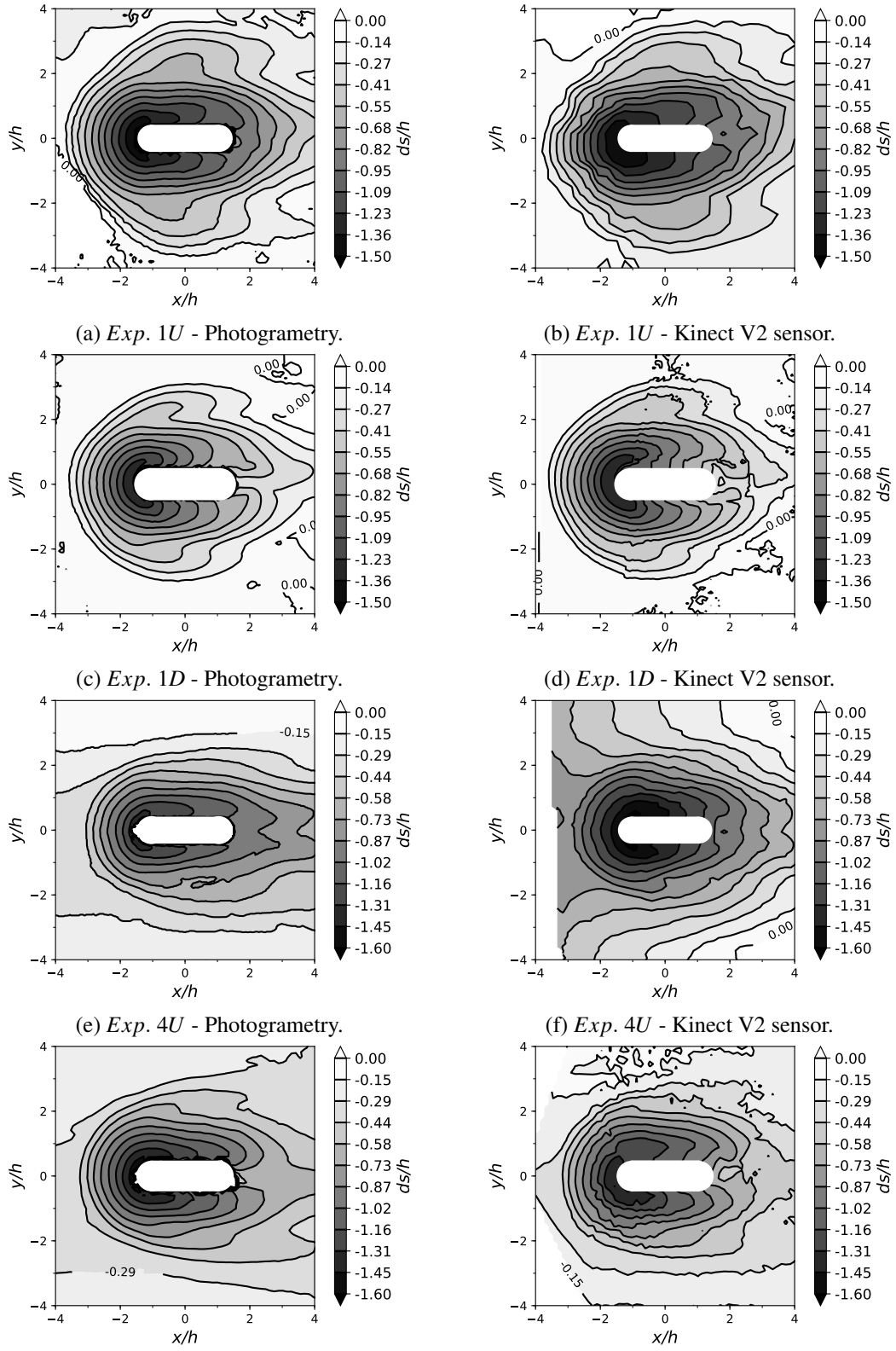

(a) *Exp*. 1*U* - Photogrametry.

(b) *Exp*. 1*U* - Kinect V2 sensor.

(c) *Exp*. 1*D* - Photogrametry.

(d) *Exp*. 1*D* - Kinect V2 sensor.

(e) *Exp*. 4*U* - Photogrametry.

(f) *Exp*. 4*U* - Kinect V2 sensor.

(g) *Exp*. 4*D* - Photogrametry.

(h) *Exp*. 4*D* - Kinect V2 sensor.

Figure 4.22: Contour bed surfaces around the oblong pier model from close-range photogrammetry (left panel) and Kinect V2 sensor (right panel).

though not affecting significantly the resulting 3D model.

The non-feeding feature of the herein live bed scour experiments (*Run* 4) explains in part the bed elevations, at the upstream reach of the sand box, lower than the respective flat bed stages. The general scouring capacity (beyond local scour) of the approach flows in $Exp.\ 4U$ and $Exp.\ 4D$ transported the eroded bed material not only from the vicinity of the pier but also from the upstream reach of the sand box, further downstream. Thus, it is understandable some lack of heaps of sand as observed for the clear water scour experiments (*Run* 1). In both live bed experiments, the sand was transported beyond the working section and the concrete stretch floor, appearing accumulated on the downstream recess box.

To aid the characterization of the scouring experiments, Figure 4.21 and Figure 4.22, an additional assessment was carried out. Bed profiles at the vicinity of the oblong bridge pier models were evaluated in line with the scheme illustrated in Figure 4.23. A direct comparison was herein performed and examined once more against the approach flow depth of each experiment as can be seen in Figure 4.24, Figure 4.25, Figure 4.26 and Figure 4.27, respectively.

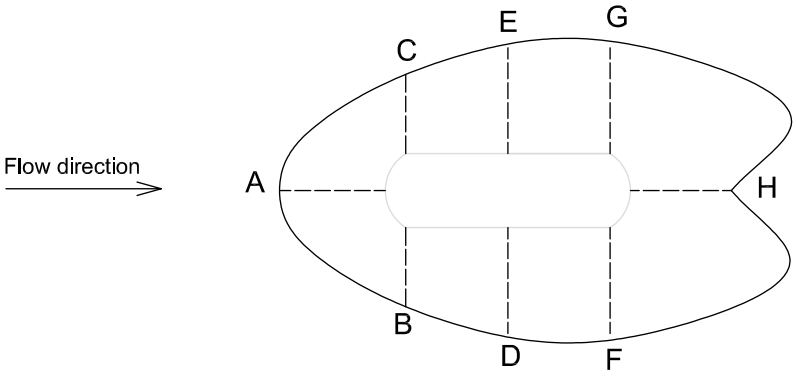

Figure 4.23: Scheme of the scour bed profiles under analysis.

The analysis performed to the 3D bed morphology models and the correspondent contour surface maps is herein corroborated by individual examinations to some representative cross-sections (Figure 4.23). The higher differences between the two image-based characterization techniques occurred for $Exp.\ 4U$ (Figure 4.26); as aforementioned, the Kinect V2 sensor was returning erroneously higher scour depth values. For that experiment, the close-range photogrammetry technique revealed to be undoubtedly the more realistic as confirmed by the 3D model and the scour depth point-wise measurement performed at 0.05 m from the pier front (Figure 4.26). For the remaining local scouring experiments, the two image-based techniques gave quite similar results (Figure 4.24, Figure 4.25 and Figure 4.27).

The slope of the "A" bed profiles returned expectable values, namely 65.51% for $Exp.\ 1U$, 65.35% for $Exp.\ 1D$, 67.60% for $Exp.\ 4U$ and 67.62% for $Exp.\ 4D$. The corresponding angles assume values between 33.17° ($Exp.\ 1D$) and the 34.07° for $Exp.\ 4D$, slightly higher than the typical angle of repose of 30° for wet sand, although within a reasonable value. The backward flow at the base of the piers eroding the foot of the upstream slope of the scour hole, as well as the

continuous sediment supply of sediments into the scour holes have been identified as the reasons for the higher angles than the wet sand angle of repose.

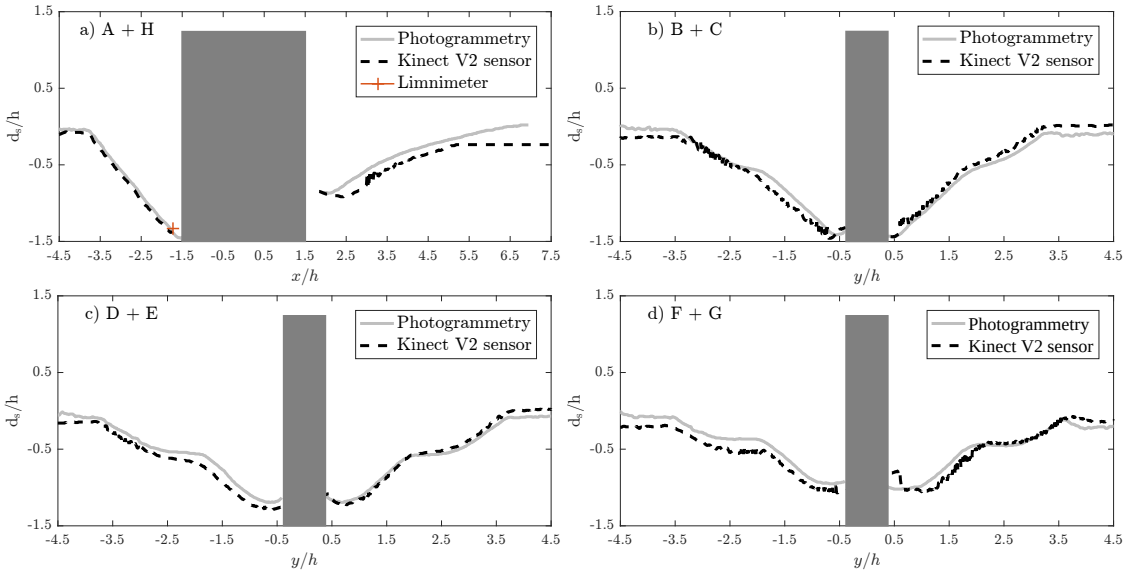

Figure 4.24: Scour bed profiles normalized by the approach flow depth from close-range photogrammetry (continuous line) and Kinect V2 sensor (dashed line) for end of *Exp.* 1*U*.

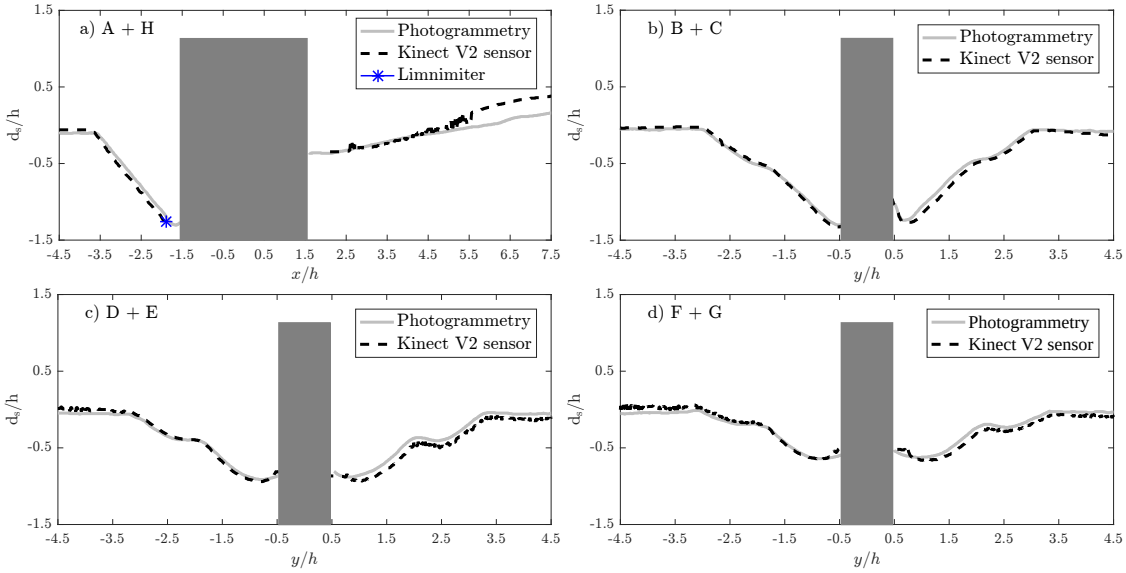

Figure 4.25: Scour bed profiles normalized by the approach flow depth from close-range photogrammetry (continuous line) and Kinect V2 sensor (dashed line) for end of *Exp.* 1*D*.

At the transverse profiles, namely “B + C”, “D + E” and “F + G” (Fig. 4.23), ring shaped portions close to the pier lateral surface are identified (although not so pronounced for the “B + C” profiles due to their proximity to the piers’ front). Over these ring shaped portions, nearly uniform slopes are observed (visible from Fig. 4.24 to Fig. 4.27), which are in accordance with

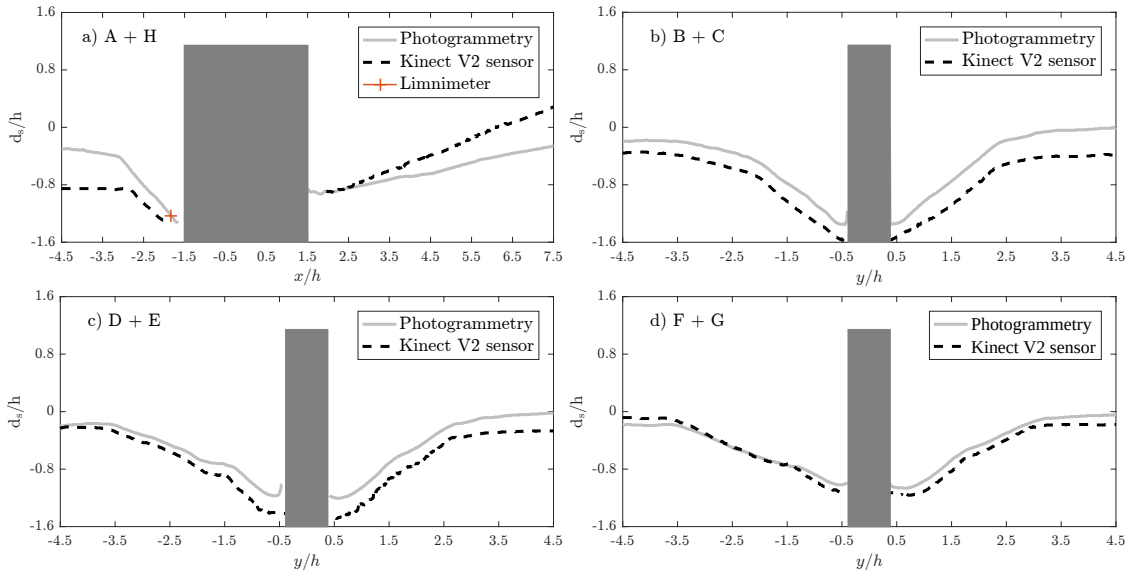

Figure 4.26: Scour bed profiles normalized by the approach flow depth from close-range photogrammetry (continuous line) and Kinect V2 sensor (dashed line) for end of *Exp*. 4*U*.

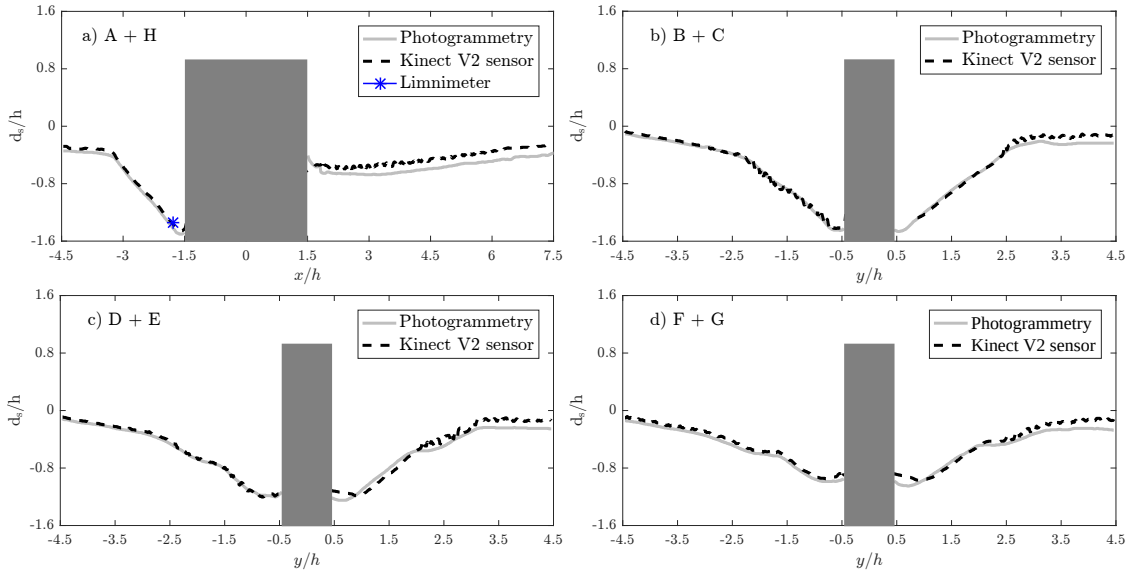

Figure 4.27: Scour bed profiles normalized by the approach flow depth from close-range photogrammetry (continuous line) and Kinect V2 sensor (dashed line) for end of *Exp*. 4*D*.

Diab (2011)'s experimental findings. These trends are noticed for all experiments, regardless of the clear water or live bed approach flow condition. The existence of scour profile breaks are also suggestive of distinct strengths of the vortex system action; higher vortex strength occurred at the lower part of the scour hole, i.e. close to the respective pier's lateral surface, as depicted in figures 4.24, 4.25, 4.26 and 4.27. Similarly, counterclockwise vortex system rotation contributes to the bed lateral stabilization.

4.3.6.4 Bed profiles during experiments

One of the novelties of the present investigation consisted in the assessment of the sand-pier border at the pier's lateral surface along the scouring phenomenon. For that purpose, a continuous monitoring of the sand-pier border evolution during *Exp.* 1*D* was enabled by the acquisition of synchronized images from four submersible cameras. Figure 4.28 shows an underwater photograph (Figure 4.28a) and 2D bed profiles of the local scouring experiment (*Exp.* 1*D*) for instants between 7.52 and 102.33 hours (Figure 4.28b). The detection of the sand-pier border and the computation of the distance of each pixel to a reference line (Figure 4.28a) was performed through a python code, developed for this particular purpose, in order to provide 2D bed profiles for several instants of the scouring experiment.

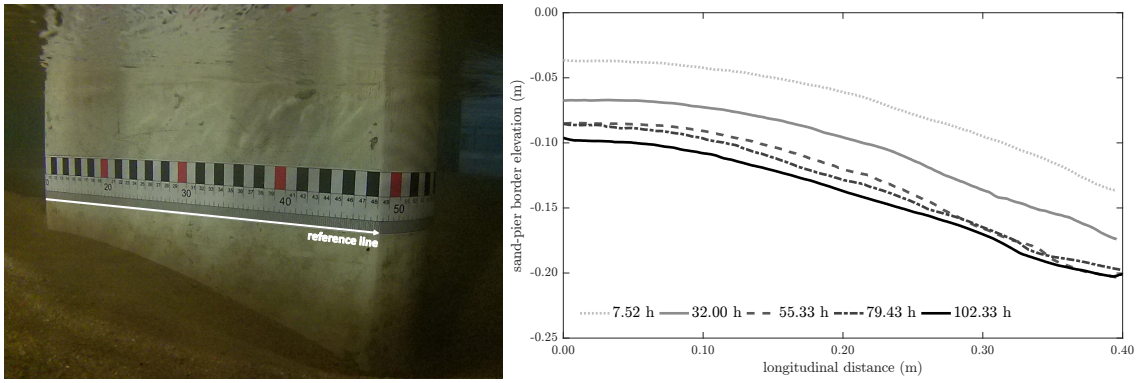

(a) Photograph acquired at 7.52 h of experiment.

(b) Sand-pier border profiles.

Figure 4.28: Underwater photograph (left panel) and 2D bed profiles at different instants of *Exp.* 1*D* (right panel).

A higher difference in the sand-pier border elevation occurred between 7.52 and 32 hours of the *Exp.* 1*D*, as can be seen in Figure 4.28b, which was consistent with the more rapidly development of the scouring process for the first day (Figure 4.20a with duration represented in seconds). At 7.52 hours of the experiment, the border was roughly at 0.037 m and 0.136 m below the reference line at the beginning and at the end of the correspondent bed's profile, respectively. An almost constant difference of 0.034 m in the sand-pier border was registered for the first two bed profiles, i.e. for 7.52 and 32.00 hours of the scouring process.

By comparing the evolution of the second with the third bed profile, computed for the 55.33^{th} hour of experiment, it is visible a decrease on the sand-pier border elevation, although less substantial. Reduction trends of 41.4% and 21.7% for the downstream and the upstream ends of *Pier* 14, were obtained when compared against the difference between the first two bed profiles. After the third day of this experiment, namely for the instant of 79.43 hours, the sand-pier evolution slightly differs from the previous profiles on the center part of the oblong pier. For the last 2D bed profile (102.33 hours of *Exp.* 1*D*), a similar trend was verified, registering not significant differences between the sand-pier border elevations at the right end of the bed profiles (Figure 4.28b). On the contrarily, the downstream end of *Pier* 14 shows a decrease of that elevation in a percentage of 11.2%.

For validation purposes of this methodology, a comparison of the herein computed scour depths at the upstream end of *Pier* 14 was performed against the point-wise measurements plotted in Figure 4.20a. Despite the different positions at which each of them were measured, they are close enough to provide results of the same orders of magnitude. The maximum scour depth obtained at 7.52 hours of $Exp.\ 1D$ was of 0.117 m, while the limnimeter registered the value 0.107 m. The bed profile extracted for 32 hours gave a scour depth of 0.155 m, which was very close to the measured 0.157 m at 0.05 m from the pier front. On the fourth day of experiment, namely for the hour 79.43, a scour depth of 0.180 m was obtained (2% higher than the measured with the limnimeter). The last 2D profile registered a maximum scour depth of 0.179 m, 2% lower than the given by the limnimeter.

Besides the detection of the sand-pier border, the methodology required an accurate definition of a reference line from which the distances between those borders could derive reliable 2D bed profiles during the scouring experiments. For the present case, the lower line of the ruler (Figure 4.28a) was adopted as reference line. In order to account with the uncertainties inherent in the determination of the points' coordinates (in both image and metric units) that led to the computation of the line's equation, the python code also included an evaluation of the associated errors in both directions (x and y). Table 4.8 presents the respective estimate errors with a 95% of confidence interval (given by $\frac{1.96\sigma}{\sqrt{n_s}}$) for each of the 2D bed profiles showed in Figure 4.28b.

Table 4.8: Statistical results in the computation of the reference lines.

Coordinates	x (m)			y (m)		
Time (h)	Mean	Std. Deviation	Estimate error	Mean	Std. Deviation	Estimate error
7.52	$5\text{x}10^{-4}$	$4\text{x}10^{-7}$	$\pm1\text{x}10^{-4}$	$1\text{x}10^{-4}$	$6\text{x}10^{-5}$	$\pm3\text{x}10^{-5}$
32.00	$5\text{x}10^{-4}$	$4\text{x}10^{-7}$	$\pm1.1\text{x}10^{-4}$	$1\text{x}10^{-4}$	$6\text{x}10^{-5}$	$\pm2\text{x}10^{-5}$
55.33	$5\text{x}10^{-4}$	$4\text{x}10^{-7}$	$\pm1.0\text{x}10^{-4}$	$1\text{x}10^{-4}$	$6\text{x}10^{-5}$	$\pm2\text{x}10^{-5}$
79.43	$5\text{x}10^{-4}$	$4\text{x}10^{-7}$	$\pm8.6\text{x}10^{-5}$	$1\text{x}10^{-4}$	$6\text{x}10^{-5}$	$\pm5\text{x}10^{-5}$
102.33	$5\text{x}10^{-4}$	$4\text{x}10^{-7}$	$\pm8.6\text{x}10^{-5}$	$1\text{x}10^{-4}$	$6\text{x}10^{-5}$	$\pm4\text{x}10^{-5}$

Regarding the process visualization, a large field of view was obtained using the four action cameras, not only due to their ultra-wide angle lenses but also owing to their strategic displacement around the oblong pier model. By this way, a redundancy on the camera's selection was gained for the current approach. The oblique placement of the cameras, inside the water, was revealed to constitute a good compromise solution, since it covered all the necessary areas, without interfering with the approach flow, and without having the disturbance of the light refraction. The use of natural light in the experiment avoids the need for lightning devices; however, a downside is that good lighting relies on the weather conditions. For those circumstances, a diffuse artificial light was used, as well as for the image-based techniques addressed in the previous subsection.

The proposed methodology has delivered promising results for studying the scouring process in the vicinity of bridge pier models in an experimental environment. It precludes the interruption of the experiment to gather data in respect to the erosion and deposition patterns of the local scouring

phenomenon. Notwithstanding, improvements can also be added, namely on the sand-pier model border detection in order to automatize such step as far as possible.

4.3.7 Conclusions

Scouring phenomenon in the vicinity of bridge piers invariably faces morphological changes due to the interactions regarding flow-structure, flow-sediment, and sediment-structure. The characterization of these type of interactions is a necessary key towards an increased understanding of the mechanism related with the scouring phenomenon. In this paper, different approaches and techniques were evaluated with the aim of fully characterizing its effect and evolution around two transitional oblong bridge pier models.

The study comprised the monitoring of the hydraulic variables and the temporal evolution of the scour depth at piers' front during four scouring experiments. The scour depth was registered with the aid of limnimeters at the upstream faces of the bridge pier models. The time required to reach 90% of the equilibrium scour depth, by Sheppard/Melville equation, was considered as a basis for the experiments' time duration. Two other formulations were also considered when predicting the maximum scour depth that could be obtained experimentally. Those formulations include the ones derived by Arneson *et al.* (2012) and Moreno (2016). The obtained scour depths were largely under-predicted by the latest version of HEC-18 (29.5%), whilst being in reasonable agreement with the Moreno (2016)'s prediction (9.2%).

A comprehensive measurement system for the three-dimensional characterization of the scouring effects and its respective ensemble was conducted, besides the point-wise measurements of the maximum scour depth at piers' front. Two image-based techniques were considered: close-range photogrammetry and Kinect V2 sensor for characterizing both the flat (initial) and the eroded (final) stages of the bed morphology. These techniques required the previous emptying of the tilting flume and a set of control points, suitably deployed to enable the spatial reference of the 3D bed morphology models. The number and displacement of the control points revealed of great importance to achieve results of the highest quality, both in terms of geometrical precision and spatial-referencing accuracy. The close-range photogrammetry returned position averages errors of the order of the median sand grain diameter (D_{50}); higher in an average of 52.3% for *Run* 1, whereas for *Run* 2 the average error was 17.4% lower than D_{50}. The Kinect V2 sensor scans were spatially referenced with a resulting Root Mean Square Error (RMSE) lower than 0.03.

The produced 3D bed morphology models provided detailed measurements with quite similar results between the image-based techniques. The exception occurred for the $Exp.\ 2U$ experiment, for which the Kinect V2 sensor erroneously over-predicted the scour depth values. For that experiment, the close-range photogrammetry technique revealed to be undoubtedly the more realistic. This was confirmed by both the 3D model and the scour depth point-wise measurement performed at 0.05 m from the pier. Thus, 16 three-dimensional (3D) maps of bed morphology at the vicinity of the oblong bridge pier models constitute a valuable database for calibration and validation of numerical models, such as Computational Fluid Dynamics (CFD) tools. In addition, contour bed surfaces and scour profiles allowed a detailed characterization of the scouring process.

The scour bed slopes (profiles "A") and the ring shaped portions (of the transversal profiles) of the four experiments confirmed the vortex system action's distinct strengths within the respective scour holes.

The ultimate contribution of this study consisted in the development of a methodology capable of performing a continuous monitoring of the sand-pier border at the pier's lateral surface along the scouring process. This methodology was based in underwater image processing and computer vision routines. The maximum scour depths for the various instants analysed were in accordance with the registered values at the pier's front. A decreasing discrepancy was registered, from 8.5% for 7.52 hours to a difference of 2% for both t = 79.43 and t = 102.33 hours. The 2D bed profiles revealed consistent trends with the scouring development observed for $Exp.\ 1D$. The results allowed the temporal characterization of the phenomenon as well as to take advantage of the increasing development of the technology of submersible cameras and processing tools. The proposed methodology has delivered promising results for the continuous and non-stop studying of the scouring process around bridge pier models in a laboratory environment.

Throughout the performed investigation, the hydraulic and scour data and results included: (i) an assessment of the uncertainty of the observations used in the evaluation of relevant variables; (ii) full details of the methods of model evaluation and performance measures undertaken; and (iii) prior assessment of the uncertainty and its propagation associated with the several experimental scouring measurement techniques.

4.3.8 Data availability statement

Some or all data, models, or code that support the findings of this study are available from the corresponding author upon reasonable request.

4.3.9 Acknowledgments

The first author acknowledges the financial support of the Portuguese Foundation for Science and Technology (FCT) through the PhD scholarship PD/BD/127798/2016, in the framework of the Doctoral Program INFRARISK - "Analysis and Mitigation of Risks in Infrastructures". This research was also supported by Centro Interdisciplinar de Investigação Marinha e Ambiental (CIIMAR) through the project with reference UID/Multi/04423/2019. The first author thanks to Luis Mendes for his help in developing the python code. The authors thank the technical assistance provided by the team of the Laboratory of Construction and Modelling and the Center of Scientific Instrumentation of the National Laboratory of Civil Engineering (LNEC).

4.4 Experimental characterization of the flow field around oblong bridge piers. *Paper under preparation*

TITLE: Experimental characterization of the flow field around oblong bridge piers[1]

Paper under preparation and to be submitted for publication in an international scientific journal

Author contributions:
All authors conceived the experimental campaign. Bento, A.M. planned and performed the experiments. Bento, A.M. analysed and post-processed the results, and wrote the manuscript. Viseu, T., Pêgo, J.P. and Couto, L. provided critical feedback and helped shape the research, analysis and manuscript.

[1] Bento, A.M., Viseu T., Pêgo, J.P. & Couto, L. (Under preparation). Experimental characterization of the flow field around oblong bridge piers.

4.4.1 Abstract

The complexity of the flow field inherent to the scour development at bridge foundations is mainly characterized and caused by separation and generation of multiple vortices. This complexity is further magnified due to the dynamic interaction between the flow and the movable bed during the development of a scour hole. Flow structures of upflow, downflow, horseshoe vortices and lee-wake vortices are well established for the hydraulic turbulent flow field around circular piers. The strength of these organized structures depends on several variables, which seem to include the bridge pier's or abutment's geometry. The present study was based on a laboratory experimental campaign planned for flow velocity measurements of the flow around oblong bridge pier models, of different width, carried out in a tilting flume of the National Laboratory of Civil Engineering. These experiments included measurements at both the flat and the eroded bed stages of the scouring development. Results obtained in terms of turbulent structure components such as distributions of mean velocities and Reynolds shear stresses are presented and discussed.

Keywords: bridge pier, flat and eroded bed, flow field, velocity profile measurements

4.4.2 Introduction

The presence of obstacles such as bridge foundations in rivers is often associated with local morphological changes as a result of altering the sediment-flow equilibrium at the immediacy of those hydraulic infrastructures. The modification of local geomorphological bed characteristics, known as local scour, should be accounted for when analysing the safety of bridges due to the severe threat that the developed scour hole can pose to its integrity. The local scour around bridge piers is one of the major threats to bridge structures founded in riverbeds and is a result of the complex flow patterns created by the flow around those foundations (Melville & Coleman, 2000; Arneson *et al.*, 2012). It is therefore important to be acquainted with the flow structure and the related scour mechanisms around the bridge pier.

The main flow processes that take place around a circular pier exposed to a steady current on a plane bed has been the subject of several flow field studies (Dargahi, 1989; Yulistiyanto *et al.*, 1998; Roulund *et al.*, 2005, among others). They comprise the horseshoe vortices formed immediately upstream the pier, the lee-wake vortices (usually in the form of vortex shedding), contracted streamlines at the side edges of the pier, and the downflow process due to the deceleration of the flow at the pier front. Few studies have been devoted to non-circular bridge piers (Lima *et al.*, 2018), although a large number of bridge foundations do not have a circular shape (Arneson *et al.*, 2012; Ettema *et al.*, 2011). The relatively limited number of flow field studies induced by the presence of an oblong bridge pier model, when compared with circular piers, motivated this investigation.

The presence of a scour hole at the vicinity of a pier radically alters the turbulent flow field and the hydrodynamic characteristics (Dey & Raikar, 2007a; Kumar *et al.*, 2012). For instance, the bed shear stress and turbulence quantities are strengthened, which induces further sediment transport and scour development at the pier vicinity. The increased horseshoe vortex and the turbulent

energy (Link *et al.*, 2012; Kirkil & Constantinescu, 2015) indicate that different mechanisms trigger the flow field structure when a scour hole is present, which needs further research to deepen the understanding of the pier scouring process. Their results also indicate that the in depth understanding of the flow and turbulence influenced by the scour hole is essential to improve the prediction of scour depth (Li *et al.*, 2020, and references therein).

Therefore, the current study aims to identify and analyse the physics of the flow disturbed by the presence of a developed scour hole around oblong bridge piers. For that purpose, flow and turbulence characteristics are analysed, on the basis of an experimental campaign, with respect to the change in pier effective width, approach hydraulic conditions and bed morphology stages, at the initial flat and the final eroded bed stages. Six fixed bed experiments were conceived and carried out in a recirculating tilting flume located in the experimental facilities of the National Laboratory of Civil Engineering (LNEC), in Lisbon, Portugal. Based on flow velocity measurements, the flow fields at the flume mid-plane surface are analysed, as well as the typical flow and turbulence characteristics in terms of the time-average velocities and Reynolds shear stress. Furthermore, space-averaged quantities were also obtained to clarify the influence of scour development on the flow and turbulence characteristics.

Following this introduction, the flow field experiments are characterized in Subsection 4.4.3. The description of the experimental facility and bridge pier models, the devices, measured variables and instrumentation are also given in Subsection 4.4.3. A particular description of the approach used for the characterization of the turbulent flow field is also included in Subsection 4.4.3. The results and their discussion are presented in Subsection 4.4.4. Finally, the main conclusions are provided in Subsection 4.4.5.

4.4.3 Flow field experiments

In the present subsection, the experimental facility and the bridge pier models are presented, as well as the instrumentation and the measuring techniques considered for the flow field characterization. The flow field experiments are identified, together with the specific tasks for the success of the flow velocity measurements.

4.4.3.1 Experimental facility and bridge pier models

The experiments were undertaken in the tilting flume of the National Laboratory of Civil Engineering (LNEC), in Lisbon, Portugal (Figure 4.29). The tilting flume, herein termed CIV, is 40.7 m long, 2.0 m wide and 1.0 m deep, with glass sides and a concrete base. Two working sections were created within the base of the tilting flume, each being approximately 5.0 m long and 0.4 m deep. These sections were filled with uniform quartz sand characterized by a density, ρ_s, of 2650 kgm^{-3}, a median diameter, D_{50}, of 0.86 mm and a standard deviation of sediment particle sizes, σ_D, of 1.28. The working sections, herein also referred as "sand recess boxes", are preceded by 2.0 m long accelerating ramps and 7.0 m long fixed bed reaches, and are followed by 3.0 m long fixed bed reaches. The accelerating ramps, placed at flume inlet and at the stilling recess boxes, conduce to uniform flow distributions in the two working sections. The stilling recess area between

the two working sections was conceived to restore the flow regime for the downstream working section, and to store the sand bed material transported by the flowing water from the upstream working section during local scouring experiments . In the upstream boundary of the working sections, fine gravel mattresses, properly levelled by the respective concrete base, allow for smooth and progressive transitions, as well as ensure a turbulent flow development.

(a) Upstream working section (b) Flume (c) Instrumentation

Figure 4.29: Experimental facility and bridge pier models.

Two oblong bridge pier models, *Pier* 11 and *Pier* 14, were placed in the upstream and downstream working sections, respectively. The piers differ in width (W), length (L), and semi-cylindrical surface ratio (R). The dimensions of *Pier* 11 are $W = 0.11$ m, $L = 0.433$ m and $R = 0.065$ m. *Pier* 14 is slightly larger, with $W = 0.14$ m, $L = 0.463$ m, and $R = 0.08$ m (Figure 4.30). The bridge pier models were placed vertically on the flume mid-plane at ≈ 2 m from the working sections' upstream borders. The contraction and wall effects were negligible to the scouring process, since the associated flume "width-to-pier width" ratio (W/B, B being the flume width) was 5.5% and 7%, both lower than the limit value of 10% indicated by Chiew & Melville (1987).

The present study comprises the hydrodynamic characterization of six experiments divided into fixed "flat bed" and "eroded bed" stages of three local scouring experiments, namely *Exp.* 1U, *Exp.* 1D and *Exp.* 4U. The letters U and D denote the pier model, being U for *Pier* 11 and D for *Pier* 14. These local scouring experiments are characterized in detail in Subsection 4.3. For simplicity, a suffix was added to the local scouring experiments' name. The suffix *Fbed* stands for the fixed flat bed, whilst *Ebed* denotes the fixed eroded bed experiments. Therefore, the six flow field experiments were labelled as follows: *Exp.* 1U *Fbed* and *Exp.* 1U *Ebed* for *Exp.* 1U; *Exp.* 1D *Fbed* and *Exp.* 1D *Ebed* for *Exp.* 1D; and, *Exp.* 4U *Fbed* and *Exp.* 4U *Ebed* for *Exp.* 4U.

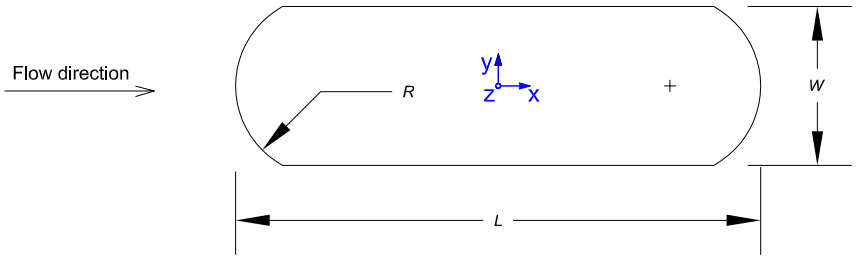

Figure 4.30: Geometry of the oblong bridge pier models.

4.4.3.2 Devices, measured variables and instrumentation

Several flow variables were measured during the experiments, namely: (i) the flow discharge at the flume entrance; (ii) the flow depth within CIV and at the immediacy of the working sections; and (iii) the instantaneous three velocity components of the flow at the piers' vicinity. The following paragraphs describe the measuring process of each variable.

A variable frequency drive was used to control the rotational speed of the pump motor in order to obtain the desired flow discharge. The flow discharge was then measured by an electromagnetic flowmeter and recirculated in the flume. At the flume entrance, stilling grids and a flow straightener were provided for damping the flow containing large scale eddies, leading to vortex free uniform flow in CIV. An adjustable sluice gate at the downstream end of the flume enabled obtaining the desirable flow depth within CIV.

The approach flow depth was monitored using the acquired signals from acoustic probes, suitably positioned within the flume so as not to interfere with the development of the experiments. The signal of the three acoustic probes was acquired at a sampling frequency of 10 Hz, whereas the signal of the electromagnetic flowmeter was acquired at 25 Hz. Movable carriages were present on the rails of the flume to allow the access to the flume for controlling and measuring purposes of both the approach flow depth and the acquisition of the flow velocity components by the connection of the downlooking vectrino to its respective acquisition firmware (*Vectrino Plus*).

The instantaneous three-dimensional velocity measurements were acquired using a downlooking vectrino (hereinafter designated as vectrino), from Nortek®, in two different moments: (i) at the beginning of the scouring process and (ii) within the respective developed scour holes. The velocity flow field was measured throughout the test section around the pier models at relative elevations for the comparison of turbulence and flow characteristics due to the scouring process (before scour *vs* after scour). An independent moving carriage system was developed to clamp the downlooking vectrino in order to move it along the different velocity measurement grid points to ease the measurement task, up to an accuracy of ± 1 mm in the three directions (x, y and z). The origin was considered at the pier center, where x, y and z denote the longitudinal, transversal and vertical axes, respectively (as can be seen in Figure 4.30).

4.4.3.3 Flow field characterization

Previously to the flow field characterization, water from the local scouring experiments was drained out and once dried, a synthetic glue was sprayed uniformly over the eroded bed. The use of a fixed bed obviously prevents processes of sediment burial and reappearance from being observed. However, a fixed bed is frequently used in flow field studies under the assumption that the results are simpler and explanatory than those from complex scenarios with a variety of acting processes (Lee & Hong, 2019, and references therein). For that purpose, a synthetic glue was sprayed uniformly over the several bed morphology (flat and eroded bed stages) in order to consolidate the surface layers of the bed material (Step 1 - Figure 4.31(a)).

(a) Step 1 (b) Step 2 (c) Step 3

Figure 4.31: Setup for the flow velocity measurements.

Once the sand beds were properly fixed, the same hydraulic conditions of the corresponding local scouring experiments (given in Table 4.5 of Section 4.3) were imposed and the flume was filled until the desired flow discharge and water depths. Since the downlooking vectrino uses the Doppler effect to measure current velocity by transmitting short pairs of acoustic waves, they must bounce off of particulate matter in the flow. In a laboratory environment, the water is usually quite clean and thus an artificial introduction of particles, commonly known as seeding particles, must be added to the flow for vectrino flow velocity acquisition purposes. The *Vectrino Plus* interface provides a readout of the parameter signal-to-noise ratio (SNR), which is an indicative aspect of the quality of the seeded flow; the higher the SNR, the better the seeding and consequently the more reliable the velocity measurements (Step 2 - Figure 4.31(b)).

Five acoustic probe tips (one transmitter and four receivers, illustrated in Figure 4.32) send and receive acoustic information in a fluid volume below the downlooking vectrino, referred to as the sampling volume. Since the instrument is inserted into the flow, the sampling volume must be far

enough away from the probe tip so as not to disturb the flow and the velocity measurements. Using acoustic waves, the vectrino directly measures in real time how far away the probe tip and sampling volume are from the bottom boundary, so adjustments were enabled whenever necessary (Step 3 - Figure 4.31(c)).

Figure 4.32: Downlooking vectrino: photo (left panel) and scheme (right panel, adapted from Quaresma (2017)).

There is always inherent uncertainty with the velocity measurements. The primary source of bias comes from computed temperature. If this is not accurately measured, or if the conditions change while the experiment was being run, the velocity measurements would be biased. Another source of uncertainty is the Doppler noise, which Nortek (2018) states as being an artefact of acoustic scattering and could be assumed to be purely random. For instance, at a sampling frequency of 200 Hz and a SNR above 15 dB, uncertainty due to Doppler noise can be estimated in 1% of the maximum velocity range. To evaluate quality of velocity measurements, one of the real time outputs that vectrino provides is a correlation statistic. This is a value ranging from 0% - 100%; the closer the correlation is to 100%, the less noisy and more reliable a velocity measurement is. A minimum correlation of 70% is strongly recommended by several researchers (Beheshti & Ataie-Ashtiani, 2010, among others).

4.4.4 Results and discussions

4.4.4.1 Hydraulic conditions of experiments

Table 4.9 presents the main hydraulic variables of the fixed bed experiments, namely the approach flow discharge (Q), flow depth (h), flow velocity (V), Froude number (Fr), flow and pier Reynolds number (Re and Re_D, respectively). The water elevation within the flume CIV, as well as the

approach flow velocities are given in the form of box-plot graphs for *Exp. 1U Fbed*, *Exp. 1U Ebed*, *Exp. 1D Fbed* and *Exp. 1D Ebed* (Figures 4.33, 4.34, 4.35 and 4.36, respectively).

Table 4.9: Hydraulic variables of the fixed bed experiments, including uncertainties.

Experiment	Q (m^3s^{-1})	h (m)	V (ms^{-1})	Fr $(-)$	Re $(-)$	Re_D $(-)$
Exp. 1U Fbed	0.0927	$0.1610\pm3x10^{-6}$	$0.2882\pm6x10^{-6}$	$0.1825\pm8x10^{-6}$	46200 ± 0.06	31600 ± 0.7
Exp. 1U Ebed	0.0925	$0.1628\pm3x10^{-6}$	$0.2849\pm4x10^{-6}$	$0.1784\pm4x10^{-6}$	46200 ± 0.02	31200 ± 0.4
Exp. 1D Fbed	0.0927	$0.1588\pm5x10^{-6}$	$0.2921\pm9x10^{-6}$	$0.1875\pm1x10^{-6}$	46200 ± 0.1	32000 ± 1.0
Exp. 1D Ebed	0.0925	$0.1579\pm3x10^{-6}$	$0.2937\pm5x10^{-6}$	$0.1896\pm6x10^{-6}$	46200 ± 0.05	32200 ± 0.5
Exp. 4U Fbed	$0.1244\pm5x10^{-7}$	$0.1952\pm1x10^{-5}$	$0.3187\pm2x10^{-5}$	$0.1665\pm2x10^{-5}$	61900 ± 0.2	34900 ± 2.0
Exp. 4U Ebed	$0.1237\pm4x10^{-7}$	$0.1486\pm5x10^{-7}$	$0.4164\pm2x10^{-6}$	$0.2856\pm2x10^{-6}$	61600 ± 0.18	45600 ± 0.2

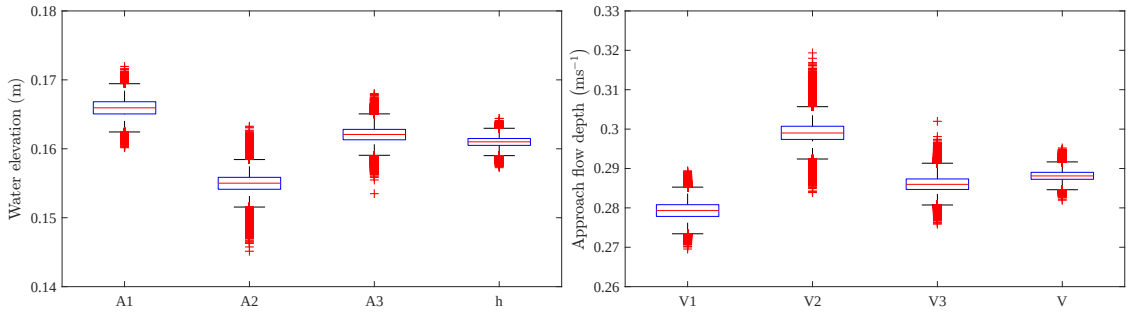

(a) Water level within the flume. (b) Approach flow velocity.

Figure 4.33: Hydraulic conditions of *Exp. 1U Fbed*.

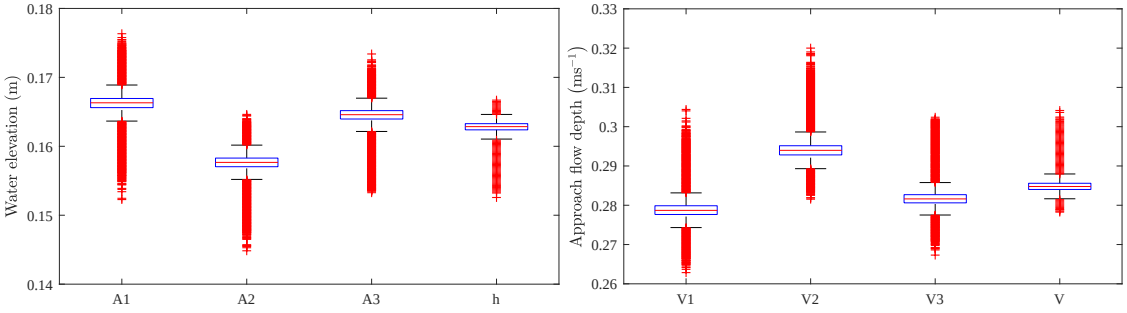

(a) Water level within the flume. (b) Approach flow velocity.

Figure 4.34: Hydraulic conditions of *Exp. 1U Ebed*.

For the experimental tests, represented in Figures 4.33 to 4.36, the water depth was monitored by using three acoustic probes, herein denoted as $A1$, $A2$ and $A3$, placed at the immediacy of each working section. For *Exp. 4U Fbed* and *Exp. 4U Ebed* experiments, the continuous monitoring of the approach flow discharge was enabled, together with the approach water depth, which explains the additional two sub-plots of Figures 4.37 and 4.38, respectively. For these experiments, the water depth was monitored by means of two resistive probes positioned at upstream and downstream ends of the respective working sections. The acquired data of the approach flow discharges was filtered by the application of different methods, namely the Butterworth filter, the Smoothing spline and

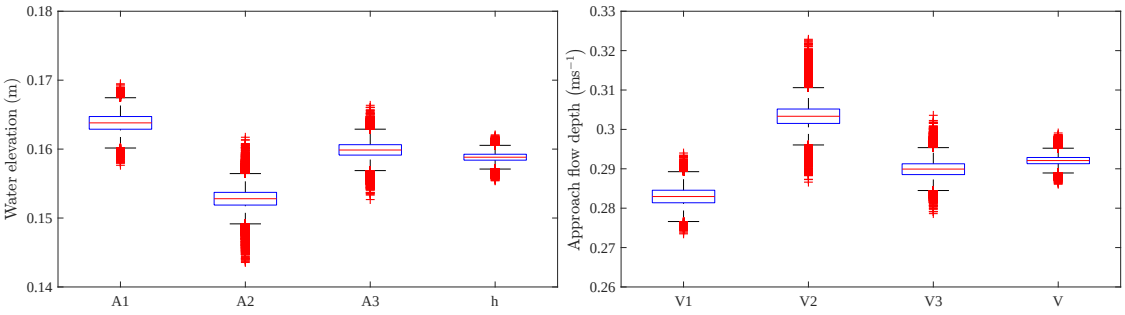

(a) Water level within the flume. (b) Approach flow velocity.

Figure 4.35: Hydraulic conditions of $Exp.\ 1D\ Fbed$.

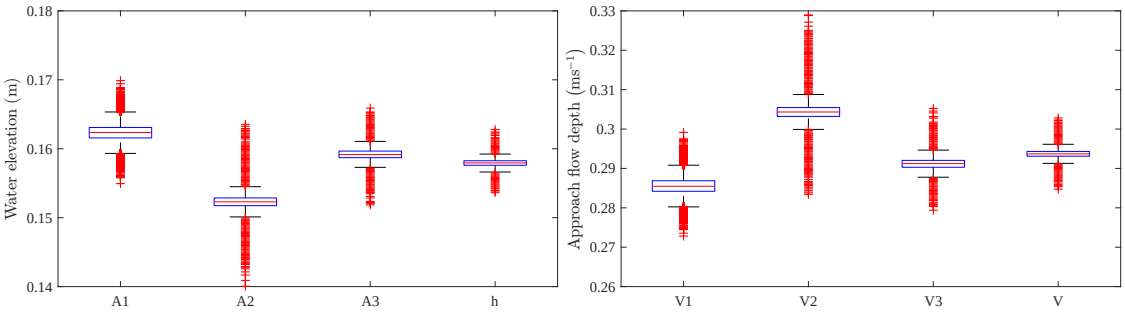

(a) Water level within the flume. (b) Approach flow velocity.

Figure 4.36: Hydraulic conditions of $Exp.\ 1D\ Ebed$.

Moving average. In both $Exp.\ 4U\ Fbed$ and $Exp.\ 4U\ Ebed$, in terms of the approach flow depth and flow velocity, the extreme outliers were removed from the analysis, whereas the mild ones were kept for the average estimate of such variables. Further results are given in Appendix C.5.

Fully developed incoming flows were obtained for all experiments, as indicated by the magnitudes of the flow and pier Reynolds numbers (Re and Re_D in Table 4.9). The experiments were performed under subcritical flow conditions ($Fr < 1$ as indicated in Table 4.9).

4.4.4.2 Velocity measurements

In the present research, instantaneous velocity maps were acquired for the fixed bed experiments, before the beginning of the scouring process, at a flat bed, and at the final stage of experiments, at an eroded bed. Figure 4.39 provides a schematic diagram of the velocity point measurements. It comprises five profiles, namely $Profile\ A$, $Profile\ J$, $Profile\ E$, $Profile\ G$ and $Profile\ I$. Each profile is composed by 4 or 5 sections, as indicated in Figure 4.39, where the flow velocity was measured for several points along the water depth. The position of the measuring spots varied for each application; it was dependent on flow depth and pier dimensions. In line with what was performed in the work of Kirkil *et al.* (2008), Chang *et al.* (2013) and Beheshti & Ataie-Ashtiani (2016), among others, the measurements in each experiment were taken in the Cartesian coordinate system (x, y, z) also indicated in Figure 4.39.

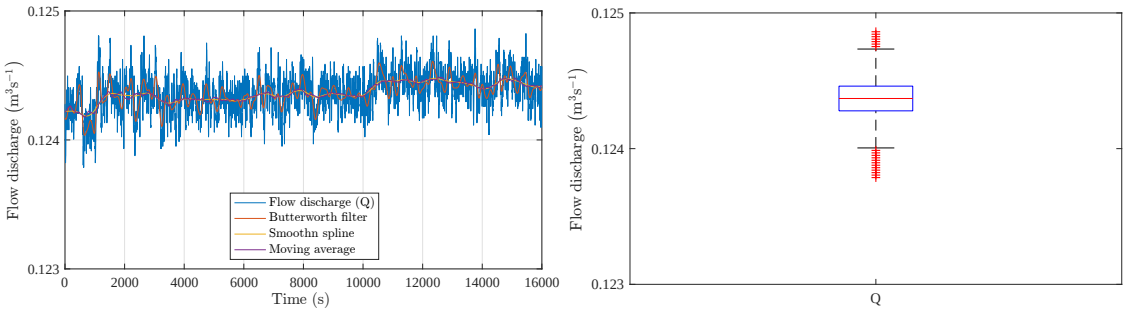

(a) Approach flow discharge (Q) time evolution. (b) Box-plot graph of Q along experiment's duration.

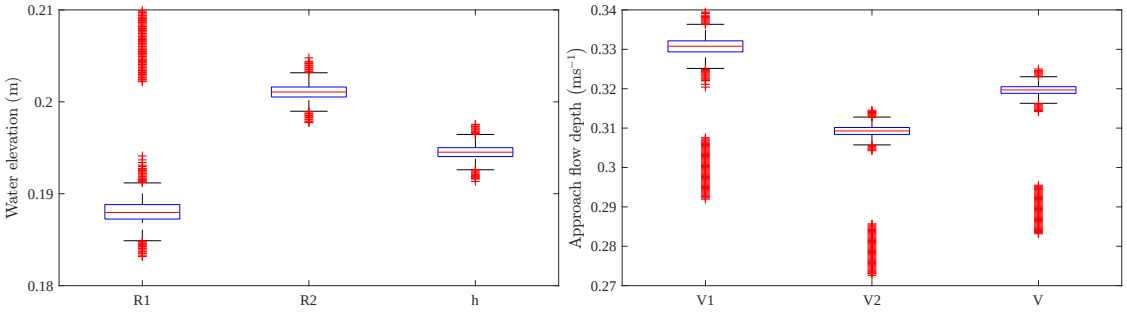

(c) Water level within flume. (d) Approach flow velocity.

Figure 4.37: Hydraulic conditions of $Exp.\ 4U\ Fbed$.

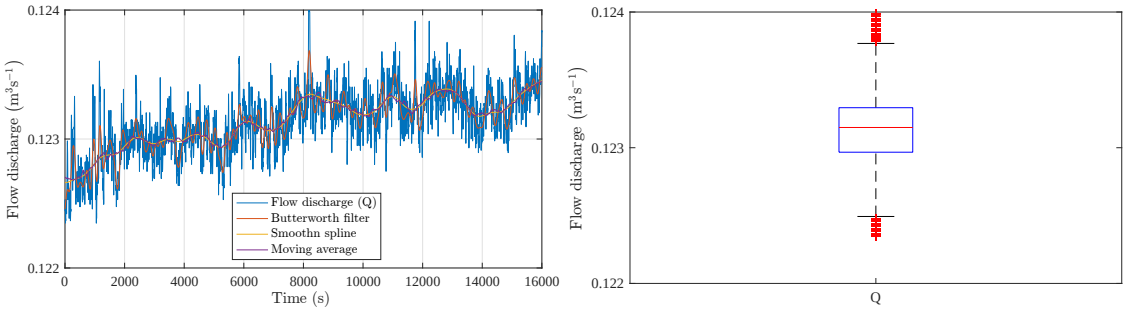

(a) Approach flow discharge (Q) time evolution. (b) Box-plot graph of Q along experiment's duration.

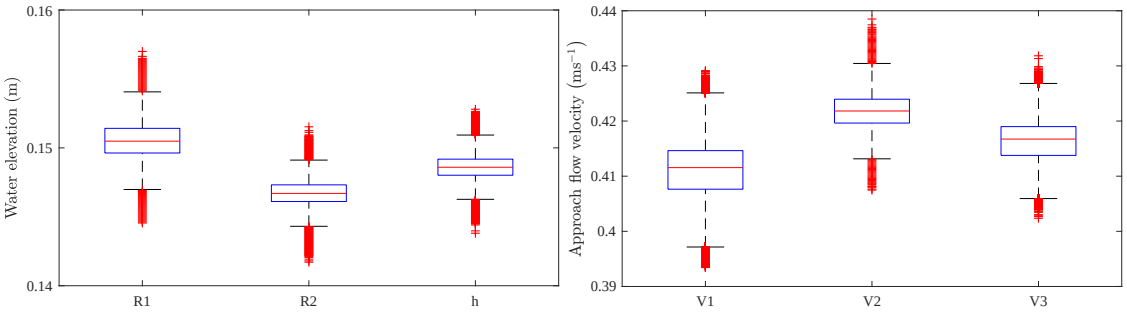

(c) Water level within flume. (d) Approach flow velocity.

Figure 4.38: Hydraulic conditions of $Exp.\ 4U\ Ebed$.

A minimum correlation of 70% and a minimum signal-to-noise ratio (SNR) of 15 dB were thus considered for ensuring the reliability of the instantaneous velocity data (García *et al.*, 2005; Montero *et al.*, 2014). During the velocity measurements, the downlooking vectrino sampling

frequency was chosen to be 200 Hz with a duration within the range of 120 to 300 seconds, depending on the magnitude of turbulence at each measuring location. These instantaneous three-dimensional velocity measurements allowed the obtaining of: (i) mean velocities (u, v and w); (ii) turbulent fluctuation velocities (u', v' and w'); and (iii) Reynolds shear stresses (*RSSes*) including $\overline{u'v'}, \overline{u'w'}$ and $\overline{v'w'}$. The derivation of such parameters provides insights of the flow magnitude and structure for the particularities of each experiment and bed morphology stage (flat *vs* eroded).

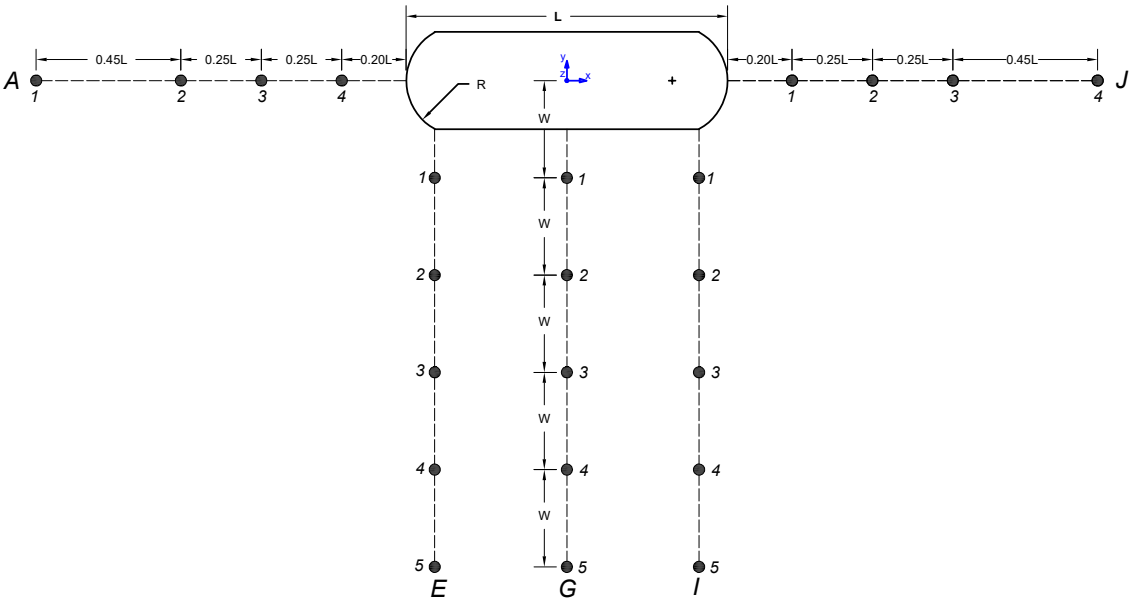

Figure 4.39: Schematic diagram of the velocity point measurements.

Prior to data analysis, all records were visually inspected to identify potential erroneous data such as spikes, trends or abrupt discontinuities in the velocity time series. The velocity data was then processed using the ExploreV software, which streamlined the analysis of the turbulent and the time-averaged 3D velocity data, as well as the statistical and the spectral analysis of the downlooking vectrino data by computing the respective skewness and kurtosis measures for each measuring point. Results including mean values, variance, skewness and kurtosis of each of the aforementioned variables, for all experiments, are available upon request, as well as exemplified in Appendix C.5 for *Profile I* of *Exp. 4U Ebed*. For sake of simplicity, a limited number of the most relevant plots, drawn up in the form of vertical profiles, are analysed in the following subsections, namely for the different sections of *Profile A* and *Profile J*. A total of 680 velocity point measurements were acquired for these two profiles.

A characterization of the approach flow was also performed. For fully turbulent flow, over hydraulically rough sand bed surface, the dimensionless stream-wise mean velocity (u/u^*, u^* being the shear velocity), was found to follow the log-law as expected (Schlichting & Gersten, 2017, and references therein). The k_s value adopted was 0.00215 m ($k_s = 2.5D_{50}$). The adjustment of the log-law to *Exp. 1U Ebed* velocity profile upstream the oblong bridge pier, for instance, allowed obtaining the shear velocity, u^*, of 0.0174 (1.7% higher than the obtained by) and constant B_s = 9.74, as shown in Figure 4.40. These values, along with the bed Reynolds number, $\frac{u^* k_s}{\nu} \approx 37$, are in

agreement with the literature for the hydraulically transitional boundary layer (Cardoso & Cunha, 1998).

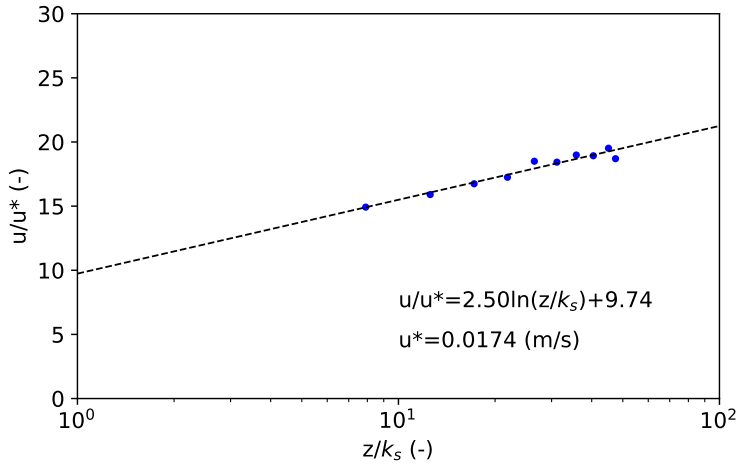

Figure 4.40: Longitudinal velocity profile measured in the flume mid-plane and at the distance 0.50 m upstream the oblong pier's front. Experimental data (○) and theoretical approximation line (dashed line).

4.4.4.3 Mean velocities

Figures 4.41 to 4.46 depict the profiles of the velocity components at the eight mid-plane profiles - *Profile A* and *Profile J* (Figure 4.39), for all experiments. The velocity points were scaled by a reference velocity equal to 0.30 m/s and 0.40 m/s (for the *Exp. 4U Ebed*), as indicated in each plot. A scale factor was used for their graphical representation.

The time average v values at the symmetry plane ($y = 0$) are nearly zero for both bed morphology stages (flat and eroded), as expected (see figures 4.41b, 4.42b). For this reason, the other v vertical distributions are not depicted for the remaining experiments (from *Exp. 1D Fbed* to *Exp. 4U Ebed*).

In the upstream area, the stream-wise component of the velocity (u) decreases when approaching the oblong bridge pier model, due to the effect of velocity reduction close to the pier's blocking effect. For the flat bed stages, this trend is common in experiments *Exp. 1U Fbed*, *Exp. 1D Fbed* and *Exp. 4U Fbed*. In *Exp. 1U Fbed*, the maximum stream-wise component of velocity, u, occurred for a $z = 0.097$ m in all the vertical profiles at the upstream side of the oblong pier (*Pier 11*); the magnitude reached a maximum value of 0.377 ms^{-1} for section 1 (Figure 4.31), whereas a magnitude of 0.313 ms^{-1} was attained for section 4. For *Exp. 4U Fbed*, such values registered a maximum of 0.509 ms^{-1} and 0.422 ms^{-1} for sections 1 and 4 of *Profile A*, respectively.

The stream-wise velocity profiles are marked by negative velocity within the developed scour holes, which indicates the occurrence of flow separation and recirculation, as can be seen in figures 4.42a, 4.43a and 4.45a. In these same figures, we can see that the downstream vertical profiles (*Profile J*) are characterized by increasing magnitudes as they move away from the oblong bridge pier.

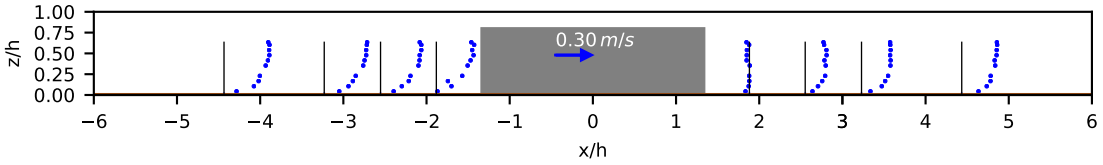

(a) Stream-wise component of velocity (u).

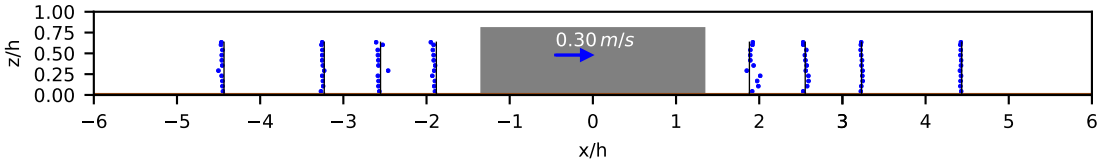

(b) Cross-wise component of velocity (v).

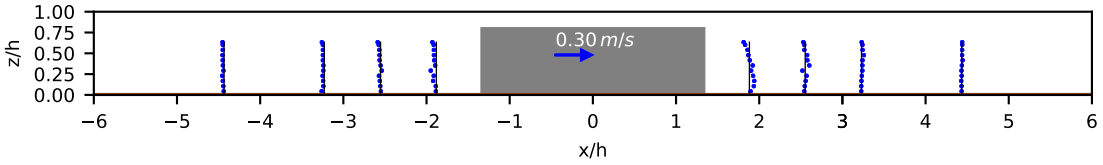

(c) Vertical component of velocity (w).

Figure 4.41: Vertical profiles of the velocity components along the mid-plane of the pier for $Exp.\ 1UFbed$.

The vertical profiles show that u increases with distance from the bed to an elevation near the pier front and then it decreases when approaching the region of decelerating flow in the pier front. The velocity measurements were also allowed within the scour hole (i.e. below the initial flat bed level). The vertical profiles of w illustrate the downward movement of flow (downflow) in front of the pier, which is more visible with the eroded bed stage (developed scour hole).

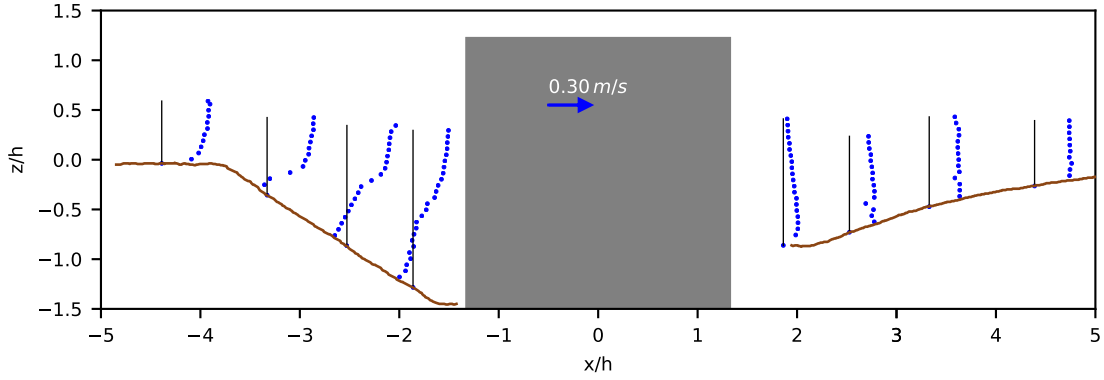

(a) Stream-wise component of velocity (u).

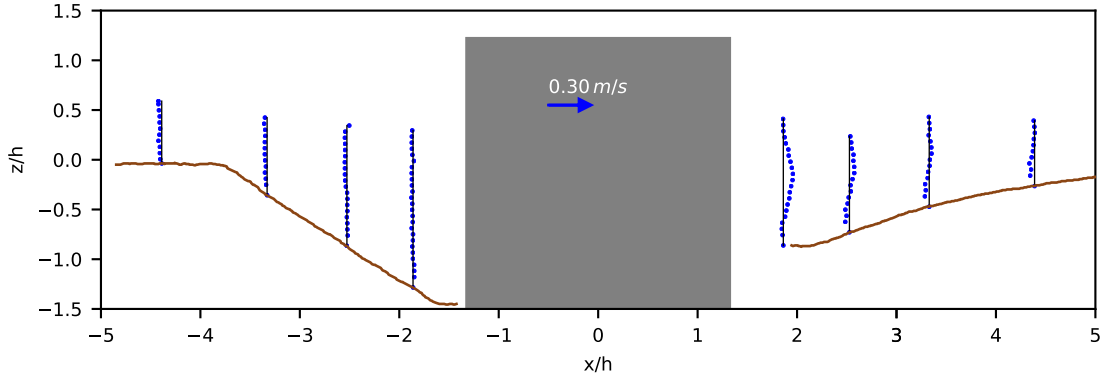

(b) Cross-wise component of velocity (v).

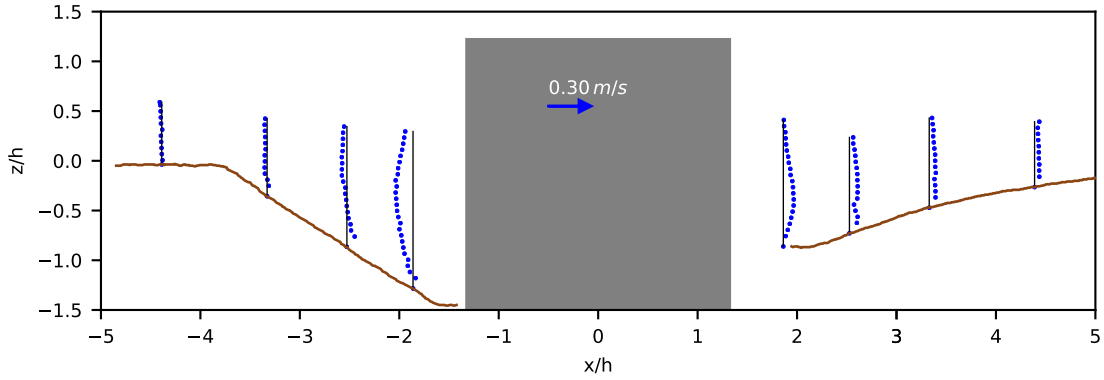

(c) Vertical component of velocity (w).

Figure 4.42: Vertical profiles of the velocity components along the mid-plane of the pier for *Exp. 1U Ebed*.

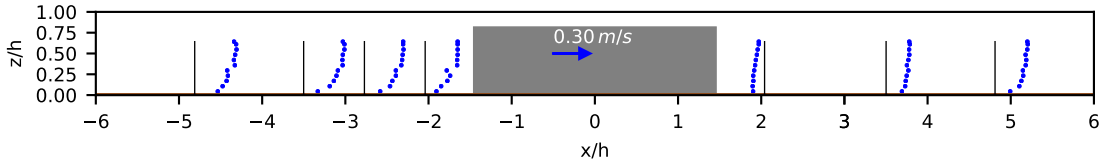

(a) Stream-wise component of velocity (u).

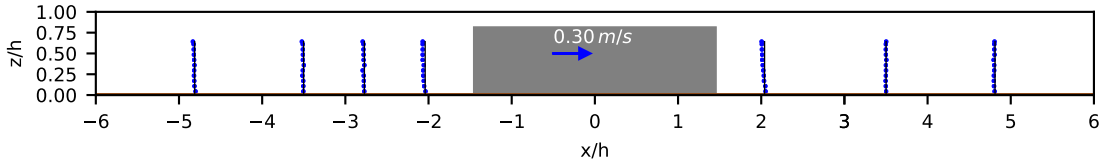

(b) Vertical component of velocity (w).

Figure 4.43: Vertical profiles of the velocity components along the mid-plane of the pier for *Exp. 1D Fbed*.

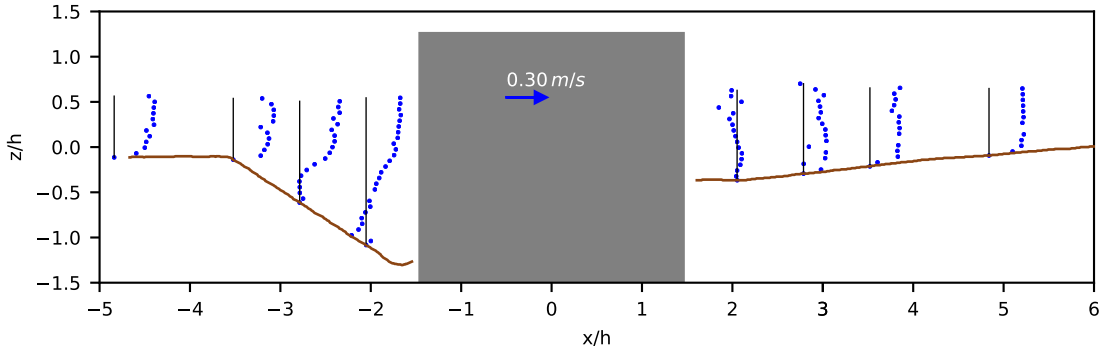

(a) Stream-wise component of velocity (u).

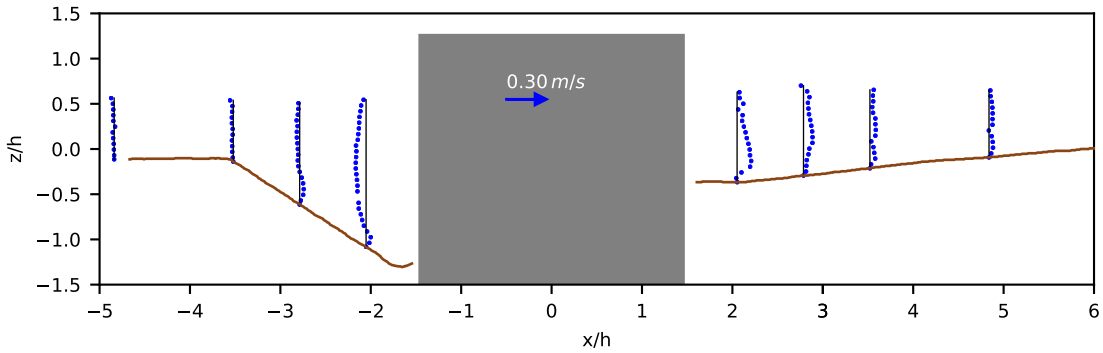

(b) Vertical component of velocity (w).

Figure 4.44: Vertical profiles of the velocity components along the mid-plane of the pier for *Exp. 1D Ebed*.

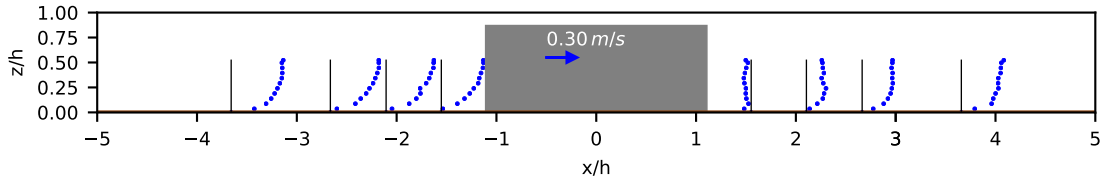

(a) Stream-wise component of velocity (u).

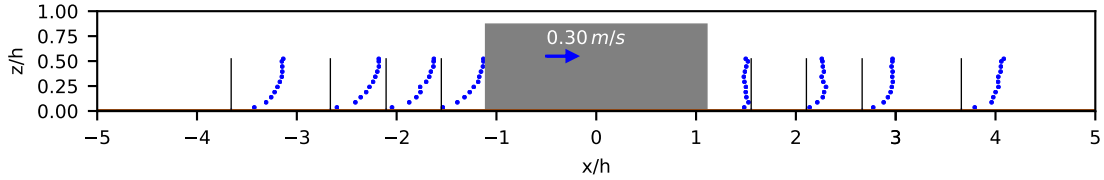

(b) Vertical component of velocity (w).

Figure 4.45: Vertical profiles of the velocity components along the mid-plane of the pier for *Exp. 4U Fbed*.

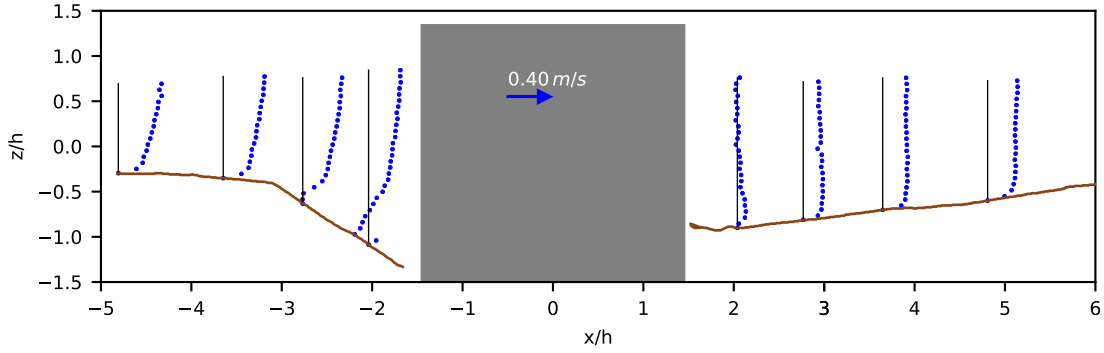

(a) Stream-wise component of velocity (u).

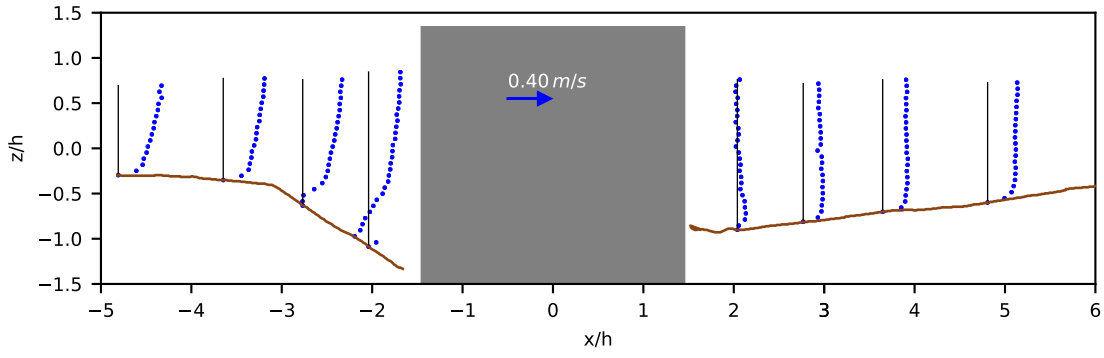

(b) Vertical component of velocity (w).

Figure 4.46: Vertical profiles of the velocity components along the mid-plane of the pier for *Exp. 4U Ebed*.

4.4.4.4 Reynolds shear stresses

The Reynolds shear stress, $u'v'$, $u'w'$ and $v'w'$, are depicted in Figures 4.47 to 4.52 for experiments $Exp.\ 1U\ Fbed$, $Exp.\ 1U\ Ebed$, $Exp.\ 1D\ Fbed$, $Exp.\ 1D\ Ebed$, $Exp.\ 4U\ Fbed$ and $Exp.\ 4U\ Ebed$, respectively.

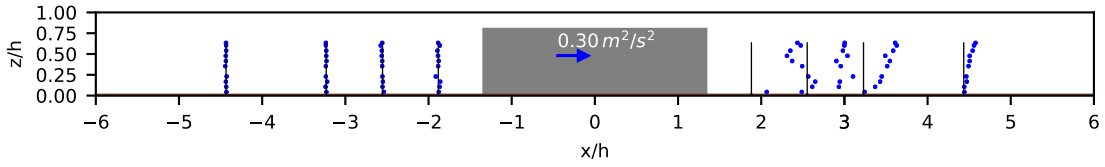

(a) Reynolds shear stresses ($\overline{u'v'}$).

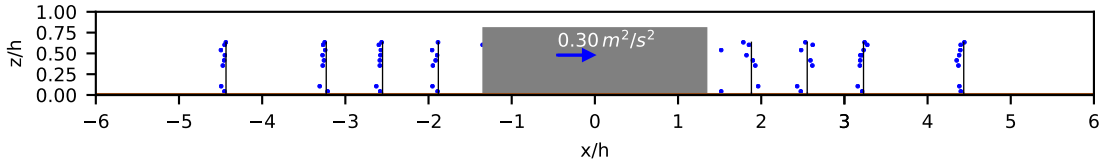

(b) Reynolds shear stresses ($\overline{u'w'}$).

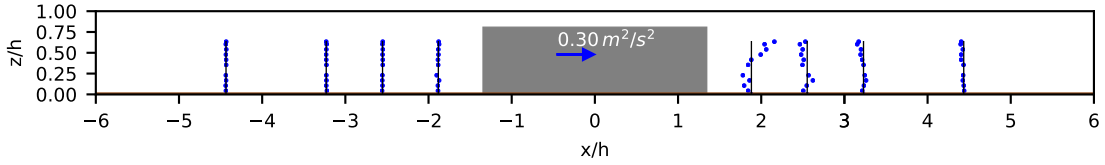

(c) Reynolds shear stresses ($\overline{v'w'}$).

Figure 4.47: Vertical profiles of the Reynolds shear stresses along the mid-plane of the pier for $Exp.\ 1U\ Fbed$.

The magnitudes of $\overline{u'v'}$ in the downstream region are greater than the corresponding points at the upstream side of the bridge pier model at both bed stages (flat and eroded). This behaviour can be attributed to the turbulent mix of fluid as a result of vortical flow in the rear side of the pier. For sections of $Profile\ J$ (Figure 4.39), the complex vortical flow is distinctly identified by the saw-toothed trend of the Reynolds shear stress $\overline{u'w'}$, magnified for the eroded bed experiments. The values of $\overline{v'w'}$ are generally less pronounced than the other components of the Reynolds shear stress, $\overline{u'v'}$ and $\overline{u'w'}$. These results, from Figure 4.47 to Figure 4.52, demonstrate that the usual assumption of isotropic turbulence is not exactly true, although it is most used as the basis of much of the theoretical analysis of turbulent flow.

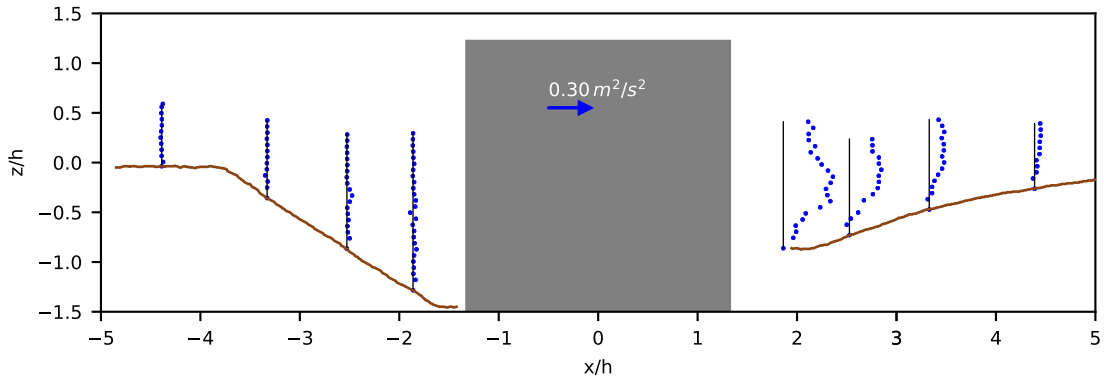

(a) Reynolds shear stresses ($\overline{u'v'}$).

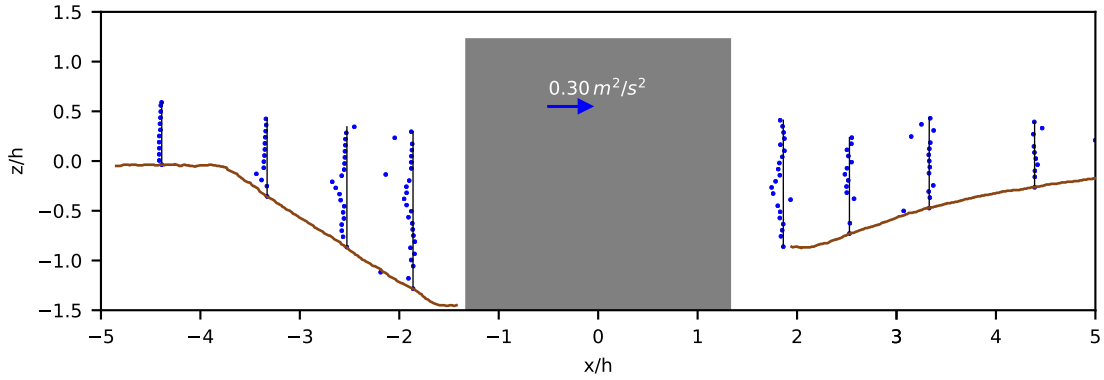

(b) Reynolds shear stresses ($\overline{u'w'}$).

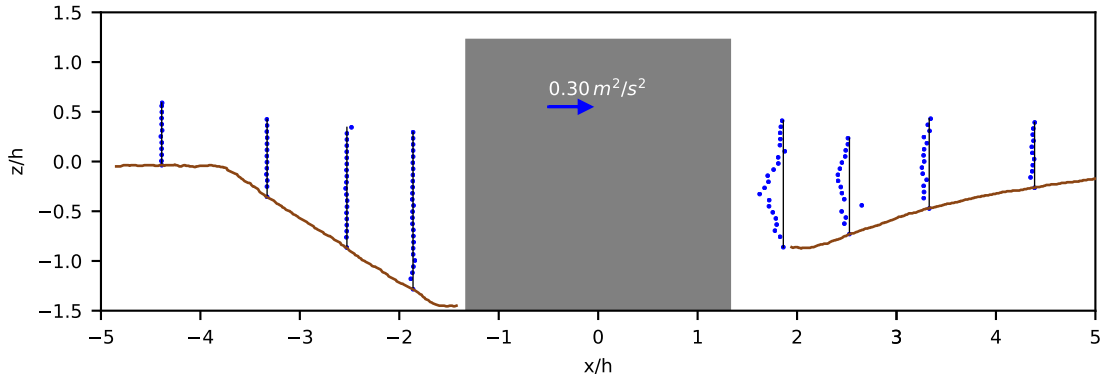

(c) Reynolds shear stresses ($\overline{v'w'}$).

Figure 4.48: Vertical profiles of the Reynolds shear stresses along the mid-plane of the pier for *Exp. 1U Ebed*.

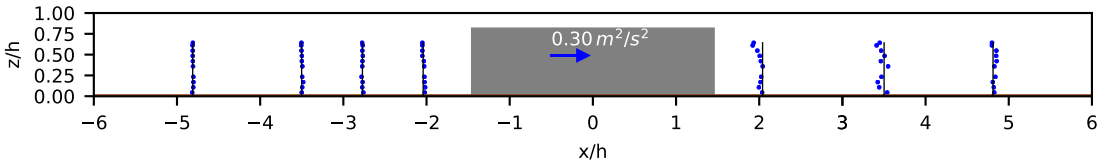

(a) Reynolds shear stresses ($\overline{u'v'}$).

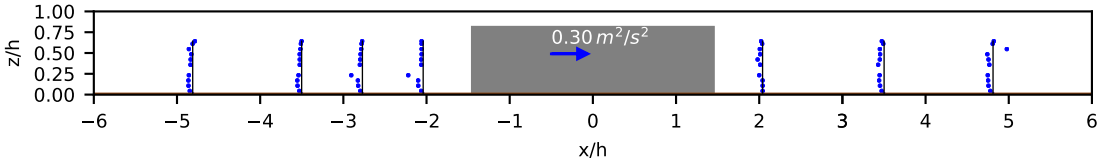

(b) Reynolds shear stresses ($\overline{u'w'}$).

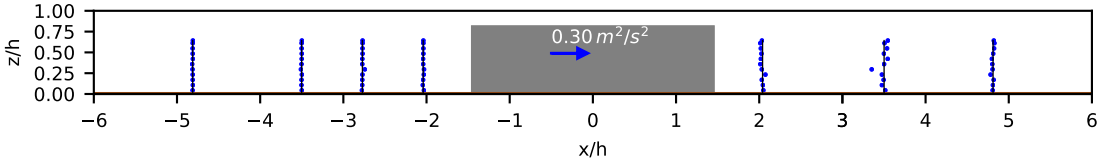

(c) Reynolds shear stresses ($\overline{v'w'}$).

Figure 4.49: Vertical profiles of the Reynolds shear stresses along the mid-plane of the pier for *Exp. 1D Fbed*.

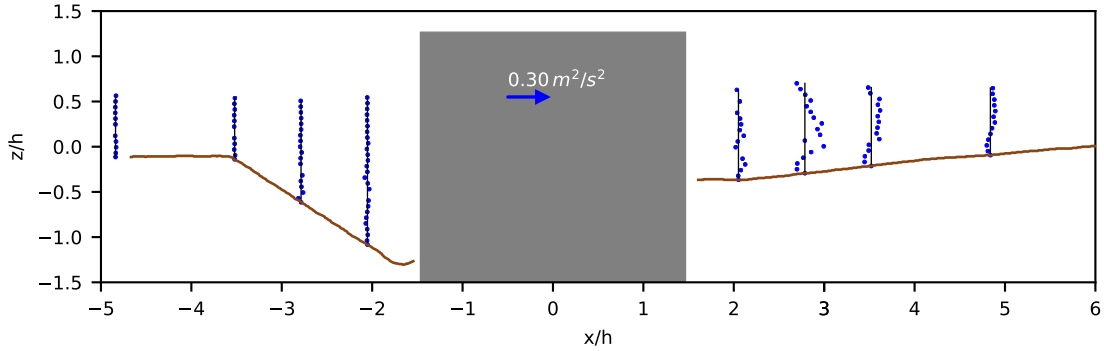

(a) Reynolds shear stresses ($\overline{u'v'}$).

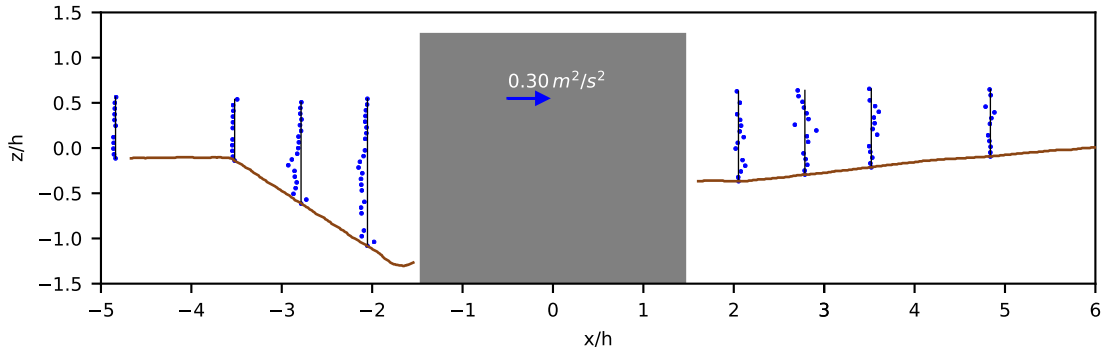

(b) Reynolds shear stresses ($\overline{u'w'}$).

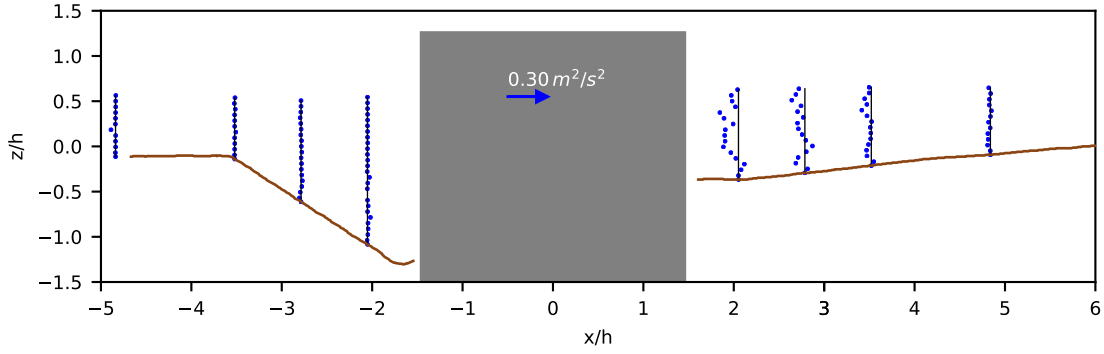

(c) Reynolds shear stresses ($\overline{v'w'}$).

Figure 4.50: Vertical profiles of the Reynolds shear stresses along the mid-plane of the pier for *Exp. 1D Ebed*.

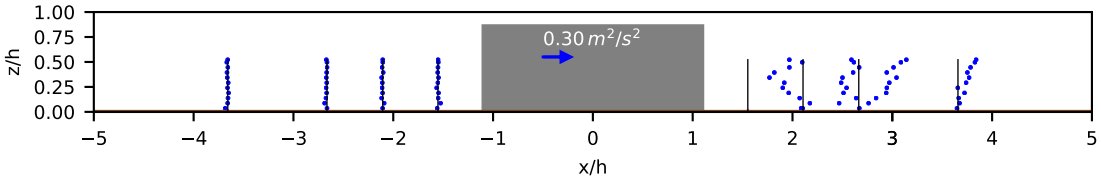

(a) Reynolds shear stresses ($\overline{u'v'}$).

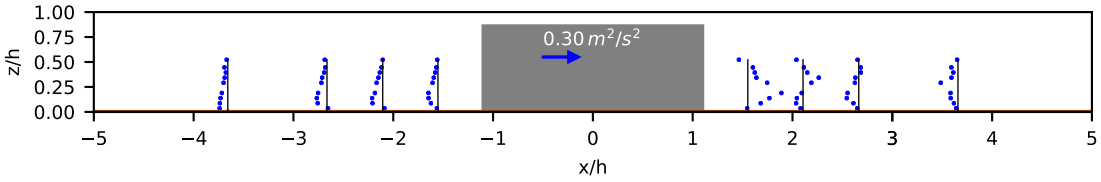

(b) Reynolds shear stresses ($\overline{u'w'}$).

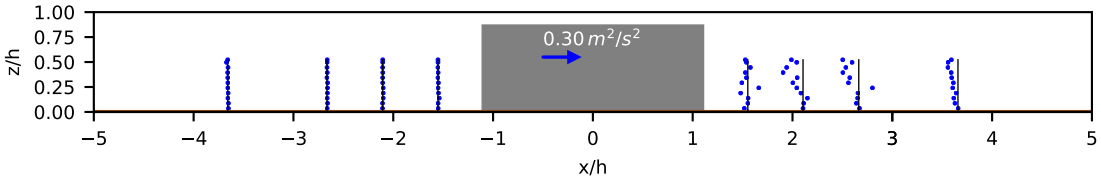

(c) Reynolds shear stresses ($\overline{v'w'}$).

Figure 4.51: Vertical profiles of the Reynolds shear stresses along the mid-plane of the pier for *Exp. 4U Fbed*.

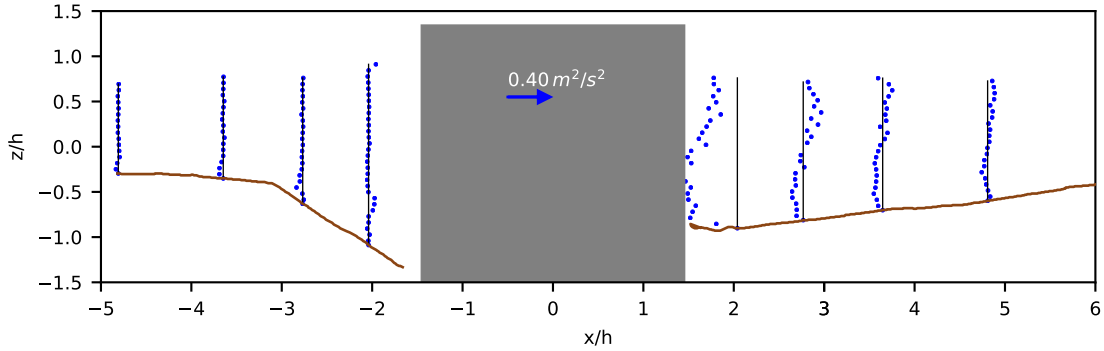

(a) Reynolds shear stresses ($\overline{u'v'}$).

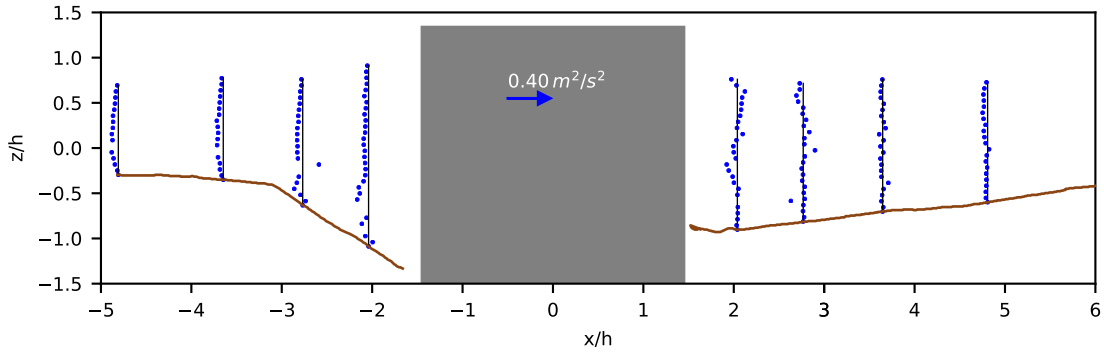

(b) Reynolds shear stresses ($\overline{u'w'}$).

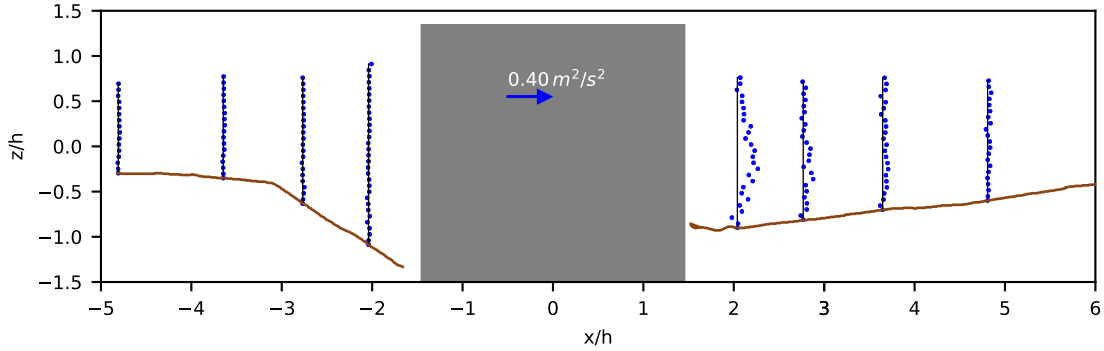

(c) Reynolds shear stresses ($\overline{v'w'}$).

Figure 4.52: Vertical profiles of the Reynolds shear stresses along the mid-plane of the pier for *Exp. 4U Ebed*.

4.4.5 Conclusions

This study aimed at characterizing the turbulent flow field at two different stages, namely (i) at the beginning of the scouring process and (ii) within the developed scour hole of three local scouring experiments. A total of six fixed bed experiments at the vicinity of oblong bridge pier models were carried out.

Measurements of stream-wise, cross-wise and vertical velocity distributions as well as the Reynolds shear stresses were performed by using a high-resolution acoustic velocimeter, namely a downlooking vectrino. The results showed that the presence of the developed scour hole, by creating extra flow resistance and augmenting the velocity difference between the four vertical profiles at the upstream side the pier, changes the velocity distribution pattern and the Reynolds shear stresses. At the rear part of the pier significant differences on flow field patterns, by the presence of the developed scour holes, were also observed. Their magnitudes were in accordance with the approach flow conditions, such as the corresponding depth and velocity.

As aforementioned, the turbulent flow field characterization of these experiments was considerably further and can ultimately guarantee a higher level of understanding of the complex flow field at the vicinity of this kind of bridge foundations through the computational of additional variables. Such variables may comprise the computation and representation of the turbulent intensities, from the turbulent fluctuation velocities (u', v' and w'), as well as the turbulence kinetic energy ($k = 0.5\ \left(\overline{u'u'} + \overline{v'v'} + \overline{w'w'}\right)$) at the different vertical sections herein considered. The derivation of such parameters contributes to a comprehensive description of the flow magnitude and structure for the particularities of each experiment and bed morphology stage (flat *vs* eroded). The collected data may also aid the calibration and validation phases of sophisticated numerical models, such as Computational Fluid Dymanics (CFD) tools.

4.4.6 Data availability statement

Some or all data, models, or code that support the findings of this study are available from the corresponding author upon reasonable request.

4.4.7 Acknowledgements

The first author thanks for financial support through a PhD scholarship PD/BD/127798/2016, in the framework of the Doctoral Program INFRARISK - “Analysis and Mitigation of Risks in Infrastructures”. This research was also supported by Centro Interdisciplinar de Investigação Marinha e Ambiental (CIIMAR) through the project with reference UID/Multi/04423/2019. The authors thank the team of the Laboratory of Construction and Modelling of the National Laboratory of Civil Engineering for the technical assistance in the experimental work.

Chapter 5

Numerical Modelling

5.1 General Considerations

Numerical modelling was considered in the present investigation for providing a fundamental importance to the bridge scour prediction problem. The methodological proposal herein developed is similar to other Computational Fluid Dynamics (CFD) applications, being one of the key steps the generation of efficient grid meshes (as summarized in Section 2.6). The mesh generation and refinement process, which relies on the selected CFD tool, is a critical and time-consuming step given the direct influence on the quality of results and the variety of possible mesh generation methods, such as algebraic and elliptical meshes. In addition, a careful preparation of the numerical setup considering the features of the experimental flume (Section 4.2), as well as the initial and boundary conditions of the experiment used as reference were adequately considered to build the computational domain of the numerical simulations. The SSIIM (acronym for Sediment Simulation In Intakes with Multiblock option) software was the selected CFD tool for the current study. Due to the amount of data and the required computational time, the platform GridFEUP (`https://grid.fe.up.pt/web/index.php?page=welcome`), provided by the Faculty of Engineering of the University of Porto (FEUP), was used to perform the numerical simulations.

The present chapter is dedicated to the numerical simulation of sediment bed transport at the vicinity of a oblong bridge pier model. The focus was devoted to modelling both the sediment bed movement and the bed shear stress in the vicinity of an oblong bridge pier model, namely *Pier* 11. Clear water scour conditions and a sand of known granulometric composition were considered, in conformity with the performed *Exp*. 1*U* experiment (Section 4.3). Expecting long time-frames, the averaged form of the Navier-Stokes equations were considered for simulating the turbulent flow fields. These approaches average the aforementioned equations in time and solve only the mean flow quantities, saving computational time. The performed numerical simulations allowed the assessment of the scour depth time evolution, as well as the deposition regions at the rear part of the bridge pier model. This paper, under preparation, is preparation in Section 5.2 and will be submitted for publication in an international scientific journal.

5.2 Numerical simulations of scour development around an oblong bridge pier laboratory model. *Paper under preparation*

TITLE: Numerical simulations of scour development around an oblong bridge pier laboratory model[1]

Paper under preparation and to be submitted for publication in an international scientific journal

Author contributions:
Bento, A.M. designed the model and the computational framework; carried out the implementation and performed the calculations; and wrote the manuscript with input from Pêgo, J.P., Viseu, T. and Couto, L. All authors discussed the results and commented on the manuscript.

[1] Bento, A.M., Pêgo, J.P., Viseu, T. & Couto, L. (Under preparation). Numerical simulations of scour development around an oblong bridge pier laboratory model.

5.2.1 Abstract

The complex flow structure around bridge piers is challenging both for the experimental and numerical studies. Thus, investigating the capabilities of CFD tools in resolving the flow structure and the mechanism of sediment entrainment in and out of the scour hole remains a challenging task. In this paper, the bed shear stress distributions in time and space, as well as the scour depth time evolution around an oblong bridge pier were numerically investigated using the Computational Fluid Dynamics (CFD) tool SSIIM (acronym for Sediment Simulation In Intakes with Multiblock option). Experimental data and results, carried out by Bento et al. (Section 4.3), were used to calibrate and validate the numerical model. The results demonstrate that calibrated numerical models can reproduce measured scour depths in the laboratory environment with significant accuracy, namely around oblong bridge piers.

Keywords: bed shear stress, bridge pier, sediment transport, scour hole, SSIIM software

5.2.2 Introduction

The local scouring phenomenon has been recognized over decades as a serious threat to the stability of bridges worldwide (Cook *et al.*, 2015; Flint *et al.*, 2017; Proske, 2018). In Portugal, the tragic accident of the Hintze Ribeiro bridge, in the Douro river, was partially due to erosion around one of its foundations (Rocha *et al.*, 2008). This phenomenon results from the dynamic interactions between the three-dimensional turbulent flow field and the movable riverbed at the vicinity of bridge foundations, which is magnified during the development of a scour hole. Due to the intervention of various complex mechanisms, mainly of hydraulic nature, the scouring process remains an challenging engineering problem after many decades (Chiew *et al.*, 2020).

Numerous experimental and numerical studies have attempted to resolve the flow structure and the mechanism of sediment entrainment in and out of the scour hole, mostly for piers of a circular cross-section geometry. Dargahi (1989) was a pioneer in experimentally investigating flow patterns, turbulence intensity and boundary shear stress distributions in the scour zone of a circular pier. The referred study was performed for different fixed scour stages under clear water conditions. Based on these results, several other experimental studies were conducted to investigate the flow mechanism and the associated scouring process around single piers (Hoffmans & Verheij, 1997; Melville & Raudkivi, 1977; Graf & Istiarto, 2002; Unger & Hager, 2006; Kirkil *et al.*, 2008; Diab, 2011, among others).

After decades of research on experimental controlled environments, fewer works have devoted their attention to the three-dimensional numerical simulation of these processes. Nevertheless, some first steps have been taken towards achieving the numerical characterization of the flow patterns (Escauriaza *et al.*, 2017) in order to accurately complement the experimental efforts. Briley & McDonald (1981) made numerical solutions of the compressible Navier-Stokes equations for a laminar steady horseshoe vortex at the junction between an elliptic strut and a flat plate, whilst Kwak *et al.* (1986) computed the laminar steady junction flow using a three-dimensional incompressible Navier-Stokes code. However, when the flow is turbulent, the computational prediction of the

separation flow is a process of crucial relevance since it influences significantly the numerical performance in reproducing the physical phenomenon. The fluctuation of turbulent flows on a wide range of time and length scales makes its numerical computation difficult and requires a specific way to model that turbulence. RANS (Reynolds-averaged Navier-Stokes) are such model equations and were employed in the first application of Computational Fluid Dynamic (CFD) tools, by Deng & Piquet (1992), to study the three-dimensional turbulent flow around an airfoil. The adoption of an iterative fully decoupled technique to compute the RANS equations revealed an attractive approach to capture the main features of horseshoe vortices although they lacked some accuracy on modelling the scour process. The rapid development of computer science has widened the application of numerical methods in many fields, for instance, for studying the local scour phenomena, as it boasts such advantages as high precision, low expenses, and modelling scale independence (Zhang *et al.*, 2017). In recent years, several numerical models have been constructed for simulating the 3D flow field and bed morphological changes around circular piers.

Olsen & Melaaen (1993) were among the first to predict local scour developing processes by combining the three-dimensional flow field with a sediment transport model around a circular pier. The work was limited to the initial stage of scouring while the entire scour process was contemplated by Olsen & Kjellesvig (1998), where good qualitative and quantitative agreement with the experimentally measured scour patterns was achieved. Richardson & Panchang (1998) performed three-dimensional simulations of the flow around a circular pier with fixed scour holes at intermediate and equilibrium phases, employing FLOW3D software. By comparing the numerical results with the experimental observations by Melville & Raudkivi (1977), they found that the FLOW3D hydrodynamic model simulates well the complex flow patterns around the bridge pier.

Wang & Jia (1999) simulated the temporal evolution of the scour hole around a bridge pier using the CCH3D software, analysing different flow effects on sediment transport. Chang *et al.* (1999) performed three-dimensional calculations of the flow around a bridge pier with a fixed bed and no scour by using a Large-Eddy Simulation (LES) model. In Tseng *et al.* (2000), simulation runs were conducted to study various properties of the three-dimensional flow around both circular and square piers by LES model, exposed to a steady current. Their model results were validated against Dargahi (1989)'s experimental results. Despite the discussion about the influence of flow patterns in the scouring process, no scour simulation was undertaken.

Chen (2002) employed the Reynolds-Average Navier-Stokes (RANS) equations to predict scour in an array of piers in a side-by-side arrangement. The bed material was cohesive and the scour rate was assumed to vary linearly with the bed shear stress. Later, Roulund *et al.* (2005) developed an experimental and numerical study of the flow and the scour around a circular pier by employing a k-ω turbulence model. The authors devoted special attention to horseshoe and lee-wake vortices, to the influence of the boundary layer thickness, Reynolds number and bed roughness on those mechanisms. Roulund *et al.* (2005) also derived a non-cohesive sediment model, obtaining equilibrium scour depths 30% larger than the experimental data.

Khosronejad *et al.* (2012b) simulated the processes of clear water scouring around piers of cylindrical, square and diamond cross-section geometries using an unsteady RANS k-ω model

and a sediment transport model. The simulation results were compared to experimental data. The computed scouring agreed well only with that of the diamond-shaped pier; the maximum scour depths were under-predicted for the cylindrical and square-shaped piers. Baranya *et al.* (2012) used a 3*D* k-ε turbulence model and a bed load model to simulate the scour hole development of multiple circular piers. Baykal *et al.* (2015) studied the flow and scour around a circular pier exposed to a steady current by using a three-dimensional hydrodynamic model that incorporates a k-ω turbulence model, a sediment transport (bed and suspended load) description and a morphological model. A detailed review of the recent advances in the numerical simulations of local scour problems is presented in Sumer (2015).

Recently, Jia *et al.* (2017) proposed a novel numerical method for simulating local scouring around bridge piers using a 3*D* free-surface RANS turbulent flow model; a good agreement between simulations and experimental data was obtained. The authors found that the downflow and the turbulent kinetic energy around the pier were the main factors in the scouring process. The three-dimensional characterization of the flow field and the evolution of the scour hole at the vicinity of bridge foundations, using numerical modelling tools, is thus nowadays more feasible due to the experimental validation and the computational cost and time reduction.

The present study aims to improve the understanding of the scouring process around an oblong bridge pier embedded in a movable bed, by characterizing the scour depth time evolution at its vicinity, as well as to assess the quality of the numerical approach by comparing the numerical results with the experimental observations. The numerical simulations were carried out with SSIIM, a general-purpose CFD tool that solves the Navier-Stokes equations using the control volume method with the SIMPLE algorithm and the two-equation closure turbulence models (Olsen, 2018a). The program computes the advection-diffusion equation for sediment transport, using empirical formulas for the bed boundary. Regarding the cells closest to the water surface, SSIIM model uses the Manning-Strickler friction coefficient, the discharge and the downstream water level as input values to generate the water level for the calculations using the standard backwater calculation, for which some cross-sections were considered fixed and used as reference during simulations. The morphological model of this CFD tool is herein analysed in order to examine whether it reproduces accurately and effectively the whole involved physics in sediment transport processes compared with experimental data. The model is calibrated and validated by using experimental data of Bento et al. (Section 4.3).

This paper is organized as follows. The hydrodynamic model and sediment transport equations used are described in Subsection 5.2.3. The experimental case study is presented in Subsection 5.2.4, whilst the numerical model setup, including mesh geometrical dimensions and boundary conditions, are given in Subsection 5.2.5. Simulations of the bed morphology and the bed shear stress around the oblong bridge pier are subsequently presented and discussed in Subsection 5.2.6. Finally, the main conclusions are drawn in Subsection 5.2.7.

5.2.3 The hydrodynamic model

5.2.3.1 Framework

SSIIM model was designed to be used in research for hydraulic/river/sedimentation engineering and was developed at the Norwegian University of Science and Technology (Olsen, 2018a). It was used in the present study due to its ability to model sediment transport and considerable numerical stability for large time steps. Its capacities permit to compute long intervals of integration with a low computation effort, thus making possible to study long time scale phenomena as is the case of local scour. A description of the hydrodynamic model used throughout the current study is herein provided.

5.2.3.2 Flow computation

The three-dimensional incompressible flow field of the numerical model used is computed by the continuity and the Reynolds-averaged Navier-Stokes (RANS) equation as follows (Equations 5.1 and 5.2):

$$\frac{\partial \overline{u_i}}{\partial x_i} = 0 \tag{5.1}$$

$$\frac{\partial \overline{u_i}}{\partial t} + \overline{u_j}\frac{\partial \overline{u_i}}{\partial x_j} = -\frac{1}{\rho}\frac{\partial \overline{P}}{\partial x_i} + \nu_T\left(\frac{\partial^2 \overline{u_i}}{\partial x_j^2}\right) - \frac{\partial \overline{u_i' u_j'}}{\partial x_j} \tag{5.2}$$

where x_i and x_j (i, j = 1, 2 or 3) stand for the longitudinal (x), transversal (y) and vertical (z) directions; $\overline{u_i}$ and $\overline{u_j}$ are the time-averaged velocity components; u_i' and u_j' are the correspondent fluctuation components; ρ is the water density, P is the non-hydrostatic pressure; ν is the kinematic viscosity and t represents time.

The first and second terms on the left side of the momentum equation, Equation 5.2, are denoted transient and convective terms, respectively. On the right side, the first term is the pressure, while the second corresponds to the diffusion term. In the third term, $\overline{u_i' u_j'}$ represents the Reynolds stresses and can be computed by using the mean flow velocity gradients and the turbulent eddy viscosity, under the Boussinesq assumption (Equation 5.3):

$$-\overline{u_i' u_j'} = \nu_T\left(\frac{\partial \overline{u_i}}{\partial x_j} + \frac{\partial \overline{u_j}}{\partial x_i}\right) - \frac{2}{3}k\delta_{ij} \tag{5.3}$$

where δ_{ij} is the Kronecker delta (1 if i=j, 0 otherwise), ν_T is the eddy viscosity and k is the turbulence kinetic energy. The last term on the right side of Equation 5.3 is incorporated into the pressure. To compute the eddy-viscosity (ν_T), the standard k-ε turbulence model was used, which requires solving two additional equations for the transport of turbulent kinetic energy (k) and turbulent dissipation (ε), Equation 5.4 (Wilcox, 2006), in which C_μ is constant and equal to 0.09.

$$\nu_T = C_\mu \frac{k^2}{\varepsilon} \tag{5.4}$$

The criterion employed to establish the convergence and numerical stability of the iterative algorithm was the reduction of all normalized residuals. It measures the local imbalance of a conserved variable in each control volume. Thus, every cell in the model has its own residual value for each of the equations being solved, which never reaches the exact value of zero. As the iteration proceeds, the variables converge to their final solution as the residuals decrease. Furthermore, the lower the residual value is, the more numerically accurate is the solution (Olsen, 2018a).

One of the difficulties in solving Equation 5.1 and 5.2 results from the non-existence of an explicit equation for the pressure. Therefore, the SIMPLE (Semi-Implicit Method for Pressure-Linked Equation) algorithm was used for the pressure coupling for all cells (Patankar & Spalding, 1972), except the closest ones to the water surface. For the cells closest to surface, SSIIM computes the water surface with a free surface algorithm, the 1D standard backwater computation, based on a given water level point at the outlet boundary. This approach was employed in the current study since it is numerically stable for the time steps approaching infinity (Hines, Jonathan, 2008).

The implicit finite volume method is employed to discretize the governing equations (Equations 5.1 and 5.2) on a structured and non-staggered grid system. This approach comprises different methods differing on how the concentration on a cell surface is calculated (Olsen & Melaaen, 1993), for which the Power-Law scheme (POW) and the Second-Order Upstream scheme (SOU) are the most used. Further descriptions of these schemes can be found in Patankar (1980), Olsen (1991), Melaaen (1992), and Versteeg (2007). The Power-Law scheme (POW) is a first-order upstream scheme that converges easily; however, its results can be largely deteriorated by false diffusion. False diffusion can either result from the adoption of a non-adequate discretization scheme for the convective terms in the Navier-Stokes equations (Equation 5.2) or by a non-appropriate grid mesh. For the case under analysis, the SOU scheme was applied to the velocity equations whilst a POW scheme was adopted for the turbulence formulations. In fact, stability problems did occur on different simulation runs if a different scheme than the First-Order Power-law (POW) was assigned for the turbulence equations.

5.2.3.3 Sediment transport equations

The equation of sediment continuity, first presented by Exner (Exner, 1920, 1925), describes the conservation of mass between sediment in the bed of a channel and sediment that is being transported either along the bed (bed load) or in suspension (suspended load). The integration of Exner's equation over the water depth emerges as (Equation 5.5):

$$(1-\lambda)\frac{\partial z_b}{\partial t}+\frac{\partial q_{tx}}{\partial x}+\frac{\partial q_{ty}}{\partial y}=0 \tag{5.5}$$

where z_b is the bed level, λ is the porosity of the bed material, and q_{tx} and q_{ty} are the total load (bed and suspended load) discharge in stream- and cross-wise direction, respectively.

The suspended load discharge results from two main transport processes developed through the walls of the finite volume: the convection and the diffusion of sediments. The combination of these two processes for a steady sediment transport is given by the convection-diffusion equation

(Equation 5.6). The variable c accounts for the sediment concentration, while w_s is for the fall velocity of the sediment particles and Γ_T denotes the diffusion coefficient.

$$u_j \frac{\partial c}{\partial x_j} + w_s \frac{\partial c}{\partial z} = \frac{\partial}{\partial x_j}\left(\Gamma_T \frac{\partial c}{\partial x_j}\right) \tag{5.6}$$

The first term on the left side of Equation 5.6 represents the convection of sediments, which is the parcel of sediments that are transported due to the water average velocity component over time. The transport due to the fall velocity (w_s) of the sediments (second term on the left side of Equation 5.6) is discretized as an extra convective term and added to the velocities in the vertical direction, z (Olsen, 1991). The right side of Equation 5.6 represents the diffusion of sediments owing to turbulent mixing and concentration gradients. The turbulent mixing process is commonly modelled with the diffusion coefficient (Γ_T). This coefficient is set equal to the eddy-viscosity (ν_T), taken from the k-ε turbulence model. However, Equation 5.6 is not solved for the grid cells closest to the bed, whereby the sediment continuity equation is usually not satisfied. The discrepancy in continuity is used to calculate bed levels changes, allowing the simulation of the interaction between the sediment that moves close to the bed and the sediment that moves in suspension. It is, therefore, necessary to define an equilibrium concentration in the cells close to the bed; Rijn (1984) proposed a formula for the equilibrium concentration (Equation 5.7) that is used in the current model.

$$C_{bed} = 0.015 \frac{D_{50}^{0.3}}{a} \frac{\left[\dfrac{\tau - \tau_c}{\tau_c}\right]^{1.5}}{\left[\dfrac{(\rho_s - \rho)g}{\rho \nu^2}\right]^{0.1}} \tag{5.7}$$

The variable C_{bed} is the equilibrium concentration at the bed, a is the distance from the concentration point to the bed, ν is the kinematic viscosity of the water, ρ_s is the sediment density, and g is the acceleration of gravity. The critical bed shear stress (τ_c) for movements of sediment particles is obtained from Shields' curve (Shields, 1936), and then internally multiplied with the reduction factor (r), derived by Brooks (1963), in order to account for the sloping bed (Equation 5.8).

$$r = \frac{-\sin\varphi_s \sin\alpha_b}{\tan\theta_s} + \sqrt{\left(\frac{\sin\varphi_s \sin\alpha_b}{\tan\theta_s}\right)^2 - \cos^2\varphi_s \left[1 - \left(\frac{\tan\varphi_s}{\tan\theta_s}\right)^2\right]} \tag{5.8}$$

The angle between the flow direction and a line perpendicular to bed plane is denoted α_b, the slope angle is represented by φ_s, and the slope parameter is given by θ_s. The reduction factor (r) is calculated and then multiplied with the critical shear stress for a horizontal surface to give the effective critical shear stress for a sediment particle (Olsen, 2018b).

5.2.4 Local scouring experimental data

The results of an experimental test performed by Bento et al. (Section 4.3) were used for calibration and validation of the hydrodynamic model. The local scouring experiment was performed in a

tilting flume 40.7 m long, 2.0 m wide, and 1.0 m deep, located in the experimental facilities of the National Laboratory of Civil Engineering (LNEC), in Lisbon, Portugal.

The flow discharge was regulated by the rotational speed of the associated pump to a constant value and monitored by an electromagnetic flowmeter (at an accuracy of $\pm 0.25\%$). The water depth within the tilting flume was adjusted by two sluice gates, one placed at the upstream section and the other at the downstream end of the flume and was monitored by two resistive probes at a sampling frequency of 25 Hz. A uniform quartz sand was used as bed material with a median grain size diameter, D_{50}, of 0.86 mm and a sediment diameter standard deviation, σ_D, of 1.28. An oblong bridge pier model, 0.11 m wide and 0.433 m long, was placed vertically in the working section on the flume mid-plane at $\approx$11 m from the flume entrance. The scouring experiment was stopped at the time required to reach 90% of the equilibrium scour depth (t_{90}, as given by Sheppard *et al.* (2011)), namely after 5.9 days. A value of 65.51%, corresponding to an angle of 33.23°, was obtained for the maximum bed hole slope. The hydraulic and scour conditions in which the experiment was developed are summarized in Table 5.1. Point-wise measurements of the scour depth time evolution (d_s) at 0.03 m from the pier's front were considered for calibration and validation purposes.

Table 5.1: Hydraulic variables of $Exp.\ 1U$.

Experiment	Q (m^3s^{-1})	h (m)	V (ms^{-1})	If $(-)$	Fr $(-)$	Re $(-)$	Re_D $(-)$
$Exp.\ 1U$	0.0923	0.1440	0.3205	1.0295	0.2696	46150	35253.47

Further details about the experimental measurement techniques can be found in Bento et al. (Section 4.3).

5.2.5 Numerical model setup

5.2.5.1 Mesh geometrical dimensions

The computational domain is commonly described as the region in 3D (or 2D space), in which the governing equations are solved by the SSIIM tool. The grid mesh was generated by dividing the computational domain into cells, in which the numerical equations are solved. In this study, the computational domains in 2D (plane xy) was divided in different zones to generate non-orthogonal grid lines and the grid points were created by means of the elliptical grid generation method (Thompson, 1982). Only the elliptical grid was herein considered since it provided better results than the algebric grid system, as stated by Alemi & Maia (2016). The elliptical grid mesh was performed through a Fortran code developed on purpose, which was then imported to the SSIIM software.

Different mesh sizes were tested to generate a three-dimensional structured grid. A 4.1 m long and 2.0 m wide computational domain (equivalent to $37W$ and $18W$, being W the pier width) was selected, which resulted in 189 and 122 computational cells in x- and y-direction, respectively. The vertical distribution of the grid points (z direction) was predefined in the numerical model as percentages of the flow depth (indicated in Table 5.1). During the SSIIM computations, the grid

points in the *x*-*y* plane were fixed whereas the ones in the *z*-direction changed according to the flow depth. The pier definition was performed by blocking out the cells where the pier was located, at a distance of 1.1 m ($\approx 10W$) from the inlet boundary.

Figure 5.1 shows the plan view of the grid mesh around the oblong bridge pier. The origin of the Cartesian coordinate system was at the left lateral edge of the oblong pier, as can be seen in Figure 5.1. The mesh is finer in the region close to the pier and bed surface, and progressively coarser with the distance. The spatial increase of the grid cell size was performed with an expansion ratio of about 1.01, taking into account that the grid should not be too coarse where vortices are expected to be developed.

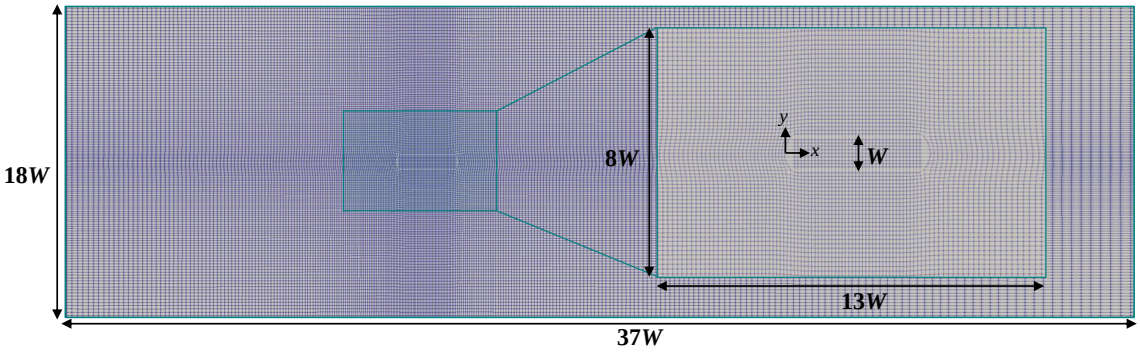

Figure 5.1: Plan view of the grid mesh around the oblong bridge pier: whole and local mesh.

5.2.5.2 Boundary conditions and input parameters

Another essential step in the numerical simulation process is to specify appropriate boundary and input parameters, which is also most subject to error. The computational domain of the numerical simulation was divided into seven different boundaries: inlet, outlet, water surface, wall, bottom, front and back sides. Specific boundary conditions for the hydrodynamic model (Equation 5.1 to Equation 5.8) were established to those boundaries.

At the inlet, Dirichlet boundary conditions must be specified (Olsen, 2012). This is relatively straightforward for velocities, although commonly more difficult to specify for turbulence. Nonetheless, Olsen (1991) outlined a procedure in which k and ε are specified based on the investigations of the magnitude (Keefer, 1971) and vertical distribution profile (Naas, 1977) of the eddy-viscosity in rivers. Given the velocity, it is also possible to estimate the shear stress at the entrance bed. Then, the turbulent kinetic energy (k) at the inflow bed is determined by Equation 5.9 based on equilibrium between production and dissipation of turbulence at the bed cell.

$$k = \frac{\tau}{\rho\sqrt{C_\mu}} \tag{5.9}$$

At the outlet, zero gradient boundary conditions were used for all variables. The flow discharge and water depth were herein defined and used to generate the water surface for the calculations in all domain using a standard backward calculation. The location of the water surface is computed by extrapolating the pressure from the inner cells to the water surface. The vertical movement of the

water surface is applied to the top grid line. The grid points below the water surface are also moved vertically according to the relative distance to that surface. At the water surface, zero gradient boundary conditions were used for the turbulent dissipation (ε), while the turbulent kinetic energy (k) was set to zero.

The flux through the wall, bottom, front and back sides is zero, i.e. the no-slip condition was imposed. However, the velocity gradient towards the wall is very steep, and it would require a significant number of grid cells to dissolve the gradient sufficiently. Alternatively, the empirical velocity wall formula for rough boundaries (Schlichting & Gersten, 2017) was used, transformed by means of integrating it over the cell closest to the bed (Equation 5.10):

$$\frac{U}{u_*} = \frac{1}{K} \ln\left(\frac{30 y_w}{k_s}\right) \tag{5.10}$$

where u_* is the shear velocity (given by $u_* = \sqrt{\frac{\tau}{\rho}}$), K is the Von Kármán constant (equal to 0.41), y_w is the distance from the wall to the center of the cell, and k_s is the roughness height, usually computed based on the bed particle median diameter, D_{50}, and τ is the local bed shear stress. The wall log-law is used for both the velocities and the turbulence parameters. The turbulent kinetic energy (k) is assumed equal to its dissipation (ε) near the wall according to Rodi's formulas (Rodi, 1993).

The input parameters were set to values assumed in the performed experiments. These included the mean approach flow discharge and flow depth at the downstream boundary of the computational domain ("outlet" side), median grain size diameter, density, angle of repose, fall velocity and critical bed shear stress. The angle of repose was assumed equal to the experimentally obtained (Subsection 5.2.4). The fall velocity was calculated by the formula present in Hoffmans & Verheij (1997), and the critical bed shear stress was set by the Shields-Rouse's equation (Guo, 2002).

5.2.6 Results and discussion

5.2.6.1 General considerations

Before initiating the simulation case, the scour development around an oblong bridge pier model, a proper calibration of the presented numerical model was performed. This process required mainly the definition of the time step and the bed roughness height.

Bearing in mind that small time steps give more accurate results but also require more computational time to reach the stability condition, a balance between results' accuracy and needed simulation time (until t = 480 min) was performed. As aforementioned, SSIIM model is numerically stable for large time steps (Hines, Jonathan, 2008; Olsen & Melaaen, 1993); a time step of 5 sec was used for the numerical simulations. Once selected, two different values for the bed roughness height were considered, namely $k_s = 3D_{50}$ and $k_s = 3D_{90}$. The agreement between experimental measurements and model results of the scour depth at 0.03 m from the pier's front was used as the main calibration criterion. The bed roughness height parameter is the main responsible for the involved uncertainties of the empirical formulas that relate it with the grain size distribution.

In accordance with Figure 5.2, a bed roughness height of 0.0051 m (in the present case, $k_s = 3D_{90}$) was thus selected, confirming the proposed relation by Van Rijn *et al.* (1993).

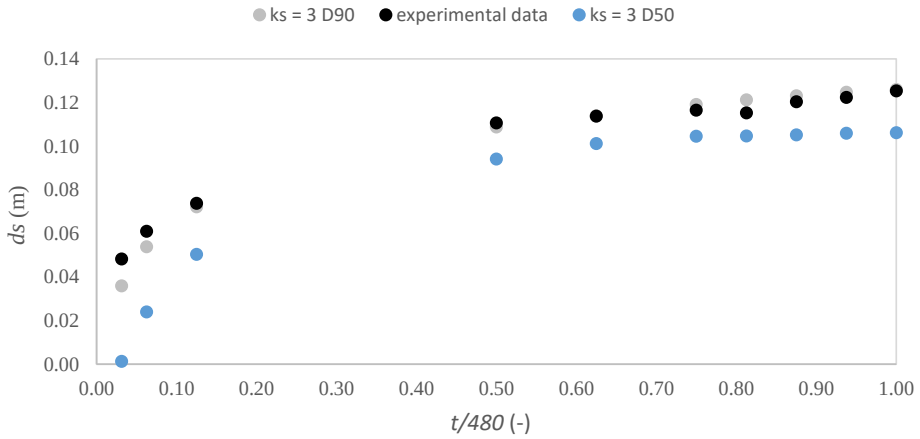

Figure 5.2: Calibration of the bed roughness height.

In the present study, the results of the numerical approach comprised the characterization of the full geometry of the bed morphology during the scouring process, as well as the bed shear stress at the vicinity of the oblong bridge pier until t = 480 min. The numerical simulations were performed in a reasonable Central Process Unit (CPU) time. The elapsed CPU time was about 36 hours by employing 16 processors in parallel. These results were compared against the experimentally measured data, given in Section 4.3.

5.2.6.2 Scour depth estimates

Figure 5.3 shows the evolution of simulated and measured scour depth at 0.03 m from the pier's front in time (relative to the time duration of t = 480 min).

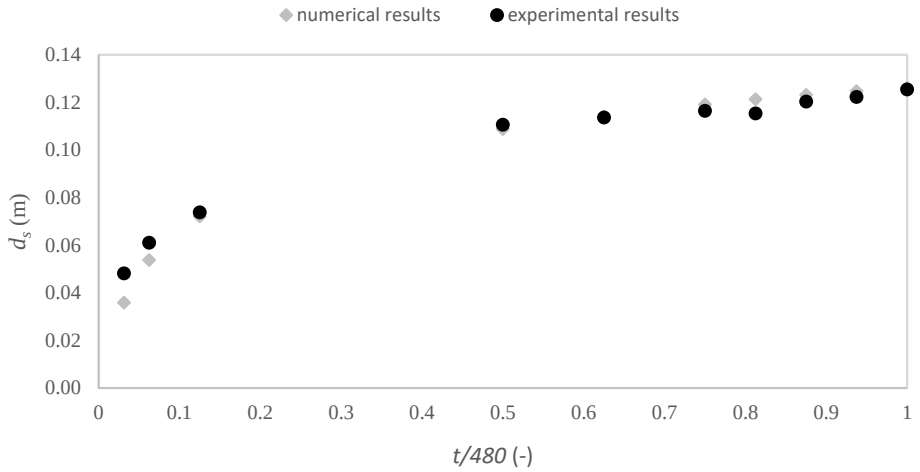

Figure 5.3: Experimental and computed scour depths.

The quantification of the deviation in the predicted and obtained experimentally scour depth, at 0.03 m from the pier's front, was assessed by performing a characterization of the relative errors, determined by Equation 5.11:

$$e_i = \frac{|d_{s,computed} - d_{s,measured}|}{d_{s,measured}} \tag{5.11}$$

where $d_{s,measured}$ is the scour depth measured experimentally along each scour bed profile, and $d_{s,computed}$ is the scour depth computed by the numerical model. These scour depths, as well as the corresponding relative errors are indicated in Table 5.2.

Table 5.2: Scour depth relative error (e_i), determined by Equation 5.11.

t (min)	$d_{s,measured}$ (m)	$d_{s,computed}$ (m)	e_i (%)
15	0.048	0.036	25.4
30	0.061	0.054	11.8
60	0.074	0.072	2.2
240	0.111	0.109	1.7
300	0.114	0.114	-0.2
360	0.117	0.119	-2.3
390	0.115	0.121	-5.2
420	0.120	0.123	-2.4
450	0.122	0.125	-2.0
480	0.125	0.126	-0.5

The simulated scour depth development ($d_{s,computed}$) began a little later than the one observed experimentally ($d_{s,measured}$). This may be caused by the simulated horseshoe vortex or the turbulent fluctuations at the initial time, which are relatively weaker than those registered experimentally. According to Table 5.2, the numerical model presents an under-prediction higher than 25% for t = 15 min, which trend reduces significantly for t = 60 min to 2.2% and 1.7% for t = 240 min. From t = 300 to t = 480 minutes, the numerical model over-predicts the experimental data, in percentages ranging between 0.2% to 5.2%. Thus, it is possible to state that the numerical model predicts with significant accuracy the measured scour depths (with an average relative error of 2.9%).

5.2.6.3 Bed morphology

Figure 5.4 gives the computed bed morphology at the vicinity of the oblong bridge pier at different instants of the local scouring experiment ($Exp.\ 1U$), from t = 15 min to t = 480 min. The zero at the vertical plane (z) corresponds to the bed level before scouring. This provides a global overview of the detailed scour and deposition processes around the oblong bridge pier laboratory model, triggered by the rich dynamics of turbulent flow.

The sediment bed transport initiated at the sides of the pier, driven by the region of larger magnitude of bed shear stress (still noticeable for t = 15 min, Figure 5.4a). At later times, the scouring development is observed at the pier lateral sides, as well as at the upstream side, which is indicative of the domination of the horseshoe vortex system in the process (see Figure 5.4b).

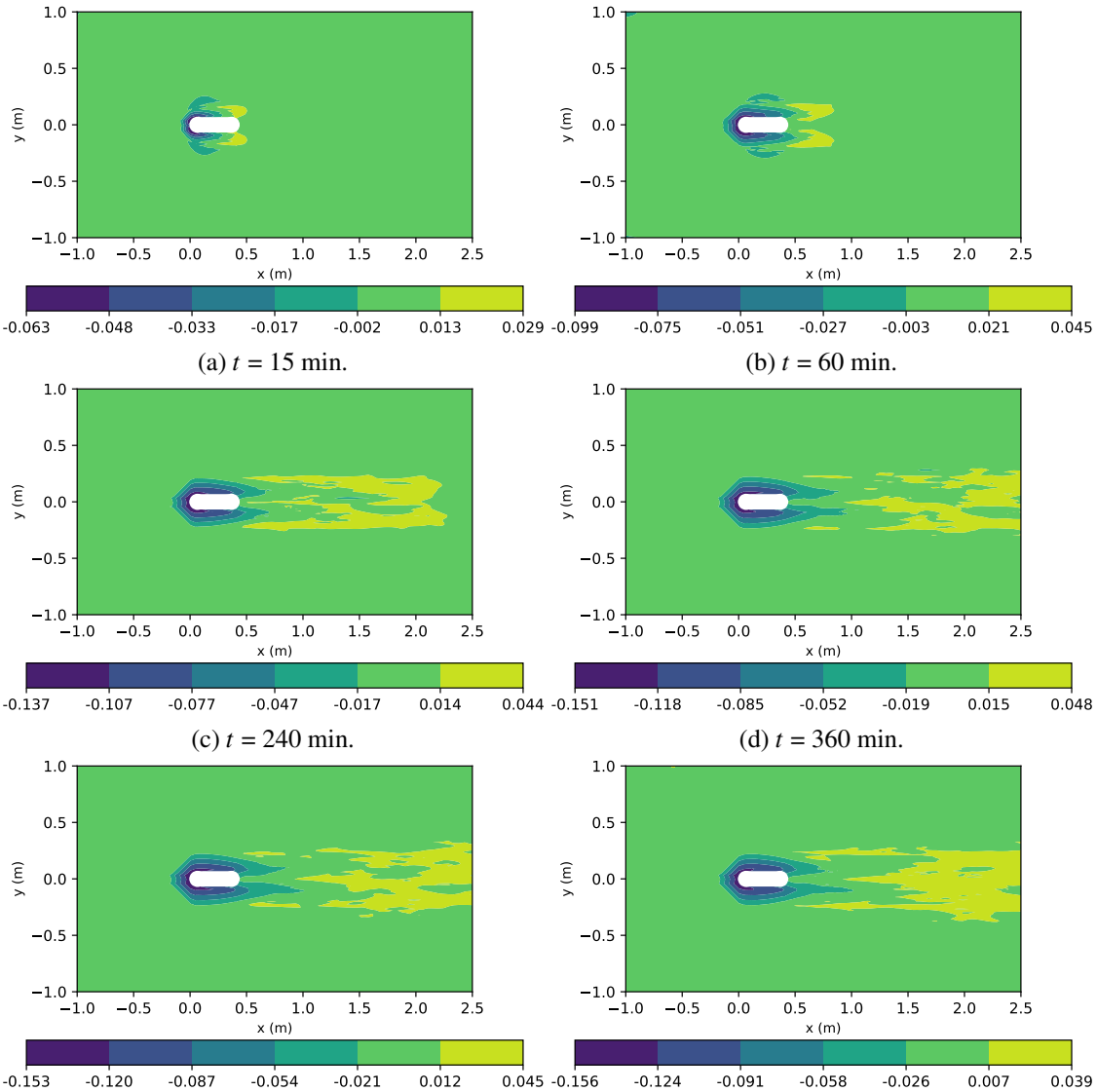

(a) t = 15 min. (b) t = 60 min.

(c) t = 240 min. (d) t = 360 min.

(e) t = 420 min. (f) t = 480 min.

Figure 5.4: Scour hole and deposition region around the oblong bridge pier (dimensions in meters).

From t = 60 (Figure 5.4b) to t = 480 minutes, the simulation exhibited a steady growth of bed scouring at the vicinity of *Pier* 11, which indicates that the acceleration effect, along with dynamics of horseshoe vortices, was a significant contribution to entrainment of sediment on the bed. The sediment transported from the pier's vicinity was deposited downstream and it slowly migrated due to periodic shedding of vortices in the wake regions. It is observed that the scour hole contours and the location of the maximum scour area at the upstream side of the pier obtained by means of the numerical model markedly coincides with the observed experimentally (Section 4.3).

To better understand the features of the scouring process around the oblong bridge pier, it is worth exploring the scoured bed profiles at different azimuth planes. Figure 5.5 depicts the numerical results of the bed profiles during time (for the aforementioned instants) on the longitudinal mid-plane (Figure 5.5a) and on the plane normal to the flow direction (Figure 5.5b).

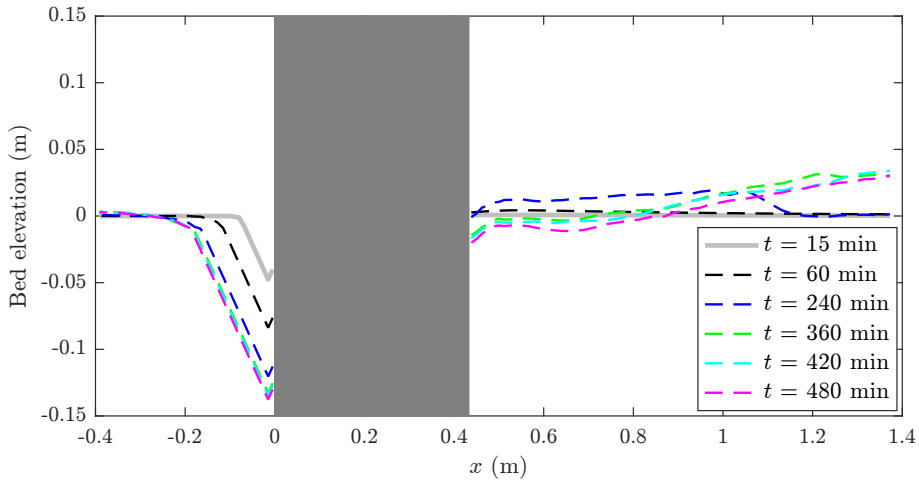

(a) At the pier's longitudinal mid-plane.

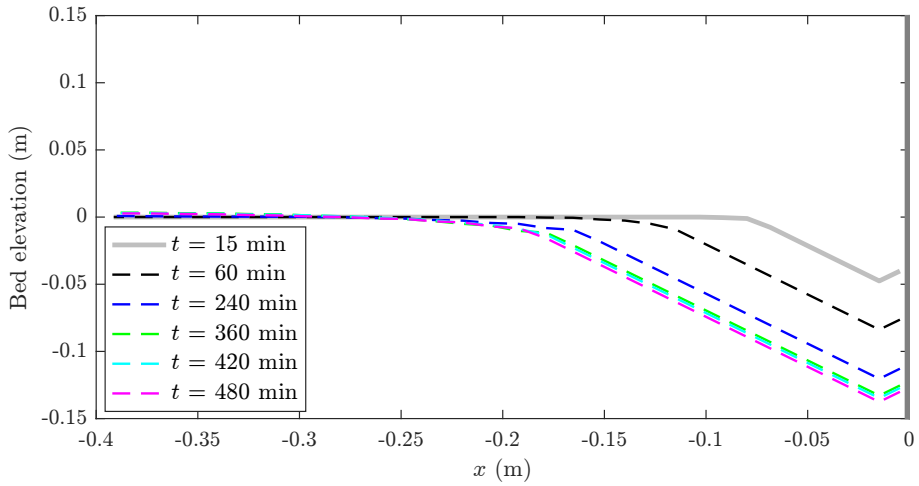

(b) At the plane normal to flow direction.

Figure 5.5: Scoured bed hole profiles on the longitudinal mid-plane (5.5a) and on the plane normal to the flow direction (5.5b). Flow direction: x-axis.

The growth rate of the scouring process slowed down with time. The width of the scour hole at the upstream of the pier ranges between $0.73W$ (t = 15 min) and $2.5W$ (t = 480 min), as can be observed in Figure 5.5a. The maximum scour depth registered along the mid-plane of the oblong pier model, a relevant parameter for the stability analysis of bridge foundations, was confirmed to occur for a distance of 0.015 m from the pier's front (equivalent to a distance of $0.14W$).

Taking into account the upstream scoured hole profile on the pier's mid-plane, the maximum bed hole slope value was computed for each of the analysed temporal instants (t = 15, 60, 240, 360, 420 and 480 minutes) and compared to the angle of repose of the sediment bed material, as well as the obtained for the end of the scouring experiment, $Exp.\ 1U$ (Section 4.3 and Subsection 5.2.4). The slope of the upstream scoured bed profile for t = 480 min was equal to 36.61°, 9% higher than the angle of repose obtained for the end of $Exp.\ 1U$ (as indicated in Subsection 5.2.4). The angles were roughly 10% and 18% higher than the classic 30° repose angle value for wet sand (Matos Fernandes, 2016) for t = 5.9 days and t = 480 min, respectively.

5.2.6.4 Bed shear stress

Contours of the normalized mean bed shear stress (τ/τ_m) around the oblong bridge pier are given in Figure 5.6, being τ_m the bed shear stress of the approach flow. It can be observed an initial preponderance of the normalized bed shear stress at the pier lateral sides, which is in accordance with the scouring development (depicted in Figure 5.4a). For the remaining instants, until t = 480 minutes, an increase of τ/τ_m was obtained immediately upstream of the pier, which is indicative of the higher scour depths at the oblong pier's front (Figure 5.6b to 5.6f). Near the upstream edge of the scour hole (the "<" shape), the bed shear stress is smaller than that in the region where horseshoe vortex system occurs, which is in line with the literature (Kirkil *et al.*, 2008).

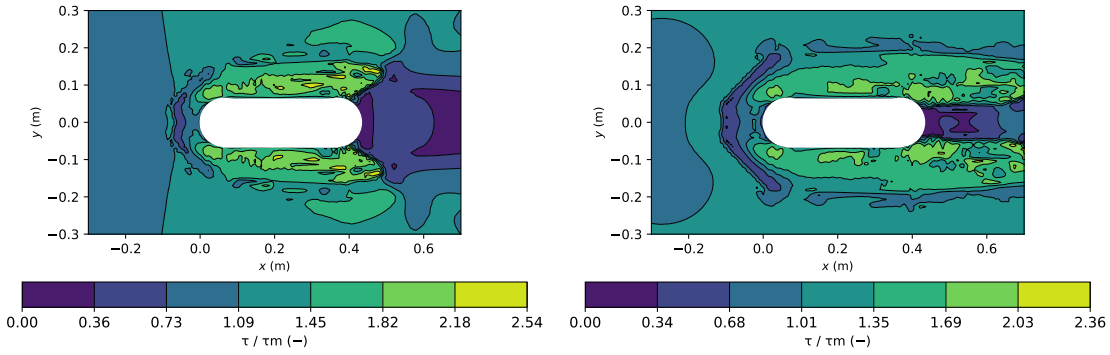

(a) t = 15 min. (b) t = 60 min.

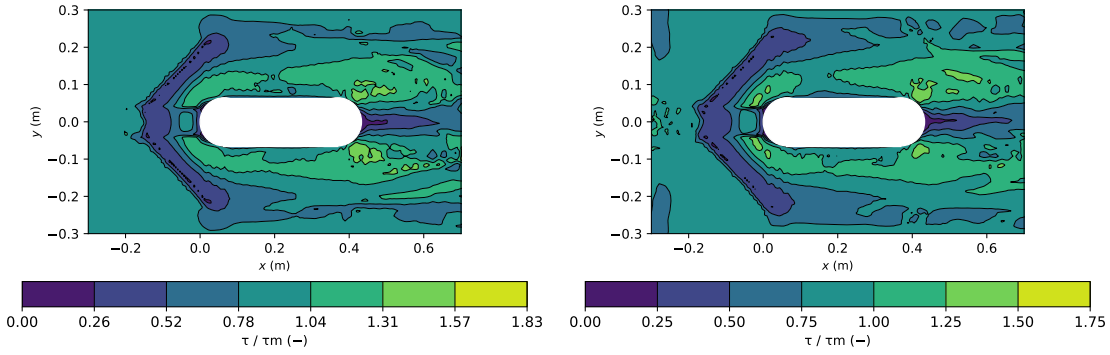

(c) t = 240 min. (d) t = 360 min.

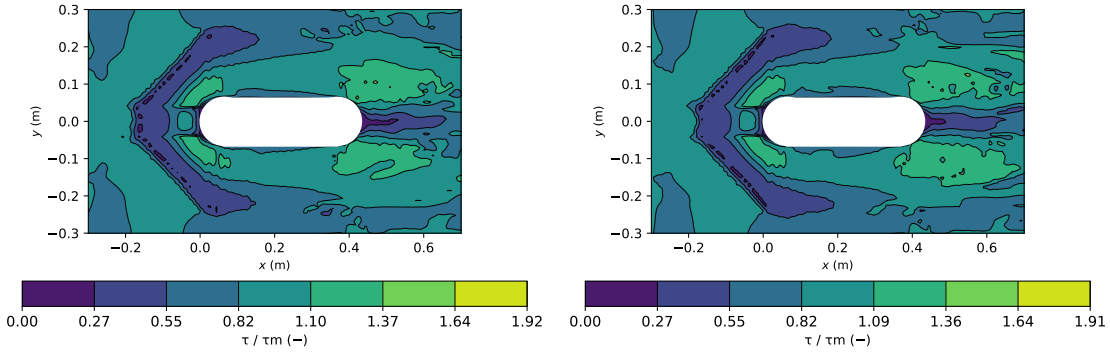

(e) t = 420 min. (f) t = 480 min.

Figure 5.6: Normalized bed shear stress (τ/τ_m) contours around the oblong bridge pier.

5.2.7 Conclusions

Local scouring results carried out in an experimental facility were used to assess the performance of a CFD numerical model, regarding the bed morphology and the bed shear stress around an oblong bridge pier, as well as to get information related to uncertainties in what concerns their prediction. The laboratory experiments performed jointly with numerical simulations showed that maximum scouring and dynamic flow characteristics near the oblong bridge pier are quite similar when a proper calibration of the numerical model is undertaken.

The numerical simulations were carried out using the CFD tool SSIIM and were designed to get insights on key particularities of flow and scouring characteristics, not all simultaneously possible when conducting a local scouring experiment. For example, the time and space distribution of the bed shear stress and scoured bed hole. Detailed measurements of the full geometry of the bed morphology and the bed shear stress at the vicinity of a 0.11 m wide oblong pier were computed.

Regarding the local scouring simulations, it is possible to conclude that the SSIIM model, properly calibrated and validated with the laboratory data (Section 4.3), predicted with a significant accuracy the measured scour depths (with an average relative error less than 3%) using reasonable computation times.

5.2.8 Data availability statement

Some or all data, models, or code that support the findings of this study are available from the corresponding author upon reasonable request.

5.2.9 Acknowledgements

The first author acknowledges the financial support from the Portuguese Foundation for Science and Tecnology (FCT), through the PhD scholarship PD/BD/127798/2016, in the framework of the Doctoral Program INFRARISK – “Analysis and Mitigation of Risks in Infrastructures”. The authors thank FCT for the funding to this research with project reference UID/Multi/04423/2019.

Chapter 6

Conclusions and Future Research

6.1 Main Conclusions

6.1.1 General considerations

The present document comprises six chapters. Chapter 1, Introduction, specified the structure of the study in three modules, from which the results are summarized in the present Chapter 6. "A Review of Bridge Scour Research", exposed in Chapter 2, covered the main issues associated with scour problem, such as type of erosion, scour process, parameters and prediction; numerical modelling, monitoring and risk assessment. The review undertaken culminated in the selection of key equations and methodology in accordance with their relevance and actual practice. Highlights were given to Equation 2.7 and 2.8 for predicting the equilibrium scour depth in both laboratory and field environments; to Figure 2.2 that depicts the main flow features around a circular pier; and to Figure 2.15 which summarizes the main steps in a numerical simulation applied for a bridge pier scour problem.

This PhD investigation comprised three key research modules that contributed to improve the prediction of the bridge scour phenomenon. First, a risk-based methodology was developed to allow bridge engineers to assess the vulnerability to scouring at bridge pier foundations. This methodology was calibrated and validated using valuable field case study data from a Portuguese bridge (Chapter 3). Then, a comprehensive experimental campaign was undertaken to characterize the flow field and the bed morphology in the vicinity of oblong bridge pier models (Chapter 4). This can be considered as a key contribution to the knowledge of morphological stability of the riverbed around bridge foundations, in addition to being useful for the calibration and validation of numerical modelling studies. Finally, numerical modelling of the turbulent flow field and scour patterns around a bridge pier model was undertaken using this study's experimental data of Chapter 4 for calibration purposes (Chapter 5). Although this module was not explored to the same level of detail as the other two, it is a subject that is sparking a growing interest in the academia and industry, thus highly relevant to this dissertation.

This PhD study carries innovative methodological and analytical value with the purpose of reaching cost-effective solutions in the concept, design and maintenance stages of bridges. The

scientific production was strongly considered, such that four conferences presentations (Appendix D) were targeted for publishing and five scientific journal papers were framed: one published in "Engineering Structures", one submitted in "Journal Hydrologic Engineering" and three under preparation for submission. This section highlights the contributions of each research module.

6.1.2 *Risk-based Analysis*

The contribution of this module should be highlighted as a new and pragmatic methodology for assessing risks associated with scour at bridge piers founded on alluvial riverbeds, which is the most onerous foundation stratum for this type of scouring process. This methodology is based on a multidisciplinary analysis which covers concepts from the large branches of civil engineering such as structural, hydraulics and geotechnical areas of expertise. Furthermore, the proposed methodology is a potential useful tool that can be considered to be incorporated into regular bridge inspection schedules, as well as being used in the hydraulic design of new infrastructures since it can help to understand and evaluate their vulnerability to scouring effects.

The proposed risk-based methodology comprises three steps: (i) hydrological modelling of extreme events (hazards); (ii) computation of flow and scour parameters to model river behaviour; and (iii) assessment of bridge scour risk by associating its relative scour depth with the priority factor of such infrastructure (vulnerability) and assigning a qualitative evaluation of the scour risk rating (level of risk). A Portuguese bridge over Douro river, the new Hintze Ribeiro bridge, was selected for validation of the developed methodology. This bridge was elected as case study after an extensive analysis of hydrological and bed level monitoring data available and among the thirteen Portuguese bridges indicated in Appendix B.

In the first step, the innovative hydrological $modified\ MM$ method was developed for providing reliable estimates of extreme discharge flows approaching hydraulic infrastructures (such as bridges) that accounts for model and parameter uncertainties, inherent to any mathematical evaluation. An extrapolation technique was developed to overcome the difficulty of satisfying the minimum required sample size for the application of flood frequency analysis on hydrological time series data. The developed technique was validated with field data. The results of this first step confirm the importance of considering the variability of hydrological events, which should be taken into account in the early stages of the design (instead of the standard model selection, MS). The proposed $modified\ MM$ method resulted in a better estimate of the design floods approaching the case study bridge as depicted in figures 3.13 and 3.12. This method accounts for model uncertainty, which derives from some degree of inadequacy of models to represent such real-world phenomena. This part of the study is included in the paper submitted to "Journal of Hydrologic Engineering".

In the second step, the methodology consolidates the relationship between the recent advances on scour depth prediction and its applicability on engineering practices by computing flow and scour variables with the 1D HEC-RAS model. The determination of the maximum scour depth, using the scour module available within HEC-RAS, proved to reasonably reproduce the scour phenomenon, with safety margins, namely at the new Hintze Ribeiro bridge foundation $P2$. Three other well-established formulations were also considered when evaluating the performance of

the HEC-RAS model. The bridge scour prediction computed by the HEC-RAS scour module over-predicted the other three estimates, whilst being in accordance with the literature and with the observed scour depth, as can be seen in Figure 3.21.

The third step of the proposed methodology provides oriented measures and practical recommendations for reducing the vulnerability and enhancing the capacity of infrastructures in coping with scouring effects based on the resulting qualitative risk rating. Specific management strategies are also suggested and recommended for the obtaining risk rating level. For the case study bridge, the frequency of underwater inspections currently being undertaken by the Portuguese authority for the conservation of bridges, once in every three years, was deemed appropriate for the level of risk obtained using the proposed methodology. Main results of the application of this methodology to the case study bridge are represented in Figure 3.22.

These advances and results are provided in the scientific paper "Risk-based methodology for scour analysis at bridge foundations", published in "Engineering Structures" (Bento *et al.*, 2020).

6.1.3 *Experimental Study*

The laboratory experimental campaign was carried out in the facility described in Section 4.2 and the set of experiments detailed in sections 4.3 and 4.4, and in Appendix C.

The main contribution of the "Experimental Study" module is the proposed comprehensive measurement system for the three-dimensional characterization of the scouring effects and its respective ensemble. The characterization comprises (i) the application of close-range photogrammetry technique and (ii) the use of the Kinect V2 sensor at two moments of the local scouring experiments: at the flat (initial) and the eroded (final) bed stages. With the use of these image-based techniques, detailed 3D models of the geometry of the scour hole and deposition zone in the vicinity of two transitional oblong bridge pier models were obtained with significant accuracy levels regardless of the type of approach flow regime, as detailed in Section 4.3.

This module also offers an innovative methodology capable of performing a continuous monitoring of the sand-pier border at the pier's wall surface throughout the scouring process. For that purpose, a continuous monitoring of the sand-pier border evolution was enabled by the acquisition of synchronized images from four submersible cameras, described in sections 4.2 and 4.3, and in Appendix C.3. The detection of the sand-pier border and the computation of the distance of each pixel to a reference line was performed using a python code specifically developed for the purpose, and employing underwater image processing and computer vision routines. The originality of the methodology raised particular interest and highlighted the need of a continuous monitoring of the scouring phenomenon in experimental environments, taking advantage of the growing development of the technology of submersible cameras and image processing tools. Examples of this characterization are illustrated in Figure 4.28, which provides good results when compared with the point-wise measurements plotted in Figure 4.20a.

The turbulent flow field developed at the vicinity of the bridge pier model was also characterized at the beginning (fixed flat bed) of the scouring process and within the respective developed scour holes (eroded bed experiments). Instantaneous three-dimensional velocity components were

measured by means of a high-resolution acoustic velocimeter for six experiments, under clear water and live bed approach flow regimes, as detailed in Section 4.4. Flow patterns such as the mean velocities and the Reynolds shear stresses were derived, providing useful insights for understanding the flow magnitude and structure for the particularities of each experiment and bed morphology stage (flat *vs* eroded); Figure 4.41 and Figure 4.47 illustrate such parameters for one of the fixed bed experiments ($Exp.\ 1UFbed$).

Throughout the performed study, the hydraulic and scour data and results included: (i) an assessment of the uncertainty of the observations used in the evaluation of relevant variables; (ii) full details of the methods of model evaluation and performance measures undertaken; and (iii) some assessment of the uncertainty associated with the several modelling results.

Measurements of scour and flow during the temporal development of the scour hole were performed successfully. Such experimental campaign led to a considerable amount of data, such as data describing the approaching flow (Figure 4.18 and Figure 4.19 of Section 4.3; Figure 4.33 to Figure 4.38 of Section 4.4), the scour depth evolution (Figure 4.20), the scour hole geometry and deposition regions (figures 4.21 and 4.22), the flow field at flat and eroded bed stages (from Figure 4.41 to Figure 4.52), among others. These results contribute to a valuable database, not only to promote the related studies of scour and flow characterizations around bridge pier models, but also to calibrate and validate the scouring process and the complex flow fields obtained by numerical models, such as Computational Fluid Dynamics (CFD) tools.

Two scientific papers under preparation, namely "Characterizing bridge scour using image-based techniques in laboratory environment" (Section 4.3) and "Experimental characterization of the flow field around oblong bridge piers" (Section 4.4), include the advances and outcomes from the laboratory experimental campaign.

6.1.4 *Numerical Modelling*

Through numerical simulations, the behaviour of the various intervening parameters of the bridge scour processes can be observed. This is a well-known motivation for the growing number of numerical studies in replicating the scouring process. With the recent developments in the methods of modelling and simulation, and the increasing computational capabilities, CFD tools are becoming an everyday tool in engineering practice. On this subject, it is essential to remind the undeniable need for accurate calibration and validation steps using experimental studies. In the present work, the "Numerical Modelling" module made use of the experimental data obtained in the laboratory experimental campaign carried out (sections 4.2, 4.3 and Appendix C) to calibrate numerical simulations of the evolution and development of the scour hole by an exploratory view of future developments not only for research but also for engineering applications.

Numerical simulations were performed by using the CFD tool SSIIM. The simulation results demonstrated that the calibrated numerical model reproduced (with an average relative error less than 3%), with significant accuracy, the bed shear stress and the mechanism of the scour hole formation, in the laboratory environment.

The results, even in an exploratory phase, provide a platform for advancements in the scouring prediction process which, in turn, can shed light on fundamental aspects of the phenomenon that may be more difficult to monitor experimentally, such as the evolution of the bed shear stress at the vicinity of the studied oblong bridge pier models in both time and space dimensions.

One scientific paper, entitled "Numerical simulations of scour development around an oblong bridge pier laboratory model", is under preparation to be submitted to an international scientific journal. Main results are given for the bed shear stress and bed morphology (Figure 5.6 and 5.4) from the numerical simulations performed for the hydraulic and boundary conditions of $Exp.\ 1U$ (presented in Section 4.3).

6.2 Future Research

The study enabled some advances in the knowledge of the scouring phenomenon mechanism through both experimental and numerical approaches. A methodology to evaluate the risks associated with scour at bridge foundations was proposed. Still, a number of aspects have been identified for future research as several questions remain unanswered. This section outlines guidelines for future research work, the key being to strengthen the interconnection of the modules' achievements.

Recent studies have demonstrated that the majority of bridge collapses have occurred for a return period less than the reference period of 100 years (Flint *et al.*, 2017; Proske, 2018; Pizarro *et al.*, 2020), so commonly considered in the design of hydraulic infrastructures worldwide (Arneson *et al.*, 2012; Highways Agency, 2012). Furthermore, some authors identified the need to incorporate a larger number of hydrological and hydraulic variables for a more rigorous evaluation of bridge collapse risk (Lagasse *et al.*, 2013; Pizarro & Tubaldi, 2019). However, this requires the access to reliable field data, given the model and parameter uncertainties related to the estimation of reliable discharge flows approaching hydraulic infrastructures. In the majority of the cases such field data are not easily available, which explains the relatively scarce studies on such topic.

However, collecting hydrological, riverbed data and bridge structural characteristics from the bridge management authority involves many resources and is still a highly time-consuming task. By contrast, the present dissertation took advantage of the provision of bathymetry data and bridge structural characteristics from one of the Portuguese authorities responsible for the conservation of most bridges (Infraestruturas de Portugal) with which the author's institutional affiliations signed a collaboration and information exchange agreement. Streamflow data was partly made accessible also thanks to a collaboration agreement with "Energias de Portugal", the Portuguese private company responsible for the management of the dams considered in the current work. For the remaining data, an extrapolation technique was developed for satisfying the minimum required sample size for a reliable application of the flood frequency analysis technique (Section 3.2). These data allowed the development of a scour risk methodology to evaluate the scouring effects at bridge foundations (Section 3.3), properly validated by a case study bridge. Since valuable data were fortunately available, future works should include:

(i) the application of the proposed scour risk assessment methodology to other bridges in order to further support and validate its potential. Among Portuguese bridge data collected in Appendix B, Duarte Pacheco bridge, crossing an important affluent of the Douro river in Portugal, the Tâmega river, presents relevant flow monitoring data and variability of the bathymetry at the bridge site, as well;

(ii) the incorporation of this methodology into regular bridge inspection schedules is suggested as useful tool for assessing susceptibility of existing bridges to the scouring effects, as well as aiding the hydraulic design of new infrastructures. This would lead to a priority rank of Portuguese bridges in regards to their vulnerability to scouring effects as a way to manage risk and the required steps to minimize/mitigate catastrophic consequences such as its serviceability and ultimately the structural failure of the bridge; and

(iii) improvements to the proposed risk-based methodology should be considered. The computation of the flow and bridge scour parameters and factors can be refined with more sophisticated models, by replacing the 1D HEC-RAS software with the Computational Fluid Dynamics (CFD) tool SSIIM (acronym for Sediment Simulation in Intakes with Multiblock option), as a way to calibrate those models with field data. Other aspect to be added to the methodology is the incorporation of other natural causes of bridge collapses, as discussed in Chapter 2 and detailed in Appendix A, in the quantification of the bridge's priority factor, such as the presence of debris or countermeasures at the foundations-bed level. This aspect is relevant for bridges where scouring effects are deemed identified as an important source of bridge instability.

To pursue the (iii) idea, having availability of calibrated and validated numerical models is of utmost importance. Despite the vast research on bridge scour, the current practices do not sufficiently address the complexities of the processes that trigger the scouring phenomenon. As well summarized by Chiew *et al.* (2020): "Scour, which represents an intriguing and complex engineering problem involving many physical mechanisms and interactions, has motivated a vast amount of research following different but complementary methodological approaches such as experimental, numerical, and field methods." The current practices are thus still insufficient in addressing all the complexities of bridge scour mechanisms.

The aim of the academia has been to understand how the scour develops and which are the main triggering mechanisms and what is the best way to mathematically model it (Pizarro *et al.*, 2020). This still remains an open question, for which image-based characterization techniques, strongly explored in the present work, namely in the laboratory experimental campaign (Section 4.3, Appendix C and Bento *et al.* (2018)), made it possible to shed more light on. A comprehensive measuring system was herein performed by the application of close-range photogrammetry and use of the Kinect V2 sensor, in addition to the continuous measuring of the bed profile at the pier lateral surface through underwater image processing tools and computer vision routines (Section 4.3). The significant levels of accuracy achieved builds trust on these image-based techniques, which

are being increasingly used in indoor applications and also in field environments. Regarding the pursued experimental methodology, the future works may go towards:

(i) the application of the two image-based techniques for other local scouring experiments as well as for field environmental applications due to its proved potential and high levels of accuracy; and

(ii) the improvement of the underwater continuous monitoring technique, in order to make it more intuitive, mainly in the detection of the sand-pier border at the pier's lateral surface. In addition, the extension of its capabilities and results allied to new laboratory experiments would also be useful and pertinent.

The extensive characterization of the turbulent flow field (Section 4.4), by means of a high-resolution acoustic velocimeter, brings insights to the flow patterns around bridge pier models that can be used for further analysis, not only for deriving the associated turbulence intensities but also for the quantification of the turbulence kinetic energy (k). This characterization has been recently published worldwide but its application to an oblong bridge pier model is probably quite new. The former, calculated by the mean square fluctuation components divided by the mean approach velocity, gives a good insight into the behaviour of the unsteady flow field around an obstacle (i.e., the oblong bridge pier model). The latter is associated with the eddies in the turbulent flow; physically, it is characterized by measured root-mean-square (RMS) velocity fluctuations. Both bring output for defining the systematic changes in the flow field associated with the categories of pier scour and the flow regimes for flat and eroded bed cases (as defined in the experimental campaign, see Section 4.1 and Appendix C).

In addition to the valuable datasets obtained through this PhD study, further laboratory experiments are recommended. Technical faults prevented the conclusion of the initially planned experimental campaign, which included a third pier, differing on width and length of the ones tested and various flow shallowness. These experiments can potentially complement the developed experimental study as well as contribute to:

(i) Define the systematic changes in both the scour patterns and the turbulent flow fields associated with the categories of pier scour (narrow *vs* transitional) and the scour conditions (clear water *vs* live bed) at different stages of the scouring phenomena; and

(ii) Generate the bed geometry for calibration and validation purposes of CFD tools.

This is a challenging experimental study since it also combines assumptions regarding spatial and temporal distribution of hydrodynamic and scour variables, which are relevant to support the calibration and validation of numerical models, performed in an exploratory phase in Section 5.2. A set of analysis, taking advantage of the vast experimental data, can be performed and contributes to increase the knowledge on the scouring process, namely:

(i) the assessment of different turbulence models to study the flow field at fixed flat (initial) and eroded (final) beds, such as the Large-Eddy Simulation (LES), Detached-Eddy Simulation

(DES) or hybrid RANS-LES, from tools as the well-known OpenFOAM or the recent LESpier code (Alemi *et al.*, 2019); and

(ii) the extension of the scouring simulation to other bridge pier geometries and flow conditions by exploring the capabilities of the selected SSIIM software, namely for better reproducing the morphological changes at the rear part of the oblong bridge pier model.

Finally, once adequately calibrated with experimental data, the numerical model can be applied to case study field data. The calibration may use the scour geometry and turbulent flow field around the bridge pier model. The bathymetry data retrieved from underwater inspections and the approach flow discharge at case study bridges are valuable sources of information that potentiate the use of numerical modelling for assessing the river behaviour, giving its ability to allow for $3D$ of the flow field and to be incorporated into the risk-based methodology, proposed in this research. In this way, by combining experimental, numerical and field studies, the three modules of research are strongly interconnected, with the ultimate aim of providing comprehensive and improved understanding of the complex bridge scouring processes.

References

AASHTO (2017). *LRFD bridge design specifications, Part I: Sections 1-6*. Washington, DC: American Association of State Highway and Transportation Officials, 8th ed. URL https://store.transportation.org/Common/DownloadContentFiles?id=1648.

ABERLE, J., RENNIE, C. D., ADMIRAAL, D. M. & MUSTE, M. (2017). *Experimental Hydraulics: Methods, Instrumentation, Data Processing and Management: Volume II: Instrumentation and Measurement Techniques*. CRC Press. URL https://doi.org/10.1201/9781315158921.

ACKERMAN, C. T., JENSEN, M. R. & BRUNNER, G. W. (2010). Geospatial capabilities of HEC-RAS for model development and mapping. In: *2nd Joint Federal Interagency Conference, Las Vegas, NV*. URL https://acwi.gov/sos/pubs/2ndJFIC/Contents/1F_Ackerman_3_1_10(2).pdf.

ACKERS, P. & WHITE, W. (1973). *Sediment Transport: A New Approach and Analysis*. Hydraulics Research Station. URL https://books.google.pt/books?id=S9RaOwAACAAJ.

AGHAEE, Y. & HAKIMZADEH, H. (2010). Three dimensional numerical modeling of flow around bridge piers using LES and RANS. *River Flow, Dittrich, Koll, Aberle & Geisenhainer (eds)* , 211–218URL https://izw.baw.de/e-medien/river-flow-2010/PDF/A1/A1_21.pdf.

AGISOFT, L. (2020). *Agisoft Metashape User Manual - Professional Edition, version 1.6*. Agisoft LLC. URL https://www.agisoft.com/pdf/metashape-pro_1_6_en.pdf.

AKAY, KOCYIGIT, B. & YANMAZ (2019). Development of a safety-inspection method for river bridges in Turkey. *Water* **11**(9), 1902. URL https://doi.org/10.3390/w11091902.

ALEMI, M. & MAIA, R. (2016). Numerical simulation of the flow and local scour process around single and complex bridge piers. *International Journal of Civil Engineering* **16**(5), 475–487. URL https://doi.org/10.1007/s40999-016-0137-8.

ALEMI, M., PÊGO, J. P. & MAIA, R. (2019). Numerical simulation of the turbulent flow around a complex bridge pier on the scoured bed. *European Journal of Mechanics - B/Fluids* **76**, 316–331. URL https://doi.org/10.1016/j.euromechflu.2019.03.011.

ÁLVARES, M. T. P. & PIMENTA, M. T. (1998). Erosão hídrica e transporte sólido em pequenas bacias hidrográficas. In: *Atas do 4º Congresso da Água, Associação Portuguesa de Recursos Hídricos (APRH)*. URL https://www.aprh.pt/congressoagua98/files/com/149.pdf.

ANDERSON, T. W. & DARLING, D. A. (1954). A test of goodness of fit. *Journal of the American Statistical Association* **49**(268), 765–769. URL https://doi.org/10.1080/01621459.1954.10501232.

ANDRIĆ, J. M. & LU, D.-G. (2016). Risk assessment of bridges under multiple hazards in operation period. *Safety Science* **83**, 80–92. URL https://doi.org/10.1016/j.ssci.2015.11.001.

ANEES, M. T., ABDULLAH, K., NAWAWI, M., RAHMAN, N. N. N. A., PIAH, A. R. M., ZAKARIA, N. A., SYAKIR, M. & OMAR, A. M. (2016). Numerical modeling techniques for flood analysis. *Journal of African Earth Sciences* **124**, 478–486. URL https://doi.org/10.1016/j.jafrearsci.2016.10.001.

APA (2016). Plano de gestão dos riscos de inundações, região hidrográfica RH3 - Douro. Zonas Críticas: Régua, Porto/Vila Nova de Gaia e Chaves. Agência Portuguesa do Ambiente, I.P. *Departamento de Recursos Hídricos* **PGRI**.

APA (2019). Avaliação preliminar de risco de inundações, região hidrográfica RH3 - Douro. Agência Portuguesa do Ambiente, I.P. *Departamento de Recursos Hídricos* **PGRI**.

APIPATTANAVIS, S., RAJAGOPALAN, B. & LALL, U. (2010). Local polynomial–based flood frequency estimator for mixed population. *Journal of Hydrologic Engineering* **15**(9), 680–691. URL https://doi.org/10.1061/(asce)he.1943-5584.0000242.

ARNESON, L., ZEVENBERGEN, L., LAGASSE, P. & CLOPPER, P. (2012). Evaluating scour at bridges. Tech. rep., United States. Federal Highway Administration. URL https://www.fhwa.dot.gov/engineering/hydraulics/pubs/hif12003.pdf.

ASHRAF, F. U. & FLINT, M. M. (2019). Analysis of peak flow distribution for bridge collapse sites. *Water* **12**(1), 52. URL https://doi.org/10.3390/w12010052.

ATAIE-ASHTIANI, B., BARATIAN-GHORGHI, Z. & BEHESHTI, A. A. (2010). Experimental investigation of clear-water local scour of compound piers. *Journal of Hydraulic Engineering* **136**(6), 343–351. URL https://doi.org/10.1061/(asce)0733-9429(2010)136:6(343).

BADGER, M. E. G. (2007). *Instruction and operation manual*. Subsidiary of Badger Meter, Inc., USA, Nurtinger Strasse 76, 72639 Neuffen, Germany. URL https://www.badgermeter.de/fileadmin/content/badgermeter/media/seiten/Service/Prospekte/Abgekuendigte_Produkte/MID/MID_PA_BA_02_0203.pdf.

BAGNOLD, R. A. (1966). *An approach to the sediment transport problem from general physics*. US government printing office. URL https://pubs.usgs.gov/pp/0422i/report.pdf.

BAKER, R. E. (1986). Local scour at bridge piers in non uniform sediment. *University of Auckland* URL http://worldcat.org/issn/01110136.

BALDASSARRE, G. D., SCHUMANN, G., BATES, P. D., FREER, J. E. & BEVEN, K. J. (2010). Flood-plain mapping: a critical discussion of deterministic and probabilistic approaches. *Hydrological Sciences Journal* **55**(3), 364–376. URL https://doi.org/10.1080/02626661003683389.

BALLIO, F., RADICE, A. & DEY, S. (2010). Temporal scales for live-bed scour at abutments. *Journal of Hydraulic Engineering* **136**(7), 395–402. URL https://doi.org/10.1061/(asce)hy.1943-7900.0000191.

BARANYA, S., OLSEN, N. R. B., STOESSER, T. & STURM, T. (2012). Three-dimensional RANS modeling of flow around circular piers using nested grids. *Engineering Applications of Computational Fluid Mechanics* **6**(4), 648–662. URL http://dx.doi.org/10.1080/19942060.2012.11015449.

BARATA, V. (2001). Memória descritiva e justificatica - Projeto de execução. *Ponte Hintze Ribeiro sobre o rio Douro* **LISCONCEBE**.

BARBETTA, S., CAMICI, S. & MORAMARCO, T. (2017). A reappraisal of bridge piers scour vulnerability: a case study in the Upper Tiber river basin (central Italy). *Journal of Flood Risk Management* **10**(3), 283–300. URL https://doi.org/10.1111/jfr3.12130.

BARKER, R. M. & PUCKETT, J. A. (2013). *Design of Highway Bridges: An LRFD Approach*. John Wiley & Sons, Inc., 3rd edition ed. URL http://eu.wiley.com/WileyCDA/WileyTitle/productCd-0470900660.html.

BAYKAL, C., SUMER, B., FUHRMAN, D., JACOBSEN, N. & FREDSØE, J. (2017). Numerical simulation of scour and backfilling processes around a circular pile in waves. *Coastal Engineering* **122**, 87–107. URL https://doi.org/10.1016/j.coastaleng.2017.01.004.

BAYKAL, C., SUMER, B. M., FUHRMAN, D. R., JACOBSEN, N. G. & FREDSØE, J. (2015). Numerical investigation of flow and scour around a vertical circular cylinder. *Philosophical Transactions of the Royal Society A: Mathematical, Physical and Engineering Sciences* **373**(2033), 20140104. URL https://doi.org/10.1098/rsta.2014.0104.

BEAUDAN, P. & MOIN, P. (1994). Numerical experiments on the flow past a circular cylinder at sub-critical reynolds number. Tech. rep., Stanford Univ. CA Thermosciences Div. URL https://apps.dtic.mil/dtic/tr/fulltext/u2/a289937.pdf.

BEHESHTI, A. A. & ATAIE-ASHTIANI, B. (2010). Experimental study of three-dimensional flow field around a complex bridge pier. *Journal of Engineering Mechanics* **136**(2), 143–154. URL https://doi.org/10.1061/(asce)em.1943-7889.0000073.

BEHESHTI, A. A. & ATAIE-ASHTIANI, B. (2016). Scour hole influence on turbulent flow field around complex bridge piers. *Flow, Turbulence and Combustion* **97**(2), 451–474. URL https://doi.org/10.1007/s10494-016-9707-8.

BENKACI, T. (2019). FFD 2.0. URL https://ch.mathworks.com/matlabcentral/fileexchange/67367-flood-frequency-distribution-ffd-2-0. Accessed: 2019-11-06.

BENTO, A., GOMES, A., PÊGO, J., VISEU, T. & COUTO, L. (Submitted). Improved assessment of maximum streamflow approaching a bridge over douro river. A case study. Submitted in Journal of Hydrologic Engineering.

BENTO, A. M., COUTO, L., PÊGO, J. P. & VISEU, T. (2018). Advanced characterization techniques of the scour hole around a bridge pier model. In: *E3S Web of Conferences*, vol. 40. EDP Sciences. URL https://www.e3s-conferences.org/articles/e3sconf/pdf/2018/15/e3sconf_riverflow2018_05066.pdf.

BENTO, A. M., GOMES, A., VISEU, T., COUTO, L. & PÊGO, J. P. (2020). Risk-based methodology for scour analysis at bridge foundations. *Engineering Structures* **223**, 111115. URL https://doi.org/10.1016/j.engstruct.2020.111115.

BETTESS, R. (2002). A review of predictive methods for general scour. In: *First International Conference on Scour of FoundationsInternational Society of Soil Mech and Foundations*. URL https://hdl.handle.net/20.500.11970/100331.

BEVEN, K. (2006). A manifesto for the equifinality thesis. *Journal of Hydrology* **320**(1-2), 18–36. URL https://doi.org/10.1016/j.jhydrol.2005.07.007.

BEVEN, K. (2019). How to make advances in hydrological modelling. *Hydrology Research* **50**(6), 1481–1494. URL https://doi.org/10.2166/nh.2019.134.

BLENCH, T. (1969). *Mobile-bed Fluviology*. Edmonton, Alta.: University of Alberta Press. URL https://www.uap.ualberta.ca/titles/868-9781772121322-mobile-bed-fluviology.

BORGHEI, S. M., KABIRI-SAMANI, A. & BANIHASHEM, S. A. (2012). Influence of unsteady flow hydrograph shape on local scouring around bridge pier. *Proceedings of the Institution of Civil Engineers - Water Management* **165**(9), 473–480. URL https://doi.org/10.1680/wama.11.00020.

BOURATSIS, P. P., DIPLAS, P., DANCEY, C. L. & APSILIDIS, N. (2013). High-resolution 3*D* monitoring of evolving sediment beds. *Water Resources Research* **49**(2), 977–992. URL https://doi.org/10.1002/wrcr.20110.

BRANDIMARTE, L. & BALDASSARRE, G. D. (2012). Uncertainty in design flood profiles derived by hydraulic modelling. *Hydrology Research* **43(6)**(6), 753–761. URL https://doi.org/10.2166/nh.2011.086.

BRANDIMARTE, L., PARON, P. & BALDASSARRE, G. D. (2012). Bridge pier scour: A review of processes, measurements and estimates. *Environmental Engineering and Management Journal* **11**(5), 975–989. URL https://doi.org/10.30638/eemj.2012.121.

BREUSERS, H. (1966). Conformity and time scale in two-dimensional local scour. Tech. rep., Hydraulic Research Laboratory, Poona, India. URL http://resolver.tudelft.nl/uuid:3e93d15f-8e86-4917-acf0-8a842ccbb799.

BREUSERS, H. N. C., NICOLLET, G. & SHEN, H. (1977). Local scour around cylindrical piers. *Journal of Hydraulic Research* **15**(3), 211–252. URL http://dx.doi.org/10.1080/00221687709499645.

BRIAUD, J.-L. (2015). Scour depth at bridges: Method including soil properties. II: Time rate of scour prediction. *Journal of Geotechnical and Geoenvironmental Engineering* **141**(2), 04014105. URL https://doi.org/10.1061/(asce)gt.1943-5606.0001223.

BRIAUD, J.-L., BRANDIMARTE, L., WANG, J. & D'ODORICO, P. (2007). Probability of scour depth exceedance owing to hydrologic uncertainty. *Georisk: Assessment and Management of Risk for Engineered Systems and Geohazards* **1**(2), 77–88. URL https://doi.org/10.1080/17499510701398844.

BRIAUD, J.-L., GARDONI, P. & YAO, C. (2014). Statistical, risk, and reliability analyses of bridge scour. *Journal of Geotechnical and Geoenvironmental Engineering* **140**(2), 04013011. URL https://doi.org/10.1061/(asce)gt.1943-5606.0000989.

BRILEY, W. R. & MCDONALD, H. (1981). Computation of three-dimensional horseshoe vortex flow using the Navier-Stokes equations. In: *Seventh International Conference on Numerical Methods in Fluid Dynamics*. Springer Berlin Heidelberg, pp. 91–98. URL https://doi.org/10.1007/3-540-10694-4_11.

BROOKS, H. (1963). Discussion on "boundary shear stresses in curved trapezoidal channels", by Ippen, AT & Drinker, PA. *J. Hydraulic Div., ASCE* **89**(3), 327–333. URL https://cedb.asce.org/CEDBsearch/record.jsp?dockey=0012592.

BROWNLIE, W. R. (1982). *Prediction of Flow Depth and Sediment Discharge in Open Channels*. Ph.D. thesis, California Institute of Technology. URL https://resolver.caltech.edu/CaltechETD:etd-12192006-152351.

BRUNNER, G. W. (2016). HEC-RAS River analysis system hydraulic reference manual. Version 5.0. Tech. rep., US Army Corps of Engineers, Hydrological Engineering Center (HEC), CA. URL https://www.hec.usace.army.mil/software/hec-ras/documentation/HEC-RAS%205.0%20Reference%20Manual.pdf.

BUMHAM, K. P. & ANDERSON, D. R. (2002). *Model Selection and Multimodel Inference: A Practical Information - Theoretic Approach*. Springer. URL https://www.xarg.org/ref/a/B000QCQT0C/.

CALVER, A., STEWART, E. & GOODSELL, G. (2009). Comparative analysis of statistical and catchment modelling approaches to river flood frequency estimation. *Journal of Flood Risk Management* **2**(1), 24–31. URL https://doi.org/10.1111/j.1753-318x.2009.01018.x.

CARDOSO, A. H. (1982). Canal de inclinação variável: Descrição do tanque de montante, canal propriamente dito, tanque de jusante e circuito de retorno (in Portuguese). Tech. Rep. Proc. 62/32/3, Laboratório Nacional de Engenharia Civil (LNEC), Lisbon, Portugal.

CARDOSO, A. H. & CUNHA, L. V. D. (1998). *Hidráulica fluvial*. Av. de Berna, Lisboa: Fundação Calouste Gulbenkian.

CARDOSO, A. H., GRAF, W. H. & GUST, G. (1989). Uniform flow in a smooth open channel. *Journal of Hydraulic Research* **27**(5), 603–616. URL https://doi.org/10.1080/00221688909499113.

CASTELLARIN, A., KOHNOVÁ, S., GAÁL, L., FLEIG, A., SALINAS, J., TOUMAZIS, A., KJELDSEN, T. & MACDONALD, N. (2012). Review of applied-statistical methods for flood-frequency analysis in Europe. *NERC/Centre for Ecology & Hydrology* **122pp (ESSEM COST Action ES0901)**. URL http://www.cost.eu/module/download/33272.

CEP (2002). Civil Engineering Disasters – Collapse of bridges. https://www.engineeringcivil.com/wp-content/uploads/2008/03/collapse_of_bridges_111.jpg.

CHABERT, J. & ENGELDINGER, P. (1956). Etude des affouillements autour des piles des ponts. *Laboratoire National d'Hydraulique, Chatou, France (in French)* **118**.

CHANG, C.-H., TUNG, Y.-K. & YANG, J.-C. (1994). Monte carlo simulation for correlated variables with marginal distributions. *Journal of Hydraulic Engineering* **120**(3), 313–331. URL https://doi.org/10.1061/(asce)0733-9429(1994)120:3(313).

CHANG, K. & CONSTANTINESCU, G. (2015). Numerical investigation of flow and turbulence structure through and around a circular array of rigid cylinders. *Journal of Fluid Mechanics* **776**, 161–199. URL https://doi.org/10.1017/jfm.2015.321.

CHANG, W.-Y., CONSTANTINESCU, G., LIEN, H.-C., TSAI, W.-F., LAI, J.-S. & LOH, C.-H. (2013). Flow structure around bridge piers of varying geometrical complexity. *Journal of Hydraulic Engineering* **139**(8), 812–826. URL https://doi.org/10.1061/(asce)hy.1943-7900.0000742.

CHANG, W. Y., LAI, J. S. & YEN, C. L. (1999). Simulation of scour depth evolution at pier nose. In: *Water Resources Publications: Proceedings of the 1999 international water resources engineering conference*. Highlands Ranch, CO. URL http://ajbasweb.com/old/ajbas/2011/July-2011/167-173.pdf.

CHEE, R. K. W. (1982). Live-bed scour at bridge piers. *Publication of: Auckland University, New Zealand* **290**. URL http://worldcat.org/issn/01110136.

CHEN, H. (2002). Numerical simulation of scour around complex piers in cohesive soil. In: *First International Conference on Scour of Foundations International Society of Soil Mech and Foundations*. URL https://core.ac.uk/download/pdf/326241061.pdf.

CHEN, L. & WU, G. (2019). Boundary shear flow past a cylinder near a wall. *Applied Ocean Research* **92**, 101923. URL https://doi.org/10.1016/j.apor.2019.101923.

CHEN, X., LI, Y., NIU, X., LI, M., CHEN, D. & YU, X. (2011). A general two-phase turbulent flow model applied to the study of sediment transport in open channels. *International Journal of Multiphase Flow* **37**(9), 1099–1108. URL https://doi.org/10.1016/j.ijmultiphaseflow.2011.05.013.

CHENG, N.-S., WEI, M., LU, Y. & CHIEW, Y.-M. (2020). Evaluation of sediment gradation effects on clear-water pier scour with densimetric froude number. *Journal of Engineering Mechanics* **146**(12), 04020133. URL https://doi.org/10.1061/(asce)em.1943-7889.0001871.

CHIEW, Y. M. (1984). *Local scour at bridge piers*. Ph.D. thesis, University of Auckland. URL http://hdl.handle.net/2292/2520.

CHIEW, Y.-M. (1995). Mechanics of riprap failure at bridge piers. *Journal of Hydraulic Engineering* **121**(9), 635–643. URL https://doi.org/10.1061/(asce)0733-9429(1995)121:9(635).

CHIEW, Y.-M., LAI, J.-S. & LINK, O. (2020). Experimental, numerical and field approaches to scour research. *Water* **12**(6), 1749. URL https://doi.org/10.3390/w12061749.

CHIEW, Y. M. & MELVILLE, B. W. (1987). Local scour around bridge piers. *Journal of Hydraulic Research* **25**(1), 15–26. URL https://doi.org/10.1080/00221688709499285.

CHOURASIYA, S., MOHAPATRA, P. & TRIPATHI, S. (2017). Non-intrusive underwater measurement of mobile bottom surface. *Advances in Water Resources* **104**, 76–88. URL https://doi.org/10.1016/j.advwatres.2017.03.009.

CHOW, V. T. (1959). *Open-channel hydraulics*. McGraw-Hill civil engineering series. McGraw-Hill. URL https://books.google.pt/books?id=OwZSAAAAMAAJ.

CHOW, V. T., MAIDMENT, D. R. & MAYS, L. W. (1988). *Applied Hydrology*. McGraw-Hill international editions. McGraw-Hill. URL https://books.google.pt/books?id=rY_yMgEACAAJ.

COLEMAN, S. E. (2005). Clearwater local scour at complex piers. *Journal of Hydraulic Engineering* **131**(4), 330–334. URL https://doi.org/10.1061/(asce)0733-9429(2005)131:4(330).

COLEMAN, S. E. & MELVILLE, B. W. (2001). Case study: New zealand bridge scour experiences. *Journal of Hydraulic Engineering* **127**(7), 535–546. URL https://doi.org/10.1061/(asce)0733-9429(2001)127:7(535).

COOK, W., BARR, P. J. & HALLING, M. W. (2015). Bridge failure rate. *Journal of Performance of Constructed Facilities* **29**(3). URL https://doi.org/10.1061/(asce)cf.1943-5509.0000571.

CROTTI, G., ISIDORI, D., CIGADA, A., BALLIO, F., INZOLI, F., CONCETTONI, E. & CRISTALLI, C. (2016). A hydraulic monitoring system on a bridge over the river Esino, italy. *Journal of Civil Structural Health Monitoring* **6**(3), 377–384. URL https://doi.org/10.1007/s13349-016-0179-2.

CUNNANE, C. (1989). *Statistical Distributions for Flood Frequency Analysis*. Operational hydrology report. Secretariat of the World Meteorological Organization. URL https://books.google.pt/books?id=MbcPAQAAIAAJ.

D'AGOSTINO, R. (1986). *Goodness-of-Fit-Techniques*. Statistics: A Series of Textbooks and Monographs. Taylor & Francis. URL https://books.google.com.br/books?id=1BSEaGVBj5QC.

DANIELS, J., HUGHES, D., RAMEY, G. E. & HUGHES, M. L. (2007). Effects of bridge pile bent geometry and levels of scour and P loads on bent pushover loads in extreme flood/scour events. *Practice Periodical on Structural Design and Construction* **12**(2), 122–134. URL https://doi.org/10.1061/(asce)1084-0680(2007)12:2(122).

DARGAHI, B. (1989). The turbulent flow field around a circular cylinder. *Experiments in Fluids* **8**(1-2), 1–12. URL https://doi.org/10.1007/bf00203058.

DASTORANI, M. T., KOOCHI, J. S., DARANI, H. S., TALEBI, A. & RAHIMIAN, M. H. (2013). River instantaneous peak flow estimation using daily flow data and machine-learning-based models. *Journal of Hydroinformatics* **15**(4), 1089–1098. URL https://doi.org/10.2166/hydro.2013.245.

DATE, A. (2009). *Introduction to Computational Fluid Dynamics*. Cambridge University Press. URL https://books.google.pt/books?id=XEpoPwAACAAJ.

DENG, G. B. & PIQUET, J. (1992). Navier-Stokes computations of horseshoe vortex flows. *International Journal for Numerical Methods in Fluids* **15**(1), 99–124. URL https://doi.org/10.1002/fld.1650150108.

DENG, L. & CAI, C. (2007). Applications of fiber optic sensors in civil engineering. *Structural Engineering and Mechanics* **25**(5), 577–596. URL https://www.dengteam.com/uploadfile/2017/0927/20170927034407790.pdf.

DENG, L., WANG, W. & YU, Y. (2016). State-of-the-art review on the causes and mechanisms of bridge collapse. *Journal of Performance of Constructed Facilities* **30**(2), 04015005. URL https://doi.org/10.1061/(asce)cf.1943-5509.0000731.

DEY, S. (2014). *Fluvial Hydrodynamics. Hydrodynamic and Sedimnet Transport Phenomena*. Springer Berlin Heidelberg. URL https://doi.org/10.1007/978-3-642-19062-9.

DEY, S. & RAIKAR, R. V. (2007a). Characteristics of horseshoe vortex in developing scour holes at piers. *Journal of Hydraulic Engineering* **133**(4), 399–413. URL https://doi.org/10.1061/(asce)0733-9429(2007)133:4(399).

DEY, S. & RAIKAR, R. V. (2007b). Clear-water scour at piers in sand beds with an armor layer of gravels. *Journal of Hydraulic Engineering* **133**(6), 703–711. URL https://doi.org/10.1061/(asce)0733-9429(2007)133:6(703).

DIAB, R., ZANKE, U. & LINK, O. (2010). 3*D* turbulent flow field at square pier in a gravel scour hole. In: *Proceedings of the River Flow 2010 Conference, Braunschweig, Germany*. URL https://izw.baw.de/e-medien/river-flow-2010/PDF/A5/A5_07.pdf.

DIAB, R. M. A. E. A. (2011). *Experimental Investigation on scouring around piers of different shape and alignment in gravel*. Ph.D. thesis, TU Darmstadt, Darmstadt, Germany. URL https://tuprints.ulb.tu-darmstadt.de/id/eprint/2561.

DIAS, A. J., FAEL, C. S. & NÚÑEZ-GONZÁLEZ, F. (2019). Effect of debris on the local scour at bridge piers. *IOP Conference Series: Materials Science and Engineering* **471**, 022024. URL https://doi.org/10.1088/1757-899x/471/2/022024.

DTMN (2013). *Bridge scour manual*. Department of Transport and Main Roads, State of Queensland, Australia. URL https://www.tmr.qld.gov.au/business-industry/Technical-standards-publications/Bridge-scour-manual.

DUANE, C. B. (1971). Close-range camera calibration. *Photogramm. Eng* **37**(8), 855–866. URL https://www.asprs.org/wp-content/uploads/pers/1971journal/aug/1971_aug_855-866.pdf.

DUBOYS, P. (1879). Le Rhône et les rivières à lit affouillable. In: *Annales des ponts et chaussees*, vol. 18(5). URL https://ccfr.bnf.fr/portailccfr/ark:/06871/0011318881.

DURÃO, D. F. G., HEITOR, M. V. & PEREIRA, J. C. F. (1988). Measurements of turbulent and periodic flows around a square cross-section cylinder. *Experiments in Fluids* **6**(5), 298–304. URL https://doi.org/10.1007/bf00538820.

EATON, B. C. & CHURCH, M. (2010). A rational sediment transport scaling relation based on dimensionless stream power. *Earth Surface Processes and Landforms* **36**(7), 901–910. URL https://doi.org/10.1002/esp.2120.

EINSTEIN, H. A. *et al.* (1950). *The bed-load function for sediment transportation in open channel flows*, vol. 1026. US Department of Agriculture Washington DC. URL https://naldc.nal.usda.gov/download/CAT86201017/PDF.

ELLINGWOOD, B. R. (2001). Acceptable risk bases for design of structures. *Progress in Structural Engineering and Materials* **3**(2), 170–179. URL https://doi.org/10.1002/pse.78.

ENGELUND, F. & FREDSØE, J. (1976). A sediment transport model for straight alluvial channels. *Hydrology Research* **7**(5), 293–306. URL https://doi.org/10.2166/nh.1976.0019.

ENGELUND, F. & HANSEN, E. (1967). A monograph on sediment transport in alluvial streams. *Technical University of Denmark 0stervoldgade 10, Copenhagen K*. URL http://resolver.tudelft.nl/uuid:81101b08-04b5-4082-9121-861949c336c9.

ESCAURIAZA, C., PAOLA, C. & VOLLER, V. R. (2017). Computational models of flow, sediment transport and morphodynamics in rivers. In: *Gravel-Bed Rivers*. John Wiley & Sons, Ltd, pp. 1–31. URL https://doi.org/10.1002/9781118971437.ch1.

ETTEMA, R. (1976). *Influence of Bed Material Gradation on Local Scour*. Department of Civil Engineering: Report. University of Auckland. URL https://books.google.pt/books?id=Z3AIyQEACAAJ.

ETTEMA, R. (1980). Scour at bridge piers. Tech. rep., University of Auckland. URL https://trid.trb.org/view/171850.

ETTEMA, R., CONSTANTINESCU, G. & MELVILLE, B. W. (2017). Flow-field complexity and design estimation of pier-scour depth: Sixty years since Laursen and Toch. *Journal of Hydraulic Engineering* **143**(9), 03117006. URL https://doi.org/10.1061/(asce)hy.1943-7900.0001330.

ETTEMA, R., KIRKIL, G. & CONSTANTINESCU, G. (2006a). Investigation of the velocity and pressure fluctuations distributions inside the turbulent horseshoe vortex system around a circular bridge pier. In: *River Flow 2006*. Taylor & Francis, pp. 709–718. URL https://doi.org/10.1201/9781439833865.ch74.

ETTEMA, R., KIRKIL, G. & MUSTE, M. (2006b). Similitude of large-scale turbulence in experiments on local scour at cylinders. *Journal of Hydraulic Engineering* **132**(1), 33–40. URL https://doi.org/10.1061/(asce)0733-9429(2006)132:1(33).

ETTEMA, R., MELVILLE, B. W. & CONSTANTINESCU, G. (2011). *Evaluation of bridge scour research: Pier scour processes and predictions*. Washington, DC: Transportation Research Board. URL https://doi.org/10.17226/22886.

ETTEMA, R., MOSTAFA, E. A., MELVILLE, B. W. & YASSIN, A. A. (1998). Local scour at skewed piers. *Journal of Hydraulic Engineering* **124**(7), 756–759. URL https://doi.org/10.1061/(asce)0733-9429(1998)124:7(756).

ETTEMA, R., NAKATO, T. & MUSTE, M. V.-I. (2006c). An illustrated guide for monitoring and protecting bridge waterways against scour. Tech. rep., IIHR-Hydroscience & Engineering, University of Iowa. URL https://www.iihr.uiowa.edu/wp-content/uploads/2013/06/TR449-Guide-for-Monitoring....pdf.

ETTEMA, R., YOON, B., NAKATO, T. & MUSTE, M. (2004a). A review of scour conditions and scour-estimation difficulties for bridge abutments. *KSCE Journal of Civil Engineering* **8**(6), 643–650. URL https://doi.org/10.1007/bf02823555.

ETTEMA, R., YOON, B., NAKATO, T. & MUSTE, M. (2004b). A review of scour conditions and scour-estimation difficulties for bridge abutments. *KSCE Journal of Civil Engineering* **8**(6), 643–650. URL https://doi.org/10.1007/bf02823555.

EXNER, F. (1920). Zur physik der dunen, akad (in German). *Wiss. Wien Math. Naturwiss. Klasse* **129**(2a), 929–952.

EXNER, F. M. (1925). Uber die wechselwirkung zwischen wasser und geschiebe in flussen. *Akad. Wiss. Wien Math. Naturwiss. Klasse* **134**(2a), 165–204. URL https://www.zobodat.at/pdf/SBAWW_134_2a_0165-0203.pdf.

FAEL, C., LANÇA, R. & CARDOSO, A. (2014). Pier shape and alignment effects on local scour. In: *SHF Conference: Small scale morphological evolution of costal, estuarine and river systems*. Societe Hydrotecnique de France. URL https://sapientia.ualg.pt/bitstream/10400.1/9039/1/2014_fael_et_al_2014_pier_shape_and_alignment_effects_on_local_scour.pdf.

FAEL, C., LANÇA, R. & CARDOSO, A. (2016). Effect of pier shape and pier alignment on the equilibrium scour depth at single piers. *International Journal of Sediment Research* **31**(3), 244–250. URL https://doi.org/10.1016/j.ijsrc.2016.04.001.

FALCO, F. D. & MELE, R. (2002). The monitoring of bridges for scour by sonar and sedimetri. *NDT & E International* **35**(2), 117–123. URL https://doi.org/10.1016/s0963-8695(01)00031-7.

FERDOWSI, B., ORTIZ, C. P., HOUSSAIS, M. & JEROLMACK, D. J. (2017). River-bed armouring as a granular segregation phenomenon. *Nature Communications* **8**(1). URL https://doi.org/10.1038/s41467-017-01681-3.

FILLIBEN, J. J. (1975). The probability plot correlation coefficient test for normality. *Technometrics* **17**(1), 111–117. URL https://www.tandfonline.com/doi/abs/10.1080/00401706.1975.10489279.

FINN, J. R., LI, M. & APTE, S. V. (2016). Particle based modelling and simulation of natural sand dynamics in the wave bottom boundary layer. *Journal of Fluid Mechanics* **796**, 340–385. URL https://doi.org/10.1017/jfm.2016.246.

FISCHLER, M. A. & BOLLES, R. C. (1981). Random sample consensus. *Communications of the ACM* **24**(6), 381–395. URL https://doi.org/10.1145/358669.358692.

FLINT, M. M., FRINGER, O., BILLINGTON, S. L., FREYBERG, D. & DIFFENBAUGH, N. S. (2017). Historical analysis of hydraulic bridge collapses in the continental United States. *Journal of Infrastructure Systems* **23**(3), 04017005. URL https://doi.org/10.1061/(asce)is.1943-555x.0000354.

FUHRMAN, D. R., BAYKAL, C., SUMER, B. M., JACOBSEN, N. G. & FREDSØE, J. (2014). Numerical simulation of wave-induced scour and backfilling processes beneath submarine pipelines. *Coastal Engineering* **94**, 10–22. URL https://doi.org/10.1016/j.coastaleng.2014.08.009.

FUKUOKA, S. (2013). *Advances in river sediment research: Proceedings of the 12th International Symposium on River Sedimentation, ISRS 2013, Kyoto, Japan, 2-5 September 2013*. Boca Raton: CRC Press.

GARCÍA, C. M., CANTERO, M. I., NIÑO, Y. & GARCÍA, M. H. (2005). Turbulence measurements with acoustic doppler velocimeters. *Journal of Hydraulic Engineering* **131**(12), 1062–1073. URL https://doi.org/10.1061/(asce)0733-9429(2005)131:12(1062).

GARCIA, M. & PARKER, G. (1991). Entrainment of bed sediment into suspension. *Journal of Hydraulic Engineering* **117**(4), 414–435. URL https://doi.org/10.1061/(asce)0733-9429(1991)117:4(414).

GARDE, R. (1970). Initiation of motion on a hydrody-namically rough surface–critical velocity approach. *Water and Energy International* **27**(3), 271–282. URL http://www.indianjournals.com/ijor.aspx?target=ijor:wei&volume=27&issue=3&article=003.

GAUDIO, R., GRIMALDI, C., TAFAROJNORUZ, A. & CALOMINO, F. (2010). Comparison of formulae for the prediction of scour depth at piers. In: *Proc., 1st IAHR European Division Congress*. Heriot-Watt University Edinburgh, UK. URL https://www.lombardi.ch/it-it/SiteAssets/Publications/1329/Pubb-0510-L-Comparison%20of%20formulae%20for%20the%20prediction%20of%20scour%20depth%20at%20piers.pdf.

GHOSN, M. & JOHNSON, P. (2000). Reliability analysis of bridges under the combined effect of scour and earthquakes. In: *8th ASCE Specialty Conference on Probabilistic Mechanics and Structural Reliability* (CITESEER, ed.). URL http://citeseerx.ist.psu.edu/viewdoc/summary?doi=10.1.1.626.4630.

GILJA, G., KUSPILIĆ, N. & BEKIĆ, D. (2012). Influence of riverbed degradation on bridge safety. In: *Congress of Croatian Builders 2012*. URL https://bib.irb.hr/datoteka/605348.2012_SHG_Utjecaj_degradacije_korita_na_sigurnost_mostova.pdf.

GOERLANDT, F., MONTEWKA, J., KUZMIN, V. & KUJALA, P. (2015). A risk-informed ship collision alert system: Framework and application. *Safety Science* **77**, 182–204. URL https://doi.org/10.1016/j.ssci.2015.03.015.

GOOGLE EARTH (n.d.). Google Earth. https://earth.google.com/web/@41.03823572,-8.2749551,197.80672835a,19361.80108811d,35y,46.03798904h,45.11819578t,0r. Accessed: 2019-12-06.

GOOGLE MAPS (n.d.). Google Maps. https://www.google.com/maps/d/edit?mid=16VVtjOhCKpH4P0oUF2Sb1YtZ4SDBdOPH&usp=sharing. Accessed: 2020-07-31.

GRAF, W. (1998). *Fluvial hydraulics: Flow and transport processes in channels of simple geometry*. Chichester New York: Wiley. URL https://www.wiley.com/en-us/Fluvial+Hydraulics%3A+Flow+and+Transport+Processes+in+Channels+of+Simple+Geometry-p-9780471977148.

GRAF, W. & ISTIARTO, I. (2002). Flow pattern in the scour hole around a cylinder. *Journal of Hydraulic Research* **40**(1), 13–20. URL https://doi.org/10.1080/00221680209499869.

GRIVALSZKI, P., FLEIT, G., BARANYA, S. & JÓZSA, J. (2020). Assessment of CFD model performance for flows around a hydraulic structure of complex geometry. *Periodica Polytechnica Civil Engineering* URL https://doi.org/10.3311/ppci.16709.

GUO, J. (2002). Hunter Rouse and Shields diagram. In: *Advances in Hydraulics and Water Engineering*. World Scientific Publishing Company. URL https://doi.org/10.1142/9789812776969_0200.

HACKL, J., ADEY, B. T., WOŹNIAK, M. & SCHÜMPERLIN, O. (2018). Use of unmanned aerial vehicle photogrammetry to obtain topographical information to improve bridge risk assessment. *Journal of Infrastructure Systems* **24**(1), 04017041. URL https://doi.org/10.1061/(asce)is.1943-555x.0000393.

HAGER, W. H. & OLIVETO, G. (2002). Shields' entrainment criterion in bridge hydraulics. *Journal of Hydraulic Engineering* **128**(5), 538–542. URL https://doi.org/10.1061/(asce)0733-9429(2002)128:5(538).

HAIMES, Y. Y., KAPLAN, S. & LAMBERT, J. H. (2008). Risk filtering, ranking, and management framework using hierarchical holographic modeling. *Risk Analysis* **22(2)**(2), 383–397. URL https://doi.org/10.1111/0272-4332.00020.

HANCU, S. (1971). Sur le calcul des affouillements locaux dams la zone des piles des ponts. In: *XIV IAHR Congress*.

HARRIGAN, E. (2012). *Evaluation of Bridge Scour Research*. Transportation Research Board. URL https://doi.org/10.17226/22714.

HASSAN, M. U., HAYAT, O. & NOREEN, Z. (2019). Selecting the best probability distribution for at-site flood frequency analysis a study of Torne river. *SN Applied Sciences* **1(12)**(12). URL https://doi.org/10.1007/s42452-019-1584-z.

HASSANZADEH, Y. (2007). Evaluation of sediment load in a natural river. *Water International* **32**(1), 145–154. URL https://doi.org/10.1080/02508060708691971.

HIGHWAYS AGENCY (2012). The assessment of scour and other hydraulic actions at highway structures. Tech. Rep. 3(4)., The Stationery Office London, UK. URL http://www.standardsforhighways.co.uk/ha/standards/dmrb/vol3/section4/bd9712.pdf.

HINES, JONATHAN (2008). A comparative study of the simple and fractional step time integration methods for transient incompressible flows. URL http://hdl.handle.net/10012/4162.

HIPÓLITO, J. R. & VAZ, A. (2011). *Hidrologia e recursos hídricos*. Editora Universitária do Instituto Superior Técnico, Lisboa.

HOETING, J. A., MADIGAN, D., RAFTERY, A. E. & VOLINSKY, C. T. (1999). Bayesian model averaging: A tutorial. *Statistical Science* **14**(4), 382–401. URL http://www.jstor.org/stable/2676803.

HOFFMANS, G. & VERHEIJ, H. (1997). *Scour Manual, vol. 96*. A.A. Balkema, Rotterdam, The Netherlands: CRC Press. URL https://books.google.pt/books/about/Scour_Manual.html?id=44VNuHmNWGUC&redir_esc=y.

HÖGE, M., GUTHKE, A. & NOWAK, W. (2019). The hydrologist's guide to Bayesian model selection, averaging and combination. *Journal of Hydrology* **572**, 96–107. URL https://doi.org/10.1016/j.jhydrol.2019.01.072.

HORRITT, M. & BATES, P. (2002). Evaluation of 1*D* and 2*D* numerical models for predicting river flood inundation. *Journal of Hydrology* **268(1-4)**(1-4), 87–99. URL https://doi.org/10.1016/s0022-1694(02)00121-x.

HSIEH, K.-H., LEE, W.-F. & WANG, C.-C. (2010). Bridge foundation failures during typhoon morakot in taiwan. In: *4th Japan-Taiwan Joint Worlshop on Geotechnical Hazards from Large Earthquakes and Heavy Rainfalls*. Sendai, Japan. URL http://ir.csu.edu.tw/bitstream/987654321/1730/1/468-%E5%85%A8%E6%96%87.pdf.

HUANG, C., KERENYI, K. & SHEN, J. (2018). Incorporation of scour uncertainty to current AASHTO LRFD bridge design specifications. In: *Scour and Erosion IX: Proceedings of the 9th International Conference on Scour and Erosion (ICSE 2018), November 5-8, 2018, Taipei, Taiwan*. CRC Press.

HUGHES, D., RAMEY, G. E. & HUGHES, M. L. (2007). Bridge pile bent number of piles and x-bracing system: Impact on pushover capacity as scour increases. *Practice Periodical on Structural Design and Construction* **12**(2), 82–95. URL https://doi.org/10.1061/(asce)1084-0680(2007)12:2(82).

JHA, S. K. & BOMBARDELLI, F. A. (2010). Toward two-phase flow modeling of nondilute sediment transport in open channels. *Journal of Geophysical Research* **115**(F3). URL https://doi.org/10.1029/2009jf001347.

JIA, Y., ALTINAKAR, M. & GUNEY, M. S. (2017). Three-dimensional numerical simulations of local scouring around bridge piers. *Journal of Hydraulic Research* **56**(3), 351–366. URL https://doi.org/10.1080/00221686.2017.1356389.

JIAO, J., YUAN, L., TANG, W., DENG, Z. & WU, Q. (2017). A post-rectification approach of depth images of kinect v2 for 3*D* reconstruction of indoor scenes. *ISPRS International Journal of Geo-Information* **6**(11), 349. URL https://doi.org/10.3390/ijgi6110349.

JOHNSON, P. & TORRICO, E. (1994). Scour around wide piers in shallow water. *Transportation Research Record* **1471**, 66–70. URL http://onlinepubs.trb.org/Onlinepubs/trr/1994/1471/1471-011.pdf.

JOHNSON, P. A. (1992). Reliability-based pier scour engineering. *Journal of Hydraulic Engineering* **118**(10), 1344–1358. URL https://doi.org/10.1061/(asce)0733-9429(1992)118:10(1344).

JOHNSON, P. A. & AYYUB, B. M. (1992). Assessing time-variant bridge reliability due to pier scour. *Journal of Hydraulic Engineering* **118**(6), 887–903. URL https://doi.org/10.1061/(asce)0733-9429(1992)118:6(887).

JOHNSON, P. A., CLOPPER, P. E., ZEVENBERGEN, L. W. & LAGASSE, P. F. (2015). Quantifying uncertainty and reliability in bridge scour estimations. *Journal of Hydraulic Engineering* **141**(7), 04015013. URL https://doi.org/10.1061/(asce)hy.1943-7900.0001017.

JOHNSON, P. A. & DOCK, D. A. (1998). Probabilistic bridge scour estimates. *Journal of Hydraulic Engineering* **124**(7), 750–754. URL https://doi.org/10.1061/(asce)0733-9429(1998)124:7(750).

JOHNSON, P. A. & NIEZGODA, S. L. (2004). Risk-based method for selecting bridge scour countermeasures. *Journal of Hydraulic Engineering* **130**(2), 121–128. URL https://doi.org/10.1061/(asce)0733-9429(2004)130:2(121).

KALLIAS, A. N. & IMAM, B. (2016). Probabilistic assessment of local scour in bridge piers under changing environmental conditions. *Structure and Infrastructure Engineering* **12**(9), 1228–1241. URL https://doi.org/10.1080/15732479.2015.1102295.

KEEFER, T. N. (1971). *The relation of turbulence to diffusion in open-channel flows*. US Department of the Interior, Geological Survey, Water Resources Division. URL https://pubs.usgs.gov/of/1972/0206/report.pdf.

KENDALL, M. (1975). *Rank Correlation Methods, Griffin, London*. Charles Griffin, London, U.K., 4^{th} edition ed.

KENNEY, J. F. & KEEPING, E. S. (1957). *Mathematics of statistics*, vol. 2. Van Nostrand. URL https://books.google.pt/books?id=AH4GxAEACAAJ.

KHOSRONEJAD, A., KANG, S., BORAZJANI, I. & SOTIROPOULOS, F. (2011). Curvilinear immersed boundary method for simulating coupled flow and bed morphodynamic interactions due to sediment transport phenomena. *Advances in Water Resources* **34**(7), 829–843. URL https://doi.org/10.1016/j.advwatres.2011.02.017.

KHOSRONEJAD, A., KANG, S. & SOTIROPOULOS, F. (2012a). Experimental and computational investigation of local scour around bridge piers. *Advances in Water Resources* **37**(2), 73–85. URL https://doi.org/10.1016/j.advwatres.2011.09.013.

KHOSRONEJAD, A., KANG, S. & SOTIROPOULOS, F. (2012b). Experimental and computational investigation of local scour around bridge piers. *Advances in Water Resources* **37**, 73–85. URL https://doi.org/10.1016/j.advwatres.2011.09.013.

KIANG, J. E., GAZOORIAN, C., MCMILLAN, H., COXON, G., COZ, J. L., WESTERBERG, I. K., BELLEVILLE, A., SEVREZ, D., SIKORSKA, A. E., PETERSEN-ØVERLEIR, A., REITAN, T., FREER, J., RENARD, B., MANSANAREZ, V. & MASON, R. (2018). A comparison of methods for streamflow uncertainty estimation. *Water Resources Research* **54**(10), 7149–7176. URL https://doi.org/10.1029/2018wr022708.

KIRBY, A. (2015). *Manual on scour at bridges and other hydraulic structures*. London: CIRIA. URL https://www.ciria.org/Resources/Free_publications/manual_on_scour.aspx.

KIRKIL, G. & CONSTANTINESCU, G. (2009). Nature of flow and turbulence structure around an in-stream vertical plate in a shallow channel and the implications for sediment erosion. *Water Resources Research* **45**(6). URL https://doi.org/10.1029/2008wr007363.

KIRKIL, G. & CONSTANTINESCU, G. (2015). Effects of cylinder reynolds number on the turbulent horseshoe vortex system and near wake of a surface-mounted circular cylinder. *Physics of Fluids* **27**(7), 075102. URL https://doi.org/10.1063/1.4923063.

KIRKIL, G., CONSTANTINESCU, G. & ETTEMA, R. (2009). Detached eddy simulation investigation of turbulence at a circular pier with scour hole. *Journal of Hydraulic Engineering* **135**(11), 888–901. URL https://doi.org/10.1061/(asce)hy.1943-7900.0000101.

KIRKIL, G., CONSTANTINESCU, S. G. & ETTEMA, R. (2008). Coherent structures in the flow field around a circular cylinder with scour hole. *Journal of Hydraulic Engineering* **134**(5), 572–587. URL https://doi.org/10.1061/(asce)0733-9429(2008)134:5(572).

KITE, G. (2019). *Frequency and Risk Analyses in Hydrology*. Water Resources Publications, LLC. URL https://books.google.se/books?id=b9OKxAEACAAJ.

KLEMEŠ, V. (2000). Tall tales about tails of hydrological distributions. II. *Journal of Hydrologic Engineering* **5(3)**(3), 232–239. URL https://doi.org/10.1061/(asce)1084-0699(2000)5:3(232).

KONDOLF, G. M., GAO, Y., ANNANDALE, G. W., MORRIS, G. L., JIANG, E., ZHANG, J., CAO, Y., CARLING, P., FU, K., GUO, Q., HOTCHKISS, R., PETEUIL, C., SUMI, T., WANG, H.-W., WANG, Z., WEI, Z., WU, B., WU, C. & YANG, C. T. (2014). Sustainable sediment management in reservoirs and regulated rivers: Experiences from five continents. *Earth's Future* **2**(5), 256–280. URL https://doi.org/10.1002/2013ef000184.

KOTHYARI, U. C., HAGER, W. H. & OLIVETO, G. (2007). Generalized approach for clear-water scour at bridge foundation elements. *Journal of Hydraulic Engineering* **133**(11), 1229–1240. URL https://doi.org/10.1061/(asce)0733-9429(2007)133:11(1229).

KOTHYARI, U. C., KUMAR, A. & JAIN, R. K. (2014). Influence of cohesion on river bed scour in the wake region of piers. *Journal of Hydraulic Engineering* **140**(1), 1–13. URL https://doi.org/10.1061/(asce)hy.1943-7900.0000793.

KOWALIK, A. (2009). Risk-based bridge evaluations — A Texas perspective. In: *Structures Congress 2009*. American Society of Civil Engineers. URL https://doi.org/10.1061/41031(341)51.

KUMAR, A., KOTHYARI, U. C. & RAJU, K. G. R. (2012). Flow structure and scour around circular compound bridge piers – a review. *Journal of Hydro-environment Research* **6**(4), 251–265. URL https://doi.org/10.1016/j.jher.2012.05.006.

KUMAR, V., RAJU, K. G. R. & VITTAL, N. (1999). Reduction of local scour around bridge piers using slots and collars. *Journal of Hydraulic Engineering* **125**(12), 1302–1305. URL https://doi.org/10.1061/(asce)0733-9429(1999)125:12(1302).

KUSUMASTUTI, D. I., STRUTHERS, I., SIVAPALAN, M. & REYNOLDS, D. A. (2007). Threshold effects in catchment storm response and the occurrence and magnitude of flood events: implications for flood frequency. *Hydrology and Earth System Sciences* **11**(4), 1515–1528. URL https://doi.org/10.5194/hess-11-1515-2007.

KWAK, D., ROGERS, S. E., KAUL, U. K. & CHANG, J. L. C. (1986). A numerical study of incompressible juncture flows. In: *Tenth International Conference on Numerical Methods in Fluid Dynamics*. Springer-Verlag, pp. 398–402. URL https://doi.org/10.1007/bfb0041823.

KYROUSI, F. (2017). *Large eddy simulations of gravity currents ovewr erodible beds*. Ph.D. thesis, Dipartimento di Ingegneria e Architettura, University of Trieste, Italy. URL http://hdl.handle.net/11368/2922531.

LACHAT, E., MACHER, H., MITTET, M., LANDES, T. & GRUSSENMEYER, P. (2015). First experiences with kinect V2 sensor for close range 3*D* modelling. *The International Archives of Photogrammetry, Remote Sensing and Spatial Information Sciences* **40**(5), 93. URL https://doi.org/10.5194/isprsarchives-XL-5-W4-93-2015.

LAGASSE, P. F., GHOSN, M., JOHNSON, P. A., ZEVENBERGEN, L. W. & CLOPPER, P. E. (2013). *Reference Guide for Applying Risk and Reliability-Based Approaches for Bridge Scour Prediction*. Washington, DC: The National Academies Press. URL https://doi.org/10.17226/22477.

LAGASSE, P. F. & RICHARDSON, E. V. (2001). ASCE compendium of stream stability and bridge scour papers. *Journal of Hydraulic Engineering* **127**(7), 531–533. URL https://doi.org/10.1061/(asce)0733-9429(2001)127:7(531).

LAGASSE, P. F., ZEVENBERGEN, L., SPITZ, W. & ARNESON, L. (2012). Stream stability at highway structures. Tech. rep., U.S. Department of Transportation, Federal Highway Administration. URL https://www.fhwa.dot.gov/engineering/hydraulics/pubs/hif12004.pdf.

LAGES MARTINS, L., PINHEIRO, A. & RIBEIRO, A. (2019). Caracterização 3D de um modelo físico reduzido de um pilar de uma ponte. *Laboratório Nacional de Engenharia Civil (LNEC)* **Rel. 318/2019 – CIC/NQM**.

LAI, J.-S., CHANG, W.-Y. & YEN, C.-L. (2009). Maximum local scour depth at bridge piers under unsteady flow. *Journal of Hydraulic Engineering* **135**(7), 609–614. URL https://doi.org/10.1061/(asce)hy.1943-7900.0000044.

LALL, U., IL MOON, Y. & BOSWORTH, K. (1993). Kernel flood frequency estimators: Bandwidth selection and kernel choice. *Water Resources Research* **29**(4), 1003–1015. URL https://doi.org/10.1029/92wr02466.

LAMB, R., ASPINALL, W., ODBERT, H. & WAGENER, T. (2017). Vulnerability of bridges to scour: Insights from an international expert elicitation workshop. *Natural Hazards and Earth System Sciences* **17(8)**(8), 1393–1409. URL https://www.nat-hazards-earth-syst-sci.net/17/1393/2017/.

LANÇA, R., FAEL, C., CARDOSO, A. *et al.* (2011). Effect of relative sediment size on clear-water equilibrium scour depth at single cylindrical piers. In: *Proceedings of the 34th World Congress of the International Association for Hydro-Environment Research and Engineering: 33rd Hydrology and Water Resources Symposium and 10th Conference on Hydraulics in Water Engineering*. Engineers Australia.

LANÇA, R. M., FAEL, C. S., MAIA, R. J., PÊGO, J. P. & CARDOSO, A. H. (2013). Clear-water scour at comparatively large cylindrical piers. *Journal of Hydraulic Engineering* **139**(11), 1117–1125. URL http://dx.doi.org/10.1061/(ASCE)HY.1943-7900.0000788.

LANÇA, R. M. M., SIMARRO, G., FAEL, C. M. S. & CARDOSO, A. H. (2016). Effect of viscosity on the equilibrium scour depth at single cylindrical piers. *Journal of Hydraulic Engineering* **142**(3), 06015022. URL https://doi.org/10.1061/(asce)hy.1943-7900.0001102.

LANE, E. W. & KALINSKE, A. A. (1939). The relation of suspended to bed material in rivers. *Transactions, American Geophysical Union* **20**(4), 637. URL https://doi.org/10.1029/tr020i004p00637.

LAUCHLAN, C. & MAY, R. (2002). Comparison of general scour prediction equations for river crossings. In: *First International Conference on Scour of Foundations. November 17-20, 2002, College Station, USA*. URL https://hdl.handle.net/20.500.11970/100333.

LAURSEN, E. M. (1960). Scour at bridge crossings. *Journal of the Hydraulics Division* **92**(3). URL https://trid.trb.org/view/170849.

LAURSEN, E. M. (1963). An analysis of relief bridge scour. *Journal of the Hydraulics Division* **89**(3), 93–118. URL https://cedb.asce.org/CEDBsearch/record.jsp?dockey=0012873.

LAURSEN, E. M. & TOCH, A. (1956). *Scour around bridge piers and abutments*, vol. 4. Iowa Highway Research Board Ames, IA. URL https://core.ac.uk/download/pdf/76635144.pdf.

LEANDRO, J., GANDER, A., BEG, M., BHOLA, P., KONNERTH, I., WILLEMS, W., CARVALHO, R. & DISSE, M. (2019). Forecasting upper and lower uncertainty bands of river flood discharges with high predictive skill. *Journal of Hydrology* **576**, 749–763. URL https://doi.org/10.1016/j.jhydrol.2019.06.052.

LEE, S. O. & HONG, S. H. (2019). Turbulence characteristics before and after scour upstream of a scaled-down bridge pier model. *Water* **11**(9), 1900. URL https://doi.org/10.3390/w11091900.

LEE, S. O. & STURM, T. W. (2009). Effect of sediment size scaling on physical modeling of bridge pier scour. *Journal of Hydraulic Engineering* **135**(10), 793–802. URL https://doi.org/10.1061/(asce)hy.1943-7900.0000091.

LENCASTRE, A. & FRANCO, F. M. (1992). *Lições de Hidrologia*. Caparica: Fundação da Faculdade de Ciência e Tecnologias da Universidade Nova de Lisboa.

LENCASTRE, A. C., FRANCO, F. M. & ANTUNES, M. T. (1984). *Lições de hidrologia*, vol. Monte da Caparica. Editora Universitária da Faculdade de Ciências e Tecnologia.

LI, J., YANG, Y. & YANG, Z. (2020). Influence of scour development on turbulent flow field in front of a bridge pier. *Water* **12**(9), 2370. URL https://doi.org/10.3390/w12092370.

LI, M., PAN, S. & O'CONNOR, B. A. (2008). A two-phase numerical model for sediment transport prediction under oscillatory sheet flows. *Coastal Engineering* **55**(12), 1159–1173. URL https://doi.org/10.1016/j.coastaleng.2008.05.003.

LI, Y., KELLY, D. M., LI, M. & HARRIS, J. M. (2014). DEVELOPMENT OF a NEW 3d EULER-LAGRANGE MODEL FOR THE PREDICTION OF SCOUR AROUND OFFSHORE STRUCTURES. *Coastal Engineering Proceedings* **1**(34), 31. URL https://doi.org/10.9753/icce.v34.sediment.31.

LIMA, M. M. C. L., CARVALHO, E. & ALEIXO, R. (2018). LDV measurements of the flow induced by an elongated bridge pier: The fixed bed case. In: *GeoPlanet: Earth and Planetary Sciences*. Springer International Publishing, pp. 307–321. URL https://doi.org/10.1007/978-3-319-70914-7_20.

LIN, C., BENNETT, C., HAN, J. & PARSONS, R. L. (2010). Scour effects on the response of laterally loaded piles considering stress history of sand. *Computers and Geotechnics* **37**(7-8), 1008–1014. URL https://doi.org/10.1016/j.compgeo.2010.08.009.

LIN, Y.-B., CHEN, J.-C., CHANG, K.-C., CHERN, J.-C. & LAI, J.-S. (2005). Real-time monitoring of local scour by using fiber bragg grating sensors. *Smart Materials and Structures* **14**(4), 664–670. URL https://doi.org/10.1088/0964-1726/14/4/025.

LINDER, W. (2016). *Digital Photogrammetry*. Springer Berlin Heidelberg. URL https://doi.org/10.1007/978-3-662-50463-5.

LINK, O., CASTILLO, C., PIZARRO, A., ROJAS, A., ETTMER, B., ESCAURIAZA, C. & MANFREDA, S. (2017). A model of bridge pier scour during flood waves. *Journal of Hydraulic Research* **55**(3), 310–323. URL https://doi.org/10.1080/00221686.2016.1252802.

LINK, O., GARCÍA, M., PIZARRO, A., ALCAYAGA, H. & PALMA, S. (2020). Local scour and sediment deposition at bridge piers during floods. *Journal of Hydraulic Engineering* **146**(3), 04020003. URL https://doi.org/10.1061/(asce)hy.1943-7900.0001696.

LINK, O., GONZÁLEZ, C., MALDONADO, M. & ESCAURIAZA, C. (2012). Coherent structure dynamics and sediment particle motion around a cylindrical pier in developing scour holes. *Acta Geophysica* **60**(6), 1689–1719. URL https://doi.org/10.2478/s11600-012-0068-y.

LIU, X. & GARCÍA, M. H. (2008). Three-dimensional numerical model with free water surface and mesh deformation for local sediment scour. *Journal of Waterway, Port, Coastal, and Ocean Engineering* **134**(4), 203–217. URL https://doi.org/10.1061/(asce)0733-950x(2008)134:4(203).

LOPES, C. (2019). Relatório de inspeção subaquática. Ponte Hintze Ribeiro. *Infraestruturas de Portugal* **IP**.

LÓPEZ, G., TEIXEIRA, L., ORTEGA-SÁNCHEZ, M. & SIMARRO, G. (2014). Estimating final scour depth under clear-water flood waves. *Journal of Hydraulic Engineering* **140**(3), 328–332. URL https://doi.org/10.1061/(asce)hy.1943-7900.0000804.

LU, J.-Y., SU, C.-C., HONG, J.-H. & CHEN, E.-J. (2012). Prediction of maximum general scour depth during a flood for intermittent rivers. In: *Proc. of 6th International Conference on Scour and Erosion*. URL https://www.academia.edu/32193806/Prediction_of_Maximum_General_Scour_Depth_during_a_Flood_for_Intermittent_Rivers.

LYN, D. A., EINAV, S., RODI, W. & PARK, J.-H. (1995). A laser-doppler velocimetry study of ensemble-averaged characteristics of the turbulent near wake of a square cylinder. *Journal of Fluid Mechanics* **304**, 285–319. URL https://doi.org/10.1017/s0022112095004435.

MAITY, R. (2018a). Frequency analysis, risk, and uncertainty in hydroclimatic analysis. In: *Statistical Methods in Hydrology and Hydroclimatology*. Springer Singapore, pp. 145–189. URL https://doi.org/10.1007/978-981-10-8779-0{_}5.

MAITY, R. (2018b). Hypothesis testing and nonparametric test. In: *Statistical Methods in Hydrology and Hydroclimatology*. Springer Singapore, pp. 191–227. URL https://doi.org/10.1007/978-981-10-8779-0{_}6.

MANES, C. & BROCCHINI, M. (2015). Local scour around structures and the phenomenology of turbulence. *Journal of Fluid Mechanics* **779**, 309–324. URL https://doi.org/10.1017/jfm.2015.389.

MANFREDA, S. (2018). On the derivation of flow rating curves in data-scarce environments. *Journal of Hydrology* **562**, 151–154. URL https://doi.org/10.1016/j.jhydrol.2018.04.058.

MANFREDA, S., LINK, O. & PIZARRO, A. (2018). A theoretically derived probability distribution of scour. *Water* **10**(11), 1520. URL https://doi.org/10.3390/w10111520.

MANN, H. B. (1945). Nonparametric tests against trend. *Econometrica* **13**(3), 245. URL https://doi.org/10.2307/1907187.

MANN, H. B. & WHITNEY, D. R. (1947). On a test of whether one of two random variables is stochastically larger than the other. *The Annals of Mathematical Statistics* **18**(1), 50–60. URL https://doi.org/10.1214/aoms/1177730491.

MARTINS, R. (1992). Estudos hidráulicos em modelos reduzidos do aproveitamento do Torrão. *Laboratório Nacional de Engenharia Civil (LNEC)* **Rel. 145/92 - DH**.

MASSEY, F. J. (1951). The Kolmogorov-Smirnov test for goodness of fit. *Journal of the American Statistical Association* **46**(253), 68–78. URL https://doi.org/10.1080/01621459.1951.10500769.

MATOS FERNANDES, M. (2016). *Mecânica dos Solos - Conceitos e Princípios Fundamentais*, vol. 1. Oficina de Textos, São Paulo. URL http://ofitexto.arquivos.s3.amazonaws.com/Mecanica-dos-solos-vol1-DEG.pdf.

MATTIOLI, M., ALSINA, J. M., MANCINELLI, A., MIOZZI, M. & BROCCHINI, M. (2012). Experimental investigation of the nearbed dynamics around a submarine pipeline laying on different types of seabed: The interaction between turbulent structures and particles. *Advances in Water Resources* **48**, 31–46. URL https://doi.org/10.1016/j.advwatres.2012.04.010.

MCKAY, S., FISCHENICH, J., RESEARCH, E., (U.S.), D. C., COASTAL, (U.S.), H. L. & (U.S.), C. I. R. P. (2011). *Robust Prediction of Hydraulic Roughness*. Technical note. U.S. Army Engineer Research and Development Center. URL https://books.google.pt/books?id=4CdUywAACAAJ.

MCMILLAN, H. K., WESTERBERG, I. K. & KRUEGER, T. (2018). Hydrological data uncertainty and its implications. *Wiley Interdisciplinary Reviews: Water* **5**(6). URL https://doi.org/10.1002/wat2.1319.

MELAAEN, M. C. (1992). Calculation of fluid flows with staggered and nonstaggered curvilinear nonorthogonal grids-the theory. *Numerical Heat Transfer, Part B: Fundamentals* **21**(1), 1–19. URL https://doi.org/10.1080/10407799208944919.

MELCHERS, R. E. & BECK, A. T. (eds.) (2018). *Structural Reliability Analysis and Prediction*. John Wiley & Sons Ltd. URL https://doi.org/10.1002/9781119266105.

MELVILLE, B. W. (1997). Pier and abutment scour: Integrated approach. *Journal of Hydraulic Engineering* **123**(2), 125–136. URL https://doi.org/10.1061/(asce)0733-9429(1997)123:2(125).

MELVILLE, B. W. & CHIEW, Y.-M. (1999). Time scale for local scour at bridge piers. *Journal of Hydraulic Engineering* **125**(1), 59–65. URL https://doi.org/10.1061/(asce)0733-9429(1999)125:1(59).

MELVILLE, B. W. & COLEMAN, S. E. (2000). *Bridge scour*. Highlands Ranch, Colorado: Water Resources Publications, LLC. URL http://trove.nla.gov.au/work/33270845.

MELVILLE, B. W. & RAUDKIVI, A. J. (1977). Flow characteristics in local scour at bridge piers. *Journal of Hydraulic Research* **15**(4), 373–380. URL http://dx.doi.org/10.1080/00221687709499641.

MERZ, B. & THIEKEN, A. H. (2005). Separating natural and epistemic uncertainty in flood frequency analysis. *Journal of Hydrology* **309**(1-4), 114–132. URL https://doi.org/10.1016/j.jhydrol.2004.11.015.

MEYER-PETER, E. & MÜLLER, R. (1948). Formulas for bed-load transport. In: *IAHSR 2nd meeting, Stockholm, appendix 2*. IAHR. URL http://resolver.tudelft.nl/uuid:4fda9b61-be28-4703-ab06-43cdc2a21bd7.

MIA, M. F. & NAGO, H. (2003). Design method of time-dependent local scour at circular bridge pier. *Journal of Hydraulic Engineering* **129**(6), 420–427. URL https://doi.org/10.1061/(asce)0733-9429(2003)129:6(420).

MILHAZES, F. (2016). Relatório de avaliação das condições hidrodinâmicas - Ponte Hintze Ribeiro. *Infraestruturas de Portugal* **IP**.

MILLARD, S., BUNGEY, J., THOMAS, C., SOUTSOS, M., SHAW, M. & PATTERSON, A. (1998). Assessing bridge pier scour by radar. *NDT & E International* **31**(4), 251–258. URL https://doi.org/10.1016/s0963-8695(98)00006-1.

MILLER, W. & SHEPPARD, M. D. (2002). Time rate of local scour at a circular pile. In: *First International Conference on Scour of Foundations. November 17-20, 2002, College Station, USA*. URL https://core.ac.uk/download/pdf/326240891.pdf.

MILLILO, J. M., RICHMOND, T. C. & YOHE, G. W. (2014). *Climate change impacts in the United States: U.S. national climate assessment*. Washington, DC: U.S. Global Change Research Program.

MILLIMAN, J. D. & KAO, S.-J. (2005). Hyperpycnal discharge of fluvial sediment to the ocean: Impact of Super-Typhoon Herb (1996) on Taiwanese rivers. *The Journal of Geology* **113**(5), 503–516. URL https://doi.org/10.1086/431906.

MOGES, E. M. (2010). *Evaluation of sediment transport equations and parameter sensitivity analysis using the SRH-2D Model*. Ph.D. thesis, MS Thesis in Universität Stuttgart. URL https://www.etis.ee/Portal/Mentorships/Display/45a5e90e-f02f-47dc-b565-9ea2147d5ae8.

MOLINAS, A. (2003). Bridge scour in non-uniform sediment mixtures and in cohesive materials: Synthesis report. Tech. rep., FHWA-RD-03-083,Federal Highway Administration, McLean, Virginia. URL https://www.fhwa.dot.gov/publications/research/infrastructure/hydraulics/03083/03083.pdf.

MONTERO, V. G. G., ROMAGNOLI, M., GARCÍA, C. M., CANTERO, M. I. & SCACCHI, G. (2014). Optimization of ADV sampling strategies using DNS of turbulent flow. *Journal of Hydraulic Research* **52**(6), 862–869. URL https://doi.org/10.1080/00221686.2014.967818.

MORAN, P. A. P. (1957). The statistical treatment of flood flows. *Transactions, American Geophysical Union* **38(4)**(4), 519. URL https://doi.org/10.1029/tr038i004p00519.

MORENO, M., MAIA, R. & COUTO, L. (2016a). Effects of relative column width and pile-cap elevation on local scour depth around complex piers. *Journal of Hydraulic Engineering* **142**(2), 04015051. URL https://doi.org/10.1061/(asce)hy.1943-7900.0001080.

MORENO, M., MAIA, R. & COUTO, L. (2016b). Prediction of equilibrium local scour depth at complex bridge piers. *Journal of Hydraulic Engineering* **142**(11), 04016045. URL https://doi.org/10.1061/(asce)hy.1943-7900.0001153.

MORENO, M., MAIA, R., COUTO, L. & CARDOSO, A. (2012). Evaluation of local scour depth around complex bridge piers. In: *River Flow 2012: Proceedings of the International Conference on Fluvial Hydraulics*. San Jose, Costa Rica. URL https://www.researchgate.net/publication/273761562_Evaluation_of_local_scour_depth_around_complex_bridge_piers.

MORENO, M., MAIA, R., COUTO, L. & CARDOSO, A. H. (2017). Subtraction approach to experimentally assess the contribution of the complex pier components to the local scour depth. *Journal of Hydraulic Engineering* **143**(4), 06016030. URL https://doi.org/10.1061/(asce)hy.1943-7900.0001270.

MORENO, M. E. C. (2016). *Experimental study of local scour around complex bridge piers*. Ph.D. thesis, Faculdade de Engenharia da Universidade do Porto, Porto, Portugal. URL http://hdl.handle.net/10216/85290.

MOSTAFA, E. (1994). *Scour around skewed bridge piers*. Ph.D. thesis, Dept. of Irrigation and Hydraulics, Alexandria University, Alexandria, Egypt.

MOUKALLED, F., MANGANI, L. & DARWISH, M. (2016). *The Finite Volume Method in Computational Fluid Dynamics*. Springer International Publishing. URL https://doi.org/10.1007/978-3-319-16874-6.

MUELLER, A. & SUMER, B. (2020). *Mechanics of Sediment Transport*. CRC Press. URL https://books.google.com.br/books?id=fMHyDwAAQBAJ.

MÜLLER, G., MACH, R. & KAUPPERT, K. (2001). Mapping of bridge pier scour with projection moiré. *Journal of Hydraulic Research* **39**(5), 531–537. URL https://doi.org/10.1080/00221686.2001.9628277.

MUZAMMIL, M., SIDDIQUI, N. & SIDDIQUI, A. (2006). A reliability analysis of bridge pier against local scour. *Water and Energy International* **63**(2), 33–42.

MUZZAMMIL, M. & GANGADHARIAH, T. (2003). The mean characteristics of horseshoe vortex at a cylindrical pier. *Journal of Hydraulic Research* **41**(3), 285–297. URL https://doi.org/10.1080/00221680309499973.

MUZZAMMIL, M., SIDDIQUI, N. & SIDDIQUI, A. (2008). Reliability considerations in bridge pier scouring. *Structural Engineering and Mechanics* **28**(1), 1–18. URL https://doi.org/10.12989/sem.2008.28.1.001.

MUZZAMMIL, M. & SIDDIQUI, N. A. (2009). A reliability-based assessment of bridge pier scour in non-uniform sediments. *Journal of Hydraulic Research* **47**(3), 372–380. URL https://doi.org/10.1080/00221686.2009.9522008.

NAAS, S. L. (1977). *Flow behavior in alluvial channel bends*. Ph.D. thesis, Colorado State University.

NAGHETTINI, M. & PINTO, É. J. D. A. (2007). *Hidrologia estatística*. CPRM. URL http://www.civil.ist.utl.pt/~mps/Geral/livro%20hidrologia%20estatistica_mauro.pdf.

NAKAMURA, Y., OHYA, Y., OZONO, S. & NAKAYAMA, R. (1996). Experimental and numerical analysis of vortex shedding from elongated rectangular cylinders at low reynolds numbers 200–10^3. *Journal of Wind Engineering and Industrial Aerodynamics* **65**(1-3), 301–308. URL https://doi.org/10.1016/s0167-6105(97)00048-2.

NAZARETH, A. & SOUSA CRUZ, J. (2002). Estudos geológicos e geotécnicos. *Ponte Hintze Ribeiro sobre o rio Douro* **LISCONCEBE**.

NEILL, C. R. (1967). Mean-velocity criterion for scour of coarse uniform bed-material. In: *12th Proceedings Congress*, vol. 3. Fort Collins, Colorado, USA. URL https://books.google.pt/books?id=hrq5MAAACAAJ.

NIKITIN, N. V., NICOUD, F., WASISTHO, B., SQUIRES, K. D. & SPALART, P. R. (2000). An approach to wall modeling in large-eddy simulations. *Physics of Fluids* **12**(7), 1629–1632. URL https://doi.org/10.1063/1.870414.

NINTO, Y. & GARCIA, M. H. (1996). Experiments on particle—turbulence interactions in the near–wall region of an open channel flow: implications for sediment transport. *Journal of Fluid Mechanics* **326**, 285–319. URL https://doi.org/10.1017/s0022112096008324.

NORTEK, A. (2018). *The comprehensive manual for velocimeters - Nortek Manuals*. URL https://support.nortekgroup.com/hc/en-us/articles/360029839351-The-Comprehensive-Manual-Velocimeters.

NOWAK, A. S. & COLLINS, K. R. (2012). *Reliability of structures*. CRC Press/Taylor & Francis Group. URL https://books.google.pt/books?hl=pt-PT&lr=&id=z98q9wLKCY4C&oi=fnd&pg=PP1&dq=Reliability+of+structures&ots=gYQFX4x6qw&sig=PeAXHrlgPhVyDjelanU6MjlrksU&redir_esc=y#v=onepage&q=Reliability%20of%20structures&f=false.

NTSB, N. T. S. B. (1988). Collapse of New York Thruway (1-90) bridge over the Schoharie Creek, near Amsterdam, New York, April 5, 1987. Tech. rep., The University of North Carolina at Charlotte. URL https://eng-resources.uncc.edu/failurecasestudies/bridge-failure-cases/the-collapse-of-the-schoharie-creek-bridge/.

OJHA, C., BERNDTSSON, R. & BHUNYA, P. (2008). *Engineering hydrology*. Oxford University Press. URL https://www.researchgate.net/publication/264895381_Engineering_hydrology.

OKOLI, K., BREINL, K., BRANDIMARTE, L., BOTTO, A., VOLPI, E. & BALDASSARRE, G. D. (2018). Model averaging versus model selection: Estimating design floods with uncertain river flow data. *Hydrological Sciences Journal* **63 (13-14)**(13-14), 1913–1926. URL https://doi.org/10.1080/02626667.2018.1546389.

OKOLI, K., MAZZOLENI, M., BREINL, K. & BALDASSARRE, G. D. (2019). A systematic comparison of statistical and hydrological methods for design flood estimation. *Hydrology Research* URL https://doi.org/10.2166/nh.2019.188.

OLIVETO, G. & HAGER, W. H. (2002). Temporal evolution of clear-water pier and abutment scour. *Journal of Hydraulic Engineering* **128**(9), 811–820. URL https://doi.org/10.1061/(asce)0733-9429(2002)128:9(811).

OLIVETO, G. & HAGER, W. H. (2005). Further results to time-dependent local scour at bridge elements. *Journal of Hydraulic Engineering* **131**(2), 97–105. URL https://doi.org/10.1061/(asce)0733-9429(2005)131:2(97).

OLSEN, N. (1991). *A Three-Dimensional Numerical Model for Simulation of Sediment Movements in Water Intakes*. Ph.D. thesis, Norwegian Institute of Technology, University of Trondhein, Norway.

OLSEN, N. (2018a). *A three-dimensional numerical model for simulation of sediment movements in water intakes with moving option - User's Manual*. The Norwegian University of Science and Technology, Trondheim, Norway.

OLSEN, N. R. B. (2012). Numerical modelling and hydraulics. Tech. rep., Norwegian University of Science and Technology. URL https://www.iahrmedialibrary.net/large_download/i003_flures6.pdf.

OLSEN, N. R. B. (2018b). A three-dimensional numerical model for simulation of sediment movements in water intakes with multiblock option. Tech. rep., Department of Hydraulic and Environmental Engineering: the Norwegian University of Science and Technology.

OLSEN, N. R. B. & KJELLESVIG, H. M. (1998). Three-dimensional numerical flow modeling for estimation of maximum local scour depth. *Journal of Hydraulic Research* **36**(4), 579–590. URL http://dx.doi.org/10.1080/00221689809498610.

OLSEN, N. R. B. & MELAAEN, M. C. (1993). Three-dimensional calculation of scour around cylinders. *Journal of Hydraulic Engineering* **119**(9), 1048–1054. URL https://doi.org/10.1061/(asce)0733-9429(1993)119:9(1048).

PAKRASHI, V., MCKEOGH, E., KERIN, I., MCAULIFFE, S. & BEKIĆ, D. (2016). Development of the bridge management system under the project bridge sms. Bridge SMS at Cost Action TU1406 Quality specifications for roadway bridges, standardization at a European level (BridgeSpec), Belgrade, Serbia. URL https://www.bridgesms.eu/wp-content/uploads/2016/04/TU1406_Belgrade_BridgeSMS.pdf.

PANICI, D. & DE ALMEIDA, G. A. M. (2018). Formation, growth, and failure of debris jams at bridge piers. *Water Resources Research* **54**(9), 6226–6241. URL https://doi.org/10.1029/2017wr022177.

PARK, C.-W., PARK, H. I. & CHO, Y.-K. (2017). Evaluation of the applicability of pier local scour formulae using laboratory and field data. *Marine Georesources & Geotechnology* **35**(1), 1–7. URL https://doi.org/10.1080/1064119x.2014.954658.

PARKER, G., KLINGEMAN, P. C. & MCLEAN, D. G. (1983). Closure to " bedload and size distribution in paved gravel-bed streams " by gary parker, peter c. klingeman, and david g. McLean (april, 1982). *Journal of Hydraulic Engineering* **109**(5), 793–793. URL https://doi.org/10.1061/(asce)0733-9429(1983)109:5(793).

PATANKAR, S. (1980). *Numerical heat transfer and fluid flow*. Washington, New York: Hemisphere Pub. Corp. McGraw-Hill. URL https://books.google.pt/books/about/Numerical_Heat_Transfer_and_Fluid_Flow.html?id=N2MVAQAAIAAJ&redir_esc=y.

PATANKAR, S. & SPALDING, D. (1972). A calculation procedure for heat, mass and momentum transfer in three-dimensional parabolic flows. *International Journal of Heat and Mass Transfer* **15**(10), 1787–1806. URL https://doi.org/10.1016/0017-9310(72)90054-3.

PFLEGER, F., RAPP, C. & MANHART, M. (2010). Experimental investigation on the sediment movement in the vicinity of a cylindrical bridge pier. *River Flow 2010* , 1701–1708URL https://izw.baw.de/e-medien/river-flow-2010/PDF/C5/C5_06.pdf.

PINHEIRO, A. & ANDRÉ, J. (2002). Estudos hidráulicos. Nota de cálculo provisória. *Ponte Hintze Ribeiro sobre o rio Douro* **LISCONCEBE**.

PINTO, A. M. & MATOS, A. C. (2020). MARESye: A hybrid imaging system for underwater robotic applications. *Information Fusion* **55**, 16–29. URL https://doi.org/10.1016/j.inffus.2019.07.014.

PIZARRO, A., MANFREDA, S. & TUBALDI, E. (2020). The science behind scour at bridge foundations: A review. *Water* **12**(2), 374. URL https://doi.org/10.3390/w12020374.

PIZARRO, A., SAMELA, C., FIORENTINO, M., LINK, O. & MANFREDA, S. (2017). BRISENT: An entropy-based model for bridge-pier scour estimation under complex hydraulic scenarios. *Water* **9**(11), 889. URL https://doi.org/10.3390/w9110889.

PIZARRO, A. & TUBALDI, E. (2019). Quantification of modelling uncertainties in bridge scour risk assessment under multiple flood events. *Geosciences* **9(10)**(10), 445. URL https://doi.org/10.3390/geosciences9100445.

POGGI & KUDRYAVTSEVA (2019). Non-intrusive underwater measurement of local scour around a bridge pier. *Water* **11**(10), 2063. URL https://doi.org/10.3390/w11102063.

POPE, S. B. (2000). *Turbulent Flows*. Cambridge University Press. URL https://doi.org/10.1017/cbo9780511840531.

PORTELA, M. M. & DA SILVA, C. D. S. R. (2014). Da regionalização de informação hidrométrica ao dimensionamento de albufeiras de regularização e a análise de incertezas. Tech. rep., Instituto Superior Técnico. URL https://fenix.ciencias.ulisboa.pt/downloadFile/844562369085982/Licao_MMPortela_Regionalizacao.pdf.

PRENDERGAST, L. & GAVIN, K. (2014). A review of bridge scour monitoring techniques. *Journal of Rock Mechanics and Geotechnical Engineering* **6**(2), 138–149. URL http://dx.doi.org/10.1016/j.jrmge.2014.01.007.

PROSKE, D. (2018). *Bridge Collapse Frequencies versus Failure Probabilities*. Springer International Publishing. URL https://doi.org/10.1007/978-3-319-73833-8.

QUARESMA, A. (2017). *Developing pool-type fishways based on experimental studies and numerical modelling*. Ph.D. thesis, Instituto Superior Técnico, Universidade de Lisboa.

RADICE, A. & TRAN, C. K. (2012). Study of sediment motion in scour hole of a circular pier. *Journal of Hydraulic Research* **50**(1), 44–51. URL https://doi.org/10.1080/00221686.2011.641764.

RAIKAR, R. V. & DEY, S. (2005). Clear-water scour at bridge piers in fine and medium gravel beds. *Canadian Journal of Civil Engineering* **32**(4), 775–781. URL https://doi.org/10.1139/l05-022.

RAMESH, A. (2012). *Response of Flood Events to Land Use and Climate Change: Analyzed by Hydrological and Statistical Modeling in Barcelonnette, France*. Springer Theses. Springer Netherlands. URL https://books.google.pt/books?id=f1EU4JxeMsMC.

RAMESH, R., DATTA, B., BHALLAMUDI, S. M. & NARAYANA, A. (2000). Optimal estimation of roughness in open-channel flows. *Journal of Hydraulic Engineering* **126**(4), 299–303. URL https://doi.org/10.1061/(asce)0733-9429(2000)126:4(299).

RAMOS, P. X., BENTO, A. M., MAIA, R. & PÊGO, J. P. (2015). Characterization of the scour cavity evolution around a complex bridge pier. *Journal of Applied Water Engineering and Research* **4**(2), 128–137. URL http://dx.doi.org/10.1080/23249676.2015.1090353.

RANGANATHAN, R. (1990). *Reliability Analysis and Design of Structures*. Tata McGraw-Hill. URL https://books.google.pt/books?id=AImhAAAACAAJ.

RAUDKIVI, A. J. (1986). Functional trends of scour at bridge piers. *Journal of Hydraulic Engineering* **112**(1), 1–13. URL https://doi.org/10.1061/(asce)0733-9429(1986)112:1(1).

RAUDKIVI, A. J. & ETTEMA, R. (1983). Clear-water scour at cylindrical piers. *Journal of Hydraulic Engineering* **109**(3), 338–350. URL https://doi.org/10.1061/(asce)0733-9429(1983)109:3(338).

RAUDKIVI, A. J. & ETTEMA, R. (1985). Scour at cylindrical bridge piers in armored beds. *Journal of Hydraulic Engineering* **111**(4), 713–731. URL https://doi.org/10.1061/(asce)0733-9429(1985)111:4(713).

RAUSAND, M. & HAUGEN, S. (2020). *Risk assessment: theory, methods, and applications*. Wiley series in statistics in practice. Hoboken, NJ: John Wiley & Sons, 2^{nd} ed. URL https://www.wiley.com/en-us/Risk+Assessment%3A+Theory%2C+Methods%2C+and+Applications%2C+2nd+Edition-p-9781119377351.

RICHARDSON, E. & DAVIS, S. (1995). Evaluating scour at bridges: Federal highway administration hydraulic engineering circular no. 18. Tech. rep., Publication FHWA-IP-90-017. URL https://www.fhwa.dot.gov/engineering/hydraulics/pubs/hec/hec18SI.pdf.

RICHARDSON, E. & DAVIS, S. (2001). Evaluating scour at bridges. *Hydraulic Engineering Circular No* **18**(4). URL https://www.fs.fed.us/biology/nsaec/fishxing/fplibrary/FHWA_2001_Evaluating_Scour_at_Bridges.pdf.

RICHARDSON, J. E. & PANCHANG, V. G. (1998). Three-dimensional simulation of scour-inducing flow at bridge piers. *Journal of Hydraulic Engineering* **124**(5), 530–540. URL https://doi.org/10.1061/(asce)0733-9429(1998)124:5(530).

RIJN, L. C. V. (1984). Sediment transport, part III: Bed forms and alluvial roughness. *Journal of Hydraulic Engineering* **110**(12), 1733–1754. URL https://doi.org/10.1061/(asce)0733-9429(1984)110:12(1733).

ROBINSON, J. S., SIVAPALAN, M. & SNELL, J. D. (1995). On the relative roles of hillslope processes, channel routing, and network geomorphology in the hydrologic response of natural catchments. *Water Resources Research* **31**(12), 3089–3101. URL https://doi.org/10.1029/95wr01948.

ROCA, M. & WHITEHOUSE, R. (2012). Scour risk assessment at river crossings. *Proceedings of ICSE6, Paris, France* URL https://eprints.hrwallingford.com/887/1/HRPP528_Scour_risk_assessment_at_river_crossings.pdf.

ROCHA, J. & ALVES, E. (2002). Plano específico preliminar de extração de inertes na albufeira de Crestuma-Lever, rio Douro. *Laboratório Nacional de Engenharia Civil (LNEC)* **Rel. 186/02 - NHE**.

ROCHA, J. S. & CARDOSO, A. (1984). Medição do caudal sólido e observação do regime aluvionar do rio Douro. Análises das observações efetuadas entre 1972 e 1974. *Laboratório Nacional de Engenharia Civil* **Rel. 137/84 - NHHF**.

ROCHA, J. S., DO CARMO, J. S. A., LEMOS, L. J. L., DA SILVA, V. D. & DA SILVA REBELO, C. A. (2008). Pontes construídas sobre fundos aluvionares: O colapso da ponte Hintze Ribeiro. *Recursos Hídricos* **29**(2). URL https://www.researchgate.net/publication/256293320_PONTES_CONSTRUIDAS_SOBRE_FUNDOS_ALUVIONARES_O_COLAPSO_DA_PONTE_HINTZE_RIBEIRO_BRIDGES_BUILT_ON_ALLUVIAL_BEDS_THE_FAILURE_OF_THE_HINTZE_RIBEIRO_BRIDGE.

RODI, W. (1993). *Turbulence models and their application in hydraulics: A state-of-the art review*. Rotterdam, Netherlands Broofield, Vt: A.A. Balkema.

RODI, W. (2017). Turbulence modeling and simulation in hydraulics: A historical review. *Journal of Hydraulic Engineering* **143**(5), 03117001. URL https://doi.org/10.1061/(asce)hy.1943-7900.0001288.

RODI, W., FERZIGER, J. H., BREUER, M. & POURQUIE´E, M. (1997). Status of Large Eddy simulation: Results of a workshop. *Journal of Fluids Engineering* **119**(2), 248–262. URL https://doi.org/10.1115/1.2819128.

ROGERS, A. (2019). *The geometric scaling of a developing scour hole*. Ph.D. thesis, University of Southampton. URL http://eprints.soton.ac.uk/id/eprint/438116.

ROGGER, M., KOHL, B., PIRKL, H., VIGLIONE, A., KOMMA, J., KIRNBAUER, R., MERZ, R. & BLÖSCHL, G. (2012a). Runoff models and flood frequency statistics for design flood estimation in Austria – do they tell a consistent story? *Journal of Hydrology* **456-457**, 30–43. URL https://doi.org/10.1016/j.jhydrol.2012.05.068.

ROGGER, M., PIRKL, H., VIGLIONE, A., KOMMA, J., KOHL, B., KIRNBAUER, R., MERZ, R. & BLÖSCHL, G. (2012b). Step changes in the flood frequency curve: Process controls. *Water Resources Research* **48**(5). URL https://doi.org/10.1029/2011wr011187.

ROULUND, A., SUMER, B. M., FREDSØE, J. & MICHELSEN, J. (2005). Numerical and experimental investigation of flow and scour around a circular pile. *Journal of Fluid Mechanics* **534**, 351–401. URL http://dx.doi.org/10.1017/S0022112005004507.

SCHLICHTING, H. & GERSTEN, K. (2017). *Boundary-Layer Theory*. Springer Berlin Heidelberg. URL https://doi.org/10.1007/978-3-662-52919-5.

SEARCY, J. & HARDISON, C. (1960). Double-mass curves. Manual of hydrology: Part I, General surface water techniques. *US Geological Survey Water-Supply Paper* **1541**. URL https://pubs.usgs.gov/wsp/1541b/report.pdf.

SHEN, H., HUNG, C. & OF CIVIL ENGINEERING, C. S. U. D. (1970). *An Engineering Approach to Total Bed-material Load by Regression Analysis*. Colorado State University. URL https://books.google.pt/books?id=DfUYcgAACAAJ.

SHEN, H., SCHNEIDER, V. & KARAKI, S. (1966). Mechanics of local scour. *US Dept of Commerce, National Bureau of Standards, Inst of Applied Technology, Washington D C* URL https://trid.trb.org/view/102951.

SHEPPARD, D. & RENNA, R. (2010). *Bridge scour manual*, vol. Tallahassee, Florida. FDOT.

SHEPPARD, D. M., DEMIR, H. & MELVILLE, B. W. (2011). *Scour at Wide Piers and Long Skewed Piers*, vol. 682. Transportation Research Board. URL https://doi.org/10.17226/14426.

SHEPPARD, D. M., MELVILLE, B. & DEMIR, H. (2014). Evaluation of existing equations for local scour at bridge piers. *Journal of Hydraulic Engineering* **140(1)**(1), 14–23. URL https://doi.org/10.1061/(asce)hy.1943-7900.0000800.

SHEPPARD, D. M. & MILLER, W. (2006). Live-bed local pier scour experiments. *Journal of Hydraulic Engineering* **132**(7), 635–642. URL https://doi.org/10.1061/(asce)0733-9429(2006)132:7(635).

SHEPPARD, D. M., ODEH, M. & GLASSER, T. (2004). Large scale clear-water local pier scour experiments. *Journal of Hydraulic Engineering* **130**(10), 957–963. URL https://doi.org/10.1061/(asce)0733-9429(2004)130:10(957).

SHEPPARD, M. D. & GLASSER, T. L. (2004). Sediment scour at piers with complex geometries. In: *Proceedings 2nd International Conference on Scour and Erosion (ICSE-2). November 14–17, 2004, Singapore.* URL https://henry.baw.de/bitstream/20.500.11970/99977/1/PAS_8.pdf.

SHIELDS, A. (1936). Application of similarity principles and turbulence research to bed-load movement. *CalTech library* URL https://resolver.caltech.edu/CaltechKHR:HydroLabpub167.

SHIROLE, A. & HOLT, R. (1991). Planning for a comprehensive bridge safety assurance program. *Transportation Research Board, National Research Council* **1290**, 39–50. URL https://trid.trb.org/view/358683.

SILVA, J. & OLIVEIRA, M. (2002). As cheias na parte portuguesa da bacia hidrográfica do rio Douro. In: *Atas do 3rd Congresso Ibérico de Gestão e Planeamento da Água*. Sevilha, Spain: Fundação Nova Cultura da Água.

SILVERMAN, B. W. (1986). *Density estimation for statistics and data analysis*. London New York: Chapman and Hall. URL https://ned.ipac.caltech.edu/level5/March02/Silverman/paper.pdf.

SIMARRO, G., FAEL, C. M. S. & CARDOSO, A. H. (2011). Estimating equilibrium scour depth at cylindrical piers in experimental studies. *Journal of Hydraulic Engineering* **137**(9), 1089–1093. URL https://doi.org/10.1061/(asce)hy.1943-7900.0000410.

SIMONOVIC, S. P. (2012). *Floods in a Changing Climate: Risk Management*. Cambridge University Press. URL https://doi.org/10.1017/cbo9781139088404.

SOAR, P., WALLERSTEIN, N. & THORNE, C. (2017). Quantifying river channel stability at the basin scale. *Water* **9**(2), 133. URL https://doi.org/10.3390/w9020133.

SOHANKAR, A., DAVIDSON, L. & NORBERG, C. (1999). Large eddy simulation of flow past a square cylinder: Comparison of different subgrid scale models. *Journal of Fluids Engineering* **122**(1), 39–47. URL https://doi.org/10.1115/1.483224.

SORDO-WARD, Á., BIANUCCI, P., GARROTE, L. & GRANADOS, A. (2014). How safe is hydrologic infrastructure design? analysis of factors affecting extreme flood estimation. *Journal of Hydrologic Engineering* **19**(12), 04014028. URL https://doi.org/10.1061/(asce)he.1943-5584.0000981.

SOUSA, J. J. & BASTOS, L. (2013). Multi-temporal SAR interferometry reveals acceleration of bridge sinking before collapse. *Natural Hazards and Earth System Sciences (NHESS)* **13**(3), 659–667. URL https://doi.org/10.5194/nhess-13-659-2013.

SPALART, P., JOU, W.-H., STRELETS, M. & ALLMARAS, S. (1997). Comments on the feasibility of LES for wings, and on a hybrid RANS/LES approach. In: *Proceedings of first AFOSR international conference on DNS/LES*. Greyden Press. URL https://www.cobaltcfd.com/pdfs/DES97.pdf.

STEDINGER, J. R. (1993). Frequency analysis of extreme events. *in Handbook of Hydrology* URL https://sites.tufts.edu/richardvogel/files/2019/04/frequencyAnalysis.pdf.

STURM, T., ABID, I., MELVILLE, B., XIONG, X., STOESSER, T., BUGALLO, B. F., CHUA, K. V., ABT, S., HONG, S., & AND (2018). *Combining Individual Scour Components to Determine Total Scour*. Transportation Research Board. URL https://doi.org/10.17226/25046.

SUMER, B. (2015). A review of recent advances in numerical modelling of local scour problems. In: *Proc., 5th Int. Conf. on Scour and Erosion*. CRC Press, pp. 61–70. URL https://doi.org/10.1201/b17703-7.

SUMER, B. M. (2007). Mathematical modelling of scour: A review. *Journal of Hydraulic Research* **45**(6), 723–735. URL http://dx.doi.org/10.1080/00221686.2007.9521811.

SUMER, B. M. & FREDSØE, J. (1997). *Hydrodynamics Around Cylindrical Structures*. World Scientific. URL https://doi.org/10.1142/3316.

SUMER, B. M., PETERSEN, T. U., LOCATELLI, L., FREDSØE, J., MUSUMECI, R. E. & FOTI, E. (2013). Backfilling of a scour hole around a pile in waves and current. *Journal of Waterway, Port, Coastal, and Ocean Engineering* **139**(1), 9–23. URL https://doi.org/10.1061/(asce)ww.1943-5460.0000161.

SUN, R. & XIAO, H. (2016). SediFoam: A general-purpose, open-source CFD–DEM solver for particle-laden flow with emphasis on sediment transport. *Computers & Geosciences* **89**, 207–219. URL https://doi.org/10.1016/j.cageo.2016.01.011.

TAKAHASHI, T. (1978). Mechanical characteristics of debris flow. *Journal of the Hydraulics Division* **104**(8), 1153–1169. URL https://cedb.asce.org/CEDBsearch/record.jsp?dockey=0008250.

TANASIĆ, N., ILIĆ, V. & HAJDIN, R. (2013). Vulnerability assessment of bridges exposed to scour. *Journal of the Transportation Research Board* **2360**, 36–44. URL https://doi.org/10.3141/2360-05.

TATO, J. F. (1966). *As cheias do rio Douro*. Documentos e memórias para a história do Porto. In: O rio e o mar na vida da cidade: Exposição documental, Câmara Municipal, 156–177, Porto.

THOMPSON, J. F. (1982). Elliptic grid generation. *Applied Mathematics and Computation* **10-11**, 79–105. URL https://doi.org/10.1016/0096-3003(82)90188-6.

THORNE, C., SOAR, P., SKINNER, K., SEAR, D. & NEWSON, M. (2010a). 4 driving processes II. investigating, characterising and managing river sediment dynamics. In: *Guidebook of applied fluvial geomorphology*. Thomas Telford Ltd, pp. 120–195. URL https://doi.org/10.1680/gafg.34846.0004.

THORNE, C., WALLERSTEIN, N., SOAR, P., BROOKES, A., WISHART, D., BIEDENHARN, D., GIBSON, S., LITTLE, C., MOONEY, D., WATSON, C. C., GREEN, T. & COULTHARD, T. (2010b). Accounting for sediment in flood risk management. In: *Flood Risk Science and Management*. Wiley-Blackwell, pp. 87–113. URL https://doi.org/10.1002/9781444324846.ch5.

TODINOV, M. T. (2006). *Risk-Based Reliability Analysis and Generic Principles for Risk Reduction*. Elsevier Science. URL https://www.xarg.org/ref/a/0080447287/.

TOPCZEWSKI, Ł., CIEŚLA, J., MIKOŁAJEWSKI, P., ADAMSKI, P. & MARKOWSKI, Z. (2016). Monitoring of scour around bridge piers and abutments. *Transportation Research Procedia* **14**, 3963–3971. URL https://doi.org/10.1016/j.trpro.2016.05.493.

TSENG, M.-H., YEN, C.-L. & SONG, C. C. S. (2000). Computation of three-dimensional flow around square and circular piers. *International Journal for Numerical Methods in Fluids* **34**(3), 207–227. URL https://doi.org/10.1002/1097-0363(20001015)34:3<207::aid-fld31>3.0.co;2-r.

TUBALDI, E., MACORINI, L., IZZUDDIN, B. A., MANES, C. & LAIO, F. (2017). A framework for probabilistic assessment of clear-water scour around bridge piers. *Structural Safety* **69**, 11–22. URL https://doi.org/10.1016/j.strusafe.2017.07.001.

UNGER, J. & HAGER, W. H. (2006). Down-flow and horseshoe vortex characteristics of sediment embedded bridge piers. *Experiments in Fluids* **42**(1), 1–19. URL https://doi.org/10.1007/s00348-006-0209-7.

USGS (2012). The Schoharie Creek bridge. http://water.usgs.gov/wid/images/NY.figure.id.3.gif.

VAN RIJN, L. C. *et al.* (1993). *Principles of sediment transport in rivers, estuaries, and coastal seas*, vol. 1006. Amsterdam, the Netherlands: Aqua Publications. URL https://books.google.pt/books/about/Principles_of_Sediment_Transport_in_Rive.html?id=gGIYAQAAIAAJ&redir_esc=y.

VERSTEEG, H. K. (2007). *An introduction to computational fluid dynamics: The finite volume method*. Harlow, England New York: Pearson Education Ltd. URL https://books.google.pt/books/about/An_Introduction_to_Computational_Fluid_D.html?id=RvBZ-UMpGzIC&redir_esc=y.

VIEIRA, A. A. B. & COSTA, F. D. S. (2017). As inundações do rio douro em 1909: um contributo para o seu estudo a partir dos arquivos históricos da agência portuguesa do ambiente. *Investigaciones Geográficas* **53**, 77–92. URL https://doi.org/10.5354/0719-5370.2017.43598.

VISCONTI, F., STEFANON, L., CAMPOREALE, C., SUSIN, F., RIDOLFI, L. & LANZONI, S. (2012). Bed evolution measurement with flowing water in morphodynamics experiments. *Earth Surface Processes and Landforms* **37**(8), 818–827. URL https://doi.org/10.1002/esp.3200.

WALD, A. & WOLFOWITZ, J. (1943). An exact test for randomness in the non-parametric case based on serial correlation. *The Annals of Mathematical Statistics* **14**(4), 378–388. URL https://projecteuclid.org/download/pdf_1/euclid.aoms/1177731358.

WALLING, D. & FANG, D. (2003). Recent trends in the suspended sediment loads of the world's rivers. *Global and Planetary Change* **39**(1-2), 111–126. URL https://doi.org/10.1016/s0921-8181(03)00020-1.

WALTON, C. M., YU, C.-P., NG, P. & TOBIAS, S. (1982). An assessment of recent state truck size and weight studies. *Center for Transportation Research, Austin, TX* URL https://library.ctr.utexas.edu/digitized/texasarchive/phase2/241-4-summary-ctr.pdf.

WANG, S. & JIA, Y. (1999). Computational simulations of local scour at bridge crossings-Capabilities and limitations. In: *Proceedings ASCE International Water Resources Engineering Conference: Past Accomplishments and New Challenges" ASCE, Seattle*.

WARDHANA, K. & HADIPRIONO, F. C. (2003). Analysis of recent bridge failures in the united states. *Journal of Performance of Constructed Facilities* **17**(3), 144–150. URL https://doi.org/10.1061/(asce)0887-3828(2003)17:3(144).

WILCOX, D. (2006). *Turbulence modeling for CFD*. La Canada, CA: DCW Industries, Inc. URL https://cfd.spbstu.ru/agarbaruk/doc/2006_Wilcox_Turbulence-modeling-for-CFD.pdf.

WOOD, E. F. & RODRÍGUEZ-ITURBE, I. (1975). A bayesian approach to analyzing uncertainty among flood frequency models. *Water Resources Research* **11**(6), 839–843. URL https://doi.org/10.1029/wr011i006p00839.

YAN, H. & MORADKHANI, H. (2014). Bayesian model averaging for flood frequency analysis. In: *World Environmental and Water Resources Congress 2014*. American Society of Civil Engineers (ASCE). URL https://doi.org/10.1061/9780784413548.189.

YANG, C. T. (1973). Incipient motion and sediment transport. *Journal of the hydraulics division* **99**(10), 1679–1704. URL https://cedb.asce.org/CEDBsearch/record.jsp?dockey=0020110.

YANG, C. T. (1984). Unit stream power equation for gravel. *Journal of Hydraulic Engineering* **110**(12), 1783–1797. URL https://doi.org/10.1061/(asce)0733-9429(1984)110:12(1783).

YANG, S.-Q., TAN, S.-K. & LIM, S.-Y. (2004). Velocity distribution and dip-phenomenon in smooth uniform open channel flows. *Journal of Hydraulic Engineering* **130**(12), 1179–1186. URL https://doi.org/10.1061/(asce)0733-9429(2004)130:12(1179).

YANG, Y., MELVILLE, B. W., MACKY, G. H. & SHAMSELDIN, A. Y. (2019). Local scour at complex bridge piers in close proximity under clear-water and live-bed flow regime. *Water* **11(8)**(8), 1530. URL https://doi.org/10.3390/w11081530.

YANMAZ, A. M. (2002a). Dynamic reliability in bridge pier scouring. *Turkish Journal of Engineering and Environmental Sciences* **26**(4), 367–376. URL https://journals.tubitak.gov.tr/engineering/issues/muh-02-26-4/muh-26-4-8-0111-6.pdf.

YANMAZ, A. M. (2002b). Reliability simulation of scouring downstream of outlet facilities. *Turkish Journal of Engineering and Environmental Sciences* **27**(1), 65–72. URL https://journals.tubitak.gov.tr/engineering/issues/muh-03-27-1/muh-27-1-8-0205-12.pdf.

YANMAZ, A. M. & CICEKDAG, O. (2001). Composite reliability model for local scour around cylindrical bridge piers. *Canadian Journal of Civil Engineering* **28**(3), 520–535. URL https://doi.org/10.1139/l01-009.

YANMAZ, A. M. & ÜSTÜN, I. (2001). Generalized reliability model for local scour around bridge piers of various shapes. *Turkish Journal of Engineering and Environmental Sciences* **25**(6), 687–698. URL http://citeseerx.ist.psu.edu/viewdoc/summary?doi=10.1.1.489.3100.

YEN, B. C. (2002). System and component uncertainties in water resources. In: *Risk, Reliability, Uncertainty, and Robustness of Water Resource Systems*. Cambridge University Press, pp. 133–142. URL https://doi.org/10.1017/cbo9780511546006.015.

YU, X. & ZABILANSKY, L. J. (2006). Time domain reflectometry for automatic bridge scour monitoring. In: *Site and Geomaterial Characterization*. American Society of Civil Engineers. URL https://doi.org/10.1061/40861(193)19.

YULISTIYANTO, B., ZECH, Y. & GRAF, W. H. (1998). Flow around a cylinder: Shallow-water modeling with diffusion-dispersion. *Journal of Hydraulic Engineering* **124**(4), 419–429. URL https://doi.org/10.1061/(asce)0733-9429(1998)124:4(419).

ZHANG, Q., ZHOU, X.-L. & WANG, J.-H. (2017). Numerical investigation of local scour around three adjacent piles with different arrangements under current. *Ocean Engineering* **142**, 625–638. URL https://doi.org/10.1016/j.oceaneng.2017.07.045.

ZHOU, K., DUAN, J. G. & BOMBARDELLI, F. A. (2020). Experimental and theoretical study of local scour around three-pier group. *Journal of Hydraulic Engineering* **146**(10), 04020069. URL https://doi.org/10.1061/(asce)hy.1943-7900.0001794.

ZHOU, L. (2017). *Numerical modelling of scour in steady flows*. Theses, Université de Lyon, France. URL https://tel.archives-ouvertes.fr/tel-01598600.

Appendix A

Bridge Failures Causes

Throughout history, many bridges have collapsed due to a variety of reasons. In Deng *et al.* (2016)'s research, the main causes of bridge collapses are categorized into natural and human factors. Natural disasters, e.g., floods, scour, earthquakes, landslides, debris flow, hurricane, and typhoon, are often unavoidable and can cause serious damages to bridges. Other researchers have demonstrated that these natural factors are the most common causes of total or partial bridge collapse (Cook *et al.*, 2015; Flint *et al.*, 2017; Proske, 2018, and references therein), as indicated in Table A.1 for a universe of 92 bridge failures.

Table A.1: Percentages of cause of bridge failure rate, adapted from Cook *et al.* (2015).

Cause of failure	Partial collapse	Total collapse	Total count	Percentage of total (%)
Hydraulic total	21	27	48	52.2
Hydraulic	-	2	2	2.2
Flood	8	18	26	28.3
Scour	12	7	19	20.7
Ice	1	-	1	1.1
Collision total	17	1	18	19.6
Collision	14	1	15	16.3
Auto/truck	3	-	3	3.3
Overload	3	8	11	12.0
Deterioration total	4	2	6	6.5
Deterioration	-	1	1	1.1
Steel deterioration	2	1	3	3.3
Concrete deterioration	2	-	2	2.2
Fire	3	-	3	3.3
Construction	1	1	2	2.2
Fatigue steel	1	-	1	1.1
Bearing	-	1	1	1.1
Soil	1	-	1	1.1
Miscellaneous	1	-	1	1.1
Total	52	40	92	100.0

The most common cause of pier failure, and consequent bridge failure, is due to pier scour that undermines piers and footings causing the loss of support of the bridge deck (Brandimarte *et al.*, 2012). Therefore, a careful analysis of bridge hydraulics is essential in bridge design as this type of structure interacts with river flow, either by piers in the main channel or road embankment on the lateral riverbanks (Gilja *et al.*, 2012). Hydraulic design of bridge elements may, thus, invoke flooding upstream of the bridge or water elevation during high flows. Water loading on exposed bridge elements under flood conditions is most likely to cause damage to the stability of the bridge. Topczewski *et al.* (2016) emphasizes the importance of understanding well the phenomena that occurs during high flows, in the area of the bridge foundations, to properly assess the current condition and to develop proper maintenance actions.

Debris flows, in turn, are usually responsible for strong impact forces on the obstacles in ways (e.g. bridge foundations and bridge deck) capable of destabilizing the supporting structures, especially when large stones are transported (Takahashi, 1978; Deng *et al.*, 2016). The accumulation of debris at bridge piers obstructs the flow, producing increased upstream water levels, large horizontal structural loadings and flow field modifications that can considerably exacerbate scour (Panici & de Almeida, 2018). This situation may dangerously result in forcing the flowing water to overtop the blocked bridge and washing the structure away (Gilja *et al.*, 2012; Dias *et al.*, 2019). This phenomenon is more frequent in unstable streams characterized by active riverbank erosion (Richardson & Davis, 1995). An example of debris accumulation in the vicinity of a Portuguese bridge piers is shown in Figure A.1.

Figure A.1: Debris effects at the vicinity of Portuguese bridge foundations (Universidade do Algarve, 2006).

Appendix B

Portuguese bridges suggested as potential case studies

Appendix B presents a summary of the thirteen Portuguese bridges suggested by Infraestruturas de Portugal (IP) as potential candidates to use as case study in the aim of the present work. Among them, the selection of the case study bridge was considered taking into account the higher number of hydrology and bathymetry data and also its importance in the national road plan. The information provided by IP aided the selection process, which was complete following the selection of the new Hintze Ribeiro bridge, N° 2335, as the most appropriate for the purpose of the current work (Chapter 3). Figure B.1 shows an indicative location of the bridges per reference number (N°) using Google Maps. The summary table provides further details, namely name, age, location, latitude and longitude, river, satellite imagery, availability of bathymetry, data bridge, deck length, and photographs.

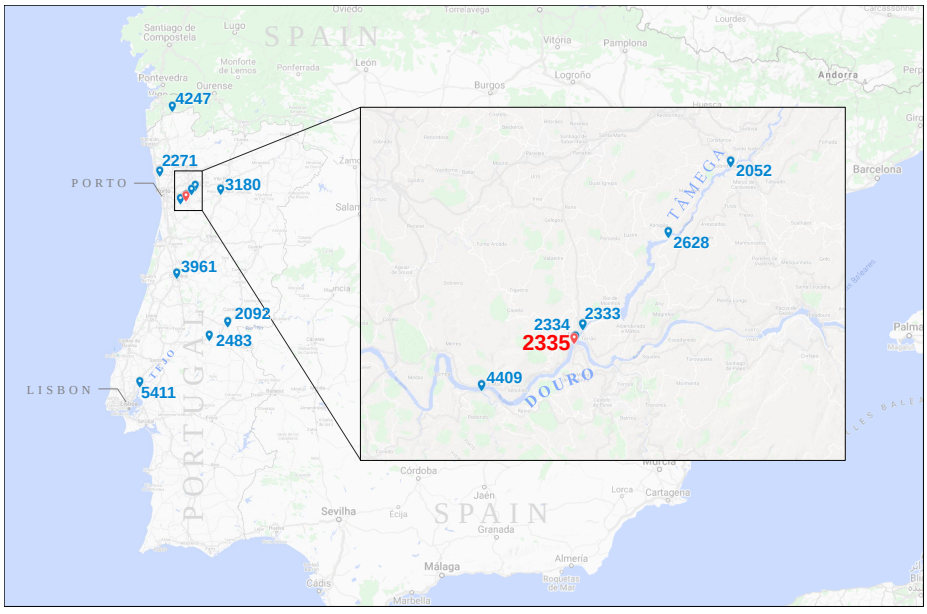

Figure B.1: Portuguese bridges suggested by Infraestruturas de Portugal as potential case studies (Google Maps, n.d.).

No.	Bathymetry	Coordinates	Location	Satellite Image	Name (Year)	River	Deck length (m)	Photographs
2052	2005, 2010, 2015	41.195238, -8.159168	Marco de Canaveses		N211 Variant	Tâmega	300	
2092	2005, 2010, 2016, 2019	39.647033, -7.676408	Vila Velha de Ródão, Castelo Branco		Portas de Ródão Bridge (1888)	Tagus	167	
2271	2005, 2010, 2015	41.356836, -8.685375	Vila do Conde		N306	Ave	150	(-)

No.	Bathymetry	Coordinates	Location	Satellite Image	Name (Year)	River	Deck length (m)	Photographs
2333	2010, 2013, 2016, 2019	41.0871389, -8.287916	Entre-os-Rios		Duarte Pacheco bridge (1941)	Tâmega	107	
2334	2010, 2013, 2017	41.080436, -8.295500	Castelo de Paiva		N224 Variant	Douro	400	
2335	2010, 2013	41.079691, -8.296765	Castelo de Paiva	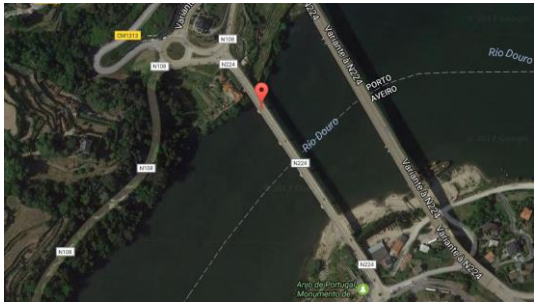	N224	Douro	336	

No.	Bathymetry	Coordinates	Location	Satellite Image	Name (Year)	River	Deck length (m)	Photographs
2483	2010, 2013	39.49130, -7.95077	Belver, Portalegre		Belver bridge (1907)	Tagus	239	
2628	2005, 2010, 2015	41.148735, -8.213696	Pombal/ Fafiães		N320	Tâmega	200	
3180	2006, 2013, 2017	41.154308, -7.780220	Peso da Régua		Régua Bridge (N2)	Douro	300	

No.	Bathymetry	Coordinates	Location	Satellite Image	Name (Year)	River	Deck length (m)	Photographs
3961	2005, 2010, 2013	40.206035, -8.430532	Coimbra	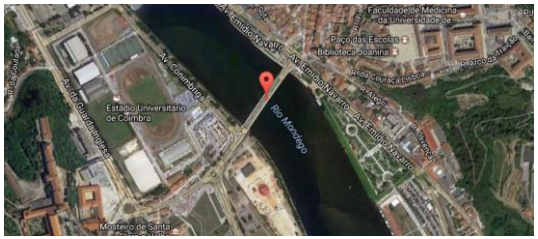	Ponte de Sta Clara (1954)	Mondego	210	
4247	2006, 2015	42.078674, -8.497915	Salvaterra de Miño	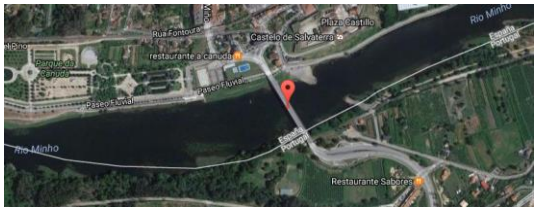	(-)	Minho	205	
4409	2006, 2013	41.047880, -8.377065	Pedorido, Aveiro		N222	Arda (Douro afluente)	100	
5411	2006 2010 2013, 2017	38.956192, -8.978878	Vila Franca de Xira		Marechal Carmona, bridge (1951)	Tagus	1224	

Appendix C

Experimental Study. Framework and Results

C.1 Experimental campaign

Initially, twelve local scouring experiments, organized in six different runs, were planned to be undertaken in the facility described in Section 4.2, as indicated in Table C.1. The letters 'U' and 'D', in experiments' notation, denote the upstream and downstream sand recess box in which the bridge pier models would be installed, respectively. However, unforeseen problems and technical faults on the components of the experimental flume had made it not possible to conclude the experimental campaign (Table C.1). On March 2020, the pandemic COVID-19 virus interfered with the continuity of the experimental campaign. The laboratory experiments performed in the present study (Chapter 4) are indicated in bold letters (see Table C.1).

Table C.1: Experimental campaign initial plan.

Scour conditions	Clear water			Live bed		
Runs / Piers	**Run 1**	*Run* 2	*Run* 3	**Run 4**	*Run* 5	*Run* 6
Pier 11	**Exp. 1U**	*Exp.* 2U	-	**Exp. 4U**	*Exp.* 5U	-
Pier 14	**Exp. 1D**	-	*Exp.* 3U	**Exp. 4D**	-	*Exp.* 6U
Pier 17	-	*Exp.* 2D	*Exp.* 3D	-	*Exp.* 5D	*Exp.* 6D

C.2 Experimental procedure

To ensure repeatability and isolate the effects of various parameters on the scouring process, a set of steps, enumerated below, were followed in sequence before, during and at the end of each experiment. The expected duration of some of the steps is also indicated.

1. Install the bridge pier models in the desired position in each sand recess box on the CIV mid-plane with the aid of a tape measure and a level - *half day*;

2. Fill the recess boxes with the graduated sand, compact and level the sand beds with the adjacent concrete bed level - *1 day*;
   Note: The area upstream of the obstacle was carefully compacted since it is a persistent site of unwanted scour at the transition between the concrete bottom to sand.

3. Protect the bridge pier models with metallic plaques (designed for that purpose) to preclude undesirable scour before reaching the desired flow conditions - *before experiments*;

4. Place the hydrometers in their respective positions according to Section 4.2.4 - *before experiments*;

5. Check all instrumentation and measuring supports - *before experiments*;

6. Operate the downstream submersible pump and check the level of the surge tank - *before experiments*;

7. Place the downstream sluice gate at least 0.20 m above the flume bottom, ensuring the slow filling of the channel during the flow stabilization, preventing, thus, flow velocities higher than the required - *before experiments*;

8. Take pre-experiment photographs - *before experiments*;

9. Fill the flume slowly and allow standing until the air trapped in the sediment has escaped. Drain the flume and compact the sediment once again - *2 days*;

10. Obtain scan images/photos of the flat bed models for further comparisons of the bed morphology at the pier models vicinity - *1 day*;

11. Fill the flume again. Increase the flow discharge and gradually adjust the level of the downstream sluice gate until reaching the hydraulic conditions defined for the experiments (Sections 4.3 and 4.4)- *half day*;

12. Check the fully developed flow upstream both working sections with the aid of a downlooking vectrino, before and during experiments - *before and during experiments*;

13. Remove the protective plaques with the aid of wires and mark the beginning of the respective experiments - *before experiments*;

14. Measure the temporal evolution of the scour depth at the piers' front. Higher periodicity is used for the first instants of experiments as scour develops very rapidly. The intervals between measurements are increased according with the scouring development. As a result, perceptive temporal evolutions, as either by linear or logarithmic trends are obtained - *during experiments*;

15. Acquire synchronized images of the scour hole at certain instants of the experiments - *during experiments*;

16. Interrupt the experiment at the pre-defined instants by switching off the pump group and drain out the flume - *during experiments*;

17. Obtain scan images/photos of the scour holes at the end of each experiment for its characterization by using the Kinect sensor and the close-range photogrammetry technique, respectively - *1 day*;

18. Fix the bed with the aid of a glue spray and let it drain and consolidate the surface layer of sand - *2 days*;

19. Restart the experiment with the same hydraulic conditions and perform flow field measurements (in a fixed eroded bed) - *7 days*;

20. Remix and clean (or even replace) the sand of both sand recess boxes - *2 days*;

21. Repeat steps 2 to 10 - *3 days*;

22. Fix the flat bed and left it drain and consolidate the surface layer of sand - *2 days*;

23. Restart the experiment with the same hydraulic conditions of step 11 and perform flow field measurements (in a fixed flat bed) - *5 days*;

24. Carry out the above steps for the completion of the experimental campaign.

C.3 Cameras calibration parameters

Four action cameras were acquired for a continuous monitoring of the scour hole development along the experiment $Exp.\ 1D$. The layout of the action cameras is indicatively illustrated in Figure C.1. The kind of camera used offers new perspectives due to its wide-angle lens (commonly called fish-eye lens), as well as for their ability to capture synchronized images in underwater environments. Nevertheless, the wide field of view leads is responsible for the inherent distortion, which has to be corrected for reliability purposes of underwater image processing analyses, and computer vision routines, undertaken in this work (see Section 4.3). For that purpose, a matlab toolbox, "Camera Calibration Toolbox for Matlab", was used for determining the intrinsic and extrinsic parameters, the radial distortion parameters and the image center for each action camera (herein referred as "CAM1", "CAM2", "CAM3" and "CAM4"). Table C.2 presents the obtained results for each action camera.

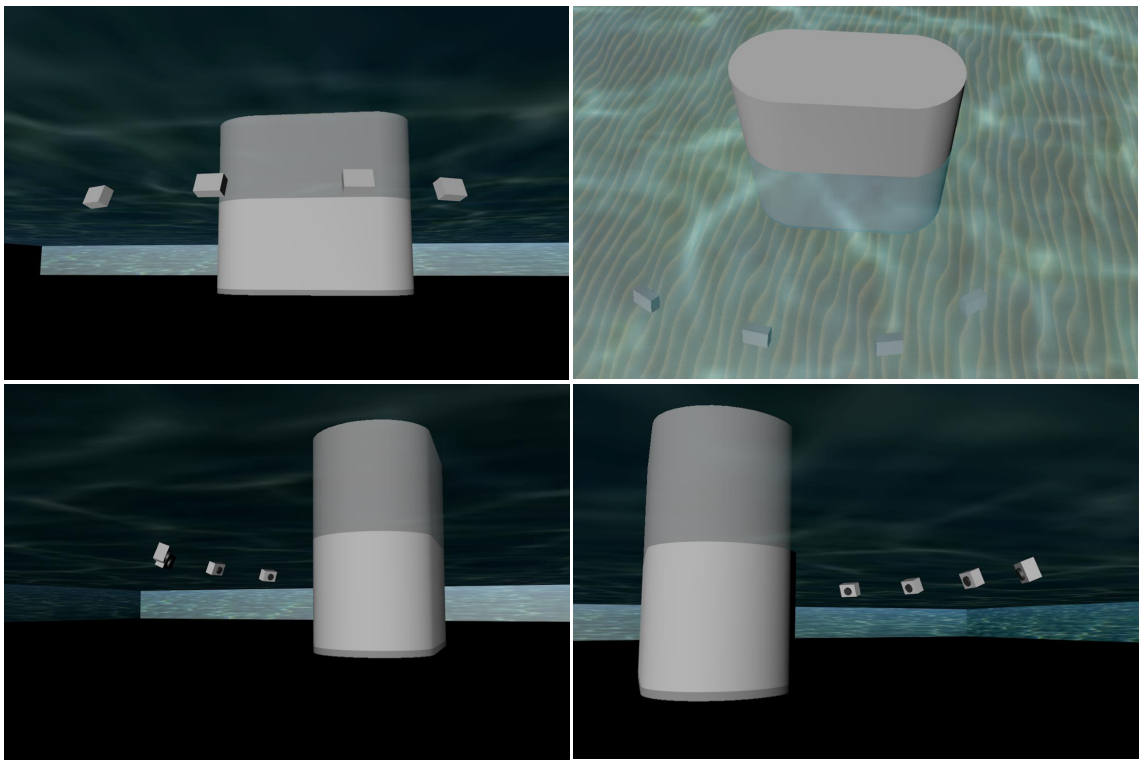

Figure C.1: Schematic layout of the camera setup adopted in the experimental study. Courtesy of Doctor Renato Henriques.

Table C.2: Intrinsic parameters of the action cameras, obtained from "Camera Calibration Toolbox for Matlab".

CAM1	Focal length	fc	2720.2749	2719.3781	-	-	-
	Principal point	cc	2026.2721	1627.2005	-	-	-
	Skew coefficient of camera	alpha_c	0.0000	-	-	-	-
	Distortion coefficients for camera	kc	-0.3567	0.1935	0.0017	-0.0007	0.0000
	Focal length uncertainty	fc_error	72.1048	71.9457	-	-	-
	Principal point uncertainty	cc_error	38.5337	38.7689	-	-	-
	Skew coefficient uncertainty	alpha_c_err	0.0000	-	-	-	-
	Distortion coefficients uncertainty	kc_error	0.0330	0.0445	0.0032	0.0024	0.0000
	Image size	nx, ny	4000.0000	3000.0000	-	-	-
	Pixel error	err	13.9855	7.3166	-	-	-

CAM2	Focal length	fc	3145.8651	3153.7730	-	-	-
	Principal point	cc	2011.7237	1534.0672	-	-	-
	Skew coefficient of camera	alpha_c	0.0000	-	-	-	-
	Distortion coefficients for camera	kc	-0.4754	0.3465	0.0014	-0.0012	0.0000
	Focal length uncertainty	fc_error	64.4150	62.3549	-	-	-
	Principal point uncertainty	cc_error	40.9840	38.7667	-	-	-
	Skew coefficient uncertainty	alpha_c_err	0.0000	-	-	-	-
	Distortion coefficients uncertainty	kc_error	0.0379	0.0736	0.0029	0.0021	0.0000
	Image size	nx, ny	4000.0000	3000.0000	-	-	-
	Pixel error	err	12.0628	6.2340	-	-	-

CAM3	Focal length	fc	3099.9248	3110.8749	-	-	-
	Principal point	cc	1964.7506	1562.4736	-	-	-
	Skew coefficient of camera	alpha_c	0.0000	-	-	-	-
	Distortion coefficients for camera	kc	-0.4709	0.3728	0.0014	0.0004	0.0000
	Focal length uncertainty	fc_error	90.2385	87.4383	-	-	-
	Principal point uncertainty	cc_error	45.9885	48.8827	-	-	-
	Skew coefficient uncertainty	alpha_c_err	0.0000	-	-	-	-
	Distortion coefficients uncertainty	kc_error	0.0469	0.0894	0.0039	0.0027	0.0000
	Image size	nx, ny	4000.0000	3000.0000	-	-	-
	Pixel error	err	15.3411	8.6106	-	-	-

CAM4	Focal length	fc	2729.7634	2764.2154	-	-	-
	Principal point	cc	2026.2053	1531.4248	-	-	-
	Skew coefficient of camera	alpha_c	0.0000	-	-	-	-
	Distortion coefficients for camera	kc	-0.3007	0.1779	0.0011	-0.0006	0.0000
	Focal length uncertainty	fc_error	168.6157	166.6165	-	-	-
	Principal point uncertainty	cc_error	66.7143	73.9747	-	-	-
	Skew coefficient uncertainty	alpha_c_err	0.0000	-	-	-	-
	Distortion coefficients uncertainty	kc_error	0.0586	0.0787	0.0054	0.0047	0.0000
	Image size	nx, ny	4000.0000	3000.0000	-	-	-
	Pixel error	err	26.2683	16.6081	-	-	-

C.4 Movable bed experiments carried out for bridge scour characterization

RUN 1

Exp. 1*U* (*Pier* 11)

&

Exp. 1*D* (*Pier* 14)

***Run* 1:** Exp.1D began on January 30th, 2019, at 10h10 while *Exp.* 1*U* started three minutes later, 10h13 on the same day. *Run* 1 lasted 5.9 days instead of the 5.62 days, obtained for the observed hydraulic conditions of the longer experiment (*Exp.* 1*D*), as discussed in Section 4.3. The hydraulic variables and bed material characteristics are given in Table C.3.

Table C.3: Hydraulic conditions and bed material characteristics of *Run* 1.

Run 1		
	***Exp.* 1*U* (*Pier* 11)**	***Exp.* 1*D* (*Pier* 14)**
Q (m^3s^{-1})	0.0923 (f = 14.35 Hz)	
h (m)	0.144	0.150
h/W (-)	1.31	1.07
U (ms^{-1})	0.3205	0.3077
U^2/gh (-)	0.0727	0.0643
D_{50} (mm)	0.00086	
U_c (Shields) (ms^{-1})	0.3048	0.3069
U_c (Neil) (ms^{-1})	0.3113	0.3126
I_f (-)	1.0295	0.9843
Fr (-)	0.2696	0.2536
Re (-)	46150	
Re_D (-)	35253.47	43073.33
t_e (days)	30.41	34.03
t_{90} (days)	4.62	5.62
$d_{se\text{-}sm}$ (m)	0.2014	0.2370
$d_{se\text{-}HEC\text{-}18}$ (m)	0.1514	0.1749
$d_{se\text{-}MM}$ (m)	0.2176	0.2509

Variables and parameters included in Table C.1 were described in Section 4.3. Scour depth measurements were taken with the aid of a limnimeter installed at the piers front, at 0.03 m from *Pier* 11 and at 0.05 m from *Pier* 14; the correspondent values are presented in Table C.4 by the variable d_s. Table C.5 indicates the pier scour dependencies of Run 1.

Table C.4: Scour depth time evolution of *Run* 1.

	Exp.* 1*U					***Exp.* 1*D***				
Day	Real time	t (min)	t (h)	Limnimeter (cm)	d_s (m)	Real time	t (min)	t (h)	Limnimeter (cm)	d_s (m)
30-Jan-19	10h13	0	0.000	17.39	0.0000	10h10	0	0.0000	18.46	0.0000
	10h18	5	0.083	20.08	0.0269	10h17	7	0.1167	20.54	0.0208
	10h31	18	0.300	22.21	0.0482	10h34	24	0.4000	22.73	0.0427
	10h48	35	0.583	23.49	0.0610	10h52	42	0.7000	23.75	0.0529
	11h15	62	1.033	24.77	0.0738	11h11	61	1.0167	24.20	0.0574
	14h06	233	3.883	28.45	0.1106	14h18	248	4.1333	26.99	0.0853
	15h19	306	5.100	28.76	0.1137	15h17	307	5.1167	28.62	0.1016
	16h15	362	6.033	29.04	0.1165	16h19	369	6.1500	28.70	0.1024
	16h47	394	6.567	28.92	0.1153	16h41	391	6.5167	29.11	0.1065
	17h14	421	7.017	29.42	0.1203	17h11	421	7.0167	29.06	0.1060
	17h46	453	7.550	29.62	0.1223	17h43	453	7.5500	29.43	0.1097
	18h16	483	8.050	29.93	0.1254	18h14	484	8.0667	29.93	0.1147
	18h48	515	8.583	30.50	0.1311	18h45	515	8.5833	29.28	0.1082
31-Jan-19	10h41	1468	24.467	32.56	0.1517	10h25	1455	24.2500	33.00	0.1454
	11h15	1502	25.033	32.50	0.1511	11h12	1502	25.0333	33.09	0.1463

	Exp. 1U					*Exp. 1D*				
	Real time	t (min)	t (h)	Limnimeter (cm)	d_s (m)	Real time	t (min)	t (h)	Limnimeter (cm)	d_s (m)
	11h46	1533	25.550	32.80	0.1541	11h40	1530	25.5000	33.16	0.1470
	12h17	1564	26.067	33.14	0.1575	12h14	1564	26.0667	33.22	0.1476
	13h16	1623	27.050	32.83	0.1544	13h19	1629	27.1500	33.38	0.1492
	14h19	1686	28.100	32.93	0.1554	14h12	1682	28.0333	33.34	0.1488
	15h48	1775	29.583	32.96	0.1557	15h52	1782	29.7000	34.00	0.1554
	18h14	1801	30.017	33.18	0.1579	18h11	1921	32.0167	33.80	0.1534
1-Feb-19	10h14	2881	48.017	33.94	0.1655	10h10	2880	48.0000	35.18	0.1672
	12h20	3007	50.117	34.26	0.1687	12h15	3005	50.0833	35.49	0.1703
	15h17	3184	53.067	34.39	0.1700	15h19	3189	53.1500	35.44	0.1698
	18h18	3365	56.083	34.82	0.1743	18h13	3363	56.0500	35.29	0.1683
2-Feb-19	11h21	4388	73.133	35.28	0.1789	11h15	4385	73.0833	36.23	0.1777
	13h04	4491	74.850	35.07	0.1768	13h08	4498	74.9667	35.93	0.1747
	17h34	4761	79.350	34.98	0.1759	17h36	4766	79.4333	35.97	0.1751
	19h08	4855	80.917	35.47	0.1808	19h05	4855	80.9167	36.46	0.1800
3-Feb-19	10h56	5803	96.717	35.91	0.1852	11h08	5818	96.9667	36.61	0.1815
	13h52	5979	99.650	35.62	0.1823	13h37	5967	99.4500	36.68	0.1822
	17h02	6169	102.817	36.18	0.1879	17h00	6170	102.8333	36.65	0.1819
	20h16	6363	106.050	36.14	0.1875	20h14	6364	106.0667	36.39	0.1793
4-Feb-19	9h54	7181	119.683	36.19	0.1880	9h52	7182	119.7000	36.96	0.1850
	12h59	7366	122.767	36.07	0.1868	12h58	7368	122.8000	37.46	0.1900
	16h36	7583	126.383	36.30	0.1891	16h32	7582	126.3667	37.31	0.1885
	19h22	7749	129.150	36.14	0.1875	19h17	7747	129.1167	37.19	0.1873
5-Feb-19	7h46/15h26	8493	141.550	36.54	0.1915	7h46/15h19	8496	141.6000	37.41	0.1895

The pier scours' dependencies of *Run* 1, in Table C.5, include the parameters described in Subsection 2.4.2.2 and in Section 4.3. As discussed in those sections, these parameters represent the relations between the approach flow depth and the pier width.

Table C.5: Pier scour dependencies of *Run* 1.

Exp.* 1*U			***Exp.* 1*D***		
d_s/W	**d_s/h**	**$d_s/(Wh)^{1/2}$**	**d_s/W**	**d_s/h**	**$d_s/(Wh)^{1/2}$**
0.000	0.000	0.000	0.000	0.000	0.000
0.245	0.187	0.214	0.149	0.139	0.144
0.438	0.335	0.383	0.305	0.285	0.295
0.555	0.424	0.485	0.378	0.353	0.365
0.671	0.513	0.586	0.410	0.383	0.396
1.005	0.768	0.879	0.609	0.569	0.589
1.034	0.790	0.903	0.726	0.677	0.701
1.059	0.809	0.926	0.731	0.683	0.707
1.048	0.801	0.916	0.761	0.710	0.735
1.094	0.835	0.956	0.757	0.707	0.731
1.112	0.849	0.972	0.784	0.731	0.757

Exp.* 1*U			***Exp.* 1*D***		
d_s/W	**d_s/h**	d_s/W	**d_s/h**	d_s/W	**d_s/h**
1.140	0.871	0.996	0.819	0.765	0.792
1.192	0.910	1.042	0.773	0.721	0.747
1.379	1.053	1.205	1.039	0.969	1.003
1.374	1.049	1.201	1.045	0.975	1.010
1.401	1.070	1.224	1.050	0.980	1.014
1.432	1.094	1.251	1.054	0.984	1.019
1.404	1.072	1.227	1.066	0.995	1.030
1.413	1.079	1.235	1.063	0.992	1.027
1.415	1.081	1.237	1.110	1.036	1.072
1.435	1.097	1.255	1.096	1.023	1.059
1.505	1.149	1.315	1.194	1.115	1.154
1.534	1.172	1.340	1.216	1.135	1.175
1.545	1.181	1.351	1.213	1.132	1.172
1.585	1.210	1.385	1.202	1.122	1.161
1.626	1.242	1.421	1.269	1.185	1.226
1.607	1.228	1.405	1.248	1.165	1.206
1.599	1.222	1.398	1.251	1.167	1.208
1.644	1.256	1.437	1.286	1.200	1.242
1.684	1.286	1.472	1.296	1.210	1.252
1.657	1.266	1.448	1.301	1.215	1.257
1.708	1.305	1.493	1.299	1.213	1.255
1.705	1.302	1.490	1.281	1.195	1.237
1.709	1.306	1.494	1.321	1.233	1.277
1.698	1.297	1.484	1.357	1.267	1.311
1.719	1.313	1.502	1.346	1.257	1.301
1.705	1.302	1.490	1.338	1.249	1.292
1.741	1.330	1.522	1.354	1.263	1.308

***RUN* 4**

***Exp.* 4*U* (*Pier* 11)**

&

***Exp.* 4*D* (*Pier* 14)**

***Exp.* 4*U* (*Pier* 11)**

Exp. 4*U* began on July 23th, 2019, at 11h37, and scour depth measurements were taken with the aid of a limnimeter installed at the pier's front (at 5 cm from the pier front). Owing to the previous usage of the flume (addition of seeding particles to the flow for velocity measurements through a downlooking vectrino V2), and besides all the provided cleaning before in the meanwhile, the column water kept presenting a high level of turbidity which prevented the underwater measurements and image acquisition. This experiment lasted 3.1 days instead of the 2.9 days obtained for t_{90} (recalculated for the observed hydraulic conditions). The hydraulic variables and bed material charateristics are given in Table C.6. The registered scour depths at the pier's front, as well as the pier scour dependencies, are presented in Table C.7.

Table C.6: Hydraulic conditions and bed material characteristics of *Exp.* 4*U* including uncertainties.

***Exp.* 4*U* (Pier 11)**	**Mean**	**Standard Deviation**	**Standard Error**	**Sample Error**	**Min**	**Max**	**Final Values**
Q (m^3s^{-1})	0.1226	$7.2761x10^{-4}$	$2.8205x10^{-7}$	$5.5281x10^{-7}$	0.1188	0.1243	$0.1226 \pm 6x10^{-7}$ (m^3s^{-1})
h_1 (m)	0.1479	0.0022	$8.5431x10^{-7}$	$1.6744x10^{-6}$	0.1416	0.1730	$0.1479 \pm 2x10^{-6}$ (m^3)
h_2 (m)	0.1426	0.0016	$6.1268x10^{-7}$	$1.2009x10^{-6}$	0.1376	0.1675	$0.1426 \pm 1.2x10^{-6}$ (m)
h (m)	0.1453	0.0018	$6.8889x10^{-7}$	$1.3502x10^{-6}$	0.1408	0.1703	$0.1453 \pm 1.4x10^{-6}$ (m)
V_1 (ms^{-1})	0.4146	0.0054	$2.1021x10^{-6}$	$4.1202x10^{-6}$	0.3460	0.4317	$0.4146 \pm 4\ x10^{-6}$ (ms^{-1})
V_2 (ms^{-1})	0.4300	0.0044	$1.7114x10^{-6}$	$3.3544x10^{-6}$	0.3575	0.4444	$0.4300 \pm 3x10^{-6}$ (ms^{-1})
V (ms^{-1})	0.4222	0.0045	$1.7586x10^{-6}$	$3.4469x10^{-6}$	0.3517	0.4336	$0.4222 \pm 3x10^{-6}$ (ms^{-1})
V_{c1} (ms^{-1})	0.3121	$4.5830x10^{-4}$	$1.7765x10^{-7}$	$3.4820x10^{-7}$	0.3108	0.3171	$0.3121 \pm 3x10^{-7}$ (ms^{-1})
V_{c2} (ms^{-1})	0.3110	$3.3545x10^{-4}$	$1.3003x10^{-7}$	$2.5486x10^{-7}$	0.3099	0.3160	$0.3110 \pm 3x10^{-7}$ (ms^{-1})
V_c (ms^{-1})	0.3116	$3.7308x10^{-4}$	$1.4462x10^{-7}$	$2.8345x10^{-7}$	0.3106	0.3166	$0.3116 \pm 3x10^{-7}$ (ms^{-1})
I_{f1} (-)	1.3284	0.0191	$7.4013x10^{-6}$	$1.4506x10^{-5}$	1.0913	1.3880	$1.3284 \pm 1.5x10^{-5}$ (-)
I_{f2} (-)	1.3827	0.0154	$5.9554x10^{-6}$	$1.1673x10^{-5}$	1.1311	1.4332	$1.3827 \pm 1.2x10^{-5}$ (-)
I_{fmean} (-)	1.3550	0.0159	$6.1599x10^{-6}$	$1.2073x10^{-5}$	1.1109	1.3951	$1.3550 \pm 1.2x10^{-5}$ (-)
Fr (-)	0.2964	0.0062	$2.4158x10^{-6}$	$4.7350x10^{-6}$	0.2105	0.3130	$0.2964 \pm 5x10^{-6}$ (-)
Re (-)	61069	362.3578	0.1405	0.2753	59185	61895	61069 ± 0.3 (-)
Re_D (-)	46254	497.0553	0.1927	0.3776	3.8529	4.7509	46254 ± 0.4 (-)
t_e (days)	34.5801	0.1039	$4.0267x10^{-5}$	$7.8923x10^{-5}$	34.3154	35.9816	$34.5801 \pm 8x10^{-5}$ (days)
t_{90} (days)	2.8984	0.1036	$4.0159x10^{-5}$	$7.8712x10^{-5}$	2.6762	4.7119	$2.8984 \pm 8x10^{-5}$ (days)
$d_{se\text{-}SM}$ (m)	0.2012	$4.8426x10^{-4}$	$1.8771x10^{-7}$	$3.6792x10^{-7}$	0.1999	0.2076	$0.2012 \pm 4x10^{-7}$ (m)
$d_{se\text{-}HEC\text{-}18}$ (m)	0.1581	$8.7786x10^{-4}$	$3.4029x10^{-7}$	$6.6696x10^{-7}$	0.1443	0.1602	$0.1581 \pm 7x10^{-7}$ (m)

Table C.7: Scour depth time evolution of *Exp.* 4*U*.

Day	**Real time**	**t (min)**	**t (h)**	**Limnimeter (cm)**	**d_s (cm)**	**d_s (m)**	**d_s/W**	**d_s/h**	**(Wh)^(1/2)**
23-Jul-19	11h37	0	0.000	18.29	0.000	0.0000	0.000	0.000	0.000
	11h42	5	0.083	20.54	2.250	0.0225	0.205	0.155	0.178
	11h47	10	0.167	22.71	4.420	0.0442	0.402	0.304	0.350
	12h07	30	0.500	25.07	6.780	0.0678	0.616	0.467	0.536
	12h37	60	1.000	26.77	8.480	0.0848	0.771	0.584	0.671
	13h07	90	1.500	27.66	9.370	0.0937	0.852	0.645	0.741
	13h37	120	2.000	28.30	10.010	0.1001	0.910	0.689	0.792
	14h37	180	3.000	28.73	10.440	0.1044	0.949	0.719	0.826
	15h37	240	4.000	30.25	11.960	0.1196	1.087	0.823	0.946
	17h37	360	6.000	32.03	13.740	0.1374	1.249	0.946	1.087
	18h07	390	6.500	33.07	14.780	0.1478	1.344	1.017	1.169

	Real time	t (min)	t (h)	Limnimeter (cm)	d_s (cm)	d_s (m)	d_s/W	d_s/h	(Wh)^(1/2)
	18h37	420	7.000	33.79	15.500	0.1550	1.409	1.067	1.226
	19h07	450	7.500	33.59	15.300	0.1530	1.391	1.053	1.210
	19h37	480	8.000	33.12	14.830	0.1483	1.348	1.021	1.173
24-Jul-19	10h07	1350	22.500	35.67	17.380	0.1738	1.580	1.196	1.375
	10h37	1380	23.000	36.56	18.270	0.1827	1.661	1.257	1.445
	11h07	1410	23.500	35.78	17.490	0.1749	1.590	1.204	1.383
	11h37	1440	24.000	35.91	17.620	0.1762	1.602	1.213	1.394
	12h07	1470	24.500	35.84	17.550	0.1755	1.595	1.208	1.388
	12h37	1500	25.000	34.91	16.620	0.1662	1.511	1.144	1.315
	13h07	1530	25.500	35.70	17.410	0.1741	1.583	1.198	1.377
	13h37	1560	26.000	35.26	16.970	0.1697	1.543	1.168	1.342
	15h07	1650	27.500	35.58	17.290	0.1729	1.572	1.190	1.368
	15h37	1680	28.000	35.93	17.640	0.1764	1.604	1.214	1.395
	16h07	1710	28.500	35.65	17.360	0.1736	1.578	1.195	1.373
	16h37	1740	29.000	35.89	17.600	0.1760	1.600	1.211	1.392
	17h18	1781	29.683	36.40	18.110	0.1811	1.646	1.246	1.432
	18h07	1830	30.500	36.04	17.750	0.1775	1.614	1.222	1.404
	19h07	1890	31.500	36.10	17.810	0.1781	1.619	1.226	1.409
	19h37	1920	32.000	35.86	17.570	0.1757	1.597	1.209	1.390
	20h07	1950	32.500	36.32	18.030	0.1903	1.639	1.241	1.426
	20h37	1980	33.000	36.14	17.850	0.1785	1.623	1.228	1.412
25-Jul-19	11h07	2850	47.500	36.94	18.650	0.1865	1.695	1.284	1.475
	11h37	2880	48.000	36.50	18.210	0.182	1.655	1.253	1.440
	12h37	2940	49.000	36.14	17.850	0.179	1.623	1.228	1.412
	13h37	3000	50.000	36.71	18.420	0.184	1.675	1.268	1.457
	14h37	3060	51.000	37.28	18.990	0.190	1.726	1.307	1.502
	15h37	3120	52.000	36.81	18.520	0.185	1.684	1.275	1.465
	16h37	3180	53.000	36.59	18.300	0.183	1.664	1.259	1.448
	17h37	3240	54.000	36.46	18.170	0.182	1.652	1.251	1.437
	18h37	3300	55.000	36.36	18.07	0.181	1.643	1.244	1.429
	19h37	3360	56.000	36.74	18.45	0.185	1.677	1.270	1.459
26-Jul-19	8h37	4140	69.000	36.41	18.12	0.181	1.647	1.247	1.433
	9h37	4200	70.000	37.07	18.78	0.188	1.707	1.292	1.485
	10h37	4260	71.000	36.55	18.26	0.183	1.660	1.257	1.444
	11h37	4320	72.000	36.46	18.17	0.182	1.652	1.251	1.437
	12h37	4380	73.000	36.06	17.77	0.178	1.615	1.223	1.406
	13h37	4440	74.000	36.25	17.96	0.180	1.633	1.236	1.421
	14h01	4464	74.400	36.160	17.87	0.179	1.625	1.230	1.413

Exp. 4D (Pier 14)

Exp. 4*D* began on September 2nd, 2019, at 11h40 and scour depth measurements were taken with the aid of a limnimeter installed at the pier's front (at 0.05 m from the pier front). In this experiment, the lack of transparency of the water column also prevented the underwater acquisition through the action cameras - Figure C.2 was taken during *Exp*. 1*D,* while Figure C.3 was acquired during *Exp.* 4*D*.

Figure C.2: Underwater capture during *Exp.* 1*U*.

Figure C.3: Underwater capture during *Exp.* 4*D*.

An additional issue arose before completing the second day of the experiment. Mechanical faults stopped the pump system and consequently the hydraulic circuit in use. From the continuous acquisition system of the flowmeter and the resistive probes, it was possible to confirm the exact moment at which the pump system stopped. According to those, the flow discharge started to decrease at 6h41min39sec (4.09.2019) and reached zero after 23 seconds of decrease, at 6h42min02sec. Thus, *Exp.* 4*D* lasted 43.7 hours (1.8 days) which corresponds roughly to 44.4% of the planned duration (criterion given by the recalculated t_{90}). The hydraulic conditions and bed material characteristics are given in Table C.8. The registered scour depths at the pier's front, as well as the pier scour dependencies, are presented in Table C.9.

Table C.8: Hydraulic conditions and bed material characteristics of *Exp.* 4*D* including uncertainties.

Exp. 4D (Pier 14)	Mean	Standard Deviation	Standard Error	Sample Error	Min	Max	Final Values
Q (m^3s^{-1})	0.1244	$9.5783x10^{-4}$	$6.6467x10^{-7}$	$1.3027x10^{-6}$	0.1212	0.1258	$0.1244 \pm 1.3x10^{-6}$ (m^3s^{-1})
h_1 (m)	0.1589	0.0011	$7.624x10^{-7}$	$1.4943x10^{-6}$	0.1541	0.1647	$0.1589 \pm 1.5x10^{-6}$ (m^3)
h_2 (m)	0.1550	0.0018	$1.2420x10^{-6}$	$2.4344x10^{-6}$	0.1494	0.1621	$0.1550 \pm 2x10^{-6}$ (m)
h (m)	0.1570	0.0011	$7.8939x10^{-7}$	$1.5472x10^{-6}$	0.1526	0.1617	$0.1570 \pm 2x10^{-6}$ (m)
V_1 (ms^{-1})	0.3916	0.0038	$2.6113x10^{-6}$	$5.1182x10^{-6}$	0.3772	0.4065	$0.3916 \pm 5x10^{-6}$ (ms^{-1})
V_2 (ms^{-1})	0.4014	0.0059	$4.0761x10^{-6}$	$7.9892x10^{-6}$	0.3801	0.4188	$0.4014 \pm 8x10^{-6}$ (ms^{-1})
V (ms^{-1})	0.3964	0.0043	$2.9646x10^{-6}$	$5.8106x10^{-6}$	0.3811	0.4104	$0.3964 \pm 6x10^{-6}$ (ms^{-1})
V_{c1} (ms^{-1})	0.3144	$2.1741x10^{-4}$	$1.5087x10^{-7}$	$2.9570x10^{-7}$	0.3134	0.3155	$0.3144 \pm 3x10^{-7}$ (ms^{-1})
V_{c2} (ms^{-1})	0.3136	$3.6081x10^{-4}$	$2.5037x10^{-7}$	$4.9073x10^{-7}$	0.3124	0.3150	$0.3136 \pm 5x10^{-7}$ (ms^{-1})
V_c (ms^{-1})	0.3140	$2.2731x10^{-4}$	$1.5774x10^{-7}$	$3.0916x10^{-7}$	0.3131	0.3149	$0.3140 \pm 3x10^{-7}$ (ms^{-1})
I_{f1} (-)	1.2456	0.0125	$8.6832x10^{-6}$	$1.7019x10^{-5}$	1.1963	1.2970	$1.2456 \pm 2x10^{-5}$ (-)
I_{f2} (-)	1.2801	0.0200	$1.3869x10^{-5}$	$2.7183x10^{-5}$	1.2070	1.3402	$1.2801 \pm 3x10^{-5}$ (-)
I_f (-)	1.2626	0.0143	$9.8935x10^{-6}$	$1.9391x10^{-5}$	1.2103	1.3104	$1.2626 \pm 2x10^{-5}$ (-)
Fr (-)	0.2575	0.0043	$2.9703x10^{-6}$	$5.8218x10^{-6}$	0.2404	0.2738	$0.2575 \pm 6x10^{-6}$ (-)
Re (-)	61977	477.0072	0.3310	0.6488	60359	62636	61977 ± 0.6 (-)
Re_D (-)	55281	595.7217	0.4134	0.8102	53148	57222	55281 ± 0.8 (-)
t_e (days)	40.8442	0.0739	$5.1305x10^{-5}$	$1.0056x10^{-4}$	40.5596	41.1471	$40.8442 \pm 1x10^{-4}$ (days)
t_{90} (days)	4.0537	0.1120	$7.7693x10^{-5}$	$1.5228x10^{-4}$	3.6881	4.4917	$4.0537 \pm 1.5x10^{-4}$ (days)
$d_{se\text{-}SM}$ (m)	0.2395	$3.6060x10^{-4}$	$2.5023x10^{-7}$	$4.9045x10^{-7}$	0.2381	0.2409	$0.2395 \pm 5x10^{-7}$ (m)
$d_{se\text{-}HEC\text{-}18}$ (m)	0.1789	$9.0544x10^{-4}$	$6.2831x10^{-7}$	$1.2315x10^{-6}$	0.1755	0.1819	$0.1789 \pm 1.2x10^{-6}$ (m)

Table C.9: Scour depth time evolution of *Exp.* 4*D* including uncertainties.

Day	Real time	t (min)	t (h)	Limnimeter (cm)	d_s (cm)	d_s (m)	d_s/W	d_s/h	$d_s/(Wh^{1/2})$
2-Sep-19	11h40	0	0.000	18.46	0.000	0.0000	0.000	0.000	0.000
	11h45	5	0.083	24.32	5.860	0.0586	0.419	0.373	0.395
	11h55	15	0.250	27.77	9.310	0.0931	0.665	0.593	0.628
	12h10	30	0.500	29.61	11.150	0.1115	0.796	0.710	0.752
	12h40	60	1.000	31.36	12.900	0.1290	0.921	0.822	0.870
	13h10	90	1.500	31.86	13.400	0.1340	0.957	0.854	0.904
	13h40	120	2.000	32.88	14.420	0.1442	1.030	0.918	0.973
	14h10	150	2.500	32.38	13.920	0.1392	0.994	0.887	0.939
	14h40	180	3.000	33.66	15.200	0.1520	1.086	0.968	1.025
	15h10	210	3.500	33.76	15.300	0.1530	1.093	0.975	1.032
	15h40	240	4.000	33.98	15.520	0.1552	1.109	0.989	1.047
	16h40	300	5.000	34.74	16.280	0.1628	1.163	1.037	1.098
	17h40	360	6.000	35.25	16.790	0.1679	1.199	1.069	1.132
	18h40	420	7.000	35.46	17.000	0.1700	1.214	1.083	1.147
	19h40	480	8.000	36.21	17.750	0.1775	1.268	1.131	1.197
	20h40	540	9.000	36.19	17.730	0.1773	1.266	1.129	1.196
3-Sep-19	8h10	1230	20.500	38.44	19.980	0.1998	1.427	1.273	1.348
	9h40	1320	22.000	38.99	20.530	0.2053	1.466	1.308	1.385
	11h40	1440	24.000	38.76	20.300	0.2030	1.450	1.293	1.369
	13h40	1560	26.000	40.03	21.570	0.2157	1.541	1.374	1.455
	15h40	1680	28.000	39.16	20.700	0.2070	1.479	1.318	1.396
	17h40	1800	30.000	39.23	20.770	0.2077	1.484	1.323	1.401
	19h40	1920	32.000	39.92	21.460	0.2146	1.533	1.367	1.447
4-Sep-19	6h42min2sec (forced interruption)	2622	43.701	39.60	21.140	0.2114	1.510	1.346	1.426

By analysis of the registered scour depths during the Exp. 4D's duration, the time required to reach 90% of the equilibrium scour depth was not reached. At the end of the first hour, the measured scour depth reached almost the value of 0.13 m. The night period (of almost 11 hours, from the last measurement performed on 2.09.2019 and the first one on 3.09.2019), registered an increase of the scour depth of 0.0225 m. During the second nocturnal period of the experiment, a slight difference of 0.0052 m was registered for the scour depth at the pier front. A reduction of slope was noticeable. Even though the experiment did not run all the planned time, it is expected that the final scour depth would be around 0.210 m, since the estimates of S/M and HEC-18 equations gave values of 0.217 m and 0.164 m, respectively (90% of the equilibrium scour depths).

C.5 Fixed bed experiments carried out for flow field characterization

Hydraulic variables of the fixed bed experiments, *Exp*. 1*U Fbed, Exp*. 1*U Ebed, Exp*. 1*D Fbed,* Exp. 1*D Ebed, Exp*. 4*U Fbed* and *Exp*. 4*U Ebed*, including uncertainties, are given in the following tables (from Table C.10 to Table C.15).

Table C.10: Hydraulic conditions and bed material characteristics of Exp. 1U *Fbed* including uncertainties.

***Exp.* 1*U Fbed* (Pier 11)**	**Mean**	**Standard Deviation**	**Standard Error**	**Sample Error**	**Min**	**Max**	**Final Values**
h1 (m)	0.1659	0.0013	3.03×10^{-6}	5.94×10^{-6}	0.1602	0.1719	$0.1659 \pm 6\times10^{-6}$ (m)
h2 (m)	0.1550	0.0140	3.25×10^{-6}	6.37×10^{-6}	0.1451	0.1633	$0.1550 \pm 6\times10^{-6}$ (m)
h3 (m)	0.1621	0.0011	2.65×10^{-6}	5.20×10^{-6}	0.1535	0.168	$0.1621\pm5\times10^{-6}$ (m)
h (m)	0.1610	7.28×10^{-4}	1.71×10^{-6}	3.34×10^{-6}	0.1573	0.1644	$0.1610 \pm 3\times10^{-6}$ (m)
V1 (ms^{-1})	0.2794	0.0022	5.10×10^{-6}	1.00×10^{-5}	0.2696	0.2894	$0.2794 \pm 1\times10^{-5}$ (ms^{-1})
V2 (ms^{-1})	0.2991	0.0027	6.29×10^{-6}	1.23×10^{-6}	0.2839	0.3194	$0.2991 \pm 1.2\times10^{-6}$ (ms^{-1})
V3 (ms^{-1})	0.2860	0.0020	4.69×10^{-6}	9.18×10^{-6}	0.2759	0.302	$0.2860 \pm 9\times10^{-6}$ (ms^{-1})
V (ms^{-1})	0.2882	0.0013	3.07×10^{-6}	6.01×10^{-6}	0.282	0.2952	$0.2882 \pm 6\times10^{-6}$ (ms^{-1})
Fr (-)	0.1825	0.0017	3.88×10^{-6}	7.60×10^{-6}	0.1748	0.1914	$0.1825 \pm 8\times10^{-6}$ (-)
Re (-)	46200	13.6773	0.032	0.0628	46200	46300	46200 ± 0.06 (-)
Re_D (-)	31600	143.4116	0.336	0.6585	30900	32300	31600 ± 0.7 (-)

Table C.11: Hydraulic conditions and bed material characteristics of Exp. 1U *Ebed* including uncertainties.

***Exp.* 1*U Ebed* (Pier 11)**	**Mean**	**Standard Deviation**	**Standard Error**	**Sample Error**	**Min**	**Max**	**Final Values**
h1 (m)	0.1662	0.0016	1.69×10^{-6}	3.32×10^{-6}	0.1523	0.626	$0.1662 \pm 3\times10^{-6}$ (m)
h2 (m)	0.1576	0.0014	1.55×10^{-6}	3.04×10^{-6}	0.1448	0.6272	$0.1576 \pm 3\times10^{-6}$ (m)
h3 (m)	0.1645	0.0014	1.55×10^{-6}	3.04×10^{-6}	0.1533	0.6266	$0.1645 \pm3\times10^{-6}$ (m)
h (m)	0.1628	0.0012	1.25×10^{-6}	2.45×10^{-6}	0.1526	0.6265	$0.1628 \pm 2\times10^{-6}$ (m)
V1 (ms^{-1})	0.2789	0.0024	2.58×10^{-6}	5.05×10^{-6}	0.074	0.3044	$0.2789 \pm 5\times10^{-6}$ (ms^{-1})
V2 (ms^{-1})	0.2941	0.0024	2.56×10^{-6}	5.01×10^{-6}	0.0739	0.32	$0.2941 \pm 5\times10^{-6}$ (ms^{-1})
V3 (ms^{-1})	0.2818	0.0022	2.36×10^{-6}	4.62×10^{-6}	0.074	0.3024	$0.2818 \pm 5\times10^{-6}$ (ms^{-1})
V (ms^{-1})	0.2849	0.0016	1.78×10^{-6}	3.50×10^{-6}	0.074	0.3041	$0.2849 \pm 4\times10^{-6}$ (ms^{-1})
Fr (-)	0.1784	0.0021	2.23×10^{-6}	4.36×10^{-6}	0.012	0.2032	$0.1784 \pm 4\times10^{-6}$ (-)
Re (-)	46200	8.8391	0.0096	0.0188	46200	46300	46200 ± 0.02 (-)
Re_D (-)	31200	180.4983	0.1955	0.3833	81100	33300	31200 ± 0.4 (-)

Table C.12: Hydraulic conditions and bed material characteristics of Exp. 1D *Fbed* including uncertainties.

***Exp.* 1D *Fbed* (Pier 14)**	**Mean**	**Standard Deviation**	**Standard Error**	**Sample Error**	**Min**	**Max**	**Final Values**
h1 (m)	0.1638	0.0013	4.70×10^{-6}	9.21×10^{-6}	0.1577	0.1695	$0.1638 \pm 9\times10^{-6}$ (m)
h2 (m)	0.1528	0.0015	5.40×10^{-6}	1.06×10^{-5}	0.1436	0.1617	$0.1528 \pm 1.1\times10^{-5}$ (m)
h3 (m)	0.1599	0.0011	4.08×10^{-6}	7.99×10^{-6}	0.1527	0.1664	$0.1599 \pm8\times10^{-6}$ (m)
h (m)	0.1588	6.76×10^{-4}	2.41×10^{-6}	4.72×10^{-6}	0.1554	0.1621	$0.1588 \pm 5\times10^{-6}$ (m)
V1 (ms^{-1})	0.2830	0.0023	8.12×10^{-6}	1.59×10^{-5}	0.2735	0.294	$0.2830 \pm 2\times10^{-5}$ (ms^{-1})
V2 (ms^{-1})	0.3034	0.003	1.07×10^{-5}	2.11×10^{-5}	0.2866	0.3229	$0.3034 \pm 2\times10^{-5}$ (ms^{-1})
V3 (ms^{-1})	0.2899	0.0021	7.39×10^{-6}	1.45×10^{-5}	0.2786	0.3036	$0.2899 \pm 1\times10^{-5}$ (ms^{-1})
V (ms^{-1})	0.2921	0.0013	4.46×10^{-6}	8.74×10^{-6}	0.2861	0.2991	$0.2921 \pm 9\times10^{-6}$ (ms^{-1})
Fr (-)	0.1875	0.0016	5.70×10^{-6}	1.12×10^{-5}	0.1799	0.1962	$0.1875 \pm 1.1\times10^{-5}$ (-)
Re (-)	46200	16.2716	0.058	0.1136	46200	46300	46200 ± 0.11 (-)
Re_D (-)	32000	137.1379	0.4887	0.9578	31300	32800	32000 ± 1.0 (-)

Table C.13: Hydraulic conditions and bed material characteristics of Exp. 1D *Ebed* including uncertainties.

***Exp.* 1D *Ebed* (Pier 14)**	**Mean**	**Standard Deviation**	**Standard Error**	**Sample Error**	**Min**	**Max**	**Final Values**
h1 (m)	0.1623	0.0011	2.53×10^{-6}	4.96×10^{-6}	0.1549	0.1699	$0.1623\pm 5\times10^{-6}$ (m)
h2 (m)	0.1523	0.0011	2.63×10^{-6}	5.15×10^{-6}	0.1401	0.1635	$0.1523 \pm 5\times10^{-6}$ (m)
h3 (m)	0.1591	8.18×10^{-4}	1.89×10^{-6}	3.70×10^{-6}	0.1519	0.1659	$0.1591 \pm 4\times10^{-6}$ (m)
h (m)	0.1579	5.57×10^{-4}	1.29×10^{-6}	2.52×10^{-6}	0.1536	0.1628	$0.1579 \pm 3\times10^{-6}$ (m)
V1 (ms^{-1})	0.2856	0.0019	4.45×10^{-6}	8.72×10^{-6}	0.2728	0.2991	$0.2856 \pm 9\times10^{-6}$ (ms^{-1})
V2 (ms^{-1})	0.3044	0.0023	5.26×10^{-6}	1.03×10^{-5}	0.2834	0.3309	$0.3044 \pm 1\times10^{-5}$ (ms^{-1})
V3 (ms^{-1})	0.2913	0.0015	3.46×10^{-6}	6.78×10^{-6}	0.2794	0.3052	$0.2913 \pm 7\times10^{-6}$ (ms^{-1})
V (ms^{-1})	0.2937	0.001	2.39×10^{-6}	4.69×10^{-6}	0.2847	0.3028	$0.2937 \pm 5\times10^{-6}$ (ms^{-1})
Fr (-)	0.1896	0.0013	3.09×10^{-6}	6.05×10^{-6}	0.1783	0.2009	$0.1896 \pm 6\times10^{-6}$ (-)
Re (-)	46200	11.5976	0.0268	0.0525	46200	46400	46200 ± 0.05 (-)
Re_D (-)	32200	113.6257	0.2623	0.5142	31200	33200	32200 ± 0.5 (-)

Table C.14: Hydraulic conditions and bed material characteristics of Exp. 4U *Fbed* including uncertainties.

***Exp.* 4U *Fbed* (Pier 11)**	**Mean**	**Standard Deviation**	**Standard Error**	**Sample Error**	**Min**	**Max**	**Final Values**
Q	0.1244	1.51×10^{-4}	2.35E-07	4.61E-07	0.1238	0.1249	$0.1244 \pm 5\times10^{-7}$ (m^3s^{-1})
h1 (m)	0.1886	0.0038	5.87E-06	1.15E-05	0.1832	0.2129	$0.1886 \pm 1\times10^{-5}$ (m)
h2 (m)	0.2018	0.0041	6.37E-06	1.25E-05	0.1977	0.2273	$0.2018\pm 1\times10^{-5}$ (m)
h (m)	0.1952	0.0039	6.03E-06	1.18E-05	0.1913	0.2192	$0.1952\pm 1\times10^{-5}$ (m)
V1 (ms^{-1})	0.3298	0.0061	9.52E-06	1.87E-05	0.292	0.3395	$0.3298\pm 2\times10^{-5}$ (ms^{-1})
V2 (ms^{-1})	0.3083	0.0058	8.95E-06	1.76E-05	0.2726	0.3148	$0.3083\pm 2\times10^{-5}$ (ms^{-1})
V (ms^{-1})	0.3187	0.0058	9.07E-06	1.78E-05	0.2832	0.325	$0.3187\pm 2\times10^{-5}$ (ms^{-1})
Fr (-)	0.1665	0.0058	9.00E-06	1.76E-05	0.1319	0.1732	$0.1665\pm 2\times10^{-5}$ (-)
Re (-)	61900	75.2589	0.1171	0.2295	61600	62200	61900± 0.2 (-)
Re_D (-)	34900	638.3998	0.9933	1.9468	31000	35600	34900± 2.0 (-)

Table C.15: Hydraulic conditions and bed material characteristics of Exp. 4U *Ebed* including uncertainties.

***Exp.* 4U *Ebed* (Pier 11)**	**Mean**	**Standard Deviation**	**Standard Error**	**Sample Error**	**Min**	**Max**	**Final Values**
Q	0.1237	5.66×10^{-4}	1.81×10^{-7}	3.55×10^{-7}	0.1216	0.125	$0.1244 \pm 4\times10^{-7}$ (m^3s^{-1})
h1 (m)	0.1505	0.0013	4.19×10^{-7}	8.21×10^{-7}	0.1446	0.157	$0.1886 \pm 8\times10^{-7}$ (m)
h2 (m)	0.1467	8.97×10^{-4}	2.87×10^{-7}	5.62×10^{-7}	0.1417	0.1515	$0.2018 \pm 6\times10^{-7}$ (m)
h (m)	0.1486	8.61×10^{-4}	2.75×10^{-7}	5.39×10^{-7}	0.1438	0.1528	$0.1952 \pm 5\times10^{-7}$ (m)
V1 (ms^{-1})	0.4111	0.0047	1.49×10^{-6}	2.92×10^{-6}	0.3934	0.4291	$0.3298 \pm 3\times10^{-6}$ (ms^{-1})
V2 (ms^{-1})	0.4218	0.0032	1.01×10^{-6}	1.99×10^{-6}	0.4075	0.4385	$0.3083 \pm 2\times10^{-6}$ (ms^{-1})
V (ms^{-1})	0.4164	0.0035	1.11×10^{-6}	2.18×10^{-6}	0.4024	0.4318	$0.3187 \pm 2\times10^{-6}$ (ms^{-1})
Fr (-)	0.2856	0.0039	1.24×10^{-6}	2.44×10^{-6}	0.2696	0.3061	$0.1665 \pm 2\times10^{-6}$ (-)
Re (-)	61600	282.1153	0.0902	0.1767	60500	62300	61600 ± 0.2 (-)
Re_D (-)	45600	380.6882	0.1217	0.2384	44100	47300	45600 ± 0.2 (-)

For illustrative purposes, the velocity data of *Profile I* (Exp. 4U Ebed) follow in the form of tables (from Table C.16 to Table C.30), in which the mean values, the variance, the skewness and the kurtosis of the instantaneous three-dimensional velocity components (*u*, *v* and *w*), their fluctuations (u', v' and w'), and their Reynolds shear stresses ($\overline{u'v'}$, $\overline{u'w'}$and $\overline{v'w'}$) are provided.

Profile I

Table C.16: Mean values of Seci1 – *Exp.* 4*U Ebed.*

Seci1						
Distance sensor	***u***	***v***	***w***	***u′v′***	***u′w′***	***v′w′***
5cm	10.000	-0.180	-0.460	0.310	-1.230	-0.060
6cm	27.390	1.340	0.970	-3.140	-1.620	0.520
7cm	28.240	1.380	0.180	-4.780	-1.590	-0.150
8cm	29.190	1.430	-0.780	-4.940	-4.350	-0.200
9cm	24.640	-0.260	-1.850	-2.350	-21.520	-1.280
10cm	27.890	1.970	-0.340	-3.140	-2.650	0.150
11cm	31.830	0.950	-0.860	-3.720	11.000	-1.330
12cm	29.680	2.410	-1.070	-1.670	-4.800	-1.000
13cm	16.650	6.630	-6.250	-14.830	56.600	-7.270
14cm	14.930	-7.070	4.100	-7.760	-223.330	10.460
15cm	10.630	5.440	1.720	-28.520	-8.790	-12.380
16cm	34.050	34.740	-0.080	-15.430	-22.310	2.610
17cm	35.490	3.490	-0.270	0.110	-3.000	0.630
18cm	36.420	3.510	-0.050	0.840	-3.060	0.810
19cm	36.850	3.540	-0.200	1.480	-2.930	0.610
20cm	36.940	3.560	0.170	1.730	-3.220	0.820
21cm	40.970	5.670	2.080	3.160	-2.060	0.060
22cm	40.030	8.180	0.880	3.160	-2.060	0.060
23cm	38.540	3.060	0.380	3.000	-2.140	1.040
24cm	36.010	0.860	0.920	3.360	-10.940	0.950
25cm	38.090	-5.450	0.640	4.030	-2.450	1.840
26cm	40.170	12.710	0.660	3.900	-7.330	0.150
27cm	36.540	9.730	0.200	4.710	-0.970	0.940
28cm	35.780	3.980	0.050	5.680	-0.210	0.310
29cm	40.960	3.840	1.010	8.800	-33.420	-0.140
30cm	37.590	4.030	1.070	9.060	0.320	-0.030

Table C.17: Variance of Seci1 – *Exp.* 4*U Ebed.*

Seci1						
Distance sensor	***u***	***v***	***w***	***u′v′***	***u′w′***	***v′w′***
5cm	6.950	46.690	0.400	325.710	5.240	17.990
6cm	25.940	23.020	4.830	720.170	132.770	111.190
7cm	25.840	24.970	6.980	754.970	180.580	162.500
8cm	36.300	41.110	8.230	2691.550	2439.430	397.700
9cm	106.360	109.020	12.340	20320.010	13821.340	1721.300

Seci1						
Distance sensor	***u***	***v***	***w***	***u′v′***	***u′w′***	***v′w′***
10cm	51.470	31.260	9.190	1555.690	3578.210	248.150
11cm	127.180	57.660	15.140	10066.460	15800.050	968.200
12cm	100.980	86.740	11.130	9360.310	4027.940	967.860
13cm	449.750	485.520	34.190	232423.540	23808.730	16851.010
14cm	921.96	771.93	60.05	776484.850	75079.700	51636.950
15cm	684.970	563.970	26.930	402501.210	18821.710	15823.680
16cm	98.020	1975.200	10.550	194711.150	15515.060	20027.700
17cm	19.430	13.580	4.880	279.230	112.730	70.890
18cm	17.340	13.480	4.940	294.200	101.640	73.840
19cm	18.650	14.040	5.270	298.780	112.030	82.320
20cm	19.080	14.590	5.660	319.690	134.290	106.300
21cm	31.100	80.470	5.590	2367.630	286.070	346.690
22cm	23.820	40.810	6.200	2367.630	286.070	346.690
23cm	19.090	20.570	5.140	586.200	135.080	122.430
24cm	55.010	41.050	7.850	1364.280	8166.830	212.230
25cm	23.300	244.410	6.250	5071.350	217.800	932.770
26cm	41.220	202.080	8.150	8144.660	5825.690	1018.940
27cm	23.530	150.370	7.700	3396.160	274.420	821.100
28cm	31.580	19.230	10.250	1104.660	493.360	280.040
29cm	163.08	31.03	21.02	4795.79	67448.89	763.53
30cm	42.350	35.150	15.990	3600.420	943.490	814.420

Table C.18: Skewness of Seci1 – *Exp. 4U Ebed.*

Seci1						
Distance sensor	***u***	***v***	***w***	***u′v′***	***u′w′***	***v′w′***
5cm	0.066	-9.269	-0.188	3.089	-3.148	7.624
6cm	0.076	-0.037	-0.279	-0.692	-0.529	-0.090
7cm	0.208	0.043	-0.138	-1.491	-0.182	-0.251
8cm	0.450	-1.424	-0.261	11.206	-29.064	-2.859
9cm	-0.024	-1.812	-0.048	1.938	-9.896	-0.622
10cm	0.879	-0.911	0.540	-1.415	2.677	-0.234
11cm	0.705	-0.924	0.527	-6.759	4.100	-5.237
12cm	-1.348	-0.296	-0.021	0.345	-2.085	0.311
13cm	-0.015	0.124	0.058	0.019	1.480	-0.913
14cm	0.344	0.263	-0.348	0.275	-2.099	-0.086
15cm	-0.799	-0.301	-0.156	-0.528	1.260	-0.907
16cm	0.425	0.158	-0.544	1.374	-11.241	-0.221
17cm	-0.219	0.017	0.033	-0.536	-3.547	0.841

Seci1						
Distance sensor	***u***	***v***	***w***	***u′v′***	***u′w′***	***v′w′***
18cm	-0.310	-0.123	0.006	-0.776	-2.074	0.809
19cm	-0.269	-0.129	-0.008	0.893	-0.319	1.018
20cm	-0.242	-0.183	-0.252	1.233	-1.450	1.871
21cm	0.120	-0.050	0.089	0.234	-1.046	-0.429
22cm	0.276	-0.336	-0.021	0.234	-1.046	-0.429
23cm	-0.344	-0.781	-0.125	3.083	1.054	3.094
24cm	-0.706	-2.571	-0.511	-0.697	-16.675	0.939
25cm	-0.367	0.083	-0.118	1.367	-1.902	-0.118
26cm	2.616	1.693	-1.067	-4.622	-17.320	-0.573
27cm	-0.285	-0.351	-0.126	0.515	2.198	-0.995
28cm	-0.286	-0.307	-0.070	2.840	-0.748	-0.125
29cm	2.607	-0.838	-1.181	0.877	-8.290	-0.394
30cm	-0.768	-0.38	-0.125	4.175	1.186	0.761

Table C.19: Kurtosis of Seci1 – *Exp. 4U Ebed.*

Seci1						
Distance sensor	***u***	***v***	***w***	***u′v′***	***u′w′***	***v′w′***
5cm	0.349	140.392	0.518	451.975	14.923	372.905
6cm	0.337	0.364	0.222	11.817	7.666	9.000
7cm	0.510	0.362	-0.022	11.243	10.067	6.098
8cm	24.634	21.567	2.475	833.727	1261.474	304.502
9cm	16.361	18.229	5.210	268.269	170.303	261.653
10cm	17.113	17.990	2.787	52.690	163.830	16.682
11cm	11.377	17.728	5.371	310.378	56.595	177.821
12cm	5.766	6.656	1.415	62.155	64.142	34.718
13cm	0.355	1.238	0.223	16.720	22.678	14.959
14cm	-0.488	-0.123	-0.577	5.520	4.570	5.599
15cm	-0.076	0.745	0.502	8.351	5.140	10.972
16cm	22.984	0.596	8.190	103.633	210.293	39.746
17cm	0.651	0.762	0.149	12.228	65.023	9.064
18cm	0.297	1.052	0.247	31.926	23.354	12.768
19cm	0.312	0.655	0.240	16.612	31.124	14.487
20cm	0.462	0.756	1.091	19.630	20.287	28.395
21cm	0.969	0.877	1.298	9.877	34.366	18.040
22cm	2.000	6.826	2.164	9.877	34.366	18.040
23cm	0.657	38.746	1.102	87.610	41.611	51.884
24cm	40.912	31.333	8.329	99.405	337.469	51.574
25cm	1.189	22.021	0.985	80.751	98.888	115.282

Seci1						
Distance sensor	***u***	***v***	***w***	***u′v′***	***u′w′***	***v′w′***
26cm	39.902	17.437	7.203	403.627	424.944	160.114
27cm	1.508	11.543	1.042	35.608	65.746	60.012
28cm	1.465	3.498	1.467	32.178	24.727	21.860
29cm	35.038	8.149	9.921	88.375	70.059	35.022
30cm	3.819	2.643	1.319	104.751	19.844	24.490

Table C.20: Mean values of Seci2 – *Exp. 4U Ebed*.

Seci2						
Distance sensor	***u***	***v***	***w***	***u′v′***	***u′w′***	***v′w′***
5cm	14.080	1.460	-0.030	0.430	-1.210	3.270
6cm	18.680	1.250	0.130	2.390	-3.630	-0.950
7cm	19.150	1.420	1.100	1.990	-4.990	-2.790
8cm	20.220	1.700	1.230	1.660	-9.250	-2.970
9cm	22.420	2.020	1.140	4.090	-39.870	-3.930
10cm	24.670	2.490	1.140	4.220	-25.280	-4.280
11cm	26.570	2.380	0.690	7.290	-13.580	-4.220
12cm	29.020	2.470	0.280	3.550	-13.750	-2.350
13cm	31.350	3.080	0.130	2.570	-15.180	-1.640
14cm	33.700	3.410	-0.180	1.900	-8.530	-2.060
15cm	35.260	2.770	-0.090	-0.110	-6.070	-1.350
16cm	35.760	3.190	-0.070	2.200	-7.310	-2.330
17cm	37.590	2.260	-0.400	-0.930	-4.020	-0.010
18cm	37.730	2.600	-0.370	-1.070	-36.550	-0.160
19cm	37.140	2.360	-0.040	-0.710	-4.180	-0.100
20cm	37.580	1.560	-0.310	-0.820	-3.090	0.310
21cm	39.790	1.910	-0.530	-0.460	-2.310	0.180
22cm	39.660	2.200	-0.660	-0.670	-2.180	0.390
23cm	40.230	2.100	-0.870	-0.440	-0.940	0.060
24cm	39.640	1.930	-0.470	0.050	-8.870	0.170
25cm	41.090	2.610	-0.780	0.190	-0.730	0.060
26cm	39.470	0.950	-0.400	-0.360	-1.040	-0.700

Table C.21: Variance of Seci2 – *Exp. 4U Ebed.*

Seci2						
Distance sensor	***u***	***v***	***w***	***u′v′***	***u′w′***	***v′w′***
5cm	25.550	23.400	2.650	687.540	75.650	86.120
6cm	38.75	43.47	7.64	1995.320	352.330	356.810
7cm	41.370	47.910	14.660	2277.000	636.160	678.310
8cm	49.650	47.950	18.190	2604.510	912.290	918.090
9cm	180.890	44.290	30.190	6962.180	70281.180	1188.160
10cm	105.680	670.150	25.700	41722.590	27561.400	12879.520
11cm	58.030	40.140	18.390	2737.860	1135.830	838.840
12cm	59.130	59.190	16.880	3138.170	1267.070	733.340
13cm	64.150	27.400	16.130	2210.140	12300.520	575.580
14cm	40.270	98.250	11.370	3314.340	787.150	682.100
15cm	29.440	18.340	10.380	920.440	640.410	327.190
16cm	30.380	18.790	9.040	705.180	483.080	186.750
17cm	23.220	16.170	5.350	458.500	2901.870	95.960
18cm	147.980	11.740	14.410	1104.480	74643.860	148.890
19cm	21.010	180.080	5.630	2797.760	199.040	285.080
20cm	18.330	23.460	4.210	494.220	118.280	90.510
21cm	13.170	13.430	3.250	207.230	61.920	42.270
22cm	11.930	7.140	3.270	134.330	64.680	30.110
23cm	11.930	7.140	3.270	134.330	64.680	30.110
24cm	7.940	5.290	2.390	60.770	32.510	16.150
25cm	36.980	4.340	4.130	143.030	8291.740	18.720
26cm	5.690	8.740	2.000	73.560	20.390	22.330

Table C.22: Skewness of Seci2 – *Exp. 4U Ebed.*

Seci2						
Distance sensor	***u***	***v***	***w***	***u′v′***	***u′w′***	***v′w′***
5cm	0.444	-0.024	-0.113	0.830	-0.669	2.807
6cm	0.269	-0.037	-0.198	0.477	-1.522	-0.082
7cm	0.254	-0.110	-0.005	-0.072	-0.794	-0.103
8cm	0.130	0.177	0.022	-0.526	-0.385	0.742
9cm	0.832	0.297	-0.201	-0.517	-7.558	0.315
10cm	0.494	-0.071	0.023	-4.330	-12.365	-0.896
11cm	-0.448	-0.202	0.624	1.401	-1.568	-0.274
12cm	-0.658	-1.523	0.713	0.392	-1.778	0.244
13cm	-0.237	-0.440	0.718	0.267	-18.485	0.015
14cm	-0.715	-1.326	0.926	-1.014	-3.151	6.953

Seci2						
Distance sensor	***u***	***v***	***w***	***u′v′***	***u′w′***	***v′w′***
15cm	-0.720	-0.324	1.199	-1.327	-4.479	-1.462
16cm	-0.571	-0.186	0.716	2.165	-3.697	-2.166
17cm	-2.233	0.906	0.869	-0.087	-48.477	-0.900
18cm	0.608	0.094	-0.896	-0.002	-7.945	-0.278
19cm	-0.441	-0.687	0.847	-0.599	-3.671	-2.679
20cm	-0.324	-0.080	0.498	-2.797	-3.304	0.351
21cm	-0.361	-0.018	0.401	-1.074	-1.998	0.428
22cm	-0.939	0.304	0.652	-1.552	-3.223	0.846
23cm	-0.741	0.095	0.523	-1.282	-1.737	0.065
24cm	1.552	0.227	-1.049	2.356	-20.256	-1.178
25cm	-0.833	0.070	0.347	-1.236	-2.386	0.162
26cm	-7.526	-0.191	-0.597	0.716	3.210	-20.304

Table C.23: Kurtosis of Seci2 – *Exp. 4U Ebed.*

Seci2						
Distance sensor	***u***	***v***	***w***	***u′v′***	***u′w′***	***v′w′***
5cm	0.464	0.288	0.606	14.587	9.547	16.900
6cm	0.230	0.213	0.627	9.586	12.844	10.580
7cm	0.273	0.232	0.111	14.277	8.428	9.425
8cm	-0.006	0.305	-0.321	11.020	8.076	18.263
9cm	30.833	8.966	4.149	80.250	83.799	15.917
10cm	34.274	9.511	2.267	196.372	222.867	64.701
11cm	0.083	4.891	0.235	27.159	8.154	12.346
12cm	0.412	68.822	0.705	62.211	8.469	25.745
13cm	37.275	5.098	4.324	45.397	448.380	18.626
14cm	1.354	56.201	1.782	77.996	19.964	325.622
15cm	1.712	3.162	3.311	79.528	41.559	31.509
16cm	1.326	0.508	1.453	30.174	31.312	15.635
17cm	79.815	134.552	7.215	141.115	2480.433	36.514
18cm	48.080	1.200	23.146	149.598	62.120	58.144
19cm	0.771	36.097	2.418	147.398	34.251	91.323
20cm	0.563	27.085	1.703	130.883	29.703	25.539
21cm	0.700	1.030	0.923	25.342	10.456	15.696
22cm	1.539	1.801	0.990	30.563	25.491	16.659
23cm	1.354	0.743	1.840	30.361	22.013	20.065
24cm	87.700	2.096	31.815	184.357	442.455	61.892
25cm	2.663	0.838	1.332	40.725	48.258	50.523
26cm	74.002	57.055	38.590	287.971	204.054	1267.291

Table C.24: Mean values of Seci3 – *Exp.* 4*U Ebed*.

Seci3						
Distance sensor	***u***	***v***	***w***	***u′v′***	***u′w′***	***v′w′***
5cm	13.090	0.060	0.180	-1.550	-0.740	1.510
6cm	21.960	0.550	0.110	-2.430	-4.560	-1.890
7cm	24.600	0.950	-0.170	0.190	-5.470	-2.070
8cm	27.030	1.420	-0.220	-1.420	-6.380	-0.770
9cm	28.720	1.690	-0.280	1.540	-10.090	-1.190
10cm	30.770	1.990	-0.340	-0.400	-4.690	-0.480
11cm	30.810	1.950	-0.290	-1.720	-4.580	-0.480
12cm	24.310	2.180	-0.550	-0.860	-4.030	0.280
13cm	33.550	2.690	-0.610	-2.120	-3.960	0.130
14cm	35.140	2.810	-0.730	-0.730	-4.810	-0.110
15cm	28.240	12.780	5.310	-1.900	-4.420	0.740
16cm	36.580	2.350	-0.810	-2.000	-2.990	0.550
17cm	38.170	0.500	-0.980	-1.560	-4.800	0.490
18cm	38.080	1.600	-0.800	-1.650	-3.070	0.610
19cm	37.520	1.640	-0.540	-1.640	-2.790	0.020
20cm	40.170	1.290	-1.060	-0.760	-1.630	0.450
21cm	39.270	-0.030	-0.830	-2.070	-1.860	0.810
22cm	40.150	1.090	-0.690	-0.660	-1.250	0.270

Table C.25: Variance of Seci3 – *Exp.* 4*U Ebed*.

Seci3						
Distance sensor	***u***	***v***	***w***	***u′v′***	***u′w′***	***v′w′***
5cm	13.290	7.370	1.350	113.920	20.930	15.560
6cm	29.950	25.330	5.510	787.690	173.820	153.470
7cm	34.950	25.920	6.610	1018.550	241.720	184.710
8cm	36.590	27.250	6.820	1127.100	285.980	175.120
9cm	54.620	532.970	8.250	17695.510	12784.040	1664.430
10cm	29.960	20.230	5.660	761.960	421.890	128.970
11cm	26.240	18.290	5.970	530.270	193.240	121.680
12cm	20.990	16.360	5.470	374.240	141.260	93.840
13cm	24.620	17.550	5.530	447.480	148.330	101.440
14cm	25.410	108.240	5.680	2410.680	1078.980	329.100
15cm	28.240	12.780	5.310	381.170	235.640	72.710
16cm	19.820	20.620	4.770	446.610	105.250	92.090
17cm	25.850	19.620	4.510	455.650	7390.300	81.060
18cm	17.700	10.610	4.340	242.560	105.660	56.340

Seci3						
Distance sensor	***u***	***v***	***w***	***u′v′***	***u′w′***	***v′w′***
19cm	17.270	8.460	3.970	177.520	87.350	44.610
20cm	11.720	27.000	2.700	305.910	51.050	44.210
21cm	14.590	75.400	3.240	1108.590	71.610	197.110
22cm	11.800	5.320	2.640	104.010	50.550	21.690

Table C.26: Skewness of Seci3 – *Exp.* 4*U Ebed*.

Seci3						
Distance sensor	***u***	***v***	***w***	***u′v′***	***u′w′***	***v′w′***
5cm	0.479	-0.306	0.118	-1.153	-0.943	3.213
6cm	0.203	-0.145	0.130	-0.818	-1.587	-1.275
7cm	0.105	-0.169	0.336	-0.030	-1.330	-0.845
8cm	-0.205	-0.418	0.264	2.760	-1.695	0.623
9cm	2.003	-0.080	-0.673	0.213	-19.640	1.698
10cm	-0.483	-1.618	0.299	2.160	-64.377	-2.579
11cm	-0.174	-0.062	0.116	0.220	-2.174	-0.541
12cm	-0.352	0.086	0.172	-0.827	-2.205	0.001
13cm	-0.132	-0.001	0.279	-0.723	-1.295	0.631
14cm	-0.279	-2.768	0.260	1.638	-56.308	1.187
15cm	-0.051	0.067	0.310	-2.154	-0.921	0.559
16cm	-0.381	-0.072	0.325	-0.490	-1.444	0.803
17cm	4.217	1.969	-0.943	5.848	-34.603	4.964
18cm	-0.697	0.178	0.483	-0.725	-2.075	0.778
19cm	-0.282	0.085	0.441	-0.856	-1.735	-0.850
20cm	-0.979	-2.112	0.475	6.931	-2.466	3.332
21cm	-0.543	0.018	0.512	-1.343	-1.667	1.110
22cm	-0.849	0.071	0.476	-1.276	-2.181	1.201

Table C.27: Kurtosis of Seci3 – *Exp.* 4*U Ebed*.

Seci3						
Distance sensor	***u***	***v***	***w***	***u′v′***	***u′w′***	***v′w′***
5cm	0.376	0.695	0.694	18.372	12.674	20.237
6cm	-0.033	0.483	0.219	10.474	8.205	10.193
7cm	0.045	0.459	0.283	10.507	5.690	13.652
8cm	0.038	40.370	0.319	145.976	7.675	61.114
9cm	56.528	12.251	13.258	33.743	525.731	62.200
10cm	4.535	36.000	0.589	238.415	7253.057	44.963
11cm	0.135	0.572	0.151	12.744	15.436	13.526

Seci3						
Distance sensor	***u***	***v***	***w***	***u′v′***	***u′w′***	***v′w′***
12cm	0.324	0.437	0.486	13.819	11.236	10.646
13cm	-0.150	0.743	0.427	10.772	7.282	14.509
14cm	21.151	61.528	1.859	150.880	3717.321	158.674
15cm	0.619	4.564	0.772	40.585	23.421	13.866
16cm	-0.009	0.526	0.585	10.553	12.094	8.730
17cm	155.250	125.249	25.414	479.492	1212.909	218.104
18cm	0.757	1.458	0.647	18.608	15.957	17.258
19cm	0.321	1.170	0.975	15.741	11.329	21.318
20cm	0.585	5.456	1.512	29.129	14.142	22.421
21cm	1.679	1.406	1.803	40.534	19.968	27.908
22cm	1.528	1.306	1.703	33.534	17.968	25.908

Table C.28: Mean values of Seci4 – *Exp.* 4*U Ebed*.

Seci4						
Distance sensor	***u***	***v***	***w***	***u′v′***	***u′w′***	***v′w′***
5cm	8.620	-1.630	-0.170	-1.550	-0.220	0.510
6cm	25.860	0.310	-0.730	-2.960	-3.190	-0.940
7cm	28.980	1.360	-0.990	-0.610	-3.860	-0.140
8cm	30.930	1.210	-0.900	-2.090	-3.650	-0.340
9cm	31.640	1.700	-0.730	-1.510	-5.800	-0.160
10cm	33.860	1.420	-0.900	-1.330	-4.630	0.060
11cm	33.250	1.500	-0.480	-2.040	-4.550	0.130
12cm	34.010	1.560	-0.710	-0.280	-4.890	0.280
13cm	36.220	2.800	-1.060	-1.080	-5.470	0.290
14cm	35.950	1.670	-0.930	-2.330	-8.170	0.300
15cm	39.450	1.320	-1.630	-1.060	-7.870	-0.150
16cm	39.150	-1.860	-1.270	-2.420	-2.900	0.280
17cm	38.190	0.230	-0.960	-1.430	-25.720	0.320
18cm	37.640	1.110	-0.520	-0.990	-3.310	0.350
19cm	39.030	0.220	-0.680	-1.180	-2.010	-0.120

Table C.29: Variance of Seci4 – *Exp. 4U Ebed*.

Seci4						
Distance sensor	***u***	***v***	***w***	***u′v′***	***u′w′***	***v′w′***
5cm	7.840	17.920	0.500	120.650	4.390	7.890
6cm	29.330	22.010	3.580	680.660	120.890	87.420
7cm	28.490	17.870	4.590	553.990	133.310	93.790
8cm	25.890	18.430	5.200	483.530	160.310	95.700
9cm	31.800	87.940	5.420	1863.790	3716.070	267.060
10cm	28.210	28.540	5.050	743.260	3197.110	94.730
11cm	26.970	17.220	5.800	481.490	157.310	95.420
12cm	26.440	15.120	5.550	389.200	148.290	83.170
13cm	29.060	27.940	5.440	703.210	4546.000	127.610
14cm	41.470	299.380	6.180	10134.690	9265.260	1069.380
15cm	36.350	9.790	5.430	325.990	340.460	55.150
16cm	19.680	33.730	3.820	683.840	97.720	121.900
17cm	107.200	22.220	10.320	1211.990	66829.160	136.920
18cm	20.850	7.080	3.840	189.990	104.680	39.090
19cm	13.890	63.510	2.930	773.560	51.070	90.230

Table C.30: Skewness of Seci4 – *Exp. 4U Ebed*.

Seci4						
Distance sensor	***u***	***v***	***w***	***u′v′***	***u′w′***	***v′w′***
5cm	0.027	0.565	0.082	1.877	-0.120	2.415
6cm	0.112	-0.003	0.009	-0.489	-1.734	-1.196
7cm	-0.046	-0.073	-0.149	-0.296	-1.126	0.429
8cm	-0.069	0.003	-0.094	-0.202	-1.297	-0.500
9cm	1.398	1.412	-0.467	-0.819	-36.960	-0.170
10cm	1.485	-3.638	-0.472	-0.425	-52.251	-0.836
11cm	-0.190	-0.036	0.052	-0.308	-1.200	0.098
12cm	-0.156	0.028	0.146	0.206	-1.245	0.275
13cm	-1.149	-0.175	0.331	-0.013	-31.006	0.631
14cm	-1.253	-0.355	0.471	26.121	-21.732	-13.791
15cm	0.401	0.229	-0.075	-0.638	-3.638	0.244
16cm	-0.577	0.293	0.466	-0.530	-1.796	0.512
17cm	-0.577	-5.291	0.048	1.627	-13.080	-0.946
18cm	-0.261	0.284	0.425	-1.041	-1.552	1.308
19cm	-0.320	-1.744	0.340	-3.684	-1.489	-1.730

Table C.31: Kurtosis of Seci4 – *Exp. 4U Ebed.*

Seci4						
Distance sensor	***u***	***v***	***w***	***u′v′***	***u′w′***	***v′w′***
5cm	0.109	237.724	0.260	278.854	10.664	278.972
6cm	-0.082	0.224	0.507	7.276	9.634	13.758
7cm	-0.162	0.424	0.360	9.903	7.769	16.386
8cm	-0.007	0.448	0.270	8.227	8.343	6.899
9cm	52.941	75.634	8.024	197.020	1448.581	198.481
10cm	52.658	174.879	8.664	295.815	2849.732	85.777
11cm	-0.280	19.964	0.061	14.551	5.028	7.045
12cm	-0.245	0.652	-0.059	8.640	4.937	7.619
13cm	78.628	1.468	9.774	43.254	1004.021	11.563
14cm	80.754	24.256	15.165	2305.323	491.222	1037.246
15cm	0.922	0.960	0.219	11.968	24.338	10.505
16cm	0.184	3.867	0.802	13.600	11.538	20.386
17cm	86.229	181.490	39.906	220.031	234.767	91.946
18cm	0.329	1.771	0.986	18.599	8.243	22.820
19cm	0.380	111.522	1.153	316.966	12.132	154.306

Table C.32: Mean values of Seci5 – *Exp. 4U Ebed.*

Seci5						
Distance sensor	***u***	***v***	***w***	***u′v′***	***u′w′***	***v′w′***
5cm	12.400	0.620	-0.190	-1.270	-11.530	-0.150
6cm	26.560	1.540	-1.650	0.630	-3.710	-0.070
7cm	26.830	2.020	-0.950	0.630	-3.940	-0.160
8cm	33.520	2.050	-1.960	-0.450	-3.400	0.480
9cm	31.270	2.370	-1.080	-1.670	-12.130	1.350
10cm	33.120	1.310	-0.830	-0.640	-4.510	0.720
11cm	33.880	1.390	-0.850	1.330	-3.790	0.500
12cm	35.550	1.240	-0.990	0.550	-4.820	0.250
13cm	36.420	0.830	-1.370	-1.410	-4.320	-0.140
14cm	34.100	1.160	-0.770	2.010	-61.070	-0.480
15cm	41.400	1.860	-3.110	0.440	-9.480	-0.290
16cm	38.040	0.950	-1.470	-0.170	2.260	0.200
17cm	38.480	0.080	-0.960	0.550	-7.870	0.260
18cm	39.310	-1.220	-0.950	-0.850	-2.290	0.670

Table C.33: Variance of Seci5 – *Exp.* 4*U Ebed*.

	Seci5					
Distance sensor	***u***	***v***	***w***	***u′v′***	***u′w′***	***v′w′***
5cm	60.030	20.250	4.030	3815.340	20217.060	235.770
6cm	28.950	20.220	2.850	680.210	92.910	63.070
7cm	23.160	16.770	3.750	412.340	95.930	72.930
8cm	21.010	17.650	4.310	385.460	100.180	80.250
9cm	56.450	323.780	6.870	7947.340	20040.820	817.550
10cm	25.000	15.620	5.150	386.900	1159.920	74.830
11cm	23.360	13.730	5.360	322.590	129.200	73.600
12cm	27.370	11.870	5.130	316.130	1164.620	66.970
13cm	25.030	145.120	5.230	2966.200	464.310	342.780
14cm	253.380	36.670	18.540	2357.320	79520.870	172.570
15cm	46.900	21.730	5.600	772.120	546.140	95.510
16cm	42.450	12.550	5.360	614.980	466.950	73.400
17cm	37.860	80.650	5.500	1897.010	11364.190	245.340
18cm	17.950	26.660	3.570	434.200	665.240	75.270

Table C.34: Skewness of Seci5 – *Exp.* 4*U Ebed*.

	Seci5					
Distance sensor	***u***	***v***	***w***	***u′v′***	***u′w′***	***v′w′***
5cm	-6.030	-7.156	6.054	96.003	-12.666	-92.025
6cm	0.044	0.089	-0.083	-0.919	-1.794	0.334
7cm	0.074	-0.036	-0.172	0.203	-1.721	-0.730
8cm	-0.039	-0.088	-0.102	0.118	-1.674	0.630
9cm	3.870	1.156	-1.974	-0.641	-16.545	2.825
10cm	-1.361	1.461	0.266	-2.455	-65.530	0.307
11cm	-0.078	-0.119	0.090	0.778	-1.049	0.510
12cm	-0.673	0.029	0.326	0.460	-53.366	0.258
13cm	-0.656	-0.362	0.378	-0.501	-59.275	-1.114
14cm	-2.279	-4.769	1.591	1.328	-6.265	-2.081
15cm	-0.056	-0.118	-0.111	0.406	-3.810	0.291
16cm	-0.229	0.035	0.754	0.116	5.641	-0.266
17cm	-2.266	-1.297	0.843	10.603	-25.110	1.702
18cm	-0.764	-0.004	0.583	0.029	88.193	0.936

Table C.35: Kurtosis of Seci5 – *Exp. 4U Ebed.*

Seci5						
Distance sensor	***u***	***v***	***w***	***u′v′***	***u′w′***	***v′w′***
81.099	144.098	83.899	12678.992	209.434	11941.004	-92.025
-0.049	0.339	0.280	20.795	8.694	9.641	0.334
-0.100	0.217	0.676	7.937	7.265	9.183	-0.730
0.061	0.159	0.331	8.226	7.890	10.048	0.630
90.198	23.089	27.984	58.671	277.539	54.768	2.825
24.439	37.494	2.617	72.356	4784.301	6.431	0.307
-0.349	0.647	-0.093	8.062	4.296	7.475	0.510
19.178	0.557	2.818	14.017	3230.522	15.655	0.258
6.938	46.655	1.114	127.406	5110.912	103.095	-1.114
17.658	130.059	12.790	94.042	41.494	46.941	-2.081
1.700	2.653	0.290	19.786	21.905	8.894	0.291
1.151	0.694	1.975	17.172	64.404	15.649	-0.266
119.679	96.196	23.887	523.265	661.485	296.627	1.702
20.902	3.038	6.137	18.891	8990.943	14.546	0.936

Appendix D

Conference Submissions and Communications

D.1 Caracterização da cavidade de erosão em torno de fundações de pontes. Relação entre volume erodido e profundidade de erosão

14° Congresso da Água

TITLE: Caracterização da cavidade de erosão em torno de fundações de pontes. Relação entre volume erodido e profundidade de erosão[1]

Paper presented in the 14° Congresso da Água

Observations: Bento, A.M. performed the experimental work, analysed and post-processed the data as well as analysed the results, and wrote the paper. Viseu, T., Couto, L. and Pêgo, J.P. helped in the analysis of the results and edited and reviewed the manuscript.

[1] Bento, A.M., Viseu T., Couto, L. & Pêgo, J.P. (2018). Caracterização da cavidade de erosão em torno de fundações de pontes. Relação entre volume erodido e profundidade de erosão. In: *14° Congresso da Água, 7−9 March 2018*, Évora, Portugal.

14º CONGRESSO DA ÁGUA
7, 8 e 9 Março 2018
ÉVORA
Évora Hotel
GESTÃO DOS RECURSOS HÍDRICOS: NOVOS DESAFIOS

CARACTERIZAÇÃO DA CAVIDADE DE EROSÃO EM TORNO DE FUNDAÇÕES DE PONTES. RELAÇÃO ENTRE VOLUME ERODIDO E PROFUNDIDADE DE EROSÃO

Ana Margarida, BENTO[1]; Teresa, VISEU[2]; Lúcia, COUTO[3]; João Pedro, PÊGO[4]

[1] Estudante de doutoramento, Laboratório Nacional de Engenharia Civil, Av. do Brasil 101, 1700-066 Lisboa / Faculdade de Engenharia da Universidade do Porto, Rua Dr. Roberto Frias, s/n 4200-465 Porto, Portugal, ana.bento@fe.up.pt

[2] Investigadora Auxiliar, Laboratório Nacional de Engenharia Civil, Av. do Brasil 101, 1700-066 Lisboa, Portugal, tviseu@lnec.pt

[3] Investigadora Auxiliar, Laboratório Nacional de Engenharia Civil, Av. do Brasil 101, 1700-066 Lisboa, Portugal, lcouto@lnec.pt

[4] Professor Auxiliar, Faculdade de Engenharia da Universidade do Porto, Rua Dr. Roberto Frias, s/n 4200-465 Porto, Portugal, jppego@fe.up.pt

Resumo

O desenvolvimento da cavidade de erosão junto de pilares e encontros de pontes coloca, frequentemente, em risco a sua estabilidade estrutural, o que poderá conduzir a perdas patrimoniais e/ou humanas como consequência do seu colapso parcial ou total. É, portanto, fundamental conhecer a morfologia do leito em torno dos elementos que constituem a fundação de pontes. Embora o fenómeno da erosão localizada tenha sido amplamente investigado nas últimas décadas, poucas formulações foram desenvolvidas para a previsão do volume erodido com base na profundidade máxima de erosão, principal parâmetro usado no dimensionamento das fundações de pontes. As equações existentes na literatura resultam essencialmente de estudos desenvolvidos em ambiente laboratorial. A presente comunicação tem como objetivo apresentar as formulações descritas na literatura que relacionem o volume erodido com a profundidade máxima de erosão ao longo do tempo bem como a aplicação de tais formulações em contribuições recentes dos autores, provenientes também de estudos laboratoriais. O trabalho experimental apresentado na presente comunicação consistiu na reprodução de um escoamento na proximidade de um pilar circular de 0,05 m de diâmetro, fundado num leito de sedimentos uniformes e sem transporte sólido generalizado. As experiências decorreram num canal do Laboratório de Hidráulica da Faculdade de Engenharia da Universidade do Porto. A evolução temporal da profundidade máxima de erosão e dos volumes erodidos foram obtidos com precisão submilimétrica através da aplicação de fotogrametria de pequena amplitude. Desta análise resultou uma equação empírica para a profundidade de erosão e o volume de escavação ao longo de todo o processo erosivo. A aplicabilidade da equação resultante é avaliada confrontando com resultados de equações descritas na literatura.

Palavras-chave: Erosão localizada, cavidade de erosão, fundações de pontes, profundidade de erosão, volume erodido.

Tema: Investigação em hidráulica e recursos hídricos

1. INTRODUÇÃO

O fenómeno de erosão localizada resulta da complexa interação entre o escoamento e o leito móvel de um rio em resultado das perturbações que se desenvolvem devido à presença de obstáculos nesse escoamento. A presença de obstáculos, como pilares e encontros de pontes, induz uma significativa alteração do campo de velocidades, resultando na erosão do leito envolvente (Melville e Coleman, 2000). Este processo erosivo constitui a principal causa de instabilidade estrutural de pontes e está frequentemente associada à rotura parcial ou total, ameaçando valores patrimoniais e, em casos mais extremos, vidas humanas (Flint et al., 2017). Uma rigorosa previsão da morfologia do leito reveste-se, assim, de grande importância para um projeto seguro e económico de novas pontes, bem como para a manutenção das já existentes (Johnson e Jones, 1993).

Este tópico tem sido amplamente investigado por recurso a campanhas experimentais, observações de campo e modelações numéricas. Uma grande parte desses estudos focou-se na previsão da profundidade máxima de erosão em torno de encontros e pilares até as condições de equilíbrio serem alcançadas, após algumas horas ou mesmo vários dias de ensaio (Kothyari et al., 2007). No entanto, diversos investigadores concordam que o equilíbrio não é representativo das condições de campo, devido à longa duração necessária de eventos de cheia que poderia proporcionar as condições para atingir a fase de equilíbrio, o que leva a uma frequente sobre-estimação da profundidade de erosão. Apesar disso, alguns investigadores concentraram-se na análise da evolução temporal da profundidade de erosão (Oliveto e Hager, 2005; Pandey et al., 2017). Embora se registe um elevado esforço da comunidade científica em fornecer informações importantes sobre o efeito de vários parâmetros na avaliação da profundidade de erosão, a compreensão física do fenómeno erosivo permanece ainda incompleta. Para melhor descrever este fenómeno deve dispor-se, ainda, de informação detalhada da morfologia da cavidade de erosão que se desenvolve, nomeadamente, sobre a relação entre a profundidade máxima de erosão e o volume erodido.

Nas últimas décadas, alguns trabalhos laboratoriais têm sido realizados com o objetivo de fornecer formulações empíricas que relacionam as profundidades máximas de erosão e os volumes erodidos, baseando-se sobretudo no balanço de massa de sedimentos à escala da cavidade de erosão experimentalmente obtida. Yanmaz e Altinbilek (1991) foram os primeiros autores a associar a geometria da cavidade de erosão à de um cone invertido de base circular ou quadrada, fornecendo uma aproximação razoável do volume erodido. Esta abordagem foi estendida a encontros de pontes por Yanmaz e Köse (2007). Couto (2000) obteve dados de profundidades de erosão e respetivos volumes erodidos na vizinhança de encontros de pontes. Funções parabólicas têm também vindo a ser apresentadas para pilares simples, de secção circular e quadrangular, fundados em diferentes tipos de sedimentos (Link e Zanke, 2004; Link et al., 2008; Diab et al., 2010; Diab, 2011), demonstrando um melhor ajuste à forma real da cavidade de erosão do que a primeira aproximação. Outros investigadores, como Dey (1999) e Ramos et al. (2016), assumiram que o volume apresenta uma função polinomial de terceira ordem da profundidade máxima de erosão, tanto para um pilar circular como para um pilar de geometria composta. Embora razoáveis, algumas dessas descrições empíricas não

são totalmente suportadas por medições experimentais extensas, podendo comprometer a fiabilidade e resolução das mesmas.

Em contraste com a maioria dos trabalhos onde os levantamentos do interior da cavidade de erosão são essencialmente pontuais, o que condiciona representações mais detalhadas da superfície erodida, existem trabalhos mais recentes onde a evolução temporal da cavidade de erosão em torno de pilares circulares se processa sem interrupção da experiência, através da aplicação de técnicas de imagem avançada (Bouratsis et al., 2013, 2017). Estas técnicas possibilitaram uma análise contínua e não-intrusiva da evolução temporal da cavidade de erosão, com resolução espacial e temporal bastante significativa, resultando em novas formulações empíricas da morfologia da cavidade de erosão. Aliada a alguns avanços da tecnologia de instrumentação laboratorial, tem-se assistido a um crescente desenvolvimento da modelação numérica do processo erosivo em torno de fundações de pontes, nomeadamente de ferramentas de dinâmica de fluidos computacional (CFD), para a qual é fundamental dispor de dados da morfologia do leito que permitam a calibração e a validação desses modelos. Uma descrição recente e mais completa das características do leito envolvente e sua relação com o campo de escoamento é, entre outros, feita por Escauriaza e Sotiropoulos (2011), cujo modelo numérico foi validado com resultados experimentais de Dargahi (1990). Uma revisão recente dos avanços numéricos nesta área é apresentada por Sumer (2015).

Não obstante estes avanços, há ainda falta de dados experimentais sobre a geometria da cavidade de erosão. Por outro lado, na impossibilidade de caracterizar tridimensionalmente a cavidade de erosão, é necessário dispor de formulações que permitam uma reprodução, ainda que aproximada, da geometria dessa cavidade e da sua relação com a profundidade de erosão, parâmetro tão comumente usado no dimensionamento das fundações de pontes.

Neste sentido, a presente comunicação apresenta uma compilação de equações existentes na literatura e procede à sua aplicação a dados experimentais. O trabalho experimental realizado consistiu na reprodução de um escoamento na proximidade de um pilar circular de 0,05 m de diâmetro, fundado num leito de sedimentos uniformes e sem transporte sólido generalizado. Os ensaios decorreram na instalação experimental do Laboratório de Hidráulica da Faculdade de Engenharia da Universidade do Porto.

As formulações disponíveis na literatura são descritas na secção 2. A instalação experimental, o modelo de pilar, o procedimento e metodologia experimental são brevemente apresentados na secção 3. Os resultados experimentais são sistematizados e discutidos na secção 4. Na secção 5 procede-se à aplicação e análise comparativa das formulações empíricas, derivada e recolhidas da literatura, que relacionam a profundidade máxima de erosão com o volume erodido. Por fim, as principais conclusões são remetidas à secção 6.

2. FORMULAÇÕES EXISTENTES E CONDIÇÕES DE APLICAÇÃO

A revisão literária efetuada indica que são poucos os dados que fundamentam as formulações empíricas, provenientes de trabalhos experimentais, que relacionam a profundidade máxima de erosão com o volume erodido junto de pilares e encontros de pontes. A Tabela 1 apresenta as condições de escoamento e as propriedades dos sedimentos usadas na derivação de algumas formulações existentes. Da análise destes elementos, verifica-se que estas formulações foram obtidas numa gama de intensidades de escoamento (U/U_c) variando de 0,5 (início do transporte sólido) a 1,5 (condições de transporte sólido generalizado). A altura de escoamento de aproximação varia entre uma a duas vezes a dimensão do elemento de fundação (exposta ao escoamento). A gama de variação da granulometria dos sedimentos do leito variam de D_{50} = 0,26 mm (areia) a D_{50} = 3,25 mm (gravilha). Os coeficientes de gradação em causa indicam distribuições uniformes dos sedimentos (σ_D inferiores a 1,5), à exceção de alguns ensaios de Couto (2000). Segue-se uma breve descrição sobre a obtenção das formulações disponíveis na literatura e indicadas na Tabela 1.

Yanmaz e Altinbilek (1991) foram os primeiros autores a associar a forma da cavidade de erosão à de um cone invertido (*frustum of an inverted cone*, na literatura inglesa) de base circular ou quadrada, consoante a secção do pilar. A formulação empírica, presente na Tabela 1, resultou de um conjunto de experiências em modelos de pilar de secção circular e quadrada, de 0,067 m de diâmetro e de comprimento lateral, respetivamente. As experiências foram interrompidas ao fim de diferentes durações, nomeadamente aos 5 min, 20 min, 60 min, 100 min e 150 min, para a caracterização da evolução da cavidade de erosão. Os modelos de pilar foram fundados em areia uniforme e sem transporte sólido generalizado. Concluíram que a geometria da cavidade permanece praticamente inalterada com o tempo, sendo a inclinação dos taludes laterais da cavidade de erosão aproximadamente igual ao ângulo de repouso da areia usada.

Link e Zanke (2004) estudaram experimentalmente a variação temporal do volume da cavidade de erosão em torno de um pilar circular, fundado numa areia de granulometria uniforme. A geometria da cavidade de erosão foi medida por recurso a um sensor de distância a laser (*laser distance sensor - LDS*, na literatura inglesa) inserido num pilar acrílico de 0,2 m de diâmetro. Oito perfis verticais, tomados em quatro direções diferentes em torno do pilar (0°, 45°, 90° and 135°), permitiram o cálculo do volume erodido para os instantes medidos. Foram consideradas três diferentes intensidades de escoamento (U/U_c), incorporando condições sem e com transporte sólido generalizado. As experiências foram realizadas numa instalação com 26 m de comprimento, 2 m de largura e 1 m de profundidade por um período de 20 horas e 6 horas, sem e com transporte sólido generalizado, respetivamente. Para cada conjunto de ensaios, a profundidade de escoamento variou de um a dois diâmetros do pilar testado.

Link et al. (2008), por sua vez, caracterizaram somente uma condição hidráulica para o mesmo pilar circular, aumentando significativamente o número de perfis verticais usados na caracterização da cavidade de erosão, 24 (em intervalos de 15°) ao invés dos 8 usados por Link e Zank (2004). Diab et al (2010) conduziram ensaios na mesma instalação experimental

e segundo a mesma metodologia de análise experimental usada em Link et al. (2008). Nesse estudo, estenderam a análise a pilares, de base circular e quadrada, fundados em gravilha uniforme. Neste âmbito, Diab (2011) desenvolveu novas formulações adimensionais relacionando os volumes erodidos com as profundidades máximas de erosão junto de pilares de secção quadrada com diferentes alinhamentos (ângulos de ataque); na Tabela 1 apresenta-se somente a formulação empírica resultante para o pilar quadrado alinhado com a direção do escoamento. A técnica de medição usada foi a mesma que em Link e Zanke (2004). Foram sugeridas formulações empíricas de determinação do volume erodido de acordo com o melhor ajuste feito aos respetivos resultados experimentais; as equações apresentam sobretudo uma relação polinomial de segunda ou terceira ordem (Tabela 1). Contrariamente aos ensaios preconizados por Link e Zanke (2004), as experiências subsequentes de Link et al. (2008), Diab et al. (2010) e Diab (2011) desenvolveram-se até aos últimos estágios de ensaio (estados considerados de equilíbrio).

Yanmaz e Köse (2007) realizaram experiências em torno dos modelos de pilar circular e quadrado, bem como na vizinhança de modelos verticais de encontros de pontes, todos fundados em areia uniforme e sem transporte sólido generalizado. As durações consideradas para os ensaios foram as mesmas estipuladas no trabalho de Yanmaz e Altinbilek (1991). Do estudo resultaram formulações empíricas adimensionais para a variação temporal do volume da cavidade de erosão e da área de superfície erodida para cada elemento de fundação. As formulações propostas para o volume de escavação junto dos elementos de fundação foram adicionalmente validadas com as profundidades de erosão obtidas pela previsão de Oliveto e Hager (2005).

Ramos et al (2016) reuniram um conjunto de 15 ensaios para a caracterização da evolução temporal da cavidade de erosão em torno de um pilar de geometria composta. O modelo de pilar era constituído por uma coluna, maciço de encabeçamento e quatro estacas de fundação. A aplicação de fotogrametria de pequena amplitude (*close-range photogrammetry*, na literatura inglesa) permitiu o estudo do desenvolvimento da profundidade máxima de erosão e do volume da cavidade de erosão, culminando na formulação empírica presente na Tabela 1.

Couto (2000) desenvolveu um trabalho laboratorial de caracterização da geometria das cavidades de erosão associadas a obstáculos salientes de margens em canal com fundo móvel arenoso, de diferentes granulometrias, bem como composto por materiais de baixa densidade (pedra pomes moída e granulado plástico). Abordou a localização das profundidades máximas de erosão, a batimetria resultante do processo erosivo junto aos obstáculos e o volume de escavação final obtido para cada ensaio considerado no estudo. O levantamento batimétrico foi efetuado por intermédio de um seguidor de fundos durante o decurso do ensaio.

Um trabalho recentemente desenvolvido por Bouratsis (2017) tirou partido de técnicas experimentais avançadas para a caracterização, sem interrupção do ensaio, das cavidades de erosão em torno de um pilar circular de 0,152 m fundado num leito de gravilha por um período de 250 min. Apesar da extensa análise dos parâmetros geométricos da cavidade de

erosão ao longo do tempo, o estudo não devolveu uma formulação empírica que relacionasse as profundidades máximas de erosão com os volumes de escavação. Deste modo, os dados deste estudo não aparecem na Tabela 1.

Na presente comunicação, as cinco formulações desenvolvidas para relacionar a profundidade máxima de erosão com o volume erodido junto ao pilar circular (Tabela 1) são aplicadas aos resultados do estudo experimental na secção 4 e posteriormente analisadas gráfica e estatisticamente na secção 5.

Tabela 1. Base de dados, formulações e respetivas condições de aplicação.

Tipo de fundação	Referência	U/U_c	h/b	D_{50} (mm)	σ_D	Formulação empírica
Pilar circular	Yanmaz e Altinbilek (1991)	<1	2,0	1,07	1,13	$V = \frac{\pi}{3\,tg\,\emptyset}\left(\frac{d_S^3}{tg\,\emptyset} + \frac{3d_S^2 b}{2}\right)$
	Link e Zanke (2004)	0,5 1,0 2,0	1,00 1,25 1,50 1,75 2,00	0,97	1,4	$V = (7d_S^2 + 5d_S)\cdot 10^{-5}$
	Yanmaz e Köse (2007)	<1	2,0	1,07	1,13	$V = 1{,}738 \cdot \left[\frac{t\,D_{50}(s\,g\,D_{50})^{0.5}}{b^2}\right]^{0{,}299} \times d_S \cdot \frac{\pi b^2}{4}$
	Link et al. (2008)	0,95	1,5	0,26	1,37	$\frac{V}{V_f} = 0{,}897\left(\frac{d_S}{d_{Sf}}\right)^2 + 0{,}021\left(\frac{d_S}{d_{Sf}}\right) + 0{,}046$
	Diab et al. (2010)	0,95	1,5	3,25	1,20	$\frac{V}{V_f} = 0{,}340\left(\frac{d_S}{d_{Sf}}\right)^3 + 0{,}680\left(\frac{d_S}{d_{Sf}}\right)^2 - 0{,}100\left(\frac{d_S}{d_{Sf}}\right) + 0{,}012$
Pilar quadrado	Yanmaz e Altinbilek (1991)	<1	2,0	1,07	1,13	$V = \frac{d_S}{3}\left[\pi\left(\frac{d_S}{tg\,\emptyset} + \frac{b}{2}\right)^2 + \left(\frac{2d_S b}{tg\,\emptyset} + b^2\right)\right]\ln tg\left(\frac{3\pi}{8}\right) - 2b^2$
	Yanmaz e Köse (2007)	<1	2,0	1,07	1,13	$V = 1{,}279 \cdot \left[\frac{t\,D_{50}(s\,g\,D_{50})^{0.5}}{b^2}\right]^{0{,}400} \times d_S \cdot \frac{\pi b^2}{4}$
	Diab et al. (2010)	0,95	1,5	3,25	1,20	$\frac{V}{V_f} = 0{,}340\left(\frac{d_S}{d_{Sf}}\right)^3 + 0{,}680\left(\frac{d_S}{d_{Sf}}\right)^2 - 0{,}100\left(\frac{d_S}{d_{Sf}}\right) + 0{,}012$

Pilar de geometria composta	Ramos et al. (2016)	0,97	1,5	0,86	1,4	$\frac{V}{V_f} = \left(\frac{d_S}{d_{Sf}}\right)^3$
Encontro	Couto (2000)	<1 - >1	-	0,32 - 4,00	1,0 - 1,58	-
	Yanmaz e Köse (2007)	<1	-	1,8	<1,5	$V = 0{,}681 \cdot \left[\frac{t\, D_{50}(s\, g\, D_{50})^{0.5}}{b^2}\right]^{0{,}265} \times d_S \cdot \frac{\pi\, b^2}{4}$

Nota: U - velocidade do escoamento de aproximação; U_c – velocidade crítica do escoamento; h – altura do escoamento de aproximação; b – dimensão do elemento de fundação (diâmetro ou comprimento lateral exposto ao escoamento); D_{50} – diâmetro médio do sedimento; σ_D - coeficiente de gradação do material; s – densidade relativa do sedimento; $\emptyset$ - ângulo de repouso do sedimento; t – instante temporal; d_S – profundidade máxima na cavidade de erosão; d_{Sf} – profundidade máxima na cavidade de erosão para o instante final; V – volume da cavidade de erosão; V_f – volume da cavidade de erosão para o instante final.

3. DESCRIÇÃO DO TRABALHO EXPERIMENTAL

3.1. INSTALAÇÃO EXPERIMENTAL E MODELO DE PILAR

Reproduziu-se experimentalmente um escoamento permanente na proximidade de um pilar circular de 0,05 m de diâmetro, fundado num leito de sedimentos uniformes e sem transporte sólido generalizado. Os ensaios realizaram-se no canal de 32,20 m de comprimento e 1,00 m de largura (Figura 1), no Laboratório de Hidráulica da Faculdade de Engenharia da Universidade do Porto (FEUP). O canal possui janelas de vidro que permitem a fácil visualização do escoamento, funcionando em circuito fechado. A água é elevada de dois reservatórios, situados a um nível inferior, por duas bombas associadas em paralelo. O caudal em circulação é regulado manualmente e controlado por dois caudalímetros eletromagnéticos, colocados a montante do canal. À entrada do canal existem macro rugosidades que garantem um escoamento turbulento bem desenvolvido. Na extremidade de jusante do canal, uma comporta plana vertical regula a altura do escoamento. O canal dispõe de duas caixas de areia: a primeira, onde se instalou o pilar circular, e a segunda, mais a jusante, onde os sedimentos transportados são retidos, ambas têm 3,40 m de comprimento e 0,35 m de profundidade. Para a realização dos ensaios usou-se uma areia de granulometria uniforme (σ_D) de 1,48, com diâmetro médio (D_{50}) de 0,86 mm e uma densidade (ρ) de 2650 kgm^{-3}. As experiências decorreram sem transporte sólido generalizado, através da adoção de uma velocidade de aproximação igual a 97% da velocidade crítica do escoamento, obtida pela fórmula de Neil (1967). Foram, portanto, impostos um caudal (Q) de 0,059 m^3 s^{-1} e uma altura de escoamento (h) de 0,18 m. O pilar circular de 0,05 m de diâmetro, de policloreto de vinilo (PVC), foi instalado na primeira caixa de sedimentos segundo o alinhamento central do canal.

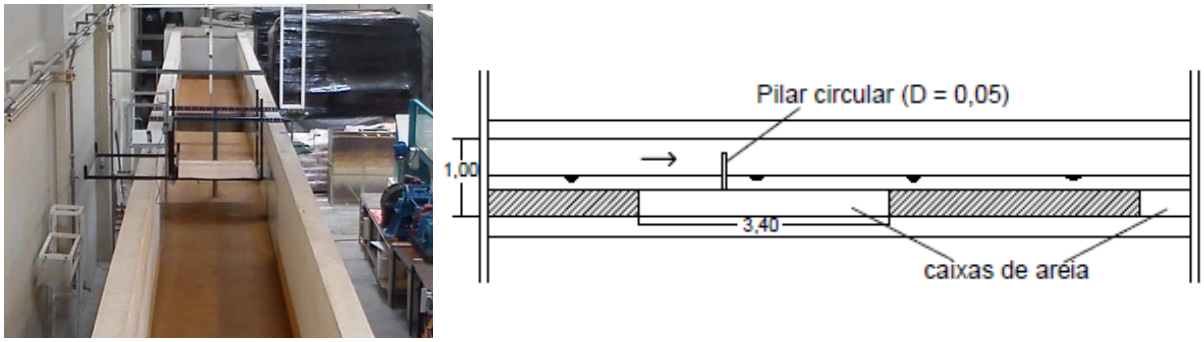

Figura 1. Canal de ensaios: fotografia (esquerda) e vista longitudinal (direita); dimensões em metros.

3.2. PROCEDIMENTO EXPERIMENTAL

Procedeu-se à fixação do pilar circular na primeira caixa de areia, posteriormente preenchida com areia até atingir o nível superior da caixa. Após uma conveniente compactação e regularização da superfície de areia, protegeu-se a zona em redor do pilar com duas grelhas metálicas, revestidas a geotêxtil, para evitar o aparecimento de erosão antes do escoamento atingir as características desejadas. Abriram-se, de forma gradual, as válvulas até atingir a altura de escoamento e o caudal de entrada pretendidos. Removeram-se as placas de geotêxtil com a ajuda de dois cordéis laterais e iniciou-se o ensaio. Decorrido o tempo estipulado para a duração do ensaio, procedeu-se ao esvaziamento gradual do canal e à secagem da areia. Este procedimento foi realizado para as seguintes durações de ensaio: 5, 10, 15, 30, 60, 120, 240, 480, 720, 1440, 4320 e 10080 minutos.

3.4. METODOLOGIA DE ESTUDO

Os ensaios experimentais permitiram: (i) a avaliação da evolução da profundidade máxima de erosão junto do pilar para a duração estipulada de cada ensaio, (ii) a representação tridimensional da cavidade de erosão, e (iii) a derivação da equação empírica para avaliação da taxa de volume erodido e da profundidade de erosão.

A cavidade de erosão, ao fim de cada ensaio experimental, foi caracterizada por aplicação de fotogrametria de pequena amplitude. Esta técnica, de precisão submilimétrica, permitiu a quantificação da distribuição espacial da erosão em torno do pilar circular em estudo. Para a obtenção de resultados fidedignos foi necessário conceber um esquema de captura fotográfica e de posicionamento de elementos de referência espacial. Foi usada uma câmara digital (Canon PowerShot SX 160 IS) para fotografar a cavidade de erosão e a zona circundante, em diversos pontos, sobre uma plataforma horizontal a aproximadamente 0,6 m do nível inicial da caixa de areia. Os elementos de referência espacial consistiram em determinadas marcas efetuadas em duas réguas graduadas, colocadas junto às paredes do canal. Utilizou-se o software “Agisoft PhotoScan Professional” (versão 1.0.4) para o processamento fotogramétrico e obtenção dos correspondentes modelos digitais de elevação (DEMs). A introdução dos DEMs no software de sistema de informação geográfica “Global Mapper” (versão 15.0) permitiu o cálculo dos níveis do leito e a medição dos volumes de

escavação. Esta informação conduziu à derivação da expressão empírica para a avaliação das profundidades máximas de erosão e dos volumes da cavidade, concretizando, deste modo, o objetivo (iii).

4. DISCUSSÃO DOS RESULTADOS EXPERIMENTAIS

4.1. EVOLUÇÃO DA PROFUNDIDADE DE EROSÃO

A configuração do leito no alinhamento central do pilar circular encontra-se ilustrada na Figura 2 para alguns dos instantes em que foram registados resultados nos ensaios. Considerou-se como critério de paragem do último estágio de ensaio, a duração correspondente a um aumento da profundidade de erosão inferior a 5% do diâmetro do pilar num período de 24 horas (Melville and Chiew, 1999). Para o ensaio final, segundo aquele critério, registou-se uma profundidade máxima de erosão de 0,115 m junto à face de montante do pilar. Este valor aproxima-se do valor de 0,11 m previsto pelo método de *Florida Department of Transportation* (FDOT, 2010).

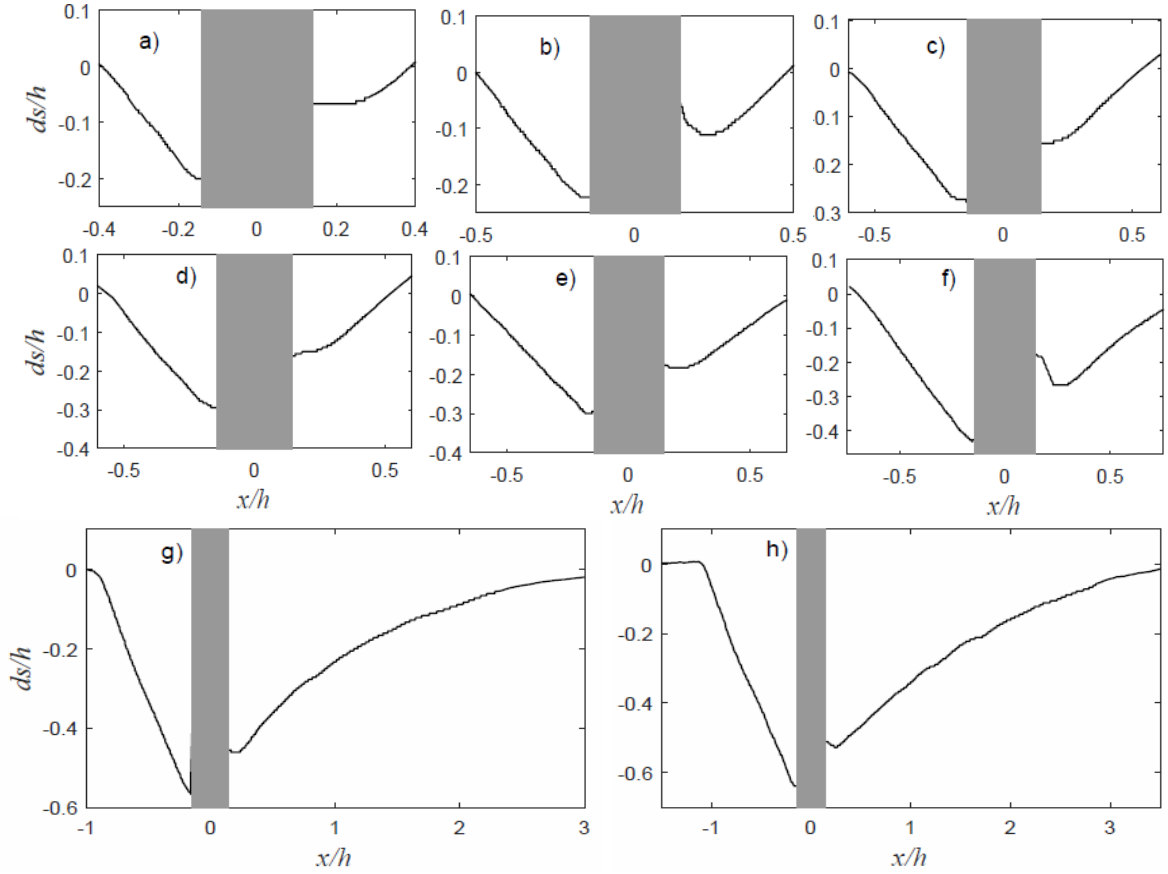

Figura 2. Perfis longitudinais do leito normalizados com a altura de escoamento, segundo o alinhamento central do pilar circular: a) t = 5 min., b) t = 15 min., c) t = 30 min., d) t = 60 min., e) t=120 min, f) t = 720 min, g) 1440 min, e h) 10080 min.

As profundidades máximas de erosão observadas segundo o alinhamento central do pilar circular e para as durações de ensaio estipuladas são apresentadas na Tabela 2 e na Figura 3. Por simplicidade de leitura, os instantes temporais são expressos em minutos na Tabela 2 e em horas na Figura 3.

Tabela 2. Profundidades máximas de erosão registadas.

t (min)	5	10	15	30	60	120	240	480	720	1440	4320	10080
d_S (m)	0,022	0,036	0,040	0,050	0,053	0,055	0,067	0,076	0,083	0,099	0,110	0,115

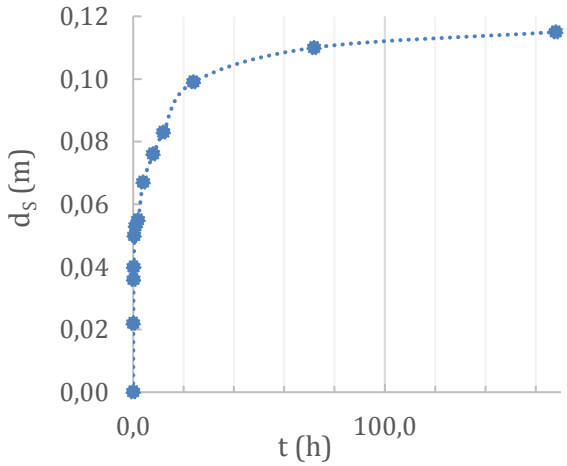

Figura 3. Evolução temporal da profundidade máxima de erosão. Instante temporal em escala logarítmica (direita).

4.2. EVOLUÇÃO DA GEOMETRIA DA CAVIDADE DE EROSÃO

A aplicação da técnica de fotogrametria de pequena amplitude permitiu a obtenção da representação tridimensional das cavidades de erosão para os instantes considerados neste trabalho experimental. Na Figura 4 apresenta-se, a título exemplificativo, a cavidade de erosão para o ensaio final, que foi atingido ao fim de sete dias de ensaio, para t = 10080 min, com o volume final (V_f) de 0,018 m^3.

Os modelos da cavidade de erosão permitem a extração de um conjunto de características geométricas, nomeadamente o volume erodido, parâmetro necessário à derivação da formulação empírica que melhor relaciona a profundidade máxima de erosão com o volume da cavidade de erosão para as condições experimentais ensaiadas. A Tabela 3 indica os valores das profundidades máximas de erosão e dos volumes erodidos, obtidos nos ensaios experimentais, normalizados pelos correspondentes valores para o ensaio de 7 dias (ensaio considerado de equilíbrio), d_{Sf} e V_f, respetivamente.

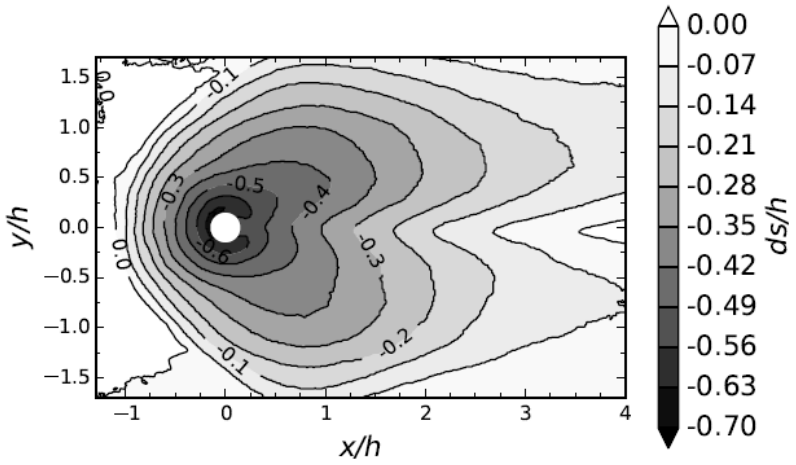

Figura 4. Cavidade de erosão para t = 10080 min.

Tabela 3. Rácios da profundidade máxima de erosão (d_S/d_{Sf}) e do volume erodido (V/V_f).

t (min)	5	10	15	30	60	120	240	480	720	1440	4320	10080
d_S/d_{Sf} (m)	0,19	0,31	0,35	0,43	0,46	0,48	0,58	0,66	0,72	0,86	0,96	1,00
V/V_f (m³)	0,009	0,012	0,017	0,034	0,034	0,049	0,080	0,097	0,146	0,314	0,567	1,000

5. ANÁLISE COMPARATIVA DAS FORMULAÇÕES EMPÍRICAS

Os dados da Tabela 3, representados na Figura 5, são usados na derivação da formulação empírica que relaciona os rácios da profundidade máxima de erosão e do volume erodido do presente trabalho experimental. A curva de melhor ajuste aos pontos experimentais, exemplificada a traço interrompido na Figura 5, levou à derivação da Equação 1. Trata-se de uma função polinomial de terceira ordem, com um coeficiente de correlação (R^2) de 0,963. As formulações recolhidas na literatura e constantes na Tabela 1, para o pilar circular, são aplicadas aos dados experimentais e os seus resultados mostrados na Figura 5.

$$\frac{V}{Vf} = 5{,}6704\left(\frac{d_S}{d_{Sf}}\right)^3 - 7{,}7411\left(\frac{d_S}{d_{Sf}}\right)^2 + 3{,}3858\left(\frac{d_S}{d_{Sf}}\right) - 0{,}429 \qquad (1)$$

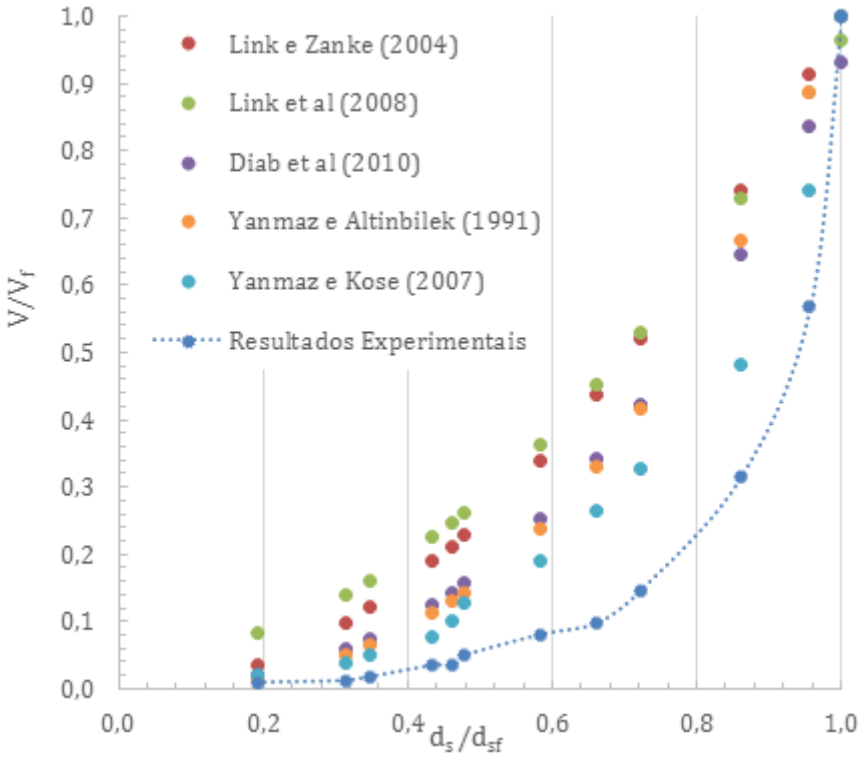

Figura 5. Aplicação das formulações empíricas aos resultados obtidos experimentalmente.

A representação conjunta dos resultados da aplicação dessas formulações com os dados experimentais na Figura 5 possibilitam a análise comparativa que se segue. De um modo geral, a aplicação das formulações empíricas apresentadas na Tabela 1, para pilares circulares, evidencia processos erosivos com evolução e desenvolvimento da cavidade mais acentuados do que os observados no presente trabalho experimental. Esta evidência verifica-se sobretudo para as experiências desenvolvidas por Link and Zanke (2004), Link et al. (2008) e Diab et al. (2010). Esta observação era expectável uma vez que a dimensão do modelo de pilar ensaiado em cada um dos trabalhos acima mencionados possuía o quadruplo do diâmetro usado nas experiências desenvolvidas no presente estudo (0,20 m em contraste com os 0,05 m). Para além da dimensão do obstáculo, também a reduzida dimensão média dos sedimentos, que compunham o fundo arenoso das experiências de Link et al. (2008), podem justificar em parte o desfasamento observado já que essa dimensão ($D_{50} < 0{,}6$ mm) conduz à formação de rugas, fenómeno que não se verificou nos ensaios preconizados no presente estudo.

As formulações propostas por Link et al. (2008) e Diab et al. (2010) diferem unicamente no tipo de sedimento usado para o leito móvel; em Link et al. (2008) trata-se de uma areia fina enquanto em Diab et al. (2010) o leito é constituido por gravilha. Embora os resultados analisados tenham sido obtidos para diferentes granulometrias (incluindo a da areia usada no presente estudo), a relação entre o diâmetro do pilar e a dimensão média dos sedimentos

(b/D_{50}) toma os valores de 61,54 e 769,23; no presente estudo experimental a relação foi de 58,14. De acordo com Lee and Sturm (2009), a profundidade de erosão é afetada pelo tipo de sedimento para b/D_{50}< 200; só em Diab et al. (2010) a profundidade de erosão e consequente volume de escavação não são afetados pela granulometria do sedimento.

Relativamente às condições de escoamento, verifica-se uma aproximação do valor da intensidade de escoamento desses estudos com as características hidráulicas da presente comunicação - 0,95 para Link et al. (2008) e Diab et al. (2010), 1.0 para Link e Zanke (2004), e 0,97 no presente estudo. No entanto, a relação entre a altura do escoamento de aproximação e o diâmetro do pilar diferem em 58,3%. Apesar da elevada percentagem, os pilares usados nos quatro casos (os três recolhidos da literatura e o do presente estudo) classificam-se como estreitos (Melville e Coleman, 2000). Para estes casos, a formação e o desenvolvimento da cavidade de erosão está intrinsecamente dependente do diâmetro do pilar. Seriam, portanto, necessários mais ensaios com diferentes diâmetros de pilares circulares (neste caso) para alargar a gama de aplicabilidade das equações empíricas de Link et al. (2008) e Diab et al. (2010).

As características do escoamento consideradas no trabalho de Link e Zanke (2004) são em muito semelhantes às utilizadas nos trabalhos da literatura mencionados acima. Apesar do modelo de pilar ter sido o mesmo que nos estudos supracitados, circular de 0,20 m de diâmetro, a formulação empírica desenvolveu-se a partir de um conjunto de onze ensaios. Para estes onze ensaios a formulação, apesar de não incluir explicitamente a dimensão do pilar, considera maiores relações entre a altura do escoamento de aproximação e o diâmetro do pilar (caso em que a altura do escoamento de aproximação toma duas vezes o valor do diâmetro do pilar). Este valor aproxima-se um pouco mais dos 3,6 assinalados para o caso experimental aqui estudado. Além deste fator, também as características dos sedimentos explica uma melhor aproximação aos dados, quando comparados com os resultados das investigações de Link et al. (2008) e de Diab et al. (2010).

No que respeita ao tipo de formulações empíricas, desenvolvida para os dados experimentais e para os estudos já mencionados, deve referir-se que se traduzem por funções polinomiais de segundo ou terceiro grau.

Os resultados da aplicação da equivalência do volume da cavidade de erosão à de um cone invertido, inicialmente proposto por Yanmaz e Altinbilek (1991), retornou valores mais aproximados dos valores observados no presente estudo experimental. Este facto deve-se essencialmente à dimensão do modelo de pilar (no caso, o diâmetro do pilar). Embora o conceito subjacente à formulação do volume de escavação pareça simplificado ou até mesmo redutor ao assumir que a forma da cavidade de erosão permanece praticamente igual ao longo do tempo, a mesma aproxima-se relativamente bem aos volumes erodidos, nomeadamente nos primeiros estágios do processo erosivo. Esse facto estará também relacionado com a duração dos ensaios que estiveram na base da formulação desenvolvida por Yanmaz e Altinbilek (1991).

Para as mesmas condições hidráulicas e sedimentológicas usadas em Yanmaz e Altinbilek (1991), Yanmaz e Köse (2007) propõem uma nova formulação para pilar circular, que é posteriormente validado com outras previsões da profundidade de erosão, nomeadamente a previsão de Oliveto e Hager (2005). Por análise da Figura 5 esta formulação é a que apresenta menores discrepâncias quando comparada aos resultados do presente estudo experimental.

Como verificação adicional, avaliaram-se os rácios dos volumes erodidos, medidos experimentalmente, $V/V_f\ (Exp)$, versus, os rácios provenientes da aplicação da Equação 1, $V/V_f\ (Eq\ 1)$, e os estimados pela mesma equação considerando o rácio das profundidades máximas de erosão dadas pela previsão de Oliveto e Hager (2005), $V/V_f\ (OH)$. A Figura 6 mostra essa comparação, bem como as regressões lineares de melhor ajuste e correspondentes coeficientes de correlação.

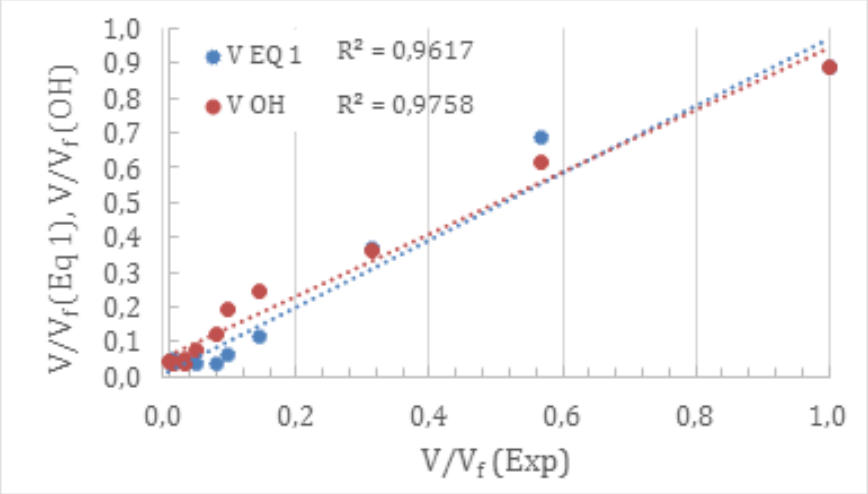

Figura 6. Comparação dos rácios dos volumes erodidos para o pilar circular do presente estudo.

Analisando a Figura 6 é possível concluir que os rácios dos volumes erodidos $V/V_f\ (OH)$ apresentam valores ligeiramente superiores aos obtidos em laboratório, $V/V_f\ (Exp)$. Os coeficientes de correlação, apresentados juntamente com a grandeza correspondente, são ambos superiores a 0,95, registando-se uma diferença pouco significativa de 1,4%. Assim sendo, as profundidades máximas de erosão medidas experimentalmente apresentam boa concordância com as estimadas pela equação de Oliveto e Hager (2005). Conclusão semelhante havia sido também extraída para os dados experimentais de Yanmaz e Köse (2007).

6. CONCLUSÕES

Nesta comunicação, foi feita uma resenha das formulações empíricas descritas na literatura, que, relacionam a profundidade máxima de erosão com o volume da cavidade de erosão, junto de fundações de pontes (pilares e encontros de pontes).

As formulações respeitantes a pilares circulares foram aplicadas aos dados experimentais obtidos num canal experimental do Laboratório de Hidráulica da Faculdade de Engenharia da Universidade do Porto. A aplicação de fotogrametria de pequena amplitude, na caracterização das cavidades de erosão, permitiu obter a evolução temporal dos volumes escavados, e, das profundidades máximas de erosão, com posterior derivação de uma nova formulação empírica.

Os pares de valores de profundidade máxima de erosão, e de volume erodido, foram comparados com as estimativas dadas por cinco formulações empíricas, para os registos experimentais obtidos neste trabalho. Os desfasamentos encontrados entre estimativas foram fundamentados; a formulação que mais se aproximou dos resultados experimentais foi a de Yanmaz e Köse (2007).

Da análise comparativa entre as formulações, recolhidas da literatura e a obtida neste estudo, pode concluir-se que estas podem fornecer indicações/orientações preliminares sobre a profundidade dos elementos de fundação, que podem ficar expostos à ação erosiva do escoamento. Podem ainda ser utilizadas para uma pré-quantificação do volume que tal cavidade de erosão pode vir a atingir ao longo do tempo. Estas informações são essenciais quer para uma abordagem mais física do fenómeno, através do uso desses resultados na modelação numérica, quer para uma vertente mais prática, usando-as como base para o dimensionamento de medidas de proteção (tapetes de enrocamento, por exemplo). Contudo, as formulações empíricas foram na maioria das vezes desenvolvidas para condições experimentais muito específicas, o que requer alguma cautela e análise crítica.

Por fim, a precisão dos rácios dos volumes erodidos por aplicação da equação desenvolvida neste estudo, e, dos rácios estimados por recurso à equação de evolução temporal de previsão da profundidade máxima de Oliveto e Hager (2005) foram avaliados confrontando-os com os coeficientes de correlação respeitantes, constatando-se uma boa correlação.

Agradecimentos

Este trabalho foi financiado pela Fundação Portuguesa para a Ciência e Tecnologia (FCT) através da bolsa de doutoramento PD/BD/127798/2016, no âmbito do Programa Doutoral INFRARISK - Analysis and Mitigation of Risks in Infrastructures. O trabalho experimental foi desenvolvido durante o projeto exploratório “Numerical and experimental study of the flow around complex bridge piers” [EXPL/ECM-HID/1663/2013] financiado pela Fundação Portuguesa para a Ciência e Tecnologia (FCT).

REFERÊNCIAS BIBLIOGRÁFICAS

Bouratsis, P.P., Diplas, P., Dancey, C.L., Apsilidis, N. (2013). High-resolution 3D monitoring of evolving sediment beds. Water Resources Research, 49(2), 977-992.

Bouratsis, P., Diplas, P., Dancey, C.L., Apsilidis, N. (2017). Quantitative Spatio-Temporal Characterization of Scour at the Base of a Cylinder. Water, 9(3), 227.

Couto, L.T. (2000). Erosões localizadas junto de esporões fluviais e encontros de pontes. Universidade Técnica de Lisboa.

Dargahi, B. (1990). Controlling mechanism of local scouring. Journal of Hydraulic Engineering, 116(10), 1197-1214.

Dey, S. (1999). Time-variation of scour in the vicinity of circular piers. Proceedings of the Institution of Civil Engineers-Water Maritime and Energy, 136(2), 67-75.

Diab, R. (2011). Experimental Investigation on scouring around piers of different shape and alignment in gravel (Doctoral dissertation, TU Darmstadt), 202p.

Diab, R., Link, O., Zanke, U. (2010). Geometry of developing and equilibrium scour holes at bridge piers in gravel. Canadian Journal of Civil Engineering, 37(4), 544-552.

Escauriaza, C., Sotiropoulos, F. (2011). Initial stages of erosion and bed form development in a turbulent flow around a cylindrical pier. Journal of Geophysical Research: Earth Surface, 116(F3).

FDOT. (2010). Bridge Scour Manual. Florida: Florida Department of Transportation.

Flint, M.M., Fringer, O., Billington, S.L., Freyberg, D., Diffenbaugh, N.S. (2017). Historical Analysis of Hydraulic Bridge Collapses in the Continental United States. Journal of Infrastructure Systems, 23(3), 04017005.

Johnson, P A., Jones, J.S. (1993). Merging laboratory and field data in bridge scour. Journal of Hydraulic Engineering, 119(10), 1176-1181.

Kothyari, U.C., Hager, W.H., Oliveto, G. (2007). Generalized approach for clear-water scour at bridge foundation elements. Journal of hydraulic Engineering, 133(11), 1229-1240.

Lee, S.O., Sturm, T.W. (2009). Effect of sediment size scaling on physical modeling of bridge pier scour. Journal of Hydraulic Engineering, 135(10), 793-802.

Link, O., Pfleger, F., Zanke, U. (2008). Characteristics of developing scour-holes at a sand-embedded cylinder. International Journal of Sediment Research, 23(3), 258-266.

Link, O., Zanke, U. (2004). On the time-dependent scour-hole volume evolution at a circular pier in uniform coarse sand. In Proceedings 2nd International Conference on Scour and Erosion (ICSE-2). November 14.–17., 2004, Singapore.

Melville, B.W., Chiew, Y.M. (1999) Time scale for local scour at bridge piers. Journal of Hydraulic Engineering, AS CE, 125 (1), 59–65.

Melville, B.W., Coleman, S.E. (2000). Bridge scour. Water Resources Publication.

Neil, C.R. (1967). Mean Velocity criterion for scour of coarse uniform bed material, Proceedings of the XII IAHR, Fort Collins, Colorado.

Oliveto, G., Hager, W.H. (2005). Further results to time-dependent local scour at bridge elements. Journal of Hydraulic Engineering, 131(2), 97-105.

Pandey, M., Sharma, P.K., Ahmad, Z., Singh, U.K. (2017). Evaluation of existing equations for temporal scour depth around circular bridge piers. Environmental Fluid Mechanics, 17(5), 981-995.

Ramos, P.X., Bento, A.M., Maia, R., Pêgo, J.P. (2016). Characterization of the scour cavity evolution around a complex bridge pier. Journal of Applied Water Engineering and Research, 4(2), 128-137.

Sumer, B. M. (2015). A review of recent advances in numerical modelling of local scour problems. In Proc., 7th Int. Conf. on Scour and Erosion, 61-70.

Yanmaz, A.M., Altinbilek, H.D.G. (1991). Study of time-dependent local scour around bridge piers. Journal of Hydraulic Engineering, 117(10), 1247-1268.

Yanmaz, A.M., Köse, Ö. (2007). Surface characteristics of scouring at bridge elements. Turkish Journal of Engineering and Environmental Sciences, 31(2), 127-134.

D.2 Evolution of local pier scour under unsteady flow conditions

5^{th} IAHR Europe Congress

TITLE: Evolution of local pier scour under unsteady flow conditions [1]

Paper presented in the 5^{th} IAHR Europe Congress

Observations: Bento A.M. performed the experimental work, analysed and post-processed the data as well as the results, and wrote the paper. Pêgo J.P., Viseu T. and Couto L. helped in the analysis of the results and edited and reviewed the manuscript.

[1] Bento, A.M., Pêgo, J.P., Viseu T. & Couto, L. (2018). Evolution of local pier scour under unsteady flow conditions. In: 5^{th} *IAHR Europe Congress, 12−14 June 2018*, Trento, Italy.

Evolution of local pier scour under unsteady flow conditions

A.M. Bento
Laboratório Nacional de Engenharia Civil, Portugal / Faculdade de Engenharia da Universidade do Porto, Portugal
J.P. Pêgo
Faculdade de Engenharia da Universidade do Porto, Portugal
T. Viseu & L. Couto
Laboratório Nacional de Engenharia Civil, Portugal

ABSTRACT

The scour depth evolution at a circular pier under unsteady flow is experimentally tested. The results are analysed along with the pier scour prediction models proposed by [4] and [5]. A reasonable agreement was achieved between measured and computed scour depths.

1 INTRODUCTION

Excessive local scour around bridge foundations is widely recognized as the major cause of bridge collapses. This phenomenon is a result of the dynamic interaction between the three-dimensional turbulent flow and the movable river bed, which is magnified during the development of a scour hole [1]. Due to the existence of various and strong mechanisms, mainly of hydraulic nature, the study of scour around bridge piers remains a complex task after many decades of research.

Though numerous researchers have focused their studies on the temporal variation of pier scour depth under steady flow and clear water flow conditions, very few have studied the temporal evolution under unsteady flow conditions [1-3]. As a result, effort on such topic is needed to improve the understanding of the scour evolution due to changes in the approach flow hydrograph as well as to examine the performance of pier scour prediction models under unsteady flows.

The main objective of this study is aimed to give a first contribution in the understanding of the scour depth time evolution under unsteady and clear water scour conditions. To attempt this, an experiment using a stepwise discharge hydrograph was conducted in a small-scale flume at the Laboratory of Hydraulics of the Faculty of Engineering of the University of Porto (FEUP). Moreover, based on the experimental data herein obtained, a comparison of predicted scour depths given by two pier scour prediction models [4, 5] was made.

2 EXPERIMENTAL WORK

A local scouring experiment was conducted in a flume under clear water scour conditions during 80 minutes, consisting on four steps of alternated flow intensities of 80% and 97%. Flow intensity is defined as the ratio of the approaching flow velocity to the critical approaching flow velocity (U/U_C). The corresponding stepwise discharges were controlled by two electromagnetic flowmeters at the flume entrance whereas the approaching flow depths were controlled by means of an adjustable electric gate provided at the flume outlet. At the upstream reach of the flume, bed macro rugosities were designed to guarantee fully developed flow. Table 1 summarizes the experimental characteristics. The longitudinal view of the experimental setup is sketched in Figure 1.

Table 1. Experimental details

Flume	32.2 m long and 1.0 m wide
Pier	Polyvinyl chloride (PVC) of 0.05 m of diameter (D) Placed at 16.15 m from the flume inlet D/B = 5% (with B the flume width)
Bed	Uniformly graded non-cohesive material Gradation coefficient (σ_D) of 1.48 Median diameter (D_{50}) of 0.86 mm Density (ρ_S) of 2650 kgm^{-3} Sediment coarseness D/D_{50} = 58.1
Flow	Four steps of alternated flow intensities (U/U_C), being U_C calculated by [6]), of 80% and 97%

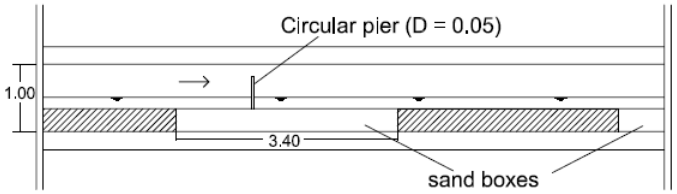

Figure 1. Longitudinal view of the experimental setup (dimensions in meters)

Before the experiment, the sediments in the sand box were levelled with the adjacent concrete bed, saturated with water and drained (at least once) to ensure their adequate compaction. Some adjustments to the lateral boundaries and around the pier were carefully performed. The area surrounding the pier was covered with thin geotextile plaques, coupled to metallic

grids, to avoid undesirable scour at the beginning of the experiments. The flume was gradually filled to the required discharge and flow depth, and once established, the geotextile plaques were carefully removed with the aid of two lateral wires to start the local scouring experiment.

3 SCOUR DEPTH EVOLUTION

The experimental data are presented graphically in Figure 2, with the upper panel showing the stepwise discharge hydrograph and the lower panel displaying the scour depths measured in the experiment as dotted line, along with the predicted depths by the two scour prediction models proposed by [4] and [5] in solid and dashed lines, respectively.

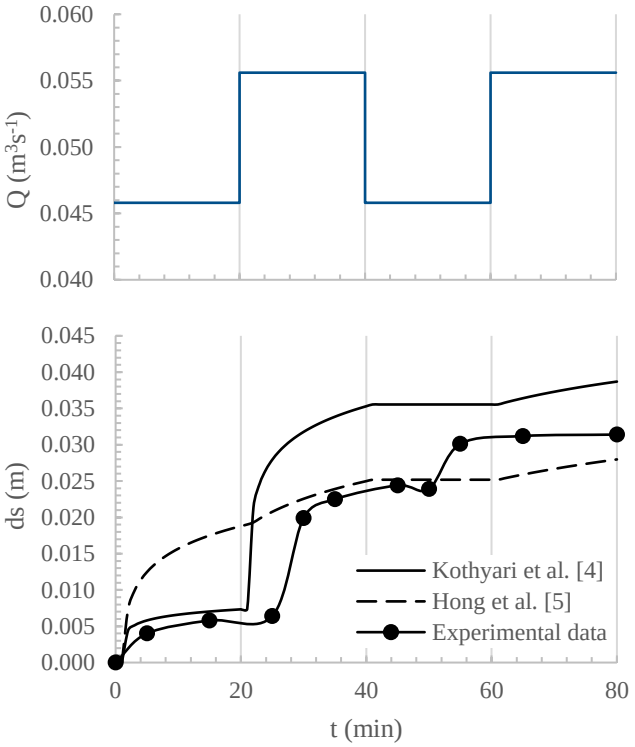

Figure 2. Stepwise discharge hydrograph (upper panel) and resultant scour depth evolution along with the predicted evolution by [4] and [5] (lower panel)

The Kothyari et al. [4] model tends to over predict the evolution of the scour depth. Very slight discrepancies are observed for the period correspondent to the first flow step whilst higher discrepancies were obtained namely for the second flow step. At the end of the experiment, a difference of 19.1% was registered between the predicted scour depth and the experimental correspondent value. The model proposed by Hong et al. [5], in turn, tends to over predict the scour depth considerably until roughly fifty-one minutes of experiment. The Hong et al. [5] model does not fit as well as [4], mainly for the correspondent first and second flow steps. From the middle of the third flow step, the model of [5] starts to under predict the scouring evolution, ending with a discrepancy of 10.5%. The accuracy of these two pier scour prediction models was also checked by comparing statistical indices, namely root mean square error (RMSE), mean absolute percentage error (MAPE) and correlation coefficient (R) as in [5] (see Table 2). The considerable mean absolute percentage errors corroborate with the discrepancies observed in Figure 2. Both models present high values of correlation coefficient.

Table 2. Statistical results for the two pier scour models

Models	RMSE (m)	MAPE (%)	R (-)
Kothyari et al. [4]	0.011	69.33	0.852
Hong et al. [5]	0.011	74.50	0.908

4 CONCLUSIONS

The temporal scour depth evolution around a circular pier was tested experimentally for a stepwise discharge hydrograph. Careful observation of the scouring phenomenon indicates that the scour depth increases significantly after a stepwise increase in discharge. Two temporal prediction scour models, proposed by [4] and [5] were applied and compared. The model [4] over predicted the scour depth whereas the model [5] showed an approach trend to the end value.

5 ACKNOWLEDGEMENT

This work was supported by the Portuguese Foundation for Science and Technology (FCT), through the PhD scholarship PD/BD/127798/2016.

REFERENCES

[1] Melville, B.W., Coleman, S.E. (2000). Bridge Scour. *Water Resources Publications*, LLC, Colorado, USA.

[2] Kothyari, U. C., Garde, R. J., and Ranga Raju, K. G. 1992. "Temporal variation of scour around circular bridge piers." J. Hydraul. Eng., 118(8), 1091–1106.

[3] Chang, W. Y., Lai, J. S., and Yen, C. L. 2004. "Evolution of scour depth at circular bridge piers." J. Hydraul. Eng., 130(9), 905–913.

[4] Kothyari, U.C., Hager, W.H., Oliveto, G. (2007). "Generalized approach for clear-water scour at bridge foundation elements." Journal of Hydraul. Eng., 133(11), 1229-1240.

[5] Hong, J.H., Chiew, Y.M., Yeh, P.H. (2014). "Comparisons of time dependent pier scour models under unsteady flow conditions." In Scour and Erosion: Proc. of the 7th Inter. Conf. on Scour and Erosion, Perth, Australia, CRC Press, 473-481.

[6] Neil, C.R. (1967). Mean velocity criterion for scour of coarse uniform bed material, Proc. of the XII IAHR, Fort Collins, Colorado.

D.3 Advanced characterization techniques of the scour hole around a bridge pier model

9^{th} International Conference on Fluvial Hydraulics

TITLE: Advanced characterization techniques of the scour hole around a bridge pier model [1]

Paper presented in the 9^{th} *International Conference on Fluvial Hydraulics*

Observations: Bento, A.M. performed the experimental work, analysed and post-processed the data as well as analysed the results, and wrote the paper. Couto, L., Pêgo, J.P. and Viseu, T. helped in the analysis of the results and edited and reviewed the manuscript.

[1] Bento, A.M., Couto, L., Pêgo, J.P. & Viseu T. (2018). Advanced characterization techniques of the scour hole around a bridge pier model. In: *River Flow: 9^{th} International Conference on Fluvial Hydraulics, 5−8 September 2018*, Lyon, France.

Advanced characterization techniques of the scour hole around a bridge pier model

Ana Margarida Bento[1,1], *Lúcia* Couto[2], *João Pedro* Pêgo[1], and *Teresa* Viseu[2]

[1]Faculdade de Engenharia da Universidade do Porto (FEUP), Rua Dr. Roberto Frias, s/n 4200-465, Porto, Portugal
[2]Laboratório Nacional de Engenharia Civil (LNEC), Avenida do Brasil, 101, 1700-066, Lisboa, Portugal

Abstract. Local scouring around bridge foundations is a major reason for bridge collapse worldwide. It occurs due to the formation of vortices around bridge foundations as a result of changing the unidirectional approach flow into the three-dimensional field in an erodible channel bed, leading to the development of a scour hole in its vicinity. In the present work, two different techniques were applied for a full characterization of the scour hole geometry developed in a sand bed flume experiment by means of a Kinect sensor and a close-range photogrammetry. These advanced survey and sensor technologies offer efficient techniques of deriving point clouds and Digital Elevation Models (DEMs), respectively. The potential, limitations and results of both techniques are herein examined and conveniently compared, including a description of measurement devices, reference points and respective software. Reliable and accurate estimates of the topographic representation of the scour hole and inherent features were obtained. The design of the bridge pier used, with a 0.14 m wide rectangular round-nose concrete column (henceforth termed as oblong pier), replicates the typical shape used in the 19th and 20th centuries, and are the most common in Portugal.

1. Introduction

The collapse of bridges inevitably leads to economically losses and not seldom is responsible for human losses. Local scouring around the foundations is the most common bridge failure cause worldwide [1, 2]. The presence of a bridge pier leads to the formation of a scour hole, from which entrainment and transport of sediments are influenced by the turbulent structures therein developed. Thus, once formed, such scour holes play a major role in the scouring process such as modifying the incoming flow patterns. The knowledge of the main scouring factors, their impact on the erosion process and their evolution in time is therefore essential for providing mechanisms and improved tools to minimise potential consequences as catastrophic failures, namely the inevitable and subsequent economical losses and human casualties. These serious threats have recently increased the awareness and interest in bridge scour research.

1 Corresponding author: ana.bento@fe.up.pt

The complex flow-pier-sediment interaction phenomenon, underlying the local lowering of the streambed elevation at the bridge pier's vicinity, has justified the considerable amount of studies performed in the past decades. The mechanism of flow and scour development near a circular pier was initially described under specific conditions [3] , while in other researches a variety of flow conditions, bridge foundations, and sediments features were considered (such as in [4] and the references therein), with the general purpose of better explaining the whole process. In spite of a notable number of scientific researches on scouring around bridge foundations, the relationships developed for the evaluation of the maximum scour depth and its temporal evolution [1, 5] are still lacking reliability. Further detailed investigations on the scour hole morphology are thus required for the development of a broader and comprehensive approach for predicting scour at bridge design phases. It is also worth highlighting that the numerical modelling of scouring, namely using Computational Fluid Dynamics (CFD) tools, is on the rise. Hence, a great demand arises for experimental approaches in order to improve the calibration and validation phases of the simulation models, which are currently used to complement laboratory-testing efforts [6].

Over decades, the most common approach for studying the scouring process was the point-wise measurements of the bed level at few locations. This has been performed either by using gauges and probe sensors [7, 8] or by employing scales that are being recorded with periscopes or cameras inside the transparent walls of the flume or of the pier model [9-11]. Other approaches involved the use of probes mounted on traversing mechanisms [12, 13]. Although capable of representing the bed surface, the intrusiveness of the technique may alter the approach flow field and consequently the scour hole features. Two and three-dimensional (2D and 3D) laser scanners have provided reliable results of the evolution of sandy beds for relatively calm free surfaces, which are difficult to guarantee in the vicinity of an hydraulic structure such as a bridge pier model. The recent advances in technology have been replacing the topographic information retrieved from traditional cross-section models by the three-dimensional (3D) and point clouds and Digital Elevation Models (DEMs).

Several efforts have involved the application of close-range photogrammetry in local scouring experiments under well-controlled conditions; this technique was successfully applied in the reconstruction of the scour hole around a single and a complex bridge pier [14, 15]. The accuracy and the minimum of financial outlay are thus of primary importance when planning a survey of three-dimensional surface maps. Another valuable and attractive alternative to expensive 3D laser scanners is the Kinect sensor [16, 17]. The application of image-based techniques constitutes, thus, a suitable way to build the three-dimensional model of the developed scour hole around a bridge pier with high spatial resolution.

Therefore, the aim of the present work is to explore the two image-based techniques - Kinect sensor and close-range photogrammetry - in a laboratory environment, for the characterization of the scour hole geometry caused by the presence of a bridge pier model in a movable bed. In the present study, an oblong pier is tested since it is the most common shape in Portuguese bridges, used in the 19th and 20th centuries.

Following this Introduction, Section 2 gives a brief description of the experimental setup, instrumentation and procedures. The two image processing techniques are also presented and their particularities explained. In Section 3, some phenomenological features of the resulting 3D scour hole are described and compared in order to highlight/outline the potential and limitations of the techniques herein applied. Finally, Section 4 presents the conclusions of this work.

2. Experimental Facilities and Methodologies

2.1 Experimental facility and conditions

A local scouring experiment, reproducing the flow at the vicinity of a small-scale bridge pier embedded in a uniform sediment bed, was performed in a 40.7 m long, 2.0 m wide and 1.0 m deep glass-sided rectangular tilting flume (CIV) at the National Laboratory of Civil Engineering (LNEC), Lisbon, Portugal.

The working section consists of a sand recess box, 5.0 m long and 0.4 m deep, preceded by a metallic grid at the inlet of the flume, ensuring the development of a uniform approach flow distribution. A 0.3 m thick and 0.2 m long fine gravel mattress, embedded at the upstream end of the recess box and properly levelled by the adjacent concrete, allowed a smooth and progressive transition, avoiding scouring at the transition between the fixed and the movable bed.

The bridge pier model does not reproduce a specific bridge pier, but its design replicates the typical shape of bridge foundations most common in Portugal. The 0.14 m wide (D) rectangular round-nose concrete column (hereinafter referred to as oblong pier) was installed in the middle of a recess box (Figure 1) filled with a uniform quartz sand, characterized by a mean sediment diameter (D_{50}) of 0.86 mm, a specific gravity (s) of 2.65, and a geometrical standard deviation (σ_D) of 1.28. The sediment coarseness ratio (D/D_{50}) assumed the value of 163, not negligible according to recent studies [18]. The influence of flume sidewall on the scour hole development was avoided [19] in this case since the pier width was lower than 10% the flume width (D/B = 7%).

The inflow discharge (Q) was regulated to the constant value of 0.120 m^3/s by an electromagnetic flowmeter, positioned on the feeder pipe. Two sluice gates of the facility, one placed at upstream and other at downstream section, enabled the approach flow depth (h) adjustment inside the flume to 0.182 m. The scour depth at the pier front was measured with a ±0.1 mm accurate limnimeter. The flow was developed under a flow intensity close to unity, assuming a critical flow velocity of u_c = 0.319 m/s [20]. The ratio of flume width to flow depth (B/h) assumed the value of 11, which allowed neglecting relevant wall effects on the flow field. A flow shallowness of 1.30 was used in the present experiment.

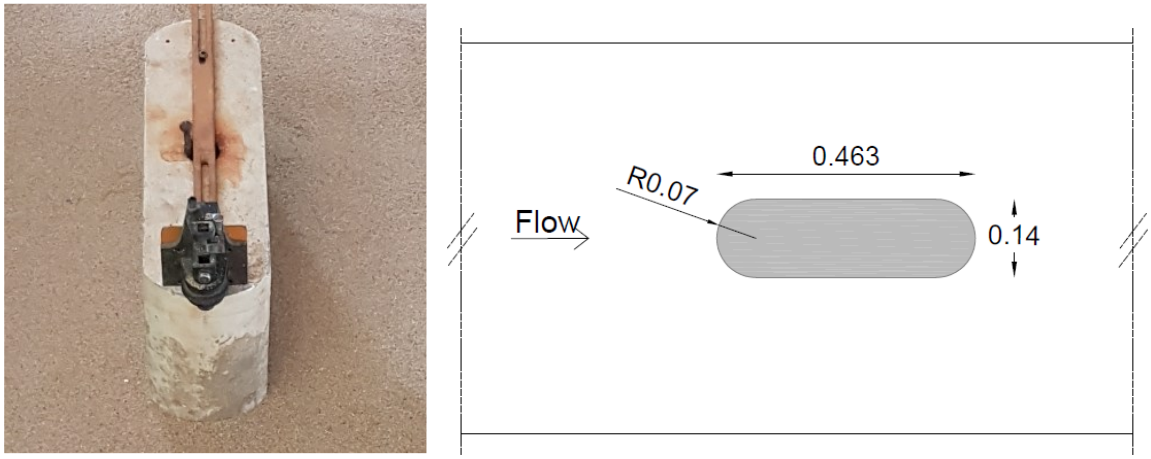

Fig. 1. Oblong bridge pier model (dimensions in meters).

2.2 Procedure and methodology

After the installation of the oblong pier, the recess box was filled with the sand, and flattened before the experiment began. In the area around the pier model, metallic plaques covering

the sand were carefully removed only when the prescribed flow condition was reached, initiating, thus, the local scouring experiment.

This experiment ran for three days with the aim of characterizing the resulting scour hole geometry, through two different image-based techniques: Kinect sensor and close-range photogrammetry. Both approaches required the previous emptying of the tilting flume and control ground points, deployed in specific points of well-known dimensions on the model, for their suitable applications. In the following subsection, the main components, instruments and procedures followed by each application are addressed.

2.3 Scour hole characterization

2.3.1 Kinect sensor

The Microsoft Kinect technique consists of a projector and two internal cameras: one *Infrared camera* and a *RGB camera* (Figure 2a). The *Infrared projector* transmits a predefined pattern of light that is deformed based on the distance of various points of the object from the sensor. The deformed pattern is captured by the infrared camera and is correlated against a reference speckle pattern projected on the surface at known distance from the sensor to build a 3D map of the object.

The procedure of obtaining the scour hole surfaces includes the post-processing of the acquired images by using a software for 3D net processing (*CloudCompare*). The resulting point clouds are also used in the creation of topographic maps using mapping software of contours and 3D surfaces.

2.3.2 Close-range photogrammetry

The application of this technique required a digital camera and a set of ground control points. The camera was used to photograph the scour hole and the surrounding affected area, at different locations at a height (*H*) of 0.50 m from the initial flatbed (Figure 2b). The ground control points, specific points in two lateral rulers, were used to accomplish the spatial reference of the model. Six ground control points were considered in this study.

The photogrammetric processing software used was *Agisoft PhotoScan Professional*. The digital elevation models (*DEMs*) were then extracted and introduced in an post-processing software (*Paraview*) to enable the creation of bed contour surfaces and profiles.

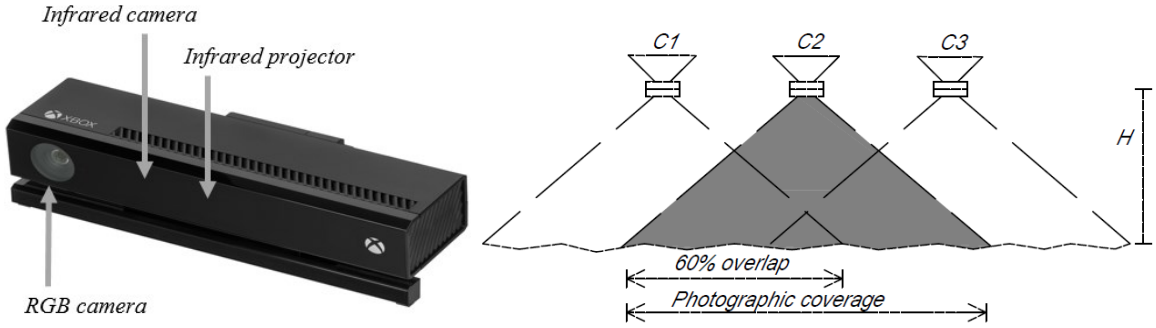

Fig. 2. Kinect sensor (a) and close-range photogrammetry scheme (b).

3. Results and comparative analysis of techniques

3.1. Scour hole

The point clouds and the digital elevation models were produced and used to compute the contour lines and the 3D surfaces. Figure 3 plots the distribution of the local scour in the vicinity of the oblong pier as a function of bed scour depth-to-approach flow depth ratio (*ds/h*). The 3D surface maps are presented in Figure 4.

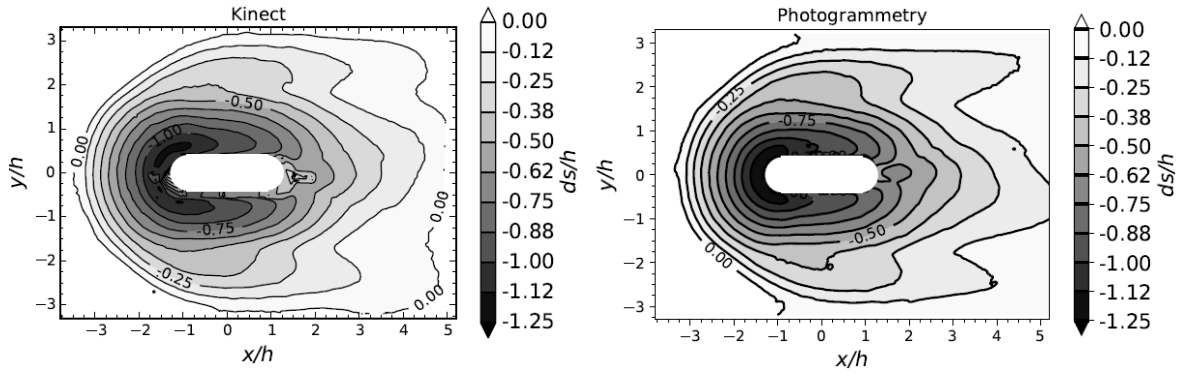

(a) (b)

Fig. 3. Contours of local scour around the oblong pier from Kinect sensor (a) and close-range photogrammetry (b).

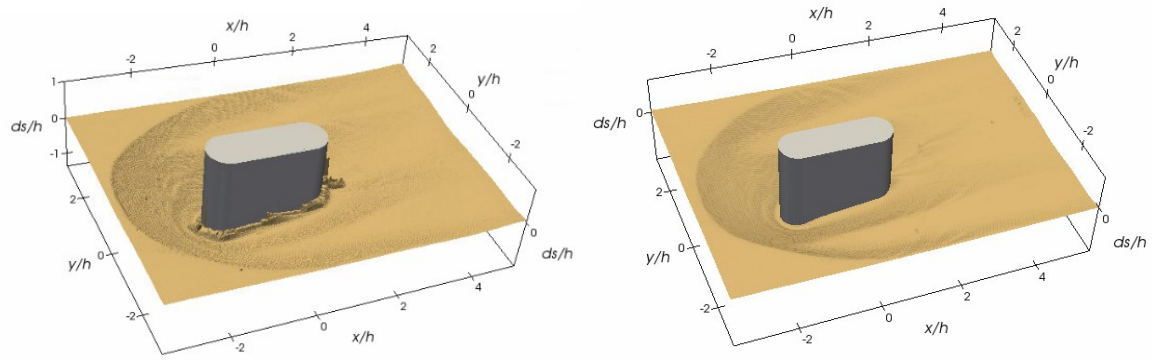

(a) (b)

Fig. 4. Three-dimensional surface maps from Kinect sensor (a) and close-range photogrammetry (b).

The contours and the 3D surface maps represent data giving a valuable insight concerning the characterization of the scour hole geometry at the vicinity of the pier model under study. The results obtained by the different techniques are clearly similar as can be seen in Figures 3 and 4, and will be better described on the following subsection.

3.2. Scour bed profiles

Figure 5 sketches the scour bed profiles considered in the present analysis. These profiles, normalized by the approach flow depth, are presented in Figure 6. A direct comparison between the aforementioned techniques can thus be performed.

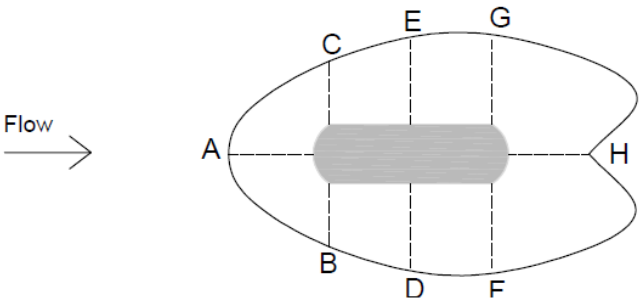

Fig. 5. Scheme of the scour bed profiles.

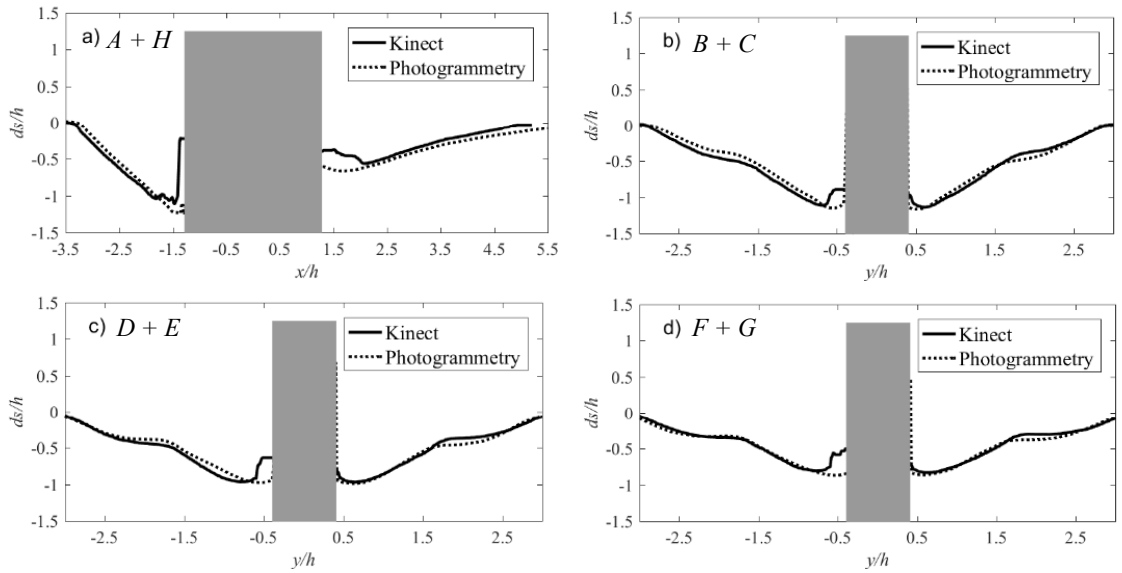

Fig. 6. Scour bed profiles normalized by the flow depth from Kinect sensor (continuous line) and close-range photogrammetry (dashed line): (a) $A + H$; (b) $B + C$; (c) $D + E$; and (d) $F + G$.

Figure 6 compares the scour depth profiles extracted from the Kinect sensor and the close-range photogrammetry at the vicinity of the oblong pier. Before analysing these profiles it should be mentioned that the structure at the top surface of the pier constituted an obstruction to the Kinect sensor, therefore the scour bed surface close to the pier wall could not be measured accurately, which justifies the erroneous results on that area. For this reason, the close-range photogrammetry results (dashed line) are herein compared with the Kinect's scour bed profiles (continuous line) measured at 0.03 m away from the pier round walls and left side (looking from upstream to downstream). Nevertheless, it can be stated that in general a good agreement was achieved.

The most affected profile in a scouring experiment is usually the longitudinal one, aligned with the approach flow direction, corresponding to profiles *A* and *H* in Figure 6a. Particular analysis is thus performed for these profiles. Very close descending slopes were registered for profile *A* by both techniques; Kinect sensor gave a value of 66.4% while the application of close-range photogrammetry returned the value of 68.1%. Even in profile *H*, on the deposition zone, the slopes were once again quite similar: 15.9% and 14.1%, for the Kinect sensor and the photogrammetry techniques, respectively. As for maximum scour depth observed in profile *A*, it was obtained a value of 0.229 m with photogrammetry, corresponding to 1.26*h* in Figure 6a. This value is corroborated by the 0.23 m observed on the limnimeter, placed at the pier front throughout the experiment. In the same way, from the analysis of the other profiles it may be concluded that both techniques were able to reconstruct the scour hole geometry with reliable detail and accuracy.

Regarding some of the main features that can be relevant in the two image-based applied techniques, emphasis should be given to the number of photos/scans, the processing complexity, the precision/accuracy, and the light conditions dependency. Only one scan was used for the application of the Kinect sensor, while a set of 100 photographs were considered in the present analysis for the close-range photogrammetry. In terms of processing complexity, the photogrammetry application followed a step-by-step procedure towards the obtaining of the DEMs. After combining the depth information for each camera, the mesh model was built after being spatially referenced with the coordinated ground control points. On the other hand, the Kinect sensor provides the mesh of the model directly, just requiring the referencing task. The identification of the control points in the scan from the Kinect sensor required greater caution than for the photogrammetry case. Accuracies of 0.001 m and 0.0005 m were obtained from the application of the Kinect sensor and the close-range photogrammetry, respectively. Neither of the techniques unveiled much dependency on light specific conditions.

4. Conclusions

This paper presents an essay on the characterization of the scour hole around an oblong pier by using two distinct image-based technique approaches: a Kinect sensor and the application of close-range photogrammetry. Both techniques were applied on the scour hole developed during a 3-days test carried out in a 2 m wide flume, with the bottom covered by uniform sand and where an oblong pier with main dimensions of 0.14 m and 0.463 m was used.

Reliable and accurate estimates of the topographic representation of the scour hole and inherent features were herein obtained, presenting solely slight discrepancies (Figure 6). The analysis undertaken revealed that both are promising approaches in the research field of local scouring phenomena since they satisfy the required precision in accessible and effortless ways. These image-based techniques allowed important insights into the whole scour geometry around the bridge pier model under study.

In the authors' point of view, the obtained results from this study constitute a positive initial step towards the numerical modelling of scour hole dimensional features around bridge piers. This task may provide, once properly calibrated, a better and a valuable insight of scouring phenomena without the limitations of measurements and scale effects.

The Portuguese Foundation for Science and Technology (FCT) supported this research work, through the PhD scholarship PD/BD/127798/2016, in the framework of the Doctoral Program INFRARISK – Analysis and Mitigation of Risks in Infrastructures.

References

1. B.W. Melville, S.E. Coleman, *Bridge Scour*. Water Resources Publications, LLC, Colorado, USA (2000)
2. W. Cook, P.J. Barr, M.W. Halling, *Bridge failure rate*. J. of Performance of Constructed Facilities, **29**(3) (2013)
3. E.M. Laursen, A. Toch, *Scour around bridge piers and abutments*, **4**, Iowa Highway Research Board, Ames, IA, USA (1956)
4. Y.W. Chang, G. Constantinescu, S. Miyawaki, W.F. Tsai, H.C. Lien, *The flow and turbulence structure at a rectangular bridge pier with a low angle of attack*. *Proceedings of River Flow 2010*, 681 – 689, Germany (2010)

5. E.V. Richardson, S.R. Davis, *Evaluating scour at bridges*. **3rd edition**, FHWA IP 90-017, Hydraulic Engineering Circular No. 18, National Highway Institute, U. S. Department of Transportation, Federal Highway Administration (1995)
6. R. Ettema, G. Constantinescu, B.W. Melville, *Flow-Field Complexity and Design Estimation of Pier-Scour Depth: Sixty Years since Laursen and Toch,* J. Hydraul. Eng., ASCE, **143**(9) (2017)
7. G. Oliveto, W.H. Hager, *Temporal evolution of clear-water pier and abutment scour*, J. Hydraul. Eng., ASCE, **128(9)**, 811–820 (2002)
8. C. Berger, B.W. McArdell, B. Fritschi, F. Schlunegger, *A novel method for measuring the timing of bed erosion during debris flows and floods*, Water Resour. Res., **46**, W02502 (2010)
9. M. F. Mia, H. Nago, *Design method of time-dependent local scour at circular bridge pier*, J. Hydraul. Eng., ASCE, **129**(6), 420–427 (2003)
10. J.-Y. Lu, Z.-Z. Shi, J.-H. Hong, J.-J. Lee, R.V. Raikar, *Temporal variation of scour depth at nonuniform cylindrical piers*, J. Hydraul. Eng., ASCE, **137**(1), 45–56 (2011)
11. R. Diab, *Experimental Investigation on scouring around piers of different shape and alignment in gravel*, PhD thesis, Darmstadt (2011)
12. F. Ballio, A. Radice, *A non-touch sensor for local scour measurements*, J. Hydraul. Res., **41**(1), 105–108 (2003)
13. O. Link, F. Pfleger, U. Zanke, *Characteristics of developing scour-holes at a sand-embedded cylinder*, Int. J. Sediment Res., **23**(3), 258–266 (2008)
14. F. Pfleger, C. Rapp, M. Manhart, *Experimental investigation on the sediment movement in the vicinity of a cylindrical bridge pier*, River Flow 2014, 1701-1708 (2014)
15. P.X. Ramos, A.M. Bento, R. Maia, J.P. Pêgo, *Characterization of the scour cavity evolution around a complex bridge pier*. Journal of Applied Water Engineering and Research, **4**(2), 128-137 (2016)
16. E. Lachat, H. Macher, M.-A- Mittet, T. Landes, P. Grussenmeyer, *First experiences with kinect V2 sensor for close range 3D modelling.* International Archives of the Photogrammetry, Remote Sensing and Spatial Information Sciences - ISPRS Archives, **40**(5W4), 93-100 (2015)
17. S. Amaral, Experimental characterization of the failure by overtopping of embankment dams, PhD thesis, Instituto Superior Técnico, Lisbon, Portugal (2017)
18. S.O. Lee, T.W. Sturm, *Effect of sediment size scaling on physical modelling of bridge pier scour*. J. Hydraul. Eng., ASCE, 135 (**10**), 793-802 (2009)
19. Y.M. Chiew, B.W. Melville, *Local scour around bridge piers,* J. Hydraul. Res., ASCE, **25**(1), 15-26 (1987)
20. C.R. Neil, *Mean velocity criterion for scour of coarse uniform bed material*. Proceedings of XII IAHR Congress, Fort Collins, Colorado, USA (1967)

D.4 Hydrological risk and associated scour risk: Case study sensitivity analysis

V International Congress on Risks

TITLE: Hydrological risk and associated scour risk: Case study sensitivity analysis [1]

Paper submitted to the V International Congress on Risks
Submitted: May 31th, 2020 / Accepted for oral communication: June 9th, 2020

Observations: Abstract accepted for oral communication.

[1] Bento, A.M., Gomes, A., Couto, L., Pêgo, J.P. & Viseu T. (2020). Hydrological risk and associated scour risk: Case study sensitivity analysis. In: *V International Congress on Risks, 12−16 October 2020*, Coimbra, Portugal (Abstract accepted for oral communication).

V International Congress on Risks
Contribution of the Science for Disaster Risk Management.
Acting today, protecting tomorrow
From 12 to 16 of October, 2020
University of Coimbra
Portugal

HYDROLOGICAL RISK AND ASSOCIATED SCOUR RISK: CASE STUDY SENSITIVITY ANALYSIS

Ana Margarida Bento
Hydraulics and Environment Department
National Laboratory of Civil Engineering
abento@lnec.pt

Andreia Gomes
Hydraulics and Environment Department
National Laboratory of Civil Engineering
andreiahmgomes@gmail.com

Lúcia Couto
Hydraulics and Environment Department
National Laboratory of Civil Engineering
luciacoutoribeiro@gmail.com

João Pedro Pêgo
Civil Engineering Department
Faculty of Engineering o the University of Porto
jppego@fe.up.pt

Teresa Viseu
Hydraulics and Environment Department
National Laboratory of Civil Engineering
tviseu@lnec.pt

ABSTRACT

Bridge collapses have been a severe problem worldwide, leading to socio-economic disruption and human casualties. The knowledge of the causes and consequent collapse modes have drawn much attention from researchers, which have also contributed to the gain of experience from real bridge failures in the design of new bridges. Bridges, like other hydraulic infrastructures, are designed to withstand a certain design flood event, ascertained by the establishment of acceptable risk and its design life. Different levels of risk can be accepted depending on the typology, importance and dimensions of a certain bridge, as well as on the consequences of its possible collapse, including possible material damage and loss of human life. Thus, the assessment of the associated hydrological risk plays a vital role in the design process, as well as during their operation, namely when bridges are founded on alluvial riverbeds. For instance, minor bridges are commonly designed with higher risk. In Portugal, the persistence of floods exceeding 8,000 m^3/s in three months has contributed to the partial collapse of the 19th century Hintze Ribeiro bridge on the night of 4 March 2001.

In structural design, the characterization of the design life of a bridge is preceded by the definition of its functional life, which depends on the maximum traffic capacity desired for that infrastructure. The functional life is often shorter than the expected design life. In that situation, the bridge should be functionally rehabilitated, for example, by increasing its width or building a new one nearby, in order to ensure that the functional quality of the crossing is maintained. In May 2002, the 19th century Hintze Ribeiro bridge was, thus, replaced by the new Hintze Ribeiro bridge, 7.5 m upstream of the old bridge's position.

Although the structural design particularities of the new Hintze Ribeiro bridge were beyond the reach of the authors, a sensitivity analysis may be performed. For instance, assuming the typical 50 years for the expected design life of such a bridge, different return periods could be plausibly used in its design process, depending on the acceptance risks. Hence, a 100-year return period of the design flood event corresponds to a hydrological risk of 40%. For a hydrological risk of 10%, the bridge would be designed to withstand the 500-year flood (Q500), whereas, for a longer design life of 100 years, a hydrological risk between 15% and 20% would be attained. The adopted return period as a design criterion, and associated design flood, also plays a significant role in the assessment of admissible scour risk (i.e., maximum scour depths at the bridge foundations level) for the bridge structural stability, which is also dependent on the priority factor attributed to that bridge. While Q500 (in 50 years) is associated with a lower hydrological risk, the water level regarding that design flood reaches the bridge deck, which adds other sources of instability in addition to the inherent scour risk.

Keywords: bridge, hydrological risk, return period, scour risk, sensitivity analysis

Panel: Panel 2 – Methodology for risk analysis and impact assessment of disasters

Type of presentation: Oral